AGARD-CP-496

1

AGARD

ADVISORY GROUP FOR AEROSPACE RESEARCH & DEVELOPMENT
7 RUE ANCELLE 92200 NEUILLY SUR SEINE FRANCE

AGARD CONFERENCE PROCEEDINGS 496

Effects of Adverse Weather on Aerodynamics

(Les Effets des Conditions Météorologiques Adverses sur l'Aérodynamique)

Papers presented and discussions held at the Fluid Dynamics Panel Specialists' Meeting held in Toulouse, France, 29th April—1st May 1991.

North Atlantic Treaty Organization
Organisation du Traité de l'Atlantique Nord

DISCLAIMER NOTICE

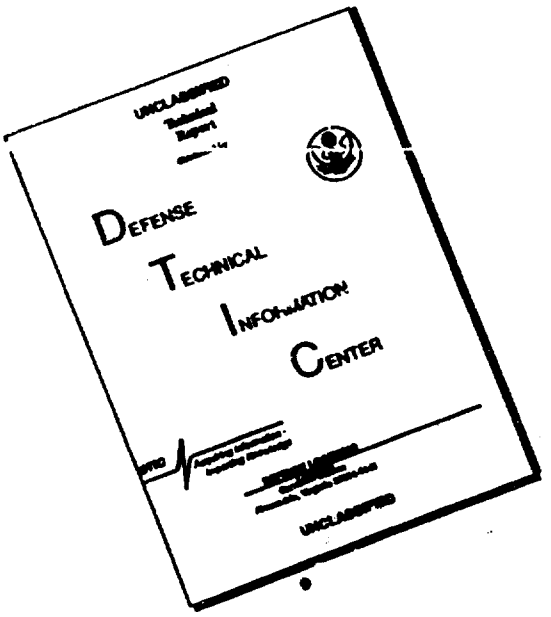

THIS DOCUMENT IS BEST QUALITY AVAILABLE. THE COPY FURNISHED TO DTIC CONTAINED A SIGNIFICANT NUMBER OF PAGES WHICH DO NOT REPRODUCE LEGIBLY.

The Mission of AGARD

According to its Charter, the mission of AGARD is to bring together the leading personalities of the NATO nations in the fields of science and technology relating to aerospace for the following purposes:

- Recommending effective ways for the member nations to use their research and development capabilities for the common benefit of the NATO community;
- Providing scientific and technical advice and assistance to the Military Committee in the field of aerospace research and development (with particular regard to its military application);
- Continuously stimulating advances in the aerospace sciences relevant to strengthening the common defence posture;
- Improving the co-operation among member nations in aerospace research and development;
- Exchange of scientific and technical information;
- Providing assistance to member nations for the purpose of increasing their scientific and technical potential;
- Rendering scientific and technical assistance, as requested, to other NATO bodies and to member nations in connection with research and development problems in the aerospace field.

The highest authority within AGARD is the National Delegates Board consisting of officially appointed senior representatives from each member nation. The mission of AGARD is carried out through the Panels which are composed of experts appointed by the National Delegates, the Consultant and Exchange Programme and the Aerospace Applications Studies Programme. The results of AGARD work are reported to the member nations and the NATO Authorities through the AGARD series of publications of which this is one.

Participation in AGARD activities is by invitation only and is normally limited to citizens of the NATO nations.

Published December 1991

ISBN 92-835-0644-8

Printed by Specialised Printing Services Limited
40 Chigwell Lane, Loughton, Essex IG10 3TZ

Recent Publications of the Fluid Dynamics Panel

AGARDOGRAPHS (AG)

Design and Testing of High-Performance Parachutes
AGARD AG-319, November 1991

Experimental Techniques in the Field of Low Density Aerodynamics
AGARD AG-318 (E), April 1991

Techniques Expérimentales Liées à l'Aérodynamique à Basse Densité
AGARD AG-318 (FR), April 1990

A Survey of Measurements and Measuring Techniques in Rapidly Distorted Compressible Turbulent Boundary Layers
AGARD AG-315, May 1989

Reynolds Number Effects in Transonic Flows
AGARD AG-303, December 1988

REPORTS (R)

Aircraft Dynamics at High Angles of Attack: Experiments and Modelling
AGARD R-776, Special Course Notes, March 1991

Inverse Methods in Airfoil Design for Aeronautical and Turbomachinery Applications
AGARD R-780, Special Course Notes, November 1990

Aerodynamics of Rotorcraft
AGARD R-781, Special Course Notes, November 1990

Three-Dimensional Supersonic/Hypersonic Flows Including Separation
AGARD R-764, Special Course Notes, January 1990

Advances in Cryogenic Wind Tunnel Technology
AGARD R-774, Special Course Notes, November 1989

ADVISORY REPORTS (AR)

Air Intakes for High Speed Vehicles
AGARD AR-270, September 1991

Appraisal of the Suitability of Turbulence Models in Flow Calculations
AGARD AR-291, Technical Status Review, July 1991

Rotary-Balance Testing for Aircraft Dynamics
AGARD AR-265, Report of WG 11, December 1990

Calculation of 3D Separated Turbulent Flows in Boundary Layer Limit
AGARD AR-255, Report of WG10, May 1990

Adaptive Wind Tunnel Walls: Technology and Applications
AGARD AR-269, Report of WG12, April 1990

CONFERENCE PROCEEDINGS (CP)

Effects of Adverse Weather on Aerodynamics
AGARD CP-496, December 1991

Manoeuvring Aerodynamics
AGARD CP-497, November 1991

Vortex Flow Aerodynamics
AGARD CP-494, July 1991

Missile Aerodynamics
AGARD CP-493, October 1990

Aerodynamics of Combat Aircraft Controls and of Ground Effects
AGARD CP-465, April 1990

Fluid Dynamics of Three-Dimensional Turbulent Shear Flows and Transition
AGARD CP-438, April 1989

Validation of Computational Fluid Dynamics
AGARD CP-437, December 1988

Aerodynamic Data Accuracy and Quality: Requirements and Capabilities in Wind Tunnel Testing
AGARD CP-429, July 1988

Aerodynamics of Hypersonic Lifting Vehicles
AGARD CP-428, November 1987

Aerodynamic and Related Hydrodynamic Studies Using Water Facilities
AGARD CP-413, June 1987

Applications of Computational Fluid Dynamics in Aeronautics
AGARD CP-412, November 1986

Store Airframe Aerodynamics
AGARD CP-389, August 1986

Unsteady Aerodynamics — Fundamentals and Applications to Aircraft Dynamics
AGARD CP-386, November 1985

Aerodynamics and Acoustics of Propellers
AGARD CP-366, February 1985

Improvement of Aerodynamic Performance through Boundary Layer Control and High Lift Systems
AGARD CP-365, August 1984

Wind Tunnels and Testing Techniques
AGARD CP-348, February 1984

Aerodynamics of Vortical Type Flows in Three Dimensions
AGARD CP-342, July 1983

Missile Aerodynamics
AGARD CP-336, February 1983

Prediction of Aerodynamic Loads on Rotorcraft
AGARD CP-334, September 1982

Wall Interference in Wind Tunnels
AGARD CP-335, September 1982

Fluid Dynamics of Jets with Applications to V/STOL
AGARD CP-308, January 1982

Aerodynamics of Power Plant Installation
AGARD CP-301, September 1981

Computation of Viscous-Inviscid Interactions
AGARD CP-291, February 1981

Subsonic/Transonic Configuration Aerodynamics
AGARD CP-285, September 1980

Turbulent Boundary Layers Experiments, Theory and Modelling
AGARD CP-271, January 1980

Aerodynamic Characteristics of Controls
AGARD CP-262, September 1979

High Angle of Attack Aerodynamics
AGARD CP-247, January 1979

Dynamic Stability Parameters
AGARD CP-235, November 1978

Unsteady Aerodynamics
AGARD CP-227, February 1978

Foreword

In recent years, a number of weather-related accidents, along with the introduction of new types of anti-icing fluids and apparent uncertainties in certification and operation procedures, have stimulated renewed research activities. Aircraft operators, the aircraft industry, as well as research institutes and certification authorities, are participating in such activities.

This situation has led the Fluid Dynamics Panel to organize a specialists' meeting on the "Effects of Adverse Weather on Aerodynamics".

Since the effects of adverse weather on aerodynamics involve a broad range of weather-related phenomena and devices — different forms of precipitation, wind shear, anti-icing fluids and devices, etc. — an in-depth coverage of these effects within the confines of a meeting required some focussing. To this end, the scope of this FDP Specialists' Meeting focussed on the degradation of aerodynamics performance due to different forms of precipitation, such as ice accretion, and due to anti-icing fluids and devices. This degradation of performance continues to be a concern in aircraft operations and is also a significant factor in aircraft design.

A complementary coverage of weather-related effects — wind shear, fog, etc. — on aircraft performance is provided in AGARD CP-470, "Flight in Adverse Environmental Conditions" (AGARD FMP Symposium held in Norway in May 1989).

The purpose of the present specialists' meeting was, in particular:

1. To provide an update of the state-of-the-art with respect to the prediction, simulation, and measurement of the effects of icing, anti-icing fluids, and various forms of precipitation on the aerodynamic characteristics of flight vehicles;
2. To communicate research results obtained in recent years on the following topics:
   - theoretical and empirical modelling of ice accretion on airfoils, wings, control surfaces, propellers, rotors, air intakes, etc.;
   - experimental and computational simulation, and flight test verification of the effects of icing on aerodynamic characteristics;
   - experimental and computational simulations of the effects of de-icing and anti-icing fluids, and devices on aerodynamics;
   - effects of (heavy) rain and other forms of precipitation on aerodynamic characteristics;
   - effects of the type of ice (rime, glaze) on aerodynamic characteristics;
   - facilities and experimental techniques (including flight tests) for simulating and measuring the effects of icing, anti-icing fluids, and heavy rain on the aerodynamics of flight vehicles and their components;
   - certification and operation procedures and regulations.

For the sake of statistics it is mentioned that of the 24 papers offered to the Programme Committee, 19 (including invited papers) could be accommodated within the time frame available.

These 19 papers were ordered into 3 sessions:

- Icing 1 Introduction and survey papers, certification issues.
- Icing 2 Prediction and simulation of ice contamination and its effect on aerodynamics.
- Effects of heavy rain and de/anti-icing fluids.

In alphabetical order of country of origin there was/were

2 papers from Belgium	1 paper from the Netherlands
3 papers from Canada	1 paper from Spain
3 papers from France	1 paper from the United Kingdom
1 paper from Germany	7 papers from the United States.

Two papers could not be presented because of sudden travel restrictions.

The Programme Committee gratefully acknowledges that 2 of the 4 invited papers were provided by the Flight Mechanics Panel (FMP) and the Propulsion and Energetics Panel (PEP) of AGARD.

It is finally mentioned that the Technical Evaluation Report, written by Mr J. Reinmann of NASA Lewis is available as AGARD Advisory Report No.306.

Professor Ir J.W. Slooff
Chairman, Programme Committee

Avant-Propos

Les travaux de recherche dans ce domaine ont repris ces dernières années à la suite d'un certain nombre d'accidents liés aux conditions météorologiques qui se sont produits, ainsi que de l'apparition de nouveaux types de liquides antigivrage et de supposées incertitudes dans les procédures d'homologation et de vol. Participent à ces activités des utilisateurs d'avions et l'industrie aéronautique en général, ainsi que des instituts de recherche et les services d'homologation.

Eu égard à cette situation, le Panel AGARD de la Dynamique des Fluides a décidé d'organiser une réunion de spécialistes sur "Les effets du mauvais temps sur l'aérodynamique".

Etant donné que les effets du mauvais temps sur l'aérodynamique couvrent un large éventail de phénomènes et de dispositifs ayant un lien avec le temps... les différentes formes de précipitation, le cisaillement du vent; les liquides et les dispositifs antigivrage etc... une mise au point s'imposait afin de permettre un examen approfondi ce des effets dans le cadre d'une réunion. A cette fin, le programme de cette réunion de spécialistes FDP a mis l'accent sur la dégradation des performances aérodynamiques due aux différentes formes de précipitation, telles que l'accumulation de glace, et aux et dispositifs antigivrage. Cette dégradation des performances continue à poser des problèmes pour l'exploitation et doit toujours être prise en compte lors de l'étude de l'avion.

Une étude complémentaire des effets du mauvais temps... cisaillement du vent, brouillard etc... est fournie par la publication AGARD CP-470 "Le vol dans les mauvaises conditions ambiantes" Symposium AGARD FMP, Norvège, mai 1989.

L'objet de la réunion FDP était:

1. De présenter une revue de l'état de l'art en ce qui concerne la prévision, la simulation, et le contrôle des effets du givrage, des liquides antigivrage, et des differentes formes de précipitation sur les caractéristiques aérodynamiques des véhicules aériens.
2. De communiquer les résultats des travaux de recherche effectués sur les questions suivantes:
   - la modélisation théorique et empirique de l'accumulation de glace sur les profils, les voilures, les gouvernes, les hélices, les rotors, les prises d'air etc...
   - la simulation expérimentale et par ordinateur, et la vérification en vol des effets du givrage sur les caractéristiques aérodynamiques des véhicules aériens.
   - la simulation expérimentale et par ordinateur des effets du dégivrage et des liquides et dispositifs antigivrage sur l'aérodynamique.
   - les effets des pluies (fortes) et d'autres formes de précipitation sur les caractéristiques aérodynamiques des véhicules aériens.
   - les effets des différents types de glace (givre, verglas) sur les caractéristiques aérodynamiques des véhicules aériens.
   - les installations et les techniques expérimentales (y compris les essais en vol) pour la simulation et le contrôle des effets du givrage, des liquides antigivrage et des pluies fortes sur l'aérodynamique des véhicules aériens et leurs composants.
   - les procédures et les règlements d'homologation.

Par égard pour la statistique il est à noter que le comité organisateur a pu inclure au programme 19 communications sur les 24 reçues (dont certaines présentées sur invitation) étant donné les contraintes de temps imposées.

Les 19 communications ont été programmées en trois séances:

- givrage 1 Communications d'introduction et vue d'ensemble, questions d'homologation.
- givrage 2 Prévision et simulation de la contamination par la glace et les effets sur l'aérodynamique.
- les effets des pluies fortes et des liquides de dégivrage/antigivrage.

Les communications présentées, par ordre alphabétique du pays d'origine, s'établissent comme suit:

2 communications de la Belgique	1 communication de Pays-Bas
3 communications du Canada	1 communication de l'Espagne
3 communications de la France	1 communication du Royaume-Uni
1 communication de l'Allemagne	7 communications des Etats-Unis

Deux communications n'ont pas pu être présentées à cause de restrictions de déplacement de dernière minute.

Le comité organisateur tient à remercier le Panel AGARD de la mécanique du vol (FMP) et le Panel de propulsion et d'énergétique (PEP) pour avoir bien voulu fournir 2 des 4 communications présentées sur invitation.

Enfin, il est signalé que le rapport d'évaluation technique, rédigé par M.J. Reinmann de NASA Lewis est publié sous la forme de AGARD Advisory Report No.306.

Professeur Ir J.W. Slooff

Fluid Dynamics Panel

Chairman: Dr W. McCroskey
Senior Staff Scientist
US Army Aeroflightdynamics Directorate
Mail Stop N258-1
NASA Ames Research Center
Moffett Field, CA 94035-1099
United States

Deputy Chairman: Professor Ir J.W. Slooff
National Aerospace Laboratory NLR
Anthony Fokkerweg 2
1059 CM Amsterdam
The Netherlands

PROGRAMME COMMITTEE

Professor Ir J.W. Slooff (Chairman)
National Aerospace Laboratory, NLR
Anthony Fokkerweg 2
1059 CM Amsterdam
The Netherlands

Professor J.A. Essers
Institut de Mécanique
Service d'Aérodynamique Appliquée
rue Ernest Solvay 21
4000 Liège
Belgium

Mr L.H. Ohman
High Speed Aerodynamics Lab.-U66
Institute for Aerospace Research
National Research Council
Montreal Road
Ottawa, Ontario K1A 0R6
Canada

M. C. Dujarric
ASE-Programme HERMES
Batiment Euler
18 avenue Edouard Belin
31055 Toulouse Cedex
France

Dr B. Wagner
Dornier Luftfahrt GmbH
Abteilung Aerodynamik
Postfach 1303
D-7990 Friedrichshafen
Germany

Professor M. Onorato
Dipartimento di Ingegneria Aeronautica e Spaziale
Politecnico di Torino
C. so Duca degle abruzzi 24
10129 Torino
Italy

Professor Dr Ir J.L. van Ingen
Department of Aerospace Engineering
Delft University of Technology
Kluyverweg 1
2629 HS Delft
The Netherlands

Professor Dr H. Norstrud
Division of Hydro- and Gas Dynamics
The University of Trondheim
Norwegian Institute of Technology
N-7034 Trondheim — NTH
Norway

Mr F. Monge
Dpt. de Aerodinamica — INTA
Crta de Torrejon a Ajalvir, Km. 4
28850-Torrejon de Ardoz
Madrid
Spain

Professor A.D. Young
70 Gilbert Road
Cambridge CB4 3PD
United Kingdom

Mr D.L. Bowers
Flight Dynamics Laboratory
WL/FIMM
Wright-Patterson AFB
Ohio 45433-6553
United States

PANEL EXECUTIVE

Dr W. Goodrich

Mail from Europe:
AGARD—OTAN
Attn: FDP Executive
7, rue Ancelle
92200 Neuilly-sur-Seine
France

Mail from US and Canada:
AGARD—NATO
Attn: FDP Executive
Unit 21551
APO AE 09777

Tel: 33 (1) 47 38 57 75
Telex: 610176 (France)
Telefax: 33 (1) 47 38 57 99

Contents

* Contribution from the Flight Mechanics Panel.

** Contribution from the Propulsion and Energetics Panel.

FLIGHT IN ADVERSE ENVIRONMENTAL CONDITIONS

by

J.F.Renaudie
1 rue Richard Mique
78000 Versailles
France

SUMMARY : The first Session of the FMP Symposium in Göl was devoted to the various techniques of measurements of wind velocity vector in severe turbulences or windshear events,both from flight test aircraft and from airline operations. Very good results are now provided, but with sophisticated means.The second Session was centered on crew warning ,crew reactions and procedures in windshears and severe disturbances, also on novel devices to improve aircraft behaviour ,and as a consequence, safety.A few papers adressed visibility in session 3, while Session 4 adressed very completely icing accretion and protection.The last Session addressed the electromagnetic interferences and lightning strikes which may effect the new electric flight control systems.

INTRODUCTION

Background

Adverse environmental conditions have four manifestations of primary interest to the Flight Mechanics Specialists : atmospheric disturbances,visibility,icing, and electromagnetic disturbances.All four manifestations can seriously influence flight safety,comfort and operational capabilities.

The Flight Mechanics Panel (FMP) has an ongoing subgroup on the topic of windshear. In addition,the Panel has sponsored two Working Groups on the topic of Rotorcraft icing .A Symposium of the FMP on "Flight in Turbulence" was held in BEDFORD , UK, in 1982. Since that time there have been many activities relative to fixed-wing aircraft concerns, e.g. JAWS,Low CAT,Wake Vortex Measurement, windshear Measurement and investigation, flow field and turbulence Measurements around geographic obstacles ,which have produced important results
Additional advances have been made in design of active control systems which can provide significant alleviation of gust loads and turbulence response : the immense growth of electronic devices in the aircraft will improve handling qualities and flight safety, e.g. fly by wire, CCV.These electrically signalled control systems and installed equipment can be significantly effected by electromagnetic disturbances, especially in flights at greater altitudes.

The increased emphasis by the military on beeing able to operate in poor weather and at night has resulted in the development of vision aids such as light intensification and infrared devices.These developments have been applied to fixed-wing aircraft and helicopters and now allow operations close to the ground in poor visibility and more adverse weather conditions.The problem has therefore expanded and there is increased need not only to make the aircraft resistant to the adverse conditions but also improve the ability to model and predict these adverse conditions so that the built-in capabilities are not exceeded.

Therefore the FMP decided to hold a Symposium on this subject in Göl, NORWAY,8-11 May 1989.

The Symposium (Fig 1)

It was structured around five Sessions:

Session 1:Atmospheric Measurements and Modelling

Session 2: Effect of Disturbances on Design and Operations

Session 3: Visibility

Session 4: Icing

Session 5: Electromagnetic Disturbances

It is a challenge to summarize these 26 excellent papers,therefore ,to give the spirit of this Symposium instead of a detailed review, I have selected those Papers presenting the most significant items,and extracted from them what I believe as essential.

SESSION 1:ATMOSPHERIC MEASUREMENTS AND MODELLING

Fig 2

1.1.Paper (6) from TOMKINS (USA) was the only one to give a broad picture of all atmospheric measurements and experiments including ground facilities,in relation with adverse atmospheric events,such as extremes of temperatures, storm, icing, lightning,electromagnetic interferences, clouds, visibility and air pollution.
All other Papers adressed the measurement of wind velocity vector (with components along all three Earth axis, including speed vector rotations).

Fig 3

Special mention must be made of Paper (3) from WINGROVE BACH and SCHULTZ of NASA because it adressed the analysis of severe atmospheric disturbances ,from airline flight records.

Fig 4

This figure presents two types of severe atmospheric disturbances

Fig 5

Again two cases of severe turbulence encounter at cruise altitudes,due either to a thunderstorm front or to the wind over a mountain range.

Fig 6

This figure presents the temperature inversion at the tropopause associated with the severe turbulences described in the previous figure.

Fig 7

This figure ,extracted from Paper (4) from VORSMAN , Germany,illustrates the challenge of this kind of measurement of very small wind vectors figures ,as differences between the airspeed and ground speed vectors of the aircraft.This is obviously the origin of all problems found ,inthe technique of atmospheric measurements.

Nevertheless the need of test aircraft with specific flight test instal'ation,at least to provide a method for deriving the atmospheric wind measurements from airline recording, is pointed out by 3 papers, (1),(2) (4),and examples chosen are modified transport aircraft (Nord 262,Dornier 128 and 228)

Fig 8

This figure ,extracted from the Paper from VORSMAN, Germany,shows the cross section of the"meteopod" system used by the Alfred Wegener Institute on Airplanes or Helicopters, to measure the wind velocities

A variety of means are used to provide accurate derivation of wind vector; nevertheless none of the papers mention the laser flow measurements which are sometime used by research establishments.

FIg 9

All papers insist on the need of good aircraft position recording by on board means (inertial reference system, or satellite positioning system) and check of position by ground radar positioning (ATC radars) :this is specifically mentioned when the purpose is to investigate wether the origin of an airline incident/accident is an atmospheric incident or not

SESSION 2:EFFECTS OF DISTURBANCES ON DESIGN AND OPERATIONS

2.0.Overview of the session:

Fig 10

Six of the papers presented adress the major subject of windshear effects on aircraft, while paper (12) from McPHERSON and ISAAC,CANADA, gives a picture of a number of atmospheric events encountered during the Canadian Atlantic Storm Programme (CASP), such as icing,snow encounter with poor visibility,high windshears and crosswinds.

The items highlighted by the authors of this session may be classified along the following headings:

- -picture of atmospheric events
- -operations in adverse weather
- -design of aircraft for bad weather
- -experimental programmes and studies

2.1.Picture of some atmospheric events

Fig 11

The Canadian Atlantic Storm Programme (CASP) describes the penetration of storm with a specifically equipped aircraft,a Twin Otter carrying a specific instrumentation system. The equipment needed to complete such a flight test campaign is the following:

-the test aircraft itself,Twin Otter specially modified to survive a penetration into severe icing environment for a long time, and equipped with instrumentation needed for water droplet size measurements,cloud water concentration,in addition to the usual flight parameters.

-a second aircraft (DC3) able to divert at greater distances than the Twin Otter and also equipped adequately.

-3 weather Radars, meteorological towers, buoys,ships.

-satellite navigation.

Fig 12

This slide shows the CASP operational area.

2.2.Operations in adverse weather

Fig 13

Four main concerns are adressed:

(a)- in flight detection of events
(b)- aircraft trajectory
(c)- crew reactions and correct crew procedure
(d)- specific case of short/vertical take off aircraft and helicopters.

(a)- in flight detection of events:

Papers adress mainly windshear detection. All authors of papers (7),(8),(9) agree on the finding that the best parameter for

detection is based on energy height (which expresses the sum of potential and kinetic energy of the vehicle).Difference between energy height,actual and expected,and their rate of variation, gives a way to introduce some phase advance,needed for proper crew reaction ,and provide the input of warning displays.

Nevertheless the usefullness of "point source sensors" is found very limited by A.E.WOODFIELD from United Kingdom in Paper (8) who concludes his written paper saying:

"Point source sensors cannot produce information on the total size of a windshear until after it has occurred.This is too late to help a pilot."

Nevertheless this judgement is not shared by all authors as shown in the following figures:

Fig 14

This slide shows a flight simulator approach in windshear condition,with an experienced pilot,with and without a windshear warning display.It is extracted from Paper (7) from SHAENZER ,Germany.It shows that the warning display help the pilot to avoid the accident, inevitable without it.

Fig 15

In the same windshear condition the less experienced pilot achieve a trajectory similar to the trajectory flown by the experienced pilot provided that the windshear warning be available.

Fig 16

Cathode tube flight instruments are probably those which provide the best flexibility to introduce such warnings,using pointers giving the energy height and its rate of change.This is extracted from the paper from BONAFE, France.

(b)- Aircraft trajectory:

Fig 17

This figure gives an example of possible trajectories during windshear conditions experienced in Dallas Aug.1985 which lead to the accident of Flight Delta 191 in an attempt to land instead of going around as Flight American 539.

Fig 18

This shows the modellisation of the microburst encountered by the two aircraft at Dallas Fort Worth.These two last figures are extracted from Paper (3) from WINGROVE BACH and SCHULTZ ,NASA,wich was illustrated by a video film explaining the accident of Flight Delta 191.I hope that the audience will have the opportunity to see this film.

(c)- Crew reactions and procedure:

They are adresssed by three papers (3),(7) and (9),only to state that the right procedure has to be found within the existing limitations of the aircraft,in terms of low speed ,stall, etc... which is not easy unless the aircraft is fully protected against them.The video film on Delta 191 accident ,used to illustrate paper (3) explains that the right crew reaction is against the instinct of the pilot to maintain the airspeed.It suggests that the lesson for Airline pilots is the following:

Fig 19

1: **avoid downburst if you can**

2: if you are **caught in a downburst:**

- **pull up** ,pitch attitude 15°
- **full throttle**
- **forget all previous experience!**

All Authors agree on the need to avoid building up of the rate of descent,even at the cost of a very low speed, close to stall speed.

(d)- Specific case of CTOL/VTOL and Helicopters :

It is adressed in Paper (18) from SCHRAGE PRASAD GAONKAR,USA:attention is driven toward the scale of atmospheric events which is usefull to consider for those vehicules which can hover and at least for helicopters: the behaviour and performances of their rotors can be severely disturbed by air motion fields whic have the same wavelength or dimensions as the rotors.

This is in particular the case of"**rotating frame turbulence** "(RFT) which is often produced by relatively small obstacles on the ground (buildings,hills,cliffs,etc...) in the air stream close to ground surface.

This "RFT" could be as important for helicopters as is the microburst for aircraft.

Fig 20

This graph illustrates the magnification of the peaks of normal acceleration due to Rotating Frame Turbulence compared to "Space Fixed Turbulence"
Parametr L/R is the Length L of the turbulence divided by the radius of the rotor R.

2.3. Design of aircraft for better behaviour in adverse weather

The papers presented adress mainly the behaviour in adverse three -dimension wind velocity situations, and means to improve safety and passenger comfort, reduce structural loads, make easier crew reactions.

Fig 21

Paper (14) from MOBES and MOLZOV,Germany gives a description of the gust load alleviation system implemented on the transport aircraft AIRBUS A320 implementing in its system a number of protections, of which at least two are specific of the windshear:

the stall protection and the "Alpha- Floor" system.

Fig 22

The stall protection system enable the pilot to pitch up the aircraft up to maximum lift, without any risk of excursions to higher angles of attack:steady flight at this maximum angle of attack is possible,without needing skillness.

The "Alpha-Floor"system takes care of preventing high rate of sink usually met at high angles of attack :the maximum available thrust is automatically triggered when A.O.A exceeds a figure depending on the configuration,and when the stick is fully deflected aft.

These protections appear as one of the major weapons of the pilots against strong wind shears,since they enable them to apply the right procedure without worrying about the stall or high rate of descent which may endanger the aircraft.

2.4 Experimental programmes or studies

Fig 23

Paper (16) from BOSRET and WINTER, Germany, presents the experimental DORNIER 28 TNT implementing the "OLGA" system to improve passenger comfort while flying through gusts.It presents a very interesting analysis of frequency response of aircraft structure, and human body.

SESSION 3 - VISIBILITY

3.2.Subjects adressed:

The objectives of this Session were only partially covered ,with two papers adressing visibility measurements , and one worthwile mentioning , Paper (20) from WRIGHT, USA

This paper points out the real need ,when flying helicopters at low altitudes,in darkness or bad visibility ,of a proper interface between man and outside world, which is still not provided.It points out that, in addition to the usual sensors providing adequate vision of the horizon in the direction of the flight (flight vector),there is a need of a good coverage of the field of view below the helicopter,not yet provided.

3.2.Gaps of this session :

The following very common factors producing poor visibility were not covered:

- clouds and precipitations,rain, drizzle,fog (in weather flying)

- smoke, smog (solid particles such as those above a battlefield,or above industrial factories,sometime mixed up with clouds)

- sand storms (often met in deserts)

Nevertheless these problems have already been studied in AGARD , in particular it was one of the aims of the Study Group that I had the great honor to chair ,AASC N°19; The title of this study was"All weather capability of combat aircraft".The following comments may be extracted from the unclassified part of the conclusions of this study:

(a)- confirmation is given of the very specific use of all infrared sensor systems for dry air nights.The range reduction in weather is such that it cannot be seriously envisaged to use them for precise tasks in weather,such as take-off and landing.

(b)- electromagnetic systems are far more promissing:the key factor is the wave length,compared to the dimensions of water particles,droplets or ice crystal.It is feasible to select the right wavelength for optimum transmission ;best transmissions are given by VHF frequencies ;millimetric wave radars provide quasi optical picture definition while having a range far better than present infra-red systems,but still not sufficient in spite of the progress made in their penetrating power.

For navigation only,when the image of a target or obstacle is not required,widely used Air Traffic Control Radar systems,operating on longer wavelength,have proven their efficiency ,from a long time ago.

New positioning systems of very high accuracy,such as the NAVSTAR Global Positioning System,operating from a set of Earth Satellites,or local radio electrical systems having the same frequency,but operating for a set of ground stations,such as the "ILOEN" (Thomson,France) are very promissing to provide new navigation aids used in all flight phases,including take-off and landing which require the highest accuracy.

For all these electromagnetic systems stealthiness remains a problem.

SESSION 4.ICING

Icing research and technology

In this session paper (22) from REINMANN SHAW and RANAUDO,USA,on NASA's programme on Icing Research and Technology meets the challenge of providing in 22 pages a very extensive presentation of almost all subjects related to icing.

Fig 25

(a) Physical mechanism of icing:
this mechanism involve a number of parameters: airspeed,outside air temperature,altitude,cloud liquid water content and concentration,cloud droplet size distribution, size or scale of models or aircraft exposed to icing,Mach and Reynolds Numbers,etc..

Ice formed in flight over the the aircraft skin results from supercooled water droplets impacting the airframe surface at the flight speed.

A number of types of ice may result from variations of the above parameters, mainly liquid water concentration and droplet size distribution in clouds. Adhesion on the skin depends on the type of icing,and roghness of surface.Basic mechanical properties of ice accreted is (1) tensile (Young's module) (2)Shear (adhesion) (3) peeling properties.

(b) Protection against icing
With the decrease of available hot air bleed of new fan engines, there is a need to develop new deicing systems using less bleed,or more efficiently,or newer systems relying on other sources of energy.

Fig 26

New systems are being developped based on electrical capacitor discharge,using external boots on the surface to protect,such as Electro-Expulsive Separation System, or Eddy Current Repulsion Deicing Boot,or installed inside the airframe, such as the Electromagnetic Impulse Deicer.All these systems provide very short duration impulses but high forces, and have been foun to be very efficient.

(c) Computation of icing accretion ; aircraft performance degradation:
Prediction of airfoil aerodynamic performance degradation due to icing is now made possible with the high capacity computers of to-day.The code of the method used at NASA LEWIS is named "LEWICE".It uses inviscid flow equations,and determines the freezing point,by solving continuity and energy equations in each control volume of the flow. Comparisons with experience give confidence in this code at least for the low incidences ;the Authors state that viscous fluid equations will have to be used for better consistency with experiments at higher angles of attack, close to CL max.

Fig 27

(d) Icing testing
The main ground testing means mentioned by REINMANN SHAW and RANAUDO is the NASA LEWIS Icing Research Wind Tunnel,which is the largest refrigerated tunnel in the world capable of testing big models of aircraft, helicopters, wing profiles etc...

Flight test research is conducted at NASA LEWIS using a modified TWIN OTTER implementing modified deicing systems instead of the basic ones.Wings and gear struts are used to flight test ice accretion and new deicing systems
Associated measurements involve a number of devices such as :
- forward scattering spectrometer probe
- optical array probe
- phase doppler particle analyser

(to measure the dimensions of water particles).

(e) New physical models:

Fig 28

REINMANN SHAW and RANAUDO made the proposal of a new physical model for ice accretion, shown by this figure.

SESSION 5.ELECTROMAGNETIC INTERFERENCES

This Session included three papers ,each of them bringing complementary information to the others.The followin items are worthwile mentioning; they are extracted from Paper (26) from FISHER, USA

Fig 29

Surprisingly,severe lightning strikes can be found where one would not expect them:

- Aircraft lightning strikes occur in both thunderstorm and non thunderstorm conditions.

- The thunderstorms regions with the highest probability for an aircraft to experience a direct lightning strike were those areas where the ambiant temperature was - 40°Celsius, where the relative turbulence and precipitation intensities were characterized as negligible to light.

- The non -thunderstorm regions with the highest probability for an aircraft to experience a direct lightning strike were those areas where the ambient temperature was between $\pm$10°C in rain, where the relative turbulence intensity is characterized as negligible to light.

- Most aircraft lightning strikes are triggered by the vehicle itself.Lightning strikesin which the aircraft intercepts a naturally-occurring lightning flash also occur,predominantly at lower altitudes.

- The presence and location of lightning do not necessarily indicate the presence or location of hazardous precipitations and turbulence.

During the discussion of this session the Special Regulatory Conditions applied to the A320 , giving the Electromagnetic Interference Model , and the Lightning model to take into account for Airworthiness Certification,were presented by the Technical Evaluation Reporter as very severe threats.The A320 was demonstrated as not effected by these threats, originated either by "natural"events , such as lightning, or from equipments made by man (powerfull ground radio stations, radars ,etc...)

CONCLUSIONS

Fig 30

As in previous meetings of this type the balance between adverse weather conditions due to windshears,gusts, turbulence on one hand, and other adverse conditions, such as flying in weather, tended to favor the iormer

- **in Session 1,** while a majority of papers adresssed wind velocity measurements, there was very little information, sometimes no information at all on the following subjects

  - high atmosphere (adressed by only one paper)
  - modelling effects of obstacles (large, such as mountain rifts,small like buildings, or installations on the deck of a carrier ship).
  - sand storms

- **in Session 4** on icingthe paper of exceptional quality given by the Specialists of NASA LEWIS is worthwhile mentioning:it covers almost the totallity of the subject.

in **Session 5** on Electromagnetic interferences and lightning strike there were three excellent and complementary papers

the **other Sessions** suffered from the unbalance already mentioned and this is the reason why ,as Technical Evaluation Reperter of this Symposium , my conclusions ,written in **AGARD TER n°277** was to **set up a follow up meeting suggested** as explained below:

a **Multi-Panel SYmposium,which would extend the subject to flight in hostile/adverse environment,for military operations.**It would be a **classified meeting** ,with high participation of military operators; three main sessions were suggested:

A- Adverse environment

B- Operational problems

C- Hostile environment

It is sincerely hoped that the F.D.P. Symposium on the subject of adverse weather, will help to fullfill the gaps left by the F.M.P meeting.

1

Session 1 - Atmospheric Measurement and Modelling

Session 2 - Effects of Disturbances on Design and Operation

Session 3 - Visibility

Session 4 - Icing

Session 5 - Electromagnetic Disturbances

2

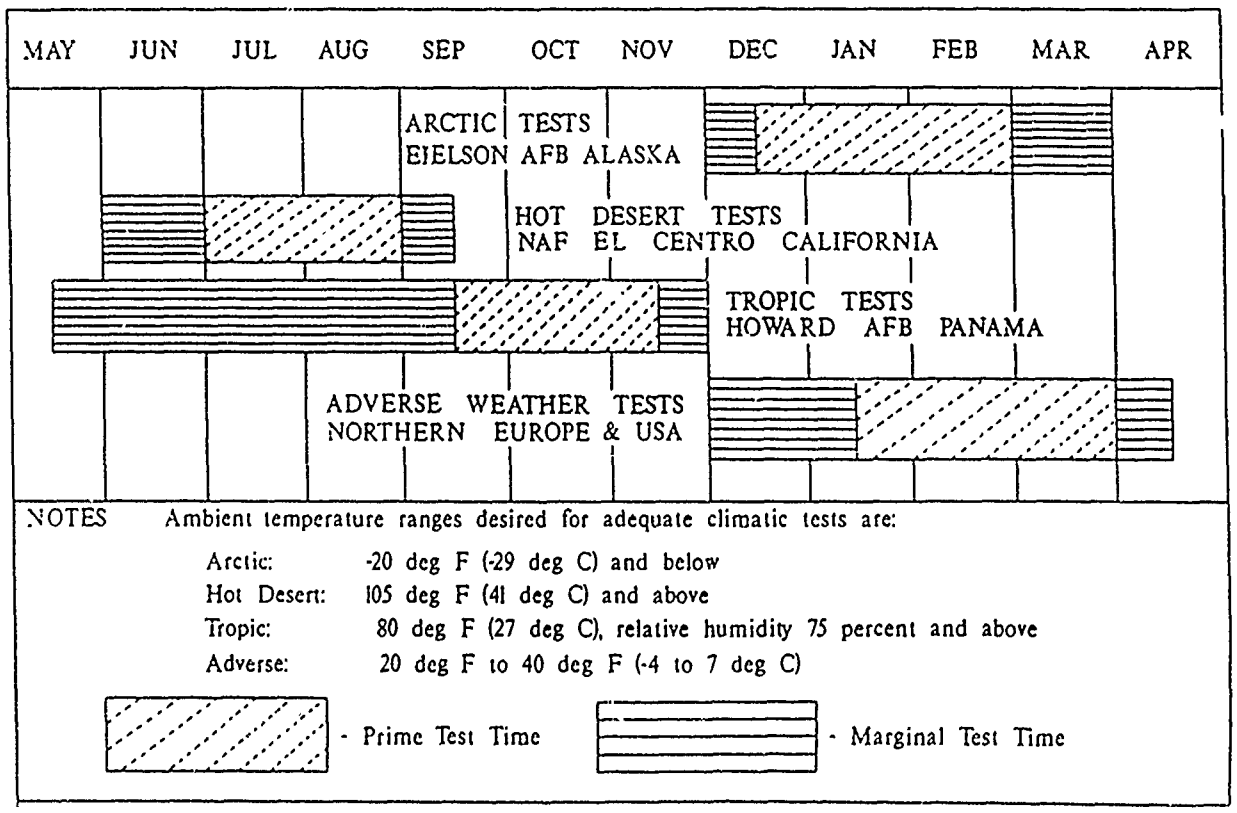

FROM PAPER 6 . TOMKINS . USA

3

TABLE I – DIGITAL FLIGHT RECORDS FROM AIRLINE ENCOUNTERS WITH SEVERE ATMOSPHERIC DISTURBANCES.

DATE	AIRCRAFT	LOCATION	OPERATION	DISTURBANCE
6/75	L1011	JFK, NY	Go-around	Microburst
11/75	DC10	Calgary, Canada	33,000'	Clear air turbulence
4/81	DC10	Hannibal, MO	37,000'	Clear air turbulence
7/82	DC10	Morton, WY	39,000'	Clear air turbulence
10/83	DC10	Near Bermuda	37,000'	Convective turbulence
11/83	L1011	Offshore SC	37,000'	Clear air turbulence
1/85	B747	Over Greenland	33,000'	Clear air turbulence
2/85	B747	Over Greenland	33,000'	Clear air turbulence
2/85	B747SP	Offshore CA	41,000'	Wind shear
8/85	L1011	Dallas/Ft.Worth, TX	Landing	Microburst
8/85	MD80	Dallas/Ft.Worth, TX	Go-around	Microburst
11/85	B747	Over Greenland	33,000'	Clear air turbulence
3/86	B747	Offshore Hawaii	33,000'	Clear air turbulence
4/86	DC10	Jamestown, NY	40,000'	Wind shear
7/86	A300	West Palm Beach, FL	20,000'	Convective turbulence
9/87	L1011	Near [illegible]	31,000'	Convective turbulence
11/87	A310	Near Bermuda	33,000'	Convective turbulence
1/88	B767	Chicago, IL	25,000'	Convective turbulence
3/88	B767	[illegible] NM	33,000'	Clear air turbulence

FROM PAPER 3 WINGROVE BACH SCHULTZ . USA

4

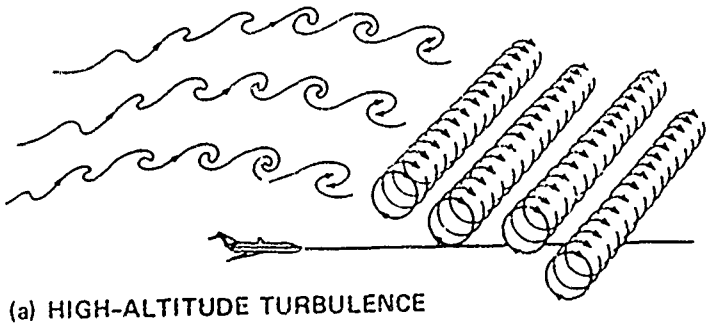

(a) HIGH-ALTITUDE TURBULENCE

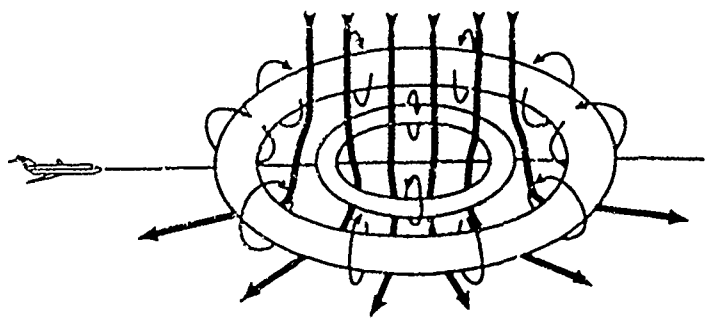

(b) LOW-LEVEL MICROBURST

Figure 1. Two types of severe atmospheric disturbances.

FROM PAPER 3 WINGROVE BACH SCHULTZ . USA

5

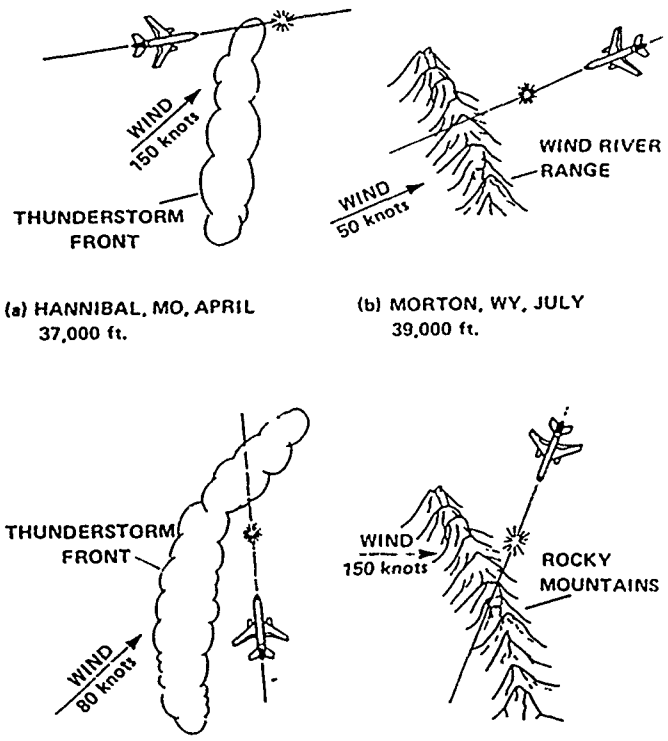

Figure 4. Overview of severe turbulence encounters at cruise altitudes.

FROM PAPER 3 WINGROVE BACH SCHULTZ . USA

6

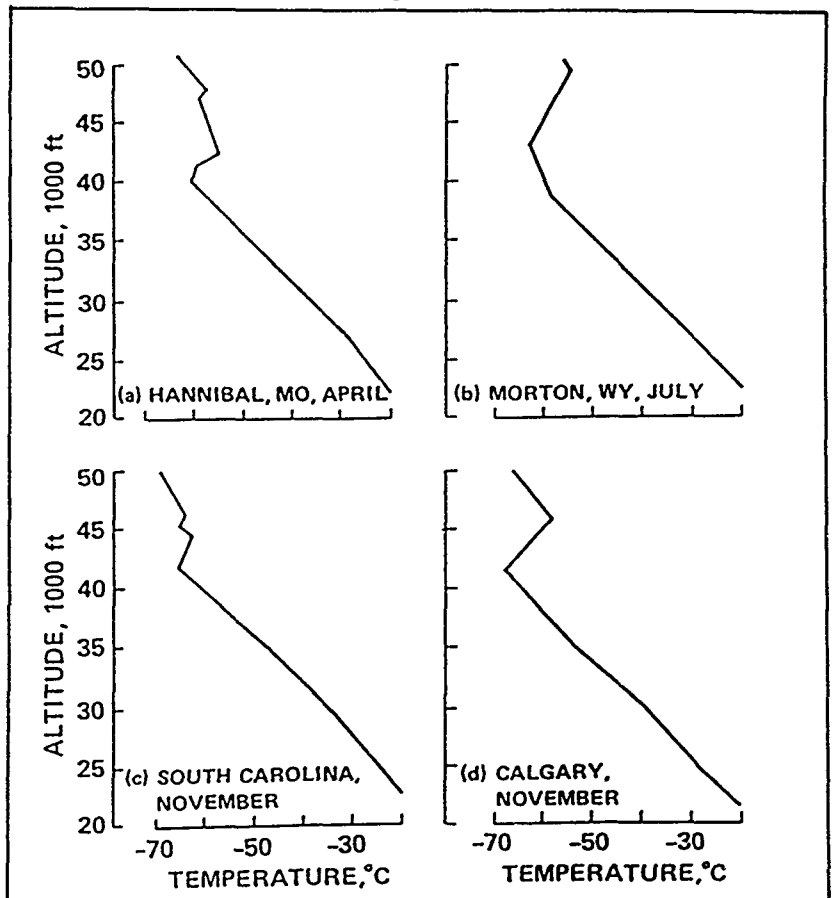

FROM PAPER 3 WINGROVE BACH SCHULTZ . USA

7

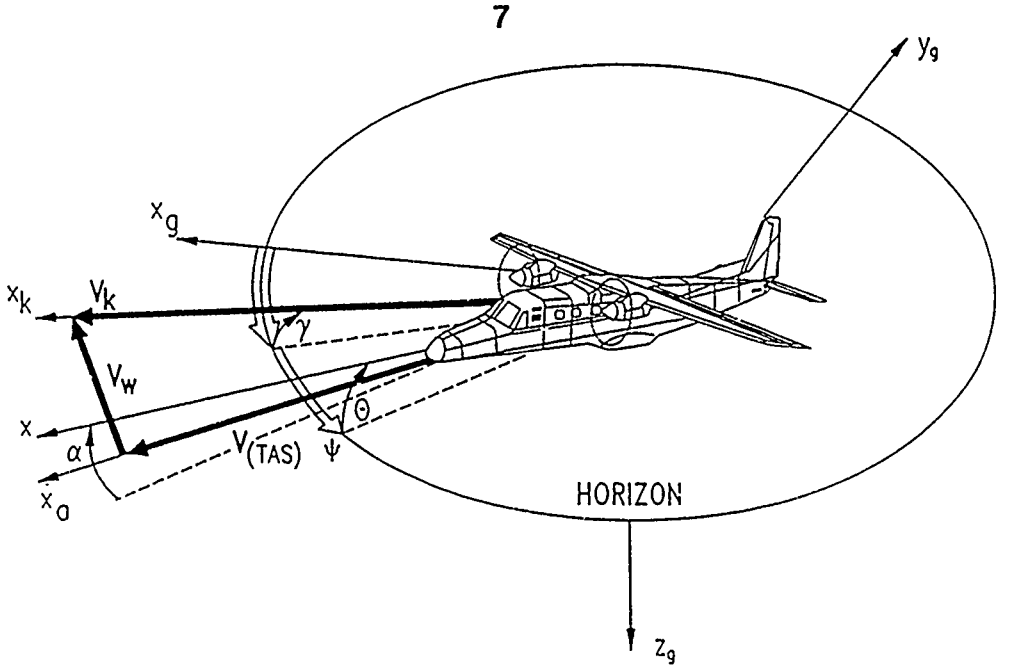

Fig 2: Determination of the Wind Vector

FROM PAPER 4 VORSMAN . GE

8

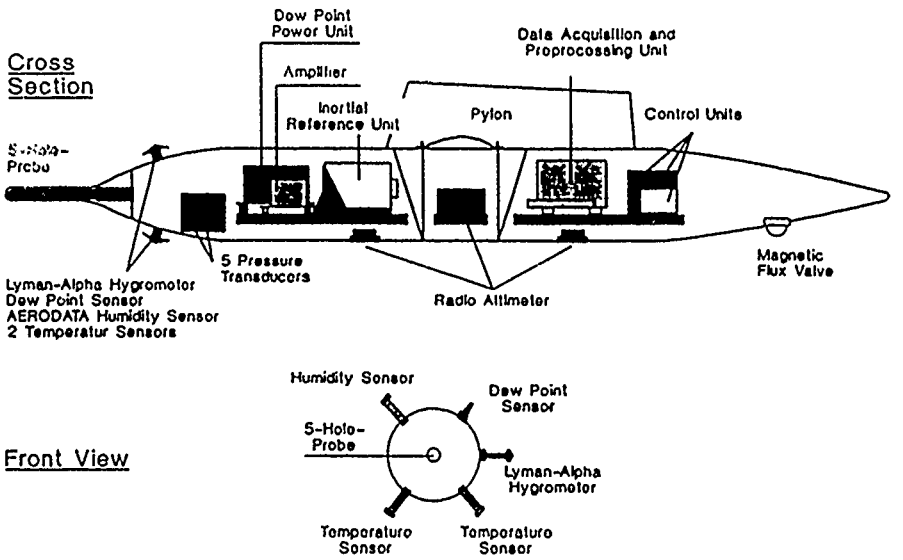

Fig. 4: Cross Sections of the Meteopod System with Hardware Locations of Sensors, Data Acquisition and Control Units

FROM PAPER 4 VORSMAN . GE

9

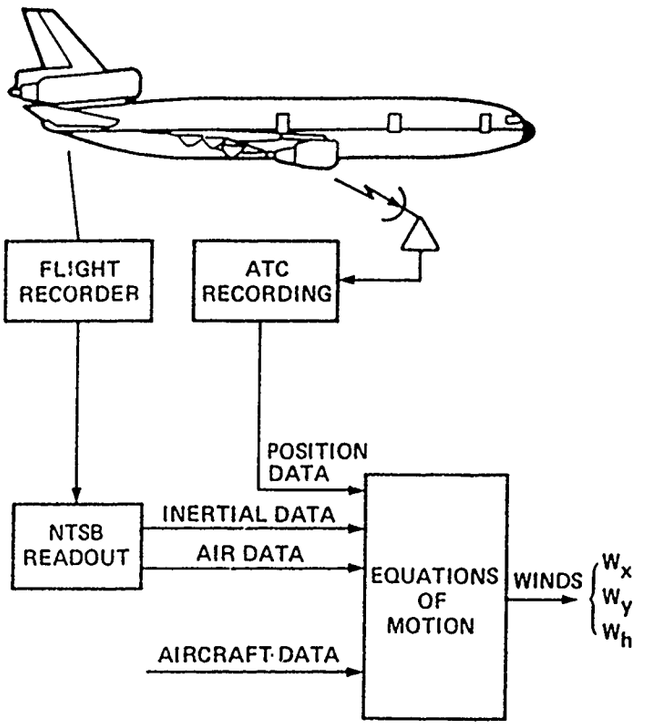

Figure 2. Reconstruction of severe winds from flight and ATC records.

FROM PAPER 3 WINGROVE BACH SCHULTZ . USA

10

OVERVIEW OF SESSION 2

Picture of Atmospheric Events

Cperations in adverse Weather

Design of Aircraft for bad Weather

Experimental Programmes and Studies

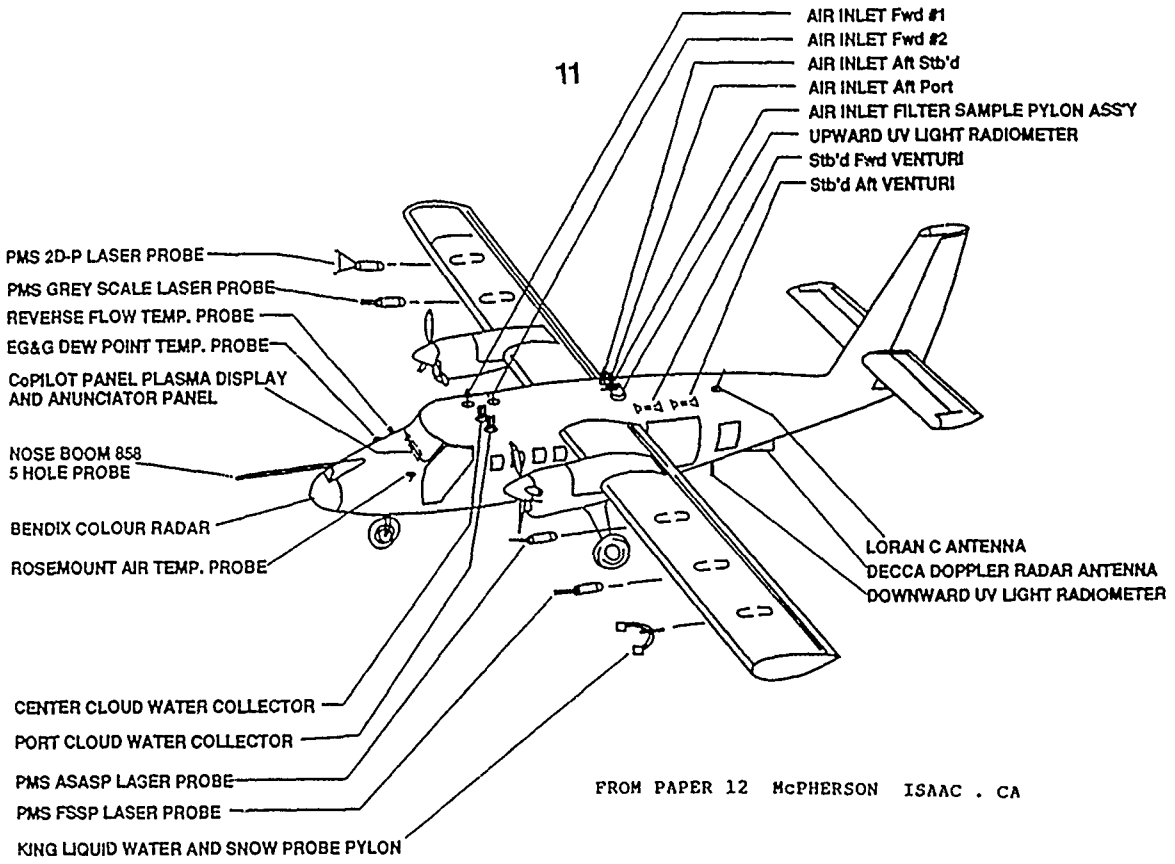

FIG. 1: NAE TWIN OTTER ATMOSPHERIC RESEARCH AIRCRAFT AS INSTRUMENTED FOR CLOUD PHYSICS MEASUREMENTS

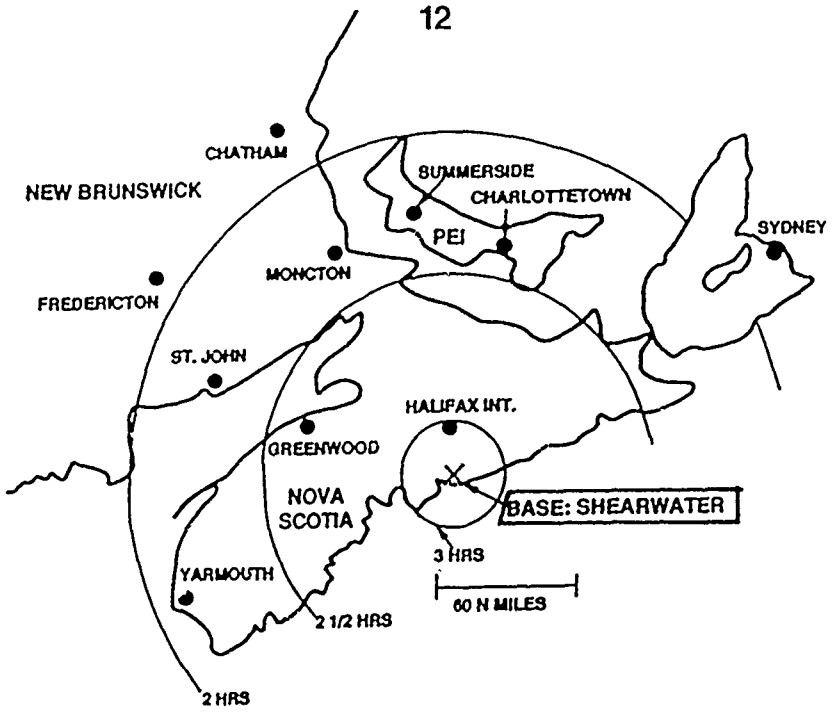

FIG. 3: THE CASP OPERATIONAL AREA

FROM PAPER 12 McPHERSON ISAAC . CA

13

OPERATIONS IN ADVERSE WEATHER

(a) in flight detection of events

(b) aircraft trajectory

(c) crew reactions and correct crew procedure.

(d) specific cases of short/vertical take off

14

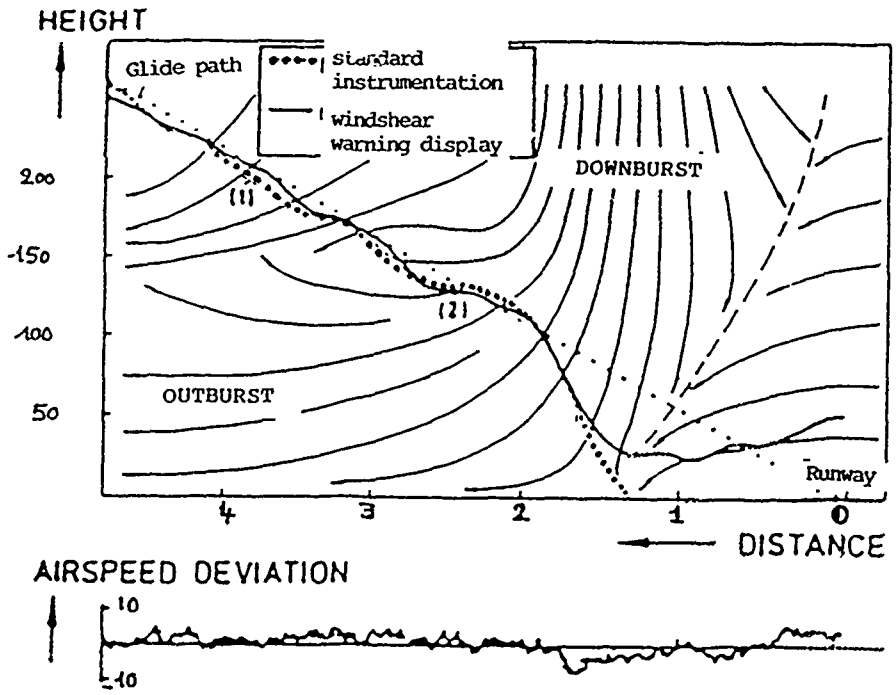

Fig. 20 : Flight simulator approach in wind shear conditions, experienced airline pilot

FROM PAPER 7 SHAENZER . GE

15

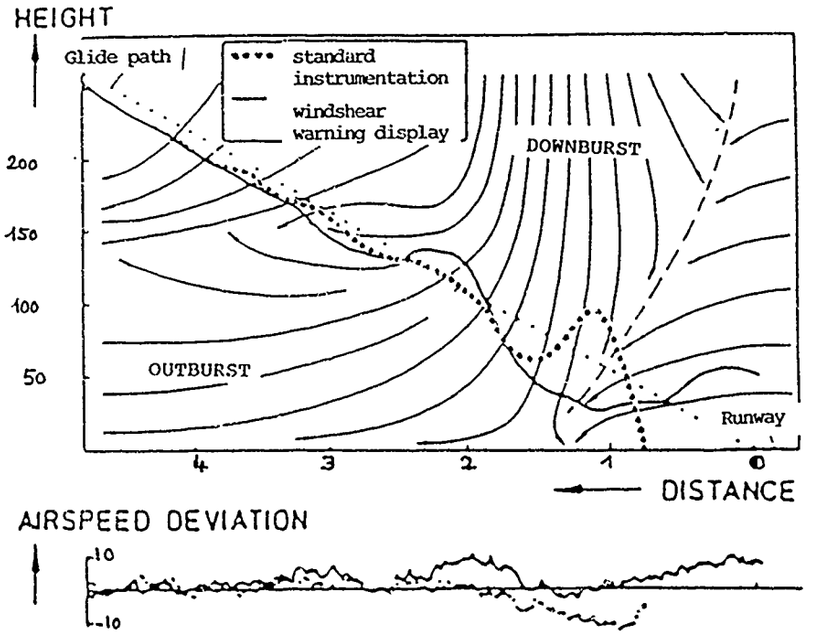

FROM PAPER 7 SHAENZER . GE

Fig. 21 : Flight simulator approach in wind shear conditions, less experienced airline pilot

16

aerospatiale — AUDIO AND VISUAL WARNING — DIVISION AVIONS

GROUND TEST 1 or 2 FAC ENGAGED
Engine not running, perform Lamp test

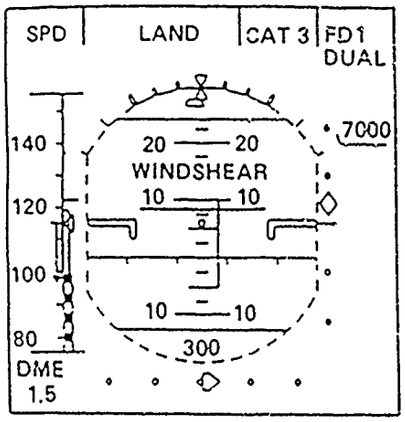

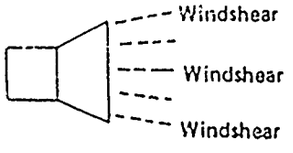

FROM PAPER 9 BONAFE . P

Windshear encounter non clean config.
and (from take off to 1000 Ft or from 1000 Ft to 50 Ft)
and WSW available 1 or 2 FAC ENGAGED.

Aural :Windshear 3 times when WSW gets on either FAC 1 or 2.

Visual :Windshear red on both PFD when WSW gets on either FAC 1 or 2 until WSW condition gets off both FAC 1 and 2 plus 15 s.

17

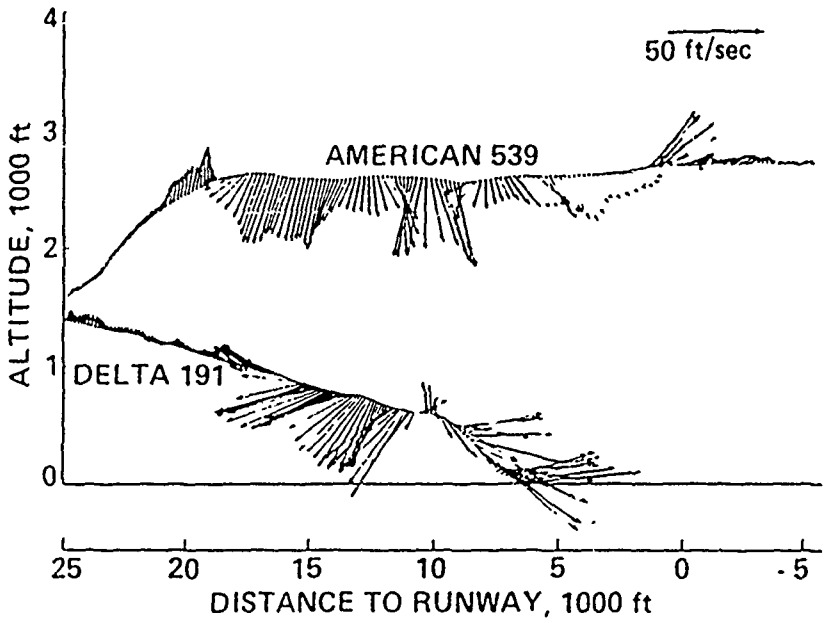

Figure 9. Wind vectors at the Dallas/Ft.Worth Airport, August 1985, reconstructed from flight records of two aircraft.

18

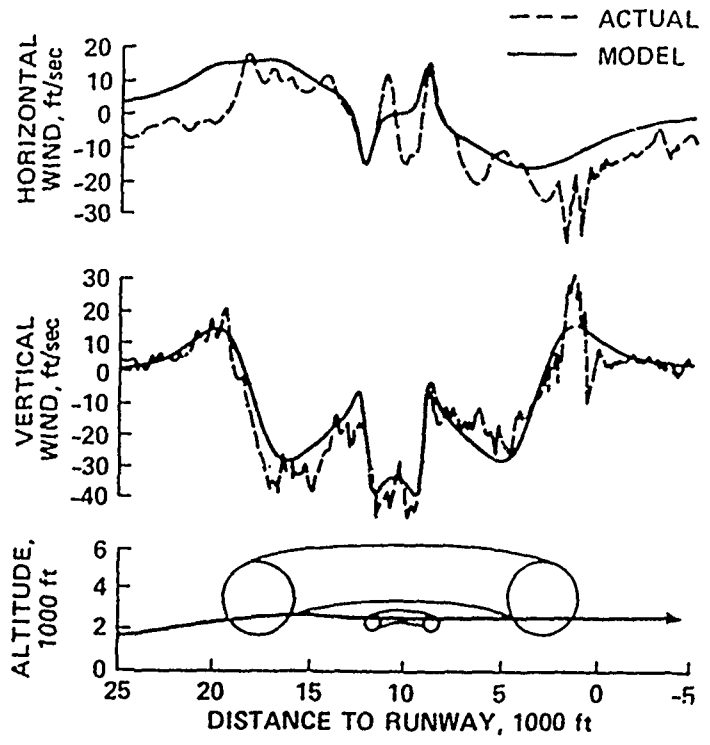

Figure 10. Multiple-vortex-ring model of the DFW microburst.

19

DOWN BURST CREW PROCEDURE:

1. AVOID DOWN BURST IF YOU CAN

2. IF YOU ARE IN A DOWN BURST:

   - pull up ,attitude 15°

   - full throttle

   - forget all previous experience

20

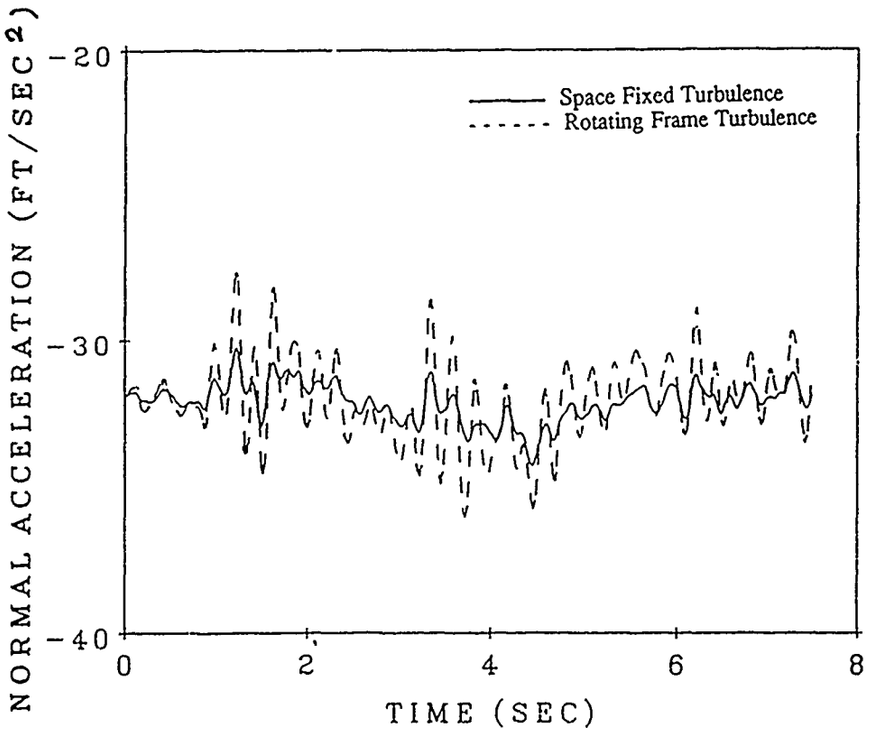

Figure 12. Effect of Turbulence on the Black Hawk Helicopter Normal Acceleration Response for L/R = 10.

FROM PAPER 18 SCHRAGE IVR PRASAD GAONKAR . USA

21

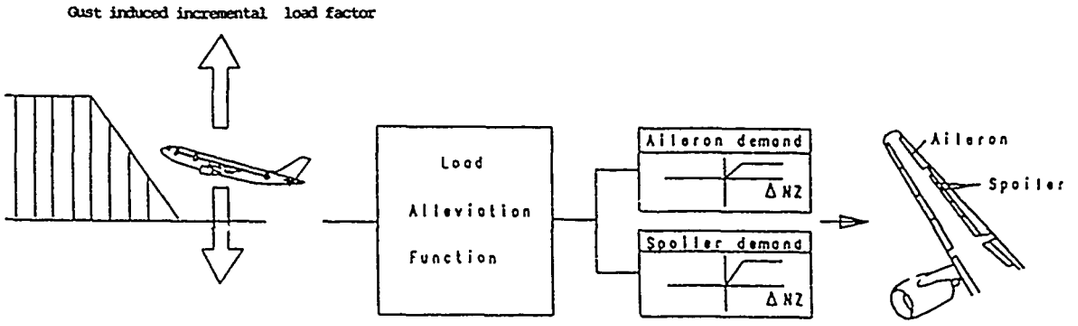

Figure 5. Gust Load Alleviation Function

FROM PAPER 14 MOBES MOLZOV . GE

22

PROTECTION SYSTEM OF THE A320

- stall protection:flying at CL max is possible

- alpha floor = automatic triggering of full thrust at high alpha or when the pilot pulls the pitch control

+

in the future

windshear warning ,and automatic reaction system

23

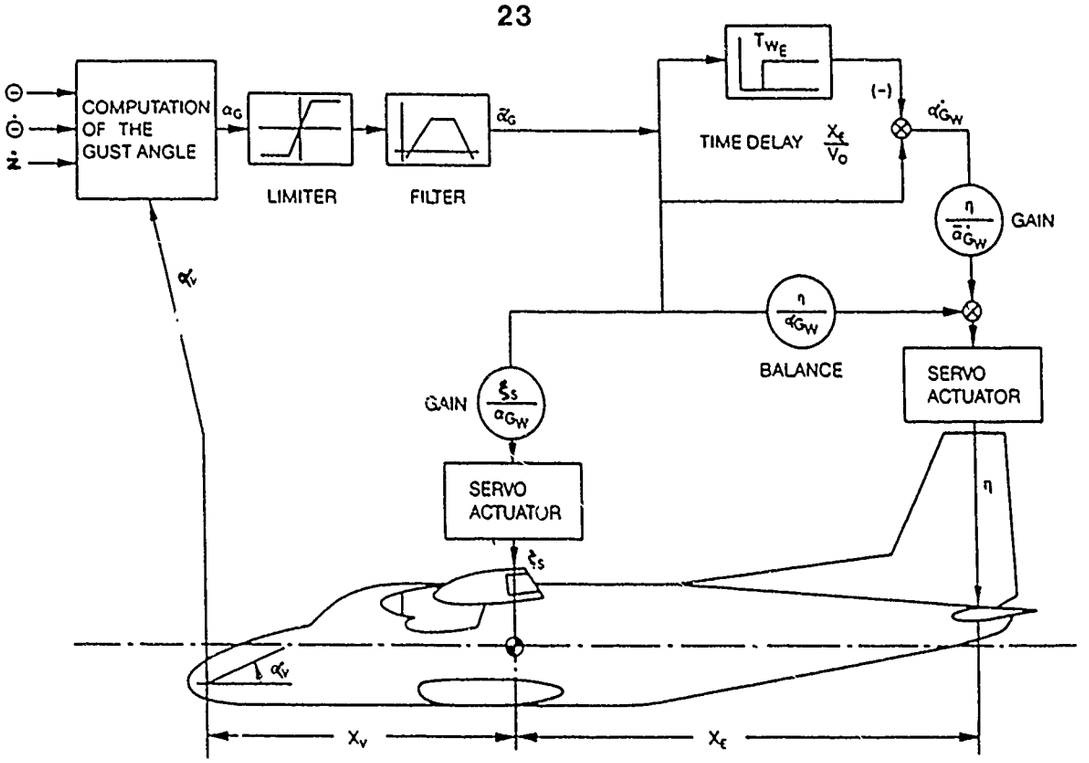

Fig. 2: Functional Diagram of the Gust Alleviation System OLGA

FROM PAPER 16 BOERET WINTER . GE

24

AGARD AASC n°19 "All Weather capability of combat aircraft"

◇ infra red systems only for dry air nights very reduced range in weather

◇ electromagnetic sensors more promising:

- λ factor wavelength compared to diameter of water droplets or cristal

- millimetric wave radars better but power must increase to get adequate range

- VHF frequencies satisfactory for navigation only (picture of target not possible)

◇ navigation systems :ATC radars , or Global Positioning System (NAVSTAR) or similar systems as the GPS using groung station (for limited coverage)

25

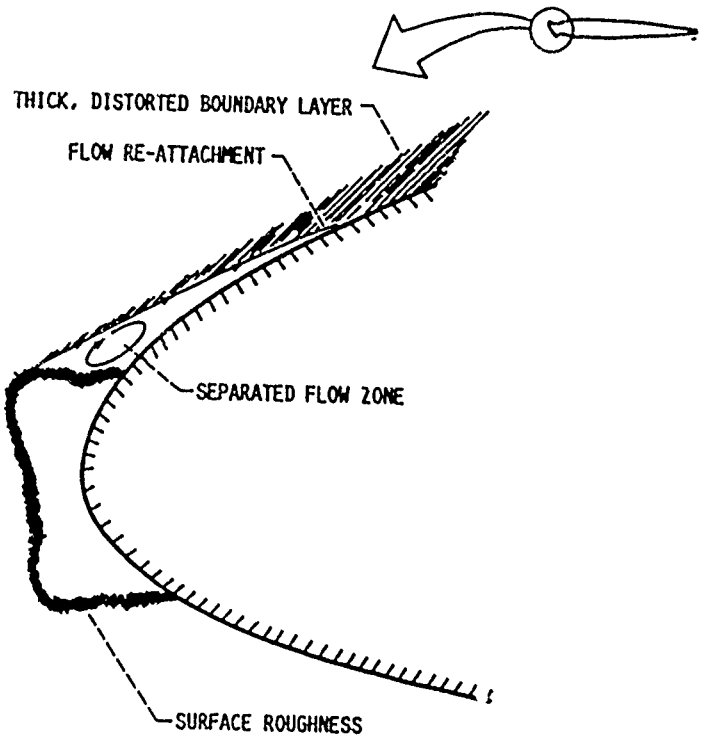

FIGURE 7. - KEY ASPECTS OF AIRFOIL ICING.

FROM PAPER 22 REINMANN SHAW RANAUDO - USA

26

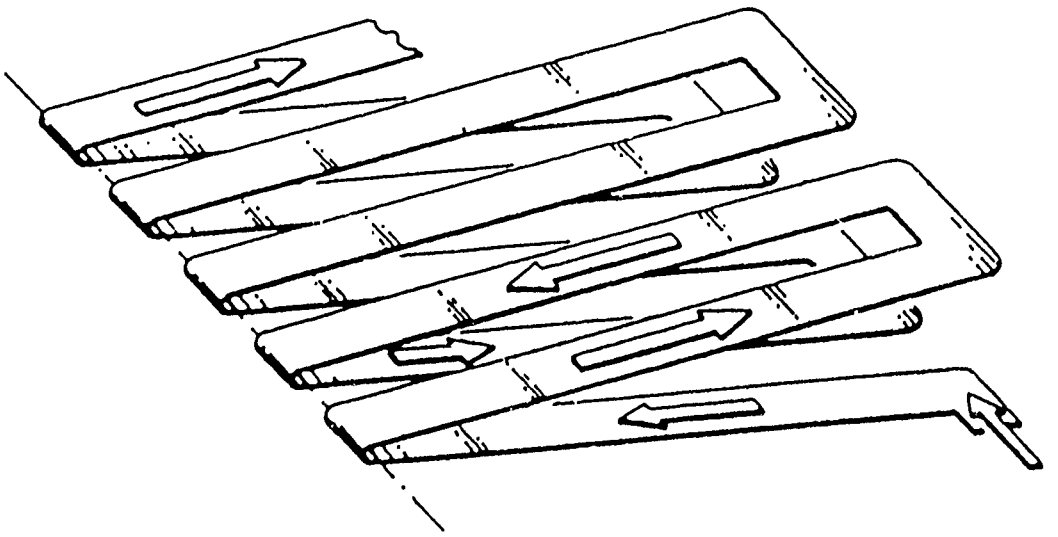

FIGURE 2. - EESS CONDUCTOR GEOMETRY.

FROM PAPER 22 REINMANN SHAW RANAUDO . USA

27

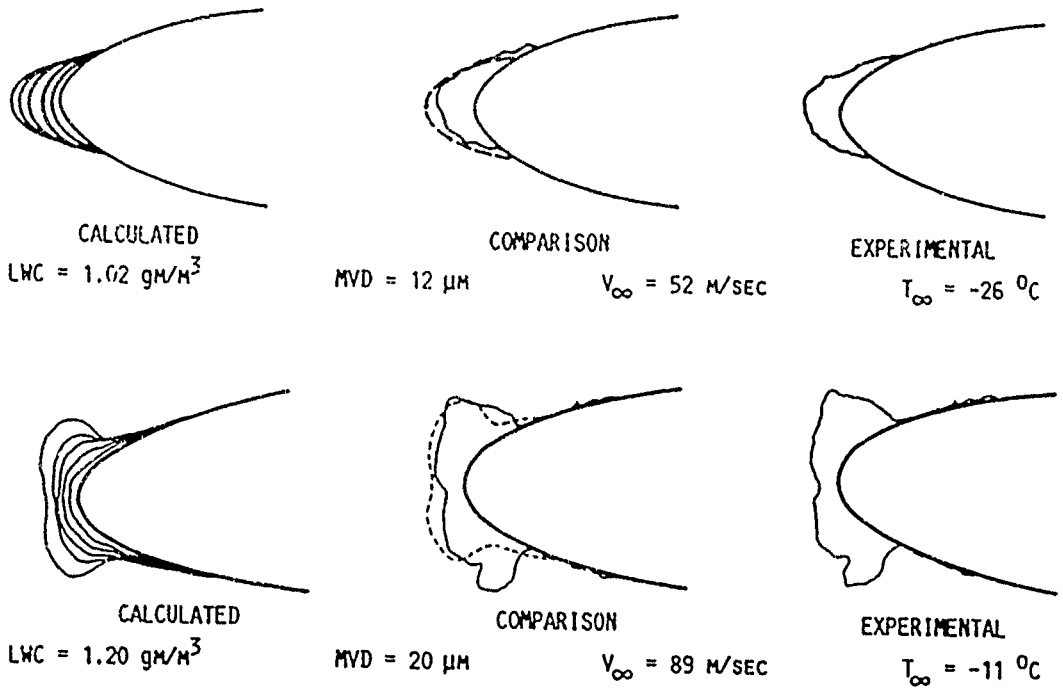

FIGURE 10. - COMPARISON OF ICE SHAPE PREDICTIONS WITH AIRFOIL ICING DATA.

FROM PAPER 22 REINMANN SHAW RANAUDO - USA

28

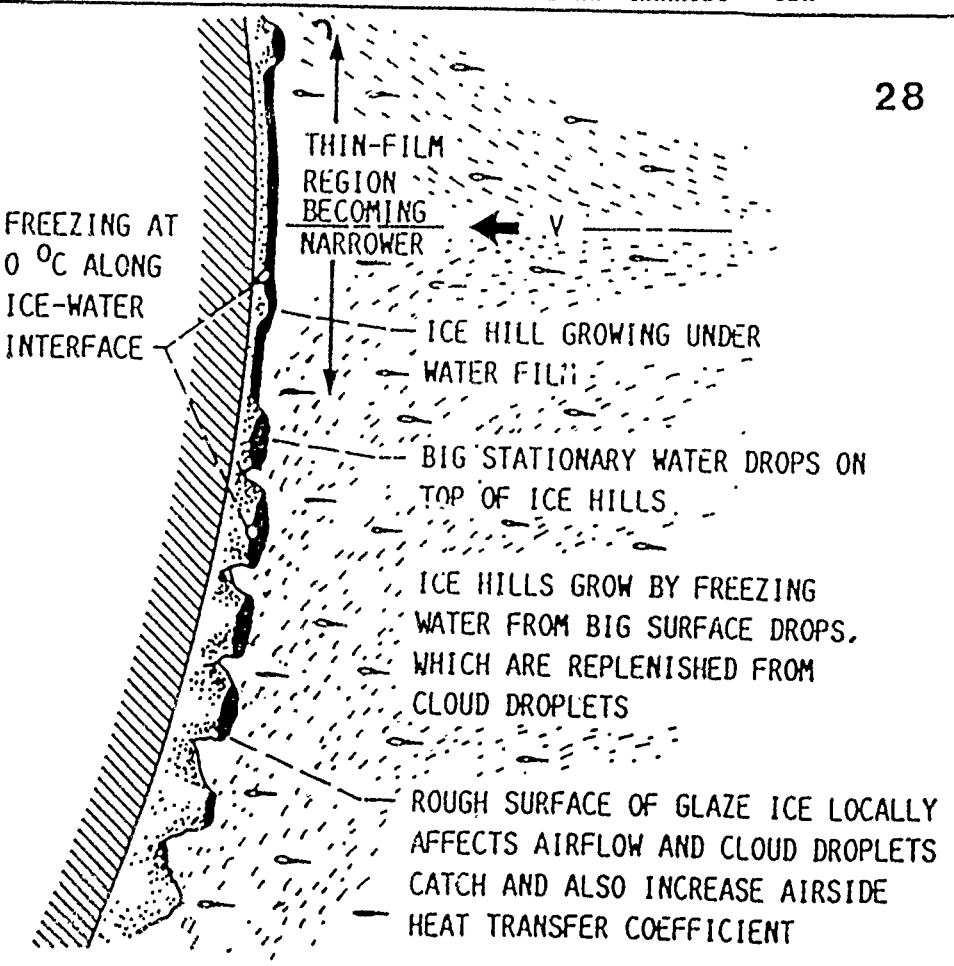

(B) FREEZING OCCURRING.

FIGURE 15. - PROPOSED NEW PHYSICAL MODEL FOR ICING PROCESS.

FROM PAPER 22 REINMANN SHAW RANAUDO . USA

29

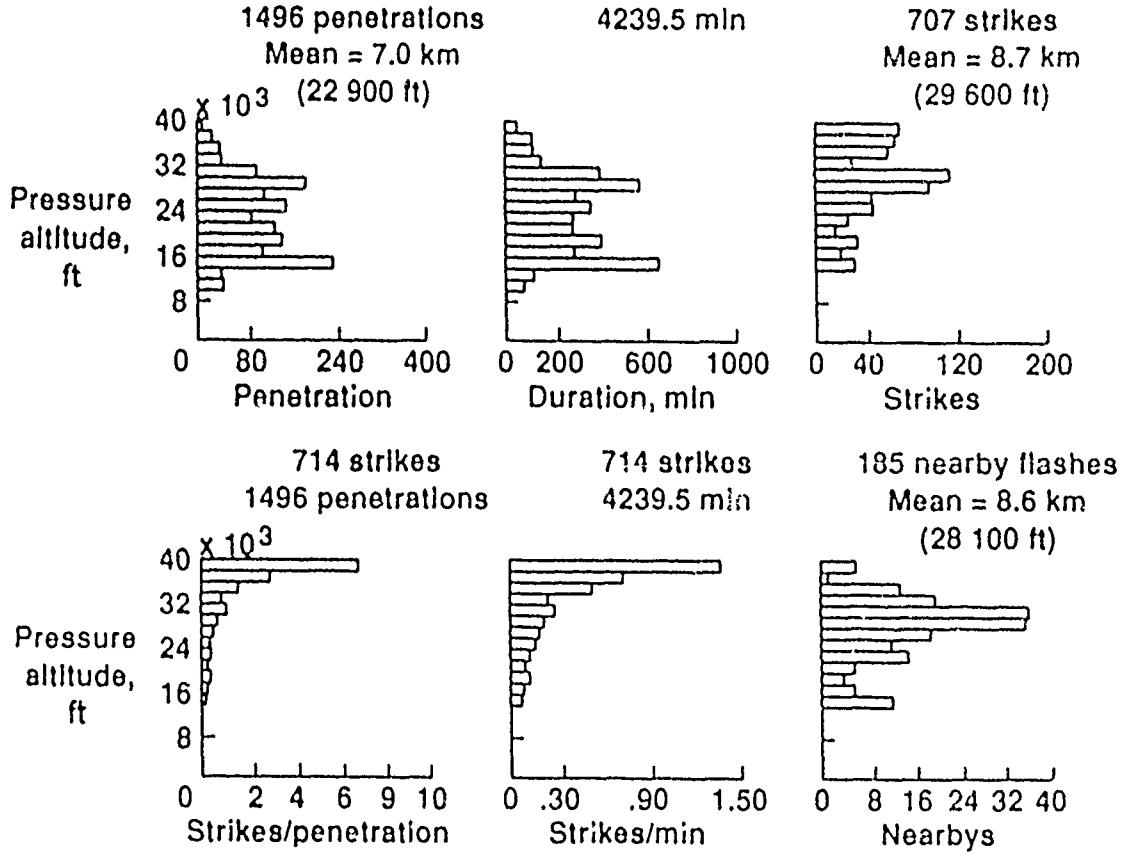

Fig 4 - THUNDERSTORM PENETRATIONS AND LIGHTNING STATISTICS AS A FUNCTION OF PRESSURE ALTITUDE FOR NASA STORM HAZARDS 1980- 1986 FROM PAPER 26 FISHER . USA

30

EFFECT OF EXTERNAL RADIATIONS ON AIRCRAFT SYSTEMS

(extracted from the J.A.A. Requirements applied to the A320)

The external threat frequency bands and corresponding average end peak levels that shall be used to establish the internal threat levels are defined as follows

Frequency range	Mean level volt /meter	Peak level kilovolt /meter
10 kiloHertz-6MegaHertz	100	
6 MegaHertz-30MegaHertz	200	
30MegaHertz-200MegaHertz	50	
200 to 400MegaHertz	50	
400MegaHertz-1GigaHertz	400	6
1 to 3 GigaHertz	200	6
3 to 8 GigaHertz	400	6
8 to 30 GigaHertz	600	6

THE EFFECT OF WING ICE CONTAMINATION ON ESSENTIAL FLIGHT CHARACTERISTICS

by
R. E. Brumby
Deputy Chief Design Engineer
MD-80/DC-9 Program
Douglas Aircraft Company
3855 Lakewood Boulevard
Long Beach, California 90846, USA

SUMMARY

Contamination of critical aerodynamic surfaces by ice, frost, and/or snow has been identified as the probable cause of a significant number of aircraft accidents. In most cases, the ice contamination has not been large ice accretions on the leading edges or thick layers of adhering snow on the top of the wings. Rather, dangerous reductions in stall margins and handling qualities can occur because of ice-related roughness equivalent to that of medium-grit sandpaper. This paper describes typical effects of such roughness on lift, drag, and pitching moment, and the corresponding effects on longitudinal and lateral control characteristics during rotation and liftoff. Of great importance is that the visual, aural, and tactile clues signaling a developing critical situation occur within a very few seconds, and usually do not correspond to any for which a flight crew has been trained or has previously experienced.

DISCUSSION

In recent years, a number of weather-related accidents has stimulated a renewed interest in the effects of adverse weather on aerodynamics. Among these effects is the contamination of aerodynamic surfaces by ice, frost, and/or snow. While such contamination can adversely affect most basic aerodynamic parameters, this presentation focuses primarily on the overall degradation of essential flight characteristics during the takeoff of an airplane that has an ice-contaminated wing.

Most regulations typically prohibit takeoff with ice on the critical surfaces of the aircraft (Table 1). For various reasons, however, flight crews will initiate a takeoff with some form of ice contamination on the wings and control surfaces. The result can range from little or no significant control problems to total disaster.

A somewhat in-between case is shown in Figure 1. This airplane made a normal approach into Sioux City, Iowa, in 1968. Mild icing was encountered during the approach, but the flight crew elected not to turn on the airfoil ice protection. During the turnaround, a light freezing drizzle was falling. The flight crew

Table 1
Federal Air Regulations Applicable to Ice, Frost, or Snow Accumulations Prior to Takeoff

PART 91 - GENERAL OPERATING AND FLIGHT RULES
§91.209 OPERATING IN ICING CONDITIONS

(a) NO PILOT MAY TAKE OFF AN AIRPLANE THAT HAS:

(1) FROST, SNOW, OR ICE ADHERING TO ANY PROPELLER, WINDSHIELD, OR POWER PLANT INSTALLATION, OR TO AN AIRSPEED, ALTIMETER, RATE OF CLIMB, OR FLIGHT ATTITUDE INSTRUMENT SYSTEM;

(2) SNOW OR ICE ADHERING TO THE WINGS, OR STABILIZING OR CONTROL SURFACES, OR

(3) ANY FROST ADHERING TO THE WINGS, OR STABILIZING OR CONTROL SURFACES, UNLESS THAT FROST HAS BEEN POLISHED TO MAKE IT SMOOTH

PART 121 - CERTIFICATION AND OPERATIONS
§121.629 OPERATION IN ICING CONDITIONS

(a) NO PERSON MAY DISPATCH OR RELEASE AN AIRCRAFT, CONTINUE TO OPERATE AN AIRCRAFT EN ROUTE, OR LAND AN AIRCRAFT WHEN IN THE OPINION OF THE PILOT IN COMMAND OR AIRCRAFT DISPATCHER (DOMESTIC AND FLAG AIR CARRIERS ONLY) ICING CONDITIONS ARE EXPECTED OR MET THAT MIGHT ADVERSELY AFFECT THE SAFETY OF THE FLIGHT

(b) NO PERSON MAY TAKE OFF AN AIRCRAFT WHEN FROST, SNOW, OR ICE IS ADHERING TO THE WINGS, CONTROL SURFACES, OR PROPELLERS OF THE AIRCRAFT

Figure 1. There Is No Such Thing as "A Little Ice"

was advised by ground maintenance personnel that there was ice on the wing and asked if the airplane should be de-iced. The flight crew declined the offer and proceeded with the takeoff. As the landing gear began to retract, the aircraft rolled violently to the right. Rudder and aileron application brought the right wing up; however, the roll continued to the left until the left wing contacted the runway. The captain succeeded in leveling the aircraft before it hit the ground about 110 feet beyond the end of the runway and skidded into a grove of trees where it came to rest, as shown in the figure.

Table 2 lists a number of icing-related accidents. While it is by no means inclusive, it does illustrate that ice contamination is quite democratic, adversely affecting straight-wing aircraft such as the Nord 262 and numerous general aviation aircraft; small turbojet aircraft with conventional airfoils such as the Learjet; larger aircraft with conventional airfoils such as the F-28, DC-9-10, and DC-8; and aircraft with leading edge high-lift devices such as the 737.

The most predominant adverse effect of ice contamination is on the lifting characteristics of the wing. It may be recalled that wing lift coefficient varies with angle of attack, as shown in Figure 2. Under normal conditions, the airflow over a wing smoothly follows the shape of the wing, as shown in the lower photograph, and lift varies directly with the angle of attack. At some fairly high angle of attack, the airflow begins separating from the wing, causing the lift curve to become nonlinear, or "break." When the airflow is essentially fully separated, as shown in the upper photograph, the wing is considered fully stalled. Between the point where the airflow begins separating and full stall is a region often called "stall onset," where flight characteristics become increasingly degraded as the angle of attack increases.

The normal variation of lift with angle of attack can be significantly altered by ice contamination. As shown in Figure 3a, the typical effect is to alter the variation of lift with angle of attack, reduce the maximum lift capability of the wing, and cause

Table 2
Some Takeoff Accidents Where Wing Ice Contamination Is Considered to Be a Contributing Factor

DATE	AIRLINE	LOCATION	ACFT TYPE	PRECIPITATION/OBSERVATIONS
27 DEC 68	OZARK	SIOUX CITY	DC-9-10	LIGHT FREEZING DRIZZLE
26 JAN 74	THY	CUMAOVAS, TURKEY	F28	PROBABLE CAUSE FROST ACCRETION ON THE WINGS
03 JAN 77	JAL	ANCHORAGE	DC-8-62	FOG
04 JAN 77		FRANKFURT	737	LIGHT SNOW/25-DEGREE WHEEL REQD AFTER LIFTOFF. RIME ICE OBSERVED ON WING
27 NOV 78	TWA	NEWARK	DC-9-10	BLOWING RAIN AND SNOW
20 DEC 78	N40SN	MINNEAPOLIS	LEARJET	PROBABLE CAUSE: SNOW AND ICE ON WINGS
19 JAN 79	N73161	DETROIT	LEARJET	PROBABLE CAUSE: PREMATURE STALL CAUSED BY ACCUMULATION OF WING ICE
12 FEB 79	ALLEGHENY	CLARKSBURG	NORD 262	LIGHT SNOW - FROZEN SNOW PHOTOGRAPHED ON EMPENNAGE AFTER ACCIDENT
18 FEB 80	REDCOTE	BOSTON	BRISTOL 253	LIGHT SNOW
13 JAN 82	AIR FLORIDA	WASH D C.	737	MODERATE-TO-HEAVY SNOWFALL
05 FEB 85	AIRBORNE	PHILADELPHIA	DC-9-10	LIGHT FREEZING RAIN, ICE AND SNOW PELLETS, FOG
12 DEC 85	ARROW AIR	GANDER	DC-8-63	LIGHT FREEZING DRIZZLE, SNOW GRAINS
15 NOV 87	CONTINENTAL	DENVER	DC-9-10	MODERATE SNOW, FOG
18 JAN 88	N2614U	NEW MEXICO	CESSNA 402	PROBABLE CAUSE: ICE/FROST REMOVAL INADEQUATE
06 FEB 88	N2832J	CALIFORNIA	CESSNA A188B	PROBABLE CAUSE: ICE/FROST REMOVAL INADEQUATE
23 DEC 88	N5570H	MONTANA	PIPER PA-11	PROBABLE CAUSE: WING ICE
10 MAR 89	AIR ONTARIO	DRYDEN	F28	HEAVY SNOW
25 NOV 89	KOREAN AIR	KIMPO	F28	DENSE FOG, ICE ON THE WING

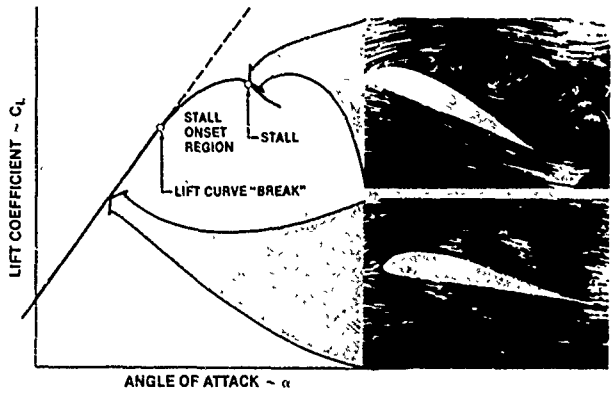

Figure 2. Airflow Over an Airfoil and Its Effect on Lift

the wing to stall at a lower than normal angle of attack. As will be shown shortly, these effects can be quite large.

Wing ice contamination can also significantly affect the airplane drag as shown, again typically, in Figure 3b. The effects on drag can be large enough that the difference between available thrust and drag can adversely affect the airplane's climb capability. This not only would make it difficult for the airplane to clear obstacles by the required distances, it could possibly result in the airplane's inability to climb at all if an engine fails during takeoff.

Figure 4 depicts a typical total airplane pitching moment curve. For an airplane trimmed for takeoff, the stabilizer is set to balance the moments due to both aerodynamic forces and center of gravity location so that the stick force at climb-out speed ranges from none to a slight pull. This balance is upset by wing ice contamination, particularly on contemporary aircraft with tapered, swept wings. With contamination on the wings, the aircraft will increasingly behave as if it was mistrimmed in the

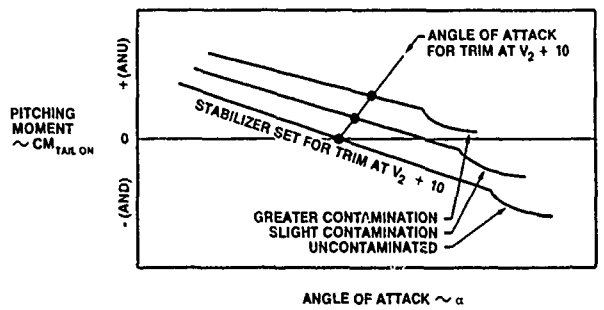

Figure 4. Effect of Wing Ice Contamination on Pitching Moment

airplane nose-up direction as the angle of attack is increased. This will result in the aircraft's pitching up more rapidly than normal during the takeoff rotation, and will require an abnormal push force to maintain the desired airspeed during climb. As with other effects, this pitch-up tendency becomes more pronounced as the amount of ice contamination increases.

During a normal takeoff, the aircraft speed schedules are established for angles of attack below that for stall onset or activation of stall-warning devices dependent on angle of attack, such as a stick shaker (Figure 5a). However, for an airplane with ice contamination, not only does stall onset occur at a lower than normal angle of attack, the airplane angle of attack must be increased in order to produce the required lift at normally scheduled speeds (Figure 5b). This compounding effect rapidly results in the aircraft's operating into the "stall onset" part of the lift curve (described earlier), and the increasingly unsteady airflow over the wing results in correspondingly degraded lateral stability, requiring larger and larger control wheel inputs to keep the aircraft from rolling off. As the amount of contamination increases, the airplane becomes increasingly unstable, eventually stalling without stick shaker activation at speeds normally scheduled for takeoff (Figure 5c).

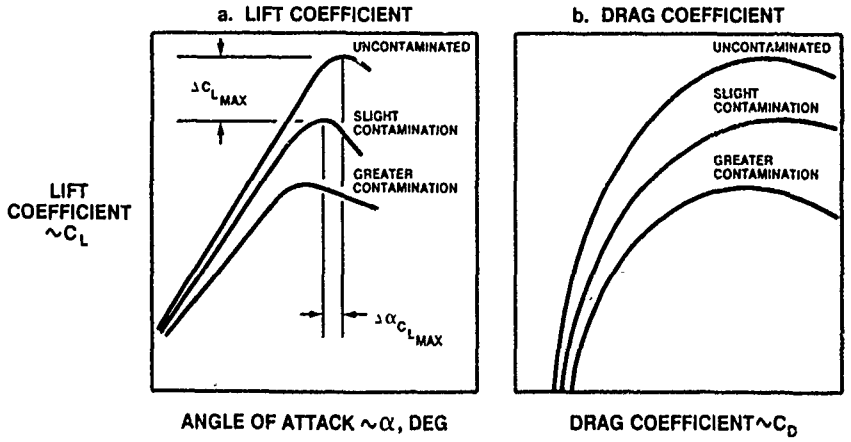

Figure 3. Effect of Wing Ice Contamination on Lift and Drag Coefficients

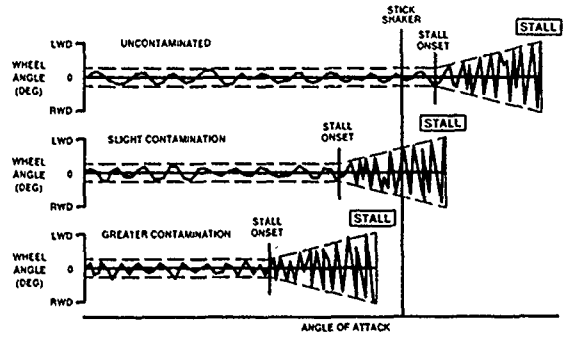

Figure 5. Effect of Wing Ice Contamination on Lateral Control Characteristics

Figure 6 shows an empirical correlation of lift loss due to wing surface roughness, including ice contamination. It is interesting to note that this simple correlation encompasses data representing a Reynolds Number range from $6x10^5$ up to $29x10^6$ and airfoil shapes ranging from simple symmetrical sections to those representative of second-generation turbojet aircraft (see Table 3).

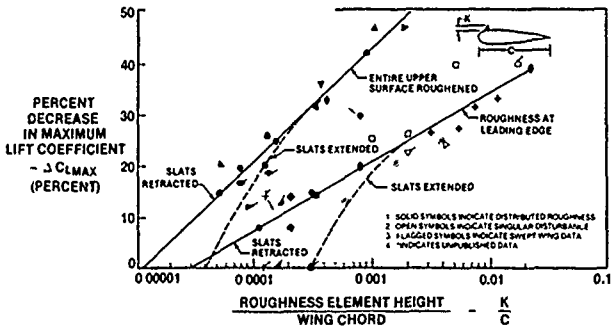

Figure 6. Correlation of the Effect of Wing Surface Roughness on Maximum Lift Coefficient

The lower line in Figure 6 shows the lift loss due to a localized strip or narrow band of contamination on the leading edge. Much of the data for the lesser amounts of contamination have been obtained from maintenance or flight training experience where some form of contamination such as insect debris, chipped paint, or burred rivets caused premature stall when the slats were retracted, but caused little or no noticeable effect when the slats were extended. Wind tunnel data indicate that as the contamination on the leading edge becomes larger, such as for in-flight ice accretions on the leading edge, slat extension will no longer recover the lift losses.

The upper line in Figure 6 shows the lift loss due to roughness on the entire upper surface of the wing, such as might be caused by frost, snow, or freezing drizzle while the aircraft is on the ground. Of particular note is the very large degradation for even the smaller amounts of contamination. Also of interest are the relatively recent data developed by Boeing during flight testing of second- and third-generation transport aircraft with slats extended. These data suggest that with essentially the entire wing upper surface covered with even small amounts of contamination, slat extension provides little or no recovery of lift losses.

Although Figure 6 shows a significant difference in lift loss between a narrow band of roughness at the leading edge and roughness over the entire upper surface, it is worthy to note that recent unpublished data for slight roughness extending aftward from the leading edge to about 7-percent chord on both the upper and lower surfaces (as might occur during a mild icing encounter) can cause lift losses similar to those caused by a fully roughened upper surface.

Figure 7 expands the data from Figure 6 into an operationally meaningful percent increase in stall speed. From this figure, the importance of maintaining the "clean wing" philosophy begins to show, because it becomes readily apparent that it takes only a relatively small amount of roughness on the wing upper surfaces to cause large increases in stall speeds even with slats extended. Further expanding the data to compare the measure of roughness (K/C) with various grades of abrasive paper, an estimate can be made (Figure 8) of the stall speed increase that would occur on an aircraft about the size of a DC-9, 737, or BAC-111 if the wing upper surface was contaminated by ice having the roughness of various grades of abrasive paper. Those familiar with the icing roughness that can occur during a freezing drizzle or when snow has partially melted and then refrozen to a surface will probably agree that this range of roughness is not at all unusual under such conditions. With the stall speed increases shown in Figure 8, stall warning margins and margins to stall decrease markedly or disappear altogether.

Table 3
References for Figure 6

SYM	REYNOLDS NO	TYPE OF ROUGHNESS	REFERENCE
	26×10^6	SAND GRAIN BAND	"THEORY OF WING SECTIONS" (ABBOT)
	31×10^6	PROTRUDING STRIP	NACA TR446
	31×10^6	MULTIPLE GROOVES	NACA TN457
	31×10^6	CARBORUNDUM GRIT	NACA TN457
	5×10^6	SAND GRAINS	"AERODYNAMSCHE PROFILE" (RIEGELS)
	63×10^5	WIRE MESH ON SURFACE	NACA TM375
	31×10^6	FWD FACING STEP	NACA TN457
	31×10^6	PROTRUDING STRIP	NACA TR446
	31×10^6	PROTRUDING STRIP	NACA TR446
	31×10^6	PROTRUDING STRIP	NACA TR446
	36×10^6	CARBORUNDUM GRIT	NACA TN457
	—	FROST (IN ICING TUNNEL)	NACA TN2962
	24×10^6	INSECT CONTAMINATION	FLIGHT TRAINING INCIDENT (DC-9)
	45×10^6	SIMULATED TAILPLANE ICE	DC-9*
	55×10^6	SIMULATED TAILPLANE ICE	DC-10
	78×10^6	SIMULATED DEICER BOOT*	C-133
	70×10^6	CARBORUNDUM GRIT	R&M 1703
	24×10	CHIPPED PAINT ON L.E.*	DC-9
	29×10^6	BALLOTINI	NPL AR1308
	24×10^6	BURRED RIVETS ON L.E.	DC-9
	32×10^6	SIMULATED FROST	FFA RPT AU 902
	18×10^6	SIMULATED WING ICE	FFA RPT AU-995
	—	SIMULATED ICE ROUGHNESS	ICAO BUL OCT 77
	$\sim 24 \times 10^6$	SIMULATED FROST	(P737) BOEING AIRLINER, OCT 83 (FROST 8)
		SIMULATED FROST	(737) VKI LECTURE (FROST 2)
		SIMULATED FROST	(757) VKI LECTURE (FROST 2)
		SIMULATED FROST	(767) VKI LECTURE (FROST 2)
		DC-9 WIND TUNNEL	TEST LB-155AN

NOTE: 737 AND 767 WITH MID SLATS

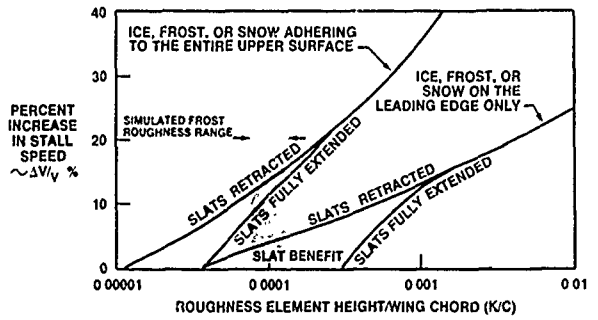

Figure 7. Approximate Effect of Wing Ice Contamination on Airplane Stall Speed

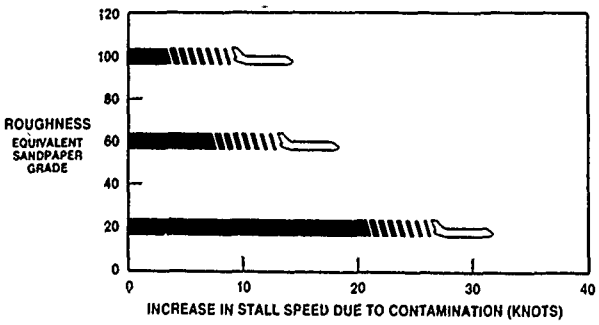

Figure 8. Approximate Effect of Wing Upper Surface Ice Contamination on the Stall Speed of a Typical Small Turbojet Transport

As noted earlier, the increases in stall speed also occur at much lower than normal angles of attack (Figure 9). This can have at least two adverse effects. First, many contemporary stall warning systems are actuated at prescheduled angles of attack. If wing ice contamination causes a stall before this prescheduled angle is reached, the flight crew will receive no warning of impending stall. Second, the reduced stall angle of attack compounds the problem of the tendency of an ice-contaminated airplane to pitch up during rotation, increasing the risk of overshooting the stall angle shortly after liftoff.

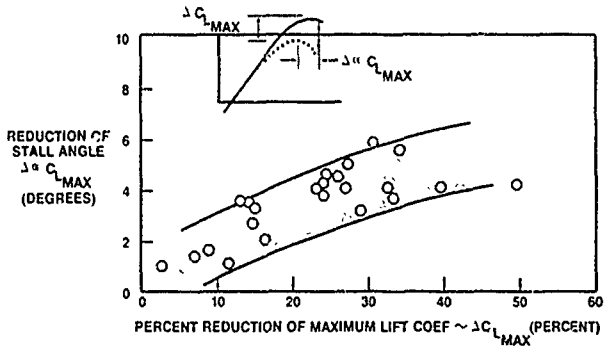

Figure 9. Reduction of the Angle of Attack at Stall Due to Wing Surface Roughness

The overall effects of wing ice contamination on various flight characteristics of an aircraft during takeoff are summarized in Figure 10. In this figure, stick force is the amount of push or pull on the control column required to manage the pitch attitude of the aircraft. Pitch attitude is the angle of the airplane with respect to a horizontal reference plane; angle of attack is the angle of the airplane with respect to its flight path; and wheel angle is the rotation of the control wheel required to manage the bank, or roll attitude, of the airplane.

For an uncontaminated airplane, the stick force to rotate and acquire the target climb speed are typically as shown by the solid line. The pitch attitude and angle of attack increase to their normal values, and there are no abnormal control wheel requirements except those caused by outside influences such as crosswinds or gusting.

The scenario changes for an ice-contaminated airplane. Part way through the takeoff rotation, the aircraft begins pitching up at a faster than normal rate, as shown by the dashed line in Figure 10. If the flight crew is familiar enough with the airplane's normal characteristics, it might recognize the abnormal rate of rotation and counter it with an immediate forward push on the control column. If done in sufficient time, there should be little pitch attitude and angle of attack overshoot into the stall onset region, and any roll perturbations will probably be controllable with prompt wheel input. If the angle-of-attack overshoot is successfully transitioned, forward pressure will likely be required to maintain the target climb speed until the stick force is trimmed out. Failure to recognize any abnormal increases in the rotation rate at, or immediately following, liftoff can result in significant angle-of-attack overshoot, accompanied by abrupt roll excursions and aerodynamic stall close to the ground.

Of great importance is the time span in which the adverse handling characteristics are manifested. Typical certified takeoff performance is based on a rotation rate of about 3 degrees per second (liftoff normally occurs at about 7 to 9 degrees pitch attitude). It is in the vicinity of liftoff attitude that the abnormal pitch-up due to ice contamination begins to become increasingly apparent and, since the airplane's angle of attack is increasing at much higher rates than in any other part of the normal flight envelope, the airplane can reach stall onset angles a very few seconds after liftoff, with full stall occurring only a second or two after that. Thus, the flight crew of an ice-contaminated airplane is placed in a situation where the visual, aural, and tactile clues of a developing critical situation occur within a very few seconds. Since this does not correspond to any situation for which they have been trained or may have previously experienced, attempting takeoff of an ice-contaminated aircraft can result in an unacceptable safety hazard.

CONCLUSION

From an aerodynamic viewpoint, there is no such thing as "a little ice." Strict attention should be focused on ensuring that critical aircraft surfaces are free of ice contamination at the initiation of takeoff.

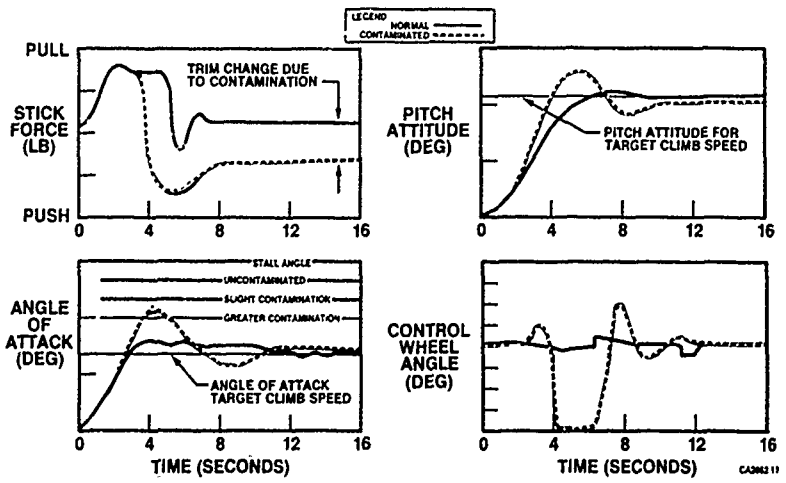

Figure 10. Effect of Wing Ice Contamination on Longitudinal Control Characteristics

LOW TEMPERATURE ENVIRONMENT OPERATIONS OF TURBOENGINES (DESIGN AND USER'S PROBLEMS)

by

Professor R.Jacques
Royal Military Academy
30 Avenue de la Renaissance
1040 Brussels
Belgium

1. Introduction.

The Propulsion and energetics panel held its symposium on "Low Temperature..." in the week from 8 to 12 october 1990.

A total of 33 conferences were presented on different problems relating to low temperature. I will not mention all the papers in this PEP symposium, but I shall try to summarize and link together the subjects and results which can be of interest to the aerodynamists, to whom I have the honour of speaking today. I thank the FDP chairman for inviting me and hope to draw your attention to the work of the PEP people without betraying the authors. At the end of this paper one can find the contents and the numbering of the papers presented at the PEP meeting. In this text I refer to these numbers.

2. Operational experience on icing.

The first problem that worries the engine engineer is closely related to your meeting: the ice build up on parts of the engine and air intake. This ice modifies the flow in front of the compressor and the airflow through the blade passages and can induce the stall and surge of the compressor. Ice pieces can detach in the front of the engine, be ingested and destroy or modify the blades shape. This can lead to unacceptable imbalance and to efficiency losses. In case of ingestion of snow paquet, a flame out can occur. As put by the first speaker, Colonel Summerton (1), in his speech on the experience of the LYNX helicopter in Norway, a normal size snowball is capable of flaming out a GEM engine, a 15cc lump of ice can cause serious damage to the low pressure compressor.

Mr Meijn of FOKKER AIRCRAFT (5) explained the experience with a turboprop in the 2000 hp class. He stressed the fact that several so-called flame-out incidents occurred in service during winter periods although the engine was qualified in the icing conditions prescribed by FAR and JAR. Extensive ground testing of the engine indicated less tolerance to ice ingestion than had been demonstrated in engine certification tests. Using commercially available miniature videosystems (fig. 1) mounted in the air intake duct, it was possible to observe some ice accretion on a seal cavity until aerodynamic forces prevailed over the adhesive forces between ice and duct wall, resulting in a periodic shedding. This would lead to a flame out. This ice accretion was formed mainly in wet snow conditions with OAT= -7° to -2°C and mean altitudes above 10000 ft. In these conditions no or little ice was collected on windshield wipers, wing leading edges and air intake lip. An engine air intake having an internal bifurcation or any other stagnation area may be prone to ice accumulation in wet snow conditions. These are generally not identified by the flight crew in the absence of external ice accretion.

Another example of this ice build up inside the air intake was given by REARDON of the Naval Air Propulsion Center (28). The F14 Aircraft engine experienced foreign object damage from ice ingestion which occurred during the carrier's landing and arrestment when ice was shed due to the shocks. The engine inlet duct is shown in figure 2. The compression ramp boundary layer is bled through a throat bleed slot and dumped overboard through the bleed/bypass door. Ice accumulated on the leading edge of the third ramp when ramp 1 and 2 were stowed as they were in low Mach conditions, this build up being a function of the amount of bleed air.

A similar surprise on a small turboprop engine was experienced by engine CT7 from G.E., as explained by Mr Blair from G.E. (20). Despite successful engine test cell and aircraft natural icing certification tests, an unacceptable level of foreign object damage was caused by ice ingestion. This engine has an integral inertial particle separator (IPS). Forward of the inlet, ice accumulates on the spinner and the propellor cuffs and inside the duct, on the inlet protection device (IPD), splitter lip and in the IPD bowl which filled up with ice (figure 3). Duct improvements, one of these being a heated IPD exhaust which reduced the FOD rate, still didn't reach the target FOD rate. As it was not possible to achieve substantial IPS performance gains within the confines of a compatible installation, the final solution was to develop ice FOD-resistant compressor blades.

3. Icing on turbo engines.

Particular attention was given to the operation of helicopter engines in icing conditions and three authors gave their experience. Small gasturbines are much more vulnerable to foreign object damage (FOD) and flame-out due to ice ingestion than the bigger turbofan engines. Flame-out can also occur due to inlet blockage by ice or snow and resulting air starvation.

Jones of Boeing Canada (6) explained the case of the inlet screens and particle separators employed as protection on the

CH113 Search and Rescue Helicopter of the Canadian Forces. The original engine inlet screen was not designed for sustained operations in an icing environment, and in these conditions the inlet screen had to be removed, resulting in an unacceptable risk of foreign object damage to the engine. New ice tolerant inlet screens have been developed and investigated and the final solution is a flat faced screen providing full time protection against FOD ingestion of particles larger than the void size. Cylindrical sides to the screen are tapered towards the inlet, forming an inverted cone. In fast forward cruise in icing conditions, the front faces ice rapidly and the air has to turn sharply to enter the sides of the cone. The sides remain clear of deposits in forward flight. The air stream sheds the majority of entrained liquid water in flowing around a sharp obstruction.

In hover the inlet flow is less unidirectional and the screen surfaces ice more uniformly. It necessitates some form of open bypass to maintain a path to feed the engine with air. The airflow distorsion at the compressor face is still acceptable. Engine cell performance tests indicated a 2% powerloss with front fan completely blocked and 75% of the sidewalls blocked. In the case when both front fan and sidewalls are completely blocked and engine air is entering solely through bypass opening, the powerloss was 37%. There is sufficient remaining power for cruise.

G.V. Bianchini of Allison Gas Turbine Division (18) presented the anti-icing system of the engine T800-LHT-800 for LH-helicopter. The engine mounted Integral Inlet Particle Separator (IPS) is a significant feature of this engine. The IPS consists of an inner dome, a casing assembly, the flow splitter, scavenge vanes and scavenge scroll. (figure 4). The large surface area results in the potential for widespread supercooled water impingement on the flow-path surface, and subsequent ice accretion. The engine's anti-icing system shall prevent ice accretion on all core flow-path surfaces of the front frame and all flow-path surfaces of the inner dome. (figure 5). The anti-icing system requires hot air from the compressor which reduces engine performance. With the anti-icing system activated in icing-conditions the power loss may not exceed 5% and the specific fuel consumption (SFC) may not increase more than 5% . The military icing test prints are given in the table underneath:

	Conditions		
	1	2	3
Engine inlet total temperature (°C)	-20	-5	-5
Mean effective drop diameter (microns)	20	20	20
Liquid water content (g/m3)	1.0	2.0	0.4
Exposure time (minutes)	10	10	60

Several anti-icing concepts were evaluated to select a system that satisfies the military or FAA requirements. After investigation, a concept of compressor split flow system was chosen. With analytical tools on heat transfer, flow system and engine performance, the required anti-ice air temperature and flow rates were determined to keep the flow-path surface at a level sufficient to prevent the icing, and the impact on engine performance was calculated. To ensure a minimal engine performance loss, a variable anti-ice flow rate was required which was obtained by a self-modulating engine mounted valve.

The test program was done on an inlet equipped with thermocouples (figure 6) and the results were compared to the analytical calculations; a comparison for a given test environment is presented in figure 7.

Mr de la Servette (35) from Aerospace presented an overview of the different air-intakes and protections against ice and snow. Aerospace optimised the concept of protection based on screens. The airflow and ice-accretion is shown in cases of high speed (V > 70 kts) and low speed (figure 8). The author highlights the danger of snow lumps detaching from the helicopter fuselage and being ingested by the engine. There is also a danger of accumulation in the inlet ducts after the inlet screen and a second screen just in front of the compressor may be necessary. This accumulation is likely to happen on a cold part of a curved duct. The author distinguishes the different critical conditions as to temperature and snow type.

The development of an anti-icing system for an inertial type inlet particle separator (IPS) by experimental methods is expensive and time consuming and leads to an anti-icing system which is not always energy efficient. Mr Mann from RR and Mr Tan from the Cranfield Institute of Technology (16) presented a predictive anti-icing design code. That could spare time in the development phase and reduce the heating requirements by 50% . The model's principal components are a Navier-Stokes flow solver, the Moore Elliptic Flow Program (MEFP) and the joint RR/Cranfield Trajectory Prediction Program. The MEFP was used in the particle separator design and as the IPS is axi-symmetric the code was run in the 2D-form. The water droplet equations of motion assume that the drag force is the only force of interaction.

E. Brook from Rolls Royce (19) presented the assessement of an engine design for icing risk. He detailed comprehensively each area of concern for the high bypass ratio turbofans. The intakes and intake ducting were already discussed (Figure 9). The non-rotating engine hardware upstream of the first rotor stage must be anti-iced because of the damage caused by ice shedding and the distorsion due to blockage of the inlet guide vanes. In the rotating stages it is impossible to provide anti-icing and the engineer has to appraise the design for its propensity to ice accumulation, how the ice will shed and the design of the surfaces on wich the ice lumps will impact.

Authors R. Henry and D. Guffond from ONERA (17) calculated the ice accretion on the inlet guide vanes (pre-rotation vanes) of a centrifugal compressor. Protection against icing is achieved by hot bleed air from the compressor and driven inside the vanes. At low engine settings, the

compressed air is at rather low temperature and is not able to avoid ice accumulation on certain parts of the vanes. A two-dimensional numerical program from ONERA was adapted to compute the ice build up on the profile. There are three distinct parts:

- a fluid dynamics computation of the flow, velocities and pressures around the vanes.
- a computation of the water droplets' trajectories for the determination of the icing surface.
- a thermodynamic balance to compute the thickness and form of the ice accumulation.

As computation in the three-dimensional field is very expensive, a two-dimensional code was used before the vanes in the (Z,R)-plan and in the (Z,θ)-plan between the vanes (figure 10).This is justified as the third component of the velocities is always small. Computation of the droplets' trajectories in the two-phase flow is based on the following assumptions:

- the flow is not influenced by the presence of a small number of droplets.
- the droplets are spherical.
- the only force on the droplet is the air-droplet interaction.

Formule: $Fg = Mg \cdot (dVg)/dt$

where: Fg = drag force
Mg = mass of the droplet
Vg = velocity of the droplet

Computation of the droplets' local captation on the impact zone showed that the captation values are low on the intrados, very high on the leading edge and that there is no captation on the extrados. The thermodynamic laws allow the computation of the ice form by determining the amount of water impacting on the zone and the wall temperature. It is based on the conservation of the mass and the heat on an elementary wall surface ds, as can be seen in figure 11. There is a clear influence of the temperature on the ice form as can be seen in figure 12, for droplets of a mean diameter of 20 µm, a liquid water content of 0.6 g/m3 and after 60 s of captation on the median height of the blades.

4.Test facilities.

The icing test facilities are necessary tools in the theoretical designs' development and in testing the engine or the inlet, or both together to demonstrate that they comply with the requirements of the icing specifications.

H. Reardon and J. Truglio (28) explained the capabilities in icing simulation at the Naval Air Propulsion Center of Trenton. The Navy specification requirements for turbofan/turbojet and turboshaft/turboprop are the baseline documents. We quote that the engine anti-icing systems allow the engine to operate satisfactorily under meteorological conditions as defined in Table 1, with no more than 5% total thrust loss and no more than 5% increase in SFC for high engine setting. No permanent performance deterioration is permitted after the meteorological conditions have been removed. The test consists of two parts:

- six power settings under the three conditions of table 1, part 1, each for a minimum of ten minutes, and rapid acceleration for transient responses.
- one hour run at idle, followed by acceleration to maximum power, under conditions of table 1, part 2. This test is very similar to that defined by FAR Part 33.68 wich requires 30 minutes idle.

It is noted that the earlier version of the Navy Specification required altitude testing. These altitude tests were deleted from the specification, in part due to the high cost of testing in the altitude chamber. In any case sea-level icing conditions represent the most severe requirements for the engine anti-icing system due to low pressure ratio in idle and static and low temperature of the bleed air combined with a high total liquid water content.

There are four small engine test cells which have sea-level as well as altitude capabilities with a maximum airflow of 25 kg/s, and two larger sea-level cells with a maximum airflow of 150 kg/s. Two basic inlet configurations are utilised at NAPC, the direct connect jet and the free jet, as depicted in figure 13. Large engines are direct connected and small engines with a mass flow less than 20 kg/s are generally configured as a free jet. Cloud simulation is accomplished with spray systems consisting of spray bars. Through the nozzles, metered air and water generate the liquid water droplets. Flow of both water and air are controlled, which provides for the setting of LWC and drop diameter. Water and air are filtered to minimize the entrained particulates which can seed the supercooled liquid water droplets causing them to freeze and form ice crystals. The flow has to be calibrated and LWC and drop diameters must be verified quantitatively and qualitatively with the forward scattering spectrometer probe and a single rotating cylinder in the duct (figure 14). The icing capabilities are depicted in figure 15, and the NAPC experienced that the production of an icing simulation in terms of LWC and droplet diameter is not an easy task and that the instruments' accuracy is not always satisfactory. We have already presented the F14A aircraft inlet icing test. The difficulties and results on engine tests are mentionned in the paper.

A second test cell was described by Riley (29) from Rolls-Royce. The Hucknall tunnel is fitted with water spray nozzles wich produce a supercooled water cloud of controllable droplet size and TLW. The liquid water content distributions and air pressure were recorded at four planes downstream of a 28 cm high reducing nozzle. Pressure and temperature profiles were measured by rakes of 25 pitots and 25 thermocouples moved in vertical planes. The nominal air velocities are 61 and 122 m/s for air temperatures of 0°C, -15°C and -30°C. Research was carried out to determine the effects of variables such as velocity and temperature on ice accretion and shedding on a steel tubing grid. The higher airspeed produced more brittle ice which shed more easily. Figure 16 shows the cross section in various test conditions. Experimental evidence showed that a reduction in water droplet size had an

effect on ice types similar to an increase in airspeed or reduction in liquid water content, producing more brittle opaque ice which shed more easily. Different temperatures produce ice of a different nature. Rime ice forms at low temperatures, is smooth, opaque and tends to follow the shape of the surface on which it is building. Glaze ice forms at temperatures approaching 0°C, is clearer and comprises forward facing "feathers" which give the classic horned shape. Glaze ice is generally a greater problem since it has a larger effect on drag and damage potential if the ice is released. But it tends to be more brittle and is more readily shed. The appearance, net quantity, shape, distribution, relative location, physical properties of the ice are a function of ambiant conditions, the collecting surface and surroundings, the external forces. Macroscopic and microscopic observation of ice accretion concluded that:

- the physical and mechanical properties of ice formed by accretion are a function of formation conditions.
- the effects of altitude, rotational speed, vibration, heat input, material type and surface finish may also influence ice properties, and these phenomena should be investigated.
- alternative techniques for microscopic observation should be investigated.

The author also explained the research on static vane sets. The vanes were set at different incidences and the test run for 30 minutes at the highest air velocity of 119 m/s. The comparison was made on the result of pressure drop, plotted non-dimensionally in the form:

$$\text{NONDIMP} = \frac{\Delta P - \Delta Po}{\Delta Po}$$

where ΔP = measured pressure drop
ΔPo = initial ΔP

An example of the pressure drop's evolution, indicating the blockage is shown in figure 17. For different speeds and temperatures, the closely spaced vanes are more prone to blockage and ice bridging, and the blockage is highly dependent on shedding propensity. We also mention from this report the research on the adhesive strength of ice formed by accretion. These experimental investigations determined the bond strength of ice build up on rotating collectors. The ice mass resulted in a centrifugal shedding force recorded by strain gauges on the collector arm front and back faces (figure 18). It was noted that failure tended to be cohesive,i.e. failure occurred within the ice at lower temperatures. At higher temperatures adhesive failure occurred,i.e. the bond between ice and metal surface was broken. The transition occurred between -6°C and -10°C air temperature, which corresponds to the transition between rime and glaze ice. Tests were carried out to investigate the effects of LWC (0.5 to 2.5 g/m3), droplet size (15 to 30 µm), impingement angle, surface preparation (clean or greased) and coatings.

Mr. E. Carr presented the icing test facility operated at Barcley in the U.K. by Aero and Industrial Technology Limited (AIT)(32). This plant is operated on a normal commercial basis and is CAA approved. Figure 19 shows the main plant schematically, and the main capabilities are: airflow of up to 5.7 kg/s at a pressure down to 38 kPa, corresponding to a pressure altitude of 7620 m. At higher altitudes up to 15240 m the airflow is reduced at 3.4 kg/s. Air temperature is supplied in the range -65°C to +75°C and rapid changes in air pressure and temperature can be achieved. The engine test cell is 12.2 m long by 4 m diameter giving a normal working space 7.9 m long by 1.8 m diameter. Based on the JAR and the FAR the correct icing conditions, such as air velocity, pressure, temperature, water content and droplet size are set for predetermined times. In addition there may be a requirement for testing the effect of ice blocks ingested by the engine. This is done by either allowing the ice accretions to shed as in service or by producing ice blocks in a refrigerator and injecting pieces of a known size into the item. A special gun can also produce and inject hailstones. The configuration of the test sections is shown in figure 20. Recently a laser equipment (Malvern 2600C) has been installed for water droplet measurement.

Scott Bartlett presented the AEDC facilities (31). These are altitude engine test facilities covering a wide range of mach numbers, pressure altitudes, inlet temperatures and icing conditions. The free-jet and direct-connect testing modes are possible. In direct-connect tests one can test engines requiring an airflow of 340 kg/s at sea-level. Bigger engines can be tested at increasingly higher altitudes. As many icing problems occur at reduced power setting meaningful icing tests can be conducted on engines for which the maximum airflow is above the facility capability. Figure 21 indicates the test limits in pressure and temperature. An interesting detail is the LWC required in a direct connecting test. Figure 22 shows that the streamtube in the real flow in front of the inlet is convergent or divergent depending on the flight mach number and the mach number in front of the fan. Thus air density increases or decreases and the LWC in g/m3 is modified. The LWC in the airflow of the straight connecting tube must be adapted to simulate the required content in the real upstream conditions set by the regulations. The icing cloud's uniformity is evaluated by the ice accreted on a calibration grid. This technique has been automated at AEDC by application of ultrasonic piezo-electric transducers. These are integrated into the grid and the ice thickness and growth rate on the transducer is calculated in real time by a signal processing system. This automation greatly reduces time for icing test preparation. The measurement effort of the cloud's liquid water content uniformity aimes at developping electro-optical diagnostics to replace the piezo-electrical transducers on the calibration grids. Using fluorescent dye in the water and exciting the droplets with a light source the uniformity of the scattered light intensity is a measure of the LWC's uniformity. Work is also conducted on the ice scaling illustrated in figure 23 obtained at AEDC.

The test facility at Pyestock was presented by Mr Holmes of the RAE (34). The capability for icing tests was incorporated at the design stage of two of the altitude

test cells intended for aero-engines. There is still work to do on improving the icing tests and one of the most important elements is the simulation of a defined cloud. Some icing clouds consist of a mixture of supercooled water droplets and particles of dry ice. These can be produced at Pyestock based on different techniques for the production of both components: ice particles are produced by milling chips of prepared ice blocks and introduced into the main flow upstream of the liquid water injection. There is a problem in measuring the uniformity of the droplet size distribution in a 2.6 m diameter cell. Therefore at RAE they calibrate individual nozzles in a controlled environment in a low speed wind tunnel especially adapted for this purpose. The two cells have large test chambers of 6 m and 7.6 m diameters, the latter can accomodate a helicopter without rotors. A majority of the aero-engine testing is done in connect mode, but it is more realistic to do it in free jet mode. The icing cloud is produced by a number of airblast water spray nozzles on rakes . A new rake for testing of large engines requires 310 nozzles for a 2.64 m duct. Five channels of closed circuit TV are available for remote viewing: one channel is a strobed view of rotating parts whilst highspeed ciné up to 1200 frames per second records the ice shedding and particle trajectories. Measuring the water content and droplets' diameter in the real test cells close to the engine is the preferred solution but it is very difficult to achieve in large scale engineering environment with delicate instruments. The alternative solution at Pyestock is an open circuit wind tunnel with a 0.37 m2 working section and 80 m/s wind speed. Spray nozzles characteristics (figure 24) show the nozzles' operational limits. Another problem is the cooling down of the droplets in the airflow. The water is injected at 20°C to prevent freezing on the nozzle; are the droplets supercooled at the time they impact on the target? The state of the droplets determines the ice accretion forms. A 10 micron droplet comes to thermal equilibrium in a -5°C airflow in under a meter, but a 30 micron droplet might require 5 meters. Thus the distance between the spray rake and the target needs to exceed 5 meters.

Mr Creismeas of C.E.Pr reported on a numerical code developed at C.E.Pr. and ONERA (30). As said in above paper the distance between spray rake and test item is in excess of 5 m and there can be a significant modification in the droplets' mean diameter. The test requires a given mean droplet diameter and it is useful to have a method to predict the evolution. The theory is based on the thermal exchanges between the liquid water and the gasflow, taking into account the hygrometry. This numerical code is named M.A.GI.C (Modélisation et Analyse du GIvrage en Caisson). The equations are based on the continuity, momentum and heat equation. The drag force of the droplet in airflow is based on the value of Cx which is taken as:

$$(24/Re).(1+0.15\ Re^{0.687})$$

Theoretical results were compared with experimental results. The starting section is 0.25 m where mass distribution in diameter intervals are given in table 2 for 4 cases. The diameters in a section 1.95 m from the injector were measured and calculated and figure 25 gives an example of the comparison.

5. Ice relevant cloud physical parameters.

Since 1983 the icing of aircraft is investigated in the DLR - Institute for Atmospheric Physics using an icing research aircraft (33). The aim is to get information about the dependance of the icing relevant cloudphysical parameters on cloud type and the height above cloud base. The total water content (fluid and solid particles), the median volume diameter and the temperature T were collected during vertical and horizontal flight through clouds. A result is shown in figure 26. The TWC of clouds of a high pressure area increases about linearly with height above cloud base. Its maximum is located just below the cloud top and has values between 0.40 and 0.50 g/m3. Temperature is decreasing with height and the median volume diameters (MVD) are rather small and are situated between 11 and 23 µm. The phase of the particles is always fluid. The MVD of clouds in the range of a warm front fluctuates strongly between small and large values and maximum values are between 100 and 460 µm. The phase of the particles in clouds in the range of a warm front would vary between fluid and solid.

6. Low temperature and fuel problems.

The low temperature operations could impact aircraft missions as the fuel can form solid wax precipitates which may cause plugging of filters or blockage of fuel transfer lines. The Naval Air propulsion center of Trenton was concerned with the problem of availability of the F-44 (JP5) fuel. This fuel with very low freezing point accounts for only a small fraction, less than 1% of total refinery production. The relaxation of the freezing point specification to that of the commercial Jet-A specification would lead to a higher fraction of the crude (25).

This study requires the determination of the fuel temperature in the fuel tanks which is very expensive if it has to be done experimentally. NAPC looked for a CFD-code that could be modified to handle the calculations. They chose the PHOENICS 84 as the base code performing fluid-flow, heat transfer and chemical reaction calculations simultaneously. The major developments are: optimum grid selection, turbulence modelling, phase change modelling and expert system. The user-friendly menu driven format allows the user to operate in a menu driven step-wise format, depicted in figure 27, where he has to input the dimensions of the tank and the amount of fuel desired. The boundary conditions are either the experimental skin temperature of the tank, or the calculated skin temperature based on air temperature and air speed. Figure 28 compares test and calculated data. The model predicts accurately, in both two and three

dimensions, fuel temperature profiles. The accuracy of the fuel holdup is not as good as that of the fuel temperature because holdup was shown to be a somewhat random phenomenon. The model is currently used to predict the effect of higher freeze point fuels on naval aircraft mission performance.

A second danger of the cold fuel is due to the presence of water dissolved in the fuel. This water under the form of ice crystals can block the filters, the fuel control and change the flow passages in the heat exchanger air-fuel. Mr Garnier of SNECMA (23) explained the mathematical model based on a heat balance oil-fuel to predict the fuel temperature during the take-off phase and cruise flight. This model was verified on a test bench built at SNECMA to verify the model and on an aircraft equipped with four CFM-56, that was put in the climatic chamber of EGLIN (Florida) where the temperature was lowered to between -21°C and -54°C.

Fuel at cold temperature can also impact the engines' starting capabilities. This is due to the low vapour pressure and the low viscosity. The droplet mean diameter increases and the fuel evaporation rate is inversely proportionate to the square of the droplet size (7,9,22). Figure 29 shows that the minimum fuel air ratio for ignition has to be increased with higher viscosity, thus lower fuel temperature. Three papers: GE (10), APU for the Tornado (11) and PW (12) explain the improvements in the starting capabilities with new fuel control schedules related to the ambient conditions.

The flame propagation model in heterogeneous phase must take into account the droplet diameters and droplet distribution, the temperatures and pressures, the fuel air ratio, the evaporation and the turbulence. In paper (24) this flame propagation is studied in the case of a multicomponent fuel to compare it with the case of a single component idealization.

CONTENTS OF THE 76th SYMPOSIUM

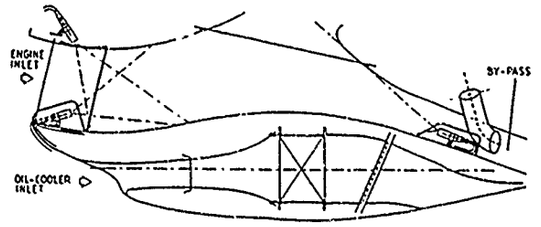

Fig 1: Positions and fields of view of cameras mounted in the air intake duct

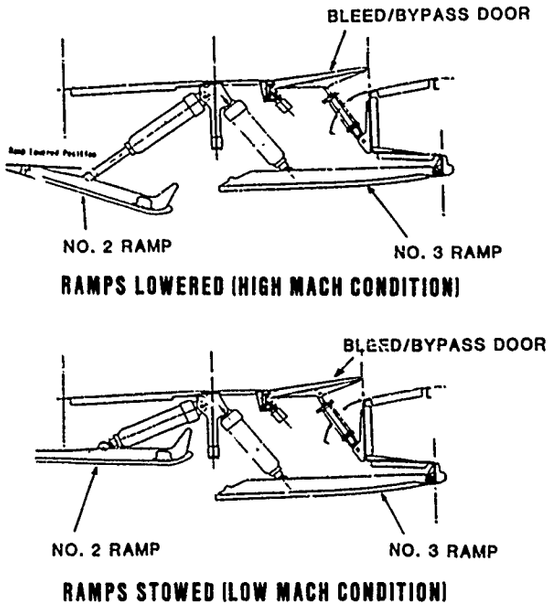

Fig 2: Engine inlet duct F 14

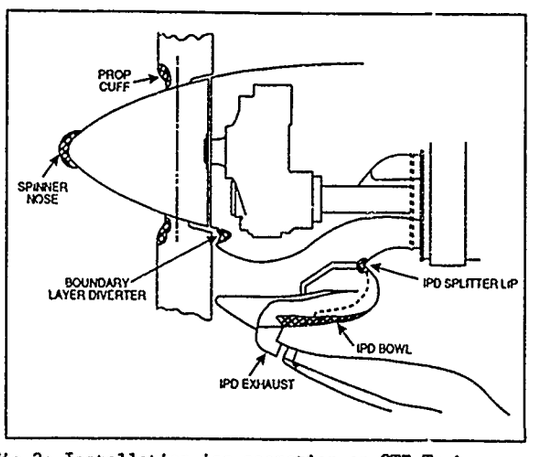

Fig 3: Installation ice accretion on CT7 Turboprop

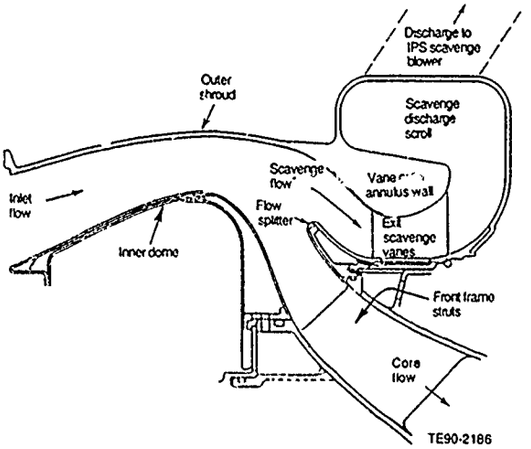

Fig 4: Inlet Particle Separator system (IPS)

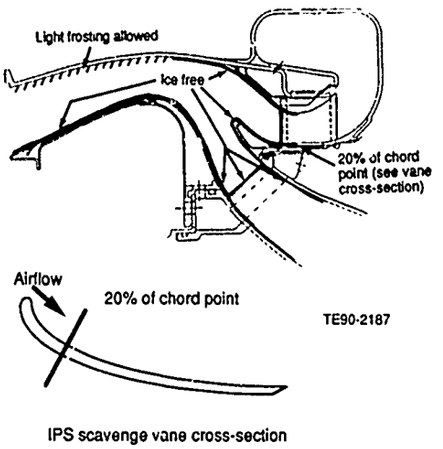

IPS scavenge vane cross-section

Fig 5: Required ice free surfaces

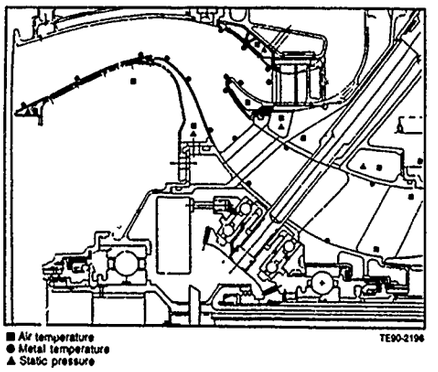

Fig 6: Preliminary Flight Rating anti-ice thermal survey instrumentation

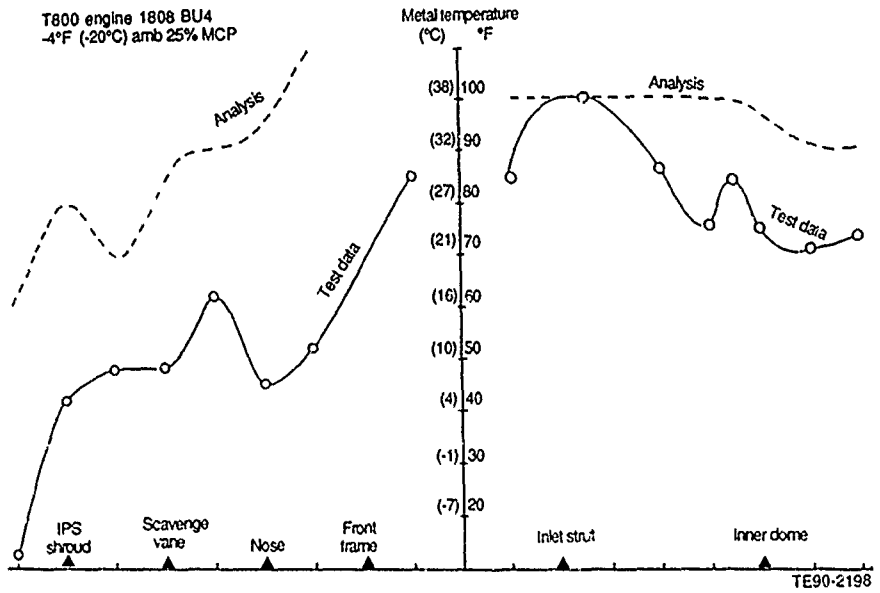

Fig 7: PFR thermal survey data; -4°F, 25%MCP

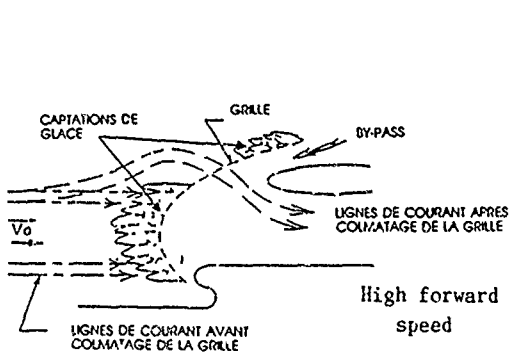

Fig 8: Icc accretion on helicopter inlet screen

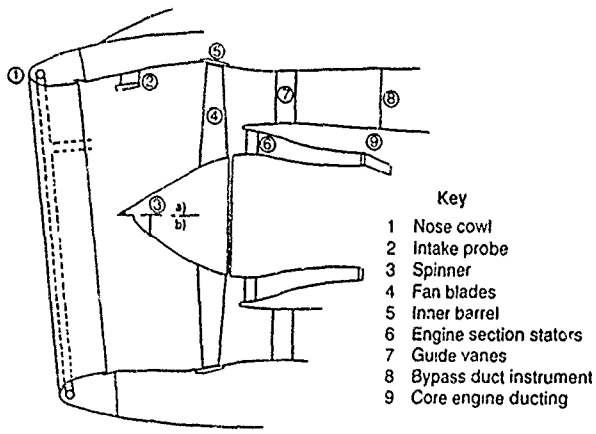

Fig 9: Engine and nacelle icing risks

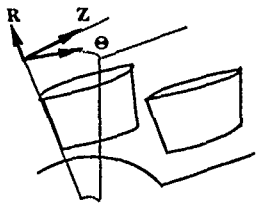

Fig 10: Reference system

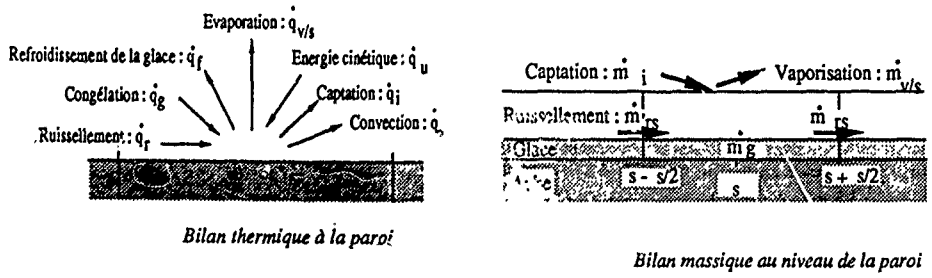

Bilan thermique à la paroi

Bilan massique au niveau de la paroi

Fig 11: Heat and mass balance on the wall

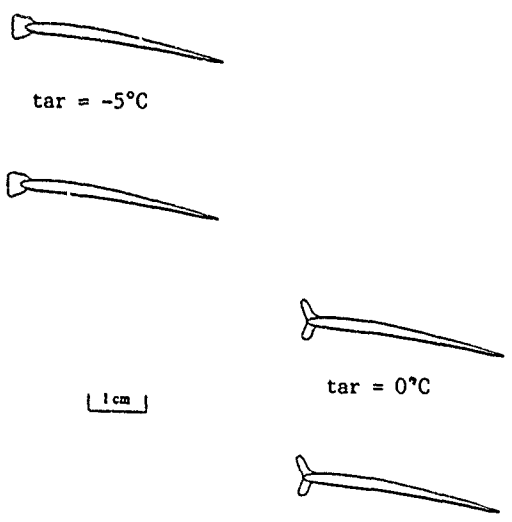

Fig 12: LWC=0,6g/m^3; DMV=20μm; Mean Diameter

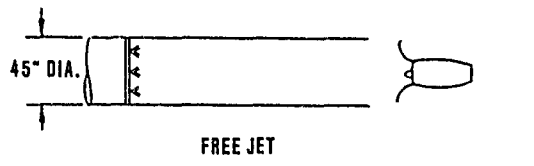

Fig 13: Icing Test inlet configurations

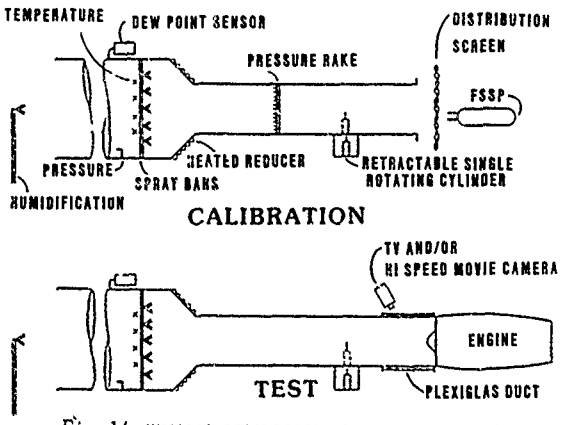

Fig 14 :TYPICAL CALIBRATION/TEST ARRANGEMENTS

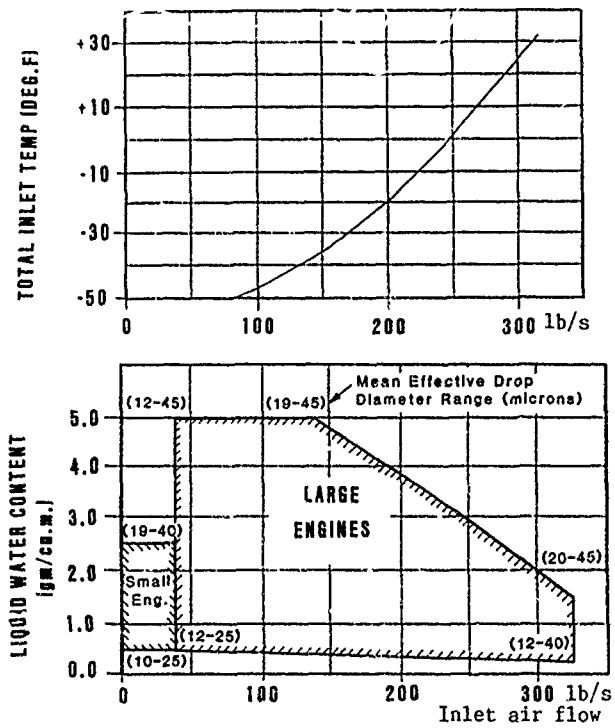

Fig 15: NAPC Icing capabilities

TABLE 1: SEA-LEVEL ANTI-ICING CONDITIONS (MIL E 005007E (AS),

	PART 1			PART 2
Engine Inlet Total Temperature	-4°F(-20°C)±1°	+15°F(-10°C)±1°	+23°F(-5°C)±1°	23°F(-5°C)±1°
Velocity	0 to 60 knots	0 to 60 knots	0 to 60 knots	0 to 60 knots
Altitude	0 to 500 ft	0 to 500 ft	0 to 500 ft	0 to 500 ft
Mean Effective Drop Diameter	20 microns	20 microns	20 microns	30 microns
Liquid Water Content (Continuous)	1 gm/m^3 ±0.25 gm/m^3	2 gm/m^3 ±0.25 gm/m^3	2 gm/m^3 ±0.25 gm/m^3	0.4 gm/m^3 ±0.1 gm/m^3

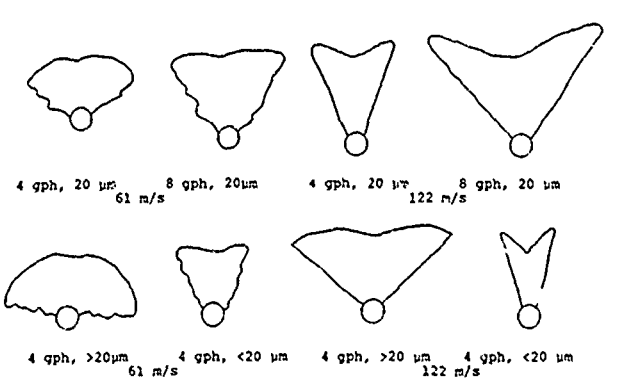

Fig 16: Profiles of grid ice accretion after 5 min at -10°C.

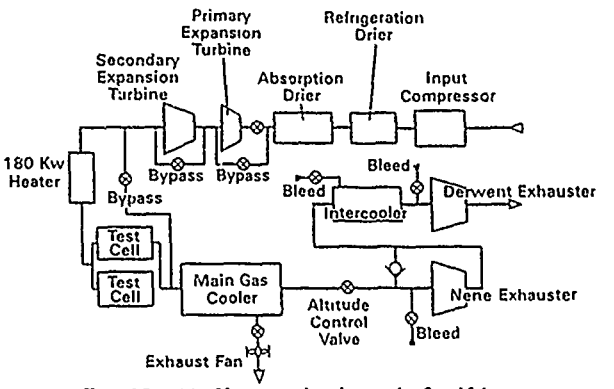

Fig 19: Airflow path through facility

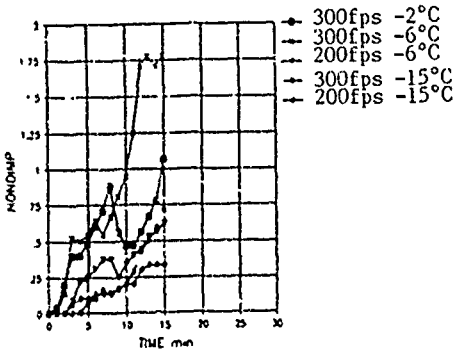

55.9 mm spacing

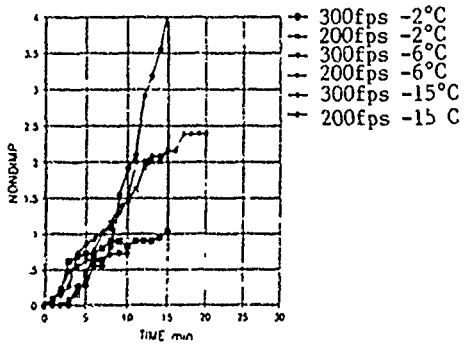

19.1 mm spacing

Fig 17: Nondimension pressure drop

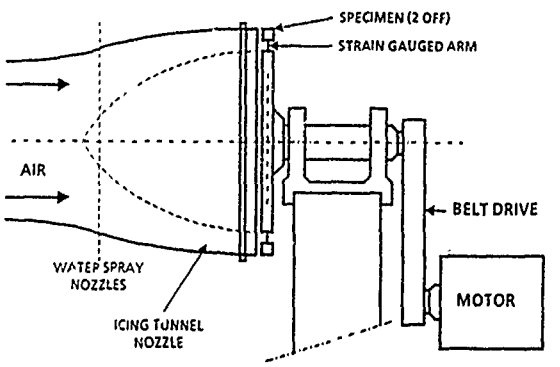

Fig 18: Testbench for adhesive strenght of ice accretion

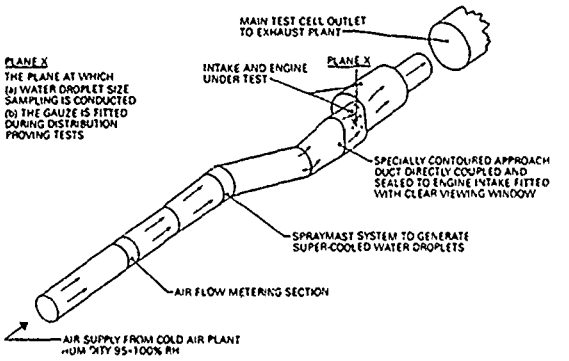

Fig 20: Typical configuration for intake icing tests

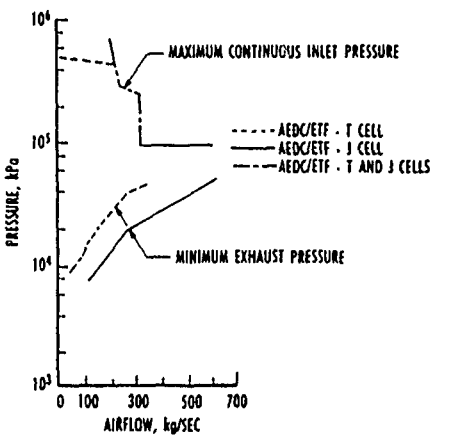

a. Air supply and exhauster capability

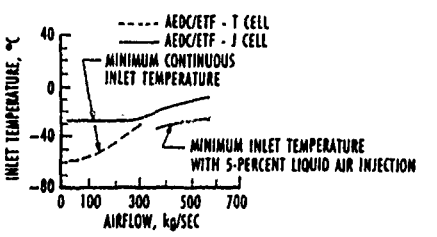

b. Estimated inlet air temperature capability

Fig 21: Facility performance capability

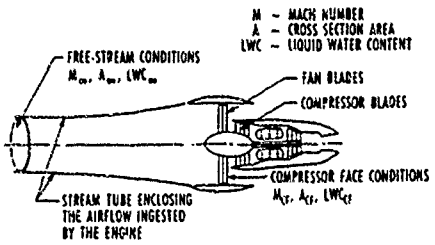

a. Inlet Mach number less than flight Mach number, $LWC_\infty < LWC_{CF}$

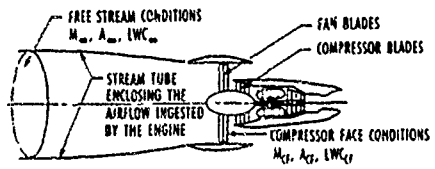

b. Inlet Mach number greater than flight Mach number, $LWC_{CF} < LWC_\infty$

Fig 22: Possible stream tube configuration for turbofan icing conditions

Table 2: Initial distribution of the droplets

19.8	9	4.7	3.5
2.5	5.3	2 4	1.5
4.3	5.2	3 4	1 3
13.5	9 8	4	2 5
14 4	9	7.6	5 8
15.3	15.3	8 9	5 4
19 6	22.3	14 7	9 2
7.4	14.2	17.1	15 9
2.4	11 2	19 2	16.8
0	0	15 8	19 4
0	0	1.5	14 5
0	0	0	3.7
0	0	0	0
0	0	0	0
0 7	0.7	0 7	0 1
cas n° 41	cas n° 42	cas n°43	cas n°44

vitesse air 13.5 m/s Hygro : 37% débit eau : 4 l/h

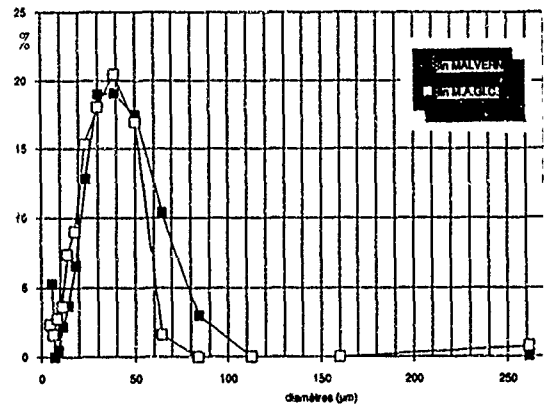

Fig 25: Calculated and measured droplet distribution at 1,95 m from injectors

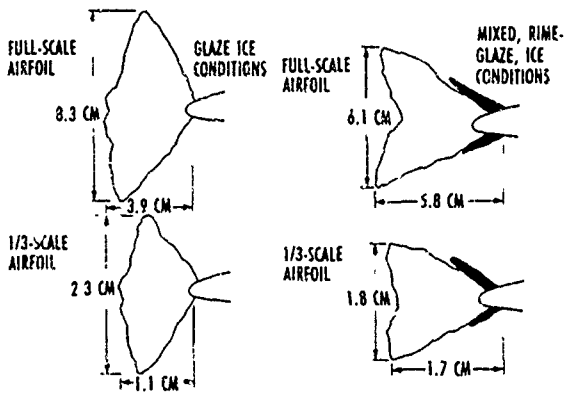

Fig 23: Ice shape scaling results, test article size, full and 1/3 scale

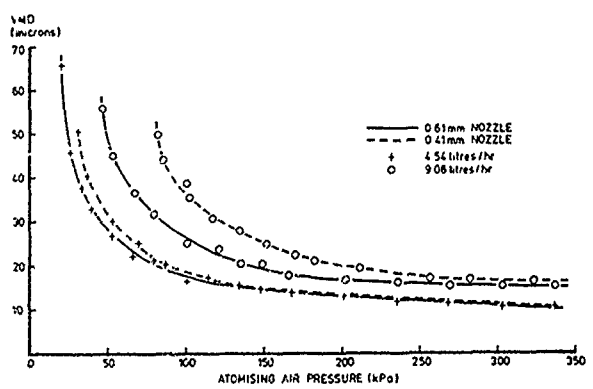

Fig 24: Spray nozzles characteristics

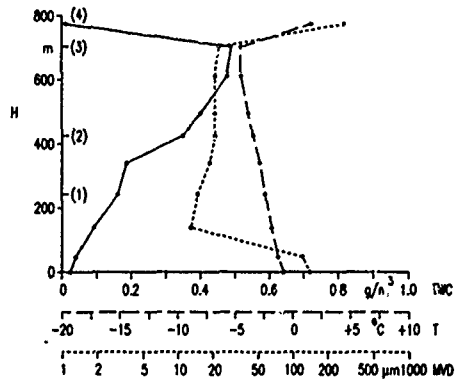

Fig 26: Total water content TWC, temperature T, and median volume diameter MVD in dependence on height above cloudbase H.
Phase of cloud particles: Fluid
Height of the cloud base: Between 400 and 500 m

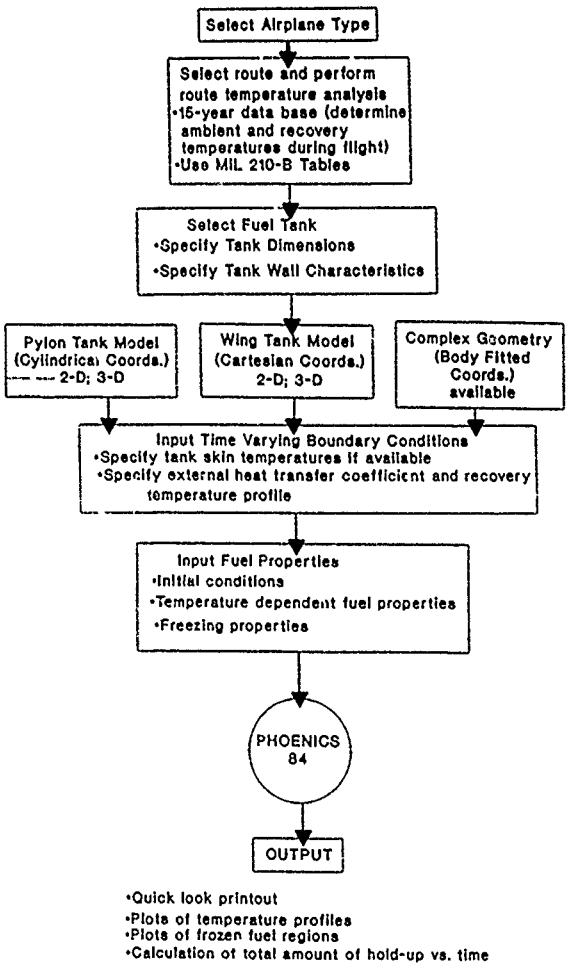

Fig 27: Flow diagram on approach to use computer model

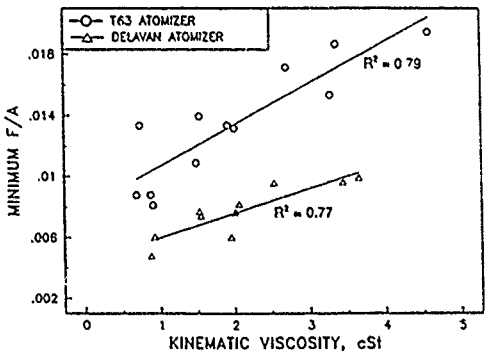

Fig 29a: Correlation of minimum fuel-air ratio for ignition with viscosity for two atomizers

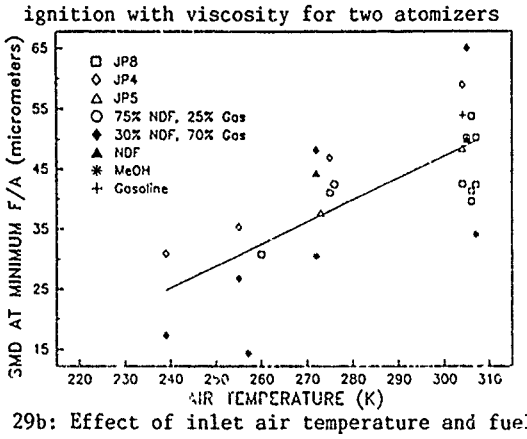

Fig 29b: Effect of inlet air temperature and fuel type on SMD required for ignition

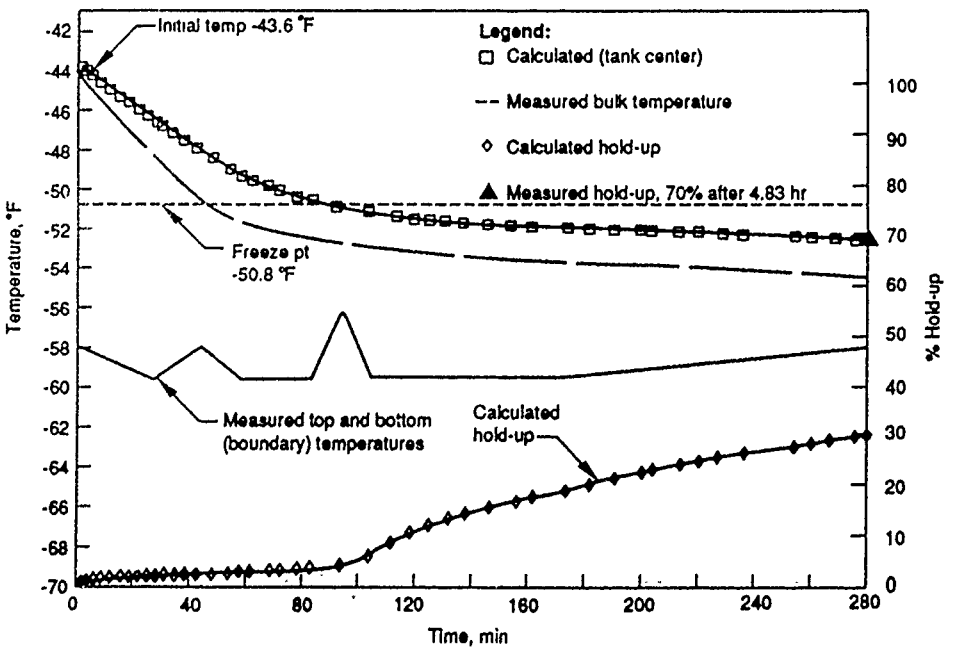

Fig 28: Comparison of calculated and measured temperatures and hold-up

EVOLUTION REGLEMENTAIRE EN MATIERE DE CERTIFICATION DES AVIONS CIVILS EN CONDITIONS GIVRANTES

par

Gilbert CATTANEO

Ingénieur Navigant d'Essais

CENTRE D'ESSAIS EN VOL 13128 ISTRES AIR

1. - RESUME

L'expérience acquise au cours de la certification de type et de l'utilisation en service des avions civils a montré qu'une évolution des règlements applicables aux conditions givrantes s'avérait nécessaire. Ce document décrit les évolutions réglementaires qui sont actuellement envisagées de manière à maintenir au cours d'un vol en conditions givrantes un niveau de sécurité comparable à celui qui est garanti hors givrage.

2. - RAPPEL DES EFFETS DE L'ACCUMULATION DE GLACE SUR LES CARACTERISTIQUES AERODYNAMIQUES D'UN AVION

On sait depuis fort longtemps que la présence de glace sur un avion dégrade de manière significative les caractéristiques aérodynamiques correspondantes.

Il existe une abondante littérature qui traite de ce sujet et de nombreuses études ont été conduites dans le monde pour en évaluer des conséquences. Nous rappelons brièvement les principales conclusions.

L'accumulation de glace sur un avion provoque :

- Une perte de portance CL a même incidence α qui s'accompagne d'une diminution du CLmax et de l'angle α (CLmax) associé.
- Une augmentation du coefficient de trainée CD.
- Une dégradation de la stabilité longitudinale et de la stabilité latérale.
- D'autres caractéristiques comme la stabilité dynamique transversale (DUTCH ROLL) peuvent aussi être affectées.

L'amplitude de l'effet étudié dépend de l'épaisseur de glace, de sa forme et dans une certaine mesure de sa rugosité (CF figures n° 1 et n° 2).

Une épaisseur même faible peut avoir un effet considérable sur le CLmax.

L'accumulation de glace sur la profondeur peut provoquer des problèmes graves de contrôle longitudinal liés à l'altération du moment de charnière observable sur les avions à commandes de vol purement mécaniques. Des dégradations significatives de l'efficacité de la profondeur ne peuvent pas être exclues sur les avions équipés de servo commandes.

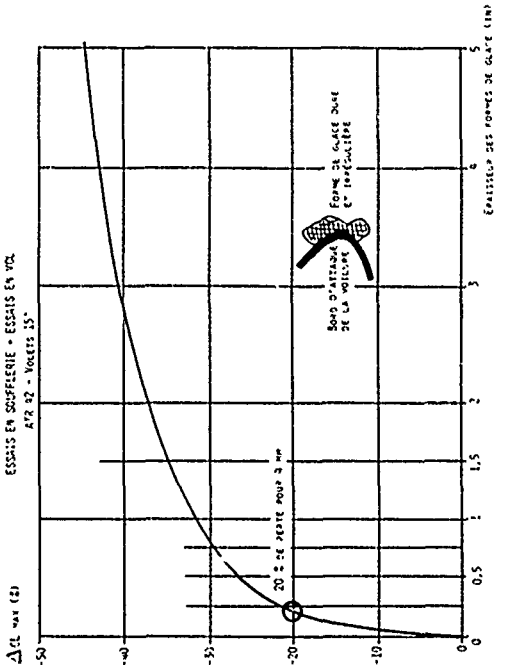

DESIGNATION :
EFFET DE L'EPAISSEUR DES FORMES DE GLACE SUR CL MAX.

AVION : AIR 42 — FIGURE n° 1

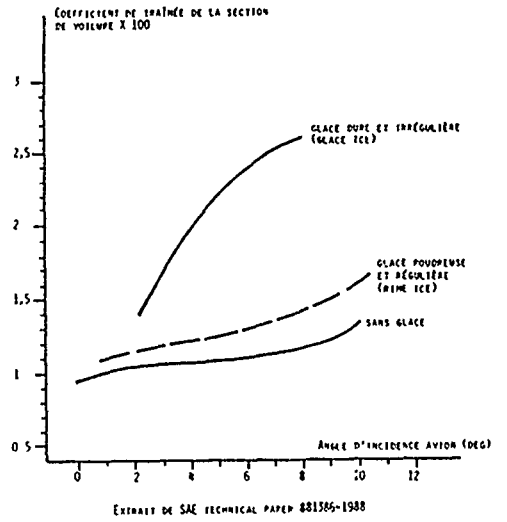

EXTRAIT DE SAE TECHNICAL PAPER 881386-1988

DESIGNATION		
EFFET DU TYPE DE GIVRAGE SUR LE COEFFICIENT DE TRAINEE CD	NACA 0012	FIGURE N° 2

Les avions peuvent être plus ou moins sensibles au givrage.

Parmi les raisons possibles qui les différencient on peut noter :

- Que les turboréacteurs ont un domaine de vol étendu et des performances élevées leur permettant d'éviter ou de traverser rapidement les zones de givrage.

- Que les systèmes de dégivrage pneumatiques à chambres déformantes (boots) n'ont pas une efficacité parfaite. De la glace s'accumule entre deux gonflages des chambres (intercycle). Par comparaison les systèmes d'antigivrage par soufflage d'air chaud évitent l'accumulation de glace.

- La mise en route différée des systèmes de dégivrage par application de la procédure garantissant l'efficacité du système, correspond à une certaine quantité de glace accumulée.

- Des conditions données de givrage peuvent avoir un effet différent en fonction du type de l'avion.

Il ressort de ces considérations que les turbopropulseurs ont plus de chance d'être "sensibles au givrage" à cause :

- De leur domaine de vol réduit.

- De leur performances limitées.

- De leur capacité limitée de prélèvement de puissance particulièrement au décollage.

- De l'absence de servo commandes.

Par contre on observe que les profils modernes ne paraissent pas présenter une sensibilité plus marquée que celle des profils anciens.

3. - LES REGLEMENTS DE CERTIFICATION EXISTANTS

On sait que pour certifier les avions civils de grande taille il existe essentiellement deux règlements de base :

- La part 25 (large aéroplanes) du titre 14 (Aéronautique et Espace) du Code des Lois Fédérales Américaines.

- La JAR 25 (Joint Aviation Requirements).

Ces règlements sont pratiquement identiques et sont complétés par des textes additionnels : Annexes, Advisory Circular Joint, etc....

Ainsi lorsque la certification en conditions givrantes est demandée en conformité avec le règlement JAR on utilisera :

a) Le texte de base chapitre 25-1419. Il précise que l'avion doit pouvoir être utilisé en toute sécurité dans les conditions de givrage maximum continu et maximum intermittent définies dans l'annexe C.

b) L'annexe C. Elle fournit les domaines de démonstrations altitude, température, étendue horizontale maximum du nuage diamètre effectif moyen des gouttelettes, concentration en eau à prendre en considération pour les conditions maximum continu et maximum intermittent (CF annexe 1).

c) L'ACJ 25-1419. Elle décrit deux méthodes de conformité.

- Une méthode empirique basée sur la pratique courante et l'expérience acquise en France et au ROYAUME UNI.

- Une méthode globale basées sur la pratique courante Américaine.

4.- INSUFFISANCE DE LA REGLEMENTATION ACTUELLE

Le développement récent d'une nouvelle génération d'avions du type Commuter et l'expérience acquise ont mis en évidence les aspects suivants :

- Les essais de certification confirment l'existence d'une dégradation importante des caractéristiques aérodynamiques : performances et qualités de vol.

- L'utilisation en service montre que la méconnaissance ou le non respect des procédures associées à la présence de glace peuvent conduire à des pertes de contrôle sévères suivies de récupérations hasardeuses qui dans un cas extrême ont entraîné la perte de l'avion et de ses occupants.

Pourtant la réglementation telle qu'elle existe paraît constituer un ensemble cohérent et complet. Pendant de nombreuses années elle a été considérée comme suffisante et parfaitement capable d'atteindre l'objectif qui lui était assigné : garantir une sécurité suffisante.

En réalité, cette réglementation, très explicite sur les conditions de givrage à étudier et sur les démonstrations relatives aux systèmes, reste extrêmement vague sur les dégradations de performance et de qualités de vol que l'on peut accepter. A titre d'exemple on peut citer le seul paragraphe qui aborde cet aspect (CF ACJ 25-1419). " Where ice can accrete on unprotected parts it should be demonstrated that the effect of such ice will not critically affect the characteristics of the aéroplane as regards safety (eg flight, structure and flutter). The subsequent operation of retractable devices should be considered."

Ces insuffisances ont conduit les autorités françaises de certification à proposer des textes complémentaires.

5.- EVOLUTION REGLEMENTAIRE

5.1. GENERALITES

Les objectifs de sécurité des textes existants étant parfaitement définies le choix s'est porté sur le maintient de ces textes et le développement de moyens d'interprétation (Advisory Material Joint). L'AMJ 25-1419 ainsi développée s'est en partie inspirée du contenu des AMA's 525/2-x et 525/5-x élaborées par les autorités canadiennes DOT.

5.2. CONTENU DE L'AMJ 25-1419

5.2.1. Généralités

- Les conditions atmosphériques sont celles définies dans l'annexe C des règlements FAR 25 ET JAR 25 (CF annexe 1).

- Les phases de vol significatives suivantes sont prises en considération. Décollage, montée, croisière, attente, atterrissage, cas de panne. Pour le décollage les systèmes de dégivrage sont supposés être mis en route à 400 feet, sauf si la procédure permet explicitement leur utilisation avant d'atteindre cette altitude.

- Les essais peuvent être effectués avec des formes de givre artificielles, les résultats ainsi obtenus doivent être recoupés par des essais en givrage naturel. Les formes artificielles doivent être déterminées à partir de modèles de calcul validés par des essais (soufflerie par exemple) et approuvés.

5.2.2. Quantités de glace accumulée

Décollage :

Supposé effectué avec une panne moteur à VEF, un rapport critique Poussée/Poids. La glace est accumulée sur l'ensemble des parties captantes de l'avion a une incidence moyenne pendant une phase de durée déterminée.

Croisière - Attente et Atterrissage :

a) Parties non protégées de l'avion.
Captation jusqu'à une épaisseur maximum de 3 pouces avec des aspérités de hauteur 3 mm et une densité de 8 à 10 grains par cm^2.

b) Parties protégées.
Les délais de mise en route des systèmes anti/dégivrages, involontaires ou liés à la procédure, sont pris en compte ; de même que la glace accumulée pendant un intercycle et que la recongélation éventuelle (runback).

Cas de panne :

Lorsque la panne affecte l'efficacité du système de dégivrage et que l'avion doit alors quitter les conditions givrantes la quantité supposée de glace déposée sur les parties protégées est fixée à 1,5 cm

Cas particulier du Sand Paper :

Une forme spécifique de captation correspondant a une faible épaisseur et une rugosité du type papier de verre a été utilisée pour qualifier le comportement de l'avion lors des manoeuvres de rendus de mains (push overs). On sait en effet par l'expérience sur différents avions tels que ATR 42. SF 340 DO 228 que ce type d'accrétion est critique pour la manoeuvre considérée.

5.2.3. Essais à exécuter

Performances :

Etablissement des vitesses de décrochage en vue du calcul des nouvelles vitesses opérationnelles associées. Validation des marges entre activation des systèmes de protection (Stall warning, stick shaker) et décrochage. Etablissement des polaires de trainée.

Qualités de vol :

Caractéristiques de décrochage. Stabilité statique longitudinale et latérale. Stabilité transversale dynamique (Dutch roll). Capacité de trim. Vibrations et buffeting. Absence de blocage des gouvernes (Jamming). Changements de configurations. Comportement longitudinal sur rendu de main aux limites du domaine de vol : n = og VFE (Push overs).

5.2.4. Essais en conditions givrantes naturelles

Le but de ces essais est de :

- Valider les formes artificielles éventuellement utilisées.

- S'assurer que les dégradations de performances et de qualités de vol observées avec les formes artificielles sont basées sur des hypothèses conservatives.

Une attention toute particulière doit être portée aux calages des protections (Stall warning/stick shaker) dans la plus large étendue possible des conditions de givrage couvrant des captations allant jusqu'à 3 cm sur les parties protégées et 1 cm sur les non protégées.

6.- APPLICATION DE L'AMJ A LA CERTIFICATION DE L'ATR 72

L'ATR 72 a été le premier avion sur lequel la proposition réglementaire nouvelle a été appliquée sous forme de la condition spéciale CS B6. Les résultats de cette application furent les suivants :

6.1. FORMES DE GIVRE ARTIFICIELLES UTILISEES

Ces formes de givre couvrant les phases décollage, croisière, ...etc. sont définies en annexe 2.

6.2. PERFORMANCE

6.2.1 Décrochage (figure n°3).

Configuration train rentré volets 0°. on constate que l'influence des formes de givre se traduit par :

- Une perte initiale des courbes Cz = F(α) qui a faible incidence est indépendante de la forme de givre.

- Une influence croissante de la forme en fonction de la sévérité du givrage. Conformément à la logique la forme critique correspond au cas de panne. Cette forme particulière affecte non seulement le niveau mais aussi l'allure de la courbe à incidence élevée $\alpha_{REF} > 9°$.

- Une perte importante de CL qui, a même incidence, peut atteindre 30 points de 100 CL pour le cas de panne.

- Les incidences d'activation du stick pusher ont été choisies pour assurer un comportement latéral satisfaisant de l'avion. Les calages sont tels que l'activation survient avant que le CLmax que peut développer l'avion soit atteint. Cette valeur de CLmax au stick pusher fixe la vitesse de décrochage associée VS1g.

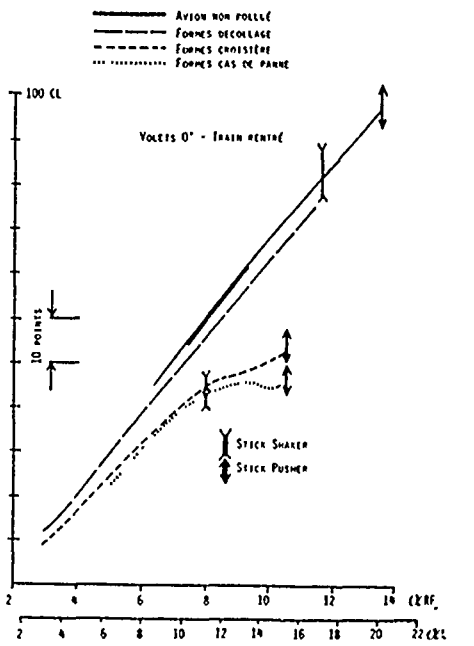

DESIGNATION : DÉCROCHAGES À TRACTION NULLE VOLETS 0°, TRAIN RENTRÉ, CENTRAGE : 19 % AVION NON POLLUÉ ET AVEC DIFFÉRENTES FORMES ARTIFICIELLES DE GIVRE	AVION ATR 72	FIGURE n° 3

Figure n° 4 (configuration volets 30° train sorti) les conclusions précédentes sont confirmées. Toutefois on observe une perte de 100 CL limitée à 15 points environ. De plus les formes de givre croisière conduisent à un blocage de CLmax pour α_{REF} >8°. La vitesse de décrochage VS1g étant alors fixée par cette valeur il n'y a a aucun intérêt à caler le stick pusher à une incidence supérieure.

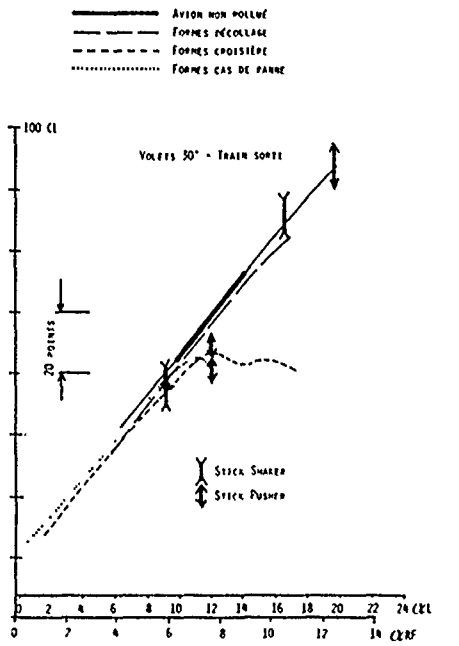

DESIGNATION :		
DÉCROCHAGES À TRACTION NULLE VOLETS 30°, TRAIN SORTI, CENTRAGE: 19 %	AVION : ATR 72	FIGURE N° 4
AVION NON POLLUÉ ET AVEC DIFFÉRENTES FORMES ARTIFICIELLES DE GIVRE		

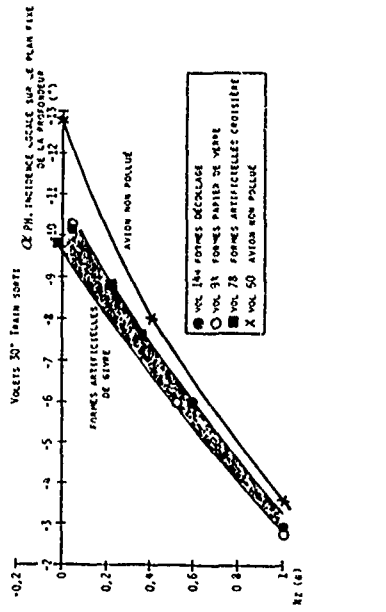

DESIGNATION :		
PUSH-OVER AVEC DIFFÉRENTES FORMES ARTIFICIELLES	AVION : ATR 72	FIGURE N° 5

6.3. QUALITES DE VOL

Un parcours complet des essais décrits au paragraphe 5.2.3 a été effectuée. Les résultats montrent que les propositions réglementaires sont réalistes et que l'exploration des qualités de vol avec les formes artificielles ne pré ıte pas de difficulté notable. A titre d'exemple on trouvera figure n° 5 les résultats d'essais de "Push overs" exécutés jusqu'à n = 0g dans la configuration critique volets 30° train sorti à VC voisin de VFE = 150 kt pour différentes formes de givre.

L'altération du moment de charnière de la profondeur est liée à l'incidence locale de l'empennage horizontal α_{PH}. Dans les conditions de l'essai, cette incidence est négative. Pour différentes pollutions par le givre, le cas critique correspond pour n = 0g à α_{PH} la plus faible. On voit qu'à ce titre le sand paper est dimensionnant (α_{PH} = -11°) et que les formes décollages donnent des résultats sensiblement équivalents.

Note : Avec un braquage de volets limité à 30°, l'ATR 72 était exempt du phénomène d'inversion d'effort à la profondeur jusqu'à n = 0g, l'avion étant ou non pollué par le givre.

6.4. ESSAIS EN GIVRAGE NATUREL

L'ensemble des essais effectués en givrage naturel est résumé dans le tableau figure n° 6.

Les conditions de captation de glace poudreuse et régulière (Rime ice) jusqu'à des épaisseurs de 58 mm (= 2,3 in) en simple corne sur les parties non protégées et intercycle sur les parties protégées ont permis un balayage complet des essais de performances et qualités de vol. Les résultats les plus significatifs sont les suivants :

Décrochages (CF figure n°7).
Pour les configurations avion étudiées le coefficient de portance CL correspondant au givrage naturel est, à toute incidence, supérieur au CL obtenu avec les formes artificielles associées. L'écart est notable à forte incidence. De plus l'altération observée sur la forme des courbes se manifeste plus tôt avec les formes artificielles.

Polaires (CF figure n°8).
Le résultat est identique, les écarts entre polaire de l'avion non pollué et de l'avion pollué par le givre sont plus faibles en givrage naturel que ceux observés avec les formes artificielles.

Qualités de vol.

D'une manière générale, les qualités de vol montrent qu'aucune caractéristique n'est plus dégradée en givrage naturel que celle observée avec les formes artificielles. Les objectifs définis en 5.2.4 sont donc atteints.

7.- BILAN DES ESSAIS

La campagne de certification de l'ATR 72 en givrage a necessité :

- 25 vols représentant 47 heures pour les essais avec formes artificielles.
- 11 vols représentant 35 heures pour les essais en givrage naturel.

Soit au total 36 vols représentant 82 heures.

Il convient cependant de remarquer ce qui suit :

Vois avec formes artificielles.

Un important travail de mise au point des générateurs de tourbillons de voilure et d'optimisation du seuil de déclenchement du stick pusher ont été rendus nécessaires pour améliorer le comportement de l'avion aux hautes incidences. Ce travail ne peut être imputé à l'application de l'AMJ, il représente 21 heures de vol.

Vols en givrage naturel.

Un certain nombre d'heures ont du être consacrées à la recherche, quelquefois infructueuse, de conditions givrantes valables. Ainsi qu'aux essais de certification des systèmes antigivrage/dégivrage équipant l'avion. Ces heures ne peuvent également pas être imputées à l'AMJ, elles représentent environ 25 heures.

Finalement l'application de l'AMJ entrainerait un surplus d'environ 25 heures de vol avec formes artificielles et 10 heures en givrage naturel soit approximativement 35 heures au total.

Cette quantité est raisonnable eu égard au coût total d'un programme de certification complet (entre 1000 et 1200 heures de vol), surtout si on considère l'amelioration importante de sécurité que les essais correspondants apportent.

ATR 72 - ESSAIS DE QUALITES DE VOL ET DE PERFORMANCES EXECUTES EN CONFIGURATIONS DE GIVRAGE REEL

TYPE DE GLACE		GLACE POUDREUSE ET REGULIERE SIMPLE COURE						GLACE DURE ET IRREGULIERE DOUBLE COURE					
NUMERO DE VOL		115	115	127	127	126	130	129	129	115	129	115	129
EPAISSEUR DE GLACE (mm) voir notes ci-dessous		14+1	30+1 MONO CHAMBRE	47-1	47+22	50+22	54+1	25+1	49+1	52+1	25+1	49+1	75+26
ESSAIS EFFECTUES	DECROCHAGES		X	X	X	X	X		X	X		X	X
	RECUPERATION DE VITESSE			X									
	PUSH-OVER VOLETS 30°	X		X	X		X	X	X		X		X
	PERTE DE MANOEUVRABILITE				X	X	X			X			
	CONTROLE LONGITUDINAL CENTRAGE AVANT						X	X				X	X
	DERAPES STABILISES			X			X						X
	EVOLUTIONS ASSOCIEES STALL MANOEUVRE VOLETS EN PANNE			X	X		X						
	TOUR DE PISTE A 200 KT						X						
	SYMETRIE CONFIGURATIONS STATIQUE CONFIGURATIONS			X			X						
	PERFORMANCE DE MONTEE AU DECOLLAGE			X			X						

1 - LA PREMIERE INFORMATION REPRESENTE L'EPAISSEUR CONTINUELLE SUR LES SURFACES NON PROTEGEES. LA SECONDE INFORMATION REPRESENTE L'EPAISSEUR EQUIVALENTE SUR LES SURFACES PROTEGEES. EXEMPLE 47+22 SIGNIFIE 47 mm SUR SURFACES NON PROTEGEES ET 22 mm SUR SURFACES PROTEGEES.

2 - QUANTITE ACCUMULEE SUR LES PARTIES PROTEGEES PENDANT UN INTERCYCLE AVEC LES CHAMPES "PROPRIETES FONCTIONNAL" DEVELOPPEMENT

FIGURE n° 6

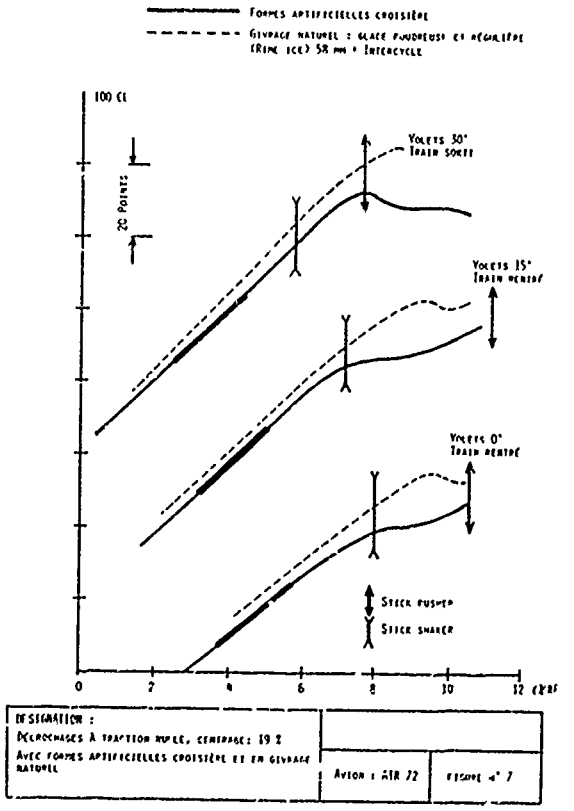

8.- APPLICATION DE L'AMJ A D'AUTRES AVIONS

A titre expérimental, l'AMJ a été appliquée sur un autre avion : le FOKKER 27 ARAT (Avion de Recherche Atmosphérique et de Teledetection). Il s'agit d'un avion FOKKER 27 modifié par adjonction :

- D'une perche de nez porte capteurs (α, β, Pp).
- D'une couronne de capteurs autour du fuselage avant.
- De points d'emports de capteurs sous voilure.

Ces modifications sont destinées à des mesures au profit de divers organismes :

- Institut Géographique National.
- Institut National des Sciences de l'Univers.
- Groupe de Télédétection Aérienne.

Les principales conclusions qui ont été tirées de cette étude sont les suivantes :

- Les essais de performances confirment l'influence notable des formes de givre sur les vitesses de décrochages (CF figure n° 9).

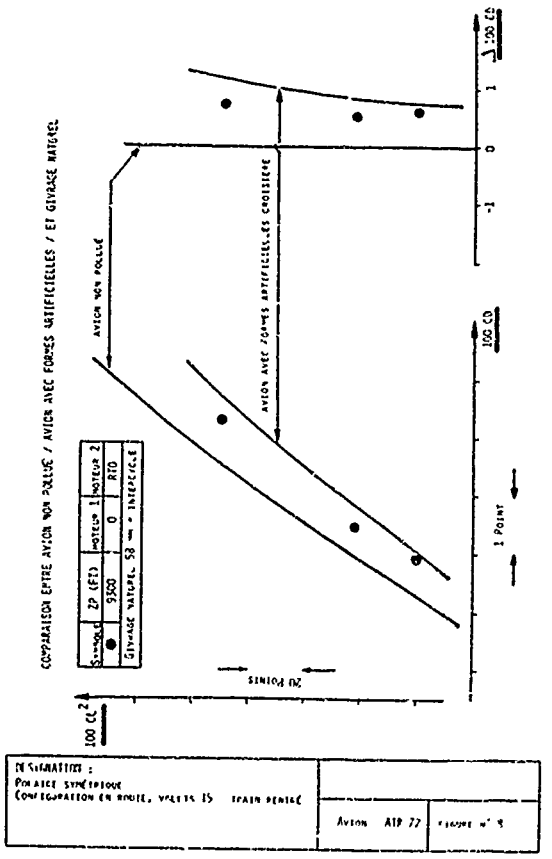

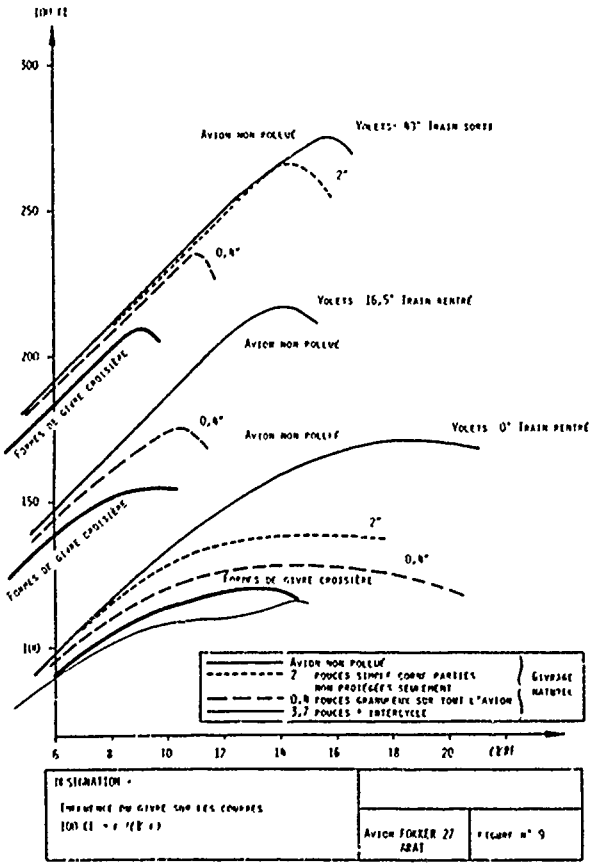

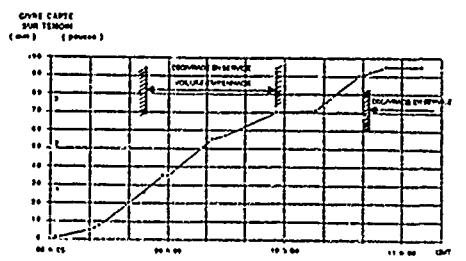

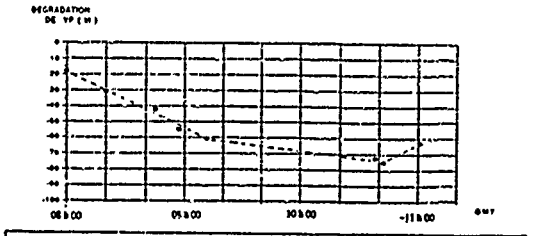

- Les formes artificielles constituent une enveloppe réaliste des accrétions naturelles de givre.

- Sur cet avion les qualités de vol sont faiblement affectées par le givrage.

- Les essais de recoupement en givrage naturel sont indispensables et permettent notamment d'avoir une idée de l'influence du givre sur la traînée (CF figure n° 10 évolution de la vitesse Vp stabilisée en palier à iso puissance en fonction de la quantité de glace accumulée).

9.- CONCLUSION

Les essais effectués sur deux avions comparables du point de vue de la motorisation et des commandes de vol mais assez différents du point de vue des formes extérieures tendent à prouver que l'AMJ 25-1419 est bien adaptée aux avions du type Commuter.

Bien que les textes correspondant ne sont pas formellement approuvés à l'heure actuelle au niveau des instances JAA, son application à des avions comme le JETSTREAM 4100, le SAAB 2000, le DORNIER 328 de même que l'A330 et l'A340 est envisagée sous forme de conditions spéciales. Ell contient en effet suffisamment d'éléments qui peuvent être transposés sans difficulté des Commuters aux Jets. Bien entendu il est nécessaire de tenir compte des particularités de ces derniers et plus spécialement des systèmes de protection en incidence.

Dans l'esprit de ses auteurs l'AMJ 25-1419 représente une exigence susceptible d'apporter une meilleure garantie de sécurité du vol en conditions givrantes.

ANNEXE 1

DEFINITION DES CONDITIONS MAXIMUM CONTINU ET MAXIMUM INTERMITTENT (ANNEXE C DES REGLEMENTS JAR 25 ET FAR 25)

1.- MAXIMUM CONTINU

Altitude Pression :
0 ≤ Zp ≤ 22 000 feet

Température extérieure :
- 30 ≤ Ta ≤ 0°C

Etendue verticale maximum du nuage :
6 500 feet

Etendue horizontale maximum du nuage :
17,4 NM

Diamètre effectif moyen des gouttelettes :
15 ≤ $\mathcal{N}$ ≤ 40 microns

Concentration en eau :
0,05 ≤ C ≤ 0,8 g/m3

2.- MAXIMUM INTERMITTENT

Altitude Pression :
4 000 ≤ Zp ≤ 22 000 feet

Température extérieure :
- 30 ≤ Ta ≤ 0°C

Etendue horizontale maximum du nuage :
2,6 NM

Diamètre effectif moyen des gouttelettes :
15 ≤ $\mathcal{N}$ ≤ 50 microns

Concentration en eau :
0.15 ≤ C ≤ 2,9 g/m3

ANNEXE 2

CONDITIONS DE CALCUL DES FORMES ARTIFICIELLES DE GIVRE SUR ATR 72

1.- FORMES DECOLLAGE (Les systèmes de protection étant inopérants).

z = 0ft

SAT = -4°C

C = 0,55 g/m3

diamètre des gouttelettes = 20$\mathcal{N}$

VC = 81 kt α_{REF} = 1°

pendant ot = 60 sec

VC = 126 kt α_{REF} = 7°

pendant ot = 120 sec

2.- FORMES CROISIERE

2.1 Parties non protégées

zp = 15000 ft SAT = -12°C
diamètre des gouttelettes = 20$\mathcal{N}$

VC croisière max 230 kt

C = 0,38 g/m3 ot = 35 mn (e = 3in max)

2.2 Partie protégées

zp = 15000 ft SAT = -20°C
diamètre des gouttelettes = 20$\mathcal{N}$

VC croisière max 230 kt

Maximum intermittent C = 1,7 gr/m3
ot = 34 sec

Maximum continu C = 0,2 gr/m3
ot = 146 sec

3.- CAS DE PANNE

Les conditions sont les mêmes que pour les parties non protégées en croisière mais pour un temps d'exposition moitié ot = 17 mn.

4.- FORMES "PUSH OVERS" sur parties protégées.

Configuration atterrissage

VC = 90 kt Zp = 5000 ft SAT = - 4°C

Diamètre des gouttelettes 20$\mathcal{N}$

Maximum intermittent

C = 2,42 g/m3 ot = 60 sec

5.- RUGOSITE DES FORMES.

Pour les accumulations importantes (e = 3in) :

hauteur des grains 3 mm
densité 8 à 10 par cm2

Pour les accumulations faibles (e < 5 mm):

hauteur des grains 1 mm
densité 8 à 10 par cm2

ICING SIMULATION: A SURVEY OF COMPUTER MODELS AND EXPERIMENTAL FACILITIES

by

M.G. Potapczuk and **J.J. Reinmann**
NASA Lewis Research Center
Mail Stop 77-10
Cleveland, Ohio 44135
United States

Summary

This paper is a survey of the current methods for simulation of the response of an aircraft or aircraft subsystem to an icing encounter. The topics discussed include: 1) computer code modeling of aircraft icing and performance degradation, 2) evaluation of experimental facility simulation capabilities, and 3) ice protection system evaluation tests in simulated icing conditions. Current research, which is focussed on upgrading simulation fidelity of both experimental and computational methods, is discussed. The need for increased understanding of the physical processes governing ice accretion, ice shedding, and iced airfoil aerodynamics is examined.

1. Introduction

The safe operation of an aircraft under icing conditions is a topic of current interest in the aerospace community. A need for development of icing simulation methods has been identified by aircraft manufacturers and certification authorities alike.[1] Reinmann, et al.[2] identified several reasons for the current interest in icing; '(1) the more efficient high by-pass ratio engines of today and the advanced turboprop engines of tomorrow have limited bleed air for ice protection, so the airframers are seeking more efficient systems; (2) airfoil designers do not want their modern, high-performance surfaces contaminated with ice, so they are intensifying pressure to develop ice protection systems that minimize residual ice and thereby allow the airframer to keep airfoil surface area to the minimum; (3) new military aircraft requiring severe weather capability are currently under development; (4) some existing military aircraft, being used primarily for training missions, are experiencing foreign object damage (FOD) due to icing conditions they would not normally encounter in combat; (5) designers of high performance military aircraft want to avoid burdening the aircraft with ice protection, so they want to know where and how much ice will build on the aircraft and whether the aeroperformance penalties are acceptable; (6) designers of future high performance aircraft with relaxed static stability need to know how their aircraft will perform with contaminated aerodynamic surfaces; (7) little is known about the effects of ice accretion on the operation and performance of advanced turboprops, and whether or not ice protection will be required; and (8) the FAA has certified only one civilian helicopter for flight into forecasted icing, which implies a strong need for support of helicopter icing.'

Satisfying these needs can require lengthy and expensive flight test programs if unassisted by icing simulation methods. Additionally, finding icing conditions over the full certification icing envelope can not be done within a reasonable time frame. Thus, various methods for simulation of icing conditions are an important and necessary part of the design and certification of aircraft and ice protection systems.

Initial efforts at icing simulation took place in the late 1920's and early 30's. These activities are described in References 3-8. World War II precipitated an urgent need for research into icing simulation and ice protection system design. In the United States, this led the National Advisory Committee for Aeronautics, NACA, to build the Icing Research Tunnel (IRT) at the Lewis Research Center in Cleveland, Ohio during the early 1940's. Initial activities in the IRT covered a broad range of icing problems. Many of these included the development of ice formations on aerodynamic surfaces and the evaluation of aerodynamic performance degradation. A complete bibliography of the NACA research activities during this period is available as a NASA TM.[9]

Icing simulation activities have increased dramatically during the period from the late 1970's to today. Wind tunnel and flight research has been conducted by many organizations in North America and Europe. In addition, the advent of high speed computer systems has allowed the development of sophisticated computer simulations of ice accretion processes and resulting performance degradation. As a result, a new role has been created for wind tunnel and flight research, that is development of code validation databases.

Despite the long history of icing research, there still remains a significant number of unresolved issues in the process of icing simulation. These issues range from the fundamental physics of the icing process to the mechanisms underlying the ice removal process. The ability of the aerospace community to predict the effects of aircraft icing and the performance of potential ice protection systems will be strengthened by addressing these issues and

incorporating an increased understanding of the icing process into simulation efforts. This paper seeks to identify the issues of current icing simulation research and to suggest how current simulation methods might be improved.

2. The Physics of Icing and Ice Protection

2.1 Ice accretion physics

Icing occurs when an aircraft encounters a cloud containing super-cooled water droplets, which impact aerodynamic surfaces and freeze, forming non-aerodynamic shapes on these surfaces. Incoming water droplets can vary in size from 2 or 3 microns to over 40 microns. Typically, smaller droplets tend to follow the airflow over the surface while larger droplets follow more straight-line paths to the surface. Upon impact on the aircraft surface, the water droplets can either freeze immediately or exist as a water/ice mixture. These two conditions are dependent on environmental parameters such as, temperature and cloud liquid water content (LWC), and on aircraft surface conditions such as, skin temperature and surface roughness.

The basics of the ice accretion process, as described above, have been known for some time. However, there are details of the process which are still not completely understood. Recent research in these areas has focused on development of alternatives to the physical model currently used in ice accretion codes.The current model was proposed by Messinger[10] nearly forty years ago and includes the following concepts: in rime icing conditions (*i.e.* air temperatures well below freezing and low LWC values), all cloud droplets freeze upon impact with the surface. In glaze icing conditions (i.e. air temperatures close to freezing and high LWC values), only a fraction of the water will freeze upon impact, and the remainder will run back. The close-up photography of Olsen and Walker,[11] as shown in Figure 1, indicates that some fraction of the water which remains in the liquid state after impact may not runback along the surface, as is currently assumed. This water may remain in pools formed by the surrounding ice, thus requiring an alteration of the current model of the ice growth process. Splashing of incoming water droplets[12,13] may occur under certain conditions, which could result in less water on the surface than indicated by droplet trajectory calculations. It is also suspected that the initial conditions of the icing process may have a significant impact on the subsequent ice growth. Factors such as the initial surface roughness, the surface tension at the air-water-airfoil interface, the water droplet size, and the boundary layer transition location can all influence the final ice shape.[12,13]

Following up on Olsen's work, Hansman, et al. [14] further studied the icing process. Figure 2 shows the test setup used to observe ice growth on a cylinder. By illuminating the ice surface with a laser sheet, they constructed a time history of the ice profile (shown in the middle diagram). This sequence of profiles suggested a three zone heat transfer model that differed significantly from the Messinger model. Hansman's model attempts to account for the changing conditions on the airfoil surface by tying the transition from the smooth to rough region to the boundary layer transition.

It is hoped that by understanding the ice accretion process more completely, some of the empiricism present in current icing models may be eliminated. This should result in more robust models providing simulation of the icing process over a broader range of the icing envelope.

2.2 Iced airfoil aerodynamics

Ice accretions on the wing leading edge lead to increases in drag, decreases in lift, changes in the moment distribution, a decrease in the value of $C_{L\,max}$, and a decrease in the stall angle. These effects are due to a change in the pressure distribution on the wing and to increased viscous losses.

From the point of view of effects on aerodynamics, ice growths have two relevant length scales. Ice growth structures on the scale of the boundary layer height can be considered as roughness elements. Structures larger than the boundary layer height and on the order of the airfoil thickness influence the aerodynamics in different ways and are typically referred to as ice shapes or ice caps.

Ice shapes can result in changes in the pressure distribution over the airfoil, development of separated flow regions, early transition of the boundary layer, and premature stall. Ice roughness can result in thickening and early transition of the boundary layer, alterations to the pressure distribution, and increased drag. Both types of ice growth can lead to a decrease in maximum lift.

The results of Ingelman-Sundberg, et al.[15]suggest that ice roughness can result in a decrease in $C_{L\,max}$ and that a glaze ice shape can result in an even larger decrease for single-element airfoils. Their results also indicate that roughness and ice caps produce approximately the same level of change in $C_{L\,max}$ for high lift configurations. Potapczuk and Berkowitz[16] have measured the changes in lift, drag, and pitching moment for a two-dimensional model of a Boeing 737-200 ADV wing section, in both cruise and high-lift configurations, as ice accumulated on the surface. Their results indicated continual increases in the effects of ice accumulation on drag. The changes to lift and pitching moment were not evident until the angle of attack was varied from the condition at which the ice was accumulated.

It is difficult to establish any clear trends applicable to all icing encounters, however, it is safe to say that the degree of aerodynamic degradation due to icing is dependent on airfoil geometry and attitude, ice accretion time, and icing cloud conditions. As a consequence of this dependence, it is apparent that simulation of iced airfoil aerodynamics is necessary to thoroughly evaluate the behavior of a given aircraft encountering icing conditions.

The changes in airfoil aerodynamics due to icing apply equally to helicopter rotors. Bond et al.[17] has shown that rotor icing can lead to increases in rotor torque on the order of 25 to 50 percent. Additional results indicate that ice shedding events can reduce rotor torque by 5 to 10 percent temporarily, thus producing loading transients which can increase system vibration. Asymmetric ice shedding can pose a considerable problem due to out-of-balance conditions which may lead to high vibratory loads on the rotor system.[18]

2.3 Ice Protection Systems

There are two approaches to aircraft protection from icing; anti-icing and de-icing. Anti-icing is the prevention of ice growth on critical aircraft lifting surfaces, while de-icing is the removal of accumulated ice before significant degradation of aircraft performance. Anti-icing methods provide the greatest safety factor but require the greatest amount of energy. De-icing methods on the other hand may provide appropriate safety with lower energy requirements.

Either approach to ice protection may be implemented in a number of ways. There are essentially three categories of ice protection techniques: chemical, mechanical, and thermal. Chemical methods typically consist of exuding some type of material on the wing surface that mixes with the ice and depresses the freezing point. Mechanical methods utilize various devices that break the ice-wing surface bond by imparting a strain or an impulse to the outer structure of the wing. Thermal methods melt or evaporate the ice by heating the wing surface through a variety of methods.

The conventional approach for protection of commercial transport vehicles for the past thirty years has been anti-icing through the use of hot compressor bleed air. Hot air flowing inside the wing raises the temperature of the leading edge above a level which will allow ice to form on the surface. Usually the temperature of the leading edge is high enough to evaporate any water on the surface. This prevents runback water from refreezing on the wing surface aft of the heated area.

But more recently, as jet engine manufacturers have begun increasing engine by-pass-ratios to achieve higher efficiencies, the engine cores have become smaller and the amount of hot bleed air available for anti-icing has shrunk significantly. First priority for bleed air is given to cabin pressurization and air conditioning. To cope with this loss of bleed air, airframers are either eliminating ice protection from selected components, or considering alternatives to compressor bleed air. Attractive alternatives are more energy-efficient deicing systems that allow some ice buildup before actuating the deicer. Helicopters, general aviation aircraft, and light transports, all with relatively small payload fractions and low power margins, have always relied on these more efficient ice protection systems.

As alternate ice protection methods are incorporated into aircraft designs, there will be a need to simulate their capabilities either computationally or in ground testing facilities such as icing wind tunnels. It therefore will be necessary to fully understand these experimental simulation activities.

3. Analytical Simulation Methods

Analytical icing simulation has been based on a combination of correlations, computer codes, and theoretical models of the icing process and its consequences. This section will discuss some of the current methods used for modeling ice accretion, aeroperformance degradation, and ice protection system performance. For further information on recent progress in analytical modeling see the report by Shaw, et al.[19]

3.1 Ice Accretion Computer Models

Ice accretion codes have been developed by several researchers.[20-23] Typically, these codes calculate the flowfield surrounding the airfoil, determine the droplet impingement pattern, and calculate the amount and shape of ice that grows on the surface. Results of these codes are compared to ice shape tracings from tests in icing wind tunnels. Comparisons to flight data have also been performed,[24] but are not as common due to the difficulty in obtaining actual in-flight ice shapes.

Current ice accretion models are based on the control volume approach, such as that of Messinger.[10] In this model, a mass balance and energy balance are performed in order to determine the amounts of water that either freeze or runback along the surface to the next control volume. This control volume approach is depicted in Figure 3. The key factors influencing the ice growth in this model are the mass of incoming water from the cloud and from the upstream control volume, the convective heat flux, and the heat flux into the surface at the ice-body interface.

The ability to accurately calculate the incoming water from the cloud has been demonstrated quite convincingly by several comparisons between calculation and experiment. The accuracy of these methods is deter-

mined by evaluating the local collection efficiency calculation along the surface of the airfoil. The local collection efficiency, in a 2D sense, is defined as the ratio of the vertical distance between two particles at the upstream release point to the distance along the airfoil surface between their impact points. An example of the collection efficiency calculation is shown in Figure 4, where the calculated value along the surface of a NACA 65-015 airfoil is shown to agree quite closely with experimental results.

The convective heat flux is influenced by the development of the boundary layer on the rough iced airfoil surface. As such, the pressure distribution, roughness level, and transition location all play an important roll in the ice growth process. Currently these effects are accounted for by correlations between the heat transfer coefficient and the cloud icing conditions. A typical example is found in the roughness correlation in LEWICE,[21] the ice accretion code developed by NASA.

Hansman, et al.[14] has indicated an alternate approach which tries to incorporate more of the physics of the process, as it is currently understood. His results have shown a marked improvement for cases of ice accretion on cylinders. Figure 5 shows a comparison of calculations using LEWICE with the original ice accretion model and with Hansman's[25] updated model. The updated analysis and experiment agree remarkably well. This multizone model is undergoing further study and refinement, especially regarding surface roughness and its effect on heat transfer and transition location.

Most computer codes treat the heat flux into the surface as a specified constant value during the entire simulation. This constant is normally taken to be zero thus prescribing an insulated boundary. However, heat flux into the airfoil surface may play an important role in the development of the ice shape, especially in the initial moments of the ice accretion. This possibility along with the desire to model thermal de-icing systems has led to the development of computational methods for evaluating the heat transfer between the ice and the underlying airfoil structure. These models will be discussed more fully in the section on ice protection system simulation.

Until recently, these computer models have been strictly two dimensional, calculating ice shapes for chord-wise slices along a wing surface. Three dimensional ice accretion codes are currently under development as extensions of the well established 2D methods. Potapczuk and Bidwell[26] have calculated the ice growth on a MS-317 wing section with 30° sweep angle. Guffond has calculated ice growth on the tip of a helicopter rotor.[27] These efforts, while promising, require further development before use as an engineering tool.

A recent research activity has been the coupling of the ice accretion code with methods for evaluation of the performance degradation due to icing. Cebeci[28] has coupled a two-dimensional interactive boundary layer (IBL) method with the LEWICE ice accretion code in order to simulate the entire icing process. Figure 6, taken from Shin et al.,[29] shows the results for several icing conditions. The most encouraging aspect of this calculation is the ability of the code to determine the drag rise at temperatures just below freezing. The results for the ice shape comparison agree quite well. The differences between the code and experiment for the actual drag values suggest that the method requires further refinement.

3.2 Performance Degradation Computer Models

Determination of an aircraft's response to an icing encounter requires the evaluation of performance changes resulting from a wide variety of ice accretion shapes. This necessitates the use of an extensive series of tests either in flight or in a wind tunnel. In either case, the use of appropriate computational methods could decrease the amount of required testing and thus decrease the cost and time requirements of the certification process. As such, computer codes currently being used for evaluation of clean or un-iced aircraft are being adapted for use in evaluation of icing performance degradation.

Until recently, performance changes for iced airfoils have been computed using empirical correlations such as those of Gray,[30] Bragg,[31] and Flemming et al..[32] These methods work well over a restricted set of environmental conditions, but are not adequate for general use by potential aircraft designers. As a result, computer codes have also been developed to evaluate the changes in performance of airfoils, wings, and rotors due to the presence of ice on critical surfaces.

Cebeci[28] has used the IBL code to evaluate the performance degradation of a NACA 0012 airfoil with a simulated leading edge ice shape. Comparisons of the IBL results with Bragg's wind tunnel data[33] are shown in Figure 7. These results indicate that the IBL method can determine the aerodynamic losses associated with ice growth on an airfoil up to stall. Further work with the IBL method has involved coupling with the LEWICE ice accretion code, as mentioned previously. An interesting result of this work is that the roughness parameters used in the ice accretion calculation were not the same values used in the viscous-flow drag calculation. There is some linkage between the role of ice roughness level in heat transfer and in boundary layer development. Further study is required to determine the influence of roughness on the ice growth process as well as on the iced airfoil boundary layer development.

Navier-Stokes calculations, while requiring more computer time, reveal interesting details of the iced airfoil aerodynamics not produced by the IBL method.

Potapczuk[34] has used the ARC2D code with a modified algebraic turbulence model to calculate the flowfield for the same iced NACA 0012 geometry that was used in the IBL calculations. Results, also shown in Figure 7, indicate good agreement with data even beyond the stall condition. The structure of the recirculation zone aft of the ice shape was also examined and compared to the measurements of Bragg,[35] as shown in Figure 8. These results reveal that the reverse flow velocity is not calculated properly. Use of a more appropriate grid or alteration of the turbulence model may be required. Additionally, results from investigations of Bragg and Khodadoust,[36] and Zaman and Potapczuk[37] suggest that there may be significant flow unsteadiness as this iced airfoil approaches stall.

The recirculation zone in the region aft of the ice shape results in complicated flow structures which are fundamentally three-dimensional in nature. An effort has begun to calculate the flowfield for a swept wing geometry with ice on the leading edge. Kwon and Sankar[38] have used a 3D Navier-Stokes code to evaluate the aerodynamics of a finite span wing model with a NACA 0012 profile and a 30° sweep angle. Figure 9 shows particle traces obtained from their calculation for an 8° angle of attack condition. The traces show the separated flow condition that occurs behind the ice shape and increases in size from the root to the tip of the wing.Their results for clean and iced conditions agree quite well with the experimental results of Khodadoust and Bragg.[39] Figure 10, which shows the comparison of spanwise lift distribution for these two conditions, supports the promising results from this simulation effort.

3.3 Ice Protection System Models

Ice protection systems have also been modeled computationally. Analysis methods for thermal systems are the most advanced. Both hot air systems and electrothermal systems have been modeled successfully. There have been fewer reported results from analysis efforts for mechanical systems. However, some recent activity in this area suggests that these systems will also be modelled computationally in the future.

Al-Khalil, et al.[40] used a 3D potential flow code, a 3D particle trajectory code, and a control volume energy analysis to evaluate a hot air anti-icing system for an engine inlet.This method holds the potential for optimization of hot air ice protection systems.

Electrothermal systems have been modeled using finite-difference methods by Keith, et al..[41] An electrothermal system consists of an array of electric heater elements embedded under the outer skin of the wing surface. The heater elements are activated during an icing encounter with enough current to melt the ice that may form on a wing surface. A typical 2D model of an electrothermal heater element is shown in Figure 11. The model simulates the thermal behavior of the composite structure and ice layer. Results indicate that temperature traces at the ice-skin interface, heater base, and substrate base agree well with measured values. Current work by Wright, et al.[42] in this area is centered on combining this analysis with ice accretion predictions in order to provide a tool for the evaluation of electrothermal anti-/de-icing system performance.

Development of methods for evaluation of mechanical ice protection systems is just beginning with some initial work on ice structural properties described in References 43-45. Computational methods to predict FOD (*i.e.* shed ice) damage to engine blades are also under development. The ability to determine the damage resulting from various sizes and shapes of shed ice will greatly enhance de-icing system design.

A mechanical system that has been evaluated computationally is the Pneumatic Impulse Ice Protection (PIIP) system. The PIIP system relies on rapid inflation of pneumatic tubes embedded the wing surface.[46] The pneumatic impulse causes a displacement of the surface which combined with the surface acceleration, cracks, debonds, and expels the ice. Ramamurthy, et al.[47] used a time dependent, compressible flow model for internal duct flow to model this ice protection system. Results to date have been encouraging however further work is required.

4. Experimental Simulation Methods

The remainder of this paper will discuss approaches to experimental icing simulation, a topic that includes both experimental facilities and the testing done in them. The prevalent approaches are as follows:

- testing in icing wind tunnels;
- testing in engine test cells that can produce supercooled clouds;
- testing in outdoor ground-level spray facilities that can produce supercooled clouds during the winter;
- testing in environmental chambers that can produce subfreezing air temperatures and supercooled clouds;
- flight testing behind aircraft spray tankers equipped with water tanks and spray booms to produce supercooled clouds; and
- testing with replicated or simulated ice shapes.

References which contain comprehensive surveys of all icing facilities in Europe and North America, and

brief descriptions of three new icing wind tunnels in North America are contained in section 4.1.3.

Principal applications of experimental icing simulation include testing of full-scale and sub-scale aircraft components, developing advanced ice protection systems, conducting basic research on the icing process and on the fundamental properties of ice, establishing empirical data bases and correlations, and developing and validating analytical models or computer codes.

4.1 Icing Simulation Facilities

The need to produce both repeatable and predictable icing test conditions for the evaluation of computer codes and ice protection systems, has led to the development of specialized icing test facilities. The following discussion centers on the requirements for and issues surrounding facilities designed to simulate the natural icing environment under controlled test conditions.

4.1.1 Icing Wind Tunnels and Test Cells

Icing wind tunnels and engine test cells undoubtedly offer the most versatile approaches to icing testing. It generally costs much less to test components in an icing wind tunnel than in flight, and conditions can be much more closely controlled and repeated. In icing tunnel testing, productivity is high and the safety risk is very low. But there definitely is an appropriate role for flight testing, and that role will be discussed later.

A schematic of the closed-loop NASA Icing Research Tunnel (IRT) is shown in Figure 12. In addition to having all the systems of a conventional dry air tunnel, an icing tunnel has two unique systems: a water spray system that injects water droplets into the airstream to create a supercooled cloud and a refrigeration system and heat exchanger that cools the air to temperatures as low as minus 30°F. The heat exchanger is in the leg just upstream of the spray bars. Closed-loop refrigerated tunnels can "dial in the weather" any time of the year and are therefore very productive. For example, in 1988, the NASA IRT logged 1330 hours of test time, making it one of NASA's most productive tunnels.

Some icing tunnels bring in subfreezing outside air to supply the cooling. Since they are restricted to operating only in the winter, their productivity is lower, and it is much harder to achieve a systematic and reproducible test program in them.

The heat exchanger and spray systems in icing wind tunnels introduce unique operational challenges. First, the air temperature and velocity profiles must remain uniform across the test section for the several hours that tests usually require, even though as time progresses the heat exchanger surfaces capture and freeze out the water injected by the spray system. Second, the cloud must be uniform over the test section. Third, the cloud must consist of supercooled droplets and no ice particles. Fourth, the spray system must be capable of reproducing nature's wide range of liquid water contents, droplet size spectra, and droplet median volumetric diameters (MVD). MVD is defined as the diameter where half of the volume of water is contained in droplets with diameters smaller (or larger) than this diameter. And fifth, the icing cloud and air temperature must be repeatable and controllable to within fairly close tolerances. In practice, no icing tunnel fully meets these requirements, but good tunnels do a reasonable job of approximating them.[48]

Another critical challenge for icing tunnels is the accurate measurement of the supercooled cloud properties. LWC can be measured to within about ±10 percent. But the accuracy of droplet sizing instruments is not known precisely, and inaccuracies greater than ±2 microns are probably typical for MVD's from 10 to 40 microns.[49] Finally, methods to detect ice particles in a cloud are primitive, and methods of quantifying the amount of ice in a cloud are not yet available.[50]

Engine test cells are used to evaluate the ice accretion patterns that may develop on engine inlets, to investigate the effects of the icing environment on engine operations and performance, and to evaluate the performance of engine ice protection systems. Engine test facilities are of two types: sea-level test stands and altitude test cells. The former having the advantage of large size and the ability to examine crosswind icing, while the latter has the advantage of being able to test over a wide range of Mach numbers, pressure altitudes, and inlet conditions without regard to prevailing weather.

The General Electric icing test facility in Peebles, Ohio, is an outdoor engine test stand located downstream of a large, free jet wind tunnel. A schematic of the facility, taken from Reference 51, is shown in Figure 13. The facility has been used to test the icing characteristics of several full-scale engines. The facility is designed to produce supercooled water droplets of 15 to 50 micron diameter at LWC levels ranging from 0.4 to 3.6 g/m^3. The facility is also designed to produce these conditions at temperatures of -20° to 0° C. The temperature conditions are of course dependent on the ambient temperature.

The lack of altitude pressure capabilities for this facility necessitates the development of adjustments to engine variables or to test variables such as LWC, drop size, and liquid/air mass flow ratios in order to simulate flight conditions. The facility is also limited to humidity conditions prevalent in the atmosphere during the scheduled test period. In order to increase the number of test opportunities available in this facility a set of scaling laws would be useful in order to adjust controllable parameters, thus allowing simulation of alternate flight conditions.

Altitude test facilities provide the capability to perform engine icing tests under conditions similar to those experienced in-flight. Examples of altitude icing facilities are the AEDC Engine Icing Test Facility at Tullahoma, Tennessee, USA;[52] the icing test cells at the National Gas Turbine Establishment (NGTE) at Pyestock, UK;[53] and the Centre d'Essais des Propulseurs (CEPr) at Orsay, France.[54] A schematic of the free jet icing test cell at AEDC, taken from Reference 52, is shown in Figure 14. This arrangement is typical of the engine icing test cells.

Testing in altitude test cells generally consists of determination of ice accretion patterns on engine component surfaces, ice protection system evaluation, and engine icing damage assessment. Since the engine models used in such facilities are generally not full-scale, the question of scaling plays a predominant role in determining test conditions. Typically, all the scaling parameters necessary for complete similitude cannot be satisfied during a single test. Hence, there is a need to develop test programs to evaluate the relative importance of scaling parameters in order to relax some of the constraints on engine icing tests. Ruff [55] and Bartlett[56] provide a more detailed discussion of similitude for engine icing tests.

4.1.2 In-flight Icing Simulators - Spray Tankers

Although computer simulations and icing tunnel testing are important steps in an icing program and hold the promise for an increased role in the future, flight testing of the full-scale aircraft is still an essential step in achieving icing certification or qualification. Before launching into an extensive flight test program in natural icing, it is sometimes advantageous to precede flights in natural icing with flights behind a spray tanker.

Icing flight testing behind a spray tanker offers important benefits: first, it offers a safety advantage because the pilot can fly the test aircraft out of the cloud and terminate the test if he encounters any problems; second, it can save development time and costs by providing cloud conditions that rarely occur in nature, yet are conditions in which the aircraft must be certified or qualified (such as higher LWC's or larger MVD's); and third, it serves to uncover major equipment problems that should be fixed before undertaking an extensive, expensive, and high risk flight test program in natural icing.

Producing a supercooled cloud with an in-flight spray tanker and calibrating that cloud presents all the challenges found in an icing tunnel plus some others. For example, the outside air humidity profoundly affects the cloud droplet size. Dryer air causes the smaller droplets to evaporate, and since any humidity from zero to 100 percent is possible on any flight, it is difficult or impossible to achieve predetermined MVD's or LWC's. Thus, before each immersion of the test aircraft in the cloud, another aircraft equipped with cloud instruments must fly through the cloud to measure its conditions. A further challenge for tanker spray systems is to provide the copious supplies of high pressure air required by the nozzles to produce the smaller droplets typically found in nature (10 to 40 microns MVD). Or conversely, the challenge is to develop a nozzle that can produce the smaller droplets with lower air pressures and flows. Nozzle research for the special needs of the spray tankers is ongoing.[57] If nozzles are developed that make small droplets with lower air pressures and flows, they will also be advantageous for wind tunnels and engine test cells, because lower nozzle air pressures will result in less droplet freeze-out.

Some of the general aviation airplane manufacturers use one of their own aircraft as a spray tanker, but the two best known spray tankers in the United States belong to the military: the Air Force's KC 135 spray tanker and the U.S. Army's Helicopter Icing Spray System (HISS).

The Air Force's spray tanker is a KC-135 aircraft equipped with a 2000 gallon water tank and a new square spray boom that extends below the aircraft's tail. The test aircraft flies 50 to 100 feet behind the boom, and depending upon the distance behind the boom, the cloud size ranges from about 5 to 10 feet square. Most testing is done at aircraft speeds from 150 kt to 300 kt indicated. The tanker is used primarily for icing tests of engines, but it is also used for tests of windshields, control surfaces, missile/aircraft interface launches, missiles, and radomes.

The Army's HISS tanker is a Boeing Chinook CH 47 D helicopter that carries an 1800 gallon water tank and a rectangular spray boom that drops down below the Chinook after the ship is airborne. The test aircraft flies about 180 feet behind the boom, where the cloud size is approximately 8 feet high by 36 feet wide. Most testing is done at aircraft speeds from 80 to 130 kt true. The HISS is used for testing both helicopters and low-speed fixed-wing aircraft.[58] Typical tests for helicopters include main rotors, tail rotors, engine inlets, fuselages, stabilators, droop stops, windshields, antennas, external stores, airspeed sensors, production ice detectors, optical system sensors (pilot night vision, and target data acquisition), refueling booms, external hoists, and various mission equipment exposed to the airstream.

As part of an overall program to assess Army and NASA cloud measurement systems, NASA flew their Twin Otter icing research aircraft behind the HISS[59] in order to acquire main wing ice shape and drag data for clouds with large MVD's, a condition that is rare in natural icing around the Great Lakes area where the Twin Otter is stationed. Figure 15 shows main wing ice shapes and drag values for two different conditions;[60] first, a flight in natural icing with a 16 micron MVD cloud, and

second a flight behind the HISS with a 35 micron MVD cloud. The HISS cloud, with the larger drop size, produced a greater extent of ice coverage and a wing section drag coefficient about 25 percent higher.

4.1.3 Surveys of Icing Simulation Facilities

Many aircraft icing simulation facilities exist worldwide. In 1981, Olsen[61] published a survey of icing simulation facilities in North America. Two excellent surveys of these facilities are listed in AGARD References 62, and 63. AGARD AR-166, surveyed all the facilities in Europe and North America as of 1981. In 1986, AGARD AR-223 amended the earlier AR-166 to delete those facilities removed from service and to add new facilities developed since 1981.

In February 1991, the Society for Automotive Engineers (SAE) sent panel members of the SAE AC-9C Activity AC-9C-90-1 a questionnaire intended to obtained a comprehensive description of all aircraft icing facilities in Europe and North America. One goal of the survey is to determine how facilities are presently calibrated. The activity also has a goal to determine if some reliable and easily performed calibration methods could be established that would allow all facilities to be compared on a common basis.

Since 1986, three new facilities were added in the United States. Fluidyne in Minneapolis, Minnesota, USA, modified a transonic wind tunnel to include an icing spray system.[64] The tunnel uses outside air during the winter to obtain the subfreezing temperatures. The test section is 22 in. x 22 in., with Mach numbers up to 0.8. This tunnel offers the potential for obtaining ice shapes and aeroperformance data on full-scale helicopter rotor blade sections.

The BFGoodrich Deicing Systems Group in Uniontown, Ohio, USA, brought on line in 1989, a new icing tunnel.[65] The test section is 22 in. x 44 in., with airspeeds up to 200 mph. This facility also includes a cold room that allows researchers to move icing samples from the test section to the cold room where they can be stored or studied further.

The Boeing Mechanical Systems Laboratory in Seattle, Washington, USA, is bringing on line the Boeing Research Aerodynamic/Icing Tunnel (BRAIT). The BRAIT will have three test section sizes: 5 ft x 8 ft (150 kt max airspeed), 4 ft x 6 ft (250 kt max airspeed), and 2.4 ft x 4.4 ft (350 kt max airspeed). The spray system will be removable for dry air testing. The tunnel is scheduled to begin testing in March 1992. Boeing estimates that the use of their new tunnel will save them up to one million dollars for each new airplane they certify for icing.

4.2 Icing Testing Techniques

Icing testing can be performed in facilities such as those described above and in addition can be done in conventional facilities such as dry air wind tunnels. In this section, several types of test programs will be described in order to illustrate the range of experimental methods used to understand the icing process and to demonstrate the efficacy of ice protection systems.

4.2.1 Ice Accretion Physics

Icing tunnels are a good place to study the fundamental processes of ice accretion because they control and repeat conditions quite well. As mentioned previously, Olsen and Walker[10] observed the icing process in the NASA IRT with close-up movies. These movies revealed accretion phenomena for glaze ice quite different from that contained in the currently used analytical model for ice accretion. These differences were discussed in the analysis section above.

In addition to the close-up movies, Olsen examined the structure of the ice deposits, the effect of ice shape on droplet catch, ice roughness effects, the effect of initial surface flow on the resulting ice shape, and the effect of droplet shedding. Olsen also discussed the use of plastic replicas of the ice shapes, developed during previous testing,[66] to evaluate the local heat transfer coefficient in a dry air wind tunnel. This illustrates the inter-relationship between testing in an icing facility and in a dry air wind tunnel.The techniques used in Olsen's test program illustrate the type of information relating to ice accretion physics which may be obtained in an icing test facility.

Personne[67] examined the effects of roughness on the type of ice developed on cylinders. He found that for low airspeeds (less than 20 m/s) surface roughness increases the droplet collection efficiency. He also suggests that rime ice roughness levels are due to the random nature of droplet trajectories caused by increased airstream turbulence near the surface.

4.2.2 Icing Effects on Aeroperformance

An important aspect of icing simulation is the experimental measurement and analytical prediction of ice accretions and their effects on wing aerodynamics. The combined use of icing wind tunnels and conventional dry air tunnels has proven effective in studying the effects of ice on airfoil aeroperformance. When conventional tunnels are employed to study icing effects, the ice is simulated by attaching a replica of an ice shape to the airfoil's leading edge. Ice replicas are obtained by several methods as discussed below.

The best method for obtaining detailed replicas of leading edge ice is from silicone rubber molds, which replicate both the ice shape and its surface texture.[68] Once the female mold is made, epoxy resin is poured into

the mold to form a casting of the ice. In a second method, chordwise cross sections of the ice are obtained by melting a thin cut in the ice around the leading edge, inserting a template in the cut, and drawing an outline of the ice on the template. A third method uses mono or stereographic photos to obtain ice shapes.

Ice replicas are typically made from wood, styrofoam, or epoxy resin. Sometimes the airfoil is machined or molded to coordinates that include the shape of the leading edge ice. Unless the surface texture is obtained from silicone rubber molds, some method of adding surface roughness is needed. Roughness can be added for example, by applying sand grain or by roughing up the surface with a knurling tool.

Ice replicas are used in conventional wind tunnels for several reasons: (1) the icing tunnel in which the ice was formed may not have the necessary force balances or flow quality to make good aerodynamic measurements; (2) making pressure measurements in a cold, moist cloud environment doesn't work well; (3) real ice sublimates and sometimes rust or dirt circulating in the tunnel erodes the ice, so unless the aerodynamic measurements are done quickly, the ice shape and surface roughness will change during the tests; (4) ice replicas allow the test to be repeated as many times as necessary to get good aeroperformance data; and (5) in the case where the experimental aeroperformance data base is to be used for code validation, ice replicas machined or molded to precise coordinates on an airfoil will allow the flow codes to model the exact airfoil shape used in the wind tunnel test.

As part of their landmark study of icing and its aerodynamic effects, the Swedish-Soviet Working Group on Flight Safety conducted testing in a Soviet icing tunnel and a Swedish dry air tunnel to study the effects of wing and tail ice on aircraft stability. In one study, they tested several configurations of a 2D, four-element wing section (1 m chord), including advanced high-lift devices.[15] And in another study, they tested two swept tailplane configurations with flaps.[69] The airfoils were tested in the Special Wind Tunnel T-4 at the Research Institute of the Ministry of Civil Aviation, USSR. The tunnel cross section was 1.5 x 2.0 m, and its speed range was 10 to 70 m/s. The tunnel was equipped with a spray system and used outside air below 0 °C for cooling. In setting the tunnel icing conditions, the Soviets applied approximate icing scaling relations to relate model test conditions to full-scale conditions. Very detailed female silicone rubber molds were made of the ice accretions. In Sweden, the molds were attached to airfoils, and epoxy resin was poured into the molds to form detailed replicas of the ice shapes. The airfoils with the ice replicas were then tested in the 3.6m diameter FFA conventional dry air wind tunnel in Sweden. These dry air tunnel tests produced a comprehensive set of curves of lift, drag, and moment for several angles of attack up to and beyond stall, and for various flap and slat configurations. The Working Group also reported results where they used emery paper to simulate frost (k/c = 1/1300) in the conventional wind tunnel tests. Figure 16, taken from Reference 15, shows the effect on C_L(alpha) and $C_{L\,max}$ of ice shapes corresponding to icing in cruise but with trailing edge flaps extended.

Olsen,[70] in a comprehensive study in the NASA IRT, systematically varied key icing tunnel and cloud parameters to obtain a series of ice shapes and resulting drag coefficients for a NACA 0012, 21 in. chord airfoil (Figure 17). Recently, Olsen's data was compared with predictions made by a version of LEWICE modified to include the interactive boundary layer (IBL) method that predicts lift, drag, and pitching moment of the iced airfoil.[29] The experimental data used in the IBL/LEWICE comparisons were from runs made at several air temperatures, while holding cloud conditions and airspeed constant. As revealed in Figure 18, air temperature strongly affects ice shape and its resultant drag, especially just below the freezing point. Figure 6 compares the IBL/LEWICE predictions with the temperature sweeps.

Potapczuk and Berkowitz[16] tested a 2D, five-element airfoil, in four different configurations (Figure 19), in the NASA IRT. The airfoil was a two-dimensional section of the Boeing 737-200 ADV aircraft wing that Boeing had used earlier as part of their ground de/anti-icing fluids evaluation in the NASA IRT. The airfoil was mounted between two splitter walls, each of which contained a turntable for varying the angle of attack and a force balance for measuring lift, drag, and pitching moments. Performance characteristics were measured at a given angle of attack during the ice accretion process and then over a range of angle of attack conditions after the accretion process was complete. All test equipment, including the data acquisition systems, were provided by Boeing.

Their results indicate the change in stall mechanism that can occur due to the presence of ice on leading edge surfaces. As seen in Figure 20, the C_L vs. alpha curve has a much lower $C_{L\,max}$ value and the slope of the curve beyond $C_{L\,max}$ changes dramatically. These differences suggest a change from trailing edge stall to leading edge stall. Changes of this sort can remain undetected at cruise conditions, yet could cause severe problems during takeoff or landing.

Flemming[32] tested several modern helicopter airfoils in the National Research Council's icing tunnel in Ottawa, Canada. The chord of the airfoils was about 6 in. Silicon rubber molds were made for many of the ice shapes. The NRC tunnel was chosen because it could be run to about Mach 0.7, which is representative of the Mach numbers near the tip of a helicopter rotor. Flem-

ming used the data to develop an empirical correlation for lift, drag, and pitching moment changes caused by icing. He has used these results in the Sikorsky Generalized Rotor Performance Code (GRP) to predict full-scale helicopter torque rises and lift loss, and more recently has used the correlations, with some modifications, to predict the performance of a sub-scale model rotor that was tested in the NASA IRT.[71] These sub-scale model rotor tests are described in a recent report by Flemming.[72]

The aerodynamics of modern swept wing aircraft is dominated by three dimensional effects. As mentioned earlier, NASA is developing 3D flow codes that can model the flow over swept, finite length wings with leading edge ice. To validate the flow codes, NASA has sponsored a parallel experimental program in a dry air wind tunnel[73] to obtain a comprehensive data base on the aeroperformance of swept, finite length wings with ice replicas on the leading edge. Figure 21 shows a 30° swept wing model in a dry air wind tunnel. The ice replica can be seen in the edge-on view. The wind tunnel has the ability to remove the boundary layer through sidewall suction at the wing root. The model is heavily instrumented for surface pressures and is attached to a three component force balance in the wind tunnel wall. Flow diagnostics include laser velocimetry and helium bubble seeding and tracking. Some typical results from this effort were discussed earlier in section 3.2.

4.2.3 Ice Protection Systems Testing

Icing tunnels are used to develop and test aircraft ice protection systems, which include pneumatic boot deicers, porous leading edge fluid deicers, electrothermal deicers, electrothermal evaporative and running-wet anti-icers, hot air evaporative anti-icers, pneumatic impulse deicers, and electro-mechanical impulse deicers. These systems apply to wings, tails, rotor blades, propellers, and engine inlets.

When considering new ice protection systems, airframers are looking for systems that offer some, or all, of the following improvements: lower weight; lower power consumption; acceptable aero-penalties that in some cases may require ice thicknesses not to exceed 0.040 in.; more reliable operation; lower maintenance time and costs; easily retrofitted to existing components; not dependent on compressor bleed air; and more economical to manufacture.

4.2.3.1 Mechanical Impulse Deicers

In their search for alternatives to compressor bleed air and energy-intensive electrothermal anti-icing systems, airframers are considering the pneumatic impulse and electro-mechanical impulse deicer systems now under early development by the ice protection system manufacturers.[46,74-76] Impulse systems have pulse times less than a millisecond and surface accelerations up to 1000 g's, imparting forces strong enough to shatter, debond, and expel the ice. The impulse systems require minimal power (i.e. on the order of the aircraft's landing light power) and they have the potential for maintaining ice thicknesses very thin, both before and after actuation.

In testing impulse deicers the following parameters are measured to characterize deicer performance: (1) maximum size of shed ice particles for a given ice thickness and pulse energy; (2) minimum thickness of ice that can be removed for a given pulse energy; (3) amount, texture, and height of residual ice remaining on the surface before and after deicer actuation; (4) energy per unit arc or per unit span length required for one deicer actuation; and (5) weight per unit area of deicer coverage.[76]

In evaluating deicer performance, the systems must be tested under the full range of expected icing conditions. Experience has shown that two conditions give impulse deicers the most trouble: near-freezing conditions that produce soft, mushy ice with water between the ice and deicer surface; and cold, rime icing conditions that cause the ice to adhere strongly to the deicer surface.[75,77] Knowledge of shed ice size would be essential if a deicer were to be used on a jet engine inlet, because engine fan blades would be damaged if the engine were to ingest ice particles greater than a prescribed size as determined by the engine manufacturer.

Power usage is so low for any these impulse systems that airframers compare them primarily on the basis of weight, complexity, ease of installation, maintainability, and aerodynamic penalties caused by the system installation and by the surface ice before and after deicer actuation.

Figure 22 contains a sequence of photos, from recent low power de-icing tests in the NASA IRT,[77] that capture an ice shedding event by means of high speed videography. Events can be captured at speeds up to 6000 frames per second on special video tapes. These tapes can be examined frame by frame with motion analysis software coupled to a micro-computer. This allows the size of the largest particles shed during an actuation to be estimated and the ice breakup process in the airstream to be followed. Special image processing software is being developed to automate the estimation of particle sizes and possibly to obtain size spectrums as well.

4.2.3.2 Water Runback in Thermal Ice Protection

Thermal deicers or anti-icers are still the most prevalent types of ice protection systems used on aircraft. If these systems are overwhelmed in severe icing, or if in the case of deicers, their on/off timing sequences are improperly adjusted, water in the form of rivulets can run back beyond the heaters and refreeze. Enough runback

water could accumulate over time to cause aerodynamic performance or stability problems, or ice could shed and be swept downstream to damage aircraft or engine components. Thus, ice protection manufacturers are beginning to develop water runback and refreeze models for their ice protection analysis and design codes. For example, see Reference 78 for runback modeling of hot bleed air anti-icers. There does not appear to be extensive experimental icing data for use in validating the runback models, but more work on development of this database is planned.

4.2.3.3 Heat and Mass Transfer from Wet Surfaces

Thermal anti-icers evaporate water that impinges on the airfoil leading edge. In general, impinging droplets are not evaporated immediately upon impact, but rather the water forms a thin film that is heated and evaporated in the process of flowing downstream along the heated surface. Heat transfer correlations for air flowing over dry airfoil surfaces are readily available to the manufacturers, but correlations for heat and mass transfer over wet airfoil surfaces are not adequate. This is an area where experimental research is still required to support validation of computer models for evaporative anti-icing systems.

4.2.4 Special Techniques for Rotorcraft

Only one civilian helicopter, the French Super Puma, is certified in the United States for flight into forecasted icing conditions. It took approximately ten years of flight testing in natural icing to receive the FAA's certification.

The U.S. rotorcraft industry estimates that, if flight testing in natural icing is the only acceptable means for certification, it would cost about 15 million dollars to certify a helicopter to the full FAA, Part 25, Appendix C criteria. This cost is prohibitively high.

For several years, NASA and the U.S. rotorcraft industry have been engaged in a joint effort to develop new methods of reducing the cost and time needed to certify and qualify U.S. rotorcraft for icing.

These methods include (1) computer codes that reliably predict full-scale rotor performance in icing and (2) experimental techniques for testing sub-scale model helicopter rotors in the IRT to acquire data for validating the codes and to develop a better understanding of the effects of icing on rotor performance.

The methods derived from these studies will also advance the state-of-the-art for predicting the effects of ice accretion and shedding for the advanced ducted propellers and other thrusting devices.

4.2.4.1 Sub-scale Model Rotor Testing in Icing Wind Tunnel

Figure 23 shows a sub-scale helicopter model being tested in the IRT. The model consists of a helicopter fuselage, four NACA 0012 blades (4.9-in. chord, 6-ft diam.), a fully articulated rotor head, and a six-component force balance housed under the fuselage.[71,72]

Some results from the sub-scale model rotor testing are shown in Figure 24. This figures shows the torque rise caused by ice accretion on the rotors versus time in icing. The experimental results are compared with an analytical prediction developed by Flemming[72] that includes an ice shedding model. The analytical prediction includes empirical airfoil performance-in-icing data that was acquired in previous tests.[32] The comparison between analysis and experiment, as shown here, was remarkably good for this particular test run. Similar agreement was also found between analysis and experiment for lift loss versus time in icing.

Another approach to sub-scale model rotor testing would involve the use of simulated ice applied to the leading edge of the rotor blades. The rotor blades with the simulated ice would be tested in a dry wind tunnel. The key to successful dry air wind tunnel testing with simulated ice would be having the correct ice shapes, with appropriate roughness, properly located on the blades. The appropriate simulated ice would be obtained from scale model testing in an icing tunnel, or from predictions with ice accretion codes. It is unlikely that sufficiently accurate ice shapes could be acquired from full-scale helicopter flights in natural icing conditions because the ice erodes and sublimates substantially during the time it takes to descend, land, and shut down.

4.2.4.2 Ice Shedding from Rotor Blades

An important problem for propellers and helicopter rotors is shedding of ice from their tips where centrifugal forces can exceed 1000 g's. When multiple rotor blades shed ice asymmetrically, the resulting imbalances cause vibrations severe enough to prevent the pilot from reading his instruments. Another concern is that shed ice particles have considerable energy and can damage aircraft structures. For example, in the design of the tilt rotor aircraft, the fuselage was covered with armor plate in those areas where ice would impact. This armor plate added a severe weight penalty.

Rigorous analytical models and supporting experimental data are needed to predict (1) shed ice events and the size of the shed ice, (2) shed ice trajectories, (3) impact energy of the ice particle and (4) structural damage caused by ice impact. A current project at NASA Lewis is attempting to address some of these issues.

4.2.5 Flight Testing with Simulated Ice Shapes

Icing flight testing with simulated ice shapes on selected lifting surfaces is done as part of the process of obtaining icing certification or qualification, or it is done to acquire a data base for use in validating computer codes that predict overall aircraft performance and stability in icing.

If ice replicas are used on liftung surfaces during flight testing as part of the process of obtaining icing certification or qualification, then the following important caution from Reference 15 must be heeded: '...It has been found that the shape of the ice deposit on an airfoil plays the main role in worsening of the aerodynamic characteristics. Flight experiments have shown that even a thin layer of ice might have a serious influence. On the other hand, cases are possible when a thick ice deposit has no significant influence on the flying characteristics...'. Therefore, when simulated ice is used in flight testing, the selection of ice shapes is critical. Ideally, it would be desirable if computer codes that predict ice shapes and resulting aeroperformance and stability could be used to judiciously select ice shapes. But until these codes have been extensively validated, which will take many years, certification testing will still depend critically on flight testing in natural icing, with the aircraft in its various multi-element wing and tail configurations. When simulated ice is used, the ice shapes should be based on extensive icing flight test experience.

In the certification process, aircraft are ordinarily tested with simulated ice shapes for two prominent reasons. First, in the event of an ice protection failure, the airplane will accrete ice that could degrade aircraft performance and stability. Thus, the airframer may elect to use simulated ice to demonstrate flight safety in the event of ice protection failure. A second reason for using simulated ice would be when an airframer deliberately chose not to protect a given component. Then the airframer would have to prove that the aircraft could fly safely with ice on the unprotected surface. They could then elect to use simulated ice to demonstrate flight safety.

As mentioned earlier, newer commercial transports are powered by advanced turbofan engines with higher bypass ratios and smaller core flows. So airframers are taking a close look at whether ice protection can be safely eliminated from certain aircraft components in order to conserve on bleed air usage.

Even in the past when commercial jet transports had copious supplies of bleed air, airframers examined the advantages and disadvantages of protecting certain components from ice, especially vertical tails. By making an unprotected vertical tail large enough, airframers could achieve acceptable tail aerodynamics for expected ice accretions. So airframers compared the amount of fuel required to carry a heavier tail against the fuel required both to carry the extra weight of hot air ducting and to overcome the loss of engine power due to use of more engine bleed air.

As a recent example for an aircraft powered by high bypass engines, the Boeing 757 was the first commercial transport to be certified by the FAA without ice protection on the outboard leading edge slats. This need to identify specific components of an aircraft system and selectively remove unnecessary ice protection was driven by the reduction in available bleed air. In the process of acquiring the certification, Boeing first used replicated ice shapes on a sub-scale model of the 757 tested in a dry air wind tunnel. The stability and control characteristics were studied in the wind tunnel tests. Next, simulated ice shapes were attached to the actual aircraft's outboard slats, and the airplane was flown in clear air, again to study the effect of the ice on performance and stability. Finally, the airplane was flown in natural icing to complete the icing certification process. Relying on their vast experience in natural icing flight testing, Boeing was able to derive empirical and analytical methods to determine the most representative ice shapes for the simulation.

In a recent research program, NASA used replicated ice shapes on the horizontal and vertical tails of their Twin Otter icing research aircraft to study the effects of tail ice on stability and control (References 79 and 80). First the Twin Otter was flown in natural icing and photos were taken of the ice formations on the tail surfaces. From these photos, styrofoam shapes were fabricated and then attached to the tail surfaces (Figure 25). The aircraft was then flown in clear air through a series of maneuvers designed to acquire a flight data base for use in determining stability and control derivatives. The flight data was analyzed by a modified stepwise regression algorithm and a maximum likelihood algorithm that yielded estimates of body-axis stability and control derivatives related to the short-period, longitudinal motion of the aircraft.

As mentioned earlier, NASA is developing a computer flow code to predict performance and stability of modern aircraft with given ice shapes on the lifting surfaces. Estimated stability and control derivatives and performance measurements from the Twin Otter will be used to validate the code at full-scale Reynolds numbers. In addition to the Twin Otter flight testing with replicated ice shapes, dry air wind tunnel testing will be conducted of a sub-scale model of a modern swept wing aircraft with replicated ice on its lifting surfaces. The wind tunnel results will provide code validation data for a modern transport aircraft. After a good data base has been acquired from the wind tunnel testing, flight tests with a modern swept wing aircraft will be conducted to acquire a validation data base at full-scale Reynolds numbers.

As noted in Reference 80, 'the successful estimation of stability and control derivatives from flight data has two important ramifications. First, the values for the derivatives can be compared with values derived from the analytical icing codes and from the IRT. These comparisons allow for an assessment of the confidence that should be put in analytical predictions and wind-tunnel results as they relate to an aircraft in flight. Second, flight-derived derivatives can be used judiciously along with those provided by analytical predictions and wind tunnel tests to upgrade simulator math models to provide a realistic set of aerodynamics for pilot-in-the-loop simulations of icing scenarios.'

4.2.6 Icing Scaling

The proposed or desired test matrix for an icing test usually involves the following variables: airspeed, outside air temperature, altitude, cloud liquid water content, cloud droplet size distribution or median volume diameter, and model size or scale. In a flight test in natural icing or in an artificial cloud behind an in-flight spray tanker, chances are that the set of variables desired will be unattainable. In a wind tunnel test, certain combinations of variables also will be unattainable. For example, most icing wind tunnels have maximum airspeeds far below the speeds of modern transport or military aircraft. And due to the practical limits on nozzle turn-down ratios and nozzle droplet size ranges, several sets of nozzles would be required to achieve the full FAA Part 25 Appendix C operating envelopes over the full speed range of the tunnel.

If the desired test variables cannot be met, the experimenter must resort to some form of scaling or similitude. Various scaling objectives can be imagined for any particular icing test, such as: (1) a geometrically similar ice shape; (2) an equivalent drag or lift coefficient; (3) the same water flux distribution around the airfoil leading edge; (4) the same heat transfer results for a thermal ice protection system; (5) rime icing conditions (*i.e.*, all water must freeze immediately upon impact); and so on. Not all of these objectives can be met simultaneously and hence the experimenter may have to chose those most appropriate for the specific test program.

Scaling laws have always been used, but never rigorously validated.[32] Flight testing in natural icing clouds will always be a required part of the certification/qualification process.

Reference 10 gives a good bibliography of the work done previously on scaling. Most of these works on scaling rely on an analysis of the ice accretion process described by Messinger.[10] As mentioned earlier, more recent studies have revealed that the Messinger model does not reflect recent observations regarding the ice accretion process.

These new results have led Bilanin[81] to formulate the scaling laws independently from any mathematical model of the icing process. He did this by applying the Buckingham pi theorem for similitude to the ice accretion problem. The pi theorem approach showed, for example, that the normalized thickness of the ice accreted on the airfoil is a function of 18 nondimensional groups. Although many of the groups can be satisfied in any scaling test, Mach, Reynolds and Weber numbers cannot all be satisfied in the same scaled test. He concluded that although competing physical effects do not in general allow a rigorous scaling methodology, an acceptable approximate scaling scheme may still be possible. Bilanin's work is continuing under NASA/FAA sponsorship.

Since rigorous scaling is not achievable, a different approach has been taken in experimental icing testing. Components are tested in conditions as close as possible to the desired conditions, or some partial scaling is used. Analytical methods are then used to predict the results of the test. The analytical methods are adjusted, if necessary, to bring the experimental results and predictions into agreement. Then the analytical methods are used to predict results for the desired conditions. This is essentially the same approach used in acquiring a data base for validating any analytical prediction. With intensified efforts to develop computer simulations of all key aspects of aircraft icing, the necessity of a prolonged experimental effort to develop and validate scaling relations may be diminished.

5. Concluding Remarks

From the preceding discussion, it is evident that aircraft icing simulations consist of three interrelated activities; analytical modeling, ground-based experiments, and flight testing. Analytical methods started as correlations of experimental data and have more recently turned to computer models based on first principles. Computer models have been doing a steadily better job of simulating the icing process and its effects. Current two-dimensional codes are being used in industry for the simulation of icing effects and for the evaluation of ice protection system effectiveness. Three-dimensional methods are currently under development and hold the promise of accurately simulating an icing encounter for a complete aircraft configuration. Ground testing in icing wind tunnels, icing test cells, and dry air wind tunnels provides (1) simulations of conditions not yet capable of being modeled correctly, (2) safer and less expensive means of testing than in-flight testing, (3) controlled, repeatable experiments at known icing conditions, and (4) a database for computer code validation. The increasing number of these facilities in the industry attests to their

importance in developing effective ice protection measures for all types of aircraft. Finally, flight testing provides a means of determining the effects of icing on complete aircraft configurations and an essential check on the fidelity of the analytical and experimental simulation methods.

The future of icing simulation is tied to this three prong approach. It is important to understand that the advancement of either analytical or experimental simulation methods will always require the need of flight test data for verification purposes. The acceptance of simulation tools by aircraft designers and certification authorities will depend on the icing modelers ability to show the accuracy of simulation methods. Additionally, the interaction of modeler, experimentalist, and pilot can lead to a more realistic and therefore more useful simulation tool.

This paper has highlighted some of the recent developments in aircraft icing simulation. Several areas requiring further research have been identified. Some of these are:

- Ice accretion physics, specifically roughness characterization, heat transfer correlations, splashing, runback, surface tension effects, and wetting characteristics.
- Ice structural properties and ice shedding.

  Stall mechanisms and post-stall behavior of iced wings. Computational simulation of these phenomena.
- Inclusion of surface roughness effects in aerodynamics codes.
- Evaluation of turbulent flow properties for iced wings and development of appropriate turbulence models
- Three-dimensional ice accretion code development.
- Computer code simulation of iced wing and iced aircraft performance. Development of performance codes for rotorcraft in icing.
- Development of computational methods for simulating ice protection systems.
- Continued development of experimental methods for simulating rotorcraft performance in icing.
- Creation and verification of icing scaling laws.

Certainly the continued development of the icing simulation methods described in this paper will continue to present an exciting challenge to the aerospace community for some years to come.

References

1) Anon., "National Aircraft Icing Technology Plan," Federal Coordinator for Meteorological Services and Supporting Research, FCM-P20-1986, U.S. Dept. of Commerce, April 1986.

2) Reinmann, J.J., Shaw, R.J., and Ranaudo, R.J., "NASA's Program on Icing Research and Technology," NASA TM-101989, presented at Symposium on Flight in Adverse Environmental Conditions, Gol, Norway, May 8-12, 1989.

3) Carroll, T.C. and McAvoy, W.H., "Formation of Ice on Airplanes," Airway Age, Sept. 1928, pp. 58-59.

4) Bleeker, W., "Einige Bemerkungen u ber Eisanatz an Flugzeugen", Meteorologishe Zeitschrift, Sept. 1932, pp. 349-354 (also available as NACA TM No. 1027).

5) Jacobs, E.N., "Airfoil Section Characteristics as Affected by Protuberances", NACA Report No. 446, 1932.

6) Jones, R. and Williams, D.H., "The Effect of Surface Roughness on the Characteristics of the Aerofoils NACA 0012 and RAF 34", British ARC, R&M No. 1708, 1936.

7) Gulick, B.G., "Effects of Simulated Ice Formation on the Aerodynamic Characteristics of an Airfoil", NACA WR L-292, 1938.

8) Comite d' Etude du Givrage Rapport du Mai 1938, Bulletin des Services Techniques No. 85, Publications Scientifiques et Techniques du Ministere de l' Air (also available as NACA TM No. 919).

9) Anon., "Selected Bibliography of NACA-NASA Aircraft Icing Publications," NASA TM-81651, NASA Lewis Research Center, Cleveland, OH, August 1981.

10) Messinger, B.L., "Equilibrium Temperature of an Unheated Icing Surface as a Function of Airspeed," Journal of the Aeronautical Sciences, Vol. 20, No. 1, 1953, pp. 29-42.

11) Olsen, W.A. and Walker, E., "Experimental Evidence for Modifying the Current Physical Model for Ice Accretion on Aircraft Surfaces," NASA TM-87184, May 1986.

12) Bilanin, A.J., "Proposed Modifications to Ice Accretion/Icing Scaling Theory," AIAA Paper 88-0203, Jan. 1988.

13) Hansman, J.R., and Turnock, S.R., "Investigation of Microphysical Factors Which Influence Surface Roughness During Glaze Ice Accretion," Fourth International Conference on Atmospheric Icing of Structures, Paris, France, Sep. 1988.

14) Hansman, J.R., Yamaguchi, K., and Berkowitz, B., "Modeling of Surface Roughness Effects on Glaze Ice Accretion," AIAA Paper 89-0734, Jan. 1989.

15) Ingelman-Sundberg, M., Trunov, O.K., and Ivaniko, A., "Methods for Prediction of the Influence of Ice on Aircraft Flying Characteristics," Swedish-Soviet Working Group on Flight Safety, Joint Report No. JR-1, 1977.

16) Potapczuk, M.G. and Berkowitz, B.M., "An Experimental Investigation of Multi-Element Airfoil Ice Accretion and Resulting Performance Degradation," NASA TM-101441, Jan. 1989.

17) Bond, T.H., Flemming, R.J., and Britton, R.K., "Icing Tests of a Sub-Scale Model Main Rotor," Proceedings of the 46th Annual American Helicopter Society Forum, May 1990, pp. 267-281.

18) Negrette, A., "The Pilot's Responsibility in Icing Conditions," Rotor and Wing International, Vol. 25, No. 1, Jan. 1991, pp. 98-99.

19) Shaw, R.J., Potapczuk, M.G., and Bidwell, C.S. "Predictions of Airfoil Aerodynamic Performance Degradation Due to Icing," Numerical and Physical Aspects of Aerodynamic Flows IV, Springer-Verlag, Berlin, 1990, pp. 19-35.

20) Lozowski, E.P. and Oleskiw, M.M., "Computer Modeling of Time-Dependent Rime Icing in the Atmosphere," CRREL Report 83-2, USAF, Jan. 1983.

21) Ruff, G.A. and Berkowitz, B.M., "Users Manual for the NASA Lewis Ice Accretion Prediction Code (LEWICE)," NASA CR-185129, May 1990.

22) Cansdale, J.T. and Gent, R.W., "Ice Accretion on Aerofoils in Two-Dimensional Compressible Flow - A Theoretical Model," Royal Aircraft Establishment Technical Report 82128, 1983.

23) Brunet, L., "Conception et Discussion d'un Modele de Formation du Givre sur des Obstacles Varies," ONERA Note Technique 1986-6, Dec. 1986.

24) Berkowitz, B.M. and Riley, J.T., "Analytical Ice Shape Predictions for Flight in Natural Icing Conditions," NASA CR 182234 and DOT/FAA/CT-88/19, Dec. 1988.

25) Hansman, J.M., Yamaguchi, K., and Kazmierczak, M., "Revision to the Icing Model in LEWICE," AIAA Paper 91-0123, Jan. 1991.

26) Potapczuk, M.G. and Bidwell, C.S., "Numreical Simulation of Ice Growth on a MS-317 Swept Wing Geometry," AIAA Paper 91-0263, Jan. 1991.

27) Guffond, D.P., "Icing and De-Icing Test on a 1/4 Scale Rotor in the ONERA S1MA Wind Tunnel," AIAA Paper 86-0480, Jan. 1986.

28) Cebeci, T., "Effects of Environmentally Imposed Roughness on Airfoil Performance," NASA CR-179639, June 1987.

29) Shin, J., Berkowitz, B., Chen, H., and Cebeci, T., "Prediction of Ice Shapes and Their Effect on Airfoil Performance," AIAA Paper 91-0264, Jan. 1991.

30) Gray, V.H., "Prediction of Aerodynamic Penalties Caused by Ice Formation on Various Airfoils," NASA TN D-2166, 1964.

31) Bragg, M.B., "Rime Ice Accretion and Its Effect on Airfoil Performance," Ph.D. Dissertation, The Ohio State University, Columbus, OH, 1981.

32) Flemming, R.J., and Lednicer, D.A., "High Speed Ice Accretion on Rotorcraft Airfoils," NASA CR 3910, August 1985.

33) Bragg, M.B. and Spring, S.A., "An Experimental Study of the Flow Field about an Airfoil with Glaze Ice," AIAA Paper 87-0100, Jan. 1987.

34) Potapczuk, M.G., "Navier-Stokes Analysis of Airfoils with Leading Edge Ice Accretions," Ph.D. Dissertation, The University of Akron, Akron, OH, May 1989.

35) Bragg, M.B. and Khodadoust, A., "Experimental Measurements in a Large Separation Bubble due to a simulated Glaze Ice Accretion," AIAA Paper 88-0116, Jan. 1988.

36) Bragg, M.B. and Khodadoust, A., "Effect of Simulated Glaze Ice on a Rectangular Wing," AIAA Paper 89-0750, Jan. 1989.

37) Zaman, K.B.M.Q. and Potapczuk, M.G., "The Low Frequency Oscillation in the Flow over a NACA0012 Airfoil with an Iced Leading Edge," NASA TM-102018, June 1989.

38) Kwon, O.J. and Sankar, L.N., "Numerical Study of the Effects of Icing on Finite Wing Aerodynamics," AIAA Paper 90-0757, Jan. 1990.

39) Khodadoust, A.and Bragg, M.B., "Measured Aerodynamic Performance of a Swept Wing with a Simulated Ice Accretion," AIAA Paper 90-0490, Jan. 1990.

40) Al-Khalil, K.M., Keith, T.G., DeWitt, K.J., Nathman, J.K., and Dietrich, D.A., "Thermal Analysis of Engine Inlet Anti-icing Systems," AIAA Paper 88-0759, Jan. 1989.

41) Keith, T.G., DeWitt, K.J., Wright, W.B., and Masiulaniec, K.C., "Overview of Numerical Codes Developed for Predicting Electrothermal De-Icing of Aircraft Blades," AIAA Paper 88-0288, Jan. 1988.

42) Wright, W.B., Keith, T.G., and DeWitt K.J., "Numerical Simulation of Icing, Deicing, and Shedding," AIAA Paper 91-0665, Jan. 1991.

43) Chu, M., Scavuzzo, R.J., and Olsen, W.A., "Measurement of Adhesive Shear Strength of Impact Ice in an Icing Wind Tunnel," Proceedings of the 3rd International Workshop on the Atmospheric Icing of Structures, May 1986.

44) Scavuzzo, R.J., Chu, M., and Lam, P.D., "Development of a Composite Technique in the Determination of the Tensile Strength of Impact Ices," Proceedings of the 3rd International Workshop on the Atmospheric Icing of Structures, May 1986.

45) Scavuzzo, R.J., Chu, M.L., and Olsen, W.A., "Structural Properties of Impact Ices Accreted at Aircraft Surfaces," NASA CR-179580, Jan. 1987.

46) Martin, C. and Putt, J., "An Advanced Pneumatic Impulse Ice Protection System (PIIP) for Aircraft," AIAA-90-0492, January 1990.

47) Ramamurthy, S., Keith, T.G., DeWitt, K.J.Putt, J.C. Martin, C.A., and Leffel, K.L., "Numerical Modeling of an Advanced Pneumatic Impulse Ice Protection System (PIIP) for Aircraft," AIAA 91-0555, Jan. 1991.

48) Ide, R.F., "Liquid Water Content and Droplet Size Calibration of the NASA Lewis Icing Research Tunnel," NASA TM 102447, AVSCOM TM 89-C-014, AIAA-90-0669, January 1990.

49) Oldenburg, J.R., and Ide, R.F., "Comparison of Drop Size Distributions from Two Droplet Sizing Systems", NASA TM 1102520, AVSCOM TM 90-C-001, March, 1990.

50) Marek, C.J., and Bartlett, C.S., "Stability Relationship for Water Droplet Crystallization With the NASA Lewis Icing Spray," NASA TM 100220, AIAA-88-0289, January 1988.

51) Keller, R.G., "Measurement and Control of Simulated Environmental Icing Conditions in an Outdoor, Free Jet, Engine Ground Test Facility," Paper No. 7 in AGARD-CP-236, April, 1978.

52) Hunt, J.D., "Engine Icing Measurement Capabilities at the AEDC," Paper No. 6 in AGARD-CP-236, April, 1978.

53) Swift, R.D., "Icing Test Facilities at the National Gas Turbine Establishment," Paper No. 4 in AGARD-CP-236, April, 1978.

54) Bongrand, J., "Installations D'essais de Givrage," Paper No. 5 in AGARD-CP-236, April, 1978.

55) Ruff, G.A., "Analysis and Verification of the Icing Scaling Equations, Vol. I," AEDC-TR-85-30 (AD-A167976), Nov. 1985.

56) Bartlett, C.S., "An Analytical Study of Icing Similitude for Aircraft Engine Testing," AEDC-TR-86-26 (AD-A173713), DOT/FAA/CT-86-35, Oct. 1986.

57) Peterson, A.A., and Oldenburg, J.R., "Spray Nozzle Investigation for the Improved Helicopter Icing Spray System (IHISS)," AIAA-90-0666, January 1990.

58) Belte, D., and Woratschek, R., "Helicopter Icing Spray System (HISS) Evaluation and Improvements," USAAEFA Project No. 83-05-3, United States Army Aviation Engineering Flight Activity, Edwards Air Force Base, Ca 93523-5000, April 1986.

59) Mikkelsen, K., Juhasz, N., Ranaudo, R., and McKnight, R., "In-Flight Measurements of Wing Ice Shapes and Wing Section Drag Increases Caused by Natural Icing Conditions," NASA TM-87307, April 1986.

60) Belte, D. and Ranaudo, R.J., "Initial Results from the Joint NASA-Lewis/U.S. Army Icing Flight Research Tests," American Helicopter Society 45th Annual Forum Proceedings, May 1989.

61) Olsen, W.A., "Survey of Aircraft Icing Simulation Test Facilities in North America," NASA TM-81707, Feb. 1981.

62) Anon., "Rotorcraft Icing--Status and Prospects," AGARD Advisory Report No. 166, August 1981.

63) Anon., "Rotorcraft Icing--Progress and Potential," AGARD Advisory Report No. 223, September 1986.

64) Idzorek, J.J., "Observations on the Development of A Natural Refrigeration Icing Wind Tunnel," AIAA-87-0175, January 1987.

65) Tenison, G.V., "Development of a New Subsonic Icing Wind Tunnel," AIAA Paper No. 89-0773, January, 1989.

66) Van Fossen, G.J., Semonian, R.J., Olsen, W.A., and Shaw, R.J., "Heat Transfer Distributions around Nominal Ice Accretion Shapes Formed on a Cylinder in the NASA Lewis Icing Research Tunnel," AIAA Paper 84-0017, Jan. 1984.

67) Personne, P., "Effect de la Rugosite sur la Croissance du Givre a Faible Vitesse: Resultats Experimentaux et Modelisation," D.Sc. Thesis, L'Universite Blaise Pascal (Clermont-Ferrand II), June 1988.

68) Reehorst, A.L., and Richter, P.G., "New Methods and Materials for Molding and Casting Ice Formations," NASA TM 100126, Sep 1987.

69) Ingelman-Sundberg, M. and Trunov, O.K., "Wind Tunnel Investigation of the Hazardous Tail Stall due to Icing," Swedish-Soviet Working Group on Flight Safety, Joint Report No. IX-2, 1979.

70) Olsen, W., Shaw, R., and Newton, J., "Ice Shapes and the Resulting Drag Increase for a NACA 0012 Airfoil", NASA TM 83556, January 1984.

71) Flemming, R.J., Bond, T.H., and Britton, R.K., "Results of a Sub-Scale Model Rotor Icing Test," NASA TM 103709, AIAA-91-0660, January 1991.

72) Flemming, R.J., Bond, T.H., and Britton, R.K., "Model Rotor Icing Tests in the NASA Lewis Icing Research Tunnel," AGARD Specialists Meeting, Effects of Adverse Weather on Aerodynamics, Toulouse, France, 29 April-1May 1991.

73) Bragg, M., Khodadoust, A., Soltani, R., Wells, S., and Kerho, M., "Effect of a Simulated Ice Accretion on the Aerodynamics of a Swept Wing," AIAA 91-0442, January 1991.

74) Goldberg, J. and Lardiere, B., "Developments in Expulsive Separation Ice Protection Blankets," AIAA Paper 89-0774, Jan. 1989.

75) Smith, S.O., and Zieve, P.B., "Thin Film Eddy Current Impulse Deicer", AIAA 90-0761, January 1990.

76) Zumwalt, G.W., Schrag, R.L., Bernhart, W.D., and Friedberg, R.A., "Electro-Impulse De-Icing Testing Analysis and Design," NASA CR-4175, 1988.

77) Bond, T.H., Shin, J., and Mesander G.A., "Advanced Ice Protection Systems Test in the NASA Lewis Icing Research Tunnel," NASA TM 103757, April 1991.

78) Al-Khalil, K., Keith, T., and Dewitt, K., "Further Development of an Anti-icing Runback Model," AIAA-91-0266, January 1991.

79) Ranaudo, R.J., Batterson, J.G., Reehorst, A.L., Bond, T.H., and O'mara, T.M., "Determination of Longitudinal Aerodynamic Derivatives Using Flight Data from an Icing Research Aircraft," AIAA Paper 89-0754, Jan. 1989.

80) Batterson, J.G., and O'Mara, T.M., "Estimation of Longitudinal Stability and Control Derivatives for an Icing Research Aircraft from Flight Data," NASA TM 4099, 1989.

81) Bilanin, A.J. "Problems in Understanding Aircraft Icing Dynamics," AIAA Paper 89-0735, Jan. 1989.

Figure 1.—Close-up grazing-angle still photos of ice formed at below freezing air temperature of –2 °C.

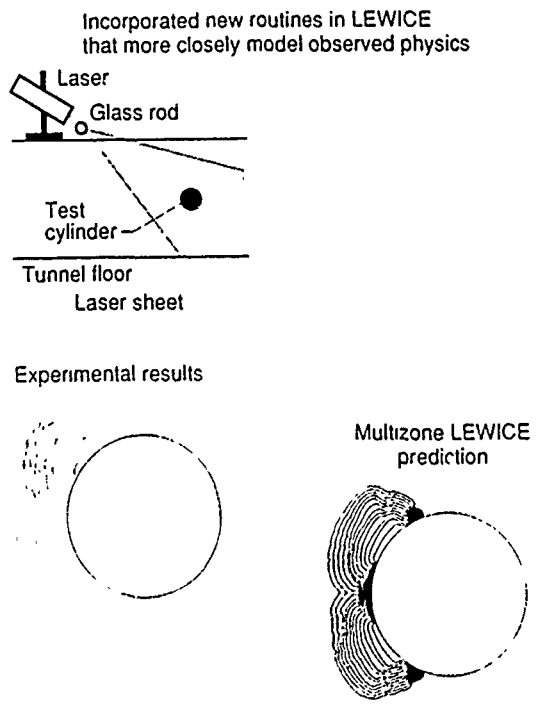

Figure 2.—Test set-up and results for ice layer growth on a cylinder.

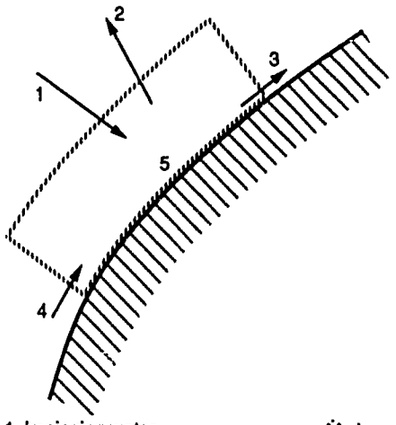

1. Impinging water	$\dot{M}_c\, i_{w,\,T}$
2. Evaporation	$\dot{M}_\theta\, i_{v,\,sur}$
3. Water flow out of CV	$\dot{M}_{r_{out}} i_{w,\,sur}$
4. Water flow into CV	$\dot{M}_{r_{in}}\, i_{w,\,sur}$
5. Ice accumulation leaving the CV	$\dot{M}_I\, i_{I\,,\,sur}$
6. Convection	$q_c\, \Delta s$
7. Conduction	$q_k\, \Delta s$

$$\dot{M}_c i_{w,T} + \dot{M}_{r_{in}} i_{w,sur} + q_k \Delta s = \dot{M}_\theta i_{v,\,sur} + \dot{M}_{r_{out}} i_{v,\,sur} + \dot{M}_I i_{I,\,sur} + q_c\, \Delta s$$

Figure 3.—Control volume for ice accretion energy balance.

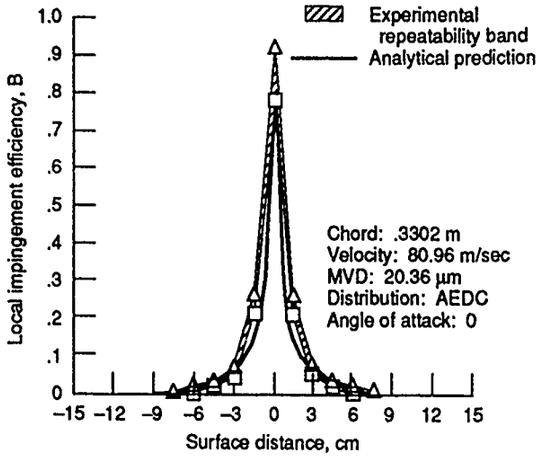

Figure 4.—Comparison of experimental repeatability and analytically predicted local impingement efficiency for a NACA 65-015 airfoil.

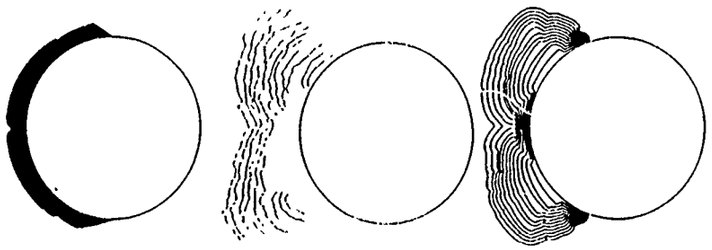

Original LEWICE prediction | Experimental results | Multi-zone LEWICE prediction

Figure 5.—Comparison of original LEWICE calculation to multi-zone LEWICE calculation for glaze ice accretion on a cylinder.

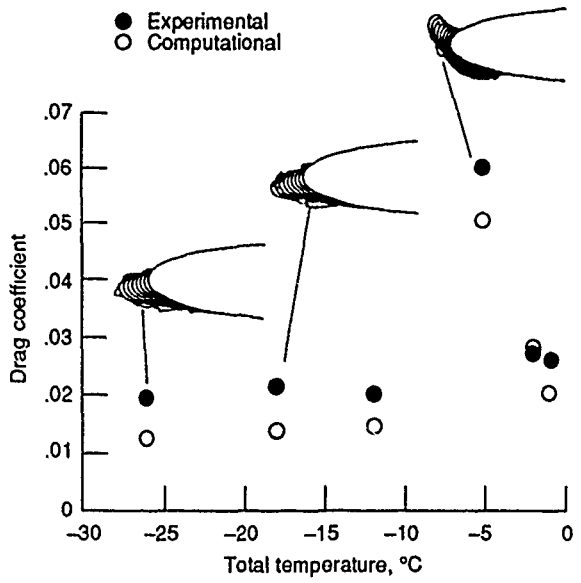

Figure 6.—LEWICE/IBL ice shape and drag coefficient predictions compared to experimental results.

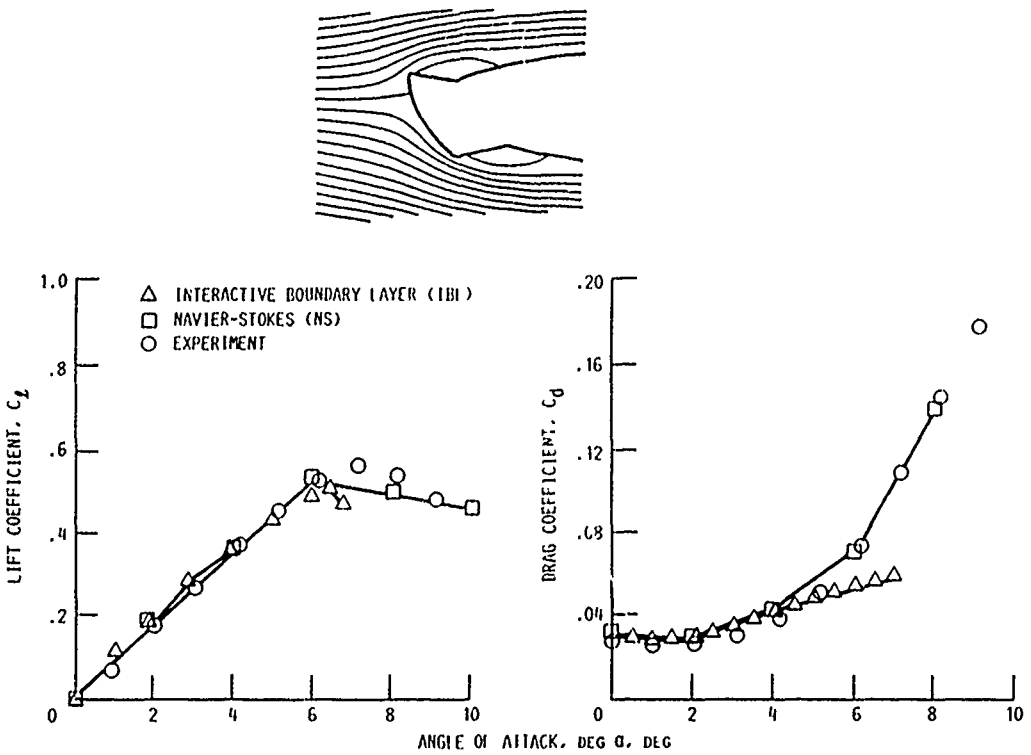

Figure 7.—Comparison of iced airfoil code predictions with experiment.

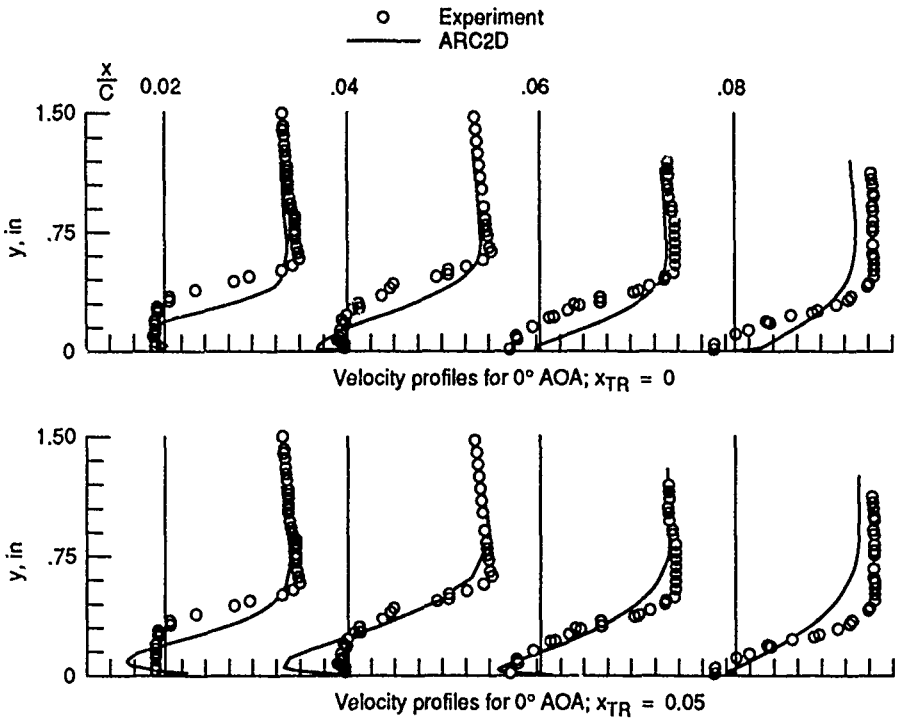

Figure 8.—Velocity profiles in the recirculation region aft of a glaze ice horn on a NACA 0012 airfoil.

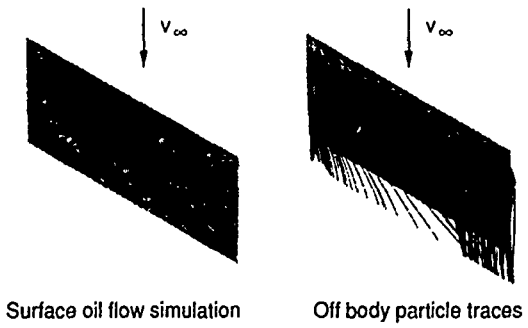

Figure 9.—Particle traces for flow over an iced swept semi-span wing at 8° angle of attack (NACA 0012 profile, 30° sweep angle).

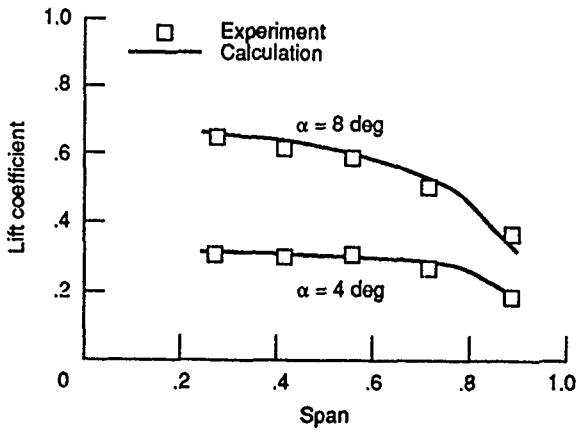

Figure 10.—Spanwise load distribution of an iced wing (NACA 0012 profile, 30° sweep angle) at 4° and 8° angle of attack.

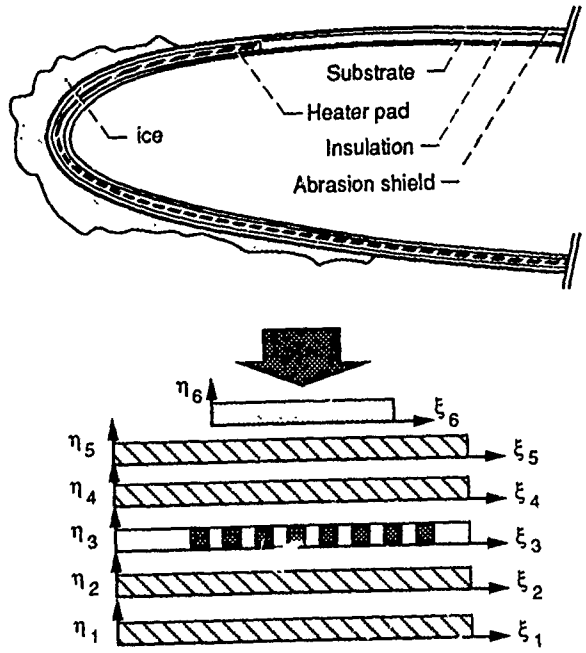

Figure 11.—Two-dimensional finite-difference model of an electrothermal heater. [Ref. 41].

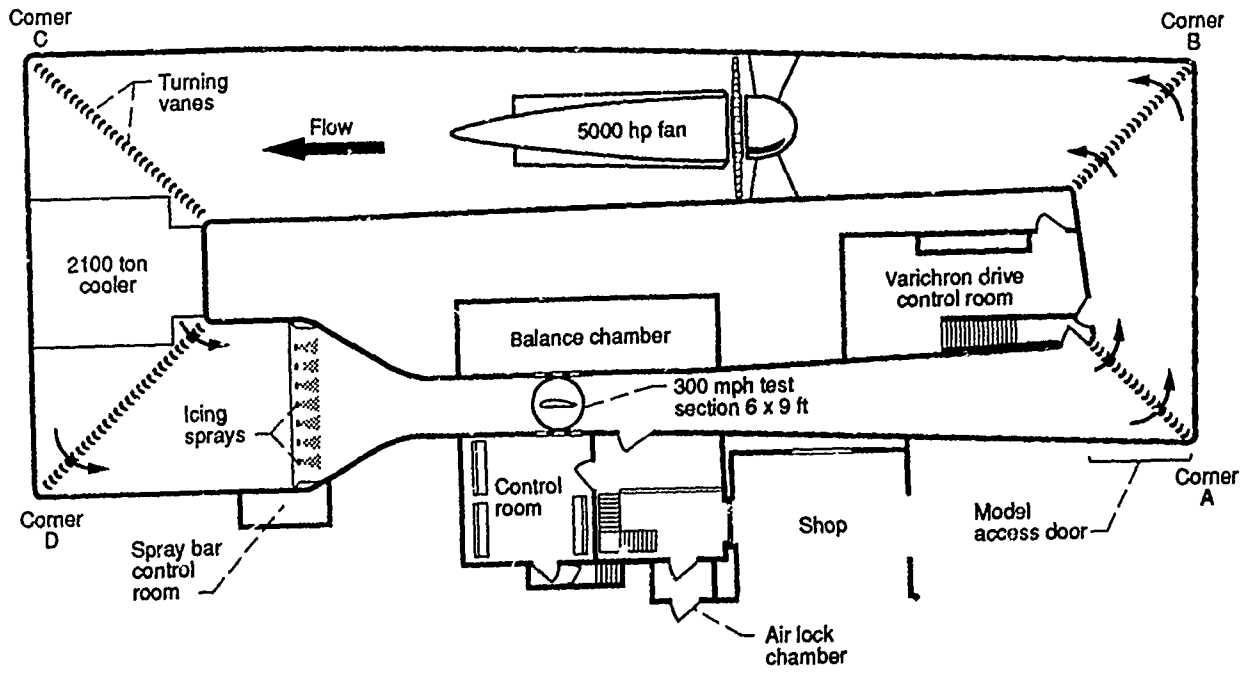

Figure 12.—Schematic of the NASA Lewis Research Center Icing Research Tunnel (IRT).

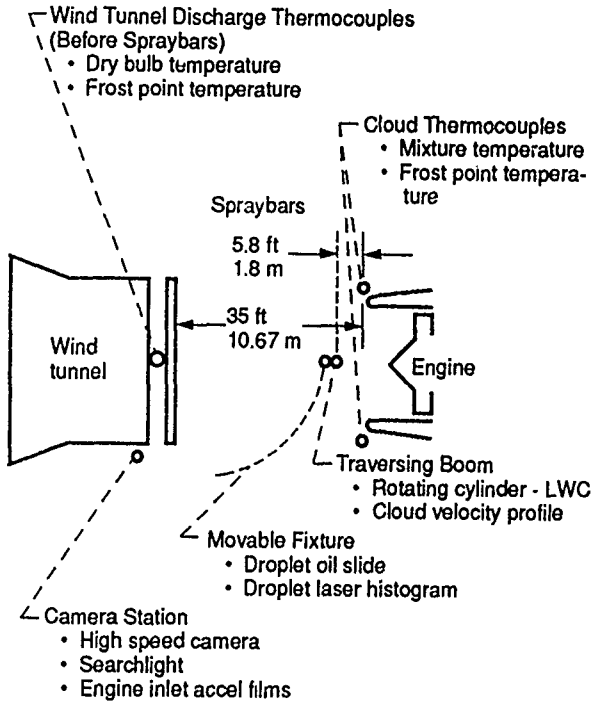

Figure 13.—Schematic of the General Electric engine icing test facility in Peebles, Ohio, USA [Ref. 51].

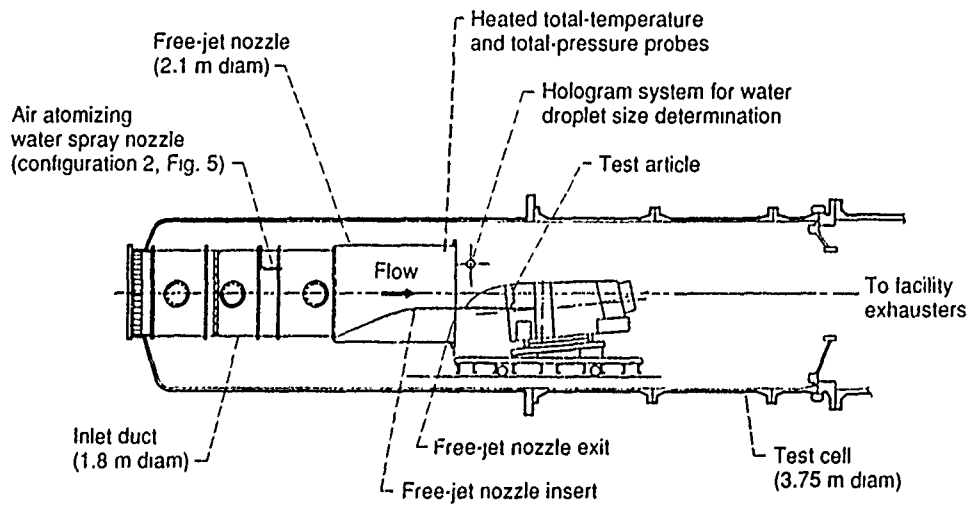

Figure 14.—Schematic of the AEDC engine icing test cell at Tullahoma, Tennessee, USA. [Ref. 52]

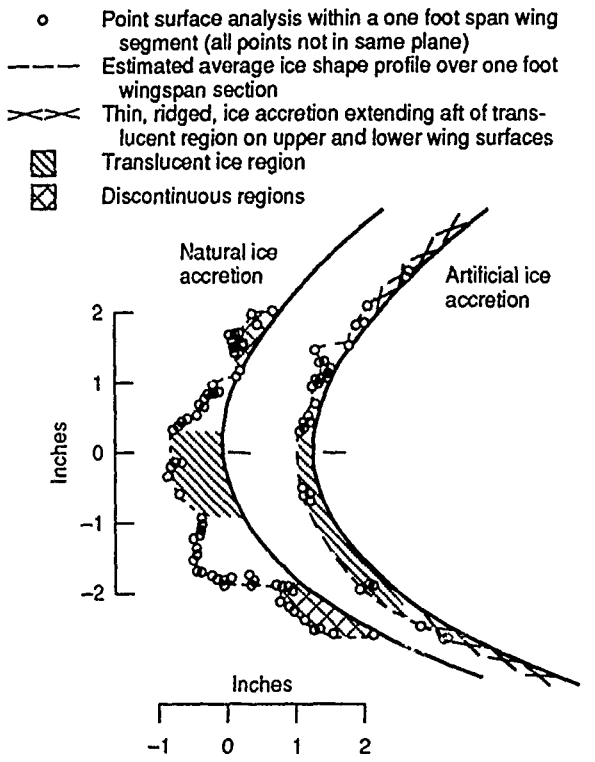

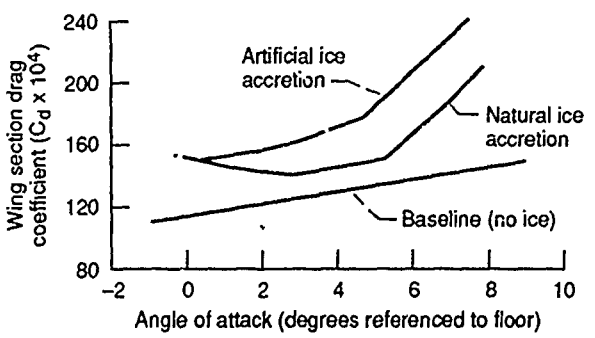

Figure 15.—Stereographic analysis of natural and artificial (HISS) ice accretions on NASA DH-6 wing section and resulting measured drag coefficients. [Ref. 60]

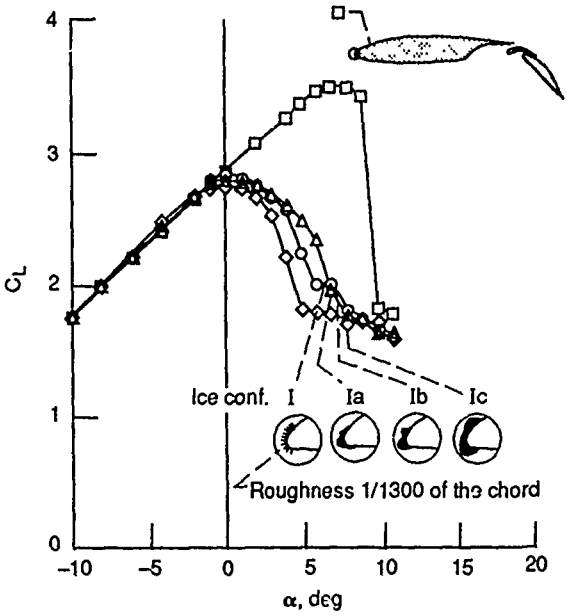

Figure 16.—The effect on $C_L(\alpha)$ and C_{Lmax} of ice shapes from the icing wind tunnel at the Research Institute of the Ministry of Civil Aviation, USSR. (Cruise condition with flaps extended). [Ref. 15]

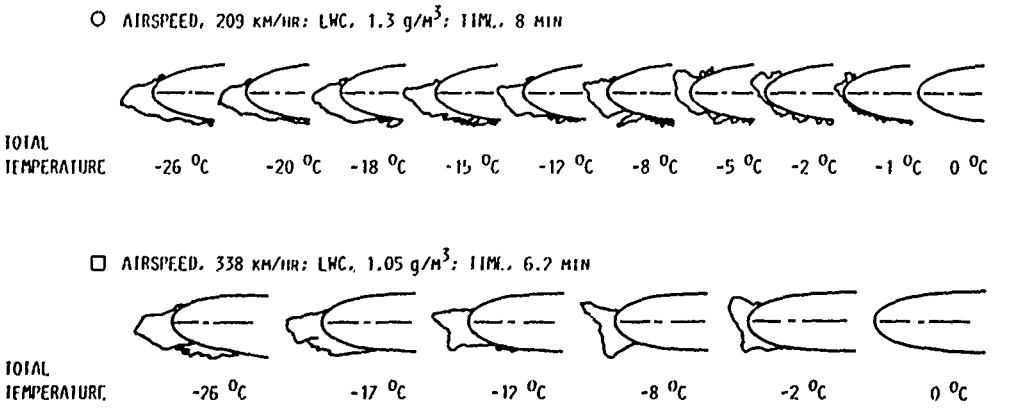

Figure 17.—The effect of total temperature on ice shape development. (LWC x V x time) = const. NACA 0012 airfoil at 4° angle of attack.

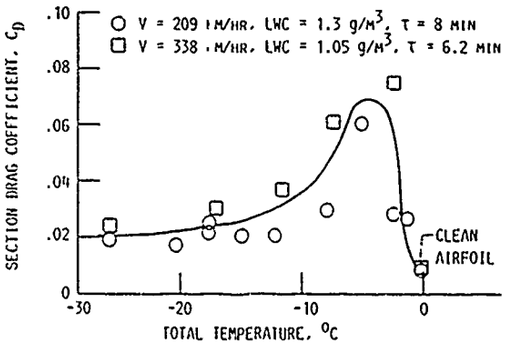

Figure 18.—The effect of total temperature on drag. (LWC x V x time) = const. NACA 0012 airfoil at 4° angle of attack.

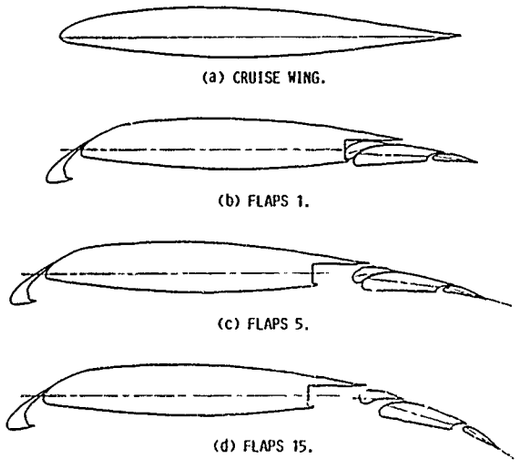

Figure 19.—Boeing 737-200 ADV wing section models tested in the NASA IRT.

Run number	Duration, min	Temperature, °F	Velocity, ft/s	LWC, g/m3	MVD, µm
17	10	26	159	0.92	14.4

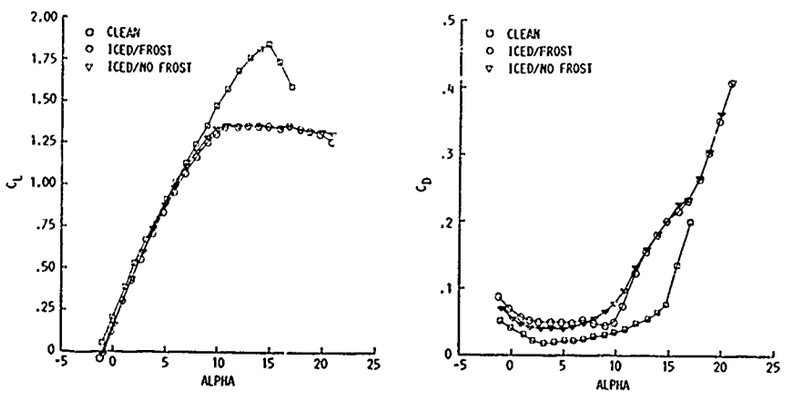

Figure 20.—Changes in lift and drag resulting from glaze ice growth on the Boeing 737-200 ADV wing model in the flaps 1 configuration.

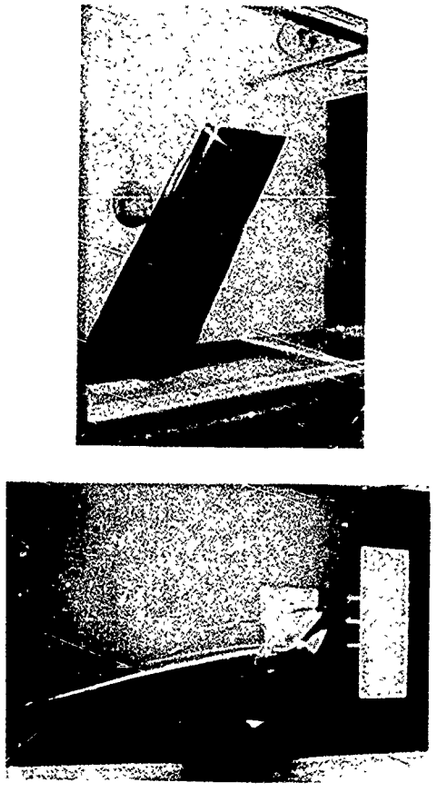

Figure 21.—Swept, finite wing with simulated ice on the leading edge installed in the University of Illinois subsonic wind tunnel.

Figure 22.—High speed video of ice shedding event during activation of a low power de-icing system.

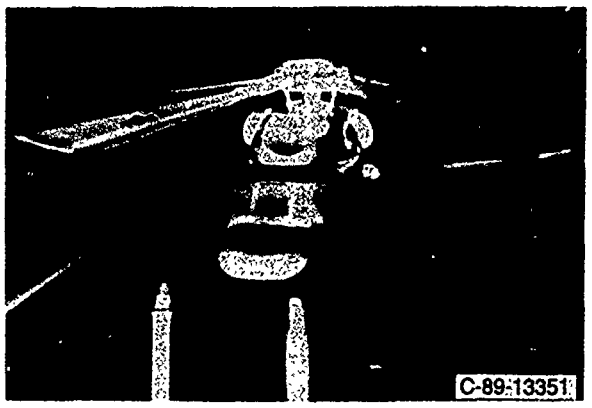

Figure 23.—Powered force model operating during simulated icing encounter in NASA Lewis Icing Research Tunnel.

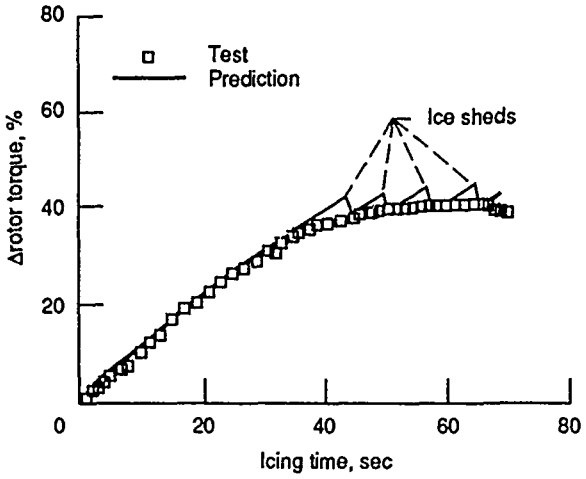

Figure 24.—Comparison of calculated and measured torque rise of PFM rotor during simulated icing encounter in the NASA IRT.

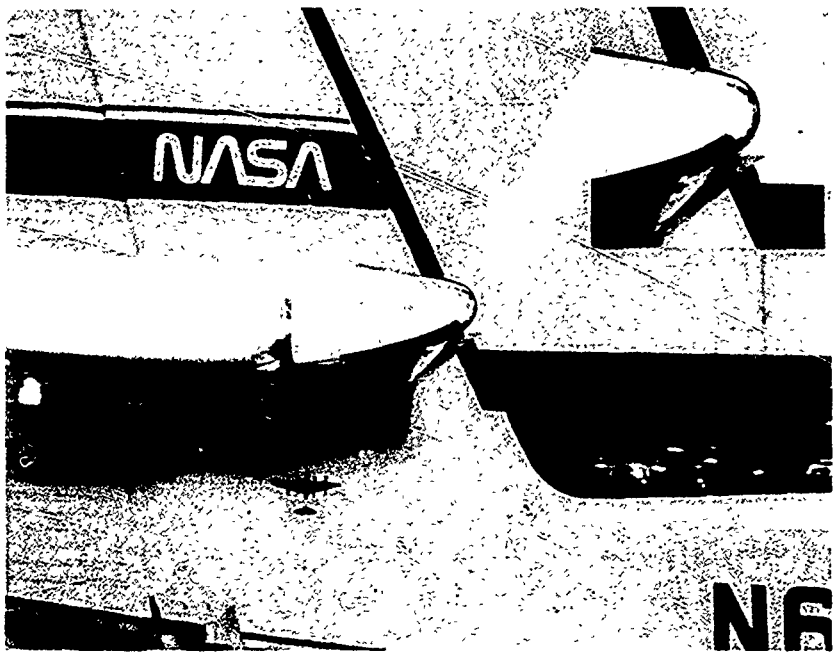

Figure 25.—Simulated ice shape attached to tail of NASA DHC-6 for evaluation of changes to stability and control characteristics.

Méthode de calcul de coefficients de concentration d'eau en tridimensionnel et ses applications industrielles

P. PREL
aerospatiale
division avions
A/DET/EG/Aéro
316, route de Bayonne
31060 Toulouse Cedex 03
France

Résumé

Cet exposé décrit successivement l'intérêt de disposer d'une méthode tridimensionnelle de calcul de coefficients de concentration de gouttelettes d'eau, ses principes généraux ainsi que le détail des codes de calcul utilisés. Des applications au positionnement de sondes sur les avions Airbus 340 et ATR 72 sont ensuite présentées, mettant principalement en évidence l'influence du diamètre des gouttes sur la concentration mesurée.

Notations

m_g	Masse de la goutte
ρ_g	Masse volumique de la goutte
D_g	Diamètre de la goutte
R_g	Reynolds de la goutte
γ_g	Accélération de la goutte
S	Surface de référence aérodynamique
F	Force exercée sur la goutte
V_r	Vitesse relative locale de la goutte par rapport à l'air
Cd	Coefficient de traînée aérodynamique de la goutte
ρ_a	Masse volumique de l'air
μ_a	Viscosité dynamique de l'air
Ec	Coefficient de concentration d'eau

Le contexte

La nécessité du vol par mauvaises conditions météorologiques s'est considérablement accrue ces dernières années du fait de l'intérêt des compagnies aériennes à mieux rentabiliser les appareils de leurs flottes. Parmi ces conditions défavorables, le givrage des différents constituants de l'avion est un risque important. Afin d'assurer un niveau de sécurité des personnes et des matériels identique à celui exigé par bonnes conditions météorologiques, il s'est avéré nécessaire de développer des compétences spécifiques dans les domaines des prévisions, mesures et protections. Ces domaines rentrant directement en ligne de compte dans les exigences réglementaires, ils intéressent particulièrement les industriels, soucieux de certifier leurs produits.

Dans cette optique, de nombreux outils utilisables au niveau industriel ont été développés. En particulier, l'accent a été mis sur les méthodes théoriques qui, une fois validées, autorisent plus de souplesse et sont d'un coût de mise en œuvre moindre que les méthodes expérimentales.

C'est dans ce contexte qu'une méthode théorique de calcul de coefficients de concentration d'eau en tridimensionnel a été mise en place par aerospatiale, et utilisée dans le cadre des différents programmes d'avions auxquels celle-ci est associée.

Intérêt de cet outil

Les accrétions de givre sont le résultat de la congélation après impact sur la paroi de l'avion des micro-gouttelettes d'eau en surfusion qui se trouvent en suspension dans les nuages givrants. De la quantité de gouttelettes captée à la paroi de l'avion va dépendre le taux de croissance du givre et finalement la forme de l'accrétion en cet endroit.

Afin de pouvoir garantir le comportement sain d'un avion dans ces conditions, il est précieux de connaître a priori les parties de l'appareil qui seront sujettes aux accrétions de glace, mais aussi les parties et les zones d'écoulement autour de l'avion qui seront masquées.

Cette connaissance permet alors de dimensionner correctement les équipements de dégivrage et d'anti-givrage et aussi de bien positionner et étalonner les sondes de mesures qui interviennent dans le processus de certification de l'avion. Pour certaines parties de l'avion (fuselage, entrée d'air,...), l'utilisation de méthodes théoriques bidimensionnelles disponibles depuis longtemps est une approximation grossière; il est alors nécessaire de prendre en compte la tridimensionnalité de l'écoulement.

Principes généraux de la méthode

Dans un premier temps, il est nécessaire de calculer le champ aérodynamique autour de l'avion considéré. Les conditions givrantes peuvent être rencontrées aux altitudes basses et moyennes, pour lesquelles les vitesses des avions de transport ne sont pas très élevées. Ceci autorise l'utilisation d'une méthode de calcul du champ aérodynamique sous les hypothèses de fluide parfait faiblement compressible, voire même incompressible.

Dans cet écoulement aérodynamique, on peut alors déterminer les trajectoires des gouttelettes d'eau provenant de l'infini amont et déviées par les perturbations aérodynamiques. Certaines gouttelettes viennent percuter la paroi de l'appareil où les paramètres aéro-thermodynamiques conditionnent alors le processus de congélation. La détermination d'un ensemble de trajectoires permet de définir les zones d'écoulement où se concentrent les gouttelettes, et celles où elles ne peuvent accéder.

La détermination des trajectoires se fait de manière balistique. L'utilisateur spécifie un point de départ d'une goutte et sa trajectoire est alors calculée de manière directe pas à pas. Comme on s'intéresse généralement à un endroit bien précis de l'avion ou de l'écoulement, il faut donc déterminer par essais successifs les points de départ qui permettent d'atteindre la zone cible. C'est pourquoi il est très intéressant de disposer en plus d'une méthode pseudo-inverse, en automatisant la recherche de la position initiale de la goutte en fonction d'un point objectif donné.

Les outils

Calcul du champ aérodynamique

Du fait de l'hypothèse de faible compressibilité de l'écoulement, un code résolvant l'équation du potentiel linéarisé par une méthode de singularités surfaciques est tout indiqué pour notre d'étude. Ce type de code présente en effet de nombreux avantages:

_ Nécessité de réaliser un maillage surfacique de la peau de l'avion et non pas un maillage volumique de l'écoulement. Ceci permet de traiter les géométries simples comme les plus compliquées.

_ Temps de calcul raisonnables permettant une utilisation intensive de la méthode. Il est ainsi possible de réaliser un ensemble de calculs correspondant à des conditions aérodynamiques différentes.

La réalisation des maillages est effectuée à partir des formes avion stockées dans l'environnement de CAO/DAO appelé MICA2 et développé au sein du département Aérodynamique. De nombreux outils permettent de générer les maillages, de les contrôler et de les visualiser.

Le code de calcul utilisé s'appelle FP3D et a été développé à aerospatiale [1]. Ses fonctionnalités sont variées: calculs de champs de vitesse, de pression, charges et efforts, lignes de courant, déflexions, débits, etc. De par sa structure modulaire et les nombreuses options offertes à l'utilisateur (type des panneaux du maillage, type des conditions aux limites sur chacun des panneaux, prise en compte de symétries multiples, corrections de compressibilité, équilibrage ou non des sillages tourbillonnaires, algorithmique,...), l'utilisation du code peut être précisément adaptée au problème à traiter.

Pour notre application, l'objectif est de représenter au mieux le champ aérodynamique dans les zones d'écoulement où seront calculées les trajectoires de gouttelettes d'eau. Pour ce faire, il est essentiel dans un premier temps de représenter précisément la géométrie proche des futures trajectoires, tandis qu'une discrétisation plus lâche du maillage est suffisante pour les parties plus lointaines.

D'autre part, l'utilisation de conditions aux limites de type "débit d'air nul" pour les panneaux de la zone proche permet d'éviter les fuites de fluide au travers du maillage. Pour les panneaux du maillage lointain, une condition de glissement suffit (vitesse normale nulle au barycentre de chaque panneau). Cette utilisation est d'autant plus nécessaire si l'on s'intéresse à un écoulement aérodynamique interne où la conservation du débit est primordiale (dans une entrée d'air par exemple).

Ces conditions aux limites demandent malheureusement un temps de calcul des singularités plus important et ne peuvent être utilisées qu'en incompressible (l'utilisation des corrections de compressibilité rend mathématiquement incorrect le calcul du débit). Cependant, si beaucoup de trajectoires de gouttes sont à déterminer, le coût du calcul initial des singularités ne représente qu'une faible part du coût de calcul global et le coût du calcul des trajectoires ne dépend pas du type de conditions aux limites utilisées dans le calcul aérodynamique.

Calcul des trajectoires de gouttelettes d'eau

Principe

Le calcul des trajectoires de gouttes d'eau repose sur une méthode développée à l'ONERA par D. GUFFOND [2]. Le code de calcul

a été adapté par aerospatiale de manière à être couplé au code de calcul aérodynamique FP3D.

Pour ces calculs, on suppose:

_ que le nombre des gouttes d'eau par unité de volume est suffisamment faible pour que l'écoulement et les caractéristiques de l'air soient identiques à ce qu'ils seraient en l'absence de gouttes. (Pour donner un ordre de grandeur, une concentration d'eau de 1 g/m^3 conduit à une distance moyenne entre deux gouttelettes égale à 80 fois leur diamètre).

_ que les gouttes sont parfaitement sphériques, de diamètre identique et constant (pertes par évaporation nulles).

_ que la seule force appliquée sur la goutte est la force de traînée aérodynamique, résultant de la différence vectorielle entre la vitesse propre de la particule et la vitesse locale de l'écoulement (pour les gouttelettes de petit diamètre les autres forces y compris le poids ne dépassent pas 1% de la force de traînée).

La force de traînée s'exerçant sur la gouttelette s'écrit donc:

$$\vec{F} = \frac{1}{2} \rho_g V_r^2 \frac{\vec{V}_r}{|\vec{V}_r|} S\, Cd$$

$$\text{avec } S = \pi \frac{D_g^2}{4}$$

Le coefficient de traînée Cd est une fonction du nombre de Reynolds R_g de la gouttelette qui s'écrit:

$$R_g = \frac{\rho_a V_r D_g}{\mu_a}$$

La loi utilisée est celle de Stokes si le Reynolds de la goutte est inférieur à 0.5, c'est-à-dire:

$$Cd = \frac{24}{R_g}$$

Pour les nombres de Reynolds supérieurs, la loi est sensiblement modifiée [2].

L'équation du mouvement de la particule d'eau s'écrit simplement:

$$\vec{F} = m_g \ddot{\vec{r}}_g$$

Le calcul des trajectoires est alors effectué par une méthode explicite d'Adams du 3ième ordre à pas de temps constant. Connaissant la position et la vitesse de la gouttelette à un instant donné t, on calcule la vitesse aérodynamique locale en ce point. La vitesse relative de la particule par rapport à l'air crée une force de traînée et donc une accélération de la gouttelette qui est intégrée pour fournir ses nouvelles position et vitesse à l'instant t+Δt.

Initialisation

Pour initialiser ces trajectoires, il faut spécifier un point de départ suffisamment en amont de l'écoulement perturbé de manière à pouvoir affecter à la particule une vitesse propre égale à la vitesse aérodynamique à l'infini amont.

Test d'impact

Pour déterminer si la particule d'eau a percuté l'avion, une boucle de calcul analyse à chaque pas sa position relative par rapport au plan moyen de chacune des facettes définissant le maillage. Si on détecte que la gouttelette est passée du côté interne de ce plan, on analyse sa position par rapport au tube formé par les quatre plans perpendiculaires à la facette et passant par ses quatres côtés. Si la goutte est à l'intérieur du tube, elle a donc traversé la facette et le calcul est arrêté.

Automatisation de la recherche du point de départ

Dans le cas d'une géométrie complexe pour laquelle l'écoulement aérodynamique est fortement perturbé, la recherche par essais successifs de la position initiale à l'amont de la goutte devant parvenir en un point cible donné peut s'avérer fastidieuse. Pour pallier cela, une méthode de recherche automatique de cette position à été couplée au programme de calcul des trajectoires.

Cette recherche s'effectue en deux étapes:

_ dans un premier temps, on calcule une ligne de courant aérodynamique en remontant l'écoulement à partir du point cible fixé. En effet, les gouttes de très petit diamètre suivent très bien les lignes de courant. Cette initialisation est donc d'autant meilleure si le diamètre réel des gouttes utilisé est faible. Le calcul de cette ligne est arrêté lorsqu'une des trois conditions suivantes est remplie:

_ la différence entre le module de la vitesse aérodynamique locale et celui de la vitesse infinie amont et l'angle formé entre ces deux vecteurs vitesse sont inférieurs à des bornes données.

_ la longueur de la ligne de courant dépasse une limite donnée.

_ le nombre de points de calculs de la ligne de courant dépasse une limite donnée.

Le premier test permet de repérer à quel moment on peut considérer que la goutte d'eau n'a pas été perturbée par le champ aérodynamique de l'avion. On peut donc lui affecter une condition initiale en vitesse égale à celle à l'infini amont.

Les deux autres tests permettent de garantir un déroulement normal du calcul (pas de stagnation ou de bouclage de la ligne de courant).

_ La position initiale de la particule déterminée, on calcule une première trajectoire de gouttes, puis deux autres qui correspondent à un léger déplacement du point de départ selon les deux coordonnées dans un plan perpendiculaire à l'axe de l'avion. Ceci nous permet donc de calculer le gradient au point initial de la fonctionnelle "carré de la distance du point d'impact au point objectif". Cette valeur du gradient nous permet de déterminer la direction de plus forte pente pour minimiser la fonctionnelle. On trouve le minimum dans cette direction par une interpolation parabolique sur trois trajectoires. A partir du minimum trouvé, on recalcule le gradient et la direction de descente conjuguée à la précédente (Méthode de Polak-Ribière [3]), puis la minimisation unidirectionnelle comme indiqué précédemment. Les itérations se poursuivent tant que la distance entre les points cible et résultat est supérieure à une borne spécifiée par l'utilisateur.

Coefficient de concentration

Pour indiquer si localement les trajectoires de gouttes d'eau ont tendance à se resserrer ou bien à s'éloigner en comparaison de l'infini amont, indiquant une augmentation ou une diminution de la concentration locale en eau, on utilise un paramètre nommé coefficient de concentration. En considérant que le flux d'eau se conserve le long d'un tube de trajectoires de gouttelettes, ce coefficient est égal au rapport des surfaces interceptées par ce tube à l'infini amont et à l'autre extrémité, ces surfaces étant prises perpendiculairement au tube (cf. Figure 1). Si le tube intercepte la peau d'un avion, on considère alors la surface généralement gauche qui est l'intersection du tube avec la paroi. Dans ce cas le coefficient obtenu est plutôt appelé coefficient de captation.

Les applications

Cas d'étude

Les résultats présentés dans la suite sont issus de deux études:

_ vérification du bon positionnement des sondes pour la certification en givrage de l'Airbus 340, et calcul des coefficients de concentration à leur endroit

_ détermination du meilleur positionnement de témoins visuels d'accrétion de givre sur ATR72 et calcul des coefficients de concentration correspondants.

Airbus A340

Pour l'Airbus 340, la condition de vol à considérer était:

Configuration lisse
Altitude: 15000 ft
Incidence: 8°
Vitesse: 250 kts TAS (130 m/s)
Température statique: 263.15 °K

La position des sondes sur la pointe avant de l'avion est indiquée sur la Figure 2. Ces trois sondes servent respectivement à mesurer l'épaisseur de glace captée (Témoin CEV), la concentration en eau liquide (LWC) et le nombre et le diamètre des gouttelettes (FSSP).

Représentation géométrique

Pour représenter le champ aérodynamique autour d'une pointe avant d'avion de transport, la question restait posée quant à la nécessité d'inclure la voilure dans le maillage de calcul. Pour nous en assurer, nous avons réalisé deux calculs avec la méthode des singularités FP3D sur un Airbus 340 avec et sans voilure. Nous avons comparé les déflexions aérodynamiques obtenues au niveau des trois sondes de givrage devant être installées pour la certification. Comme attendu, ces calculs montrent que les différences de déflexions sont d'autant plus importantes que l'on est proche de la voilure, ce qui induit au niveau de la sonde la plus proche une différence en déflexion de plus de 1°. Par conséquent, nous avons choisi de garder le maillage avec voilure pour les calculs de trajectoires de gouttes.

En toute rigueur, pour représenter le mieux possible le champ aérodynamique, il serait nécessaire d'assurer une valeur réaliste de l'incidence de l'avion ainsi qu'une valeur correcte de la circulation autour de la voilure (et par conséquent son coefficient de portance). En fait, lorsque l'incidence aérodynamique de l'avion est fixée et si le maillage de calcul représente la géométrie réelle de la voilure, le calcul aérodynamique fluide parfait tend à surestimer le coefficient de portance. Il faudrait donc modifier légèrement la géométrie de

calcul pour obtenir le bon coefficient de portance. Cette remarque prend tout son sens si l'on s'intéresse à une zone de l'écoulement fortement influencée par la voilure et dans les cas où le coefficient de portance est élevé (à forte incidence ou en configuration hypersustentée). Dans nos exemples d'application suivant, cela n'a pas été réalisé.

Pour l'A340, le maillage utilisé contient 1500 panneaux peau pour le demi-avion (cf. Figure 3). La pointe avant de l'avion est finement discrétisée et l'utilisation de conditions aux limites de type débit nul au travers de ces panneaux impose d'effectuer le calcul aérodynamique FP3D à Mach nul.

ATR 72

Pour l'ATR72, ont été étudiées les trois conditions suivantes:

1. Phase de vol: Max Cruise
Altitude: 15000 ft
Incidence: 0.2 °
Vitesse: 147.2 m/s
Température statique: 253.15 °K

2. Phase de vol: Take-off
Altitude: 0 ft
Incidence: 5.8°
Vitesse: 63.8 m/s
Température statique: 269.15 °K

3. Phase de vol: Landing
Altitude: 5000 ft
Incidence: 3.7°
Vitesse: 43.m/s
Température statique: 269.15 °K

L'implantation des témoins visuels de givre est indiquée sur la figure 4. Ce sont de petites tiges profilées installées en vue des pilotes et censées capter du givre le cas échéant. Ils renseignent donc l'équipage sur la nécessité ou non de mettre en route les systèmes de dégivrage ou d'anti-givrage.

Pour cet avion, le maillage utilisé dans tous les cas contient 2440 panneaux peau pour le demi-avion (cf. Figure 3). Comme pour l'A340, la pointe avant de l'avion est finement discrètisée et l'utilisation de conditions aux limites de type débit nul au travers de ces panneaux impose d'effectuer le calcul aérodynamique FP3D à Mach nul.

Détermination de la trajectoire arrivant en un point donné

Les figures 5 et 6 présentent une visualisation des trajectoires de gouttes calculées pour l'ATR72 lors de la recherche automatique du point de départ de la trajectoire arrivant en un point cible donné. Pour la compréhension, seules les trajectoires calculées dans la première direction de descente trouvée ont été représentées, en plus des trajectoires ayant permis de déterminer le gradient au point de départ initial.

Positionnement des sondes

Le graphique 7 présente les valeurs des coefficients de concentration calculés pour les trois sondes de l'A340, en fonction du diamètre des gouttelettes d'eau. Ces sondes sont bien positionnées, car la concentration d'eau mesurée est supérieure de 10% seulement à celle de l'infini amont, et est peu sensible au diamètre des gouttes. En effet, la figure 8 montre l'allure classique de l'évolution du coefficient de concentration en fonction de la distance à la paroi de l'avion. A la zone d'ombre (ou couche limite de givrage), dans laquelle aucune trajectoire de goutte ne peut parvenir, succède une zone d'intense surconcentration, ce coefficient tendant ensuite vers l'unité à mesure que l'on s'éloigne de la paroi. Cela signifie donc que les sondes A340 ont été positionnées suffisamment loin de la peau de l'avion pour éviter la zone de très forte surconcentration dont la position est très dépendante du diamètre des gouttelettes considéré. Les mesures faites pourront donc être considérées comme représentatives des conditions de givrage ambiantes.

Le graphique 9 est analogue au précédent mais pour les témoins de l'ATR72. Pour le témoin latéral en cas de vol de croisière, la surconcentration mesurée est très dépendante du diamètre des gouttes d'eau. En effet, le témoin de givre considéré est fixé sur la peau de l'avion et très près de celle-ci. Pour les gros diamètres de gouttes, le témoin se trouve alors dans la zone de très forte concentration. Pour des diamètres supérieurs à 50 µm, il se trouverait certainement dans la zone d'ombre, ou couche limite de givrage, dans laquelle les trajectoires de gouttelettes ne peuvent pénétrer et où la concentration est nulle par conséquent. Cette position de témoin n'est donc pas conseillée, sa captation étant très sensible au diamètre des gouttes rencontrées.

Pour le témoin de pare-brise, le coefficient de concentration est peu influencé par le diamètre des gouttelettes et reste voisin de l'unité, ce qui est l'assurance comme pour l'A340 d'une bonne représentativité des conditions de givrage ambiantes. De plus, le cas de vol n'a lui non plus que très peu d'influence sur le coefficient de concentration, ce qui permet de garantir une efficacité du témoin quelle que soit la phase de vol.

Visualisation de l'évolution du coefficient de concentration

Il est difficile de donner une image en tridimensionnel de l'évolution spatiale d'un paramètre, pour notre cas du coefficient local de concentration d'eau. D'autant plus que la valeur de celui-ci est obtenue en faisant le rapport de surfaces interceptées par des tubes de trajectoires de gouttes qu'il serait beaucoup trop coûteux de calculer dans tout l'espace. Néanmoins, lorsque l'on s'intéresse à l'évolution de ce paramètre autour d'un point précis, il est possible de combiner à la recherche de la trajectoire de goutte arrivant en ce point, le calcul d'une grille de trajectoires environnantes. A partir de cette grille de trajectoires, il est possible de calculer les surfaces amont et aval des tubes de trajectoires et d'en déduire le coefficient de concentration. Cette valeur est alors affectée au barycentre de la surface aval du tube. L'évolution du coefficient dans une portion du plan d'arrivée est alors représentée à l'aide de moyens graphiques bi ou tridimensionnels. Les figures 10 à 12 présentent de telles visualisations pour la sonde latérale de l'ATR72, pour les diamètres de gouttes de 20 et 50 µm. Pour 50 µm, la zone d'intense surconcentration apparaît nettement près de la paroi de l'avion, tandis qu'au même endroit la surconcentration est beaucoup plus faible pour 20 µm.

Les coûts

Pour qu'une méthode soit utilisable au niveau industriel, il est nécessaire qu'elle soit d'une mise en œuvre rapide et que les coûts d'utilisation soient en rapport avec les services rendus. Pour montrer ce qu'il en est des outils présentés ici, nous détaillons dans la suite les temps d'exécution des calculs sur le supercalculateur CRAY XMP116 dont nous disposons.

Pour le maillage ATR72 à 2440 panneaux peau:

Coût du calcul du champ aérodynamique par la méthode des singularités FP3D:

510 s CPU

Coût de la recherche automatique de la trajectoire de gouttes arrivant au niveau de la sonde latérale:

910 s CPU

Coût du calcul de la grille de trajectoires de gouttes environnant le point cible (24 trajectoires):

1560 s CPU

On voit donc ainsi que l'outil est tout à fait compatible avec des exigences industrielles, apportant une aide au positionnement et à l'étalonnage de sondes et capteurs dès le stade de la conception au niveau du bureau d'études.

Conclusion

Cette méthode théorique de détermination des coefficients de concentration d'eau autour d'un avion est à présent tout à fait opérationnelle. Elle a permis de définir en particulier les positions de sondes de givrage sur différents avions, Airbus et ATR. Des essais en vol avec ces sondes installées devraient permettre dans un proche avenir de la valider plus complètement.

Références

[1] "Méthode d'analyse tridimensionnelle de systèmes hypersustentateurs", RIVOIRE V., EICHEL P., AEROSPATIALE NT 443.528/87, juillet 1987.

[2] "Programme de calcul du facteur de correction de la teneur en eau liquide autour d'un nez d'avion", GUFFOND D., ONERA RT 27/5146SY, septembre 1985

[3] "Introduction à l'analyse numérique matricielle et à l'optimisation", CIARLET P.G., éditions MASSON, 1988, pages 198 à 201.

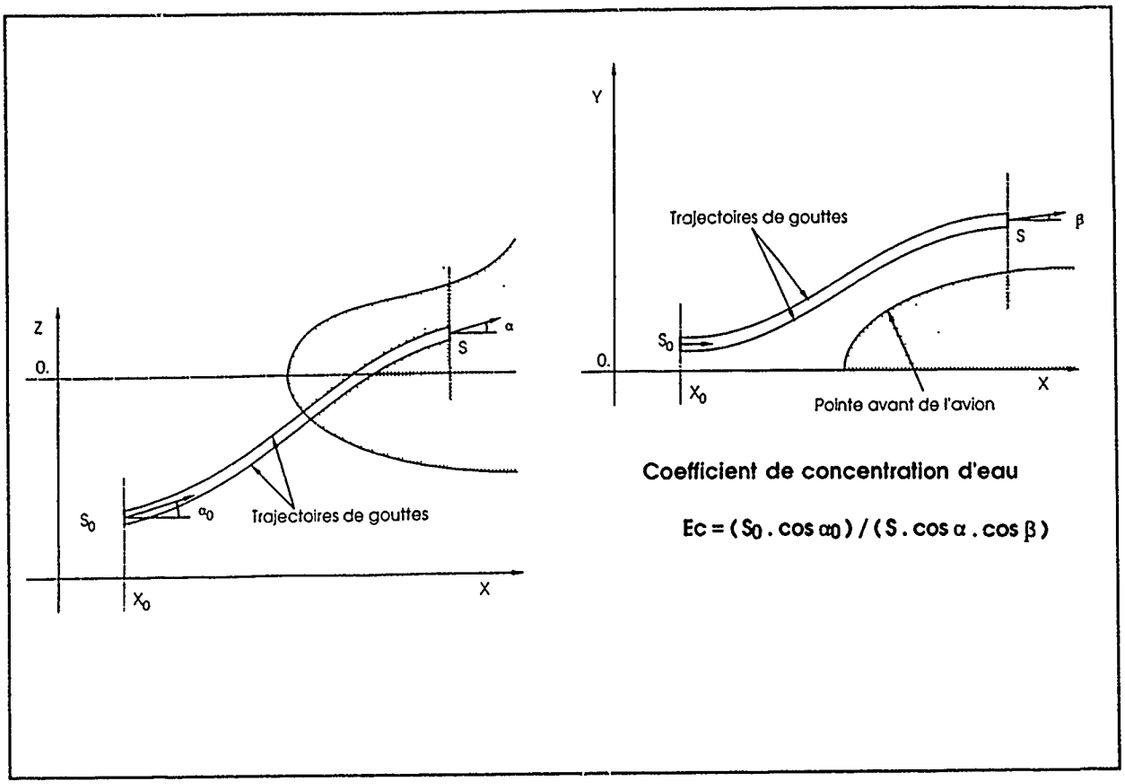

Figure 1 - Définition du coefficient de concentration d'eau

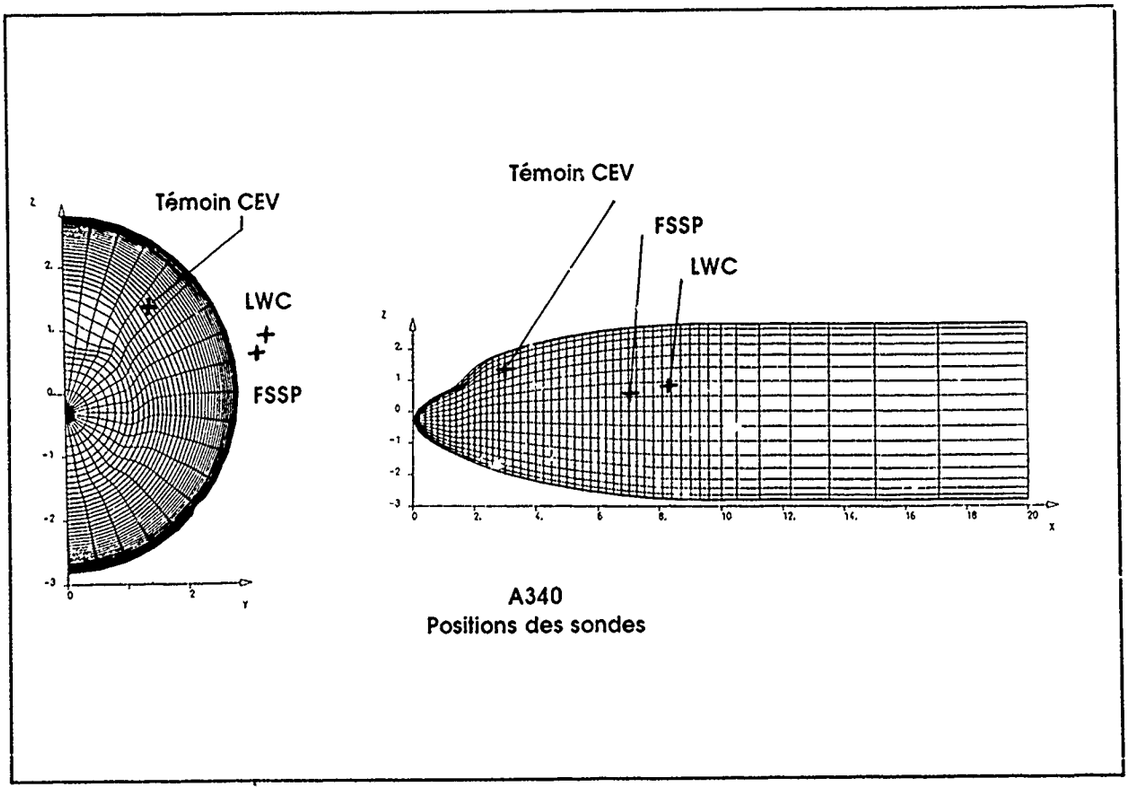

Figure 2 - Positionnement des sondes sur Airbus 340

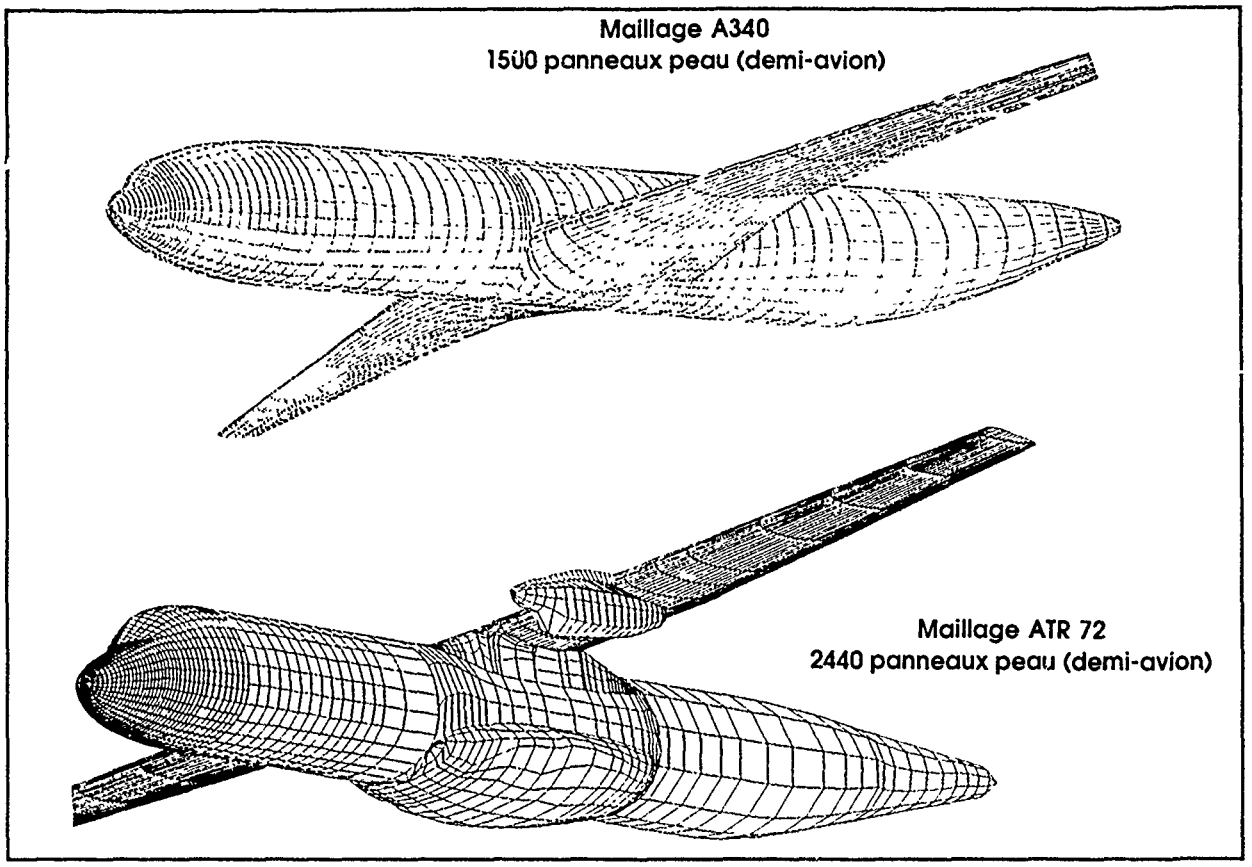

Figure 3 - Maillages ATR et Airbus pour le calcul aérodynamique

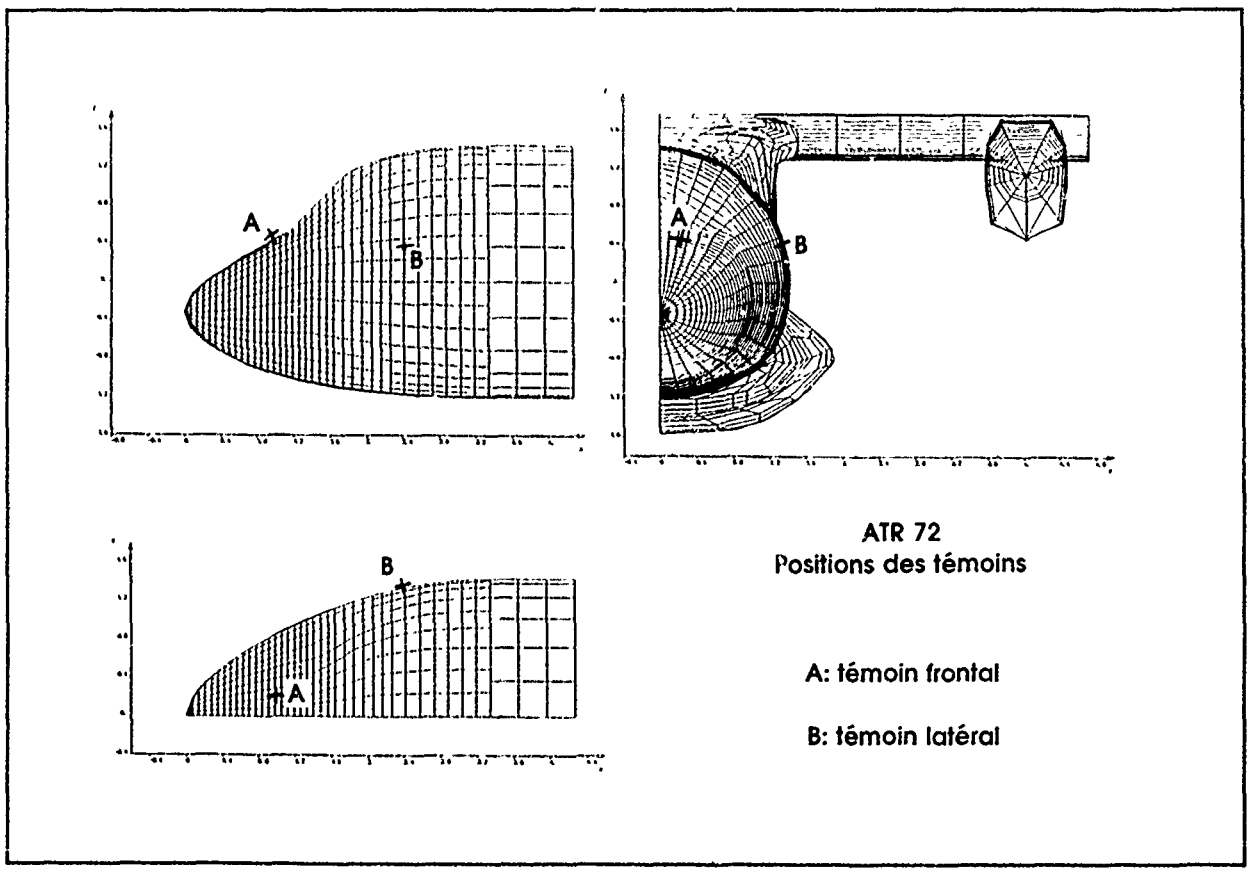

Figure 4 - Positionnement des sondes sur ATR

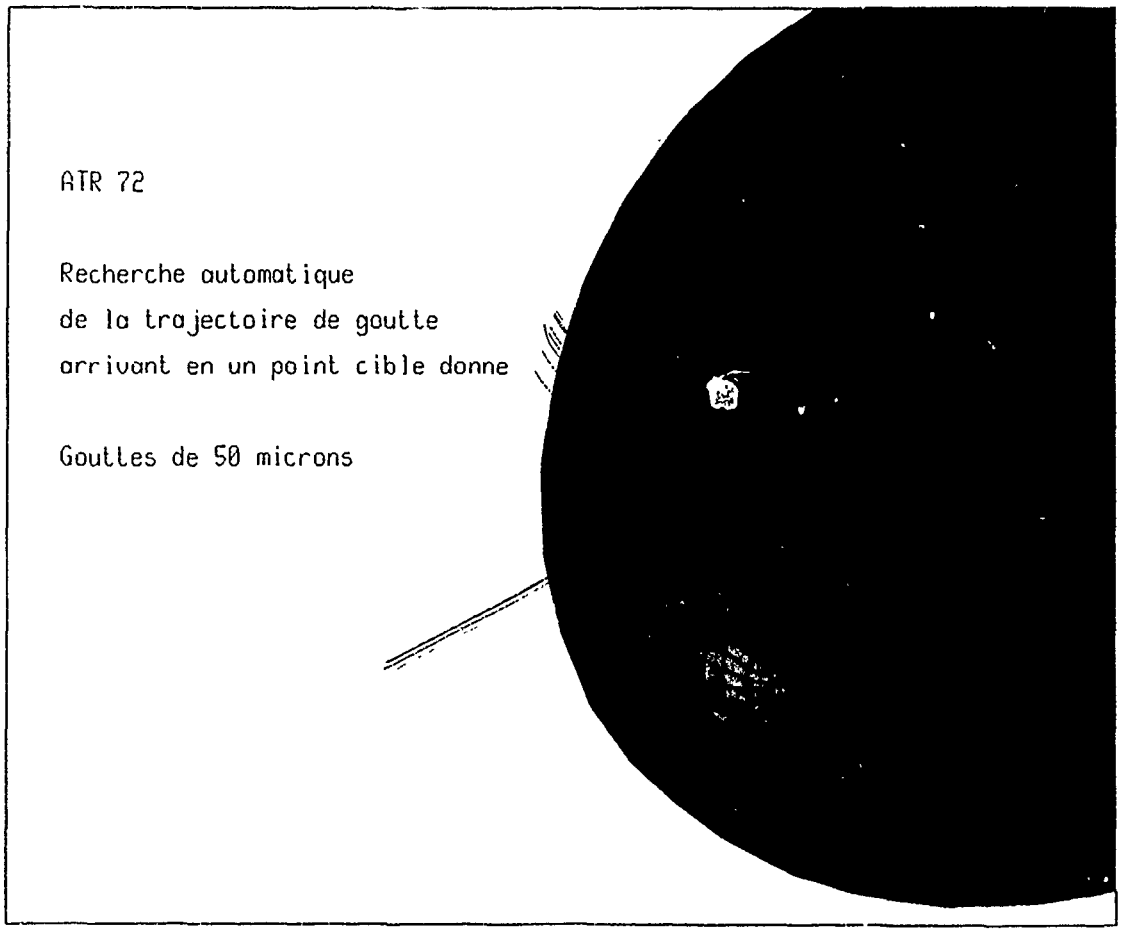

Figure 5 - Recherche automatique du départ des trajectoires

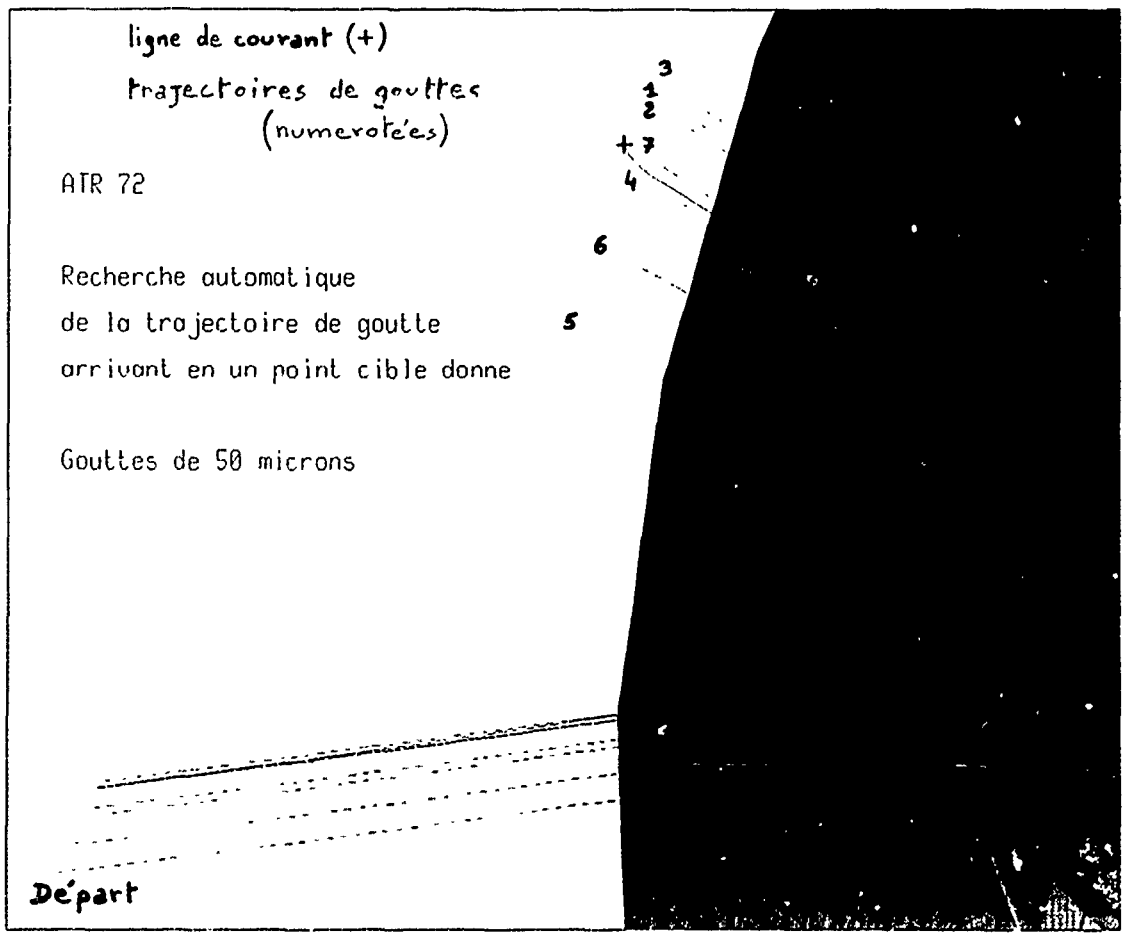

Figure 6 - Recherche automatique du départ des trajectoires (détail)

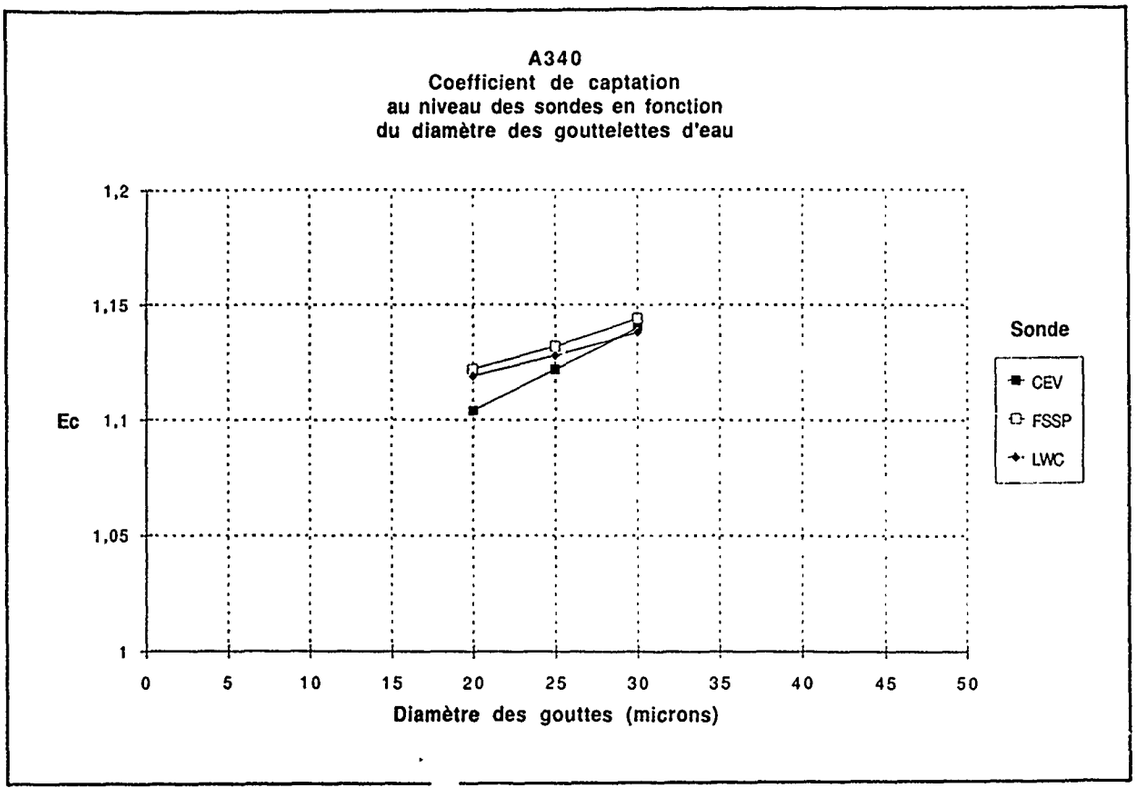

Figure 7 - Evolution du coefficient de concentration avec le diamètre des gouttes d'eau pour l'A340

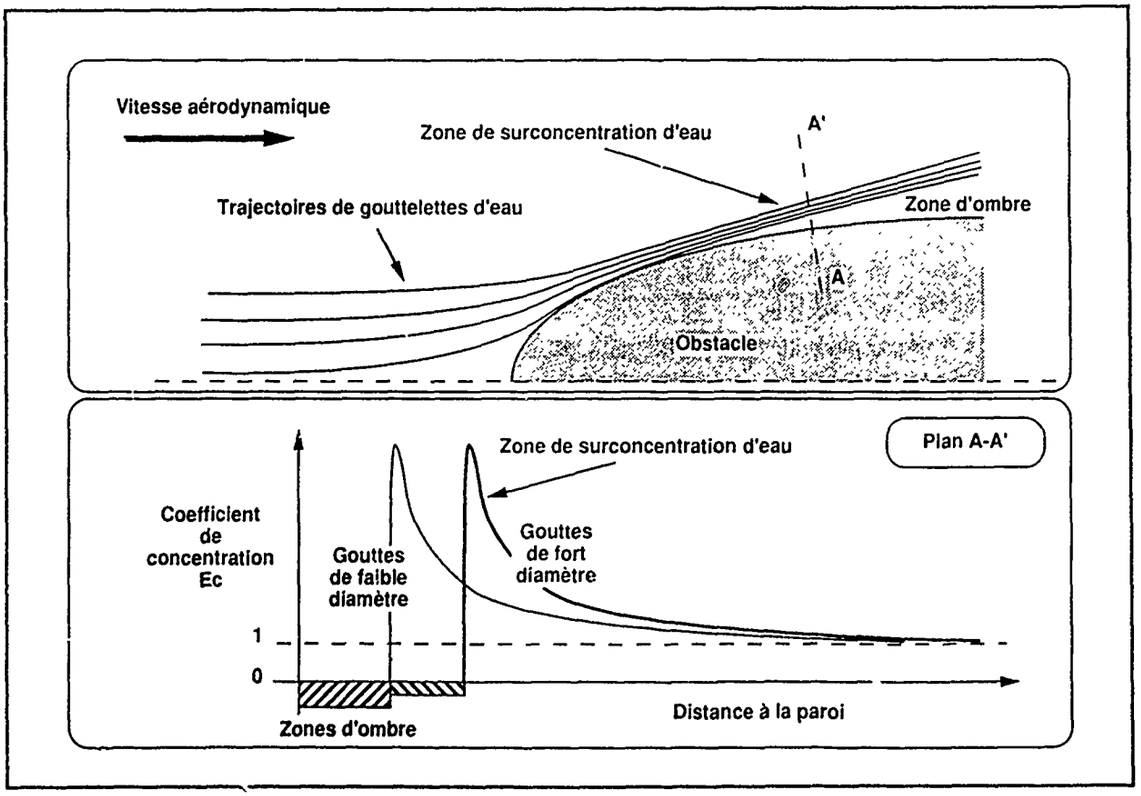

Figure 8 - Evolution schématique du coefficient de concentration avec la distance à la paroi

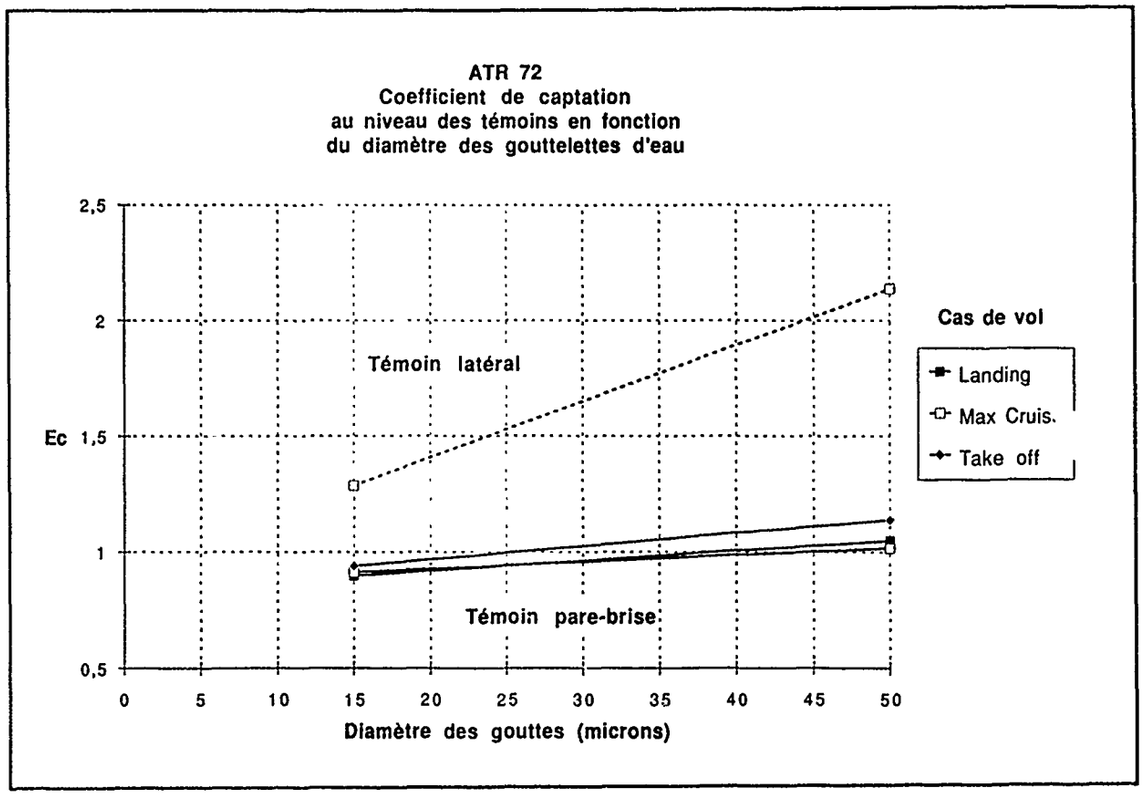

Figure 9 - Evolution du coefficient de concentration avec le diamètre des gouttes d'eau pour l'ATR

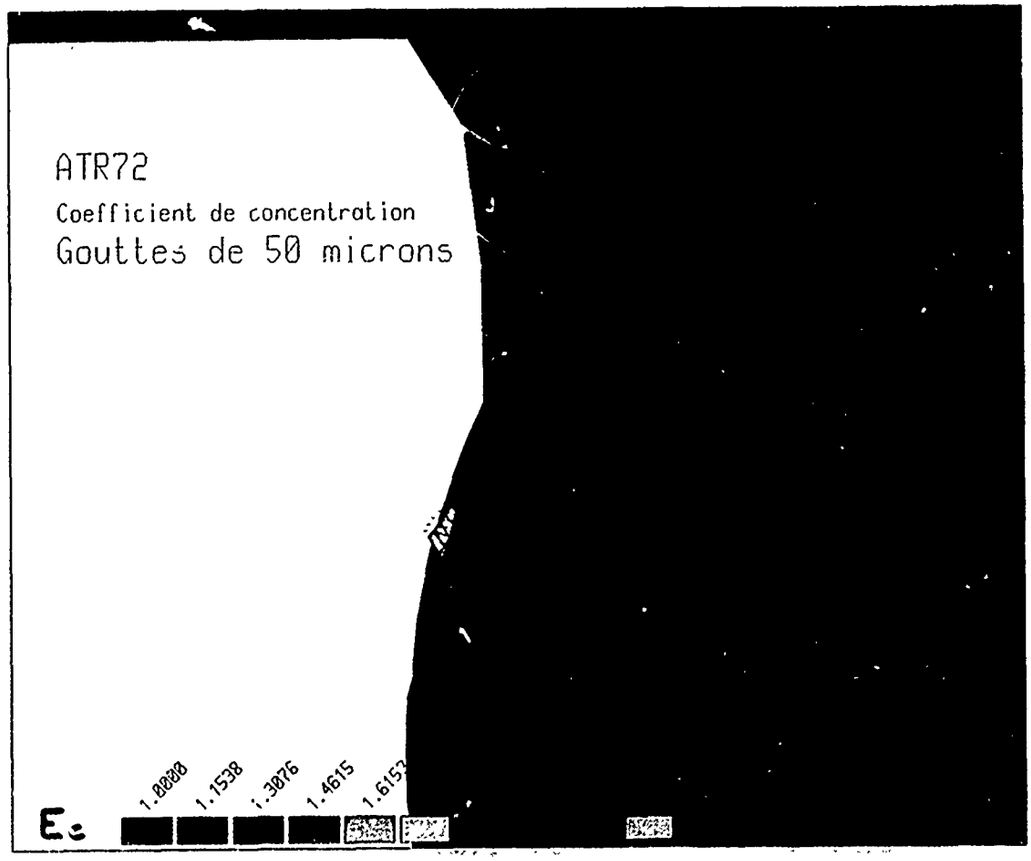

Figure 10 - Grille de trajectoires de gouttes et coefficient de concentration au niveau du témoin latéral de l'ATR

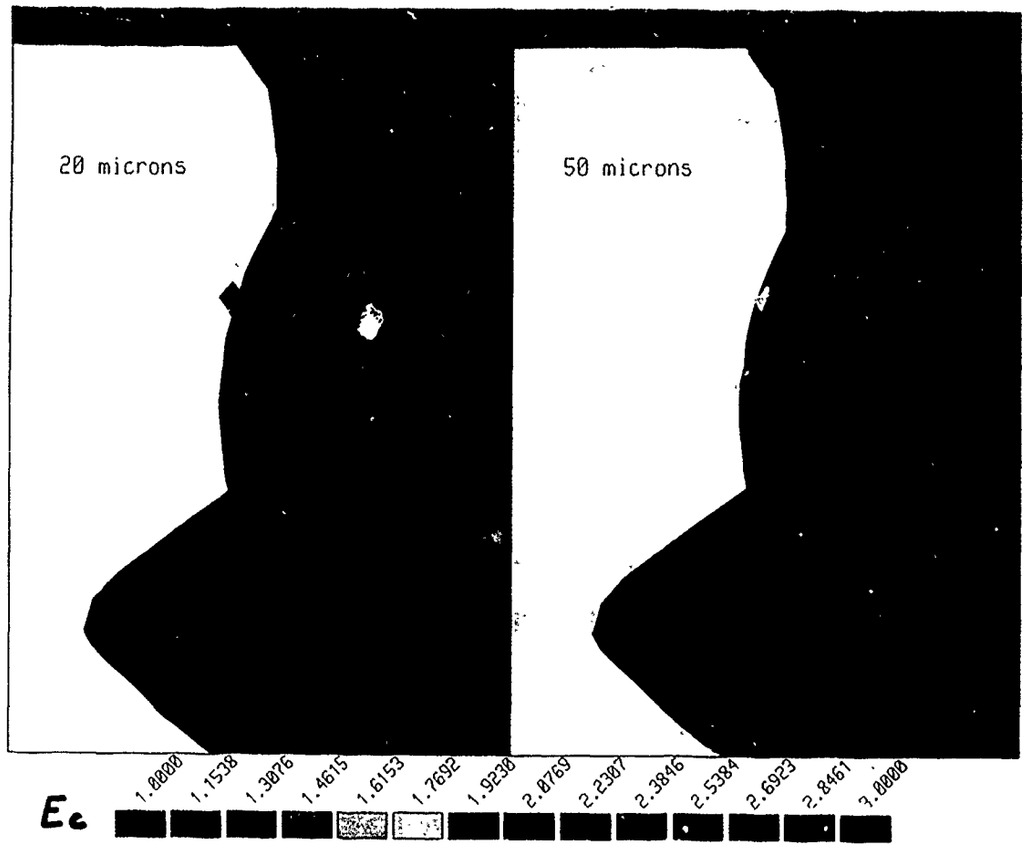

Figure 11 - Comparaison pour deux diamètres de gouttes des coefficients de concentration au niveau du témoin latéral de l'ATR

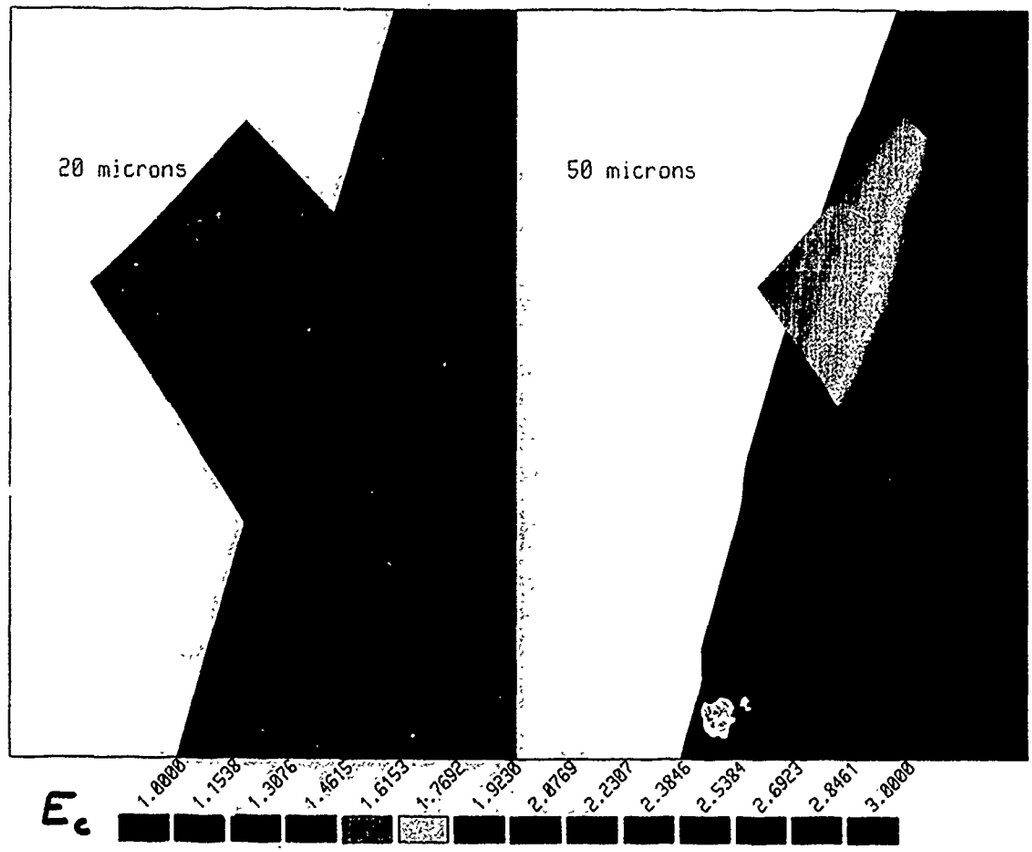

Figure 12 - Comparaison pour deux diamètres de gouttes des coefficients de concentration au niveau du témoin latéral de l'ATR (détail)

Simulation of Iced Wing Aerodynamics

M.G. Potapczuk
NASA Lewis Research Center
Cleveland, Ohio 44135
M.B. Bragg
University of Illinois at Urbana-Champaign
Urbana, Illinois 61801
O.J. Kwon
L.N. Sankar
Georgia Institute of Technology
Atlanta, Georgia 30332

Summary

The sectional and total aerodynamic load characteristics of moderate aspect ratio wings with and without simulated glaze leading-edge ice are studied both computationally, using a three-dimensional, compressible Navier-Stokes solver, and experimentally. The wing has an untwisted, untapered planform shape with NACA 0012 airfoil section. The wing has an unswept and swept configuration with aspect ratios of 4.06 and 5.0, respectively. Comparisons of computed surface pressures and sectional loads with experimental data for identical configurations are given. The abrupt decrease in stall angle of attack for the wing, as a result of the leading edge ice formation, is demonstrated numerically and experimentally.

List of Symbols

b	span length at leading edge
C_l	sectional lift coefficient
C_L	wing lift coefficient
C_p	pressure coefficient
F,*F*	inviscid flux vector
G,*G*	inviscid flux vector
H,*H*	inviscid flux vector
q,*q*	flow properties vector
R,*R*	viscous terms
S,*S*	viscous terms
T,*T*	viscous terms
t	time
x	Cartesian coordinate
y	Cartesian coordinate
y	spanwise coordinate
z	Cartesian coordinate
η	curvilinear coordinate
t	time
ξ	curvilinear coordinate
ζ	curvilinear coordinate

1. Introduction

The adverse effects of ice formation on the aerodynamic characteristics of wings and helicopter blades are well known.[1,2] It is known that icing may cause premature flow separation and lead to stall at angles of attack as low as 6 degrees. Techniques for quantitative prediction of the 3D leading edge ice formation process and the effects of icing on the aerodynamic performance of wings and rotors are however not well developed. Reliable techniques for quantitative prediction of the above phenomena are urgently needed, so that next generation aircraft and rotorcraft may be designed to cope with icing. Additionally, experimental iced wing flow field data is required for code validation efforts.

Recognizing the need for improved understanding of the aircraft icing phenomena, a multi-disciplinary research program has been underway under the funding and direction of NASA Lewis Research Center, for the past several years. Work performed under this program covers areas such as:

- Numerical modeling of the ice accretion process and development of an associated code validation database
- Experimental studies of the effects of icing on the aerodynamic characteristics of finite wings
- Efficient engineering tools based on a combination of panel methods and interactive boundary layer schemes to predict aerodynamic characteristics up to stall onset
- Research tools based on 3D Navier-Stokes equations to study the pre- and post stall characteristics of finite wings

These activities, although only a portion of the overall icing effort, constitute a major part of the program for simulation of an icing encounter for a fixed wing aircraft.

Initial research on development of analytical and computational tools for simulation of iced airfoil aerodynamics was centered on two-dimensional flows.[3-5] This was supported by an extensive experimental program for characterization of the 2D iced airfoil flow field.[6-8] Results of that research indicated reasonable agreement between code and experiment for angle of attack conditions up to stall. There is still some concern over the role of turbulence models in the prediction of massive separation at stall condition.[4,9]

The present work describes the NASA sponsored effort to develop a validated 3D Navier-Stokes solver for study of the aerodynamic characteristics of isolated wing configurations for non-iced and iced conditions. The computer code was developed by Sankar, et al.[10-12] and the current calculations were performed by Kwon and Sankar.[13,14] The experimental results were produced by Bragg and his students.[8,15,16] The wing geometry being considered has an untwisted, untapered planform shape with NACA 0012 airfoil section. The wing has an unswept and swept configuration with aspect ratios of 4.06 and 5.0, respectively.

The results presented have been documented in previous publications.[8,13-16] However, this paper provides an opportunity to assess the current status of the simulation effort for iced aircraft aerodynamics, to discuss the issues as yet unresolved, and to suggest the direction for future research. Detailed comparisons with experiments of the surface pressures and sectional airloads are used to provide a basis for the discussion.

2. Code Description

2.1 Governing Equations

The equations governing unsteady three-dimensional flow are the full Navier-Stokes equations, and may be written in a Cartesian coordinate system as:

$$q_t + F_x + G_y + H_z = R_x + S_y + T_z \qquad (1)$$

Here, q is the unknown flow properties vector; F, G and H are the inviscid flux vectors; R, S, and T are the viscous terms. To facilitate treatment of arbitrary planforms and airfoil shapes, the equations are solved in a body-fitted coordinate system. The following general curvilinear coordinate system is used:

$$\xi = \xi(x, y, z, t) \qquad \eta = \eta(x, y, z, t)$$
$$\zeta = \zeta(x, y, z, t) \qquad \tau = t \qquad (2)$$

In such a coordinate system, the governing equations may be written in the following strong conservation form:

$$q_\tau + F_\xi + G_\eta + H_\zeta = R_\xi + S_\eta + T_\zeta \qquad (3)$$

The quantities **q, F, G, H, R, S, T** are related to their Cartesian counterparts through the metrics of transformation. For a detailed description of the flow and flux vectors in the Cartesian and transformed coordinate systems, the reader is referred to Reference 12.

A two layer Baldwin-Lomax eddy viscosity model patterned after the well known Cebeci-Smith model has been used in this work. Use of such a simple model in massively separated flows may be considered questionable. In order to address this concern, studies of 2D stalled flows for iced airfoils using other models have been conducted by Potapczuk[4,9] and Wu.[17] Potapczuk used a modified mixing length model and found some improvement in the simulation for conditions at stall, however those results require further investigation for 3D calculations. Wu's results indicate that the use of higher order turbulence models does not significantly improve the accuracy of the simulation for iced airfoils. In order to keep the computer time resources small, the Baldwin-Lomax model has been used in all the 3D calculations presented here.

2.2 Solution Procedure

The governing equations are parabolic in time, and may be advanced in time using a suitable stable, dissipative scheme. Standard second-order accurate, central differences are used to approximate the spatial derivatives and to compute the metrics of the transformation. The flux vectors **F** and **H** are linearized while the spanwise flux vector, **G**, is treated semi-implicitly, thus requiring no time linearization. The viscous terms are treated explicitly. The time derivative is approximated as a first-order accurate, two-point backward difference.

2.3 Grid Generator

An algebraic C-grid generator has been built in to the computer code, and can generate computational grids around arbitrary planforms and arbitrary airfoil sections. The grid generation methodology is based on the sheared parabolic coordinate scheme. The user needs to prescribe the leading edge coordinates and the section chord and twist at chosen stations. The grid generation routines perform the necessary interpolation (linear along the span and cubic in the chordwise direction) to enrich the input wing shape. After the sheared parabolic grid is generated, the points along the grid lines in the direction approximately normal to the wing surface are redistributed so that, the first point off the wall is at a user specified distance off the surface, and an adequate number of points are placed within the boundary layer. A typical grid for a swept wing is presented in Figure 1 which shows the upper half of the computational domain at the

wing root plane and on the surface of the wing. The grid at the wing root plane can be used as a reflection plane or as a solid surface representing the wind tunnel wall.

2.4 Boundary Conditions

In the present numerical procedure, all the boundary conditions are applied explicitly after each time step. Since these cases deal with low subsonic Mach numbers, the flow quantities at the far-field are set to be the undisturbed freestream conditions. To satisfy this condition, the far-field boundaries are placed at least 6 to 7 chord lengths from the surface of the wing. At the downstream boundary, the pressure is assumed to recover to freestream values and all the other flow properties are extrapolated from the interior. The C-grid generated by the present algebraic transformation created a cut that originates from the trailing edge. On this cut the flow quantities are averaged from above and below.

Two types of boundary conditions have been used at the wing root location. The experimental model is a semi-span wing with a splitter wall at the root location. This splitter wall is used to minimize the effects of the tunnel wall boundary layer on the flow over the wing. The wing-splitter wall intersection results in the development of a vortical flow region which reduces the effective angle of attack at the wing root. This effect is minor for the non-iced geometry but can play an important role in the aerodynamics of the iced wing. In order to properly capture this phenomena, a no-slip boundary condition is applied at the wing root-splitter plate junction for the iced geometry. The spanwise spacing of nodal planes in this region is quite small in order to capture these effects, thus resulting in a significant increase in the number of grid points to be computed. In the case of a non-iced geometry, a reflection plane was used at the root, thus allowing coarser grid spacing in the spanwise direction and hence a less costly computation.

3. Description of Experiment

3.1 Apparatus

The experiments described in this report were conducted in the Ohio State University (OSU) subsonic wind tunnel located at the Aeronautical and Astronautical Research Laboratory and later in the subsonic wind tunnel at the University of Illinois. The OSU tunnel has a three-by-five foot test section, eight feet in length. The tunnel operates at speeds from zero to 200 feet per second at Reynolds numbers of up to 1.3×10^6 per foot. The tunnel is an open return type and uses four turbulence screens and honeycomb in the settling chamber to reduce tunnel turbulence. The University of Illinois tunnel is of similar design with a three -by-four foot test section, eight feet in length. The Illinois tunnel operates at speeds from zero to 240 feet per second at Reynolds numbers of up to 1.5×10^6 per foot.

The model used in testing is a semi-span wing having a NACA 0012 airfoil section with a variable (i.e. 0° or 30°) sweep angle. Results have been obtained using both sweep angles. The model has a chord of 15 inches perpendicular to the leading edge and a span of 35.18 inches. The chord length was chosen to provide as large an aspect ratio as possible with minimum tunnel wall interference and high Reynolds number. The model has a removable leading edge, thus allowing simulation of a non-iced or iced wing geometry. The iced leading edge is a simulation of a measured ice accretion on a NACA 0012 airfoil taken from the NASA Lewis Icing Research Tunnel. A cross-sectional view of the simulated glaze ice shape is shown in Figure 2.

The model is equipped with surface static pressure taps, as shown in Figure 3. The taps are located in 5 major rows plus a row on the tip section. Only the 5 major pressure tap rows are shown in the figure, as they were the ones used for comparison to the computations. The centerline row of taps has 80 taps in the no-ice configuration and 83 in the iced configuration. The other 4 rows on the main element have 40 and 41 taps in the no-ice and iced configurations, respectively. The wing tip section has 21 taps. The total number of pressure taps on the model is thus, 261 in the no-ice configuration and 268 in the iced configuration.

Pressure measurements were made using a Scanivalve system. Six Scanivalves capable of measuring 48 pressures each were used. No cut-off valves were used during the testing. For the zero-sweep tests, a single traversing total-pressure probe was used to measure the airfoil wake. The probe was located approximately one chord length downstream of the model trailing edge and at the spanwise station, $y/b = 0.417$, which is between the second and third tap rows.

3.2 Pressure Data Reduction

The model pressures were converted to pressure coefficients using the measured tunnel dynamic pressure taken from each of the Scanivalves. The pressure coefficients were integrated over the surface of the model to produce the section lift coefficient.The total pressure deficit, measured by a wake probe, was integrated to obtain the airfoil section drag for the zero sweep model. Note that when span loads are shown, y is taken parallel to the leading edge and C_l is taken along the tap lines perpendicular to the leading edge. When the span loads are integrated to obtain model C_L, the sectional lift coefficient at the wing root is taken as equal to value for the first tap row and the C_l at the tip is approximated as 1/2 that of the last tap row.

Further details regarding the equipment used for data acquisition and reduction are provided in References 6-8, 15, and 16.

3.3 Helium-Bubble Flow Visualization

Helium-bubble flow visualization was conducted using a bubble generator manufactured by Sage Action, Inc. The bubbles are approximately 1/16 inch in diameter and are formed by injecting helium into a special soap film using a concentric injection tube arrangement.[18] The helium-filled bubbles are approximately neutrally buoyant and are able to follow the complex separated flows found on iced airfoils. Two bubble generator heads producing a total of 800 bubbles per second were located in the tunnel settling chamber just aft of the turbulence screens.

The bubbles are illuminated from a point orthogonal to the viewing position. For the planform or top view shown later in this paper, the light beam entered the tunnel through the side window, over the wing tip. Photos were then taken through a plexiglass window in the tunnel floor and the model was mounted inverted, upper surface down.

Details regarding the photographic equipment and video recording equipment used to capture the bubble images are contained in Reference 16.

4. Results and Discussion

The experiments and computations were carried out for a combination of conditions encompassing the iced and non-iced geometry, the 0° and 30° sweep angles, and 4° and 8° angle of attack conditions. This discussion will center on a review of progress to date, issues that remain unresolved, and on what activities are planned to address those issues.

4.1 Rectangular Wing

The pressure distributions at several spanwise locations for the non-iced unswept wing at the 8° angle of attack condition are shown in Figure 4. These results show very good agreement at all the span locations. The pressure peaks near the leading edge are captured quite well. Some differences are seen near the trailing edge region, most likely due to poor grid resolution. The profile at the 85 percent span location indicates an overprediction of the C_p values by approximately 5 percent for the first 20 percent chord.

The effect of the wall boundary condition is also seen in Figure 4. The differences in C_p due to the wall, at the measurement locations, is not large. However, differences are apparent when the calculated results using either set of wall boundary conditions are compared at locations inboard of the 17 percent span location. Figure 5 shows these differences. The wall boundary condition actually increases the lift. No measurements have been taken in this region, however the effects of the splitter-wall boundary layer will be investigated in future testing through the use of a side-wall suction mechanism.

Figure 6 shows the spanwise distribution of the computed and measured airloads (i.e. measured surface pressures integrated over the chord) at 4° and 8° angle of attack for a non-iced unswept wing. The computed airloads are generally in good agreement with the measured loads over the span, even though the rate of decrease along the span between the mid semi-span and the tip is smaller than in the experiment. This gives slightly higher loading in this range. These discrepancies are partly attributable to the lack of spanwise grid points which are necessary to properly handle the concentrated vortex shedding off the wing tip.

The addition of the ice shape to the leading edge causes a considerable change to the surface pressure distributions. The recirculation region behind the ice shape alters the pressure peaks at the leading edge. The typical flat profile of a separated flow region is indicated by the experimental results for the 4° angle of attack condition, as seen in Figure 7. The calculated results, also shown in Figure 7, indicate a much larger pressure spike at the leading edge than the experiments suggest. This phenomenon has been seen by other researchers[4,5] and has yet to be examined in detail. It has been suggested that this may be due coarse grid code resolution around the ice horn. The spanwise distribution of the computed and measured airloads are shown in Figure 8. The results indicate very good agreement for the 4° angle of attack condition.

At 8° angle of attack, the importance of the wall boundary condition becomes apparent. Figures 9 and 10, C_p distributions at several spanwise locations, show the results of using the no-wall and wall boundary conditions, respectively. It is suggested that the interaction of the separation region behind the ice shape with the wing-wall vortex at the root leads to reattachment of the separated flow. Neglecting this interaction, as in the calculations for Figure 9, results in separation over the entire length of the wing at the root sections and underprediction of the C_p suction peak. The spanwise load distributions (Figure 8) also show the influence of the wall boundary condition on the computed results.

The grid required to incorporate the wall boundary conditions consisted of a 151 by 42 by 43 array of nodal points. Obviously, this is a significant increase in the computational requirements of the calculation when compared to the no-wall calculation, which has a 131 by 19 by 30 array of nodal points. This doubling of the size of the grid is necessary in this case because the no-wall

boundary condition misses a significant part of the physics of this problem.

The other point to be made here is that the wall boundary condition must be included in all calculations, if the code is to be used as a predictive tool. Since it is not known beforehand at what angle of attack the recirculation zone will develop into a completely separated region, the wall boundary condition must be used to insure that the code does not prematurely predict separation and stall of the iced wing. This also suggests that two-dimensional calculations for the stall of an iced wing will undoubtedly result in conservative predictions for the performance behavior.

4.2 Swept Wing

The effect of sweep on the wing model is seen in Figure 11 which shows the integrated lift values for positive and negative angles of attack, as measured in the wind tunnel. The swept wing has a lower lift-curve slope and a higher stall angle than the rectangular wing model.

The influence of the wall boundary condition is seen in Figures 12 and 13, which show C_p distributions and spanwise lift distributions, respectively. Both figures indicate that the wall does not significantly influence the aerodynamics of the non-iced swept wing.

The pressure distributions at several spanwise locations for the 4° angle of attack condition are shown in Figure 14. The comparisons to experiment indicate good agreement except for the pressure spike at the horn of the ice shape and the oscillation in the pressure trace at the trailing edge. As mentioned in the discussion of results for the rectangular wing, the leading edge pressure spike has been attributed to lack of resolution in the computations,[4,5,13] although no attempt has been made to systematically verify that contention. A similar argument is made for the evaluation of the trailing edge region. The large number of grid points needed to characterize the iced wing geometry has led to some compromise on accuracy of the solution in non-critical regions. This compromise has not resulted in poor agreement between computation and experiment for the airloads, as seen in Figure 15.

Particle traces developed from the calculated results are shown in Figures 16 and 17. The figures indicate a separation zone near the leading edge of the wing covering most of the span. Figure 16, a surface oil flow simulation, indicates the reattachment line at 10 percent chord and the spanwise flow from root to tip. Figure 17, consisting of particle traces ranging from zero to one chord length above the wing surface, shows the vortical nature of the flow in the separation zone. This figure can be compared to the photograph of a helium bubble flow visualization experiment, conducted in the Univ. of Illinois wind tunnel, shown in Figure 18. The photograph also shows the vortical flow in the separation zone, albeit with fewer traces due to the random nature of the bubble entrainment process.

The 8° angle of attack results indicate the onset of stall for the wing, progressing from the tip towards the root. The pressure distribution comparisons, Figure 19, show regions of increasing flow separation moving from the root to the tip. The comparisons between the calculated results and the measurements are quite good, even at the outboard stations. The spanwise load distributions, shown in Figure 15, are also in good agreement. The code appears to be capable of indicating the onset of stall for the iced wing.

Figures 20 and 21 are particle traces from the calculated results, as was described for the 4° angle of attack case. The surface oil flow simulation, Figure 20, indicates a much larger region of flow separation. The reattachment line starts at the leading edge near the root and moves toward the trailing edge near the wing tip. At the tip region, the flow separation due to the ice shape merges with the wing tip vortex, thus producing the complex flow pattern seen in the figure. The off-body particle traces, Figure 21, show the center of the vortical flow moving back along the chord as it progresses from the root to the tip. Interaction with the tip vortex causes the center to curve towards the trailing edge very rapidly over the last 30 percent of span. This can also be seen in the change in slope of the lift distribution curve (Fig. 15). Flow visualization experiments are underway in order to verify the existence of the flow patterns seen in the computations.

5. Concluding Remarks

A three-dimensional Navier-Stokes solver has been used to study the performance of non-iced wings and wings with simulated glaze leading-edge ice at 4° and 8° angles of attack. A corresponding wind tunnel test program is underway to provide highly detailed code validation information. The calculated chordwise pressure distribution and the integrated sectional loads of non-iced wings and iced wing at 4° angle of attack are in good agreement with experiments. The locally separated flow region at the iced wing leading edge is reasonably well predicted. At 8° angle of attack, the flow over the iced wing is massively separated. Accurate prediction of chordwise pressure distribution and sectional loads under these conditions requires representation of the tunnel end wall boundary condition due to the highly 3D nature of the flow field.

These results indicate the need for further investigation of the flowfield characteristics of the iced swept wing. Detailed measurements of the velocities above the wing surface are required to validate the computational

predictions of the vortical spanwise flow. These measurements will also confirm the changes in flow structure seen as the angle of attack increases. Current plans call for the use of a laser-doppler velocimeter system to obtain the detailed flow measurements required for validation. This system should also provide information on turbulence levels in the flow which will add further to the evidence for validation of the computations. Additionally, a force balance system is being developed to provide integrated lift, drag, and moment measurements for the wing model. Flow visualization experiments will be continued to provide qualitative assessment of the correspondence between calculation and experiment.

On the computational side, more cases must be run to address some of the issues identified above. Grid resolution near the leading and trailing edge regions must be increased to provide better agreement for the pressure distribution on the wing. The grid resolution near the wall region should also be investigated with the goal of decreasing the number of spanwise stations necessary while maintaining accurate reproduction of the flowfield in that region.

References

1) Preston, G. M. and Blackman, C. C., "Effects of Ice Formations on Airplane Performance in Level Cruising Flight," NACA TN-1598, May 1948.

2) Korkan, K. D., Dadone, L., and Shaw, R. J., "Performance Degradation of Helicopters due to Icing -- A Review," Presented at the 41st Annual Forum of the American Helicopter Society, Ft. Worth, Texas, May 15-17, 1985.

3) Potapczuk, M. G., "Numerical Analysis of a NACA 0012 Airfoil with Leading Edge Ice Accretions," AIAA Paper 87-0101, Jan. 1987.

4) Potapczuk, M. G., "Navier-Stokes Analysis of Airfoils with Leading Edge Ice Accretions," Ph.D. Dissertation, The University of Akron, Akron, OH, 1989.

5) Cebeci, T., "Effects of Environmentally Imposed Roughness on Airfoil Performance," NASA CR-179639, June 1987.

6) Bragg, M. B. and Spring, S. A., "An Experimental Study of the Flow Field about an Airfoil with Glaze Ice," AIAA Paper 87-0100, Jan. 1987.

7) Bragg, M. B. and Khodadoust, A., "Experimental Measurements in a Large Separation Bubble due to a Simulated Glaze Ice Accretion," AIAA Paper 88-0116, Jan. 1988.

8) Bragg, M. B. and Khodadoust, A., "Effect of Simulated Glaze Ice on a Rectangular Wing," AIAA Paper 89-0750, Jan. 1989.

9) Zaman, K.B.M.Q. and Potapczuk, M.G., "The Low Frequency Oscillation in the Flow over a NACA 0012 Airfoil with an "Iced" Leading Edge," NASA TM-102018, June 1989.

10) Sankar, L. N., Malone, J. B., and Schuster, D., "Euler Solutions for Transonic Flow past a Fighter Wing," Journal of Aircraft, Vol. 24, No. 1, Jan. 1987.

11) Sankar, L. N., Wake, B. E., and Lekoudis, S. G., "Solution of the Unsteady Euler Equations for Fixed and Rotary-Wing Configurations," Journal of Aircraft, Vol. 23, No. 4, April 1986.

12) Wake, B. E. and Sankar, L. N., "Solution of the Navier-Stokes Equations for the Flow About a Rotor Blade," Journal of the American Helicopter Society, Vol. 34, No. 2, April 1989.

13) Kwon, O. and Sankar, L., "Numerical Study of the Effect of Icing on Finite Wing Aerodynamics," AIAA Paper 90-0757, Jan. 1990.

14) Kwon, O.J. and Sankar, L.N, "Numerical Study of the Effect of Icing on Fixed and Rotary Wing Performance," AIAA Paper 91-0662, Jan. 1991.

15) Khodadoust, A. and Bragg, M. B., "Measured Aerodynamic Performance of a Swept Wing with a Simulated Ice Accretion," AIAA Paper 90-0490, Jan. 1990.

16) Bragg, M. B., Khodadoust, A.,Soltani, R., Wells, S., and Kerho, M.,"Effect of Simulated Ice Accretion on the Aerodynamics of a Swept Wing," AIAA Paper 91-0442, Jan. 1991.

17) Wu, J.C., "A Study of Unsteady Turbulent Flow Past Airfoils," Ph.D. Dissertation, Georgia Institute of Technology, Atlanta, GA, 1988.

Acknowledgment

The wind tunnel measurements were performed by M.B. Bragg and A. Khodadoust at the Ohio State University and at the University of Illinois.

The computations were performed by O.J. Kwon and L.N. Sankar of the Georgia Institute of Technology on the NASA Lewis Research Center CRAY-YMP.

M.G. Potapczuk is the technical monitor of these activities. This work was sponsored by NASA Lewis Research Center under grants NAG3-768, NAG3-28, and NAG3-1134.

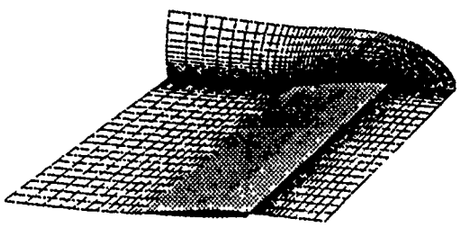

Fig. 1 Grid system for iced wing with 30° sweep angle. Grid : 151x42x43.

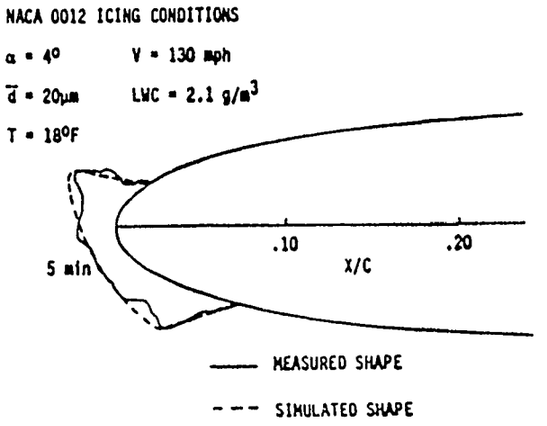

Fig. 2 Simulated glaze ice accretion.

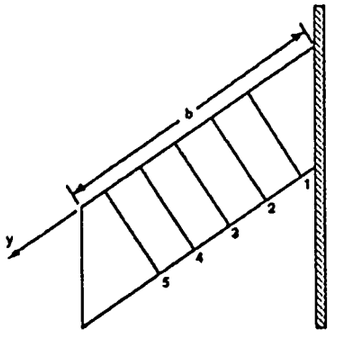

Tap flow	y/b
1	0.267
2	0.421
3	0.509
4	0.723
5	0.895

Fig. 3 Semi-span swept wing model including pressure tap locations.

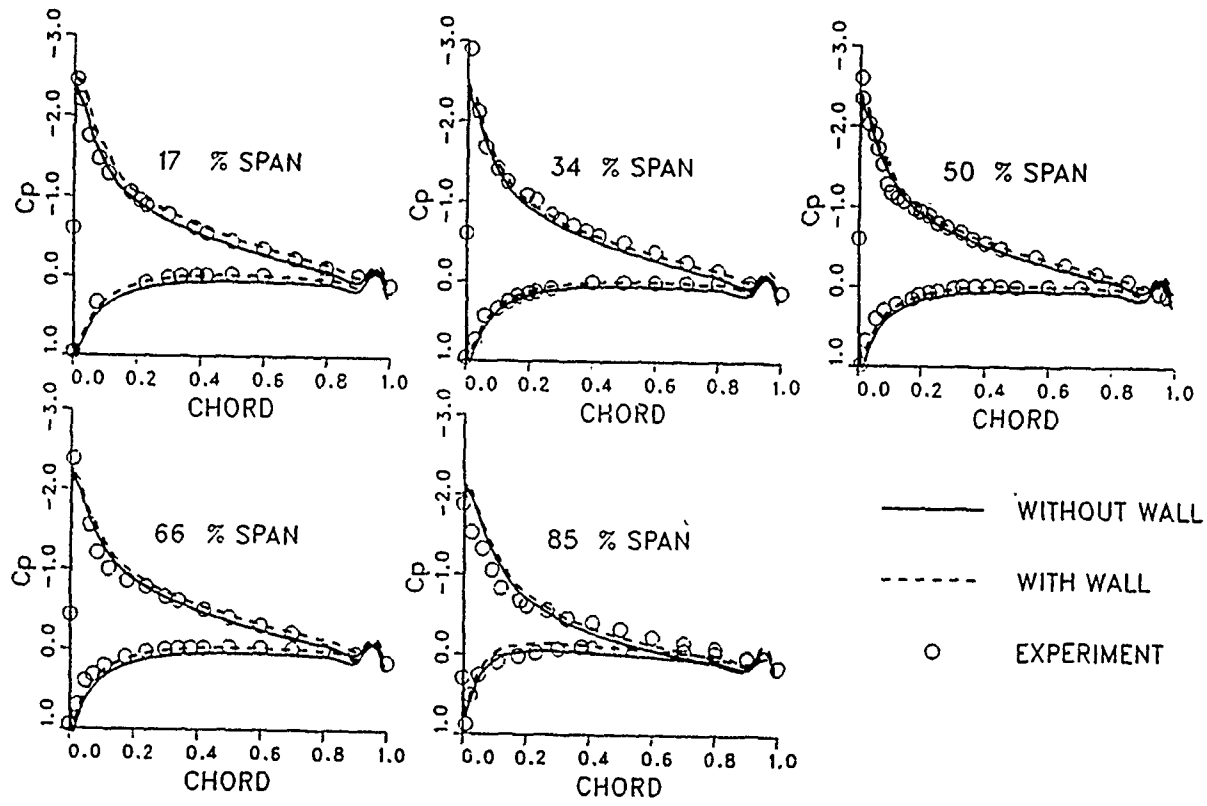

Fig. 4 Surface pressure distributions for the non-iced unswept wing at 8° angle of attack. Wall and no-wall boundary at root section.

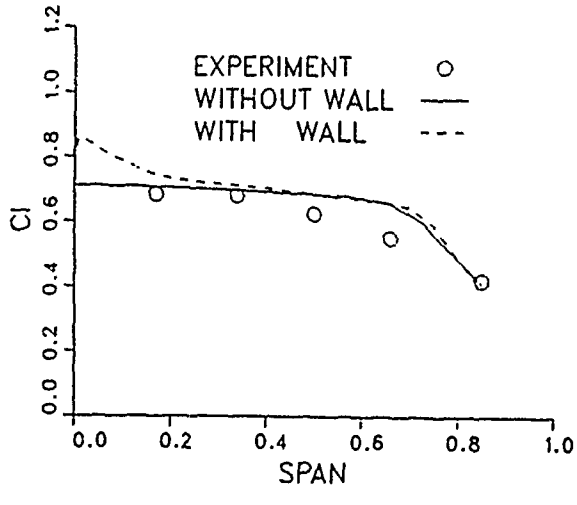

Fig. 5 Spanwise load distributions for the non-iced unswept wing at 8° angle of attack. Wall and no-wall boundary at root section.

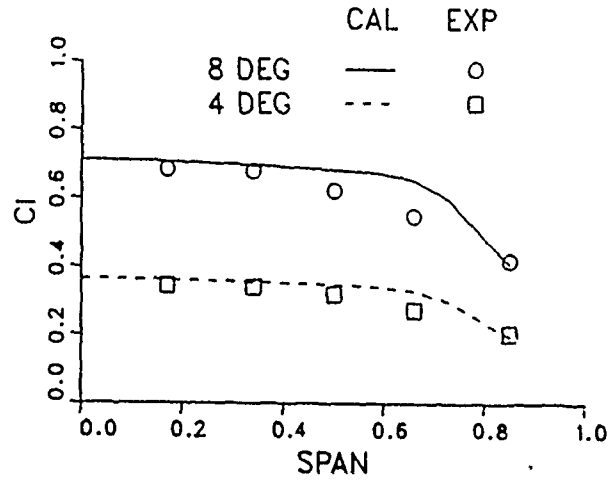

Fig. 6 Spanwise load distributions for the non-iced unswept wing at 4° and 8° angle of attack.

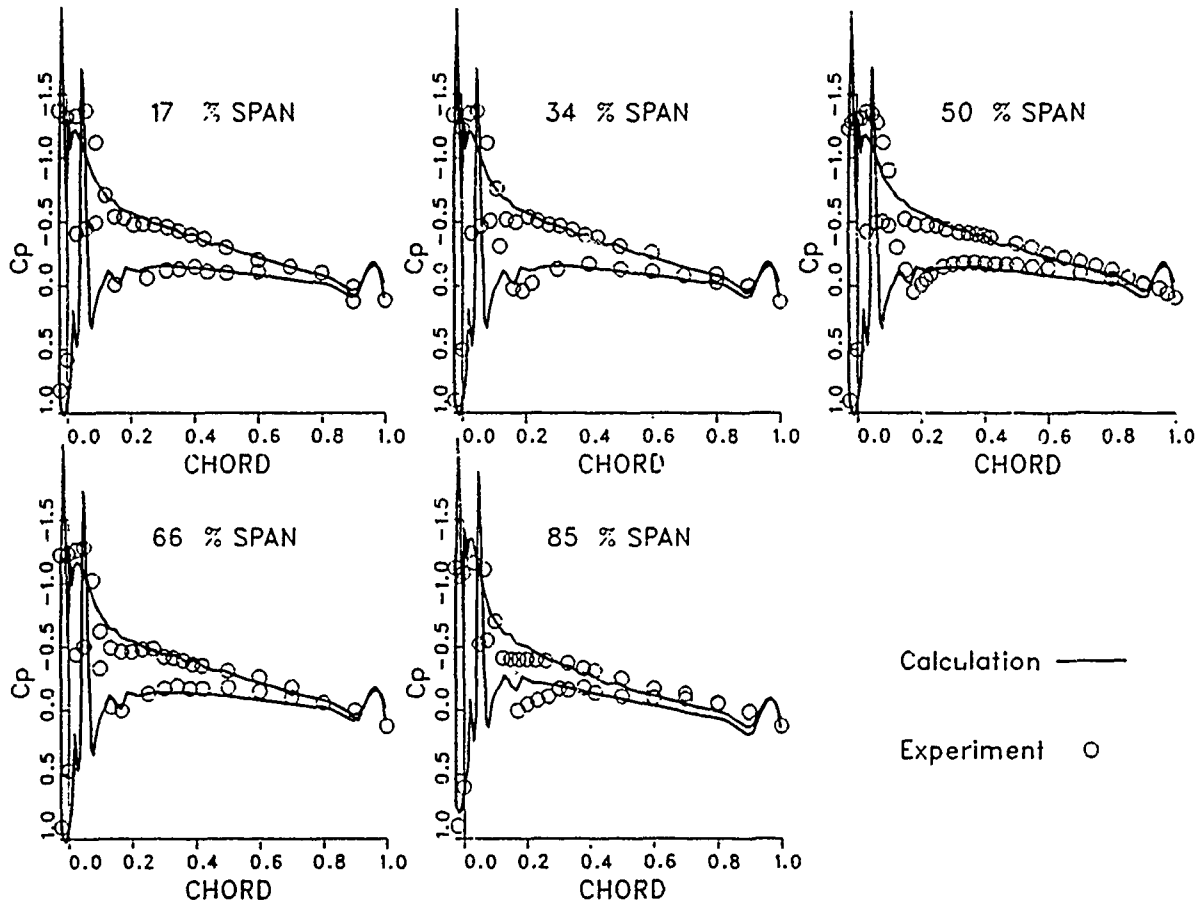

Fig. 7 Surface pressure distributions for the iced unswept wing at 4° angle of attack. No-wall boundary at root section.

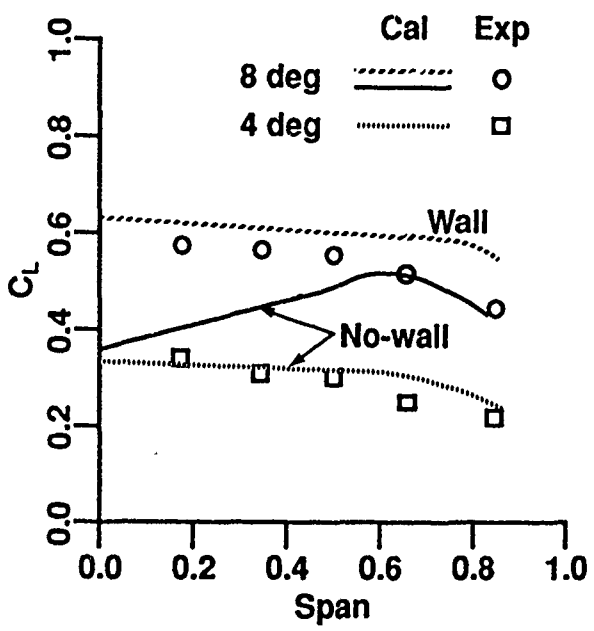

Fig. 8 Spanwise load distributions for the iced unswept wing at 4° and 8° angle of attack. No-wall and wall boundary conditions used.

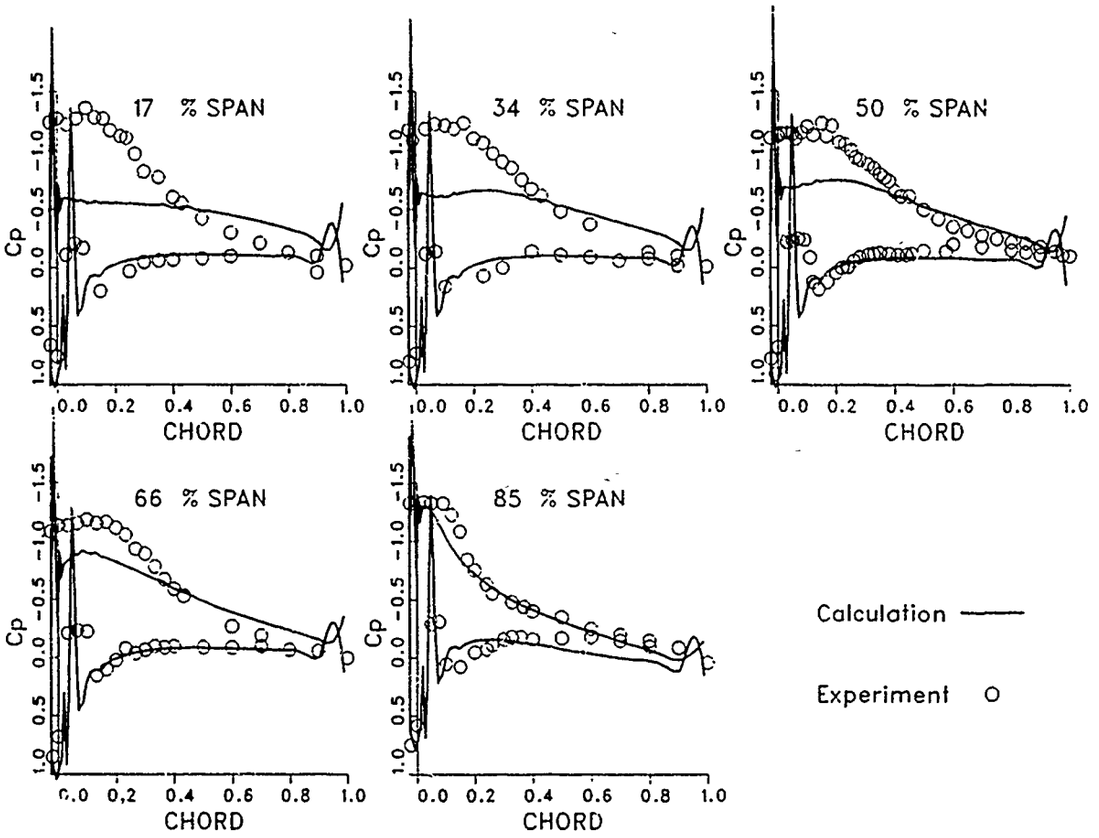

Fig. 9 Surface pressure distributions for the iced unswept wing at 8° angle of attack. No-wall boundary at root section.

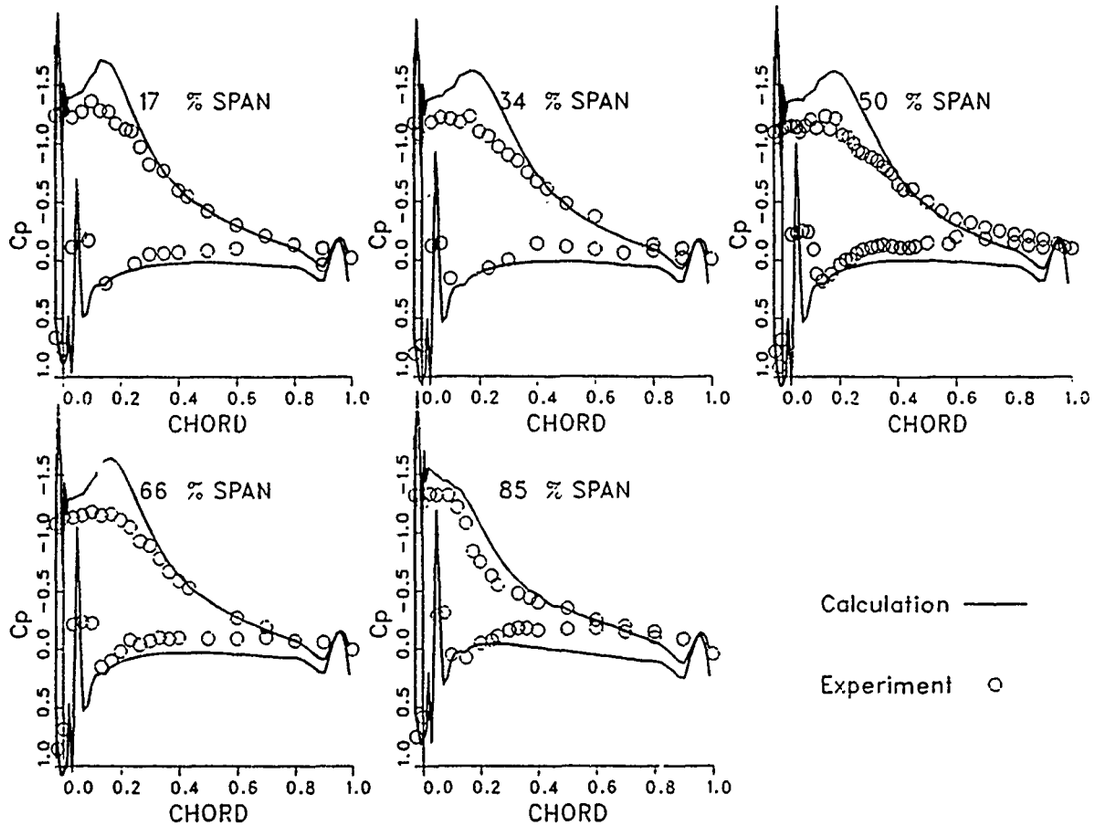

Fig. 10 Surface pressure distributions for the iced unswept wing at 8° angle of attack. Wall boundary at root section.

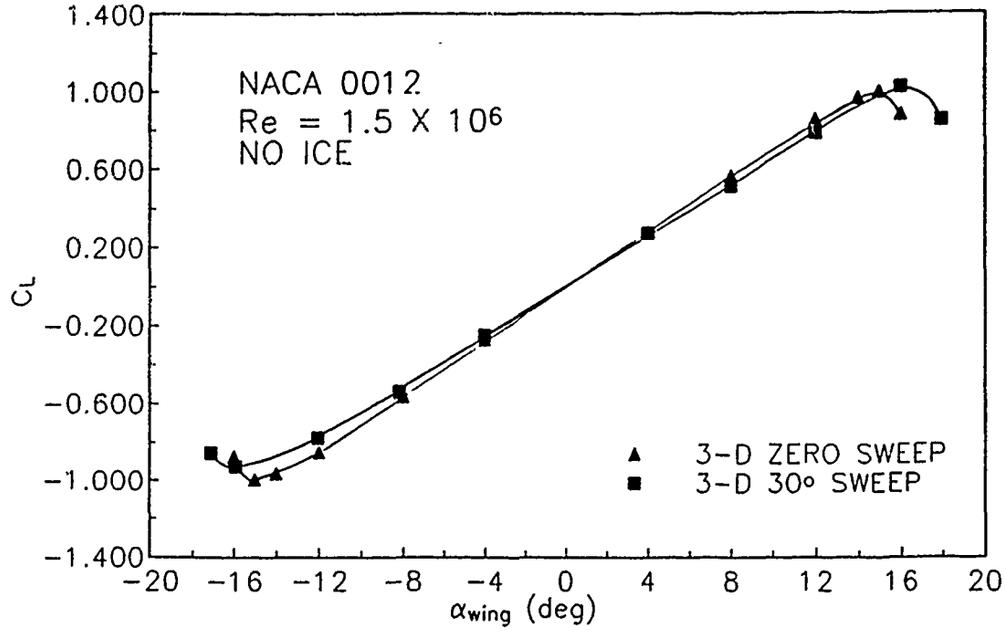

Fig. 11 3D lift performance of the swept wing compared to the unswept wing.

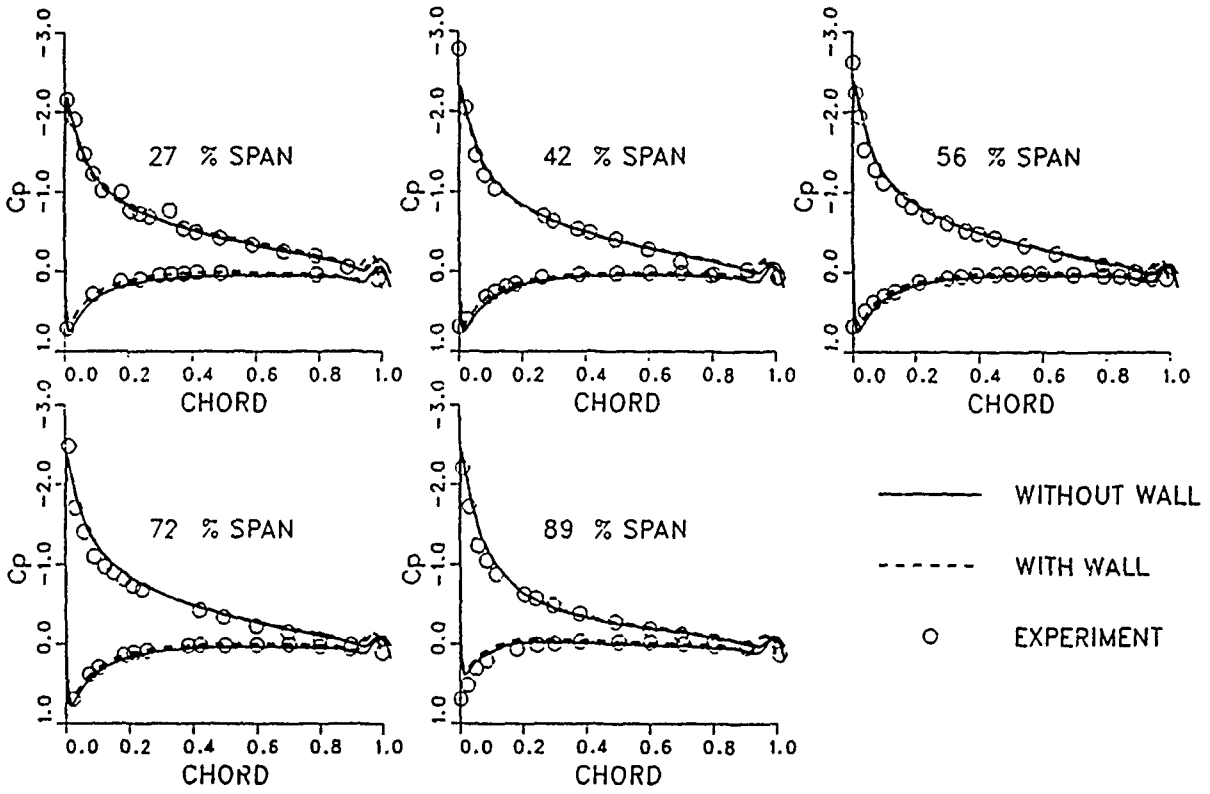

Fig. 12 Surface pressure distributions for the non-iced swept wing at 8° angle of attack. Wall and no-wall boundary at root section.

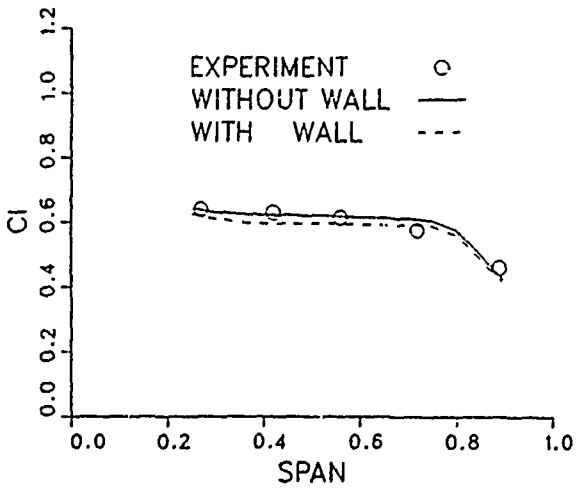

Fig. 13 Spanwise load distributions for the non-iced swept wing at 8° angle of attack. Wall and no-wall boundary at root section.

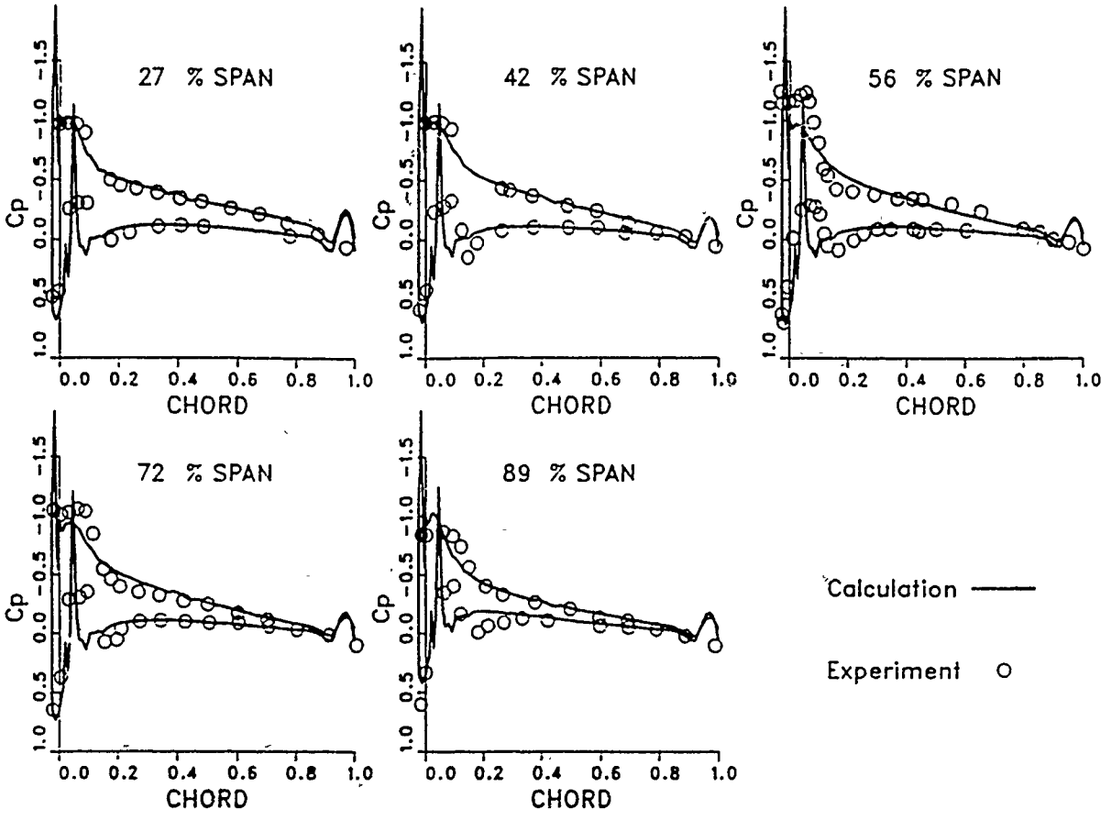

Fig. 14 Surface pressure distributions for the iced swept wing at 4° angle of attack. Wall boundary at root section.

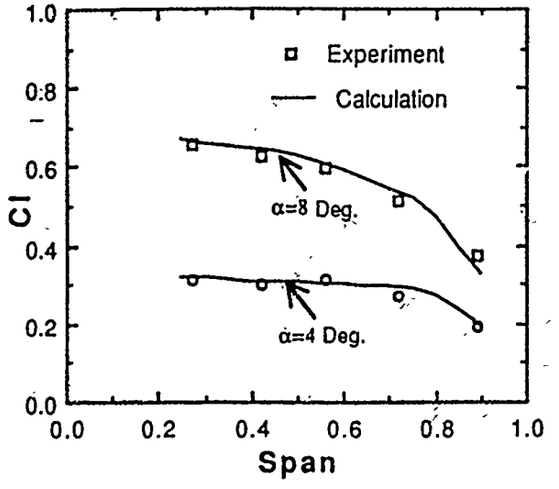

Fig. 15 Spanwise load distributions for the iced swept wing at 4° and 8° angle of attack.

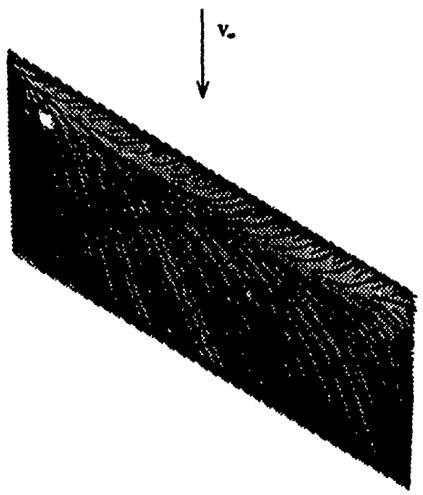

Fig. 16 Surface oil flow simulation for 30° swept wing at 4° angle of attack.

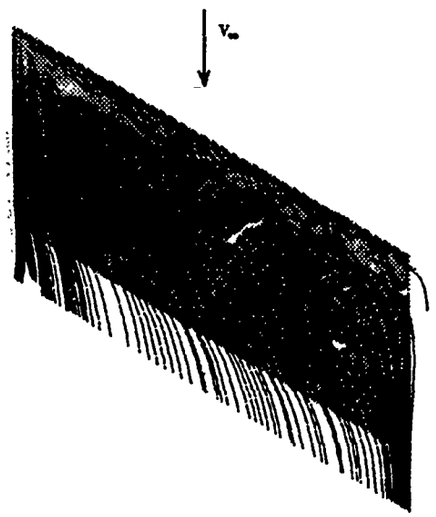

Fig. 17 Off-body particle traces for 30° swept wing at 4° angle of attack.

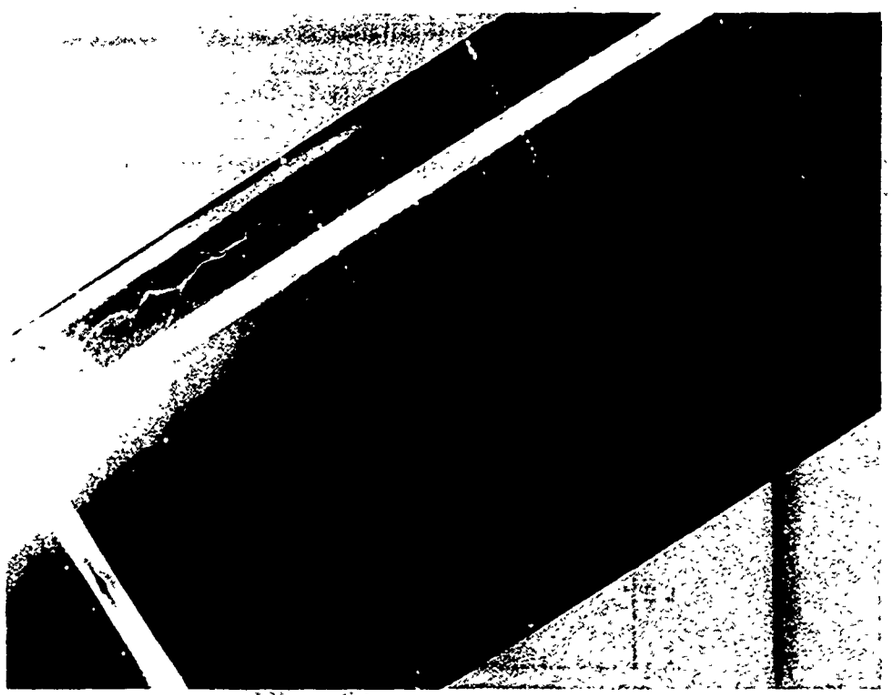

Fig. 18 Helium-bubble streaks over the upper surface of a swept wing with simulated glaze ice. $Re = 6 \times 10^5$, $\alpha = 4°$.

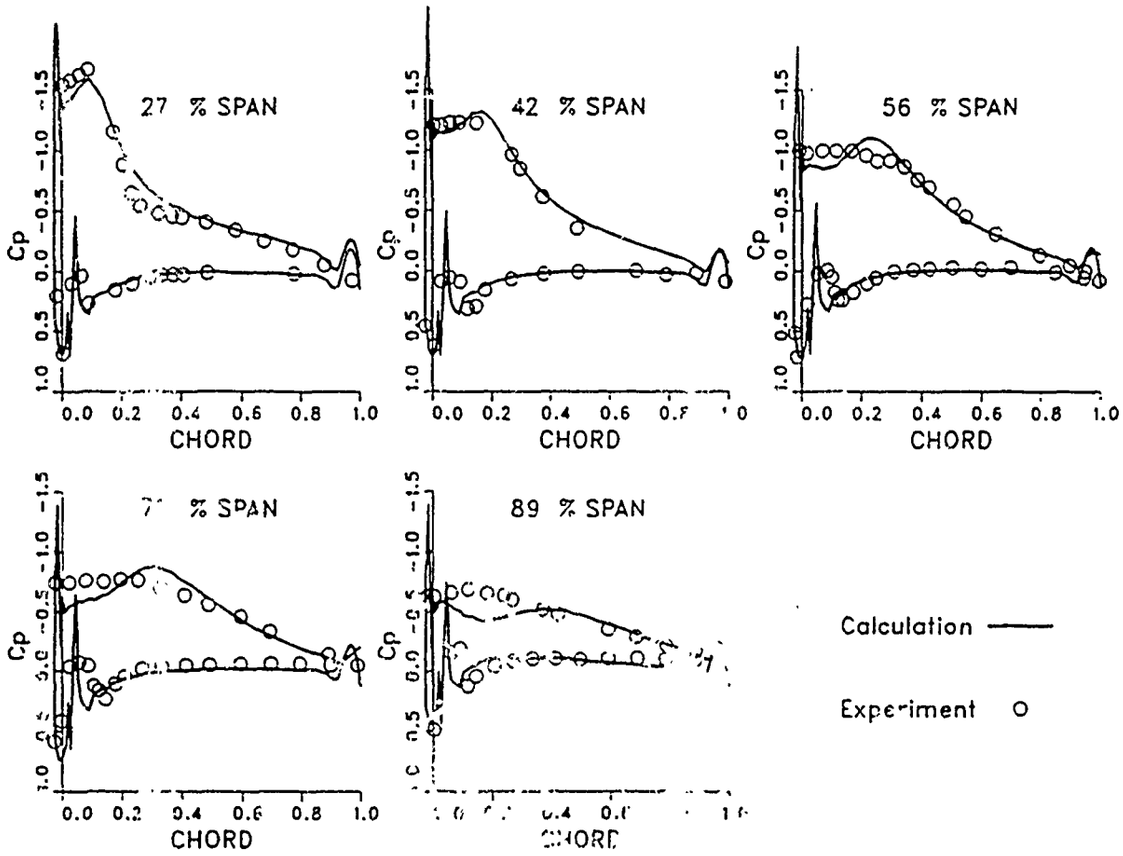

Fig. 19 Surface pressure distributions for the ideal swept wing at 8° angle of attack. Wall boundary at root section.

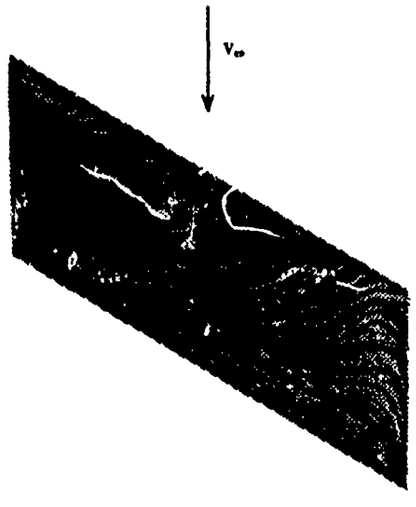

Fig. 20 Surface oil flow simulation for 30° swept wing at 8° angle of attack.

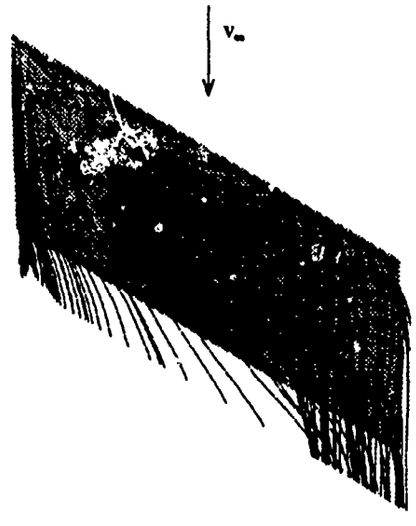

Fig. 21 Off-body particle traces for 30° swept wing at 8° angle of attack.

EFFECTS OF FROST ON WING AERODYNAMICS AND TAKE-OFF PERFORMANCE

by
R.J. Kind
Professor
and
M.A. Lawrysyn
Graduate Student (now with Canadian Forces)
Department of Mechanical and Aerospace Engineering
Carleton University
Ottawa, Ontario K1S 5B6

ABSTRACT

Computations have been done to predict the effects of various extents of frost coverage on the airfoil, wing and take-off performance of two hypothetical aircraft, a small light aircraft and a large transport aircraft. Airfoil performance was computed using rough-wall boundary layer calculations coupled to an inviscid vortex panel method which includes a capability for modelling stalled flow conditions. The roughness parameters determined for one of the frost samples were used for this purpose. A lifting line analysis was used to determine wing performance from the airfoil results.

The results indicate that frost having an effective height of only 0.4 mm in the leading-edge region of a wing can cause serious performance degradation even for a very large aircraft. On the other hand, frost coverage beginning well downstream of the suction peak, for example at about one-quarter chord, was predicted to have little effect.

1. Introduction

It is well known that frost on lifting surfaces can seriously degrade the take-off perfomance of aircraft[1]. This paper examines the effects of frost roughness on wing aerodynamics and on the take-off performance of two hypothetical aircraft, a light aircraft and a large jet transport. The main parameters of the two aircraft are given in Table 1.

Previous investigations into the effects of frost have generally relied upon experimental data obtained using artificial roughness, such as sand, to represent frost. The present work included wind tunnel measurements of the aerodynamic effects of accurately preserved real frost. These experiments enabled us to determine appropriate values for effective roughness height and roughness spacing parameters. This information is used to calculate the aerodynamic behaviour of the airfoils and wings of the two aircraft, as well as their take-off performance, with various amounts of frost coverage on the wing upper surface.

2. Frost Experiments

Six different frost samples were tested. These were grown naturally by exposing flat aluminum plates to the night sky. The samples were preserved using a dissolved plastic solution. Figure 1 shows photographs of a frost specimen before and after preservation. It can be seen that the configuration of the preserved frost is virtually identical to that of the actual frost. Figure 2 presents photographs of three of the six samples that were tested.

The plates, covered with preserved frost, were placed on the test-section floor of a low speed wind tunnel. Boundary layer development on the 1.8 m long plates was measured. Effective roughness height and spacing parameters of the frost roughness were determined from the measurements as outlined below.

Over rough surfaces in nominally zero pressure gradient the velocity profile in the inner region of the boundary layer assumes the form[2]

$$\frac{u}{u^*} = A \log\left(\frac{yu^*}{\nu}\right) + B - \frac{\Delta u}{u^*} \qquad (1)$$

Except for the term $\Delta u/u^*$ this is the familiar log law. In the logarithmic region of boundary layers the only effect of surface roughness on mean velocity profiles is a shift, $(\Delta u/u^*)$, in the intercept of the log law. For aerodynamically rough surfaces the shift is given by[2,3]

$$\frac{\Delta u}{u^*} = A \log\left(\frac{ku^*}{\nu}\right) + C[\lambda] \qquad (2)$$

Here k is the roughness height and C is a function of a suitable roughness spacing parameter, λ.

For each of the six frost samples the skin friction coefficient, C_f, and the friction velocity, u^*, were determined from the velocity profile data by two methods. One method used the momentum-integral equation

$$\frac{C_f}{2} = \frac{d\theta}{ds} + (H + 2)\frac{\theta}{U}\frac{dU}{ds} \qquad (3)$$

where θ and H are the momentum thickness and shape factor of the velocity profile, U is the velocity outside the boundary layer and s is the streamwise distance. The other method compared the measured velocity profiles with the velocity defect law[2]. Results from the two methods were in reasonably good agreement except near the ends of the frost samples. Once values for u^* were established, values of $\Delta u/u^*$ could be determined by plotting the data as in Fig. 3. The frost in each of the six samples consisted of relatively high formations scattered over the surface with relatively low 'background frost' covering the intervening space. The effective roughness height, k_f, of the frost was taken as the average measured height of the highest 20 percent of the frost formations. With values of u^*, $\Delta u/u^*$ and k established, the spacing function $C[\lambda]$ could be determined using equation (2).

Following Simpson[4], the spacing parameter, λ, for the frost samples was defined as

$$\lambda = D^2/A_F \qquad (4)$$

where A_F is the average frontal area of the roughness elements and $1/D^2$ is equal to the number of 'significant' elements per unit surface area. D can easily be determined by counting the number of significant frost formations present in an area of the sample. Of course deciding which formations should be counted (i.e. considered significant) is a matter of judgment. The average frontal area, A_w, was estimated using the relation

$$A_F = \phi_1 \phi_2 \phi_3 k_f^2 \qquad (5)$$

Here ϕ_1 represents the average width-to-height ratio of the significant frost formations, ϕ_2 represents the ratio of the average height of all the significant formations to the height, k_f, of the highest 20 percent of the formations and ϕ_3 is a factor to account for the effects of the background frost. ϕ_1 and ϕ_2 were estimated visually. ϕ_3 was assigned a value of either 1 or 1.5, when background frost was judged to be either unimportant or important, respectively.

The parameters of the six frost samples are presented in Table 2. The values of C and λ are plotted in Fig. 4. Dvorak's[3] correlation line, which was also used by Simpson[4], is included in Fig. 4. Not surprisingly, the frost results are quite widely scattered. Nevertheless they fit in reasonably well with the other data which are also widely scattered.

Table 2 includes values of k_s/k_f, the ratio of standard-sand-roughness height to the effective frost roughness height. These were determined using equation (2) with C assigned the value -4.0 for standard sand roughness[5]. The values of k_s/k_f are seen to vary widely.

A more detailed presentation of the frost experiments is available in reference 6.

3. Effects of Frost on Airfoil Performance

The first step in assessing the effects of frost on take-off performance is to assess its effects on airfoil performance. Computational methods were used for this purpose. The hypothetical aircraft of Table 1 use the NACA-2412 section and the BGK1 section. The latter is representative of a relatively modern supercritical section. For simplicity, flaps are not present. The airfoil calculations were carried out for Reynolds number, based on chord, c, of 3×10^6 and 22.5×10^6 for the NACA-2412 and BGK1 sections, respectively. These correspond to free stream velocity and chord length of 30 m/s, 50 m/s and 1.5 m, 6.7 m for the two airfoils respectively, at sea level.

Calculations were done for only one set of frost characteristics: $k_f = 0.4$ mm and C = -2.5. As seen from Table 2, these are the parameters determined for Frost Plate 3. The frost height to chord length ratios are $k_f/c = 0.00027$ and 0.0000595 for the NACA-2412 and BGK1 airfoils, respectively.

The viscous/inviscid interaction approach was used for the airfoil computations. Inviscid flow computations for the airfoil sections were done using a vortex panel method developed at Carleton University. Voricity varies linearly along the panels and is continuous at the junction points between panels. Linearly varying source distributions on the panels were used to model boundary-layer displacement effects. Where flow separation occurred, its effects were modelled by incorporating the Maskew-Dvorak[7] model, wherein two free vortex

sheets originating at the separation points are used to represent the free shear layers which bound the separation bubble. Blascovich[8] found that this model is very good for analyzing low-speed high-angle-of-attack cases.

The pressure distributions obtained from the inviscid computations provided the free-stream velocity distributions for computation of boundary-layer development along the upper and lower surfaces of the airfoil. For each surface the computations began with the stagnation-point solution given by Moran[9], followed by Thwaites[9] method for the laminar boundary layer. Transition on the upper surface was assumed to occur at the suction peak while transition on the lower surface was forced to occur at 16 percent chord. The momentum thickness, θ, was assumed to remain constant through transition. The shape factor, H, was normally assigned the value 1.32 at the start of the turbulent boundary layer calculations. Instantaneous transition was assumed. In the present work frost roughness always began at or downstream of the suction peak; attempts to begin the roughness further upstream were abandoned as this always produced immediate separation at the suction peak even at only moderate angles of attack.

Head's[10] entrainment method was the basis of the turbulent boundary layer calculations. This method has its limitations but it performs quite well for pressure distributions of the type typically found on airfoils. Dvorak[3] extended Head's method to deal with rough surfaces. This version of the method was used in the present work.

The boundary-layer computations provided two inputs for the inviscid flow computations, namely the displacement thickness required to determine the strength of the surface-source distribution and the upper-surface separation point location. The lower-surface flow always separated at the trailing edge.

Figure 5 schematically illustrates the airfoil-flow computational model. Thirty five vortex panels were used to represent the airfoil surface. For separated flow cases six panels were used for each of the two free vortex sheets. The length of these sheets is governed by an empirical wake-length factor; this was assigned the recommended value[7] of 2.0. The shape and position of the free vortex sheets must be determined iteratively, such that the velocity normal to each of the wake panels is zero. About 14 iterations were found to be adequate for this purpose. Of course there must also be an overall iteration between the inviscid and the boundary-layer computations. Typically 4 to 8 iteration cycles were necessary for convergence in separated flow cases. Only one cycle (inviscid-viscous-inviscid) was used for fully-attached flow cases.

Computations were done for various extents of frost coverage on the upper surface of the airfoils. These are shown in Fig. 6, where designation codes are also assigned. The roughness height was made to increase approximately linearly over a short distance at its upstream edge. This is both more realistic than an abrupt start and also avoids potential difficulties with the boundary layer computations that an abrupt start with large k/θ might have caused. Details are given in Fig. 6. Step lengths used in the boundary-layer computations ranged from $\Delta x/c = 0.005$ to 0.02. The shortest step length was required to avoid dependence of results on step size for most of the BGK1 computations because of the steep pressure gradient near the suction peak and the steep rise of the roughness height at its upstream edge for the 95 and 99 frost coverage cases. The lower airfoil surface was smooth in all computations.

The computed lift and profile-drag results are shown in Fig. 7 and 8 for the NACA-2412 and BGK1 sections respectively. Lift was determined by pressure integration. The drag results are not particularly accurate; pressure integration tended to give slightly negative values of drag coefficient when there was little or no flow separation. The plotted drag results were determined using the boundary-layer momentum thicknesses at the separation points in the Squire and Young[11] formula and adding the pressure-integration drag if it was positive. The computed results for the clean NACA-2412 section agree quite well with the experimental data from ref. 12 (see Fig. 7). This inspires confidence in the computed results.

From Fig. 7 and 8 it is clear that the frost roughness is predicted to produce substantial effects only if it extends close to the leading edge. Frost beginning at quarter-chord has little effect on the computed lift and drag performance of either airfoil. This can be ascribed to two factors: first, the severity of the adverse pressure gradient at quarter chord has decreased substantially compared to that near the suction peak and second, the ratio of frost height to boundary-layer thickness has become relatively small so that the roughness has little effect on the skin friction and on boundary layer growth. The latter effect also explains why the BGK1 performance is little affected by frost extending as close as $x/c = 0.009$ to the leading edge (Case 95). While this is close to the suction peak, the chord of the BGK1 section is much larger than that of the NACA-2412 section (6.7 vs 1.5 m) so that the ratio of roughness height to boundary layer thickness at a given x/c is much less for the BGK1 section. This can be seen from Figures 9

and 10 which show pressure distributions and development of boundary layer parameters for the two airfoil sections. The small effect of the frost roughness downstream of quarter-chord is also evident in Figures 9 and 10. It should be noted that the results of Fig. 7 and 8 do not mean that the BGK1 section has superior tolerance of surface roughness. Rather, these results show the importance of the ratio k/c. As is to be expected, roughness of a given height has less effect on a large airfoil than on a small one. The 0.4 mm roughness nevertheless has a dramatic effect on the performance of the 6.7 m chord BGK1 section when the roughness starts at the suction peak (Case 99). The results indicate that even on large aircraft, frost in the leading-edge region is hazardous.

4. Effects of Frost on Wing Performance

A simple lifting line analysis was used to compute the aerodynamic performance of the aircraft wings. Figure 11 schematically illustrates the flow model. The method uses a single spanwise row of horseshoe vortices. It calculates effective angle of attack at any particular spanwise station and looks up the corresponding lift and parasite drag coefficients from the airfoil performance curves, Fig. 7 and 8, generated by the airfoil calculations. The process is iterative because the strength of the horseshoe vortices is directly related to local lift coefficient. The method determines lift, parasite and induced drag coefficients for the wing.

The results for the two wings of Table 1 are shown in Fig. 12 and 13. The wing performance clearly reflects the performance of the airfoil sections.

5. Effects of Frost on Take-Off Performance

Two hypothetical aircraft are considered. their main parameters are given in Table 1.

The forces considered in the take-off analysis are: weight, wing lift and drag, drag of the other aircraft components, thrust and rolling friction.

Lift-off angle of attack and speed were chosen to give a 20 percent speed margin above stall; that is $C_L = C_{Lmax}$ at lift-off. Of course C_{Lmax} is dependent on frost coverage and C_{Lmax} values are given by Fig. 12 and 13. Rotation speed was set at 85 percent of lift-off speed.

The variation of C_L with angle of attack was taken from Fig. 12 and 13 for each frost-coverage condition. The aircraft drag-polar relations were set up such that C_{D_o} = (0.015 + wing zero-lift drag coefficient) and such that the wing drag varied with angle of attack approximately as given by the appropriate drag curves in Fig. 12 and 13. The variation of fuselage and empennage drag with angle of attack was approximated by assuming this caused a reduction of 0.1 in the value of the span-efficiency factor.

Thrust was assumed to vary with velocity: linearly for the turbofan aircraft and such that axial kinetic energy imparted to the slipstream air is constant for the propeller aircraft. The ratio of axial kinetic energy flux increase to propeller shaft power was assumed to be 0.85.

The results of the take-off computations are shown in Fig. 14 for the two aircraft. They indicate that frost in the leading-edge region of wings can cause take-off distances to increase dramatically; an increase of more than 80 percent is predicted in one case.

6. Discussion

The work presented in this paper indicates that even thin hoar frost in the leading-edge region of aircraft wings can have serious negative effects on take-off performance. Hoar frost having a height of only 0.4 mm produced much-degraded wing performance and much-increased take-off distances for both a small light aircraft and a large transport aircraft. Serious performance degradation was, however, only predicted when the upstream edge of the hoar frost coverage was at, or very close to the suction peak in the pressure distribution. Frost coverage beginning at quarter-chord or further downstream was predicted to have little effect.

In fig. 9 and 10 is can be seen that in the two cases where the frost has serious regative effects (NACA 2412, Case 95 and BGK1, Case 99) the frost begins at a point where its roughness height is several times greater than the boundary layer momentum thickness, θ. The skin-friction coefficient, C_f, accordingly rises to a high value. This causes relatively rapid growth of the momentum thickness and the pressure gradient term in the momentum equation (3) in turn exacerbates the growth rate of the thicker boundary layer in the adverse pressure gradient downstream of the suction peak. Consequently the boundary layer becomes more prone to separation.

Frost coverage beginning upstream of the suction peak would probably have even more drastic effects than those seen in the present results.

The present boundary-layer calculations did not stabilize, and predicted almost immediate separation, for frost coverage beginning at s/c values only a few percent upstream of the suction peak. Judging from the behaviour of the calculated shape parameter, H, (see Fig. 9, 10) the present calculations stablized satisfactorily for the 95 and 99 coverage cases, despite the choice of a rather low initial value for H. Head's method is known to be insensitive to the starting value of H and to rapidly adjust to a more appropriate value if the initial choice is poor.

Wings having a large chord length can be expected to be less sensitive to frost, as discussed in Section 3. However the present results indicate that they are far from immune. It seems probable that airfoil sections which produce a relatively gentle adverse pressure gradient downstream of the suction peak should be less sensitive to roughness effects. This remains to be investigated.

The parameters used to aerodynamically characterize hoar frost in the present work were obtained from flow measurements with actual, preserved, frost. They can therefore be considered to be reliably representative of real frost similar to the measured samples. The remainder of the work, however, rests on computations. Particularly crucial are the boundary-layer development calculations used to predict the effects of frost roughness on flow separation.

While the authors are confident that the predictions are basically correct, experimental confirmation would be desirable. Current regulations prohibit take-off with any frost on lifting surfaces. Until experimental confirmation of the present results in available, the regulations should not be relaxed to require frost removal from leading-edge regions only.

7. Conclusions

Boundary layer developments over six preserved samples of natural hoar frost were measured. The data have enabled determination of effective height and spacing parameters for each sample.

The effects of various extents of frost coverage on airfoil lift and drag performance were predicted using a viscous/inviscid interaction computation method. The results indicate that frost coverage beginning at or near the suction peak can cause serious degradation of airfoil, wing and take-off performance. Frost coverage beginning well downstream of the suction peak, for example at one-quarter chord, is predicted to cause little performance degradation, at least for $k/c < 0.0003$.

There appear to be two key factors which influence the severity of frost effects. The first is the severity of the adverse pressure gradient just downstream of the suction peak and the second is the ratio of boundary layer thickness to the effective roughness height of the frost. A large ratio results in less effect. Because of the second factor, airfoils or wings of large chord length are less sensitive to frost. Apparently however, they are by no means immune - they can only tolerate frost coverage beginning a few percent of chord closer to the leading edge than on wings of small chord length.

REFERENCES

1. Luers, J.K., "Wing Contamination: Threat to Safe Flight", *Astronautics and Aeronautics*, November 1983, pp. 54-59.

2. Clauser, F.H., "The Turbulent Boundary Layer", *Advances in Applied Mechanics*, Vol. 4, 1956, pp. 1-51.

3. Dvorak, F.A., "Calculation of Turbulent Boundary Layers on Rough Surfaces in Pressure Gradient", *AIAA Journal*, Vol. 7, 1969, pp. 1751-1759.

4. Simpson, R.L., "A Generalized Correlation of Roughness Density Effects on the Turbulent Boundary Layer", *AIAA Journal*, Vol. 11, 1973, pp. 242-244.

5. Grigson, C.W.B., "Nikuradse's Experiment", *AIAA Journal*, Vol. 22, 1984, pp. 1000-1001.

6. Kind, R.J. and Lawrysyn, M.A., "Aerodynamic Characteristics of Hoar-Frost Roughness", presented at AIAA 29th Aerospace Sciences Meeting, Reno, NV, Jan. 1991, AIAA paper 91-0686.

7. Maskew, B. and Dvorak, F.A., "Investigation of Separation Models for the Prediction of C_{Lmax}", *American Helicopter Society* Paper 77.33-01, May 1977.

8. Blascovitch, J.D., "A Comparison of Separated Flow Airfoil Analysis Methods", *Journal of Aircraft*, Vol. 22, 1985, pp. 208-215.

9. Moran, J., *An Introduction to Theoretical and Computational Aerodynamics*, J. Wiley & Sons, 1984, pp. 206-209.

10. Head, M.R., "Entrainment in the Turbulent Boundary Layer", *Aeronautical Research Council* (Great Britain) R & M 3152, 1958.

11. Young, A.D., *Boundary Layers*, AIAA Education Series, 1989, pp. 206-207.

12. Abbott, I.H. and Von Doenhoff, A.E., *Theory of Wing Sections*, Dover Publications, Inc., New York, 1959.

ACKNOWLEDGMENTS

The authors gratefully acknowledge support from a Natural Sciences and Engineering Research Council of Canada operating grant. Thanks are also due to S.A. Bittle who incorporated the stalled flow model into the computer software.

Table 1

Main Parameters of the Two Aircraft

	Aircraft A (light aircraft)	Aircraft B (turbofan transport)
Gross mass (kg)	1,400	135,000
wing area (m^2)	16.5	290.
Wing span (m)	11.0	48.
wing taper ratio	1.0	0.25
mean aerodynamic chord	1.5 m	6.72 m
wing sweep (1/4 chordline)	0	30°
wing twist	3° washout	2° washout
flaps	-	-
airfoil section	NACA-2412	BGK1
Powerplants	175 kw; 2m. dia. prop.	2 x 50000 lb_f static thrust 2 x 40000 lb_f at 50 m/s
Fuselage + gear + empennage drag coefficient (based on wing area)	0.015	0.015
Rolling friction coefficient	0.025	0.025
Screen height	35 ft.	35 ft.

Table 2

Average Parameters of the Six Frost Roughness Samples

Frost Plate	mom eqn. C_f	u*/U	$\Delta u/u^*$	k_f (mm)	$k_f u^*/\nu$	C	$1/D^2$ (cm^{-2})	ϕ_1	ϕ_2	ϕ_3	ϕ	λ_s	k_s/k_f
1	0.0047	0.048	6.2	1.0	140	-5.9	1.8	3	0.7	1	2.1	26	0.46
2	0.0041	0.045	4.3	0.5	70	-6.1	5.0	1.5	1	1	1.5	53	0.43
3	0.0053	.0 51	7.6	0.4	62	-2.5	4.5	3	1	1.5	4.5	31	1.8
4	0.0049	0.049	6.1	0.37	56	-3.7	4.5	1	1	1.5	1.5	108	1.1
5	0.0036	0.042	2.8	0.35	47	-6.5	3.0	1	1	1.5	1.5	181	0.36
6	0.0042	0.046	4.9	0.27	40	-4.1	2.5	10	1	1	10	55	0.96

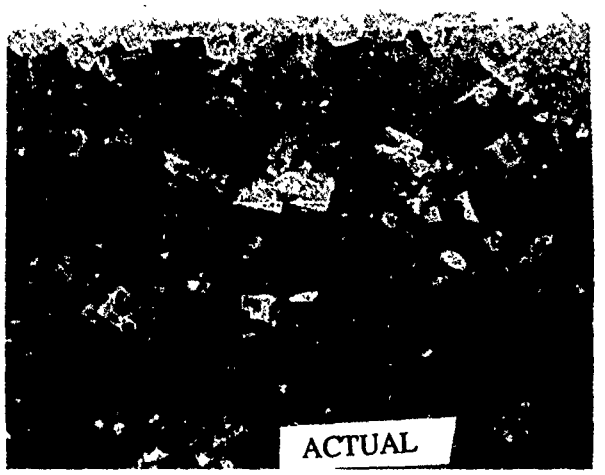

Fig. 1 Actual and Preserved Frost Sample

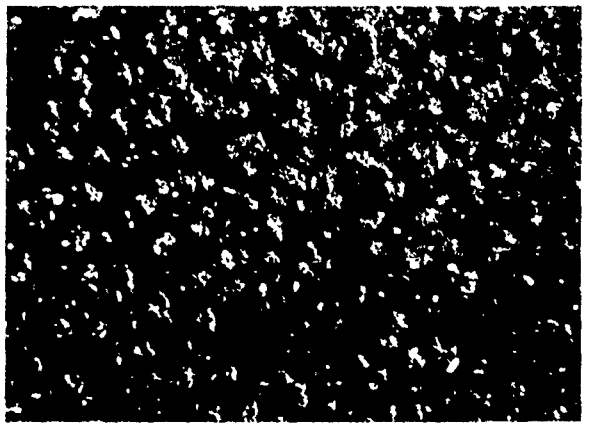

Frost Plate 2

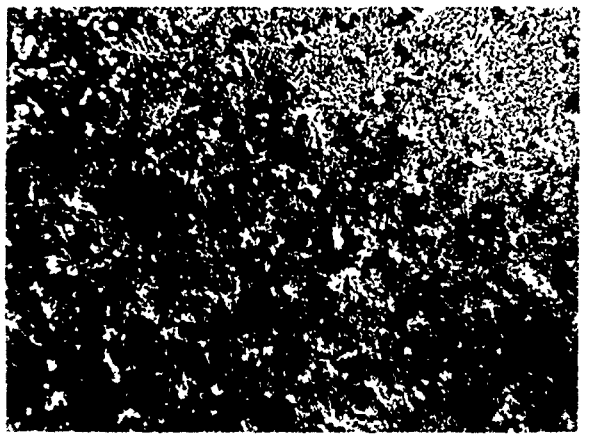

Frost Plate 3

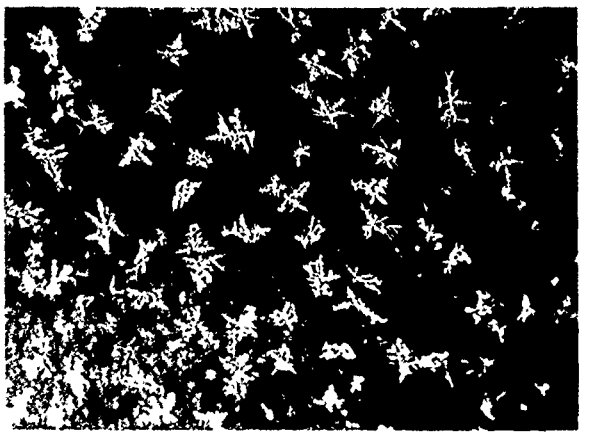

Frost Plate 6

Fig. 2 Partial Photographs of 3 of the Tested Frost Samples

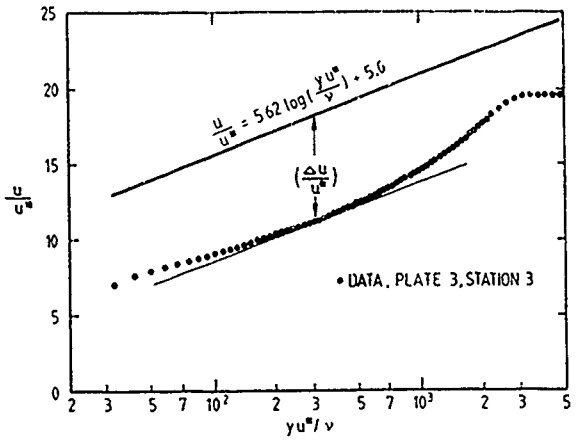

Fig. 3 Technique for Determining $\Delta u/u^*$

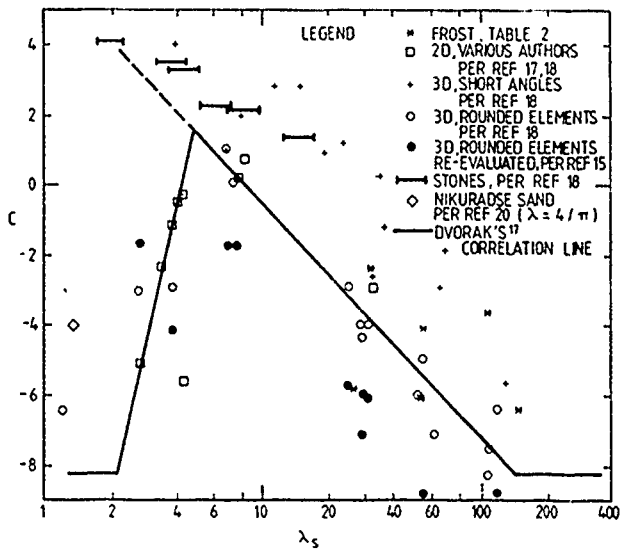

Fig. 4 Correlation Between Law-of-the-Wall Intercept Shift and Roughness Spacing Parameter (after Dvorak[3] and Simpson[4])

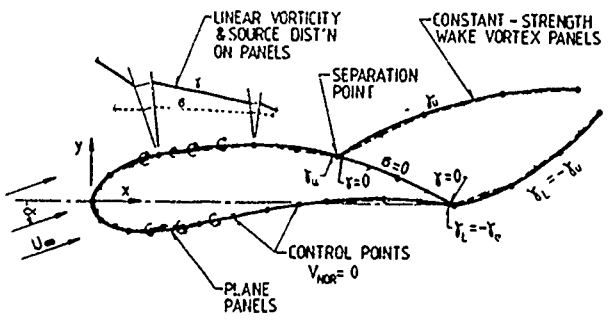

Fig. 5 Inviscid Airfoil Flow Model (after ref. 7)

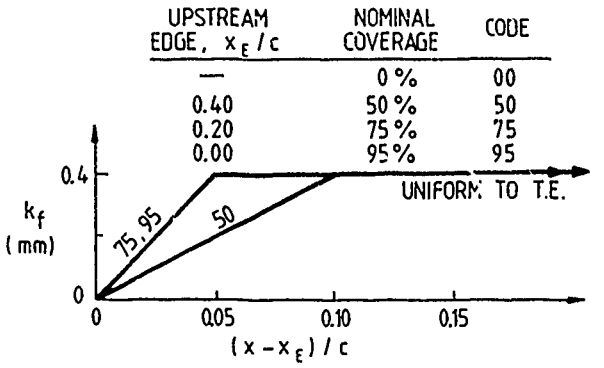

(a) LIGHT AIRCRAFT, NACA-2412
(SUCTION PEAK AT $x/c \approx 0.00$ FOR $\alpha \geq 15°$)

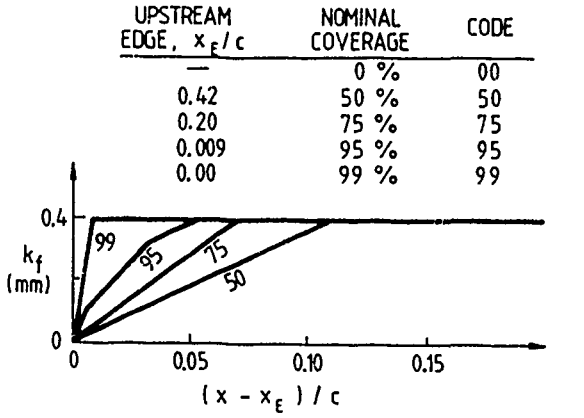

(b) TRANSPORT AIRCRAFT, BGK1
(SUCTION PEAK AT $x/c \approx 0.002$ FOR $\alpha \geq 12°$)

Fig. 6 Frost Coverage Information

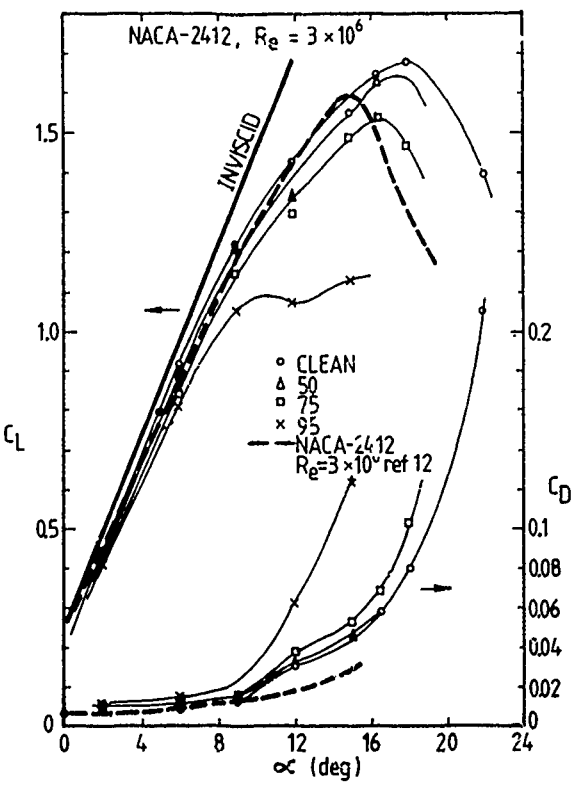

Fig. 7 Lift and Drag Coefficients for the NACA-2412 Section With Various Extents of Frost Coverage ($K_f/c = 0.00027$; points determined by computation)

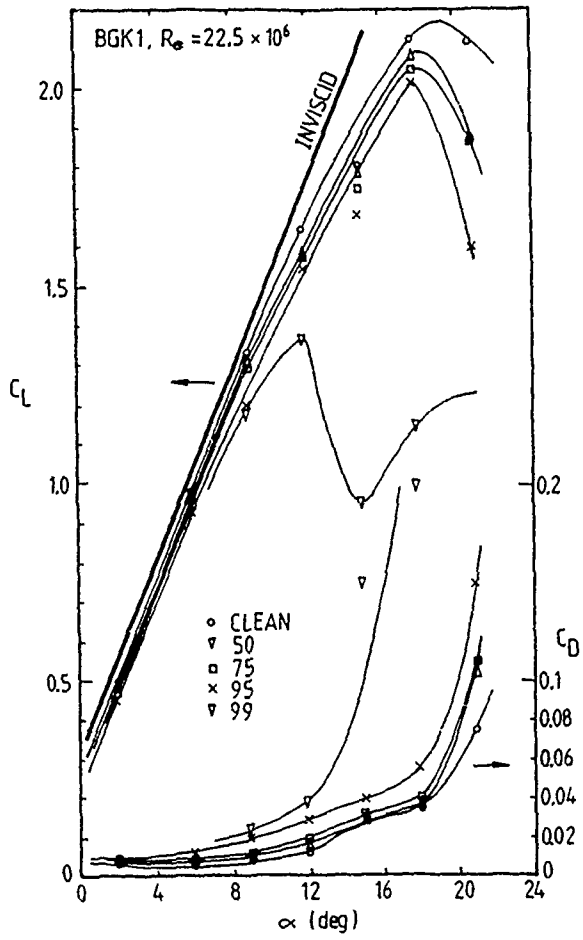

Fig. 8 Lift and Drag Coefficients for the BGK1 Section with Various Extents of Frost Coverage (k_f/c = 0.0000595; points determined by computation)

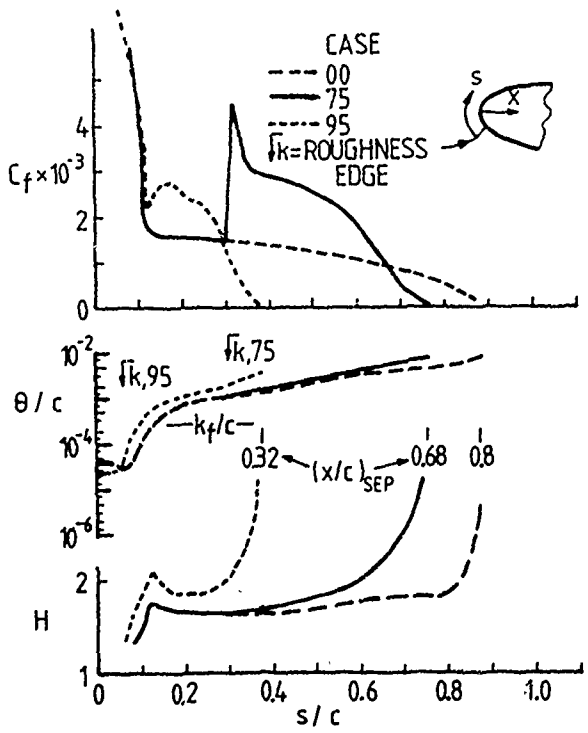

Fig. 9

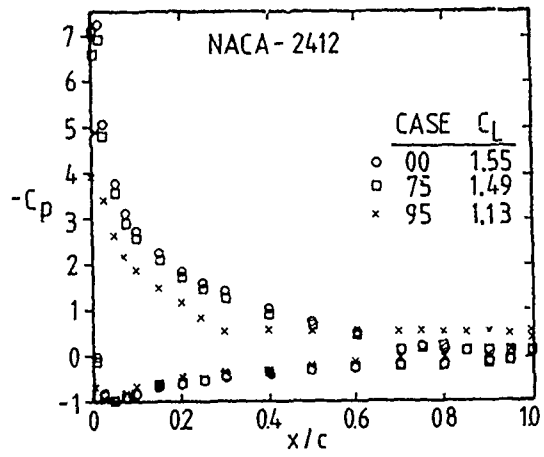

Fig. 9 Pressure Distributions and Boundary Layer Parameters for NACA-2412 Section, α = 15°, Re = 3 x 10^6, Clean, 75 and 95 Frost Coverages (k_f/c = 2.7 x 10^{-4})

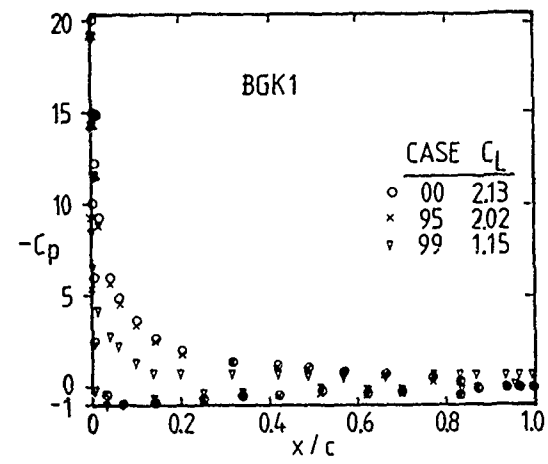

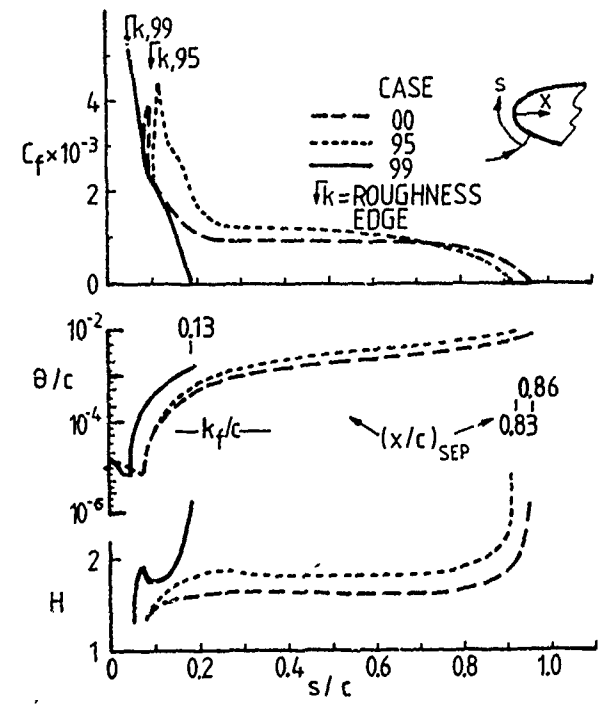

Fig. 10 Pressure Distributions and Boundary Layer Parameters for BGK1 Section, α = 18°, Re = 22.5 x 10^6, Clean, 95 and 99 Frost Coverages (k_f/c = 6 x 10^{-5})

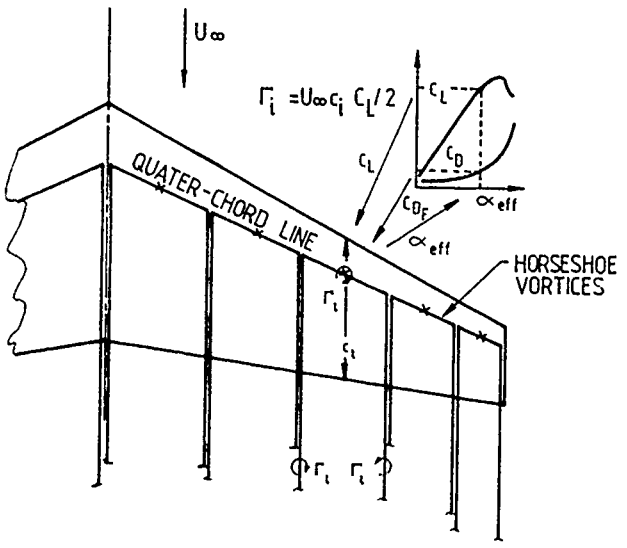

Fig. 11 Lifting Line Flow Model

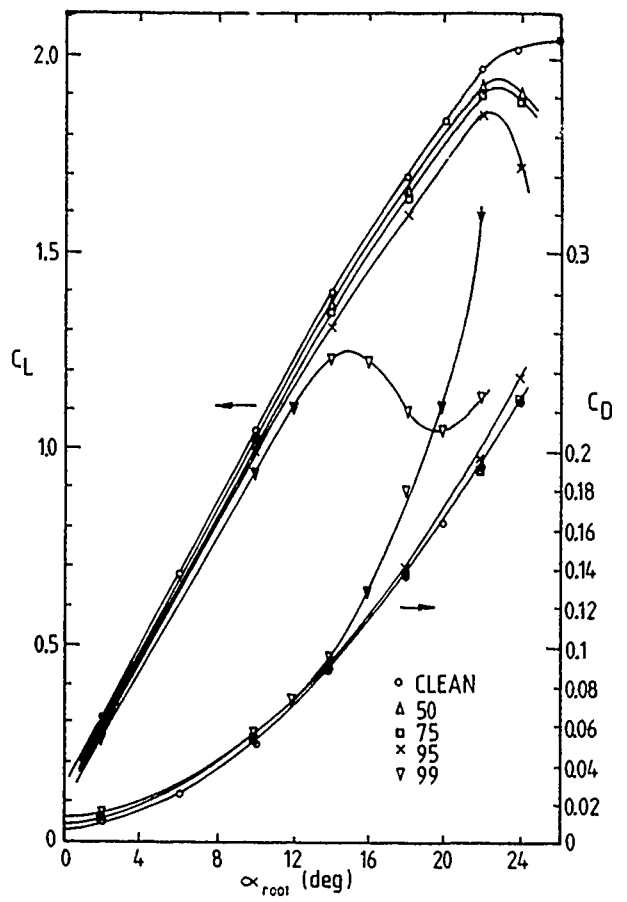

Fig. 13 Lift and Total Drag Coefficients for the Transport Aircraft Wing

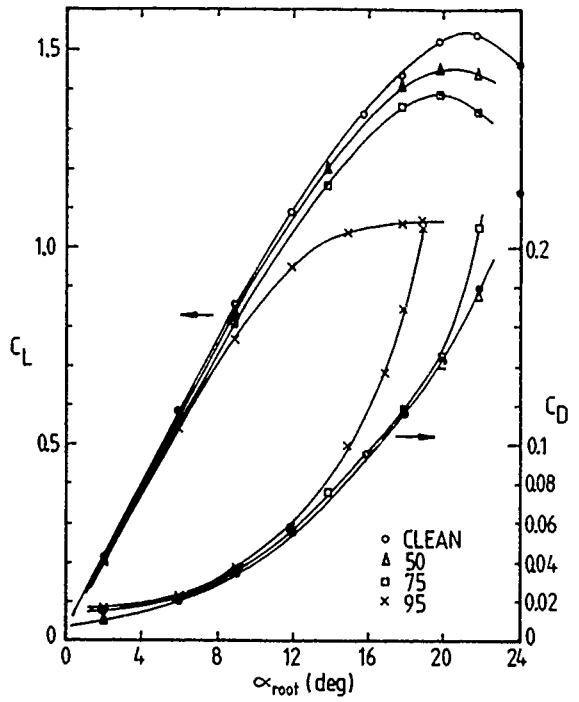

Fig. 12 Lift and Total Drag Coefficients for the Light Aircraft Wing

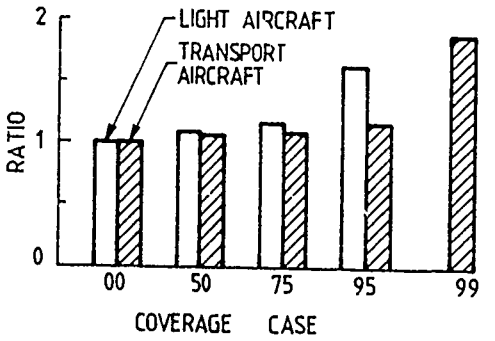

Fig. 14 Effect of Frost Coverage on Take-Off Distance Over 35 ft. Screen (RATIO ≡ distance when frost covered/distance when clean)

MODEL ROTOR ICING TESTS IN THE NASA LEWIS ICING RESEARCH TUNNEL

Robert J. Flemming
Senior Design Engineer
Sikorsky Aircraft Division, UTC
6900 Main Street
Stratford, Connecticut 06601-1381
USA

Randall K. Britton
Icing Research Engineer
Sverdrup Technology, Inc.
NASA Lewis Research Center Group
2001 Aerospace Parkway
Brookpark, Ohio 44142
USA

and

Thomas H. Bond
Aerospace Engineer
NASA Lewis Research Center
21000 Brookpark Road
Cleveland, Ohio 44135
USA

SUMMARY

Tests of a lightly instrumented two-bladed teetering rotor and a heavily instrumented sub-scale articulated main rotor were conducted in the NASA Lewis Research Center Icing Research Tunnel (IRT) in August 1988 and in September and November 1989, respectively. The first was an OH-58 tail rotor which had a diameter of 1.575 m (5.17 ft) and a blade chord of 0.133 m (5.25 in.), and was mounted on a NASA designed test rig. The second, a four bladed articulated rotor, had a diameter of 1.83 m (6.00 ft) and the 0.124 m (4.9 in.) chord blades were specially fabricated for this experiment. This rotor was mounted on a Sikorsky Aircraft Powered Force Model, which enclosed a rotor balance and other measurement systems. The models were exposed to variations in temperature, liquid water content, and median droplet diameter, and were operated over ranges of advance ratio, shaft angle, tip Mach number (rotor speed), and weight coefficient to determine the effect of these parameters on ice accretion. In addition to strain gage and balance data, the test was documented with still, video, and high speed photography, ice profile tracings, and ice molds. This paper presents the sensitivity of the model rotors to the test parameters, and compares the results to theoretical predictions. Test data quality was excellent, and prediction methods for ice accretion and rotor performance reproduced the respective trends observed in the test. Adjustments to the correlation coefficients to improve the level of correlation in the performance predictions are suggested in this paper.

LIST OF SYMBOLS

CL/σ lift coefficient/solidity

CQ/σ torque coefficient/solidity

LWC liquid water content, g/m^3

MVD droplet diameter, um

T static air temperature, °C

σ solidity

μ advance ratio

ΩR rotor tip speed

Δ change over a period of time due to icing

INTRODUCTION

Because of the trend toward design of all-weather rotorcraft, it is necessary to develop and validate experimental techniques to understand the effects of ice on rotor performance and to determine the design requirements for rotor ice protection. Analytical methods are now being developed to predict rotor performance in icing, including ice accretion and ice shedding. The use of a model rotor to provide a less expensive and more repeatable source of test data will aid in the validation of these analytical methods and support the overall goal toward more expedient certification procedures. The French undertook a model icing program where a 1/4-scale model rotor was tested in the ONERA S1MA wind tunnel at Modane, France (Ref. 1). This testing showed that a model program had promise, but the data acquired were too limited to provide a correlation base. However, this testing prompted the interest of rotorcraft icing researchers in the United States. NASA Lewis Research Center undertook a program with a university and industry consortium to demonstrate the usefulness of the model rotor test technique as an approach for obtaining meaningful icing data for rotating systems (Ref. 2).

TECHNICAL APPROACH

The Rotor Icing Consortium operated under a NASA Lewis Research Center (Lewis) grant to Texas A&M University, which then subcontracted work to each of the four major U.S. helicopter companies: Bell Helicopter Textron, Boeing Helicopters, McDonnell Douglas Helicopters, and Sikorsky Aircraft Division of United Technologies. The consortium worked during the early part of the program to identify the necessary tasks and the means to achieve them, and each of the members had specific responsibilities that lead to the successful testing of the two models. The U.S. Army Aviation Research and Technology Activity-AVSCOM provided additional funding (Propulsion Directorate), and icing tunnel hardware support (Aeroflightdynamics and Propulsion Directorates) during the actual testing.

A two model approach was selected as the most effective means to accomplish the program goals. A lightly instrumented OH-58 tail rotor (Fig. 1) that had been modified to approximately operate as a main rotor was chosen as the initial test article. This would be followed by the more sophisticated Sikorsky Powered Force Model (PFM) (Fig. 2) to provide detailed rotor performance measurements. The OH-58 IRT entry established operational techniques for the more complex model and gathered preliminary data. Ice was accreted on the blades in a variety of rotor and tunnel operating conditions and documentation of the resulting shapes was performed. The OH-58 model test was completed in October 1988 (Ref. 3).

The initial PFM IRT entry was scheduled for an 8 week period during July to September, 1989. During this time the model was installed and icing testing began. A total of 44 icing

encounters occurred in the 14 days of testing. At the end of this initial test period, the model was removed and a second entry scheduled for November 1989. Between tests, the model was serviced, data reviewed, high speed motion picture capability added, and methods for improving blade track were prepared. This second entry resulted in 41 icing encounters in 8 test days, expanded the temperature envelope, and included variations in liquid water content and droplet diameter (Refs. 4 to 6).

MODEL AND FACILITY DESCRIPTIONS

Icing Research Tunnel

The IRT (Fig. 3) is a closed-loop refrigerated wind tunnel. A 5000 hp fan provides airspeeds up to 134 m/sec (300 mph). The 21 000 ton capacity refrigeration heat exchanger can vary the total temperature from -1.1 to -42 °C. The spray nozzles provide droplet sizes from approximately 10 to 40 μm median volume diameter (MVD) with liquid water content (LWC) ranging from 0.2 to 3.0 g/m^3. The tunnel test section is 1.8 m (6 ft) high and 2.7 m (9 ft) wide.

Armor plates were attached to the walls of the tunnel test section during the model rotor test to protect personnel in the control room. Video systems were installed to monitor the test area and ice accretions on the blades, and to provide tracking information. For several runs 0.635 mm (0.025 in.) aluminium sheets were placed on energy absorbing material and attached to the armor plating in line with the rotor disk plane. The shed ice made permanent dents in the sheets that will be calibrated to calculate the impact energy of the ice that struck them. A high speed 16 mm camera was used to capture ice shedding from the blades. The movies were taken at 2000 frames per second and capture approximately a 60° arc of the rotor rotational field. These results will not be discussed in this paper.

OH-58 Tail Rotor

The tail rotor assembly was composed of the tail shaft, hub, teetering components, and rotor blades from an OH-58 helicopter. The rotor blades had NACA 0012 airfoils with a chord of 0.133 m (5.25 in.) and a span of 0.73 m (28.74 in.). The total diameter of the rotor assembly is 1.575 m (5.17 ft) (Fig. 1). This assembly was mated, through an adapter, to a 2.1 m long NASA-designed drive shaft. The extended drive shaft allowed the rotor blades to be run in the horizontal plane in the middle of the test section of the IRT while the 40 hp motor and other drive system hardware remained below the tunnel turntable (Fig. 4). A hydraulically operated collective pitch control provided the ability to change blade angle quickly to the desired condition. The drive housing was bolted to the tunnel floor plate via two gimbal pins. For this test the rotor shaft was set at 5° forward tilt to simulate forward flight of a helicopter.

A differential measuring device recorded reaction torque changes from the drive system. A set of redundant rotational speed pick-ups were located on the drive shaft.

Vibration output was recorded to detail the severity and timing of shedding events with respect to the torque data. Motor horsepower was calculated and recorded to verify the torque data. Finally, the collective pitch angle was noted to document the rotor blade angles for the specific icing encounters.

Powered Force Model

The Sikorsky PFM is a self-contained, general purpose rotor test rig. The load measuring systems, rotor power, and control mechanisms are located within the model frame. The rig is capable of accepting a fuselage and powered tail rotor, each containing its own balance system. For this project, only the main rotor balance was installed. The main rotor was located 1.01 m (3.33 ft) above the tunnel floor, about 0.10 m (0.33 ft) above the tunnel centerline. The US Army UH-60A model skins were used to enclose the balance and rotor hardware (Fig. 2). While the fuselage skins are scaled for a 2.86 m (9.37 ft) rotor, tunnel dimensions dictated the use of a 1.83 m (6.00 ft) rotor for this test.

The rotor head used for this project (Fig. 5) was a Sikorsky-designed NASA Langley owned general purpose, four bladed, fully articulated head with coincident flap and lag hinges at the 8.3 percent (76 mm or 3.00 in.) radial station. The hub has adjustable lead-lag dampers and for this test it had a zero pitch-flap coupling (δ_3). In order to preserve a consistent lead-lag damping coefficient during the variation in IRT temperature, the rotor viscous dampers were electrically heated to maintain the fluid at about 10 °C. Potentiometers mounted on the flap, lead-lag, and pitch axes provide positional information for the rotor system relative to the shaft.

The PFM main rotor was driven by two Able 3-phase variable frequency induction electric motors. As installed, the motors can rotate at speeds up to 8000 rpm. A 3.5 to 1 reduction gear box operates the rotor shaft speed to a maximum of 2286 rpm, which equates to a rotor tip speed of 219 mps (718 fps). Each motor has a continucus rating of 60 hp. Rotor speed was measured using an optical encoder. Model power was supplied by a variable frequency motor-generator set provided by the Aeroflightdynamics Directorate, US Army Aviation Research and Technology Activity. The motor-generator set featured a digital closed-loop rpm feedback control, which maintained a set rotor speed under the power variations that occurred due to ice accretion, shedding and control changes.

The rotor forces and moments (except torque) were measured using a strain gage balance, gimbal-mounted to the model frame with a soft spring attachment. The balance was electrically heated to maintain it at the calibration temperature of 20 °C. Rotor torque was obtained by measuring the reaction force between the gearbox (which was mounted on bearings) and the gearbox frame with a load cell. A 102 channel slipring was used to transfer the rotating system signals from blade gages, pushrods, motion hardware, and accelerometers to the fixed system. It also provided power to the damper heaters. The swashplate control components consisted of rotating pushrods and scissors, the swashplate, three electromechanical actuators, and a stationary scissors. Control inputs were made at the control console with cyclic and collective joystick controllers. The input signals were electronically mixed by the controller which then moved the model actuators. Resolved shaft axis cyclic and flapping first harmonic coefficients were obtained from potentiometers located on the rotorhead. These values were displayed graphically and numerically to facilitate rotor trimming. Shaft angle for this test was set using a remotely driven linear actuator located on the test rig support frame. A pitch arm transferred the linear motion of the actuator to the rotating motion of the

model shaft. This resulted in both a translational and model pitch motion for the rotor. The model support shaft angle range was from -10 to +3°. The angles set by the shaft angle control were corrected by the gimbal deflection angle and aerodynamic wall corrections to obtain the true total shaft angle.

The main rotor blades were designed and built by the McDonnell Douglas Helicopter Company using molds built by Sikorsky Aircraft. The blades had NACA 0012 airfoils with a chord of 0.124 m (4.88 i...), a -10° linear twist, and a taper ratio of 1. In order to stay within rotorhead stress limits at the design speed, the blade weight was kept to a minimum. This resulted in a thin walled hollow spar, an unsupported trailing edge, and an unpainted airfoil surface. Two of the blades were instrumented with strain gages in the flatwise, edgewise, and torsional axes to provide blade loading information for safety of flight. The data from the edgewise strain gages proved to be very useful in identifying shedding events. This prompted the addition of root edge-wise strain gages to the noninstrumented blades prior to the second entry. The rotor blades were marked on their upper surfaces with the blade number and spanwise decade percentage marks to provide identification of the blade being monitored and the relative location of the ice that was shed (Fig. 2).

DATA SYSTEM AND INSTRUMENTATION

The test techniques used in the IRT were developed during the July to October 1988 OH-58 tail rotor entry in the tunnel and used during the PFM test. Each icing run was recorded on the Dynamic Data Acquisition System (DDAS) and video systems. The video provided a viewing history of the ice accretion and shedding. There were three separate video systems: one for safety monitoring, one for blade tracking (which also provided good ice profile shapes near the blade tip), and one that allowed close-up images of the rotor blades. The three systems were strobe driven by a signal off the rotor shaft angle encoder. This gave a "frozen" image of the blade. The close-up data video system was installed on a tilt and pan mechanism along with a 35 mm camera that had a 400 mm zoom lens. The data video system had the capability of traversing the entire diameter of the main rotor while allowing zoom shots of as small a span as 0.10 m (3.94 in.) of the blade leading edge. The 35 mm camera was focused on the same close-up viewing area as the video camera, allowing pictures with greater resolution and clarity to be taken. Both the data video and the 35 mm camera were triggered from the same strobe to provide an accurate replication of the video image for the 35 mm camera.

The measured PFM test parameters fell into two main categories - those that were of research interest and those that were required solely for safety-of-flight. The parameters in the first category were processed by the DDAS and saved on both digital tape and floppy disks. Derived parameters were also computed using the DDAS and saved for further analysis. The test parameters used for analysis are the following:

Main rotor balance loads
- Normal force element number 1
- Normal force element number 2
- Axial force element
- Side force element number 1
- Side force element number 2
- Rolling moment element

Main rotor torque load
Main rotor speed
Tunnel parameters
- Total temperature
- Static pressure

- Total pressure
- Johnson-Williams Liquid Water Content

Instrumented blade positions
- Collective pitch
- Lateral cyclic pitch
- Longitudinal cyclic pitch
- Lead-lag angle
- Pitch angle
- Flapping angle
- Resolved lateral flapping angle
- Resolved longitudinal flapping angle
- Resolved coning angle

Model strut angle

Pushrod loads
- Blade number 1
- Blade number 3

Accelerations
- Gimbal lateral
- Gimbal longitudinal
- Rotor head aligned to blades 1 and 3
- Rotor head aligned to blades 2 and 4

Blade loads
- Flatwise load at blade station 11.4
- Flatwise load at blade station 16.5
- Flatwise load at blade station 21.7
- Flatwise load at blade station 26.9
- Edgewise load at blade station 11.4
- Edgewise load at blade station 16.5
- Edgewise load at blade station 21.7
- Edgewise load at blade station 26.9
- Root torsional load at blade station 10.1
- Torsional load at blade station 11.6 (r/R = 0.32)
- Torsional load at blade station 27.3 (r/R = 0.28)
- Blade 1 root edgewise load at blade station 10.1
- Blade 2 root edgewise load at blade station 10.1
- Blade 3 root edgewise load at blade station 10.1
- Blade 4 root edgewise load at blade station 10.1

A number of the derived parameters from the transducer outputs were computed and displayed at a rate of once per second to allow the model operator and Safety Of Flight (SOF) engineer to monitor loads and set target test conditions. These values accounted for tunnel blockage and buoyancy corrections, coordinate transformations, moment transfers, and balance interactions.

The heart of the DDAS digital system was a Digital Equipment Corporation PDP11/34 minicomputer. Simultaneous sample and hold amplifiers froze the analog channels before digitizing to maintain time correlation of each parameter in each time frame (i.e., in each data snapshot). Data were acquired at a rate of 16 samples per rotor revolution during the icing test. Data acquisition hardware and software were developed to reduce the quantity of stored data. Data were digitized only for the first 10 revolutions of each second (160 samples per data burst), and transferred from the DDAS to a PC/AT computer for further processing.

An integral part of the DDAS processing was the correction of the wind tunnel data for the effects of the tunnel walls. These corrections increase the effective tunnel speed and alter the rotor wake flow angles. Use of nondimensional terms normalize the data for day-to-day changes in ambient pressure, rotor speed fluctuations, and temperature variations. Data corrections must also be made for shaft torque tares, gravity tares, the induced angle of attack, and three dimensional buoyancy and solid blockage effects. The coordinate systems, data correction equations, and a description

of the derived parameters will be included in a future NASA Contractor Report.

TEST PROCEDURE

During the test run, information was collected on the data systems and the video systems, and the tunnel conditions were monitored. Liquid water content information (rise time, cloud stabilization, and spray bar lag from spray initiation) was recorded from the Control Room console output. A Johnson-Williams (J-W) LWC meter was also used during the PFM test.

Post-run information was gathered by taking 35 mm camera photographs, recording ice tracings, noting visual observations, and making ice molds. Pictures were taken of the blade planform, an end profile, and any unusual ice formations. Close-up shots of ice growths were taken to record their minute detail. A heated aluminum block with a cut-out contour of the airfoil shape was used to make a clean slice through the ice formation. A template was then held against the ice shape and a tracing made. Measurements of the ice thickness along the profile were taken at various chord locations. Visual observations were recorded about the kind of ice, any secondary growth, and frost formation. Molds were taken for several test conditions during each test.

The liquid water content and droplet diameter of the spray cloud are dependent on the spray bar water and air pressures, and the tunnel velocity. The pressure values are generated from a set of calibration equations. The above approach gives an accurate setting for LWC, but it does not provide any history of the spray which is necessary to understand the cloud time lag between spray on and model inundation, rise time to the target LWC, and cloud characteristics during the spray. A Johnson-Williams (J-W) liquid water content meter was installed during the PFM test slightly in front of and below the rotor (Fig. 2), providing cloud time history information.

TEST DATA

Accuracy and Repeatability

The ability to repeat a test condition was a major goal of this test program. Rotorcraft icing flight test data has been subject to considerable data scatter, making the application of that data to code validation and basic research difficult. A portion of the observed scatter occurs due to variations in the accretion of ice on an airfoil (Ref. 7), but most of the scatter comes from uncontrolled variation in the cloud. The IRT provides a much more controlled environment as is shown by the LWC repeatability for two settings in Fig. 6. The trends from the IRT test data show some scatter, but the data appear to be of much better quality than previous data available in the public domain. Overall ice shape repeatability was found to be very good during both tests. For a given set of rotor conditions and at a given radial location tracings of the two-dimensional shape were made and compared to obtain a measure of this repeatability. These two-dimensional shapes were found to agree best at colder temperatures where the formation was of a rime nature and was fairly smooth and easily traceable. The ice tracings tended to vary more at warmer temperatures due not necessarily to actual variation in the shapes but to difficulties in obtaining accurate tracings of these relatively small but complex geometries. However, even with the tracing difficulties the repeatability will be shown to be quite good at these warmer temperatures.

Figure 7 illustrates the quality of ice shape repeatability for one particular condition which was run several times during the OH-58 tail rotor test. As may be seen the ice shape at the measurement location was of a glaze nature with a slight double horn shape and some degree of roughness and secondary ice formation behind the primary shape. In making the cut in the ice to get to a two-dimensional tracing, often much of the detail in the secondary formations was lost due to melting when the cut was made. Some of the roughness and finer details of the primary shape were also affected by partial melting during the cut. Even with some loss of detail though, it can be seen that the ice shapes tended to repeat quite well from run to run. Because more care was taken later in the test to preserve the roughness and secondary formation detail, the final two tracings better illustrate the actual ice shape which existed at this condition throughout the rest of the OH-58 test. This same degree of two-dimensional ice shape repeatability was seen at other test conditions as well. Figure 8 shows ice shape comparisons for two different PFM repeat conditions and illustrates the small amount of variance between typical runs. The occurrances of ice shedding were also repeatable (Refs. 3 and 5). Figure 9 is a plot of lift and torque coefficients as a function of icing time for the PFM. Results for the 5 test runs show excellent repeatability. Other repeat conditions also showed very good agreement.

The accuracy of the OH-58 tail rotor torque measurement was not determined during the test. The 2σ accuracy of the PFM rotor loads was estimated to be:

Balance full scale, percent		Typical measurement, percent
Lift	0.2	1.1
Drag	.2	10.5
Torque	.7	2.5

TEST CONDITIONS

The test matrices were set up to include a range of conditions for a number of rotorcraft performance parameters under varied IRT conditions. For the OH-58 tail rotor test the temperature range was -6.7 to -26.1 °C, the LWC range was 0.25 to 0.50 g/m^3, and the MVD range was 10 to 15 μm. Maximum rotor tip speed was 173 mps (568 fps). For the PFM test the temperature range was -1.7 to -30.5 °C, the LWC range was 0.35 to 1.24 g/m^3, and the MVD range was 13 to 23 μm. The predominant PFM condition was at -15 °C, 0.50 g/m^3 LWC, and 15 μm MVD at a rotor tip speed of 206 mps (675 fps). Icing encounter times were from 44 to 158 sec. PFM thrust, propulsive force, advance ratio, and model rpm were changed, within the above tunnel conditions, to provide a wide scope of performance mapping.

OH-58 TAIL ROTOR DATA ANALYSIS

Ice accretion on the OH-58 tail rotor produced a rotor torque rise which was linear with time for a fixed set of rotor and tunnel conditions. The speed with which torque rose with time was dependent upon the specific rotor and tunnel conditions chosen. Below roughly 7° collective, the rate of torque rise with time in icing appeared relatively constant and

independent of collective. At collectives greater than 7° in icing, torque rise was more rapid. Clean rotor torques at high collectives also showed a significant increase in slope over the base torque at lower collectives, and any ice accreted on the blades will then further the torque rise.

The torque rise rate was also found to be dependent on cloud conditions (lower liquid water content and lower drop size give slower torque rise) and temperature (there is some "worst" temperature at which ice is predominantly glaze and extends to the tip without shedding). Because several different parameters affect the accretion and shedding characteristics of a system, the conditions which produce the highest torque rise rate will vary from one configuration to another. The worst case will most likely occur at some intermediate temperature which is conducive to glaze ice formation in the tip region. For this test that temperature appeared to be in the neighborhood of -15 °C.

Figure 10 presents a typical torque history in a case where multiple sheds occurred. Here torque rose smoothly until shedding occurred, at which time the torque dropped somewhat. As ice continued accreting on the blade, the torque rose again until another shed took place. If the accretion had been allowed to continue long enough, an "equilibrium" time would be reached at which shedding and accretion would roughly balance each other out. Torque would then level off at some final equilibrium value.

As expected, ice accretion on the rotor blades tended to increase vibration (measured with accelerometers) due to added mass on the blades and distortion of the flow field around the blades' leading edges. Because the accretion was symmetric, vibration rise before shedding was gradual. Occasionally, depending primarily on collective and somewhat on temperature, vibration rose to high enough levels to necessitate stopping the spray before any shedding occurred. Otherwise, vibration would rise gradually until shedding took place. At this time the vibration would either decrease if the blades shed relatively symmetrically or increase if the shedding occurred on only one blade. The direction and magnitude of the vibration change at shedding was generally sufficient to indicate symmetric or asymmetric shedding to the operator without any visual indicator.

A wide range of tunnel total temperatures from -26.1 to -6.7 °C were run in this test which encompassed the rime, mixed, and glaze ice regimes. Temperature was found to have a significant effect on the rotor ice accretion and shedding characteristics. Tunnel total temperature combined with the rotational effect of kinetic heating on the local blade temperatures influenced both ice type and transition location from rime to glaze ice. In addition, the existence and size of secondary ice formations typically in the form of ice feathers were affected by the local temperature. Figure 11 illustrates the change in ice type at a given location and condition over a range of tunnel total temperatures. The shedding characteristics are strongly influenced by temperature because of the material properties of ice. Above 23 °F, both the tensile and shear strength of impact ice decrease as the temperature increases (Ref. 8). Thus, at warmer temperatures one would expect to see see more shedding at shorter icing times. Although no concentrated study has been performed to date on shedding aspects of this test, this particular dependence on temperature was observed during the experiment.

Variations in cloud liquid water content (LWC) and median volumetric droplet diameter (MVD) were found to produce a measurable change in the accretion characteristics of the rotor blade ice formations. The liquid water content and drop size were always varied in tandem in the OH-58 tail rotor test, precluding determination of the effect of each specific parameter alone on the resulting ice shape, but the test still yielded insight into the changes which cloud parameters had on the resulting rotor ice shapes. The LWC/MVD combinations run in this test were 10 μm and 0.25 g/m^3, 12 μm and 0.40 g/m^3, and 15 μm and 0.50 g/m^3. Each produced markedly different accretions for a given set of conditions as Fig. 12(a) shows. Increasing the LWC/MVD had the effect of further encouraging glaze ice formation at a given temperature and given radial location.

Cloud liquid water content and drop size were seen to have a significant effect on rotor torque and vibration by influencing the size and type of ice which formed on the rotor blades. Each of the three sets of cloud conditions produced markedly different ice shapes and therefore distinctly different torque levels for a given rotor operating condition and temperature. As Fig. 12(b) illustrates, going from the clean blades to a 2-min icing spray at a liquid water content of 0.25 g/m^3 and median droplet diameter of 10 μm, caused no measurable change in torque. Further raising the cloud density to 0.4 g/m^3 and the droplet diameter to 12 μm raised the torque values by about 16 N-m. An even more substantial torque rise was produced by going to a liquid water content of 0.5 g/m^3 and droplet diameter of 15 μm. Here the torque was found to rise by about 32 N-m at each collective.

Rotor rpm was found to have a substantial effect on the nature of the ice which formed on the blades under a given condition. Increasing rpm had the effect of increasing the local velocity at some radial station which then encouraged a more glaze-oriented formation than did the lower speeds. This in turn had the effect of shifting the rime-to-glaze ice transition zone further inboard on the blade as rpm was increased. Figure 13 illustrates this rpm effect for a given set of conditions.

PFM DATA ANALYSIS AND CORRELATION

Baseline Data

The analysis presented in this section concentrates on the effect of icing time on performance parameters, primarily rotor lift and rotor torque. The hovering performance of the rotor was determined during tests in the Sikorsky model rotor test facility. The measured hover performance is compared with the model rotor predictions of the CAMRAD/JA code (Ref. 10). These data show that the rotor performance matched theory, using a Δc_d of 0.0026 to adjust the full-scale (chord = 0.41 m or 16 in.) NACA 0012 airfoil data for the effect of Reynolds number on profile drag. This profile drag increment is consistent with that derived using Ref. 11 methodology.

Determining the Onset of Icing

One step in the analysis of the effect of icing on a rotor is the determination of the time that the spray cloud reached the model, the onset of icing time. An accurate determination of the onset of icing is important to provide a valid reference

point for data and theoretical comparisons. The data were reviewed to determine experimentally the time for this onset of icing. This onset time was based on the Johnson-Williams (J-W) LWC probe (when available) or the beginning of the change in rotor torque and lift. This approach minimized random variations in spray development time and improves the overall data quality for the analysis for parameter comparisons.

Liquid Water Content

For this test, the duration of the spray generally ranged from 44 to 158 sec, including the spray stabilization time. The rate of ice accretion is directly related to the chord size. The smaller the chord, the faster the non-dimensional ice growth. Because of this, sub-scale experiments must use shorter spray times to simulate full-scale icing encounters. A plot of the J-W LWC data for a number of runs (Fig. 14) indicates that there was some rise time prior to reaching the target value (with the rise time increasing at the higher LWC runs). However, the spray condition remained relatively close to the desired setting after the ramp up. The cloud reached the model about 10 sec after the "spray on" command was given.

Ice Shedding

The ice shedding process is a very important factor in a propeller or rotorcraft icing encounter; this phenomenon dominates the outcome of the entire icing event. Figure 15 shows a plot of the root strain gage output for each of the blades as a function of time. When a shed occurred there was a large fluctuation in the strain gage reading. There were two major shedding events for this run; one at approximately 25 sec and another at about 38 sec. For both events blade number 4 experienced a shed first, followed by sheds from the other blades. Rotor torque, also shown in Fig. 15, exhibited a small reduction during minor shedding, with more pronounced changes in torque at major shedding events. There were instances where ice was shed asymmetrically, but the model vibration load limits were not exceeded. Figure 16 shows an example of a section of a blade with ice shed. While this shows a relatively clean break in the ice, the majority of the time there is some residual ice left on the blade after a shed.

Lift and Torque Increments

The rotor balance was sized to accommodate the vibratory loads due to ice shedding, and was, therefore too large to measure precisely the low propulsive force (power required to maintain a forward velocity) levels at the primary test speed of 31.1 m/sec (80 kt). However, the data show that shaft angle, and hence propulsive force, are of secondary importance in the data trends (Ref. 5).

The Δ lift data from the first of the two entries shows a rapid lift loss at the beginning of the ice encounter, indicative of a significant roughness effect on the lift curve shape. Data from the second entry does not exhibit the large initial lift loss, more consistent with current theoretical predictions (see Correlation with Theory section of this paper). Other data obtained in this test program show that variation in C_L/σ has no effect on lift loss or torque rise due to icing, i.e., the percent loss in lift and the percent rise in torque are independent of initial rotor lift.

The model was tested over an advance ratio range consistent with the blade envelope. For the advance ratio

range tested there is no statistically significant effect on either Δ lift or Δ torque.

The data followed expected trends when the LWC was increased. The torque data increased and the lift at constant collective pitch decreased (Fig. 17).

The median volume droplet diameter was changed in a range from 13 to 23 μm at a constant LWC of 0.75 g/m^3. The results indicate that an increase in MVD has the expected effect of increasing the torque and decreasing lift (Fig. 18).

Temperature was varied from near-3.7 to -30.5 °C. Figure 19 shows a plot of the power increase for temperatures ranging from -3.7 to -15.2 °C. The torque increases as temperature decreases because, in this temperature range, the radial icing extent increases and the outer extent is composed of more glaze ice than rime. As more of the rotor blade is iced the performance penalties become more severe. Figure 20 shows another plot of torque rise for a much colder temperature range, -15.2 to -30.5 °C. Here, the torque rise trend reverses and actually decreases with temperature. As the temperature decreases the ice shape changes from glaze to rime, and the performance penalties are less. Figures 19 and 20 show plots of the lift loss for these ranges of temperature. The trend is consistent with that of the torque with the exception of the extremely cold temperature (-30.5 °C).

The effects of icing on rotor torque at different tip speeds is shown in Fig. 21. For the higher tip speeds a balance between shedding and accretion appears to have been reached such that the torque levels off after roughly 50 sec of icing time. However, the torque trace for the lowest tip speed indicates a much higher torque towards the end of the data run, since this lower tip speed has not induced shedding.

Comparison With Theory

Comparison with theoretical methods can involve accretion, shedding, and rotor performance. The correlation presented in this paper uses LEWICE for ice accretion, and computes performance using the Sikorsky Generalized Rotor Performance (GRP) forward flight performance code with the rotorcraft icing subroutine of Ref. 7. This sub-routine is based on an empirical correlation with experimental data.

The ability to adequately predict a given ice shape is critical to a rigorous methodology which predicts performance degradation during an icing encounter. The results presented here were obtained with the computer analysis LEWICE (Ref. 12), which was developed at NASA Lewis. LEWICE is a two-dimensional code which, given the geometric and atmospheric conditions, will predict the cross-sectional ice shape for a specified icing time. Several comparisons have been made between the predictions of LEWICE and these experimental data (Ref. 6). The local angle of attack was determined with the Boeing Helicopters B65 computer performance code. The Mach number and angle of attack were azimuthally averaged for input into LEWICE as shown to be appropriate by Korkan, Dadone, and Shaw (Ref. 13) and Flemming and Lednicer (Ref. 7). The guidelines for time step size and surface roughness were those described by Korkan and Britton (Ref. 14). Figure 22 shows two sample comparisons for a rime condition. The overall agreement is quite good with slight overprediction by LEWICE on the lower

(pressure) surface. Detailed comparisons have been made for both rime and glaze conditions and the results have been encouraging (Ref. 6).

The icing correlation can be broken into two time regimes. The first regime exists prior to ice shedding, thereby limiting the analysis solely to a study of ice accretion. The second regime exists after ice shedding begins, adding a somewhat random factor to the correlation.

The correlation centered on prediction of incremental rotor lift ($\Delta C_L/\sigma$) and incremental rotor torque ($\Delta C_Q/\sigma$) for input shaft angles and flapping angles. Collective pitch was held constant at the predicted clean rotor trim solution and the performance of the rotor system was allowed to degrade. The ramp in LWC that occurred during the start of the icing encounter (Fig. 14) has been ignored and a step change assumed. Emphasis has been placed on the evaluation of the effects of tip speed, rotor lift, LWC, droplet diameter, icing time, and temperature on rotor lift and torque. These variables encompass the major terms in the Ref. 7 icing relationships.

A key element in the prediction of iced rotor lift and torque changes is the prediction of radial ice extent. Figure 23 shows a comparison between the observed ice extents from the PFM test and the Ref. 7 prediction. Since some shedding of ice may have occurred prior to the post run ice extent observations, it would be expected that the data would fall on or below the Ref. 7 line. The points that fall above the line imply that the Ref. 7 ice extent boundary temperature could be increased for future correlation work.

Figures 24 and 25 present the predicted effect of temperature on changes of lift and torque. The Ref. 7 method underpredicts warm icing cases. The observed ice extent from the warm temperature icing ranged in span from 32 to 49 percent. The predicted ice extent is 48 percent, excellent agreement considering that some ice may have shed from the blade between the ice accretion and the post tunnel shutdown observations. Ice thicknesses for these cases were not quantified, but the run log noted that the ice thicknesses were small. The predicted ice thickness ranges from 0.25 mm (0.01 in.) to 2.29 mm (0.09 in.), consistent with the "small thickness" observations. The large increments in power at warm icing temperatures have been reported by pilots, but these occurrences are not well documented. Further research in this area is warranted.

Once the blade is fully iced, comparison using Ref. 7 relationships is much better. Figures 24 and 25 show that the agreement is very good at -10, -15, and -20 °C. However, the prediction is conservative at colder temperatures. An examination of the predicted drag coefficients shows that the Ref. 7 code can produce rime drag coefficients that are greater than comparable glaze drag coefficients for small icing times. A reduction in rime drag coefficients can improve correlation significantly. The code has been modified to use glaze ice drag coefficients when those coefficients are less than the predicted rime ice drag coefficients.

CONCLUSIONS

Scaling

It should be noted that these tests did not deal with scaling in a truly rigorous way. The rotor chord was kept as large as possible in order to reduce Reynolds number effects. This resulted in a high solidity because tunnel geometry constrained the

rotor diameter. To minimize scale effects, the model was operated at full-scale tip speeds and full-scale tunnel speeds. Tunnel temperatures and pressures represent full scale conditions. These give a model Reynolds number that is lower than the full-scale value by a factor of the full to model scale chord ratio. While liquid water content and droplet diameter are important, spray cloud limitations prevented strict scaling of these parameters. Scale relationships have been presented to account for these effects (Refs. 4, 5, and 9).

CONCLUDING REMARKS

The testing of the OH-58 Tail Rotor Rig represented a positive and crucial first step in model rotor icing tests. Data gathered in this test was repeatable in terms of the nature of the accretions and their effect on rotor performance. Techniques for testing of a model rotor in an icing wind tunnel were developed and served to enhance the follow-on testing of the PFM, and set the capability for future testing of other models of rotating systems in icing.

The examination of the data from the Powered Force Model testing has provided encouraging results. The quality of the test data appears to be excellent. The changes in lift and torque are well documented and are remarkably repeatable. The model instrumentation clearly shows the time of shedding events.

The data show the effects of temperature, rotor speed, liquid water content, and droplet diameter on icing. The data trends are generally as expected. Test procedures established for rotorcraft testing in the IRT provided a safe operating environment and produced high quality data for performance analysis. The lift at a constant control collective dropped by up to 15 percent due to icing. Torque increases of 50 percent and more were common. The techniques employed have been validated by the results obtained, and the data will be useful for code and scaling research and development.

Comparisons were made between the experimental ice accretion data and the analysis of LEWICE. The results for the rime condition were excellent. Results for the glaze condition were mixed with a slight tendency to overpredict the thickness. Overall, it is felt that the predictability of the ice shape data was good.

Comparison of test results were made with the Sikorsky Generalized Rotor Performance (GRP) code predictions. Excellent prediction of moderate temperature ($-20° < T < -10$ °C) performance degradation was achieved. The code slightly overpredicted colder temperature torque rise due to an overprediction of rime ice profile drag. The code underpredicts warmer torque rise, a phenomenon that must be researched further.

Future Plans

The near term goal is the completion of the data analysis for the PFM entries and the continuation of correlation studies. High speed 16 mm movies will be processed, and this information used with the energy impact data to support ice accretion and shedding model development. Molds taken during the testing will be used to make ice castings for use in simulated ice experiments. The next experimental effort will be a re-entry of the OH-58 model rotor in the IRT with a calibrated impact energy measurement device. This test will concentrate on documentation and analysis of the ice shedding process.

Longer term goals include further PFM model icing tests, coordinated with full-scale rotorcraft icing flight testing. This would follow a logical progression for development and verification of the model rotor test techniques and the analytical methods, and identify where their use in main rotor design is appropriate.

REFERENCES

1. Guffond, D.P.: Icing and De-icing Test on a 1/4 Scale Rotor in the ONERA S1MA Wind Tunnel. AIAA Paper 86-0480, Jan. 1986.

2. Reinmann, J.J.; Shaw, R.J.; and Ranaudo, R.J.: NASA's Program on Icing Research and Technology. Flight in Adverse Environmental Conditions, AGARD CP-470, 1989 (Also, NASA TM-101989).

3. Miller, T.L.; and Bond, T.H.: Icing Research Tunnel Test of a Model Helicopter Rotor. NASA TM-101978, 1989.

4. Bond, T.H.; Flemming, R.J.; and Britton, R.K.: Icing Tests of a Sub-Scale Model Main Rotor. Proceedings of the 46th Annual American Helicopter Society Forum, Vol. 1, May 1990, pp. 267-281.

5. Flemming, R.J.; Bond, T.H.; and Britton, R.K.: Results of a Sub-Scale Model Rotor Icing Test. AIAA Paper 91-0660, Jan. 1991.

6. Britton, R.K.; and Bond, T.H.: A Review of Ice Accretion Data From a Model Rotor Icing Test and Comparison Theory. AIAA Paper 91-0661, Jan. 1991.

7. Flemming, R.J.; and Lednicer, D.A.: High Speed Ice Accretion on Rotorcraft Airfoils. NASA CR-3910, 1985.

8. Scavuzzo, R.J.; and Chu, M.L.: Structural Properties of Impact Ices Accreted on Aircraft Structures. NASA CR-179580, 1987.

9. Armand, C., et al.: Techniques and Facilities Used at the ONERA Modane Centre for Icing Tests. Aircraft Icing, AGARD-AR-127, 1978, pp. A6-1 to A6-23.

10. Johnson, W.: CAMRAD/JA, A Comprehensive Analytical Model of Rotorcraft Aerodynamics and Dynamics: Johnson Aeronautics, Palo Alto, CA, 1988.

11. Keys, C.N., et al.: Estimation of Full-Scale Rotor Performance from Model Rotor Test Data. Journal of the American Helicopter Society, vol. 30, no. 4, Oct. 1985, pp. 22-29.

12. Ruff, G.A.; and Berkowitz, B.M.: Users Manual for the NASA Lewis Ice Accretion Prediction Code (LEWICE). NASA CR-185129, 1990.

13. Korkan, K.D.; Dadone, L.; and Shaw, R.J.: Performance Degradation of Helicopter Rotor Systems in Forward Flight Due to Rime Ice Accretion. AIAA 83-0029, Jan. 1983.

14. Korkan, K.D.; and Britton, R.K.: A Study of Ice Shape Prediction Methodologies and Comparison With Experimental Data. AIAA Paper 90-0753, Jan. 1990.

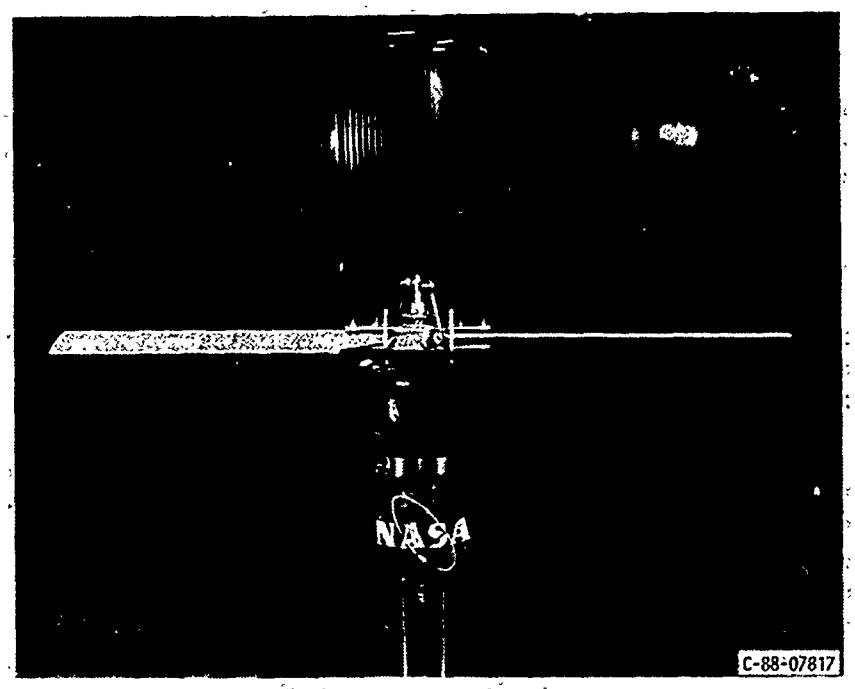

FIGURE 1. - OH-58 TAIL ROTOR ASSEMBLY.

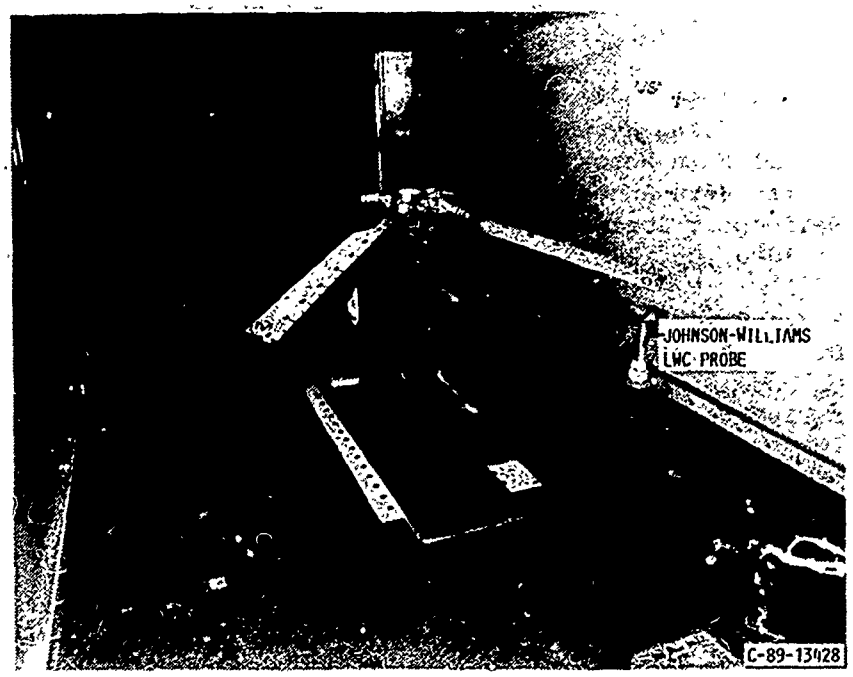

FIGURE 2. - MODEL MAIN ROTOR ASSEMBLY IN THE IRT.

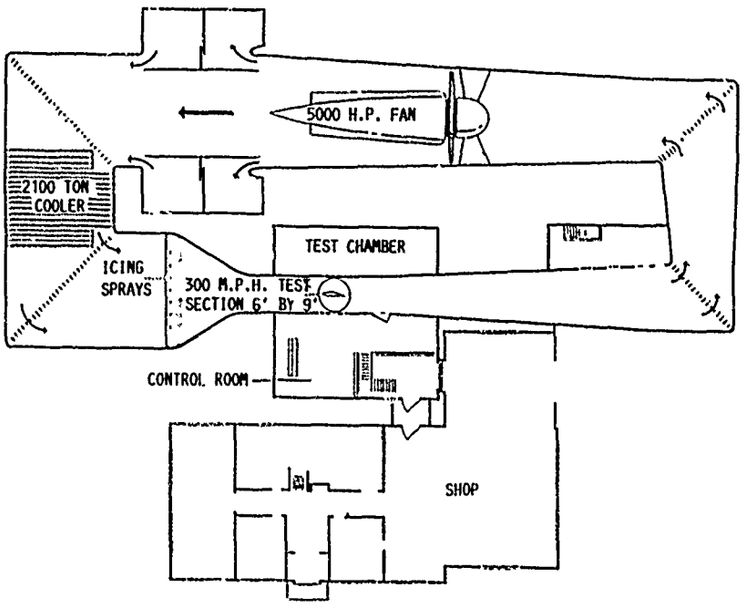

FIGURE 3. - NASA LEWIS ICING RESEARCH TUNNEL.

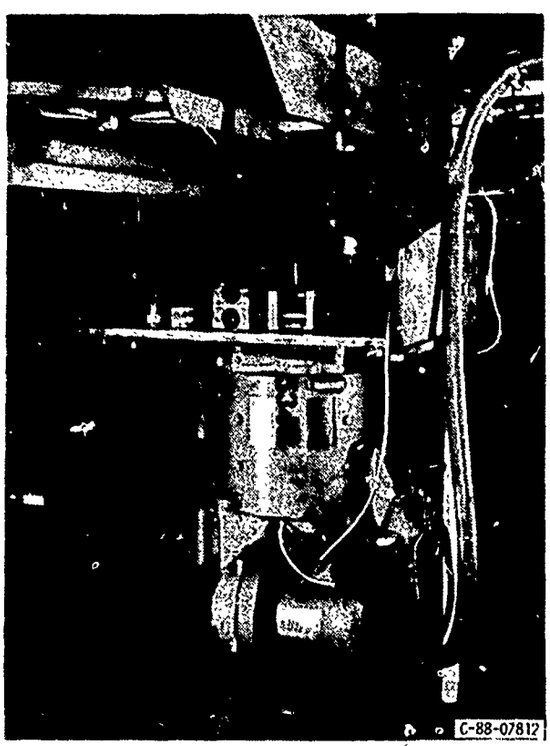

FIGURE 4. - OH-58 MODEL ROTOR DRIVE ASSEMBLY.

Figure 14 shows the results obtained

calculation. The program in current use considers 11 spanwise stations. For each of

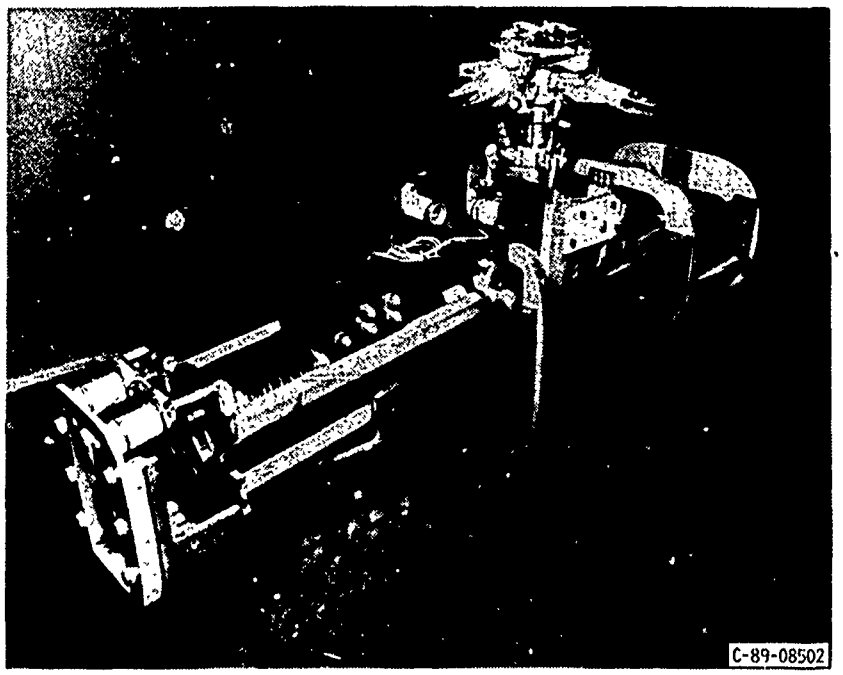

FIGURE 5. - SIKORSKY PFM ROTOR HEAD AND FORCE BALANCE ASSEMBLY.

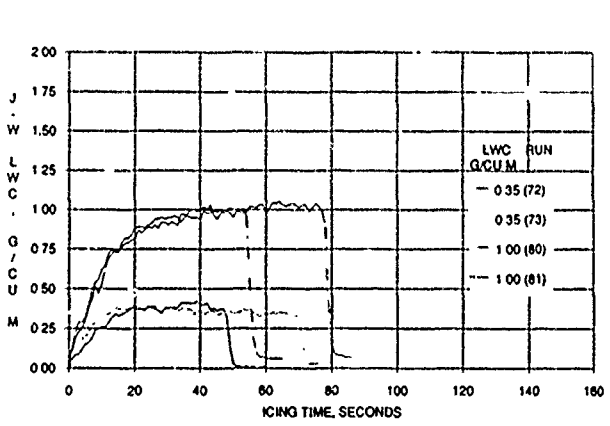

FIGURE 6. - LWC REPEATABILITY VERSUS ICING TIME (MVD = 15 μm, μ = 0.20 m/s, C_L/σ = 0.064, T = -15 ^{o}C).

drag coefficient with ambient

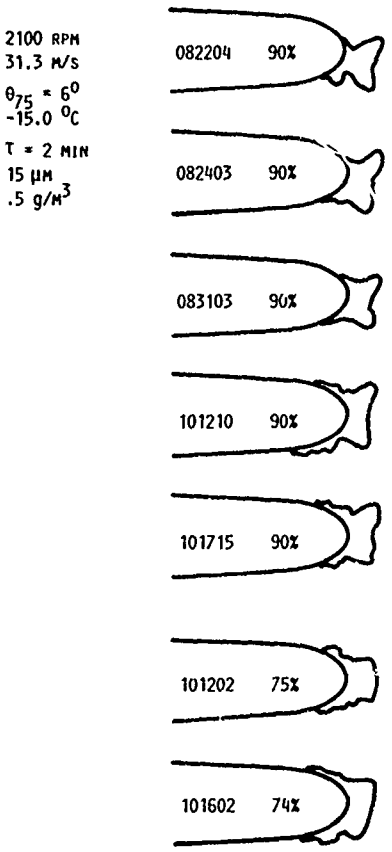

FIGURE 7. - ICE SHAPE REPEATABILITY FOR OH-58 TEST.

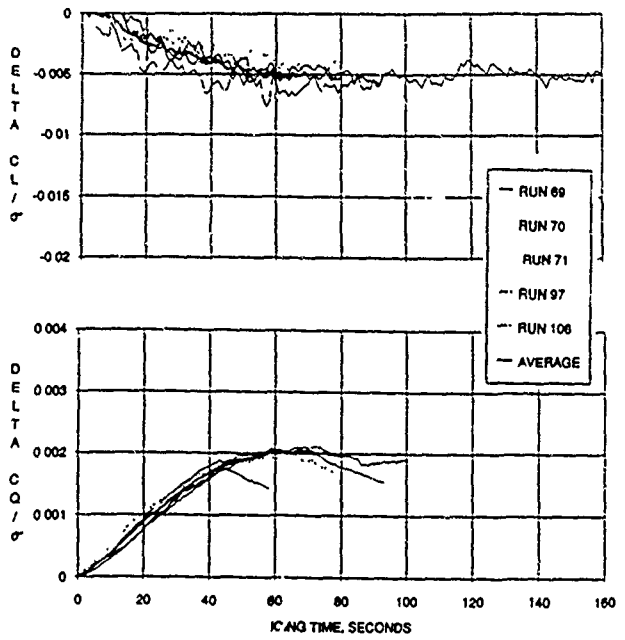

FIGURE 9. - REPEATABILITY FOR PFM TEST (ΩR = 205.7 m/s, T = -15 °C).

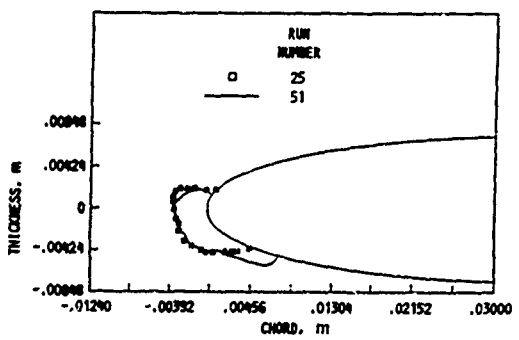

FIGURE 8. - TWO DIMENSIONAL ICE PROFILES FOR PFM TEST. (LWC = 0.5 g/m³, MVD = 15 μm, μ = 0.20 ΩR = 183 m/s, C_L/σ = 0.064, T = -15 °C).

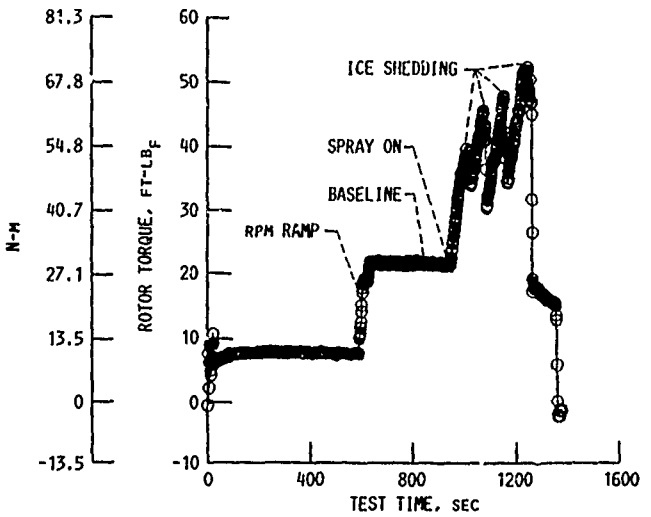

FIGURE 10. - ROTOR TORQUE VERSUS TEST TIME FOR OH-58 TEST, 2100 RPM, τ = 5.4 MIN, 15 μM, 31.3 M/S, -9.4 °C, .5 g/M³, θ_{75} = 4° FOR OH-58.

negative) the

2100 RPM
31.3 M/S

$\theta_{75} = 2^0$
T = 2 MIN

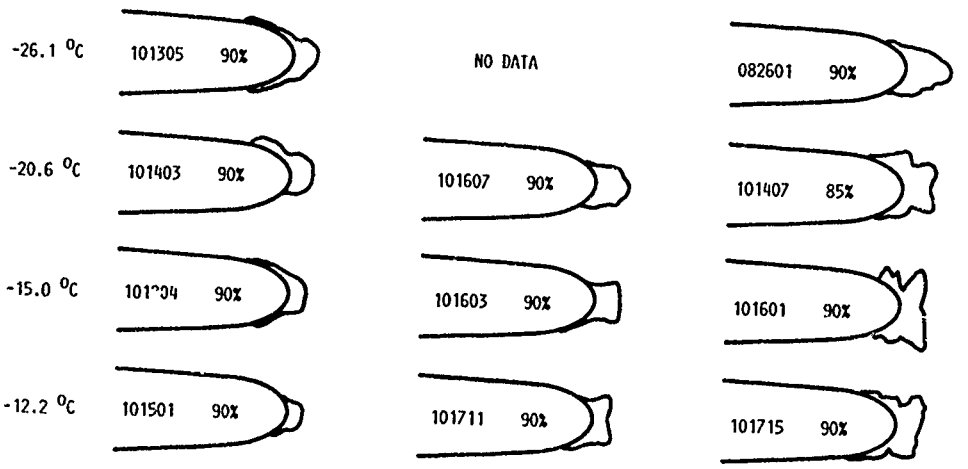

FIGURE 11. - TEMPERATURE EFFECT ON ICE ACCRETION FOR OH-58 TEST.

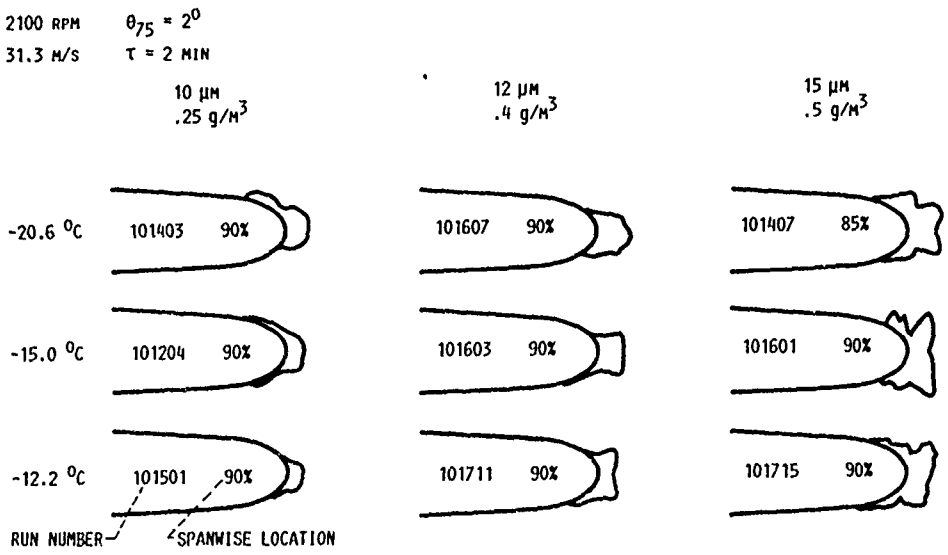

FIGURE 12(a). - LWC AND DROP SIZE EFFECT ON ICE ACCRETION FOR OH-58 TEST.

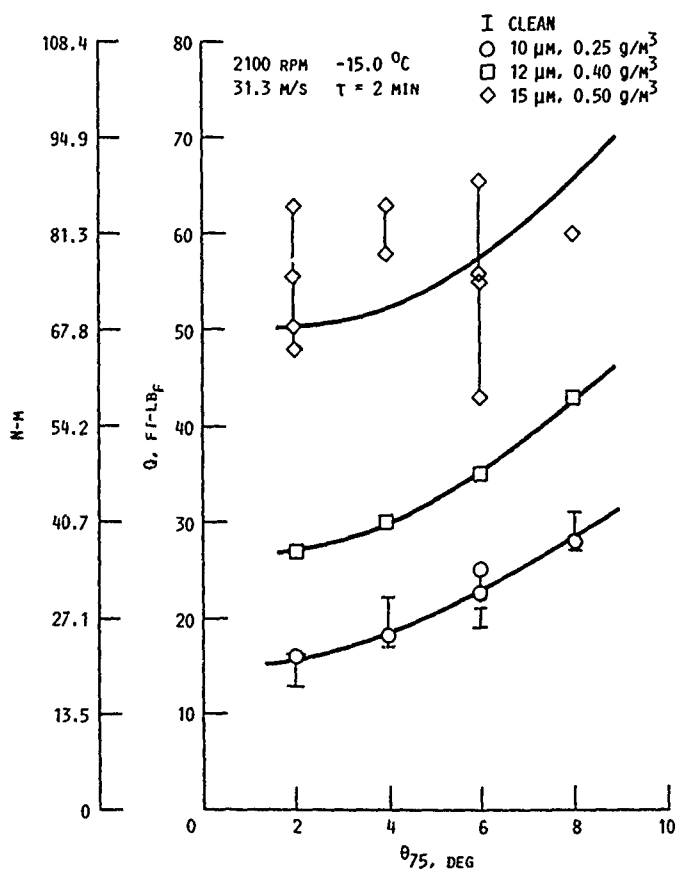

FIGURE 12(b). - LWC/DROPLET SIZE EFFECT ON TORQUE FOR OH-58 TEST.

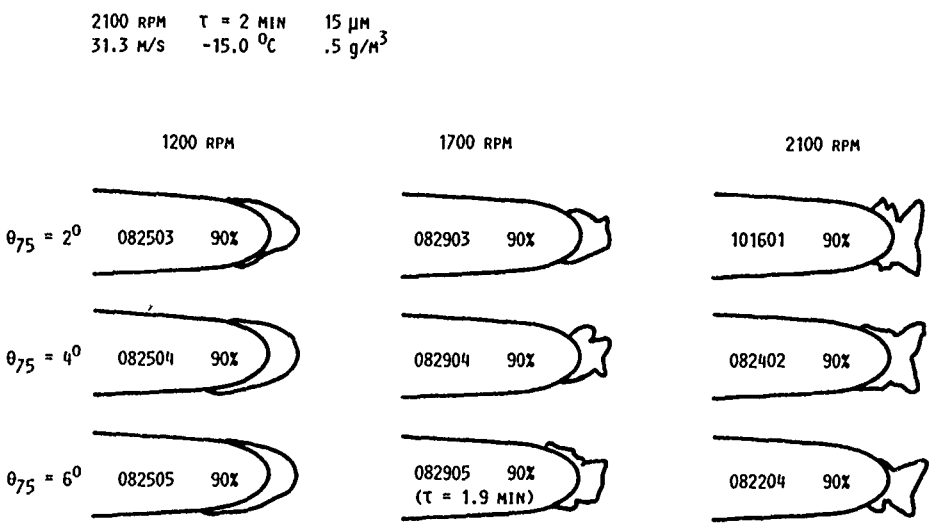

FIGURE 13. - RPM EFFECT ON ICE ACCRETION FOR OH-58 TEST.

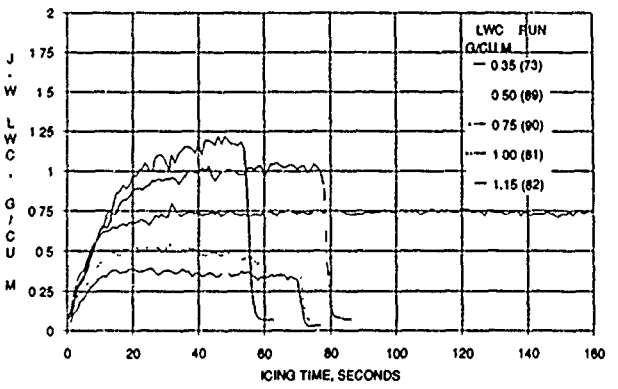

FIGURE 14. - LWC RISE TIME FOR PFM TEST (MVD = 15 μM, μ = 0.20, ΩR = 206 M/S, C_L/σ = 0.064, T = -15 °C).

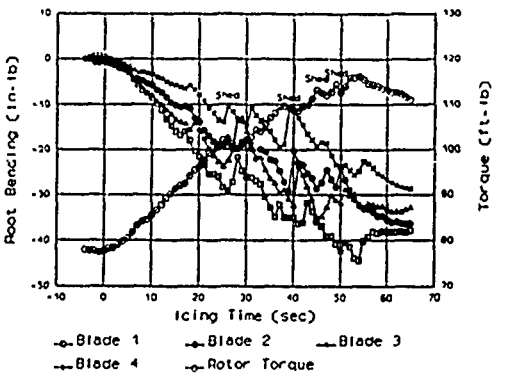

FIGURE 15. - BLADE ROOT BENDING AND TORQUE RISE VERSUS ICING TIME FOR PFM TEST. (LWC = 1.0 g/M³, MVD = 15 μM, μ = 0.20, ΩR = 206 M/S, C_L/σ = 0.064, T = -15 °C).

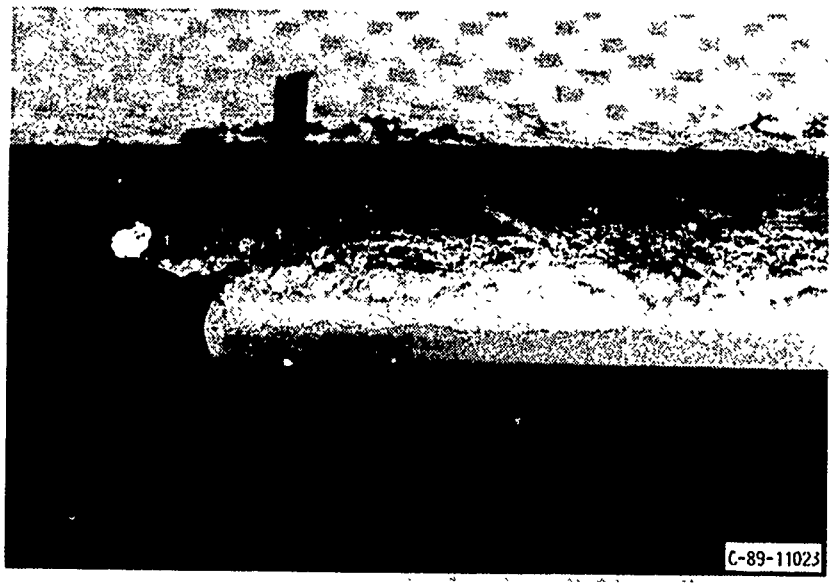

FIGURE 16. - CLOSE-UP DETAIL OF SHED ICE FROM PFM TEST.

FIGURE 17. - EFFECT OF LIQUID WATER CONTENT FOR PFM TEST. (T = -15 ^{o}C).

FIGURE 18. - EFFECT OF DROPLET DIAMETER FOR PFM TEST. (LWC = 0.75 g/M^{3}).

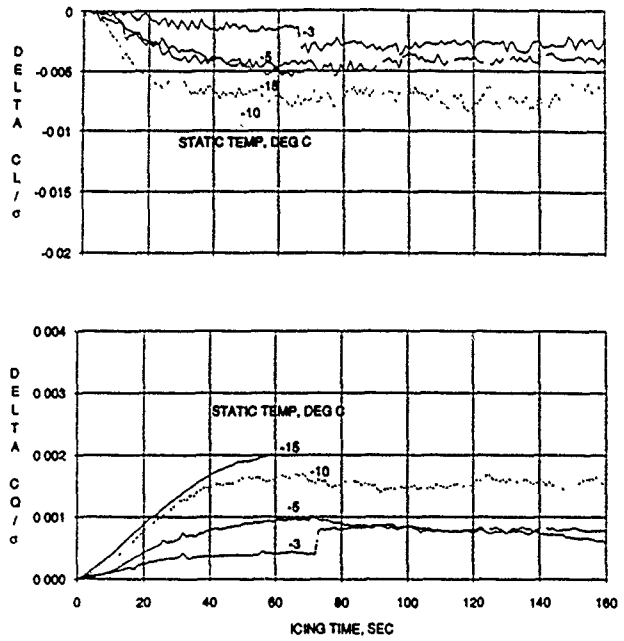

FIGURE 19. - EFFECT OF TEMPERATURE FOR PFM TEST. (ΩR = 205.7 M/S, WARMER TEMPERATURE).

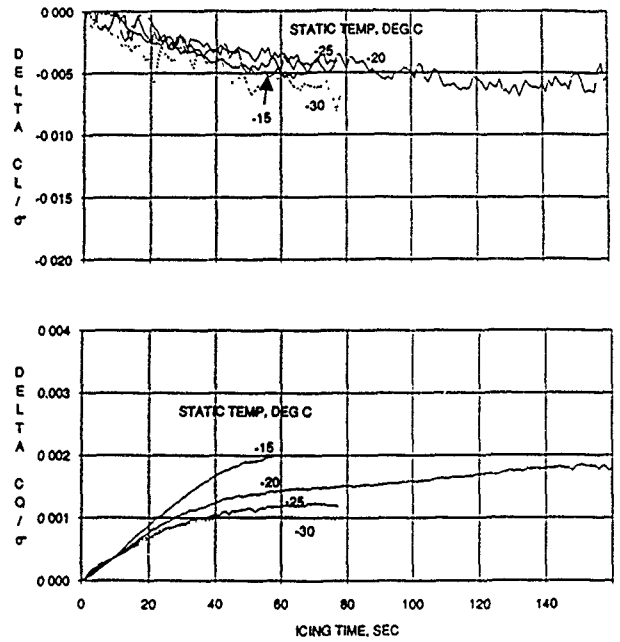

FIGURE 20. - EFFECT OF TEMPERATURE FOR PFM TEST. (ΩR = 205.7 M/S, COLDER TEMPERATURE).

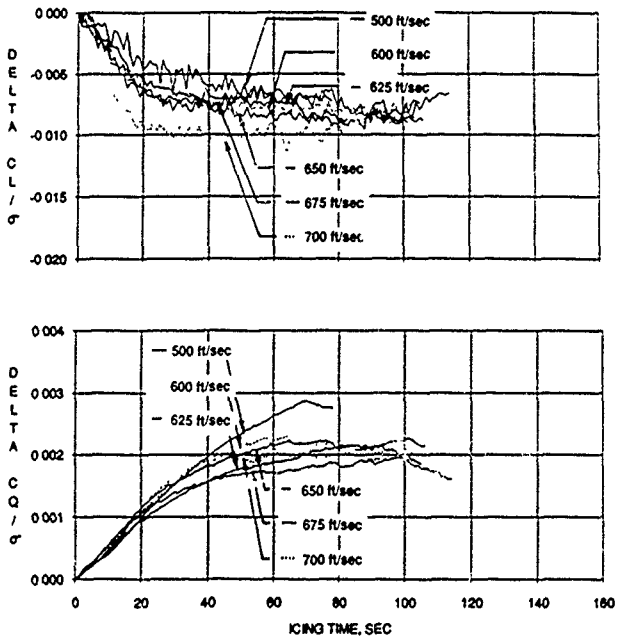

FIGURE 21. - EFFECT OF TIP SPEED FOR PFM TEST.

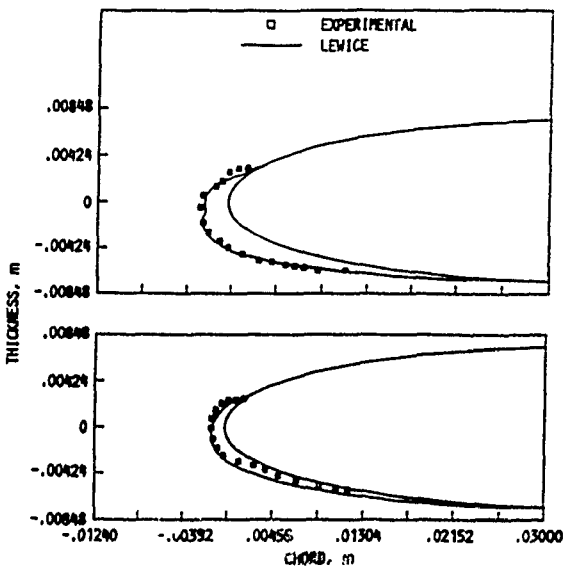

FIGURE 22. - COMPARISON BETWEEN EXPERIMENTAL AND THEORETICAL ICE SHAPES FOR PFM TEST. (LWC = 1.0 g/m^3, MVD = 15 μm, μ = 0.2, ΩR = 206 M/S, C_L/σ = 0.064, T = -15 ^{0}C).

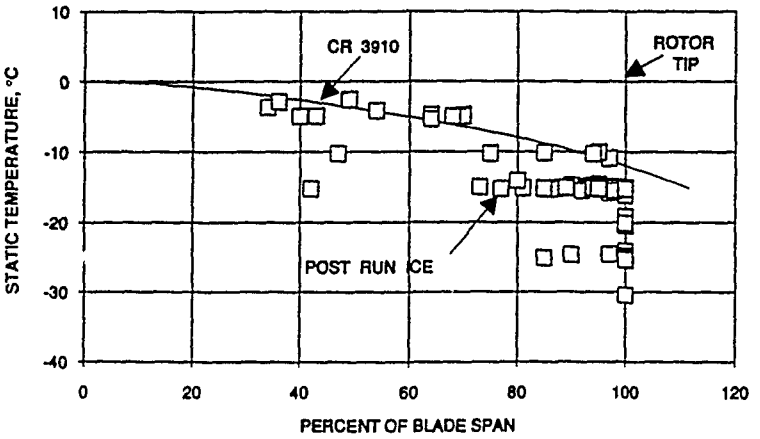

FIGURE 23. - OBSERVED AND PREDICTED MODEL ROTOR ICE EXTENT FOR PFM TEST.

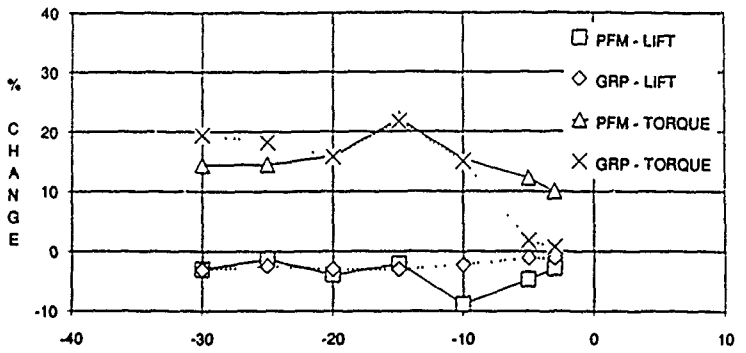

FIGURE 24. - LIFT AND TORQUE CHANGE SUMMARY FOR PFM TEST. (τ = 20 SEC, LWC = 0.5 g/M^3).

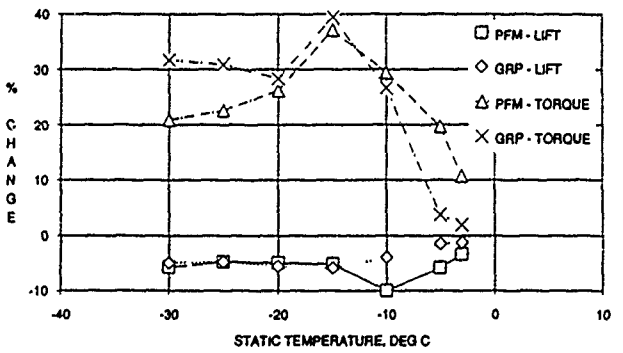

FIGURE 25. - LIFT AND TORQUE CHANGE SUMMARY FOR PFM TEST. (τ = 40 SEC, LWC = 0.5 g/M^3).

A REVIEW OF ICING RESEARCH AT THE ROYAL AEROSPACE ESTABLISHMENT

by
R.W. Gent
Royal Aerospace Establishment
Farnborough
Hampshire, GU14 6TD
England

SUMMARY

This paper provides a brief review of the computer models developed by RAE for the analysis of natural rotor icing and rotor protection against icing. Experimental results are then presented for the increase in profile drag due to rime, glaze and beak type icing. This data, combined with other published data, have been used to obtain correlations for iced aerofoil performance which have been included in a computer model of helicopter performance. This enables the prediction of the increase in rotor power required by a helicopter with unprotected rotors during flight in icing conditions. Comparisons between model prediction and both rig and flight test data are given.

NOMENCLATURE

C_D	drag coefficient
C_L	lift coefficient
CQ/s	torque coefficient/solidity
L,F	correlation factors for glaze ice
LWC	liquid water concentration, g/m^3
N_f	freezing fraction
OAT	outside (static) air temperature, °C
x/c	chordwise distance
α	incidence, degrees
α_o	zero lift incidence, degrees
τ	accretion time, min
Δ	difference with icing time

INTRODUCTION

Ice accretion resulting from flight in cloud at temperatures at or below 0°C still poses a significant hazard to most military and civil helicopters leading to unacceptable limitations in the available flight envelope. While some helicopters have limited clearances, based on engine, windscreen and pitot protection only, very few have fully developed and certificated rotor protection systems. It was these constraints on helicopter operations that led RAE to increase effort on icing research in the late 1970's. The aim was to provide an understanding of the rotor icing problem and to provide engineers with the tools needed to design the necessary rotor protection systems.

This paper provides a brief review of the computer models developed by RAE for the analysis of natural rotor icing and rotor protection against icing. Experimental results are then presented for the increase in profile drag due to rime, glaze and beak type icing. This data, combined with other published data, has been used to obtain correlations for iced aerofoil performance which have been included in a computer model of helicopter performance. This enables the prediction of the increase in rotor power required by a helicopter with unprotected rotors during flight in icing conditions. Comparisons between model prediction and both rig and flight test data are given.

ICE TYPES

This paper makes reference to three types of ice accretion which can form on a helicopter rotor. These are rime, glaze and beak type ice accretion. For the reader unfamiliar with icing terminology, the accretion types are defined below and illustrated in Figure 1.

At combinations of low airspeed, low ambient temperature or low cloud liquid

water concentration (LWC), the super-cooled water droplets freeze on impact tending to form a streamlined accretion which is white and opaque due to the presence of trapped air bubbles. The accretion may become less streamlined as the size of the accretion increases.

At certain combinations of speed, ambient air temperature and LWC, not all of the water freezes on impact, some running back along the surface which can freeze at aft positions on the aerofoil. The tendency is for this accretion to exhibit a horn on each of the upper and lower surfaces. This type of accretion is termed glaze ice. The central region where runback water is present tends to be translucent in appearance, although the accretion further aft may again become white and opaque like rime ice; the water droplets in this region freezing on impact.

At combinations of high speed and warm ambient temperature, close to 0°C, the only place where ice can form is in the region of low pressure on the upper surface near the leading edge. Under these circumstances, a "slushy" ridge of ice forms, termed beak ice.

Due to the variation in local velocity with span along a helicopter rotor, it is possible for all three types of accretion to be present at the same time. Rime ice can form at inboard stations, a region of glaze icing may form further out, and finally a region of beak icing may form near the tip of the rotor.

ICING ANALYSIS METHODOLOGY

Figure 2 shows the overall aims of the RAE approach to icing analysis. Starting with a given combination of flight conditions, environmental conditions, and body geometry it is first necessary to calculate the flowfield about that geometry. This enables the trajectories of cloud water droplets to be calculated, which is necessary to determine where and at what rate the droplets impact the surface i.e. the determination of the water droplet collection efficiency distribution.

With the collection efficiency distribution known, the next stage is to predict how this water will freeze to form an ice accretion. This is achieved by carrying out a thermodynamic analysis (or heat balance) over a section of the leading edge. Having determined the ice profile, the next stage is to evaluate the aerodynamic performance penalty; primarily a large increase in profile drag, although a reduction in lift coefficient and increase in pitching moment coefficient are also possible. This is at the component level; the calculations then need to be repeated for other parts of the wing or rotor and the results input to a model of the whole aircraft, wing or rotor to predict the total degraded performance of the unprotected aircraft.

In Figure 1, the box labelled experimental data has been included since at present there is no CFD prediction capability for iced aerofoil performance in the UK. At present therefore, the only alternative is to measure the degraded performance either directly in icing tunnels or indirectly with replicas of the ice shape tested in a conventional wind tunnel. The measured aerodynamic data is then used either directly in a prediction of performance or, as is more convenient, to generate correlations for the ice degraded aerofoil performance.

Results such as collection efficiency distribution or ice shape obtained from application of the ice accretion prediction programs can be input to a model of an aerofoil ice protection system. Alternatively, sections of code from the icing analyses can be embedded directly into a model of the ice protection system in order to predict the heat transfer from the aerofoil surface and hence any resulting ice accretion. At RAE, interest has been confined to electrothermal ice protection systems, anti-icing or de-icing using electrical heating elements, since these remain the only viable means for protecting helicopter rotors at present. The analysis capability is necessary for the design, optimisation and certification of the protection system. The aim is to predict the transient temperature response,

at the surface and at internal positions, of a multi-layered structure with embedded electrical heating strips while taking account of the complex heat balance at the aerofoil/ice surface. The designer is interested in determining how much electrical power to use, how long to activate a particular heating element in a de-icing system and how much ice is melted and shed. With the advent of glass and carbon fibre composites, the engineer is particularly interested in determining the maximum temperature arising within the heated structure.

ANALYSIS CAPABILITIES DEVELOPED AT RAE

Figure 3, shows the main programs that have been developed at RAE over the past decade. It is not appropriate in this paper to discuss each of the programs in detail. Such information is provided in the appropriate references. In this paper, only the main attributes of the programs are discussed, along with the conclusions that RAE has drawn from the application of these programs.

RAE has developed two droplet trajectory calculation programs; both assume steady, two dimensional flow conditions. The first program to be developed was based on an aerodynamic code that treats compressible flow, and also has the ability to introduce a correction for viscous effects [1]. However, it was found that both compressibility and viscous corrections had a negligible effect on the predicted water droplet trajectories and so, subsequently, a second code was developed which is more user friendly. This code [2] is based on a simpler aerodynamic analysis that assumes incompressible, potential flow.

For ice accretion prediction RAE began with simple 1D codes. These allow the freezing fraction at a single chordwise position to be assessed. The stagnation point is usually the position at which the calculation is applied. The freezing fraction is the proportion of the total incident water which freezes in unit time. A freezing fraction of one implies rime icing; between one and zero glaze icing (or beak icing at a position aft of the stagnation point on the upper surface); and zero, no icing. These 1D calculations are particularly useful for predicting the type (rime, glaze or beak ice) and radial distribution of ice accretion along a rotor.

The next step was to develop two-dimensional analyses, which predict the shape and size of the accretion. Development began with a steady two-dimensional, compressible flow model, which neglected the effect of heat conduction within the rotor blade, or aerofoil [3]. This was followed by an investigation of the effect of heat conduction within the blade [4]. Results showed that for most practical rotor blade constructions, the effect of heat conduction within the blade was negligible.

The next model addressed the effects of cyclic varying airspeed and incidence, appropriate to a helicopter rotor in forward flight [4]. This was a pseudo unsteady analysis. The azimuth was divided into a number of segments, typically 100, and the distributions for collection efficiency, pressure and convective heat transfer coefficient were calculated using the instantaneous value of airspeed and incidence. A transient heat conduction analysis applied around the rotor azimuth was used to determine the equilibrium ice accretion rates which where then averaged over the rotor azimuth.

The results from this program confirmed that harmonic pitch variation increased the limits of droplet impact, but did not have a significant effect on the profile of the ice at the leading edge. Cyclic variation of local velocity was found to have a small effect in terms of the threshold for ice accretion, but again the ice shape was not significantly affected. However, the predicted glaze ice shapes from this model were never entirely satisfactory. The problem was attributed to the modelling of the convective heat transfer which assumed distributions obtained for static conditions could be applied under

periodically varying conditions. This assumption led to the stagnation point varying with pitch much more than was likely in practice. Nevertheless, the program provided valuable information on the likely effects of cyclic variations in local velocity and incidence, and spawned a separate computer program which was efficient for rotor calculations in the hover [5].

In view of the negligible effects of compressibility on water droplet impact, of heat conduction within the blade, and of the transient effects, RAE developed a more user friendly ice accretion prediction program. This program neglected heat conduction within the blade and assumed incompressible flow conditions. In fact the latest droplet trajectory program and the simplified accretion program are combined into a single program called TRAJICE2 [2]. This program has been released to a large proportion of the UK aerospace industry for calculations on both fixed and rotary wing aircraft. The application of this program to the prediction of ice accretion on fixed wing aircraft has included work required for certification.

For the analysis of rotor protection systems, RAE has developed both one- and two-dimensional programs to predict the transient temperature response of an electrically heated rotor blade. The 1D program [6] addresses heat flow into and out of the blade in a direction normal to the aerofoil surface at a specified chordwise position, while the 2D program models a chordwise section of the rotor blade. Both programs simulate ice accretion, melting and have a crude simulation of ice shedding. These programs have been released to Westland Helicopters Limited and are currently being employed in the development of the rotor protection system for the EH101 helicopter.

The final area of modelling addressed by RAE, which is the topic considered in the rest of this paper, is that of aerodynamic performance. RAE is currently developing a program to predict the increase in drag and loss of lift on a two-dimensional aerofoil which uses correlations based on measured performance data rather than obtained from CFD prediction. This code has been embedded in an existing helicopter performance code to predict the power increase due to ice accretion on the main rotor of a conventional helicopter without rotor protection. This topic is discussed in more detail later in this paper.

MEASUREMENTS OF DRAG INCREASE DUE TO ICING

RAE conducted a short series of tests [7] in the icing wind tunnel operated by Lucas Aerospace located at Artington, near Guildford. The main aim of the testing was to compare the effect of rime, glaze and beak type ice accretion upon the drag coefficients of two helicopter rotor aerofoils. No balance mechanism was available and so no data on lift or pitching moment coefficient was obtained.

The two aerofoil sections selected for the tests were, NACA0012 representing that used on the older generation of rotorcraft such as Wessex and Sea King helicopters, and RAE9645 which is a modern cambered design used on the EH101 helicopter. Both sections have a thickness to chord ratio of 12%.

Figure 4 shows the experimental configuration used for the drag coefficient measurements. The tests employed a 0.15 m (6 inch) chord model mounted downstream of a water spray rake. With the 0.3 m (1 ft) square test section used, the highest Mach number available for test was 0.4. Approximately one chord length downstream of the trailing edge was situated a traversing wake survey pitot-static probe which could be parked behind a shield while the icing was in progress. The method adopted was to establish dry air conditions and then switch on the spray for a specified period; maximum two minutes. After the icing period the spray would be turned off, and the wake survey commenced immediately. The ice shapes were then documented.

To minimise the amount of data the tests were carried out only at Mach 0.4,

and the temperature and cloud liquid water concentration were selected to produce one example each of rime, glaze and beak ice. Measurements were made at geometric incidences of 0°, 4° and 8°.

Figures 5 and 6 show the rime and glaze ice shapes obtained during the tests respectively. The rime accretions had a maximum thickness of about 0.02 x/c, while the glaze accretions had a maximum horn thickness of about 0.05 x/c.
The wavy line aft of the main accretion in the glaze ice shapes of Figure 7, represents the approximate size and extent of rime feather ice at the time of recording. Rime feathers are localised three-dimensional accretions which have a surface structure which resembles that of a bird feather. The detailed, three-dimensional, features of rime feather accretions are difficult to record accurately.

Beak ice sheds very easily and it was not possible to retain the ice long enough to allow documentation, hence there are no details of the beak ice profiles.

In order to reduce the number of figures presented in this paper, only the experimental data obtained for the RAE section is presented, although appropriate comparisons with the NACA section data are also given.

Figure 7 shows a comparison between the drag coefficient for the clean, RAE9645 aerofoil measured in the Artington tests with previously measured data for the aerofoil obtained in a conventional wind tunnel. The agreement is good despite the high turbulence level of the icing tunnel.

Figure 8 shows the measured drag coefficient for the RAE9645 section with rime ice accretion. The results are plotted against accretion time, and three curves are shown representing the three geometric incidences used in the tests. In all cases, the drag initially increases rapidly and then approaches an equilibrium level. This "levelling off" was less marked for the NACA section. The levelling off of the drag coefficient with accretion time is consistent with flight test data recorded during helicopter natural icing flight trials which has shown an increase in and then a levelling off of torque requirements.

Figure 9 shows the same data as Figure 8, re-plotted against incidence. Note here that the ice appears to cause a change in C_{Do} which is largely independent of incidence.

Figure 10 shows a comparison between the two aerofoils with rime ice accretion under similar lifting conditions. The zero lift incidence of the RAE section is about -2°. The data for 1 and 1.5 minute ice accretion are omitted to improve clarity. The data of Figure 10 suggests to a rough first order approximation that the two aerofoils experience similar drag increase for similar thickness of rime ice accretion.

Figure 11 shows results for the variation of drag coefficient with ice accretion time under glaze icing conditions. The trend is similar to that for the rime ice case except that the magnitude of the increase in the drag coefficient is considerably larger. The increase in drag was typically about a 100% for rime ice whereas the glaze ice data shows increases of about a factor of 4. The tendency for the drag coefficient to stabilise at a higher value is again indicated.

Figure 12 shows the same results as Figure 11 re-plotted against incidence. The variation with incidence again suggests a shift in C_{Do} with the difference (iced-clean) with incidence remaining fairly constant.

Figure 13 compares the drag coefficients with glaze ice accretion for the two aerofoil sections under similar lifting conditions. The drag coefficients are similar at the 0.5 min accretion period, but at the larger icing periods, the NACA section appears to be more severely affected than the RAE section.

Figure 14 shows the results obtained for beak ice on the RAE section. Some difficulty was experienced in obtaining corresponding trend data for the NACA section in the time available for the icing tunnel tests. The trend with beak ice accretion appears to indicate a linear increase in drag coefficient with time, up to some point at which the ice sheds. Note that there is no data for 0° incidence. This case was not attempted since it was felt that there would be insufficient suction to both form and retain the beak ice. The end points of the two curves in Figure 14; 1.5 minutes at 4° and 2 mins at 8° incidence, represent the maximum that could be achieved in the icing tunnel. It was found that the ice started to shed shortly after these icing times. Note that the effect of the beak ice was to produce an increase in C_{Do} of approximately a factor of three compared to the baseline non-icing condition.

Based on the data gathered, it was only possible to compare the drag characteristics of the two aerofoils for the one minute period of beak ice accretion. These results are shown in Figure 15 and appear to indicate that the two aerofoils are affected to similar degrees by beak icing, although more data is required to confirm this conclusion.

ICED ROTOR PERFORMANCE PREDICTION

The final topic of this paper addresses the prediction of the power increase experienced by a helicopter rotor due to flight in icing conditions. The program under development at RAE performs the following tasks as illustrated in Figure 16. The first step is to calculate the power required for the clean aircraft given the necessary aerodynamic lift and drag coefficient data. It is assumed that the lift slope is constant. The drag coefficient is expressed as a function of aerodynamic incidence over a range of Mach number. The power required calculation for the clean aircraft allows the mean incidence to be calculated at each of the spanwise stations used in the power calculation. The program in current use considers 11 spanwise stations. For each of the 11 stations a routine is used to calculate the type of ice, the ice thickness at the stagnation position, or the maximum ice thickness on the upper surface in the case of beak ice. The increment to the lift and drag coefficient is then estimated using correlations, and the degraded aerofoil characteristics are fed back into the power required prediction program to obtain a solution for the ice degraded rotor. A comparison with the power required for the clean aircraft enables the power increase to be determined.

An existing helicopter power required prediction code has been used which is a forerunner of that described in Reference 8. The program calculates the power required in hover or forward flight for any conventional, main rotor / tail rotor helicopter. The program is based on a lifting line analysis and assumes linear aerodynamics.

A correlation for drag increase due to rime and beak ice accretion was obtained using the experimental data from the RAE tests. For the reduction in lift coefficient in icing, a correlation was obtained based on the data reported by Flemming [9] for measurements in the NRC tunnel. The correlation is crude and is based solely on the thickness of ice at the stagnation line and assumes that rime ice forms. While the effect on the maximum lift coefficient can be significant the change in the lift slope appears to be relatively small. To date therefore, the reduction in lift coefficient due to icing represented in the program is small. It is important to remember that at this stage it is not intended to predict the forward flight envelope of the helicopter and so a knowledge of the effect of icing on the maximum lift coefficient is not required. At present only icing of the main rotor is considered. Icing effects on the fuselage and tail rotor are neglected.

The RAE correlation for glaze ice uses a different approach to that used by other Researchers in the field [9,10]. Figure 17 shows the expected variation in profile

drag coefficient with ambient temperature (or freezing fraction). This trend has been recorded by Olsen [11] and Flemming [9]. The left side of the curve represents rime icing under cold ambient conditions. As the ambient temperature increases (i.e. proceeding from left to the right of the curve), the drag coefficient initially increases up to some maximum value as glaze ice forms. Further increases in ambient temperature, corresponding to further reductions in freezing fraction, cause the ice to become more wet and of reduced thickness and hence reduced drag until at some point only beak ice accretion forms. Still further increases in ambient temperature will eventually produce no icing with the aerofoil running wet but without an appreciable increase in drag coefficient. The approach adopted by RAE to obtain the drag increase due to glaze ice accretion is based on correlating this form of the drag variation with freezing fraction. The approach was chosen so as to complement the research being conducted in the USA.

The RAE approach is intended to establish the load factor, L, which is the ratio of glaze ice drag increase to the rime ice drag increase. The load factor can be unity, greater than unity or zero. The actual value is at present assumed to be a function of the ice thickness, a maximum enhancement factor, F, and a reference freezing fraction, Nfr. at which the highest drag coefficient is obtained.

The following sections compare predicted results with available experimental data obtained during both flight test and rig experiments.

In Figures 18 and 19, the program has been used to predict the maximum, stabilised, torque increase recorded during natural icing flight trials for two helicopters with unprotected rotors. In these comparisons the cases which are most likely to give best agreement with the program have been selected from the range of measured test data. That is, considering only the first encounter with icing, so that the fuselage and rotor are not pre-iced and hence enabling an accurate prediction of the true baseline power required for the clean aircraft. Cases were also chosen which had the highest LWC; frequently mean LWC values of 0.1 g/m³ or less are reported in natural icing flight tests on helicopters. With values below 0.1 g/m³, the accuracy of the LWC measurement instrumentation becomes significant as are the possible effects of ice sublimation.

Figure 18 shows the measured and predicted power increase due to icing on a Puma helicopter with unprotected rotors for 18 cases in which the OAT varied from -0.8°C down to -9.9°C. As ambient temperature decreases with all the other ambient conditions fixed, the power required in icing (or torque since rotor speed is governed) increases. This is because the spanwise extent of the ice increases with progressively more icing on the outboard stations of the rotor as ambient temperature reduces. In Figure 18, there is a band of data close to zero which is not predicted well. Subsequent preliminary analysis of the actual traces showing the recorded flight test data, showed that in at least one case the rotor torque remained constant during the encounter. This suggests that the quoted torque increase was attributable to a different source. The remaining cases in Figure 18 show some scatter but the trend is generally good.

Figure 19 shows a similar comparison between predicted and measured power increase for a Sea King helicopter with unprotected rotors. There are fewer cases, but the agreement is generally good, with the exception of the cases with OAT of -6°C and -7°C.

Figures 20 to 22 show comparisons between prediction and test for the data reported in Reference 12 for a model main rotor in the NASA icing research tunnel. Figure 20 shows comparisons for the change in torque coefficient with icing time for four ambient temperature conditions spanning the range from -30.5°C to -15.2°C. The correlation is generally good particularly at the coldest condition when only rime ice is expected to form on the rotor. As the OAT increases (less

negative), the program predicts slightly higher values for torque increase than measured. This is attributed to the increase in the extent of glaze ice on the rotor. Note that at present there is no allowance in the predictions for the effects of ice shedding which could reduce the magnitude of the predicted torque increase.

Figure 21 shows similar comparisons over the temperature range -15.2°C to -3.7°C. The tendency for the program to predict a slightly higher value for the torque increase is repeated. Note however, that in cases (a) and (b) of Figure 21 the scale maximum on the vertical axis has been reduced by a factor of four compared to that used for cases (c) and (d). The actual torque increase in the former cases is therefore small and the difference between prediction and measured is probably similar to the accuracy to which the rotor could be flown in the icing wind tunnel.

The final set of comparisons given in Figure 22 show the effect of LWC on the torque increase. Five cases are shown with LWC varying from 0.34 g/m³ to 1.24 g/m³. The correlation is generally good with the program predicting slightly higher values for torque increase.

Overall, the current development standard of the program is considered to predict well the trend of the power increase with ambient conditions. Some differences are shown between predicted and measured power which it is hoped can be removed or at least reduced by further development of the program.

CONCLUSION

RAE has developed an extensive analysis capability for the prediction of two-dimensional ice accretions and the protection of aerofoils against icing. As part of a continuing international collaborative activity with the United States and with France, the development of a 3D ice accretion code is being considered as an activity for future work. RAE is currently developing an analysis capability for helicopter performance in icing, using the correlation approach to obtain the ice degraded aerofoil performance. It is hoped that it will not be too long before the necessary capability is developed to enable the prediction of the degraded aerofoil section characteristics using CFD methods. This represents the missing link preventing a fully theoretical treatment of aircraft icing.

REFERENCES

1. Gent, R.W.: Calculation of water droplet trajectories about an aerofoil in steady, two-dimensional, compressible flow. RAE TR 84060, 1984.

2. Gent, R.W.: TRAJICE2 - A combined water droplet trajectory and ice accretion prediction program for aerofoils. RAE TR 90054, 1990.

3. Cansdale, J.T; Gent, R.W: Ice accretion on aerofoils in two-dimensional compressible flow. RAE TR 82128, 1983.

4. Gent, R.W.; Markiewicz, R.H.; Cansdale, J.T: Further studies of rotor ice accretion and protection. Vertica, vol. 11, No. 3, pp. 473-492, 1987

5. Gent, R. W.: HOVACC - an aerofoil ice accretion prediction program for steady, two-dimensional, compressible flow conditions. RAE TR 88052, 1988.

6. Gent, R.W.: HRB1D - A computer program for the design and assessment of electrothermal rotor deicing systems. RAE TR 88047, 1988.

7. Gent, R.W.; Beauchamp, A.R.: Measurement of drag increase due to ice accretion on aerofoils of NACA0012 and RAE9645 section. RAE TR 87013, 1987

8. Young, C.: A basic approach to predicting the power required by a helicopter. RAE TR 89043, 1989

9. Flemming, R.J.; Lednicer, D.A.: Correlation of airfoil icing relationships with two-dimensional model and full scale rotorcraft test data. AIAA 23rd Aerospace Sciences Meeting, January 14-17, 1985, Reno, Nevada.

10. Johnson, R.C.; Peterson, A.A; Britton, R.K.; Korkan, K.D.: Analytical determination and experimental comparison of performance degradation on a helicopter main rotor due to ice accretion. Presented at the 44th AHS Annual Forum and Technology Display, Washington D.C, June 1988.

11. Olsen, W.; Shaw, R.J.; Newton, J.: Ice shapes and the resulting drag increase for a NACA0012 airfoil. NASA TM 83556, 1984.

12. Bond, T.H.; Flemming, R.J.; Britton, R.K.: Icing tests of a model main rotor. Presented at the 46th AHS Annual Forum and Technology Display, Washington D.C, May 1990.

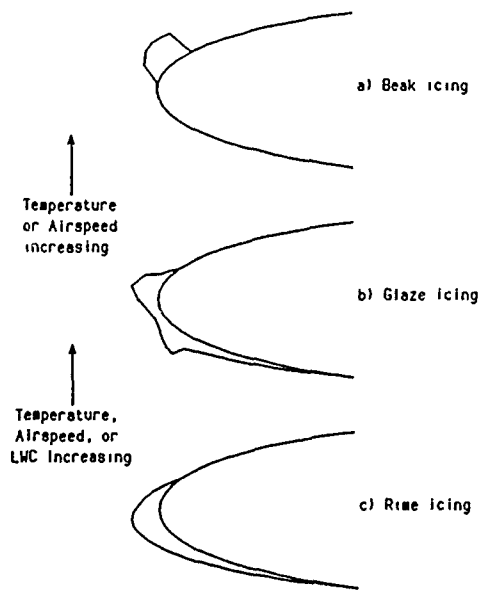

Figure 1. Types of ice accretion

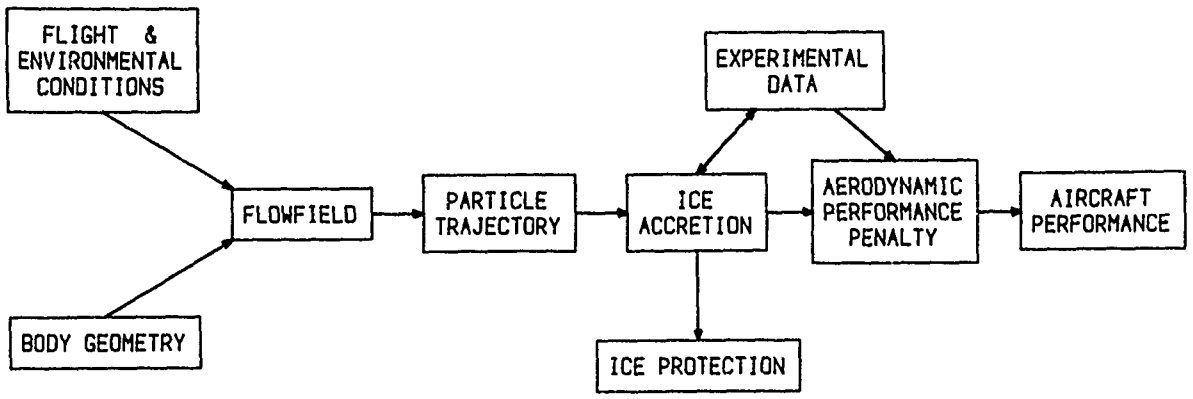

Figure 2. Icing and ice protection analysis methodology

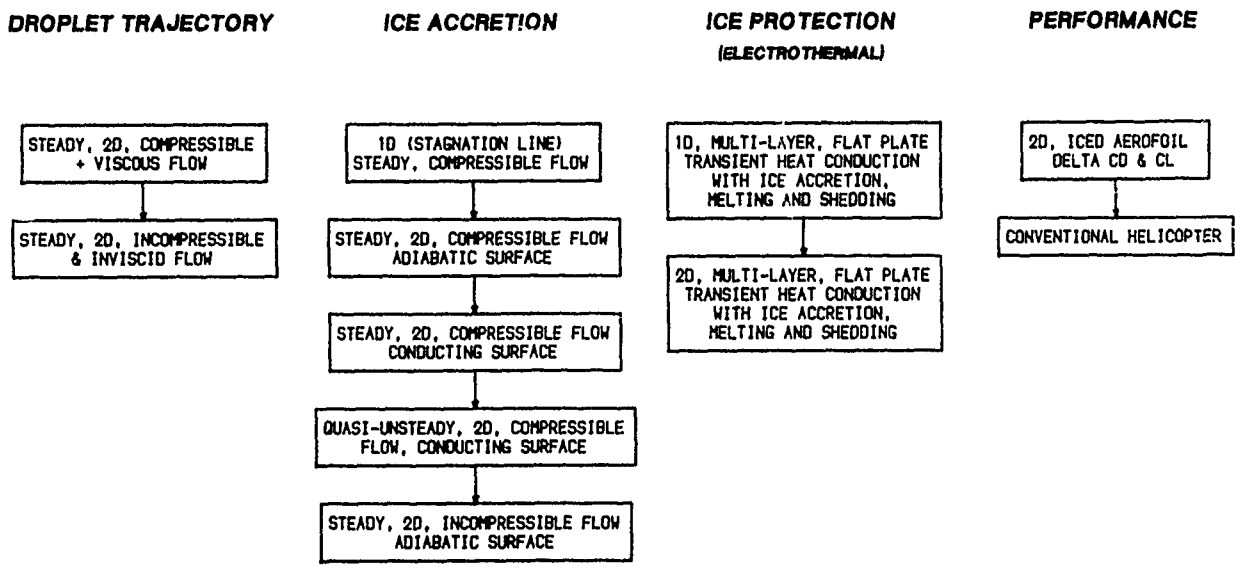

Figure 3. Analyses developed at RAE

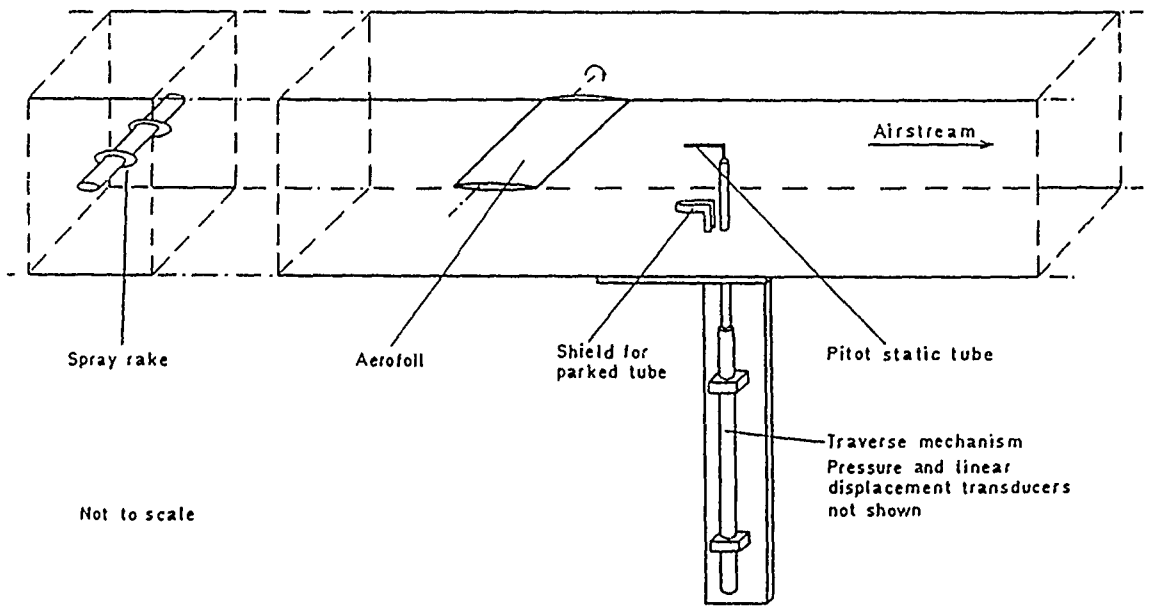

Figure 4. Test configuration

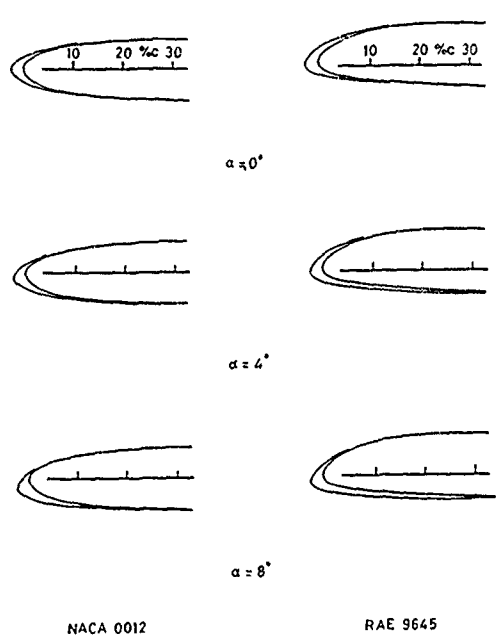

Figure 5. Rime ice accretion profiles

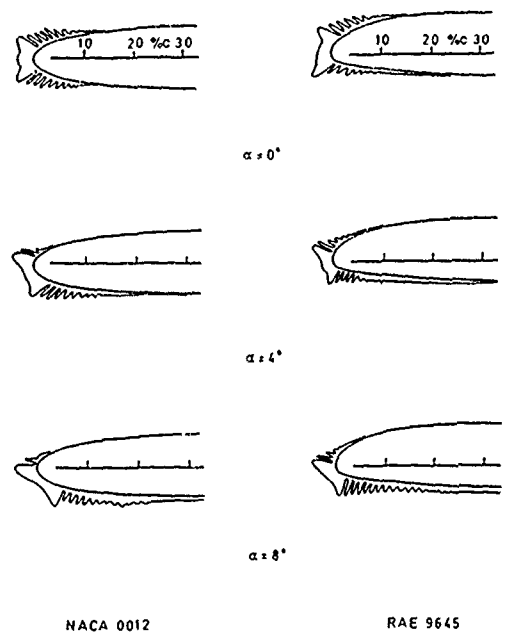

Figure 6. Glaze ice accretion profiles

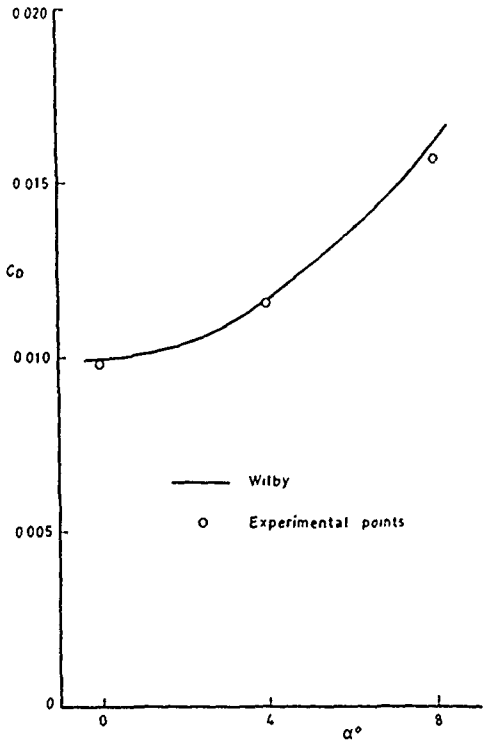

Figure 7. Clean aerofoil drag characteristics; RAE9645

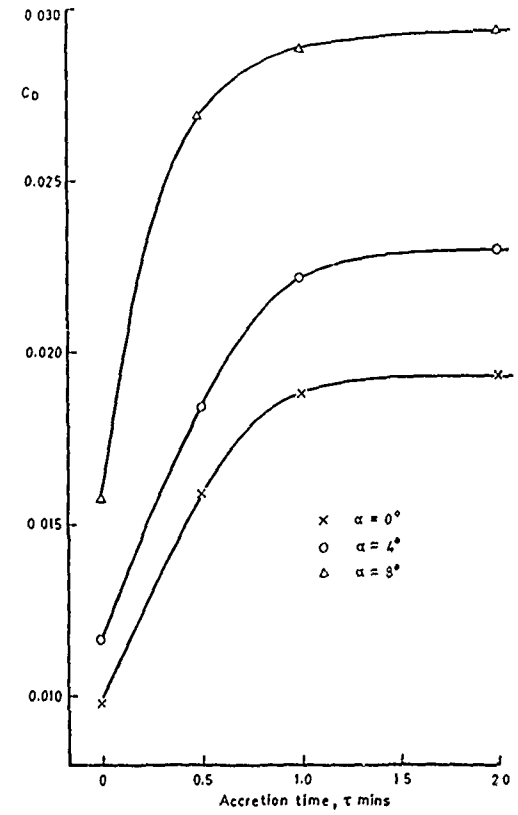

Figure 8. Effect of rime ice accretion on the drag coefficient of the RAE 9645 Aerofoil

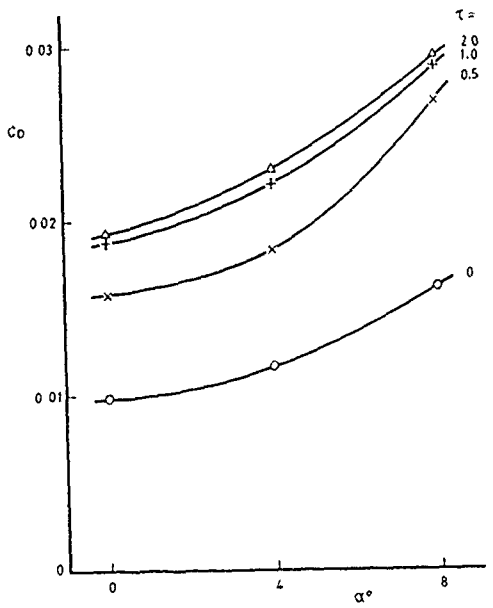

Figure 9. Measured drag coefficients for the RAE9645 aerofoil clean and with rime ice accretion

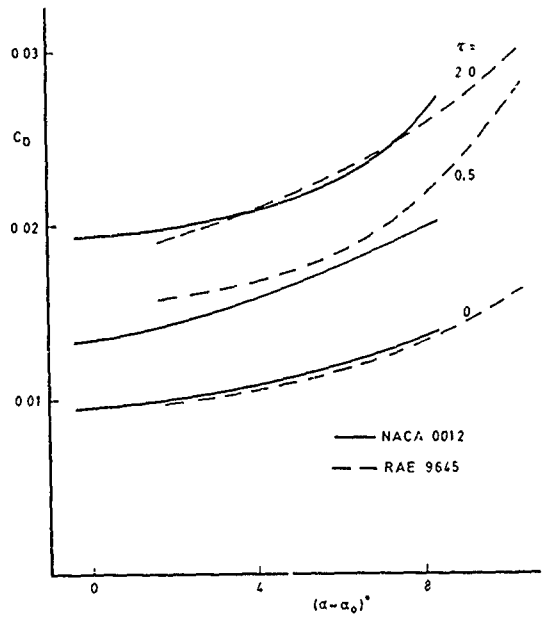

Figure 10. Comparison of drag coefficients for similar lifting conditions, clean and with rime ice accretion

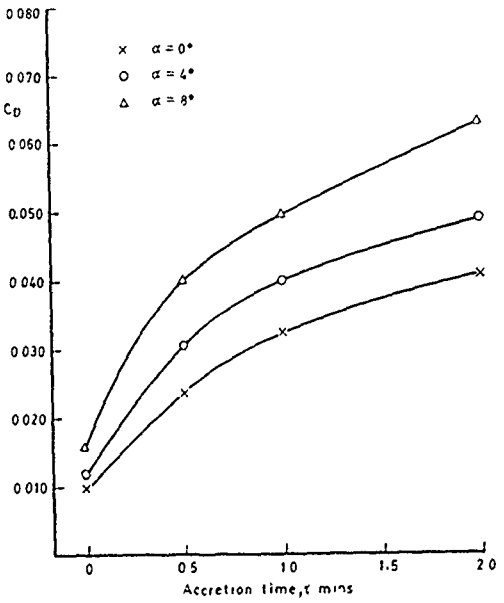

Figure 11. Effect of glaze ice accretion on the drag coefficient of the RAE 9645 Aerofoil

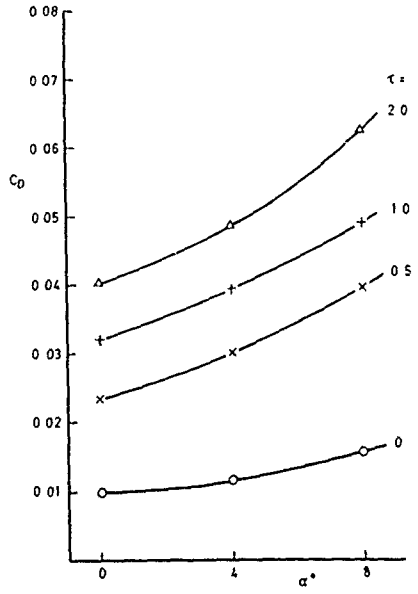

Figure 12. Measured drag coefficients for the RAE9645 aerofoil clean and with glaze ice accretion

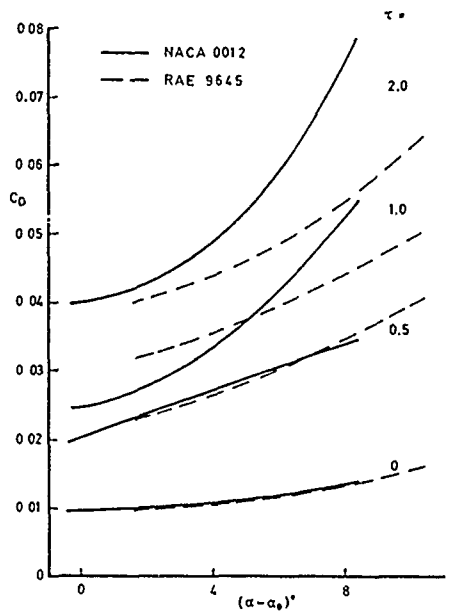

Figure 13. Comparison of drag coefficients for similar lifting conditions, clean and with glaze ice accretion

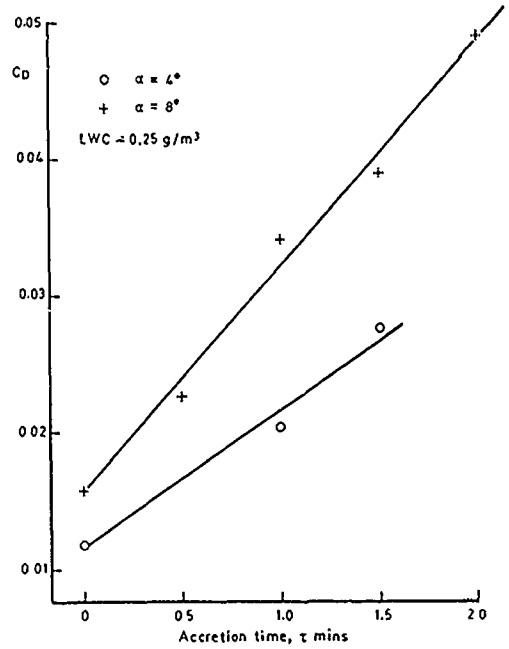

Figure 14. Effect of beak ice accretion on the drag coefficient of the RAE 9645 Aerofoil

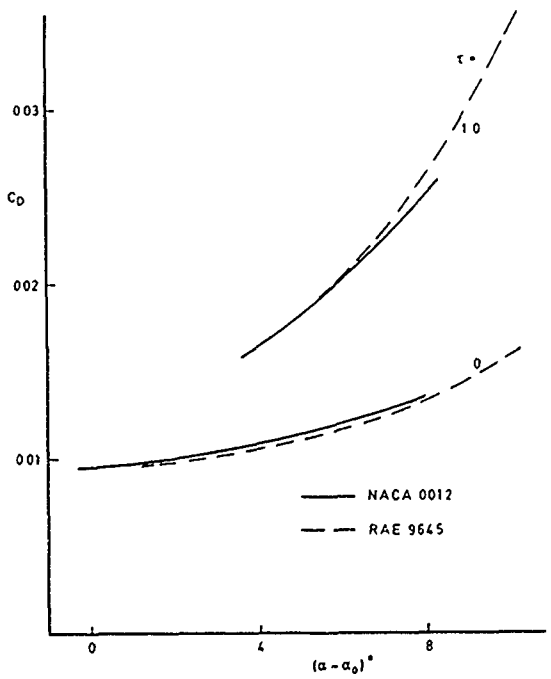

Figure 15. Comparison of drag coefficients for similar lifting conditions, clean and after 1 minute beak ice accretion

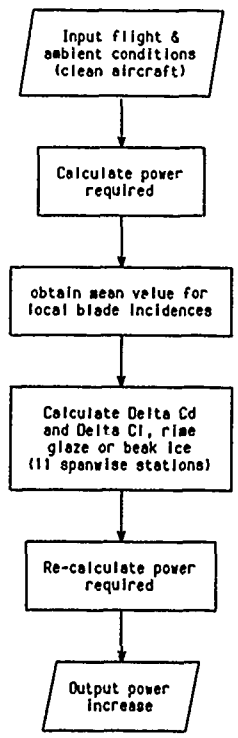

Figure 16. Helicopter iced rotor performance prediction methodology

Assume:

$$\text{Load Factor, } L = \frac{\Delta C_{Dg}}{\Delta C_{Dr}} = f(x_i/c, F, N_{fr})$$

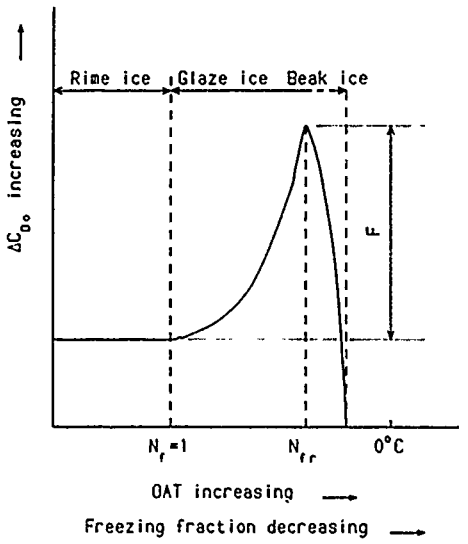

Figure 17. Observed variation in drag coefficient with ambient temperature

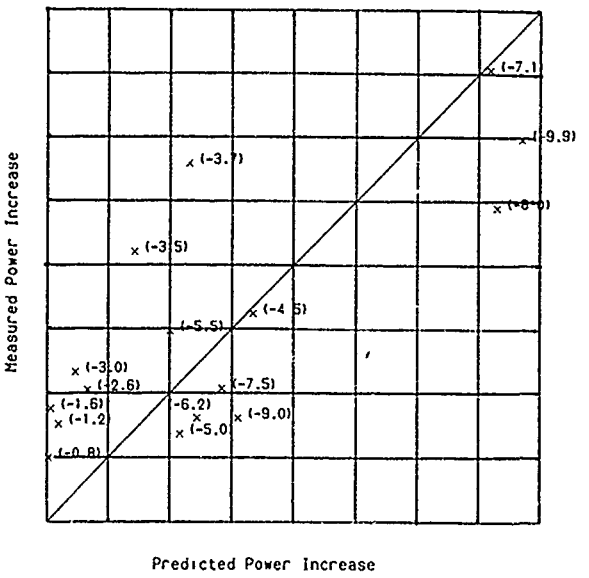

Figure 18. Power increase due to icing - cold rotor; Puma HC Mk1

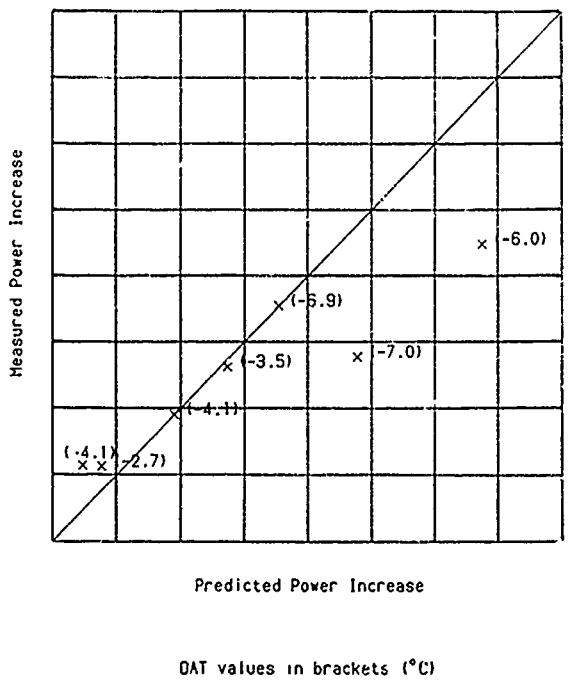

Figure 19. Power increase due to icing - cold rotor; Sea King Mk2

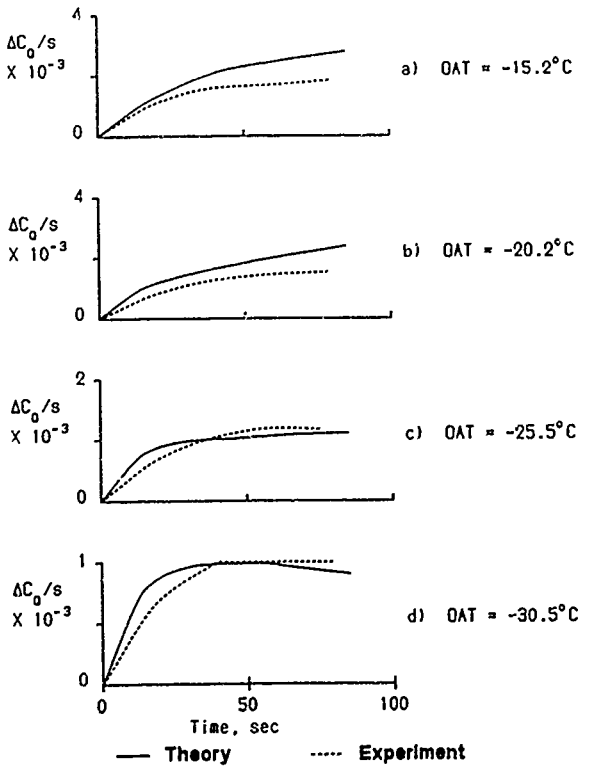

Figure 20. Torque increase due to icing; Model Rotor Effect of Ambient Temperature - Low OAT range

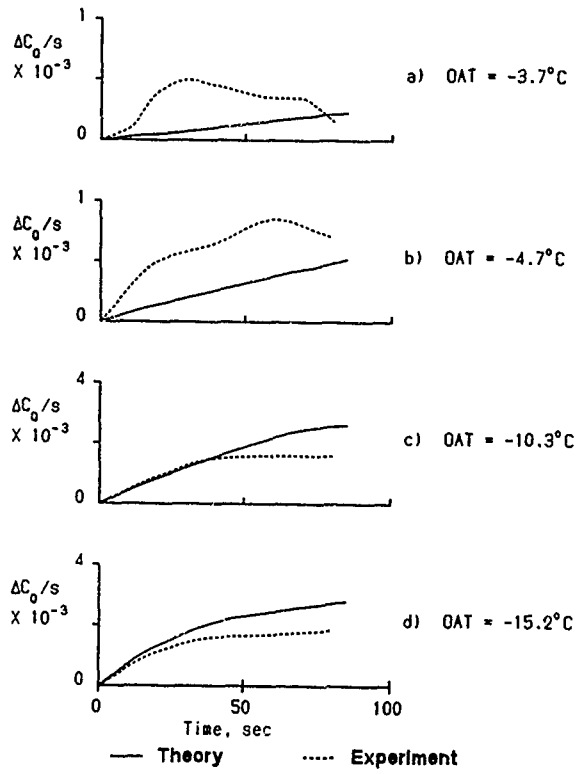

Figure 21. Torque increase due to icing; Model Rotor
Effect of Ambient Temperature - High OAT range

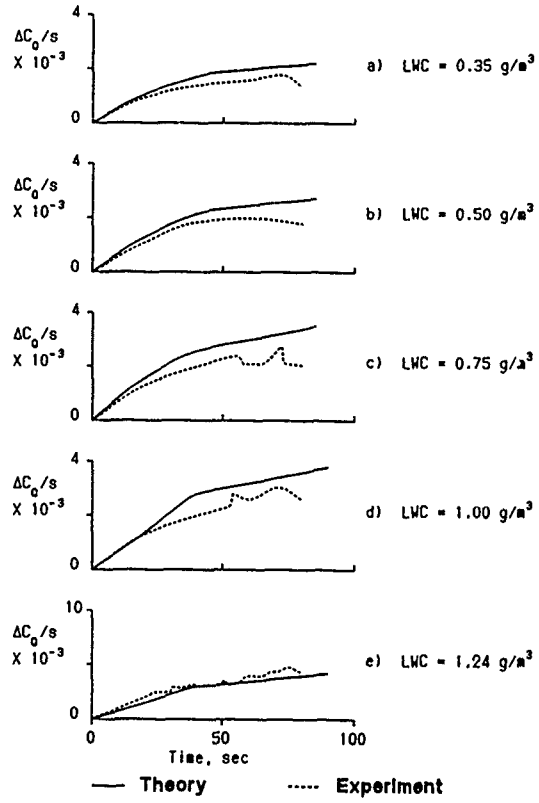

Figure 22. Torque increase due to icing; Model Rotor
Effect of LWC

WIND TUNNEL INVESTIGATION OF A WING-PROPELLER MODEL PERFORMANCE DEGRADATION DUE TO DISTRIBUTED UPPER-SURFACE ROUGHNESS AND LEADING EDGE SHAPE MODIFICATION

R.H. Wickens and V.D. Nguyen
Applied Aerodynamics Laboratory
Institute for Aerospace Research
National Research Council Canada
Ottawa, Canada K1A 0R6

SUMMARY

A wind tunnel investigation has assessed the effects of distributed upper surface roughness, and leading edge ice formation on a powered wing propeller model.

In the unpowered state, it was found that roughness reduces the lift slope, and maximum lift by 30 to 50 percent, depending upon particle size and Reynolds number. The leading edge region is especially sensitive to these disturbances, however removal of the roughness over a small portion of the nose restored the wing to close to its original performance.

The application of power to the wing, with an increase of slipstream dynamic pressure increases the lift slope and maximum lift; however this benefit is lost if the wing is roughened. Subtraction of the propeller reactions indicated that the slipstream interaction accounted for half the lift increase, and also resulted in reduced drag for the clean surface. This drag reduction was removed when the wing was roughened, indicating that the degradation of wing performance due to roughening is relatively greater when a slipstream is present, compared to the unpowered wing.

Leading edge ice accretion causes similar large losses in lift and increases of form drag although a comparison of the two types of contamination showed that leading edge ice produces a smaller reduction of lift slope prior to flow separation. In both types of contamination, Reynolds number is important, and emphasizes the necessity of testing under near full-scale conditions.

List of Symbols

C_L	lift coefficient	$\frac{L}{\frac{1}{2}\rho V^2 S_w}$
C_D	Drag coefficient	$\frac{D}{\frac{1}{2}\rho V^2 S_w}$
C_m	moment coefficient	$\frac{M}{\frac{1}{2}\rho V^2 S_w c}$
c	wing chord	
S_w	wing area	
C_{Tp}	propeller thrust coefficient	$\frac{T_p}{\rho N^2 D^4}$
C_{Np}	propeller normal force coefficient	$\frac{N_p}{\rho N^2 D^4}$
C_{mp}	propeller pitching moment coefficient	$\frac{M_p}{\rho N^2 D^5}$
C_c	wing chord force coefficient	$\frac{C_c}{\frac{1}{2}\rho V^2 S_w}$
C_{Do}	parasite drag coefficient (unpowered)	

C_{L_s}, C_{D_s}, C_{m_s} wing coefficients with the propeller reactions removed

C_s leading edge suction coefficient

D propeller diameter

N propeller rotation speed (RPS)

J propeller advance ratio $\frac{V}{ND}$

k roughness particle size

INTRODUCTION

Recent flying accidents resulting from adverse weather conditions in the form of freezing rain or snow, have focussed attention on the degradation of aerodynamic surfaces. Investigations of the effects of uniform roughness on airfoils shows clearly that stalling is premature, loss of maximum lift can be as high as 50%, (depending on Reynolds Number) and form drag reaches very high levels at angles of attack below normal clean wing stall.

The effect of upper surface roughness on complete aircraft configurations is less well known; however there is a long history of aircraft accidents related to flight in icing conditions, and several recent incidents involving swept-wing jet aircraft have highlighted the problem. In these situations it was observed that early flow separation and stalling was a characteristic result of ice and snow contaminants on the wing. Flow breakdown was accompanied not only by a loss of lift and an increase of drag, but also wing-dropping as a result of outer panel flow separation and wing tip stall prior to inboard wing stall. Experimental data on simulated upper surface contamination on a swept-wing model of a typical jet-commuter aircraft have confirmed what was suspected from flight experience, and have also demonstrated that large changes of trim will occur on the full-scale aircraft.

Figure (1a) from ref. (1) shows, for various two-dimensional airfoil configurations, losses in maximum lift and reductions the angle of attack for maximum lift that result from simulated hoar frost contamination. Large increases of drag also occur, and are attributed to form drag after separation and stall. Early wind tunnel tests on the effects of upper surface roughness on maximum lift of airfoils is also reported in reference (2), for conventional airfoils. This data shows that the loss of maximum lift is critically dependent on Reynolds Number, and also roughness particle size. For example at Reynolds Number greater than 10 million (typical for takeoff) the loss in maximum lift approaches 50% of the clean airfoil value. In comparison, at the Reynolds number values typical of low speed wind tunnel testing the loss of maximum lift is much lower, thus highlighting the dangers of assessing wing contamination effects at other than full-scale conditions. There is little or no corresponding data for modern, supercritical airfoil shapes.

Wing drag also increases as a result of surface roughness. This is due to an increase in skin friction in unseparated flow, but mainly from increases in form drag after premature separation has occurred. If the roughness elements protrude above the laminar sublayer of the turbulent boundary layer in attached flow, the result is an increase of skin friction and the production of more turbulence. Increasing the Reynolds Number aggravates this effect and increases the probability of separation particularly around the nose, since the sub-layer will be thinner. This would presumably explain the higher losses in maximum lift incurred at high Reynolds number.

If the roughness height is large in comparison to the laminar sub-layer (as would be the case for freezing rain or ice accretion) then the frontal drag of these elements determines the average tangential force, and their shape, orientation and distribution become important, and increased turbulence and dissipation in the thickened boundary layer will lead to premature flow separation and stall.

Propeller-driven aircraft, where the slipstream passes over the wing surface, are thought to be less sensitive to the effects of upper surface contamination compared to the typical swept-wing configuration. This is due in part to the effects of sweep, that reduce the wing lift-slope, compared to a straight wing; and the effects of slipstream interaction, that augment span loading locally, increase wing lift slope, and also delay flow separation at high angles of attack. Thus the rotation angle on takeoff of a straight wing propeller-driven aircraft is likely to be less than that for an equivalent swept wing aircraft, with no slipstream interaction, and the likelihood of a premature stall may not arise.

Notwithstanding this apparent beneficial comparison, the propeller-driven aircraft may still experience significant losses of lift and large increases of drag if premature flow separation occurs when the wing upper surface is

contaminated. Figure 1b from Ref. (1) for the Fokker F-27 turboprop transport wind tunnel model indicates however, that smaller losses in maximum lift may be expected from a contaminated wing, compared with the airfoil test results of Figure (1a). The corresponding reduction in critical angle of attack is also small and in some cases positive, and was attributed to a significant change in the wing-slipstream stall pattern. The extent to which the slipstream may remain attached to the wing surface is unknown but its influence may affect the overall stall pattern even when roughened by ice.

In view of the unknown nature of the complex interactions of wing boundary layer, propeller slipstream and distributed roughness, and the lack of experimental data, it was decided to use the half-wing propeller model of reference (3) to obtain some preliminary data on the effects of upper surface roughness in a slipstream and also the effects of typical in-flight ice accretion shapes on the leading edge. The utility of the data to aircraft design or performance estimation will be limited; the model configuration is not typical of current propeller transport configurations, and the test Reynolds Number was low (Re = 1.3 million).

MODEL

The general arrangement of the rectangular, unswept half-wing model is shown in figure 2. The wing, having a NACA 4415 airfoil section, was untwisted and was equipped with a 30 percent chord plain flap extending along the semi-span. The aspect ratio was 4.85. A nacelle containing a 20 hp water-cooled induction motor was underslung on the wing approximately one chord length above the floor. The four-bladed propeller was located 70% chord in front on the leading edge and was equipped with an adjustable pitch-setting mechanism. The two foot diameter propeller was the same model used in the investigations reported in references (3) and (4). In these reports full aerodynamic characteristics of the isolated propeller and also the interference effects of this wing model are reported. The relevant geometry of the propeller is listed as follows:

Propeller

Diameter	2.0 ft.
No. of blades	4
Solidity	0.127
Blade section at 0.75R	65 Series (design Cl = 0.7)

The complete model installation Figure, (2a), (2b), was mounted on the wind tunnel balance at the 30% chord location. The propeller motor was supported in a slender nacelle but did not have a separate thrust or normal force balance in this experiment. The wind tunnel balance thus measured the combined effects of wing and propeller reactions.

EXPERIMENTAL PROCEDURE

The wing was pitched through an angle of attack range from 6 to 26 degrees. A complete stall and flow breakdown was not achieved with this model due probably to the effects of the low aspect ratio, Reynolds number and the half-model configuration. Maximum lift was achieved however, and this was used as a basis of comparison for the effects of roughness. Model lift, drag and pitching moment were measured on the wind tunnel balance. Pitching moment was taken about the 30% chord location. The measured forces include the propeller reaction comprised of thrust, normal force and pitching moment. The test Reynolds Number was 1.3 million (2.3 million for the unpowered wing only).

Propeller static thrust was measured on the wind tunnel balance under wind-off conditions. At the desired test conditions thrust was varied by adjusting the blade pitch settings to a value that corresponded approximately to the take off thrust coefficient of a typical turbo-prop aircraft. Under wind-on conditions at a dynamic pressure of 25 psf, and a propeller rotational speed of 3000 rpm, this thrust coefficient C_{Tp} was estimated from the data of ref. (5) to have a value of 0.115. Propeller thrust and normal force change with incidence, and the variation of these quantities, used in other section of this report, were also determined from the data of Ref. (5).

SIMULATED ROUGHNESS

Roughness, in the form of a uniform distribution of carborundum grit was applied over various portions of the chord. Three grades of standard grit were used: 150(.0041"), 80(.0083"), 46(.0165"). These correspond approximately to average roughness heights of .03", .06", and .11" respectively on a full-scale wing of 10 ft. chord. The roughness height/chord ratios for this test were 0.000227, .000461 and .000916 respectively. In addition a heavy grade (50 grit) of commercial sandpaper was applied to the wing surface. The roughness height and concentration of this application was considered to be significantly greater than the standard grit particles applied manually to the wing surface.

The roughness was applied initially to the upper surface from the leading edge stagnation region to the flap hinge line. Since only the forward portion of the chord was found to be sensitive however, most of the investigation was performed with only the first 25-30% of the chord roughened and the results presented in this report are for 30% coverage. The density of application was not varied or determined precisely.

In addition to distributed roughness application, shapes representing rime and glaze ice accretions were applied to the wing leading edge. The shapes were similar to those of ref. (6) and are shown in Figure (2c).

PRESENTATION OF RESULTS

Unpowered Wing

The unpowered wing data presents the effects of various grit sizes (46, 80, 150) deposited on the upper surface, and also a heavy grade of sandpaper attached to the upper surface. The amount of coverage along the chord corresponded to about 30%. Tests were also done at a higher Reynolds number (2.3 million), for the unpowered wing only.

Figure 3 shows the behaviour of Cl, Cd, and Cm for the unpowered wing in the clean and contaminated states for standard grit sizes at the test Reynolds number of 1.3 million, and for heavy sandpaper at Re = 2.3 million. The main effect of wing contamination is a reduction of lift slope and maximum lift by amounts that range between 20 - 25% for a Reynolds number of 1.3×10^6, and larger losses for the higher Reynolds number. The angle of attack for maximum lift (clean) was 20 degrees; this was reduced to about 15 degrees with contamination on the upper surface.

Drag is also increased at angles of attack below stall, and large increases of form drag occur when the flow separates. In general these losses, particularly at maximum lift, increase with particle size, with the highest loss occurring where sandpaper was applied to the wing (Fig. 3a). All reductions of lift increase with increasing Reynolds number as Reference (2) points out, and this is also the case in this test. The effect of roughness on pitching moment was small at angles of attack below stall; there appears to be a slight nose-up shift of the Cm versus α curve, and its magnitude increases slightly with grit size. The application of rough sandpaper at the high reynolds number increases this nose-up shift slightly.

The most significant parameters appear to be roughness size and Reynolds number, however it was observed that when a small portion (15%) of the leading edge was cleaned off, wing lift and drag was restored to close to its clean performance, however moment was not fully restored.

Powered Wing

With the blades installed and set to the angle for take-off thrust, the propeller was operated wind-on at an advance ratio of 1.4. This was much higher than a typical takeoff advance ratio, however it was the only way a high thrust coefficient could be achieved due to current and temperature limitations of the motor. As mentioned before propeller forces were not measured separately, however both thrust and normal force were inferred from the isolated propeller data of references (3) and (5) for further analysis of these results.

Figure (4) shows the effects of propeller thrust on lift, drag and pitching moment on the unpowered clean wing at a Reynolds number of 1.3 million. A higher Reynolds number test condition was not possible in the powered tests due to limitations of the motor. The application of power with the resulting slipstream interaction results in an increase of both the lift slope and the maximum lift by about 25%, and stalling angle is increased by about 4 degrees. The drag polar is shifted by an amount that corresponds to the thrust force plus a leading edge thrust on the wing due to increased suction. The drag equivalent of the estimated propeller thrust has a value of about 0.085, which, when subtracted from the total wing force at zero lift, apparently produces a negative drag or thrust on the wing. This effect, known as the "Squire Effect", has been alluded to before (Ref. 7), and is attributed to the effects of flow rotation in the slipstream.

The pitching moment shown in figure (4c) exhibits an increased nose-up tendency due to the effects of the propeller and slipstream flow. The slope of the pitching moment curve vs α is increased with the application of power and beyond maximum lift there is a large nose-down shift of the pitching moment. The large change in moment is attributed mainly to the propeller normal force acting about the wing centre of rotation (Figure 2).

Effects of Roughness - Powered Wing

With roughness applied to the wing upper surface there appears to be a loss of lift slope and maximum lift of about 25 to 35% depending upon roughness element size. (Figure (5)). In effect, the benefits of powered lift,

resulting from slipstream interaction, is lost. Drag also increases as the flow separates prematurely, and there also is an increase in the parasite drag at zero lift due to roughness, and increased dynamic pressure in the slipstream. The effect of roughness on wing pitching moment is small at angles of attack below stall, ($\alpha < 10°$) but the moment becomes more nose down as roughness size increases.

The application of the heavy sandpaper roughness further deteriorated the wing performance under power at the Reynolds number of 1.3 million. Maximum lift decreased slightly, as did the lift slope; although the stall was not sharply defined. Drag also increased near zero lift but the pitching moment did not change significantly, although the tendency continued to be nose-down.

A comparison was made between the powered and unpowered wing drag polars to show the relative effects of roughness with and without power (Figure 6). It is clear from these graphs that roughness, especially when it reaches the heavy proportions of sandpaper coverage, has a much more adverse effect on drag of the powered wing than for the unpowered wing in uniform flow. The lift curves exhibit about the same degree of degradation of performance between powered and unpowered configurations. The pitching moment change appears to be smaller when the wing is powered and is accompanied by an increase in slope (Cm vs alpha) and a small displacement in the nose up direction.

In order to simulate the scrubbing action of the slipstream, a portion of the roughness was removed at the propeller location. This resulted in a modest improvement of performance.

Wing-slipstream characteristics

In order to separate the propeller from the total wing forces, and to compare unpowered wing characteristics with those with the wing immersed in a slipstream, the isolated propelier data were estimated from Reference (5) and (Figure 7) and were removed from the wind tunnel balance data as follows:

$$C_{L_s} = C_L - (2/J^2)(D^2/S_w)[C_{T_p} \sin\alpha + C_{N_p} \cos\alpha] \quad (1)$$

$$C_{D_s} = C_D - (2/J^2)(D^2/S_w)[C_{T_p} \cos\alpha - C_{N_p} \sin\alpha] \quad (2)$$

$$C_{M_s} = C_M - (2/J^2)(D^2/S_w)\left[C_{N_p}\left(\frac{\bar{x}}{c}\right) + C_{T_p}\left(\frac{\bar{y}}{c}\right) + C_{M_p}\left(\frac{D}{c}\right)\right] \quad (3)$$

No attempt was made to correct the propeller data for the blockage and upwash effects of the wing; however the comments of Ref (8) and the experimental data of Ref (4) suggest that these interactions may be small.

The powered cr n wing characteristics with the propeller reactions removed are shown in Figure (8). The lift curve lies between t owered and unpowered curves, suggesting that the slipstream interaction contributes about half of the powered lift increment to maximum lift, and lift-slope.

The drag polar (Figure 8) indicates significantly less drag due to the effects of the slipstream flow, particularly at low values of C_L (< 0.4), and near zero lift the wing actually produces a thrust. This has been attributed to the effects of slipstream rotation (Ref. 7), with the wing acting as a flow straighener. This result should probably be taken with caution, however, since no direct measurement of propeller thrust or normal force was available.

There appears to be a nose-down change in pitching moment when propeller forces are removed, since neither thrust or normal force are contributing (Figure 8c). The slipstream interaction evidently produces a lesser slope of the Cm vs α curve, and more nose-down moment, compared with the unpowered wing. A partial explanation of this change is given in Reference 4, and is attributed to changes in chordwise pressure distribution over the region of the wing covered by the slipstream.

Slipstream Interaction - Roughness

The loss of performance due to distributed roughness for the wing-slipstream interaction, appears to be somewhat larger than that for the unpowered wing in steady uniform flow. This may be due to the high thrust coefficient of this test, and the resulting augmentation of local pressures on the wing. Figure (9) shows lift ,drag and moment for the unpowered wing and for the wing immersed in a slipstream. Also shown is a shaded boundary that indicates the changes in drag due to increasing roughness in each case. The shaded areas in both graphs represent the maximum loss incurred by distributed roughness of varying grit size, including the heavy sand paper application. The negative drag generated on the wing near zero lift (Figure 9b) is all but removed by the action of the contamination on the nose and upper surface of the wing. In contrast the unpowered wing incurs a slightly lower drag loss due to roughness. At a lift coefficient Cls of about .36, the net drag is zero on the clean powered wing. For values of lift greater than this, drag rises rapidly, and eventually exceeds that of the unpowered wing since thrust is

CHORD FORCE C_C 1.6 DRAG C_D FIGURE

now no longer contributing a force in the streamwise direction and lift is reduced by the amount of the propeller normal force contribution. The effect of increasing roughness in both cases increases drag, particularly before stall.

The propeller contribution to pitching moment is mostly unstable (i.e. nose up). Therefore, removal of the propeller forces makes Cm more negative, and decreases the slope of the Cm vs α curve. The changes to pitching moment are relatively smaller when roughness is applied to the wing (Figure 9) compared to the clean condition. The slipstream interaction on the clean wing results in a slightly more stable pitching moment curve (Cms vs α) compared with the unpowered wing. The application of roughness causes, in both cases, a loss of stability in the pitching moment curves.

Leading edge ice accretion

In addition to uniform roughness on the wing upper surface, tests were also made with modifications to the leading edge that represented rime and glaze ice accretion (Figure 2). The data shown in Figure (10) for the unpowered wing show that such gross changes to the leading edge profile cause losses of maximum lift in the 30 to 50 percent range. Reynolds number is important and a further reduction of maximum lift of 15 to 20% will occur when reynolds number is increased to 2.3 million. Similar significant changes to pitching moment also arise from these leading edge shapes, particularly at high Reynolds numbers.

With the application of power, lift slope and maximum lift are increased but the wing performance is well below normal and the drag polars indicate high drag levels at all lift coefficients. Figure (11) shows a comparison between uniform contamination and leading edge accretion of heavy rime ice, for the drag polars and pitching moments of the ice-contaminated wing for the powered configuration. Leading edge ice results in less reduction of lift slope before stall, but a larger lift loss after stall.

Figure (11d) shows the effect of a slipstream interaction on the wing lift and drag for a medium and heavy leading edge rime accretion. As with distributed roughness, leading edge ice contamination effectively removes the benefits of slipstream flow rotation.

Chord force and leading edge suction

The effective performance of an airfoil or wing depends on the production of negative pressures along the leading edge, and a leading edge suction force that ensures that the aerodynamic force becomes normal to the relative wind. The determination of the chord force coefficient C_c and the leading edge suction coeffcient C_s indicate the degree to which lifting efficiency can be achieved.

C_c and C_s can be determined from experimental data as follows:

$$C_c = C_D \cos\alpha - C_L \sin\alpha \quad (4)$$

and for small angles

$$C_s = C_{D_o} - C_c \quad (5)$$

C_c and C_D can also be determined from the parabolic drag polar relationshipo (Ref. 9). Figure 12a shows the relationship between unpowered wing drag C_D and chord force C_c, and the effects of distributed roughness on both parameters, for the unpowered wing. It appears that roughness has a relatively larger effect on drag than on chord force.

Corresponding values of leading edge suction coefficient for the unpowered wing also show the effects of contamination. Below stall C_s is not greatly diminished by contamination around the nose, but drops suddenly beyond maximum lift.

Figure (12c) shows chord force vs. lift coefficient for the powered wing with leading edge ice and roughness, and with the propeller forces removed. The accretion of ice tends to lower the leading edge force at low values of C_{L_s}, but distributed roughness appears to have a more serious effect at higher lift coefficients.

CONCLUSIONS

1) The main effect of distributed upper surface roughness on an unpowered wing is to reduce lift slope and maximum lift by as much as 30 to 50 percent, depending upon roughness size, Reynolds number, and to a lesser extent, coverage.

2) The magnitude of the loss of maximum lift increases with roughness size, and also with Reynolds number and testing of roughened wings should be done at as high a Reynolds number as possible.

3) Roughness increases the parasite drag at zero lift and also results in a premature stall with resulting large increases of form drag.

4) The leading edge region is especially sensitive to distributed roughness regardless of particle size; there is a significant increase in drag and corresponding decrease of leading edge suction at angles of attack below stall. Conversely, removal of the roughness over a small portion of the nose restores the wing to almost clean performance.

5) If the wing is powered and clean, the slipstream interaction increases lift slope and maximum lift by 25 percent, for thrust coefficients appropriate to the take-off condition. If roughness is applied, maximum lift decreases by more than 25%, thus producing a lifting performance somewhat below the unpowered wing in the clean state. This may have significance in the event of an engine failure; the contaminated wing will suffer a further loss in maximum lift in the unpowered state.

6) An attempt was made to isolate the slipstream interaction on the wing by subtracting estimated propeller forces. When comparing the performance of the powered and unpowered wings, it was noted that roughness produced slightly higher losses on the wing immersed in the slipstream.

7) Loss of lift due to an accretion of rime or glaze ice on the leading edge of the wing may reach as high as 50 percent even when the wing is powered, and is sensitive to Reynolds number. Loss of maximum lift is greater for heavy rime ice than for heavy distributed roughness.

LIST OF REFERENCES

1. Wing Tips - Fokker product support division, #14, December 1989.

2. Jones, R., Williams, D.H. - The effect of Surface Roughness on the Characteristics of Airfoils. RAE R&M 1708, Feb. 1936.

3. Nishimura, Y. - An Experimental Investigation by Force and Surface Pressure Measurements on a Wing Immersed in a Propeller Slipstream. Part I: Force and Moment Measurements. NRC-CR-501, March 1968.

4. Nishimura, Y. - Surface Pressure Measurements Part II, NRC LR-525, June 1969.

5. Wickens, R.H. - Aerodynamic Force and Moment Characteristics of a Four-Bladed Propeller Yawed through 120 Degrees. NRC-LR-454. May 1966.

6. Olsen, W., Shaw, R., Newton, J. - The Shapes and the Resulting Drag Increase for a NACA 0012 Airfoil, NASA TM 83556, 1984.

7. Squire, H.B., Chester, W. - Calculation of the Effect of Slipstream on Lift and Drag. ARC R&M 2368, 1950.

8. Durand, Vol II. Aerodynamic Theory.

9. Schlichting, H., Truckenbrodt, E. - Aerodynamics of the Airpiane - McGraw-Hill 1979.

(roughness) As can be seen from

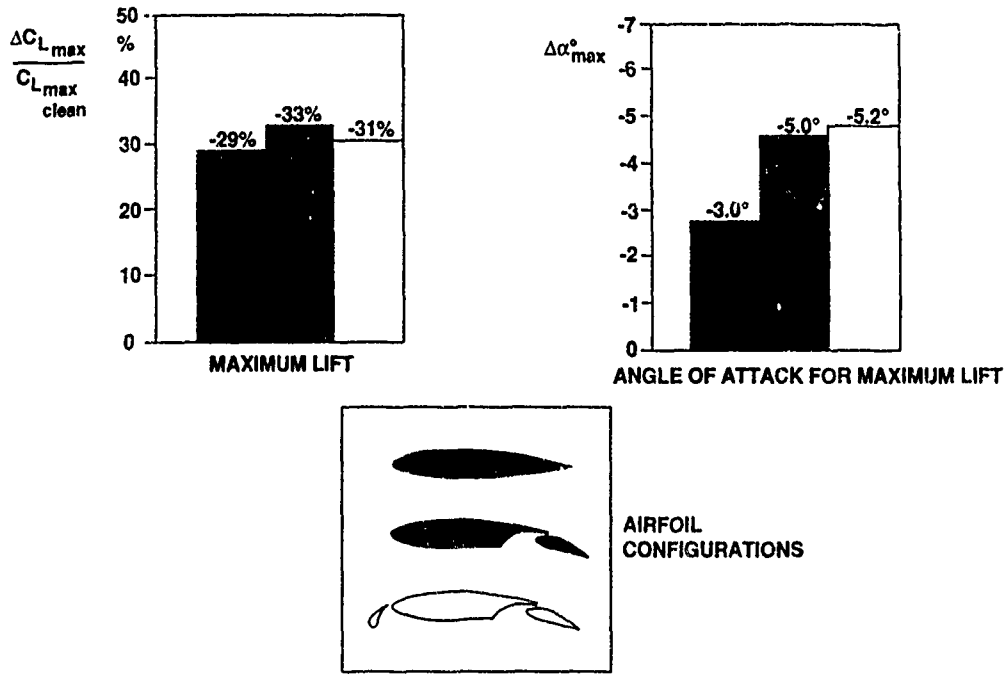

WING-ROUGHNESS-INDUCED LOSS OF MAXIMUM LIFT AND REDUCTION IN ANGLE OF ATTACK FOR MAXIMUM LIFT (REF. 1)

FIGURE 1

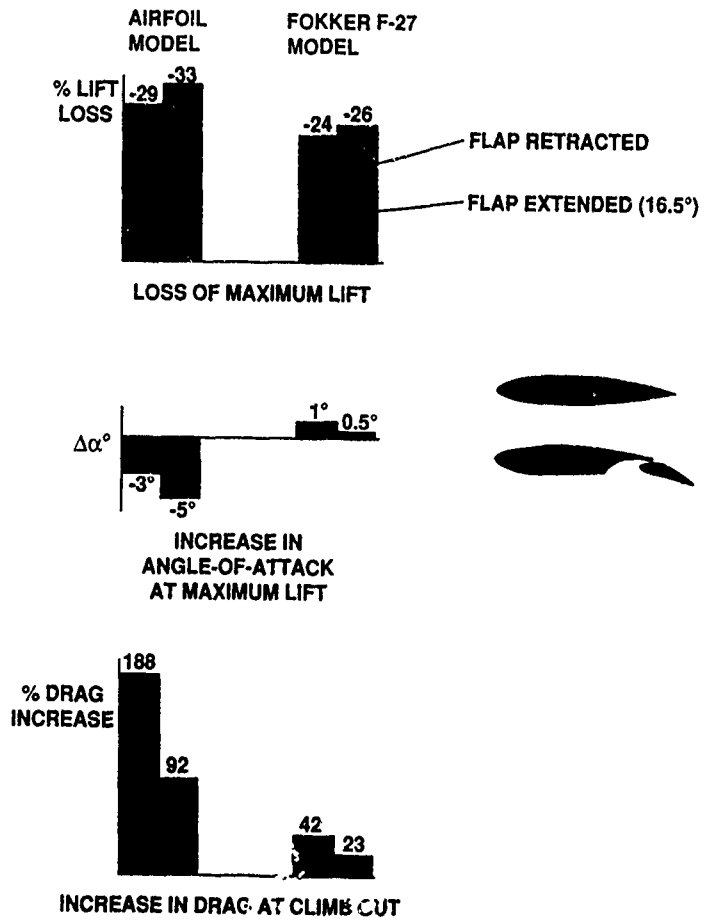

COMPARISON OF LIFT LOSS AND DRAG RISE FOR AIRFOIL AND PROPELLER-SLIPSTREAM MODELS

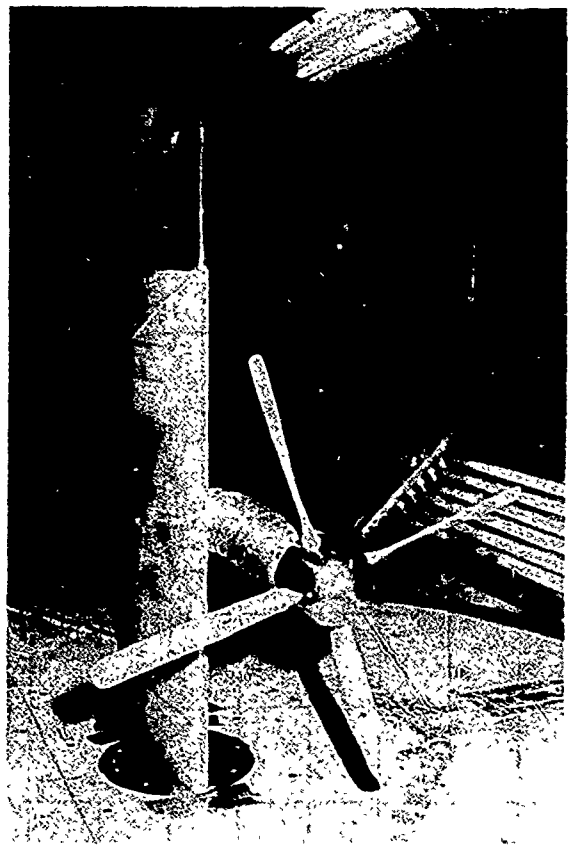

WING-PROPELLER MODEL WITH DISTRIBUTED ROUGHNESS

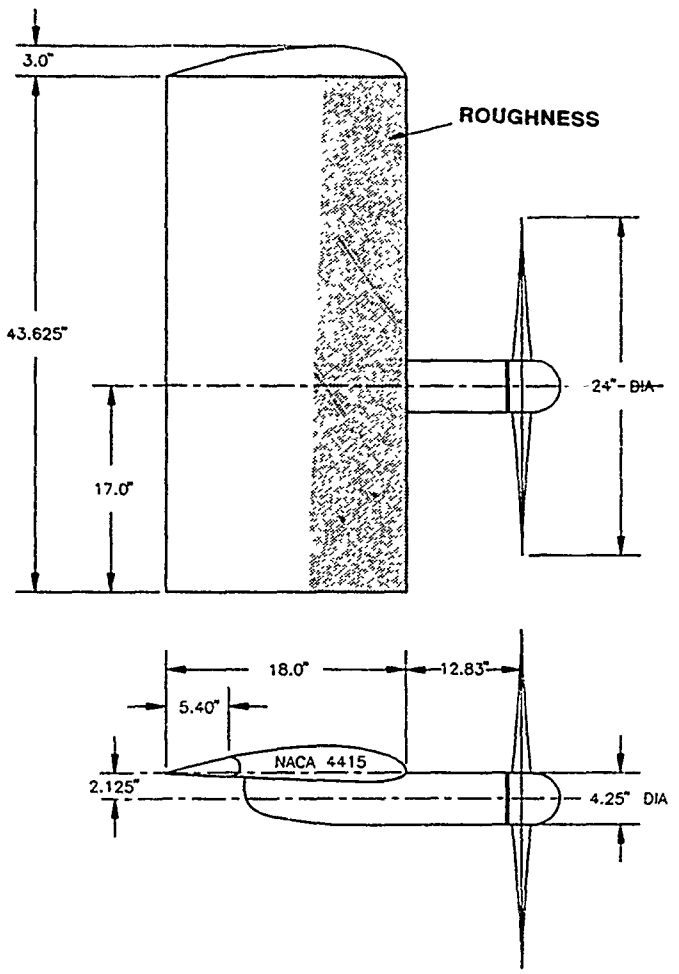

PLAN AND CROSS-SECTIONAL VIEW OF MODEL

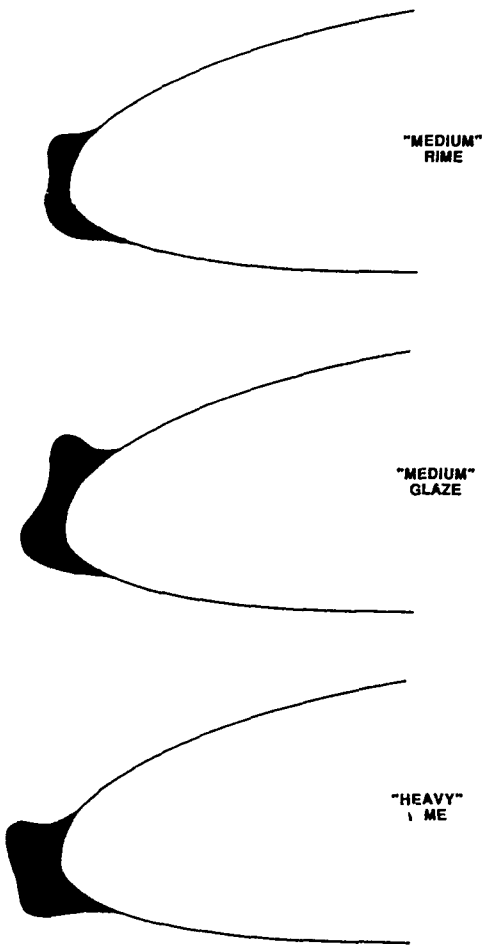

VARIOUS SHAPES OF THE LEADING EDGE GEOMETRY MODIFICATION

FIGURE 2

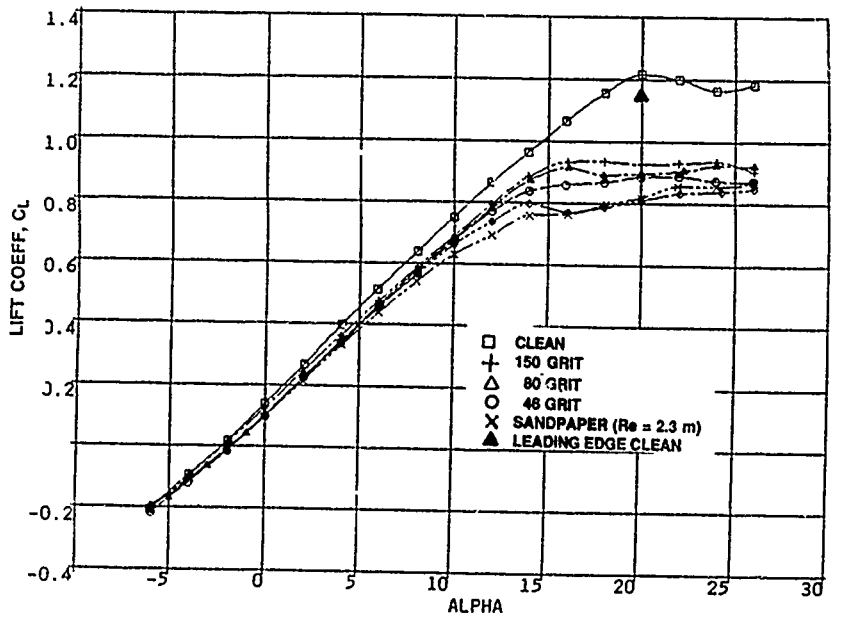

b) DRAG POLAR

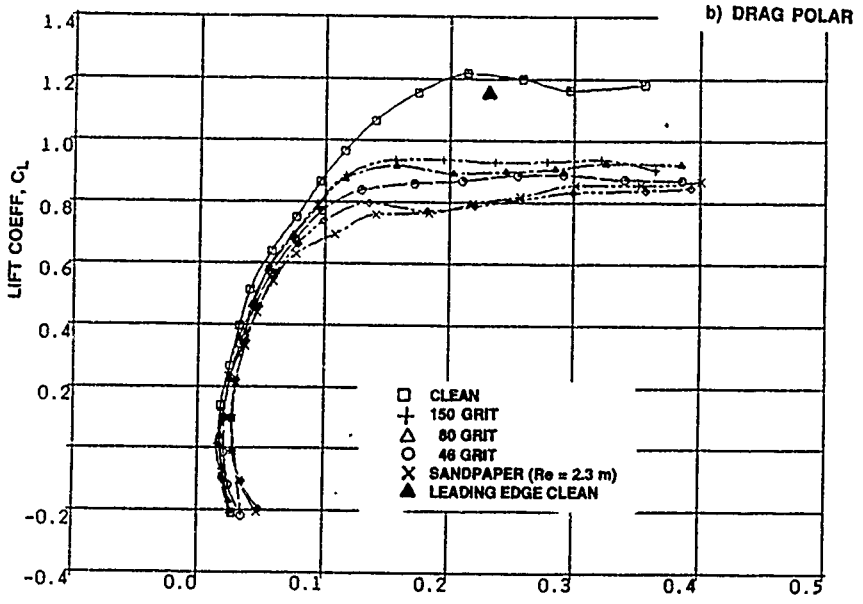

c) PITCHING MOMENT

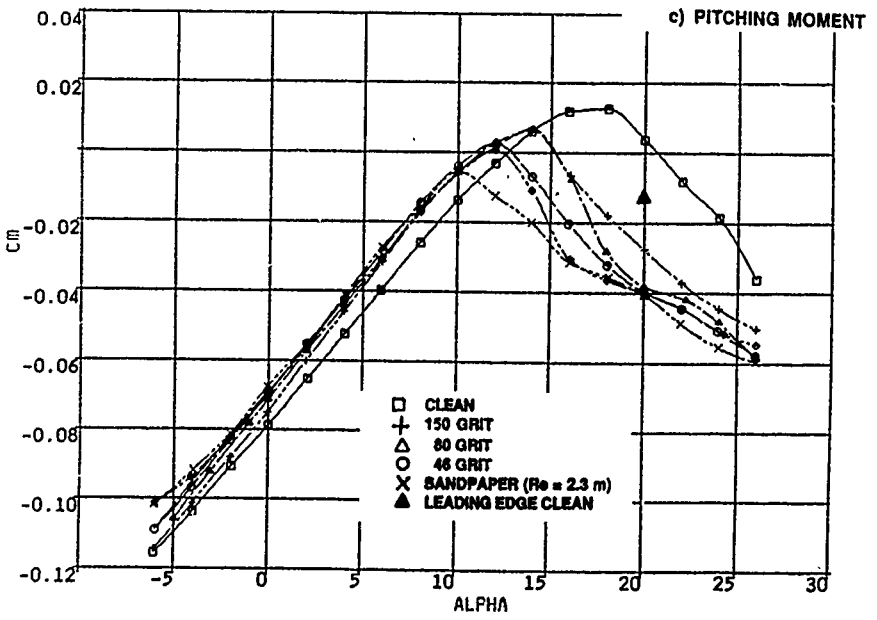

FIGURE 3

EFFECTS OF UNIFORM ROUGHNESS ON UNPOWERED WING PERFORMANCE, Re = 1.3 m, 30% COVERAGE

FIGURE 4

COMPARISON OF POWERED AND UNPOWERED CLEAN WING PERFORMANCE C_{T_p} = 0.115, Re = 1.3 m

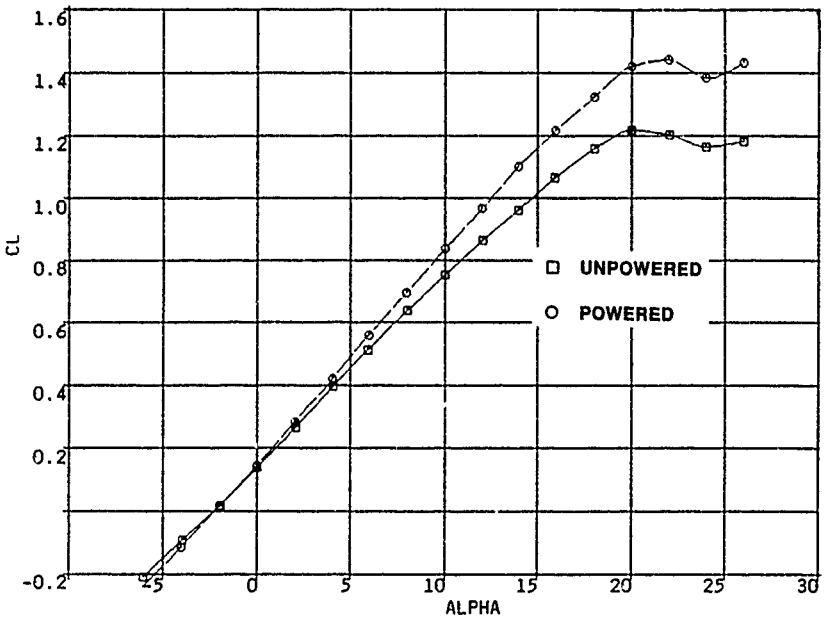

a) LIFT

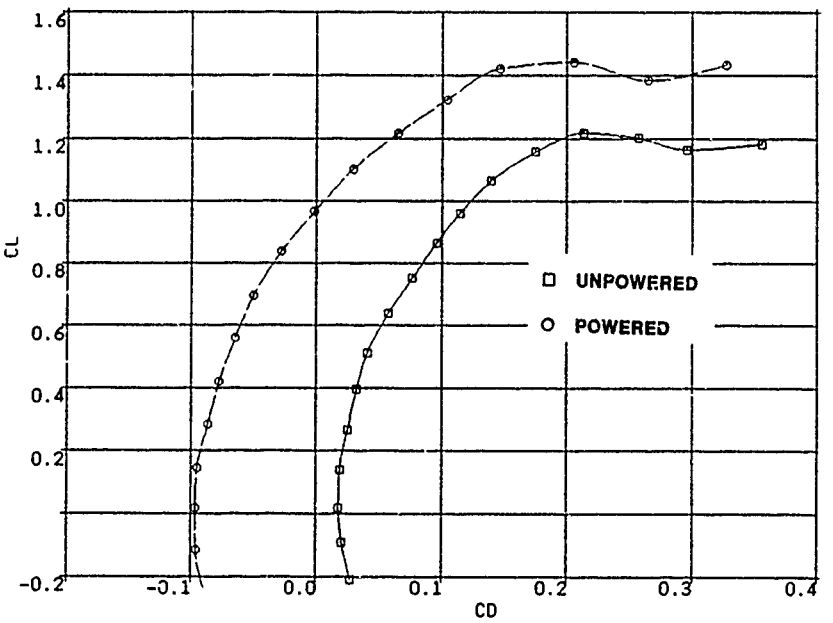

b) DRAG

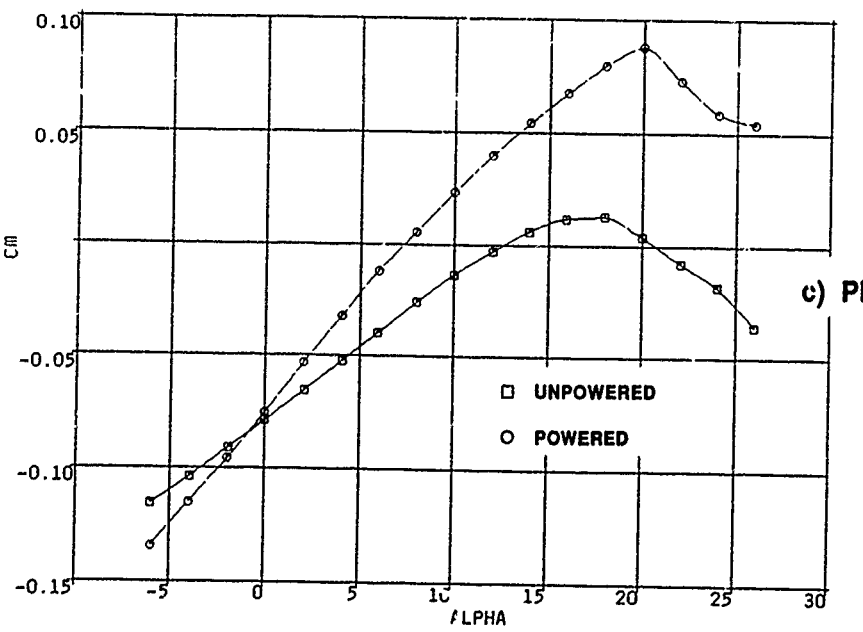

c) PITCHING MOMENT

FIGURE 5

EFFECT OF UNIFORM ROUGHNESS ON POWERED WING PERFORMANCE, C_{T_p} = 0.115, Re = 1.3 m

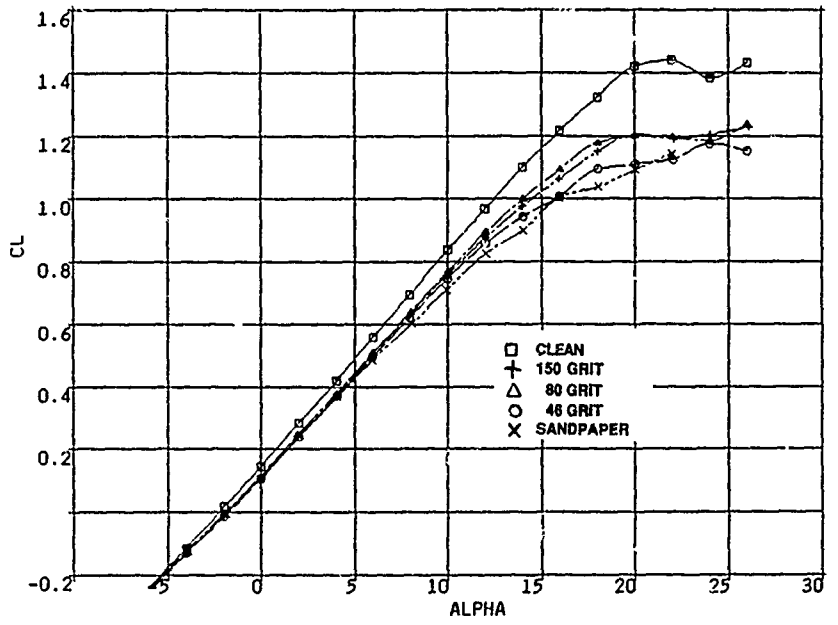

a) LIFT

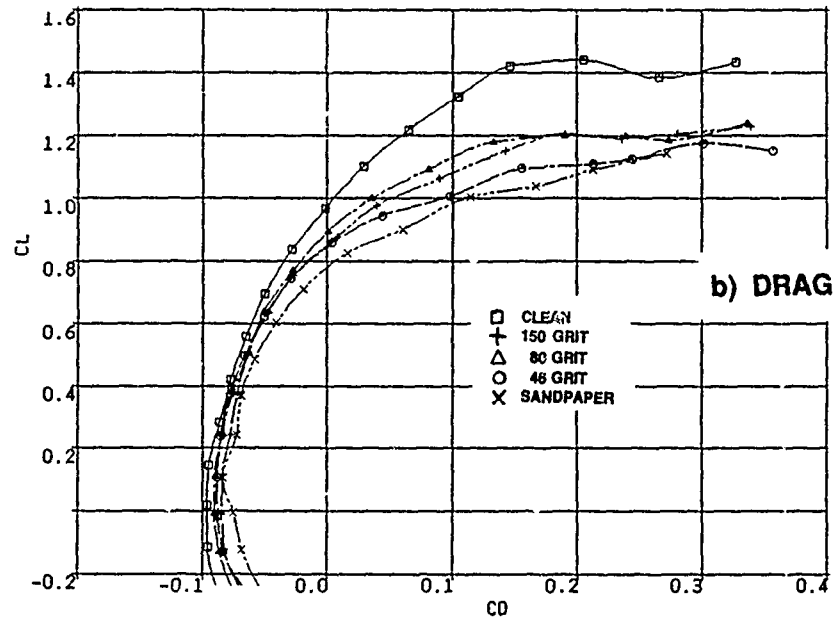

b) DRAG POLAR

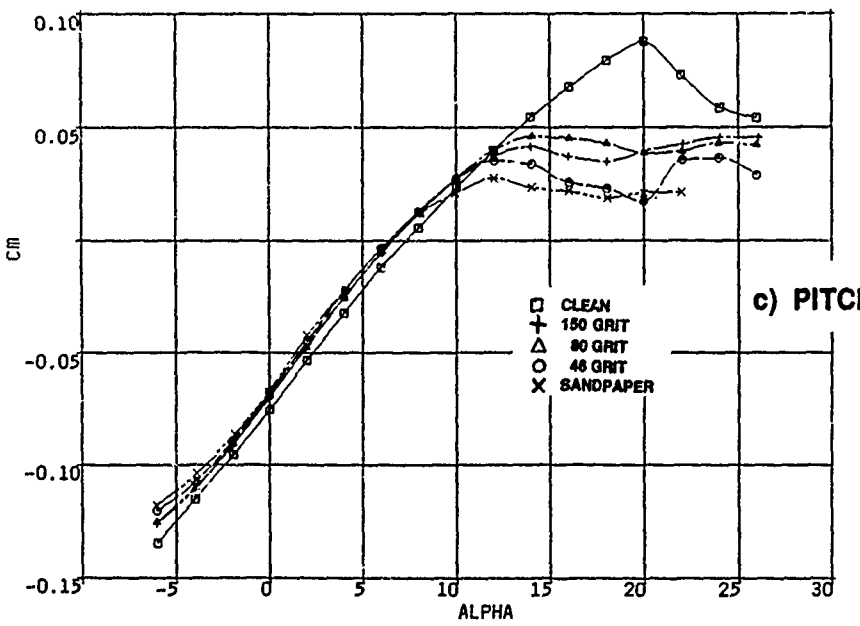

c) PITCHING MOMENT

FIGURE 6

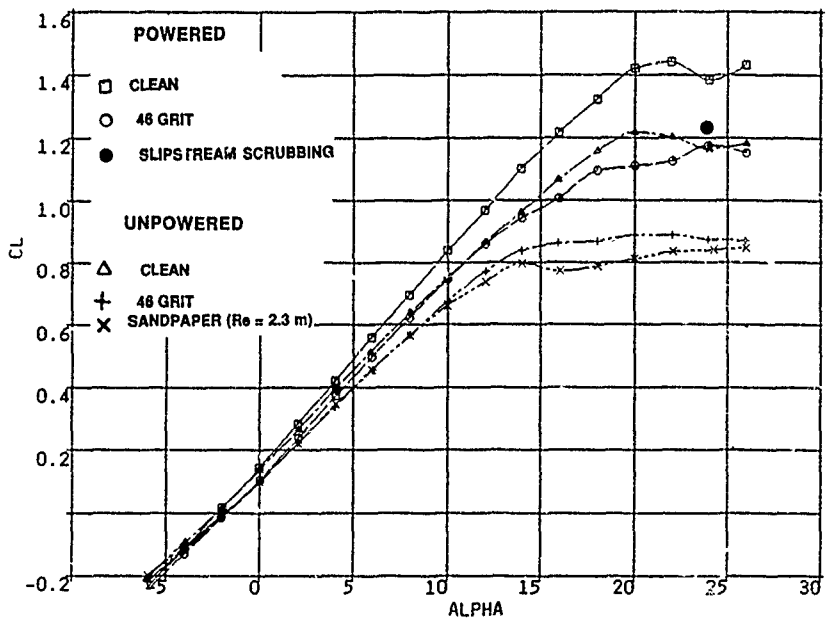

a) LIFT

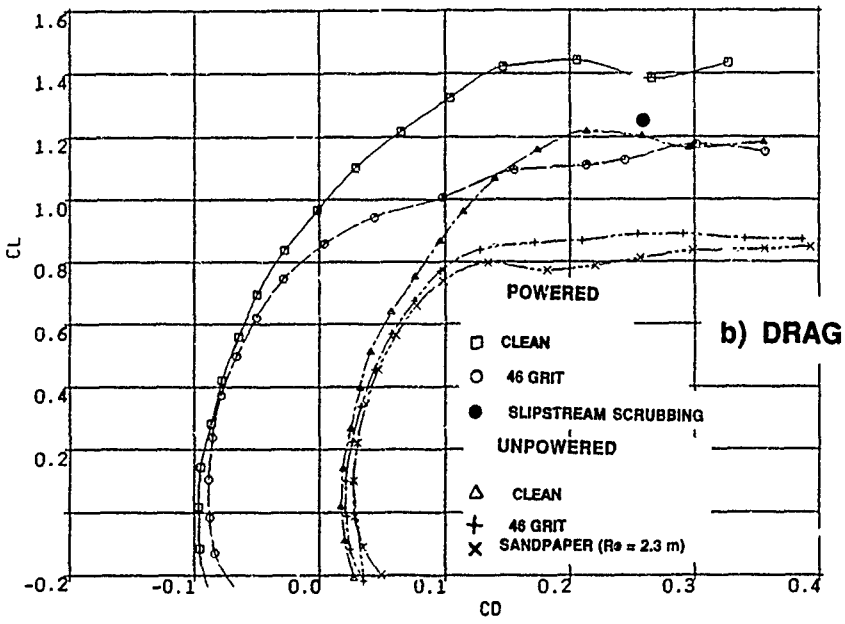

b) DRAG POLAR

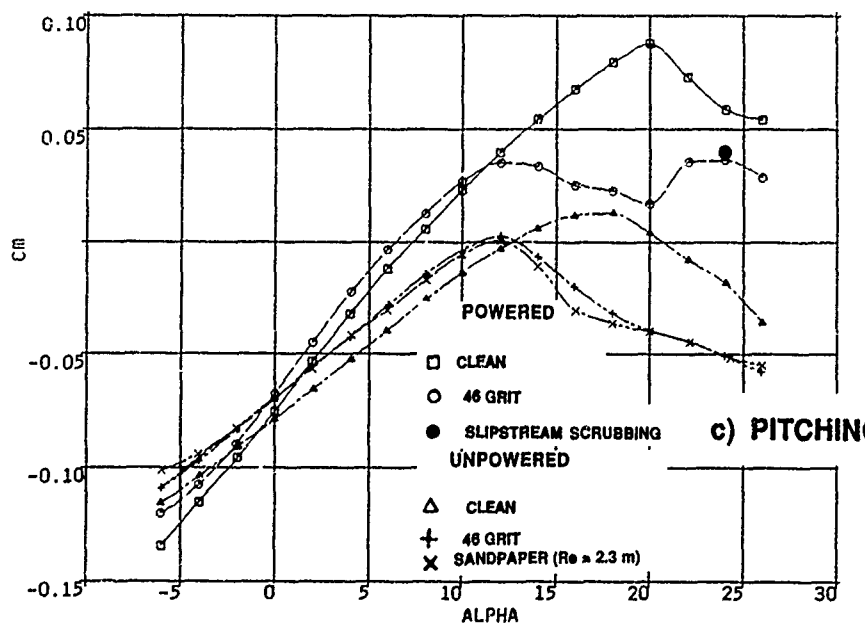

c) PITCHING MOMENT

COMPARISON OF EFFECTS OF UNIFORM ROUGHNESS ON POWERED AND UNPOWERED WING, 46 GRIT, 30% COVERAGE, C_{T_p} = 0.115, Re = 1.3 x 10^6

PROPELLER THRUST, NORMAL FORCE AND PITCHING MOMENT
(REF)

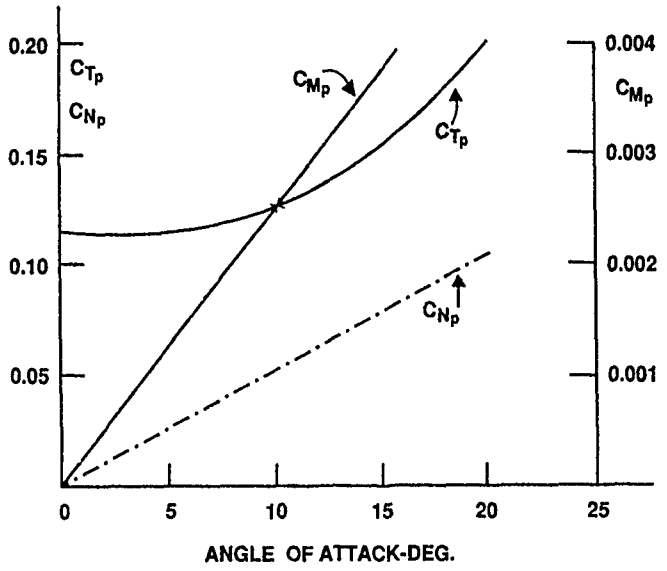

FIGURE 7

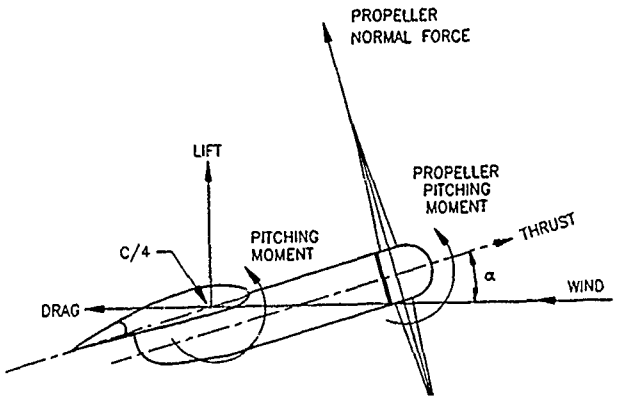

CONVENTION OF FORCES, MOMENTS AND ANGLE

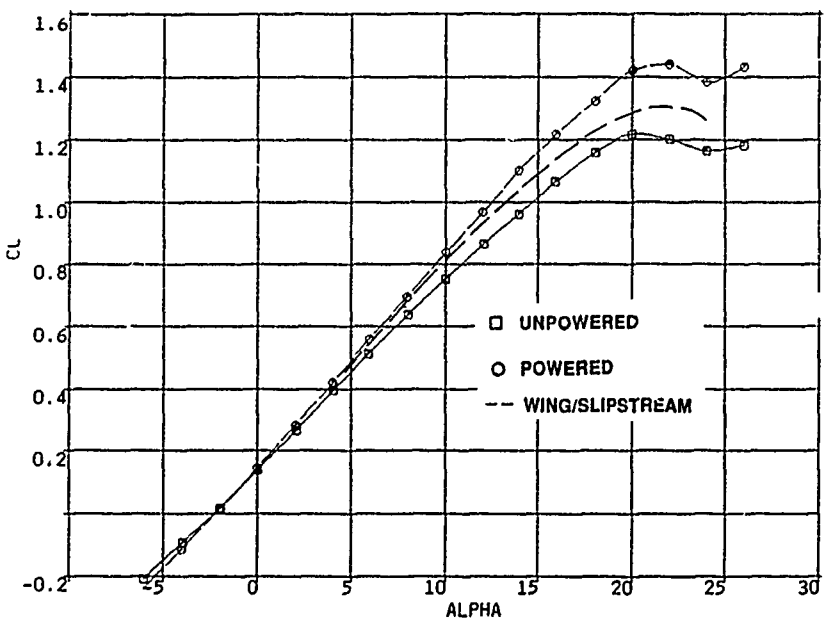

FIGURE 8

a) LIFT

REMOVAL OF PROPELLER REACTIONS FROM THE CLEAN, POWERED WING, C_{T_p} = 0.115, Re = 1.3 m

FIGURE 8

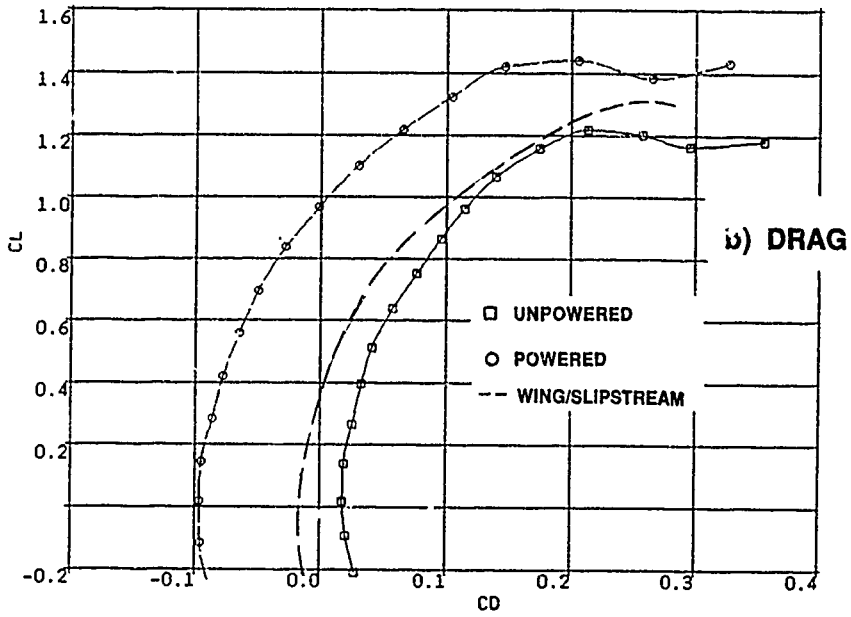

REMOVAL OF PROPELLER REACTIONS FROM THE CLEAN, POWERED WING, C_{T_p} = 0.115, Re = 1.3 m

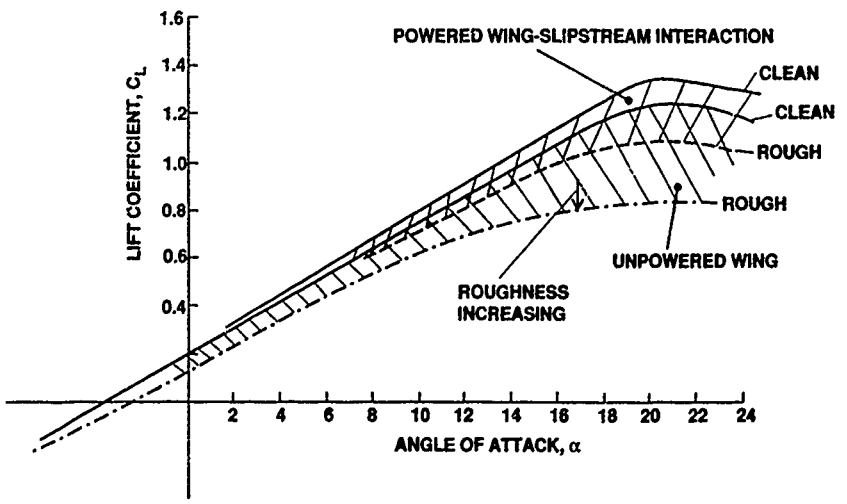

FIGURE 9

COMPARISON OF LIFT LOSS DUE TO DISTRIBUTED ROUGHNESS, OF AN UNPOWERED WING, AND A POWERED WING WITH PROPELLER REACTIONS REMOVED. C_{T_p} = 0.115, Re = 1.3 x 10^6

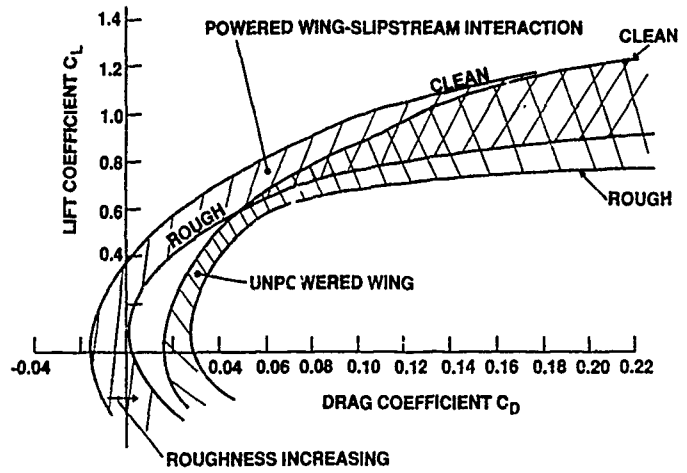

FIGURE 9

COMPARISON OF DRAG LOSSES DUE TO DISTRIBUTED ROUGHNESS, OF AN UNPOWERED WING AND A POWERED WING WITH PROPELLER REACTIONS REMOVED.
$C_{T_p} = 0.115$, Re = 1.3×10^6

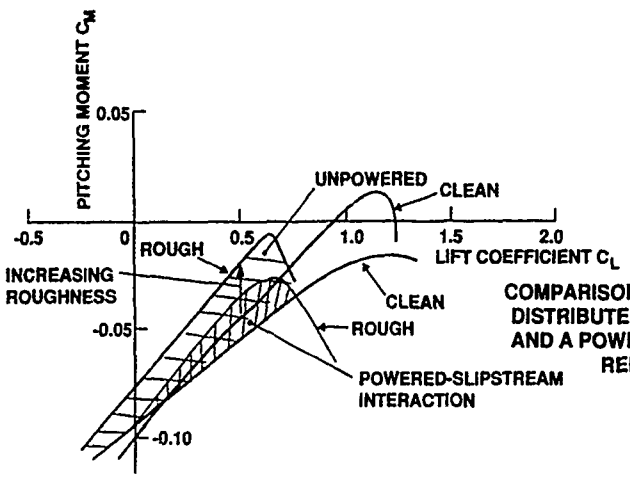

COMPARISON OF PITCHING MOMENT CHANGES DUE TO DISTRIBUTED ROUGHNESS, OF AN UNPOWERED WING AND A POWERED WING WITH PROPELLER REACTIONS REMOVED. $C_{T_p} = 0.115$, Re = 1.3×10^6

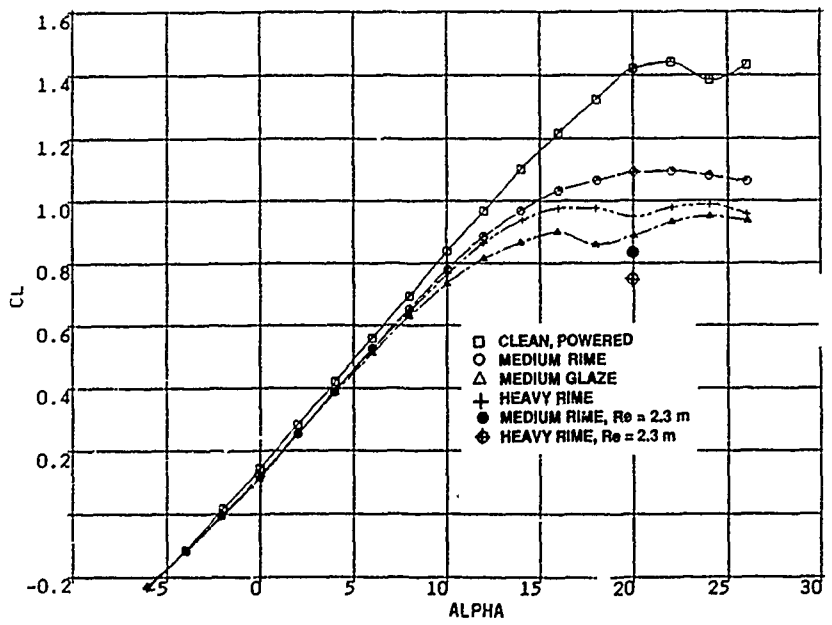

FIGURE 10

a) LIFT

EFFECT OF LEADING EDGE ICE ON POWERED WING PERFORMANCE,
$C_{T_p} = 0.115$, Re = 1.3 m

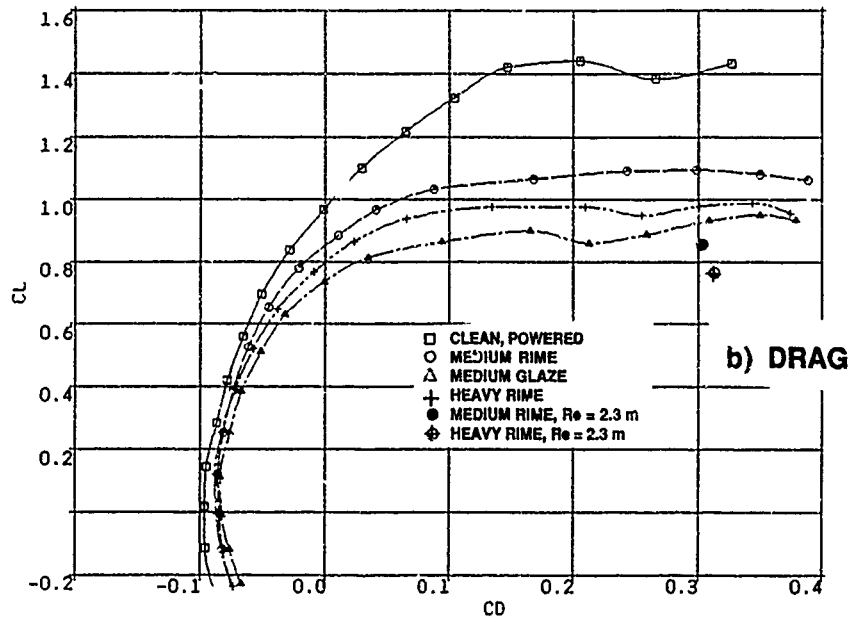

b) DRAG POLAR

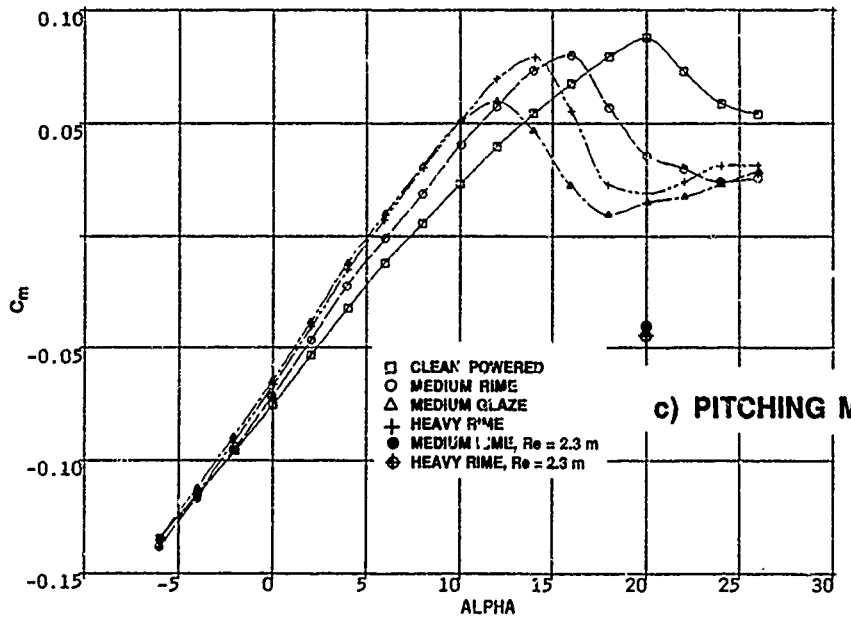

c) PITCHING MOMENT

FIGURE 10

EFFECT OF LEADING EDGE ICE ON POWERED WING PERFORMANCE, C_{T_p} = 0.115, Re = 1.3 m

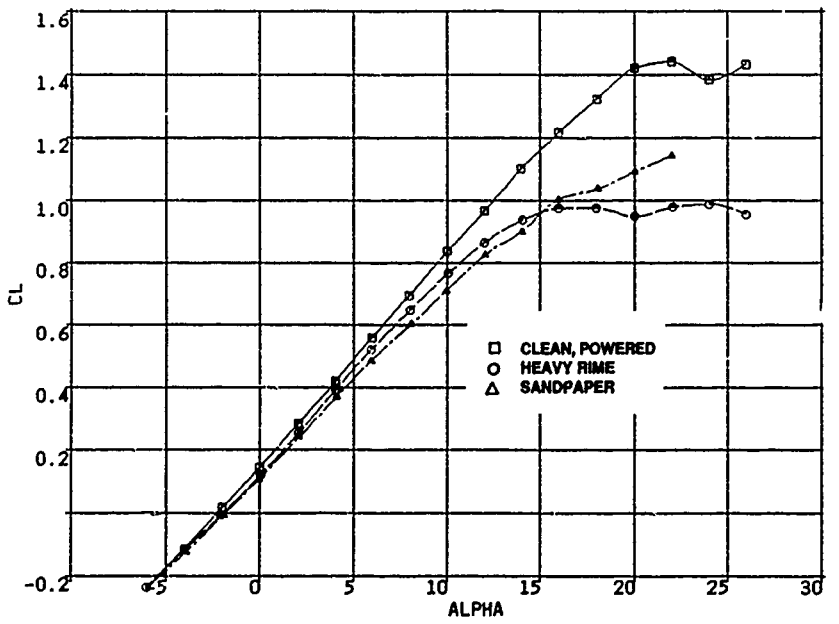

a) LIFT

FIGURE 11

COMPARISON OF LEADING EDGE ICE AND UNIFORM ROUGHNESS, C_{T_p} = 0.115, Re = 1.3 m

FIGURE 11

COMPARISON OF LEADING EDGE ICE AND UNIFORM ROUGHNESS, C_{T_p} = 0.115, Re = 1.3 m

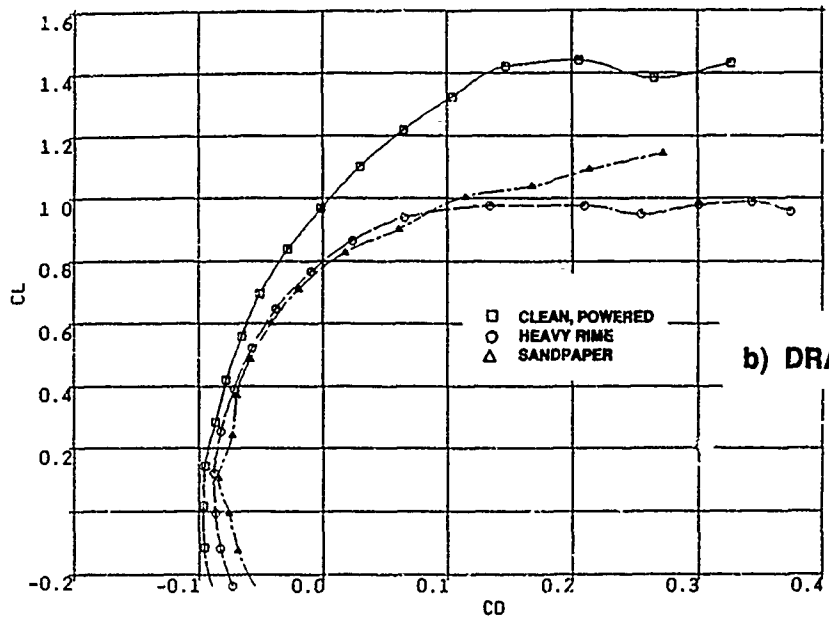

b) DRAG POLAR

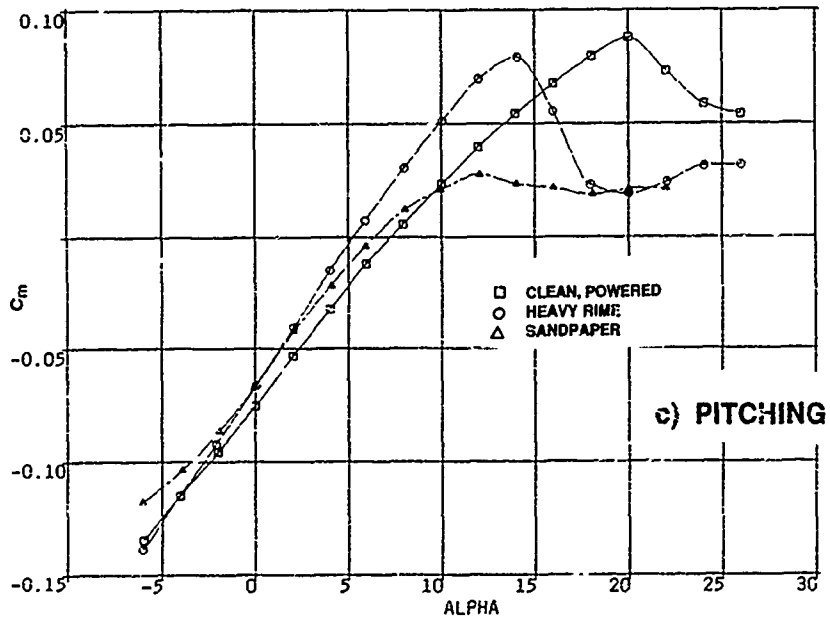

c) PITCHING MOMENT

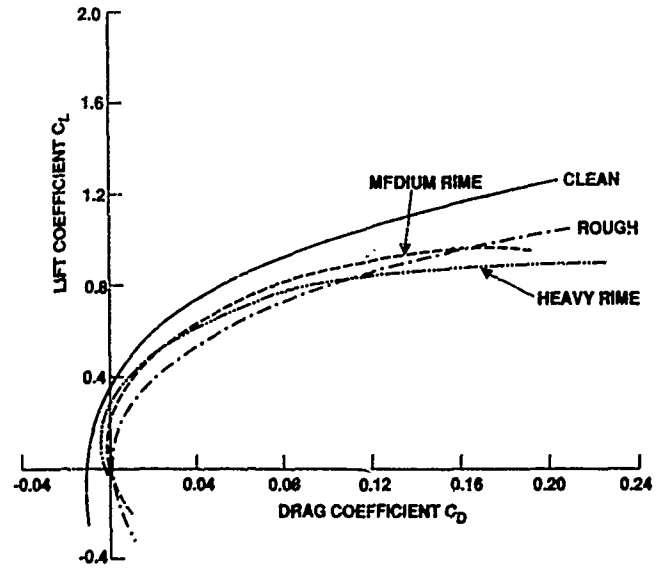

DRAG POLAR
COMPARISON OF DISTRIBUTED ROUGHNESS (50 GRIT SANDPAPER) AND LEADING EDGE ICE FOR POWERED WING-SLIPSTREAM INTERACTION (PROPELLER REACTIONS REMOVED) C_{T_p} = 0.115, Re = 1.3 x 10^6

FIGURE 12

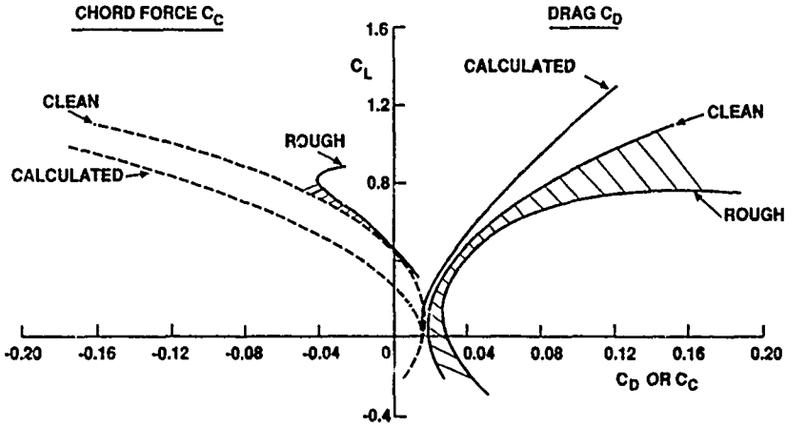

COMPARISON OF DRAG AND CHORD FORCE FOR CLEAN AND ROUGHENED UNPOWERED WING (50 GRIT SANDPAPER)

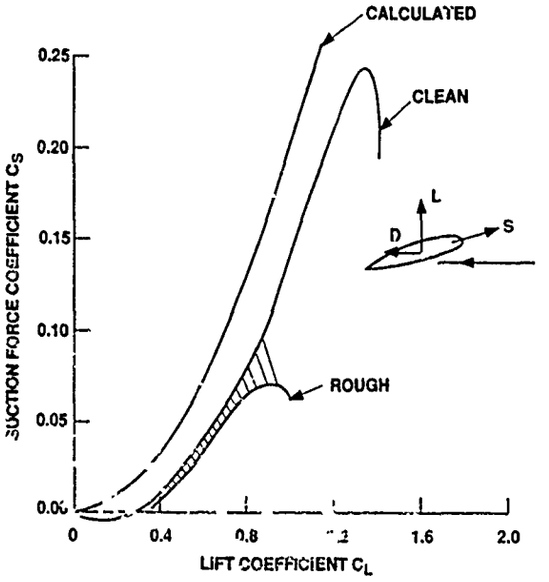

LEADING EDGE SUCTION FORCE COEFFICIENT FOR CLEAN AND ROUGHENED UNPOWERED WING

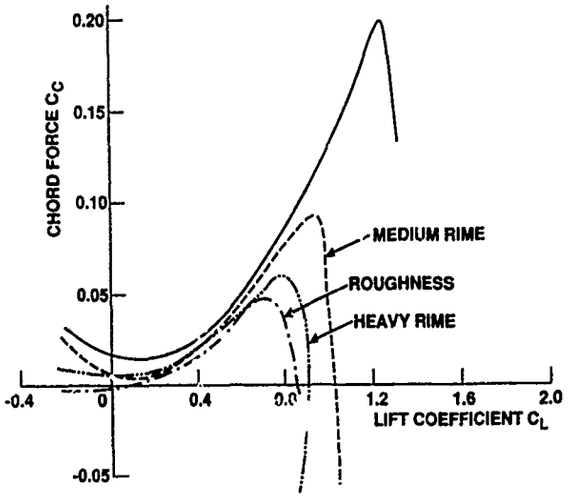

CHORD FORCE vs LIFT COEFFICIENT
COMPARISON AND LEADING EDGE ICE FOR POWERED WING-SLIPSTREAM INTERACTION (PROPELLER REACTIONS REMOVED) $C_{T_p} = 0.115$, Re = 1.3×10^6

THE ADVERSE AERODYNAMIC IMPACT OF VERY SMALL LEADING-EDGE ICE (ROUGHNESS) BUILDUPS ON WINGS AND TAILS

by

Frank T. Lynch and Walter O. Valarezo
Aerodynamics Technology
Douglas Aircraft Company
3855 Lakewood Blvd., Long Beach, CA 90846, USA

and

Robert J. McGhee
Fluid Mechanics Division
NASA Langley Research Center
Hampton, VA 23665-5225, USA

SUMMARY

Systematic experimental studies have been carried out to establish the aerodynamic impact of very small leading-edge simulated ice (roughness) formations on lifting surfaces. The geometries studied include single element configurations (airfoil and 3-D tail) as well as multi-element high-lift airfoil geometries. Emphasis in these studies was placed on obtaining results at high Reynolds numbers to insure the applicability of the findings to full-scale situations. It has been found that the well-known Brumby correlation for the adverse lift impact of discrete roughness elements at the leading edge is not appropriate for cases representative of initial ice buildup (i.e. distributed roughness). It has further been found that allowing initial ice formations of a size required for removal by presently proposed de-icing systems could lead to maximum lift losses of approximately 40 percent for single-element airfoils. Losses in angle-of-attack margin to stall are equally substantial - as high as 6 degrees. Percentage losses for multi-element airfoils are not as severe as for single-element configurations, but degradations of the angle-of-attack-to-stall margin are the same for both.

NOMENCLATURE

α	angle-of-attack
C_p	pressure coefficient
k/c	ratio of roughness height to airfoil chord
M_o	freestream Mach number
$\% \Delta C_{l_{max}}$	percent loss in maximum lift coefficient
R_N	Reynolds number based on chord
$\sqrt{x/c}$	stretched nondimensional coordinate
x/c	nondimensional coordinate

1. INTRODUCTION

We have learned from observations in icing tunnels that the initial ice accumulation on the leading edge of airfoils, particularly at temperatures just below freezing, looks very much like distributed roughness, with a disturbance height nominally equal to the thickness of the ice buildup. For some years, an empirical correlation originally assembled by Brumby[1] has been used to estimate the reductions in (1g) maximum lift capability caused by this leading-edge roughness, and therefore to set limits for the amount of leading-edge ice buildup (or residual) that might be permitted if de-icing systems are to be used as alternatives to the widely used anti-icing systems with their demanding engine bleed-air requirements. Use of this correlation (Figure 1) implied that if the thickness (k/c) of the ice buildup or residual was kept below 6×10^{-5} for installations without auxiliary leading-edge devices, or below 4×10^{-4} when leading-edge devices are deployed, then the reductions in (1g) maximum lift would be less than 5 percent (about 2 percent in stall speed). While these "allowable" ice buildups were quite small, they were still in the range that was thought to be achievable by the developers of de-icing systems, particularly for large transport aircraft.

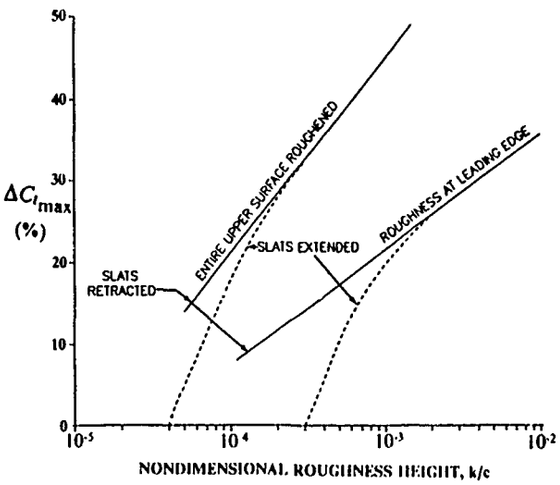

Figure 1. Brumby Correlation for Roughness Effects

However, test results obtained in 1985[2] on a single element airfoil over a wide Reynolds number range in the NASA Langley Low Turbulence Pressure Tunnel (LTPT)[3] provided an initial indication that usage of the Brumby correlation for the effects of leading edge roughness significantly underestimated the loss in maximum lift that is experienced with a representative leading-edge ice buildup/residual

(roughness). As can be seen from Figure 2, the 1985 test results for a k/c of $4x10^{-4}$ showed that the actual performance impact is closer to that expected when the entire upper surface is roughened. In fact, the loss in maximum lift (nearly 30 percent) was about three-quarters of that experienced with a simulated glaze ice buildup with horns. Cebeci[4] (at the California State University at Long Beach) then carried out a computational study to estimate the effects of these small ice (roughness) buildups on the maximum lift capabilities of single element airfoils for a range of roughness heights. These calculations, using an interactive boundary-layer method wherein the turbulence model was modified as prescribed by Cebeci and Chang[5] to account for roughness effects, predicted losses in maximum lift capability that were close to those measured in the LTPT at the same roughness height. More importantly, the predicted results, also shown in Figure 2, suggested that the maximum lift penalties at very small roughness heights ($k/c \sim 4x10^{-5}$) were very substantial (~15%), not unlike those previously expected for having the entire upper surface roughened.

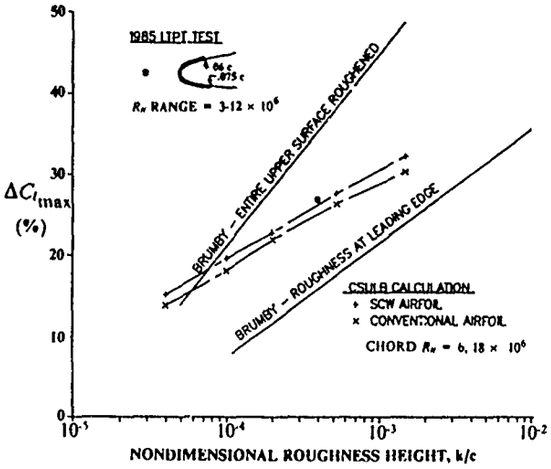

Figure 2. Initial Challenges to Interpretation of Brumby Roughness Correlation for Single-Element Airfoils

As a consequence of these two new inputs, which clearly suggested that the adverse effects of very small ice (roughness) buildups on the leading edge of a single-element wing or tail could be significantly greater than previously estimated, Douglas Aircraft and NASA Langley Research Center expanded an ongoing cooperative test program in the LTPT in order to identify representative penalties over a range of small roughness heights for both single- and multi-element airfoil configurations. Additional tests with very small roughness heights on a 3-D tail configuration were also carried out by Douglas in the ONERA F-1 facility to help assess the 2-D LTPT results. The objective of this paper is to demonstrate, by interpreting the subject test results, that there is no such thing as just a little bit of ice buildup on a wing or tail, in particular, with respect to de-icing applications. Analyses of the test data are presented which illustrate significant degradations in stall speeds and angle-of-attack margins for even the smallest amount of leading-edge ice buildup.

2. LTPT TEST FACILITY

Nearly all the experimental results presented in this paper were obtained from tests conducted in the Langley Low Turbulence Pressure Tunnel (LTPT). The LTPT is a single-return, closed-throat wind tunnel that can be operated at tunnel total pressures from near-vacuum to 10 atm[3]. A sketch of the tunnel circuit arrangement is shown in Figure 3. The tunnel test section is 3 feet wide, 7.5 feet high, and 7.5 feet long, which, when combined with a 17.6-to-1 contraction ratio, makes the LTPT ideally suited for two-dimensional airfoil testing. The tunnel can obtain a maximum Reynolds number of 15 X 10^6 per foot at a Mach number of 0.24, although most of the testing reported here was conducted at a Mach number of 0.20 with Reynolds numbers of 10 X 10^6 per foot or less as indicated.

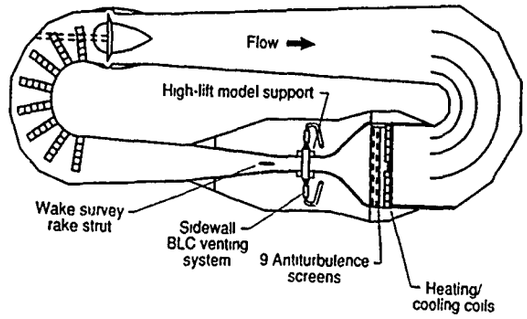

Figure 3. Sketch of the Langley Low-Turbulence Pressure Tunnel (LTPT)

To ensure spanwise uniformity of the flow field when testing high-lift airfoils at and below maximum lift coefficients, some form of tunnel sidewall boundary-layer control (BLC) is needed. The large adverse pressure gradients induced on the tunnel sidewalls by multi-element high-lift airfoils, particularly near maximum lift, can cause the sidewall boundary layer to separate with a corresponding loss of spanwise uniformity of the flow on the airfoil surfaces, and even lead to tunnel operating difficulties (surging, etc.). In order to provide adequate sidewall boundary-layer control for high performance high lift designs, a passive suction/venting system was developed and installed in the LTPT for this ongoing cooperative test program. This system consists of eight porous regions on each endplate through which the sidewall boundary layer is removed. The total porous area provided is illustrated in Figure 4. The suction/venting process is driven by the higher-than-atmosphere test section total pressure, and the appropriate sidewall venting area for each type of configuration was developed by simply taping off portions of the porous endplate surfaces on both sidewalls. Selection of the proper pattern was based on an examination of spanwise pressure variations at several chordwise location.

3. MODEL GEOMETRIES

The two-dimensional high-lift model used

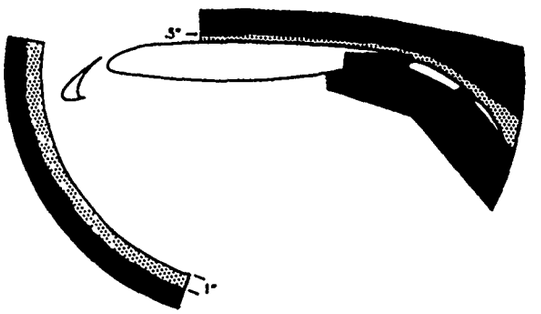

Figure 4. Sidewall Suction/Venting Area

for this investigation of leading-edge roughness effects in the LTPT was an aft-loaded-type airfoil equipped with a leading-edge slat and a two-segment flap. The cruise airfoil chord was 22 inches, and the maximum thickness-chord ratio was 11.55 percent. Leading-edge slat, forward flap segment, and aft-flap elements have respective chords of 14.48, 20.93, and 14.03 percent of the (unextended) cruise chord. The high-lift configuration with slat and two-segment flap deflected was instrumented with 142 centerline chordwise surface pressure taps which are used to determine the individual component and total configuration lift and pitching moment characteristics. Five spanwise rows of 10 taps each were also provided. Leading-edge roughness effects at high-lift conditions were measured for a representative approach/landing configuration, with slat and flap deflections of 30°, 35°, and 15°, respectively. Optimized slat- and main-element-flap riggings (gaps and overhangs) were used for this portion of the study.

The three-dimensional horizontal tail model that was tested in the ONERA F-1 facility, and used to validate the two-dimensional single-element airfoil roughness effects obtained in the LTPT, did not have aft-loaded airfoils. This configuration, which was mounted on top of a swept vertical tail, had an average maximum thickness-chord ratio of 11.37 percent, quarter-chord sweep angle of 33°, aspect ratio of 5, and taper ratio equal to 0.33.

4. SINGLE ELEMENT AIRFOIL/TAIL TEST RESULTS

In order to establish a sound basis for the experimental portion of this investigation, a water impingement analysis was performed for the single-element airfoil configuration to be tested in the LTPT to determine where to place the roughness elements to realistically simulate the effects of an initial ice buildup. The method employed, the Douglas Viscous Neumann (DACVINE) panel method[6], is capable of predicting the impingement of water droplets onto any desired surface by means of a particle trajectory and impingement calculation. The calculation takes into account the flowfield (multiple bodies), gravity, and the drag force on each particle, and is deemed appropriate to simulate the initial stages of ice accretion for the purpose of producing a realistic impingement pattern. Based on this study, for a range of conditions, it was determined that the pattern used in the 1985 LTPT test[2], which covered the entire leading edge from 6-percent chord on the upper surface to 7.5-percent chord on the lower surface, was representative. Hence, the same pattern was selected for the current investigation in order to provide a basis for comparison. Incidentally, a post-test analysis using the modified LEWICE method[7] confirmed the validity of this choice.

Several roughness heights were applied to the leading edge of the aft-loaded single-element airfoil in the LTPT to simulate either the initial ice buildup which would occur in an icing encounter, or the residual which might remain after a de-icing system cycle. The roughness sizes (heights) used were 0.0016, 0.0045, and 0.0117 inches, which resulted in non-dimensional roughness heights (k/c) of 0.00007, 0.0002, and 0.00053, respectively. Carborundum grit was used for the largest, while Ballotini beads were utilized for the smaller two. Tests were conducted for an angle-of-attack range through stall for each roughness height, as well as the clean airfoil, at 0.20 Mach number for chord Reynolds numbers from 2.5 X 10^6 to 18 X 10^6. The resultant percentage loss in maximum lift capability for this Reynolds number variation is presented in Figure 5. It can be seen that even the smallest roughness height caused a 20-percent loss in maximum lift capability for chord Reynolds numbers of 5 X 10^6 and above. The results obtained at a chord Reynolds number of 2.5 X 10^6 are clearly not representative especially for the smallest roughness height. The reason for this non-representative behavior at 2.5 X 10^6 Reynolds number is addressed subsequently in this section.

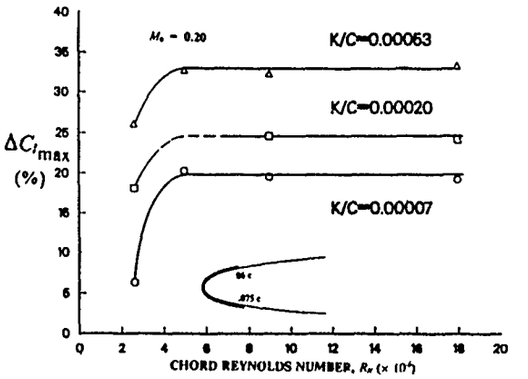

Figure 5. Reynolds Number Effect on Maximum Lift Loss Due to Leading-Edge Roughness on Single Element Airfoil

The measured reduction in maximum lift capability at chord Reynolds numbers of 5 X 10^6 and above is compared in Figure 6 to the Brumby correlation [1] and the 1985 LTPT test results [3]. It can be seen that the present results are consistent with the previous LTPT measurements, and validate the trend predicted by Cebeci[4] indicating the Brumby correlation for the entire upper surface roughened is clearly more representative of the effect of the typical initial leading-edge ice (roughness) buildup than the correlation based on more

discrete leading-edge roughness elements, particularly for the smaller roughness heights. This behavior can probably be attributed to the failure of the boundary layer to negotiate the very large adverse pressure gradient that exists just aft of the leading edge that leads to flow breakdown and consequent earlier stall. The reduction in sustainable leading-edge peak pressure with increasing roughness height that was observed at 9 X 10^6 Reynolds number is illustrated in Figure 7. Whereas a peak suction pressure coefficient of -13 can be sustained prior to stall on the clean airfoil, -8 is the best that can be done with even the smallest roughness height. As can be seen from Figure 7, and also as illustrated with the analogous lift curves shown in Figure 8, the corresponding reduction in angle-of-attack margin to stall with the smallest roughness is over 3°, and increases to about 5° for the largest size tested.

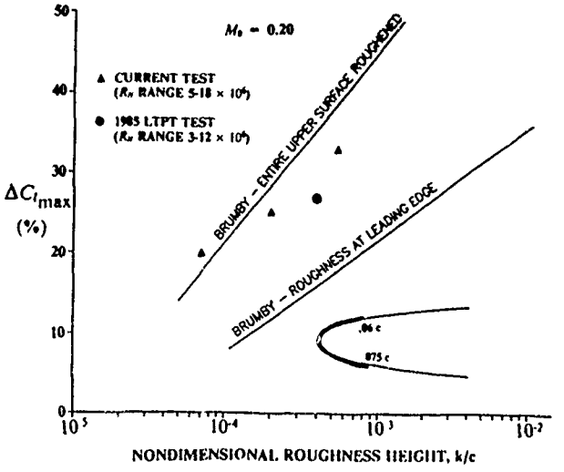

Figure 6. Leading Edge Roughness Effects on Single Element Airfoils in LTPT

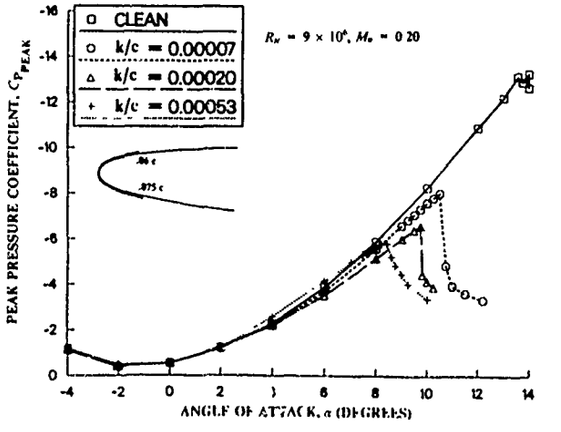

Figure 7. Effect of Leading-Edge Roughness on Peak Suction Pressure for Single Element Airfoil

As indicated earlier, too-low test Reynolds numbers can lead to erroneous indications of the reductions in maximum lift capability incurred with leading-edge ice (roughness) buildups. Results obtained in the present test program at a chord Reynolds number of 2.5 X 10^6 provide an example of how this occurs. The erroneous trend arises since the maximum lift

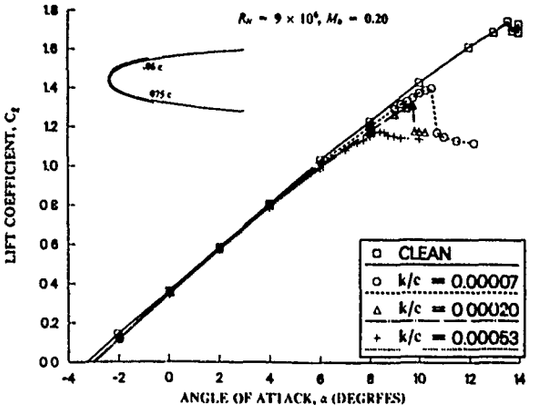

Figure 8. Effect of Leading-Edge Roughness on Single-Element Airfoil Lift Characteristics

without roughness is a strong function of Reynolds number whereas the maximum lift with roughness is not. This is illustrated in Figure 9 by the comparison of the lift curves for the clean airfoil, and with the smallest roughness applied, at chord Reynolds numbers of 2.5 X 10^6 and 5 X 10^6. The maximum lifts with roughness applied are nearly identical for the two test Reynolds numbers, but the maximum lift at 2.5 X 10^6 Reynolds number on the clean airfoil is substantially lower due to the existence of a leading-edge laminar separation bubble that is not present at the higher Reynolds number. The existence of the laminar bubble at the lower Reynolds number is indicated by the bulge in the chordwise pressure distribution seen just aft of the suction peak in Figure 10. Several attempts were made to eliminate this laminar bubble by fixing transition ahead of the bubble location, a technique reported to have been successfully used by others in avoiding the non-representative adverse consequences of having a bubble present. However, none of these attempts were successful in increasing the clean airfoil maximum lift capability at this Reynolds number. Hence, extreme caution must be exercised when planning or interpreting results for any low Reynolds number tests for leading-edge ice (roughness) buildup effects.

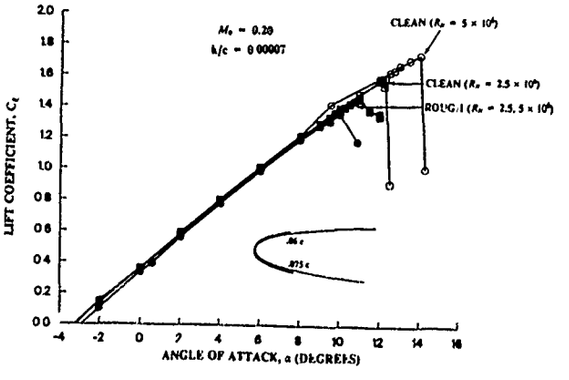

Figure 9. Reynolds Number Effects on Single-Element Airfoil Lift Characteristics With and Without Leading-Edge Roughness

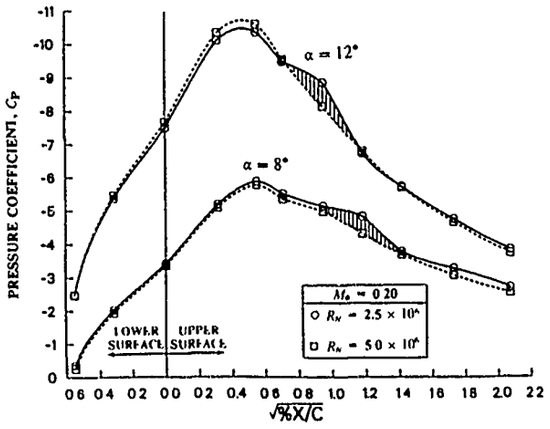

Figure 10. Indicated Laminar Separation Bubble on Clean Single-Element Airfoil at Chord Reynolds Number of 2.5 X 10^6

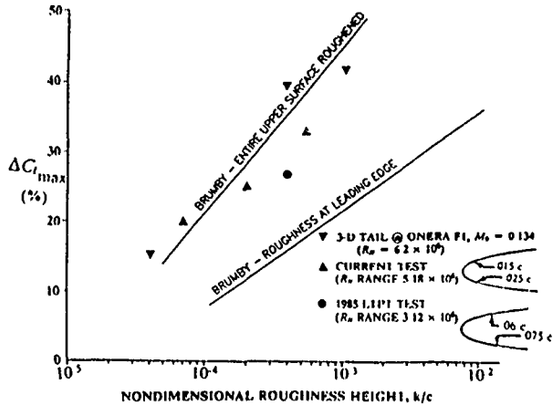

Figure 11. Comparison of Two- and Three-Dimensional Test Results for Effect of Roughness on Maximum Lift Characteristics of Single Element Configurations

With any two-dimensional tunnel tests involving leading-edge flow separation characteristics, regardless of the test Reynolds number, there is always some concern regarding the direct applicability of the results to the real three-dimensional flow situations that exist on practical airplanes. To address this concern, several roughness heights were applied to the leading-edge region of a three-dimensional, single-element horizontal tail configuration that was being evaluated in the ONERA F-1 facility. The roughness sizes used resulted in non-dimensional roughness heights (k/c) of 0.00004, 0.00036, and 0.00105, based on the tail MAC. The roughness heights covered the leading edge from 1.5-percent chord on the suction surface to 2.5-percent chord on the pressure surface, a smaller coverage than used in the LTPT investigation. Test conditions were 0.134 Mach number, and a MAC Reynolds number of 6.2 X 10^6. The corresponding percentage losses in maximum lift capability observed in these tests are compared to the LTPT results in Figure 11, where it can be seen that the three-dimensional results at the lowest roughness height are consistent with the two-dimensional results, at the two larger roughness sizes, the three-dimensional results are a bit more pessimistic. However, taken together, the two sets of data strongly suggest that the Brumby correlation based on having the entire upper surface roughened is a good indicator of the losses in maximum lift capability that will be incurred due to the initial ice buildups on wings and tails that do not have leading edge devices deployed.

A comparison of the indicated reduction in angle-of-attack margin to stall for the two sets of test results is shown in Figure 12. The reductions vary from a minimum of 3° at the lower roughness heights to around 7° at the higher roughness heights, with the three-dimensional results clearly being more adverse at the larger roughness heights. These reductions need to be addressed when considering the adequacy of stall warning systems when anti-icing protection is not provided.

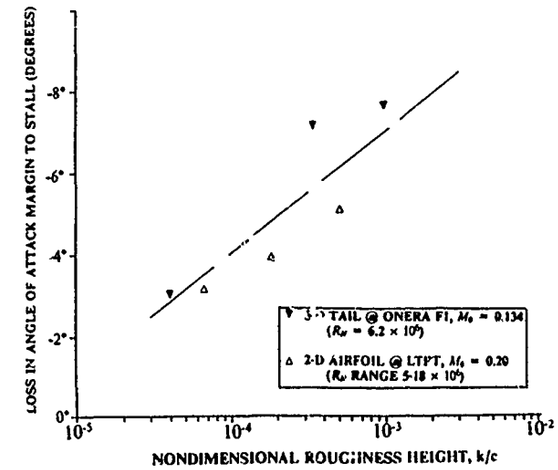

Figure 12. Comparison of Two- and Three-Dimensional Test Results for Loss in Angle-of-Attack Margin to Stall Due to Leading-Edge Roughness on Single Element configurations.

5. MULTI-ELEMENT AIRFOIL TEST RESULTS

To expand upon the study of leading-edge ice (roughness) buildup effects on single-element airfoils in the LTPT, a complementary investigation was undertaken to quantify the degradation of the maximum lift characteristics of a four-element (including two-segment flap) high-lift airfoil configuration resulting from similar small ice (roughness) buildups on the leading-edge slat at approach conditions. As was done with the single-element airfoil, a water impingement analysis was carried out to determine where the distributed roughness should be placed on the slat. Typical results from this water impingement analysis are illustrated in Figure 13 for an approach condition. On the basis of the impingement analysis, the principal area covered was the initial 4.5-percent (unextended airfoil) chord on both the upper and lower surfaces of the slat. A photograph of the roughness

installation is shown in Figure 14. In order to correlate the sensitivity of the maximum lift losses to the extent of the area covered with roughness, an additional configuration with the entire upper surface of the slat covered was also evaluated.

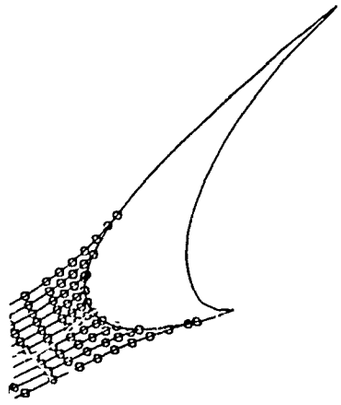

Figure 13. Analysis of Water Impingement on Slat

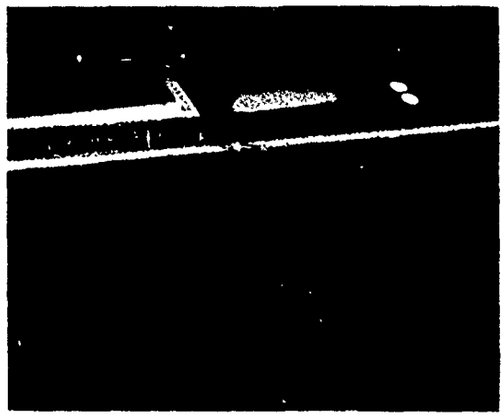

Figure 14. Roughness Applied on Slat

Tests of the four-element high-lift configuration, first without simulated ice, and then with the same three roughness sizes as used in the single-element study, were conducted at a freestream Mach number of 0.20, and at (unextended) chord Reynolds numbers of 5 X 10^6, 9 X 10^6, and 16 X 10^6. The resultant degradations in maximum lift capability (for the roughness coverage to 4.5-percent chord) as a function of the non-dimensional roughness height (k/c) are shown in Figure 15 for the intermediate Reynolds number, compared to the Brumby estimate[1] for configurations with slats extended. The observed (percentage) losses, which, incidentally, are relatively insensitive to Reynolds number variations over the range tested, are much lower than those seen on single-element airfoils. The losses in maximum lift capability range from about 5 percent at the smallest roughness to just over 10 percent at the largest, compared to losses of from 20 percent to over 30 percent for the single-element cases. However, as will be seen subsequently, the actual reductions in angle-of-attack margin to stall are remarkably similar.

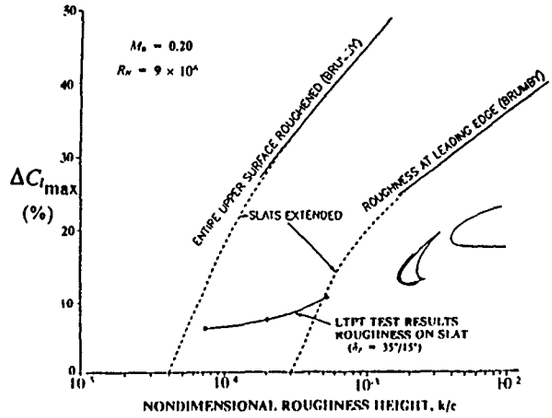

Figure 15. Effects of Roughness on Leading-Edge Slat

The impact of roughness on the slat on the total (four element) configuration lift characteristics is illustrated in Figure 16. In addition, the impact on the individual contributions of the slat and main airfoil element (behind the slat) is shown. It is the main element that is losing the lift that leads to the reduction in maximum lift capability, most likely due to the influence of a larger wake from the slat. Examination of the leading-edge peak suction pressures on both the slat and main element (see Figure 17) for these cases with roughness on the slat clearly shows that there is an alteration of the flow pattern around the leading edge of the main element concurrent with the flow breakdown on the slat.

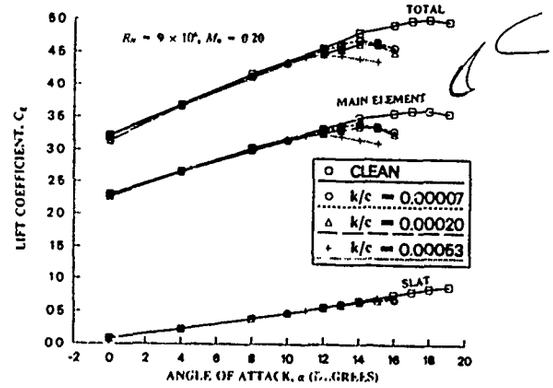

Figure 16. Effects of Slat Roughness on Four-Element Airfoil Lift Characteristics

As indicated previously, the roughness coverage area with the smallest roughness height (k/c = 0.00007) was also extended to cover the entire upper surface of the slat to determine the sensitivity of the measured losses in maximum lift to the extent of the roughened area. The measured lift characteristics for the two coverage patterns are shown in Figure 18 compared to the clean configuration. It can be seen that there is very little difference in the measured maximum lift characteristics for the two roughness coverage areas. What is

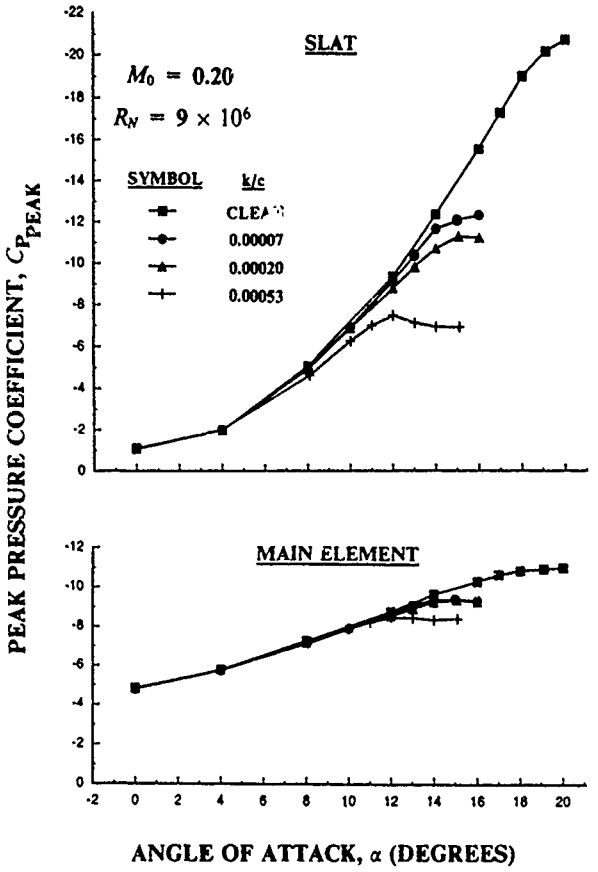

Figure 17. Effects of Slat Roughness on Peak Suction Pressures for Multielement Airfoil

clearly dominant in controlling the flow breakdown on the slat is having over the region of adverse pressure gradient just aft of the roughness elements suction peak. Extending the roughness coverage further aft is inconsequential.

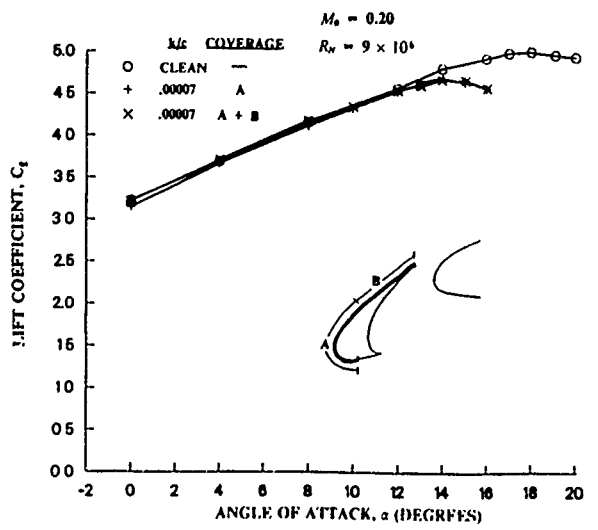

Figure 18. Effects of Slat Roughness Coverage on Four-Element Airfoil Total Lift Characteristics

A most interesting correlation is observed when comparing the indicated reductions in angle-of-attack margin to stall due to the ice (roughness) buildup for this multi-element high-lift airfoil case to the same data for the single-element airfoil cases. It can be seen from Figure 19 that they are all essentially coincident. Hence, this correlation provides a relatively quick way to assess the maximum lift penalties incurred for a leading-edge ice (roughness) buildup on any representative wing or tail configuration. It also provides the information needed to check on the adequacy of stall warning systems when anti-icing protection is not provided.

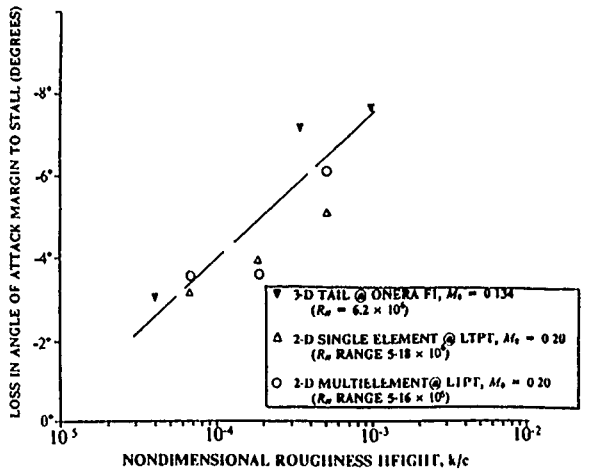

Figure 19. Correlation of Single-Element and Multi-Element Airfoil Test Results for Loss in Angle-of-Attack Margin to Stall Due to Leading-Edge Roughness

6. PRACTICAL CONSIDERATIONS

It is clear that potential applications of de-icing systems (in lieu of anti-icing systems) for wings and tails of new transport aircraft need to be carefully reassessed in light of the present test results. The identified reductions in maximum lift capability on configurations without leading-edge devices extended are very large, even for extremely small leading-edge ice (roughness) buildups. For example, roughness heights of around 0.005 inch would result in reductions in the maximum-lift capability of 20 percent at the critical spanwise stations on the wing or tail of a representative 200-seat transport. Obviously, the concern is even greater for smaller aircraft. Increasing the leading-edge roughness size to at least 0.03 inch, perhaps the minimum ice buildup that can be reliably eliminated by a de-icing system, would result in losses in maximum lift capability of up to 40 percent for the 200-seat aircraft. If the wing or tail surface areas for a particular configuration are sized by maximum lift capability, then corresponding increases in surface areas would be required, with all the attendant performance penalties (drag, weight, etc.).

Lower percentage losses in maximum-lift capability due to leading-edge ice buildups are experienced if the ice buildup occurs on an extended/deflected leading-edge device such as a slat. The maximum-lift penalty for the 0.03 inch ice buildup on a slat would be about 10 percent at typical landing flap settings. However, the penalty could well be near 20 percent on the wing for lower takeoff flap settings, or for a tail (without deflected flaps). Again, these penalties would all be increased for smaller aircraft. The correlation for reductions in angle-of-attack

margin to stall as a function of the non-dimensional roughness buildup as presented in Figure 19 should permit a representative assessment of reductions in maximum lift capability for any relatively conventional configuration. However, if a leading-edge device is to be deployed to reduce the maximum lift penalties due to an initial ice accumulation, then the impact of the extra drag incurred whenever operating in icing conditions must be taken into account.

In addition to the reductions in maximum lift capability that would be incurred on any aerodynamic surface using a de-icing system for ice protection, there are a myriad of related practical issues that need to be addressed. Specifically, there are likely certification issues such as determination of the most critical spanwise regions on a wing or tail, identification of a most adverse roughness configuration over the range of icing conditions that might be encountered, definition of the most adverse residual (after a de-icing system cycle) roughness configuration with subsequent additional buildup (until the next cycle), etc. These are all formidable issues, with a large associated risk in terms of potential performance penalties.

7. CONCLUSIONS

A systematic experimental investigation has been carried out to establish the reductions in maximum lift capability that would be incurred by both single-element and multi-element aerodynamic surfaces (airfoil, wings, tails, etc.) due to the initial leading-edge ice (roughness) buildup that would occur if de-icing systems are employed. Emphasis in this study was placed on obtaining results at high Reynolds numbers in order to assure the reliability of the finding. Analysis of the results from this investigation has led to the following conclusions:

1. Use of the "Brumby" correlation for the impact of discrete roughness elements at the leading edge of single-element configurations to estimate maximum lift losses is overly optimistic for the representative initial ice (roughness) buildups that occur. However, the correlation for the entire upper surface roughened, which predicts much greater losses, is a good indicator of the losses observed experimentally.

2. Losses in maximum-lift capability of 40 percent are indicated on single-element configurations for the typical minimum initial ice buildups that can be removed with de-icing systems being studied presently.

3. The authenticity of maximum-lift losses observed in two-dimensional tests at chord Reynolds numbers of 5 X 10^6 and above has been verified by three-dimensional test results. However, two-dimensional test results obtained at lower Reynolds numbers are misleading.

4. Lower percentage losses in maximum-lift capability due to leading-edge ice buildups are experienced if the ice buildup occurs on an extended/deflected leading-edge device such as a slat. Losses of from 10- to 20-percent are indicated, dependent upon whether trailing-edge flaps are deployed or not.

5. A correlation of the reduction in angle-of-attack margin to stall due to leading-edge ice buildup has been established which allows the assessment of likely losses in maximum-lift capability for any relatively conventional configuration. Reductions in angle-of-attack margin of 6 degrees are indicated for the typical minimum initial ice buildups ($k/c \sim 0.0005$) that could (possibly) be removed by de-icing systems on a representative 200-seat transport.

REFERENCES

1. Brumby, R.E., "The Effect of Wing Ice Contamination on Essential Flight Characteristics," Presented to SAE Aircraft Ground De-Icing Conference, Sept. 20-22, 1988.

2. Morgan, H.L., Ferris, J. C., and McGhee, R. J., "A Study of High-Lift Airfoils at High Reynolds Numbers in the Langley Low-Turbulence Pressure Tunnel," NASA TM-89125, July 1987.

3. McGhee, R. J., Beasley, W. D., and Foster, Jean M., "Recent Modifications and Calibration of the Langley Low-Turbulence Pressure Tunnel," NASA TP2328, 1984.

4. Cebecí, T.: Private Communication, CSULB, 1989.

5. Cebeci, T. and Chang, K. C., "Calculation of Incompressible Rough-Wall Boundary-Layer Flows," AIAA Journal, Vol. 16, No. 7, July 1978, pp. 730-735.

6. Hess, J. L., Friedman, D. M. and Clark, R. W., "Calculation of Compressible Flow About Three-Dimensional Inlets with Auxiliary Inlets, Slats, and Vanes by Means of a Panel Method", McDonnell Douglas Report No. MDC J3789, 1985, NASA CR-174975, and AIAA Paper no. AIAA 85-1196.

7. Shin, J., Berkowitz, B., Chen, H. H., and Cebeci, T., "Prediction of Ice Shapes and Their Effect on Airfoil Performance," AIAA Paper no. 91-0264, 1991.

THE EFFECT OF HOAR-FROSTED WINGS ON THE FOKKER 50 TAKE-OFF CHARACTERISTICS

J. van Hengst * and J.N. Boer **
* Head Aerodynamics and Aeroelasticity Department
** Manager Applied Aerodynamics
Fokker Aircraft B.V.
P.O. Box 7600
1117 ZH Schiphol
Holland

SUMMARY

This paper reviews how contamination resulting from ice, snow or frost accumulated during ground icing, degrades the Fokker 50 aircraft aerodynamics and leads to reduced flight safety during take-off.

List of symbols and Abrreviations

$\alpha°$	angle of attack (alpha)
c	wing chord
C_D	coefficient of drag
C_L	coefficient of lift
CAS	calibrated air speed
DE	elevator deflection
Δ	increase/decrease (delta)
FAA	Federal Aviation Administration
FAR	Federal Aviation Regulations
FFA	Flygtekniska Försöks Anstalten
k/c	relative roughness height
kt	knot
LST	Low Speed Tunnel
mac	mean aerodynamic chord
RN	Reynoldsnumber
V_2	take-off safety speed
V_r	rotation speed
W	clean wing
WF	wing with trailing edge flaps extended
WFS	wing with leading and trailing edge flaps extended

1.0 INTRODUCTION

In December 1982, following a number of accidents involving ground icing, the US Federal Aviation Administration (FAA) re-circulated its Advisory Circular AC 20-117 on the subject. The purpose of AC 20-117 is to emphasize the 'clean aircraft concept' following ground operations in conditions conductive to icing. It also provides information to assist in compliance with the requirements of the circular.

The wording of AC 20-117 (Figure 1) confirms that the regulations on the icing hazards as established by the US Civil Aeronautics Board in 1950 and cited under FARs 121.629, 91.209 and 135.227, remain unaffected. Regrettably however, accidents involving ground icing have continued to occur since re-publication of the circular (Table 1).

Windtunnel tests were performed to investigate the degradation of the low-speed aerodynamic characteristics of the Fokker 50 when the wings were contaminated by hoar-frost. The hoar-frost was simulated by means of carborundum grit on the wing upper surface.

The windtunnel test results were used to investigate the degradation in performance and handling qualities of the aircraft during take-off. The investigations were done on a fixed base engineering simulator.

This present paper reviews how contamination resulting from ice, snow or frost accumulated during ground icing, degrades the Fokker 50 aircraft aerodynamics and leads to reduced flight safety during take-off.

2.0 Windtunnel tests

2.1 FFA Windtunnel tests

A wind tunnel investigation of simulated hoar frost on a two-dimensional wing section was carried out in the early 1970s by Björn L.G. Ljungström of the Aeronautical Research Institute of Sweden (FFA).[1] The investigation was unique in that it comprised tests with differing levels and degrees of roughness on the same basic wing section at representative take-off configurations. The model configurations considered (Figure 2) consisted of a wing alone (W), a wing with trailing edge flap extended (WF), and a wing with leading and trailing edge flaps extended (WFS). The RN was 2.6 million, based on the wing chord.

The airfoil selected was a NACA 65_2 A215 section. Abrasive paper of three particle sizes was used to simulate the hoar frost. The profile shape and density of the coarsest paper was $k/c = 80 \times 10^{-6}$. At full scale, this roughness level corresponded to a particle size of 2.0 mm for a chord of 2.50 m (i.e. comparable with the mac of the Fokker 50).

A roughness coverage of '100%' was defined as corresponding to the practical situation of a parked aircraft with high lift devices retracted and its complete wing upper surface and a significant part of the lower surface at the leading edge covered with frost contamination from ground icing. By extending the leading edge and/or trailing edge flap, a portion of the main wing and/or trailing edge flap remains clean (Figure 3).

Test results from this investigation have been used here to compare the effects of leading edge and/or trailing edge flap deflection on the aerodynamics of a contaminated wing section.
Test results are presented in Figure 4.

Severe losses in maximum lift and large reductions in angle of attack for maximum lift were measured.

Roughness of this level and coverage, representative of hoar frost formation, increased the boundary layer over the upper surface in such a way that the wing section was physically 'de-cambered'.
This resulted in loss of lift and increase in drag for a given angle of attack. Degradation in lift and drag does not therefore occur solely at the angle of attack for maximum lift.

The test results clearly demonstrated that between slatted and non-slatted wing configurations, there is no difference in aerodynamic degradation due to hoar frost roughness.

2.2 Fokker Windtunnel tests

Fokker Aircraft performed power-off windtunnel tests on a complete model of the F27 (scale 1:20) with roughness over the complete wing upper surface, simulating frost contamination due to ground icing.

The F27 model was tested in the 1.80 x 1.25 m^2 low speed test facility (LST) at Delft University of Technology. The RN based on the mac was 0.9 million.

The model was tested without horizontal tail. Three take-off flapsettings were tested, flaps IN, flaps 8 and flaps 16 deg.

Two roughness configurations were tested indicated 100% and 85%. Configuration 100% consisted of carborundum 80 distributed uniformely from 0% to 100% wing chord over the flaps up wing upper surface.
In configuration 85% the carborundum 80 was distributed uniformely from 15% to 100% wing chord on the wing upper surface. The roughness was applied at a high density.
The configurations are shown in figure 5.

Carborundum 80 corresponds to a roughness level $k/c = 137 * 10^{-6}$ which was a coarser roughness than $k/c = 80 * 10^{-6}$ as used in the FFA tests. When corrected for Reynoldsnumber effect on boundary layer thickness using a $RN^{1/3}$ relation, the carborundum 80 on the F27 model corresponded to a roughness height of k = 2.2 mm at full scale.

Measurements without roughness were also carried out for reference purposes. The test data are expressed in terms of increments with respect to the relevant clean (reference) configuration.
Results are presented in figure 6.

The model test results showed that while the loss in maximum lift compared well with the FFA test results, the reduction in angle of attack for maximum lift did not. In fact a small increase in maximum lift angle of attack was measured on the F27 model.

The latter condition was most probably caused by a change in wing stall behaviour at this low Reynoldsnumber. Normally for a clean wing, a combined leading and trailing edge type of stall starts in the vicinity of the engine nacelle and progresses gradually inboard and outboard.
In contrast to this, for the roughened wing, a pure trailing edge type of stall occurs simultaneously over the entire wing span.

Wings are normally designed so as to ensure that stalling commences at an inboard wing station. This is in order to retain lateral control for as long as possible and to have favorable pitching moment characteristics throughout the stall. The results of the previously-mentioned wind tunnel tests revealed that model roughness simulating ice, frost and snow accumulation over the entire wing span, seriously jeopardizes such design features. When the roughness accumulation is distributed unsymmetrically over the wing span, early stall of one wing may occur, resulting in severe wing-drop at lift-off.

The losses in lift during ground roll and at climb conditions also compared well with the FFA test data.

It should be noted that the drag increments of the F27 model cannot be directly compared with the FFA results because the reference 'clean drag' of the model consists not only of wing drag but also of drag contributions from the fuselage, nacelles and vertical stabilizer.

From the windtunnel tests it is concluded that a roughness coverage of 100% representative of hoar frost contamination considerably deteriorates the aerodynamic characteristics of the Fokker 50 aircraft.

The tests also showed that cleaning the leading edge area up to 15% wing chord will not restore the clean wing lift and drag characteristics.

3.0 Simulator investigation

To study the effects of hoar frosted wings on the performance and flight handling characteristics during take-off a simulator investigation was performed.

The results of the Fokker wind tunnel tests were introduced into the aerodynamic data base of the Fokker 50 for further investigation on the Fokker Aircraft fixed-base engineering flight simulator.
The aerodynamic data base is very detailed and comprises flight-test-updated data packages.
The changes in lift-, drag and pitching moment coefficients due to roughness, as measured on the F27 model, were directly applicable for the Fokker 50 study as wing planform and sections of both aircraft are the same.

Simulated frost was applied only to the wing upper surface, because the most significant aerodynamic effects would result from frost contamination on the wing's upper surface. During take-off the horizontal stabilizer's lower surface is critical. Normally the lower surface would be frost free.

The simulator study comprised a series of take-off's at sea level ISA-20°C conditions on a dry runway.
Normal take-off technique with both engines operative was used. The take-off weight was 20,000 kg and the center of gravity was set at 30% mean aerodynamic chord. Two flap positions, flaps IN and flaps 15 were investigated. Normal (clean wing) speed schedules were applied, resulting in V_2 of 116 and 102 kt CAS for flaps IN and flaps 15 respectively. It is noted that on the aircraft flaps 15 is used to indicate a flap deflection of 16 deg.

The simulator tests were done in two sessions.

In the first session the take-off's were performed off-line which means without pilot in the loop.
Rotation was initiated by a commanded elevator deflection resulting in a constant pitch rate towards 8 deg pitch attitude. Results are presented in figures 7, 8 and 9.

Both the 100% and the 85% contamination have a deteriorating effect on the aircraft behaviour at rotation.

The pitch rate in a normal rotation is about 3 deg/sec. With a contaminated wing the (peak) elevator input to initiate a 3 deg/sec rotation is considerably larger compared to the clean wing configuration.

The (nose down) pitching moment due to the frost contamination requires a fair amount of (negative) elevator deflection at lift-off to maintain constant pitch attitude.

The tests show a large increase in take-off distance from brake release until 35 ft screen height.
With 100% contaminated wings take-off distance is increased by 40% with flaps IN and by 80% with flaps 15, the largest Fokker 50 take-off setting.
Ground roll distance until rotation was hardly affected however. The increase in take-off distance is found between initiation of rotation until 35 ft height.

It was observed that after the aircraft with contaminated wings was rotated to 8 deg pitch it remained on the runway until accelerated to a higher speed at which it eventually lifted-off.
As a consequence the peak angle of attack in the rotation increased to 8 deg with frost contaminated wings.

In the second session the take-offs were performed with a pilot in control. After lift-off flight director is followed which commands the aircraft towards a pitch attitude of about 8 deg belonging to an airspeed of V_2 + 10 kts. For flaps 15 results are shown in figure 10.

The pilot confirmed that the deteriorating effect of frost contaminated wings on the aircraft behaviour will not be noticed ahead of reaching rotation speed. At rotation however, the changes in moment equilibrium in pitch due to the frost contamination results in a slow pitch response to elevator input. Extreme stickforces are required for a rotation to 8 deg pitch attitude. After lift-off the aircraft is in a mistrim condition which requires very large pull forces.

No improvement in take-off performance or handling characteristics was found by using smaller flapsettings, or by increasing V_R by 10 kts or reducing the pitch rate at rotation. The stickforces needed for rotation remained extreme.

Finally a take-off was simulated with 100% contamination on the LH wing with the RH wing clean, being the most hazardous asymmetric condition.
In the take-off heading could be maintained by rudder deflection. However, immediately after lift-off full aileron deflection could not prevent the aircraft from rolling to 13 deg bank.

From the second session it was concluded that in the case of a take-off with frost contaminated wings the large stickforces would compel the pilot to abort the take-off.

4.0 Conclusions

Simulator tests were performed to investigate the effect of frost contamination from ground icing on the performance and flight handling characteristics of the Fokker 50 during take-off.

From the tests it is concluded that wing contamination due to ground frost seriously deteriorates the aircraft behaviour in take-off leading to reduced flight safety.

The pitch response to elevator input is slow. Extreme stickforces are required for rotation.
After lift-off the aircraft is in a mistrim condition which requires very large pull forces.

A large increase in take-off distance is experienced.

No improvement was found from cleaning the wing leading edge only or by increasing rotation speed.

The results clearly demonstrates the importance of Advisory Circular AC 20-117 emphasizing the 'clean aircraft concept' under adverse weather conditions before take-off.

5.0 References

1. B.L.G. Ljungström Windtunnel investigation of simulated hoar frost on a two-dimensional wing section with and without high lift devices.
Report FFA-AU-902, April 1972.

DATE	AIRLINE	LOCATION	ACFT TYPE	PRECIPITATION/OBSERVATIONS
27 DEC 68	OZARK	SIOUX CITY	DC-9-10	"LIGHT FREEZING DRIZZLE"
26 JAN 74	THY	CUMAOVAS, TURKEY	F28	PROBABLE CAUSE: "FROST ACCRETION ON THE WINGS"
03 JAN 77	JAL	ANCHORAGE	DC-8-62	"FOG"
27 NOV 78	TWA	NEWARK	DC-9-10	"BLOWING RAIN AND SNOW"
12 FEB 79	ALLEGHENY	CLARKSBURG	NORD 262	"LIGHT SNOW" FROZEN SNOW PHOTOGRAPHED ON EMPENAGE AFTER ACCIDENT
18 FEB 80	REDCOTE	BOSTON	BRISTOL 253	"LIGHT SNOW"
13 JAN 82	AIR FLORIDA	WASH. D.C.	737	"MOI· ·ATE-TO-HEAVY SNOWFALL"
05 FEB 85	AIRBORNE	PHILADELPHIA	DC-9-10	"LIGHT FREEZING RAIN, ICE AND SNOW PELLETS, FOG"
12 DEC 85	ARROW AIR	GANDER	DC-8-63	"LIGHT FREEZING DRIZZLE, SNOW GRAINS"
15 NOV 87	CONTINENTAL	DENVER	DC-9-10	"MODERATE SNOW, FOG"
03 MAR 89	AIR ONTARIO	DRYDEN	F28	"STEADY SNOW"

Table 1 SOME TAKEOFF ACCIDENTS WHERE WING UPPER SURFACE ICE CONTAMINATION IS CONSIDERED TO BE A CONTRIBUTING FACTOR

US Department of Transportation
Federal Aviation Administration

Advisory Circular

CONSOLIDATED REPRINT

This consolidated reprint incorporates Change 1

Subject: HAZARDS FOLLOWING GROUND DEICING AND GROUND OPERATIONS IN CONDITIONS CONDUCIVE TO AIRCRAFT ICING

Date: 12/17/82 AC No: 20-117
Initiated by: AWS-100 Change:

1. PURPOSE. To emphasize the "Clean Aircraft Concept" following ground operations in conditions conducive to aircraft icing and to provide information to assist in compliance.

2. RELATED FEDERAL AVIATION REGULATIONS (FAR) SECTIONS. Sections 121.629, 91.209, and 135.227.

§ 121.629 Operation in icing conditions.

(a) No person may dispatch or release an aircraft, continue to operate an aircraft en route, or land an aircraft when in the opinion of the pilot in command or aircraft dispatcher (domestic and flag air carriers only), icing conditions are expected or met that might adversely affect the safety of the flight.

(b) No person may take off an aircraft when frost, snow, or ice is adhering to the wings, control surfaces, or propellers of the aircraft.

§ 91.209 Operating in icing conditions.

(a) No pilot may take off an airplane that has—

(1) Frost, snow, or ice adhering to any propeller, windshield, or powerplant installation, or to an airspeed, altimeter, rate of climb, or flight attitude instrument system;

(2) Snow or ice adhering to the wings, or stabilizing or control surfaces; or

(3) Any frost adhering to the wings, or stabilizing or control surfaces, unless that frost has been polished to make it smooth.

§ 135.227 Icing conditions: Operating limitations.

(a) No pilot may take off an aircraft that has—

(1) Frost, snow, or ice adhering to any rotor blade, propeller, windshield, or powerplant installation, or to an airspeed, altimeter, rate of climb, or flight attitude instrument system;

(2) Snow or ice adhering to the wings or stabilizing or control surfaces; or

(3) Any frost adhering to the wings, or stabilizing or control surfaces, unless that frost has been polished to make it smooth.

Figure 1 FAA Advisory Circular 20-117

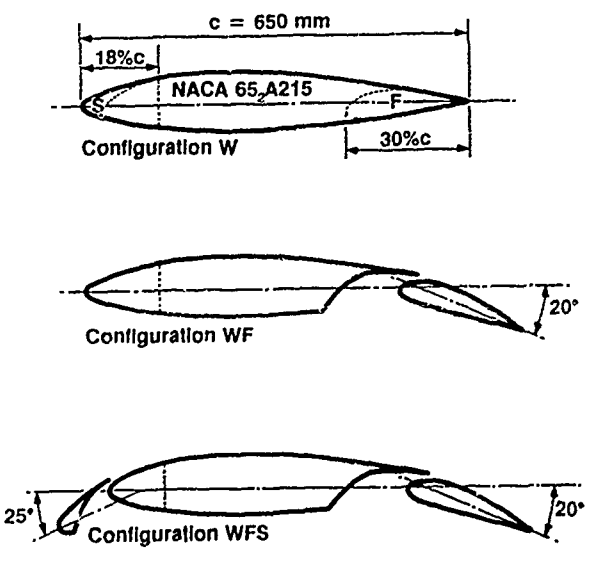

Figure 2

Model configurations FFA test

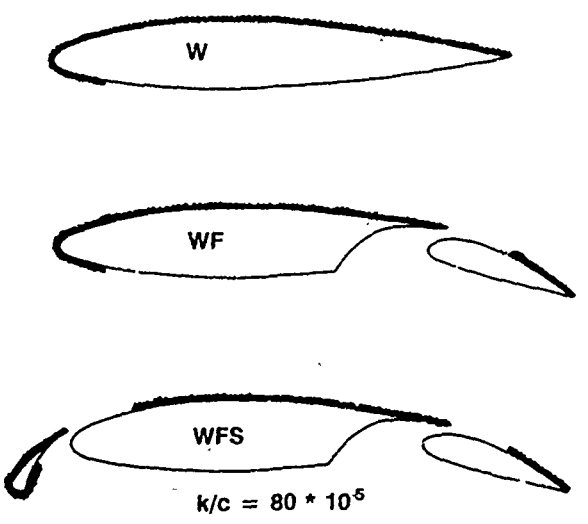

Figure 3

100% Roughness coverage, FFA test

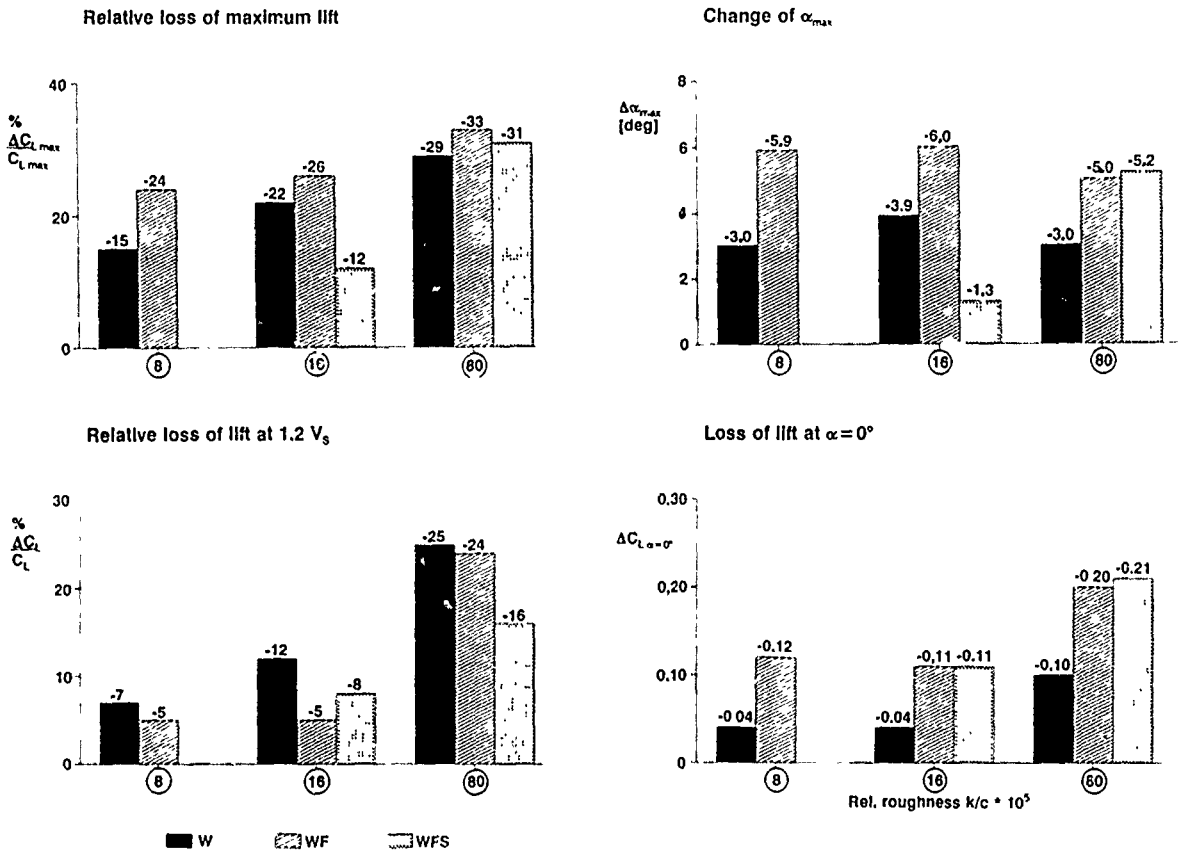

Figure 4 FFA test results
100% roughness coverage

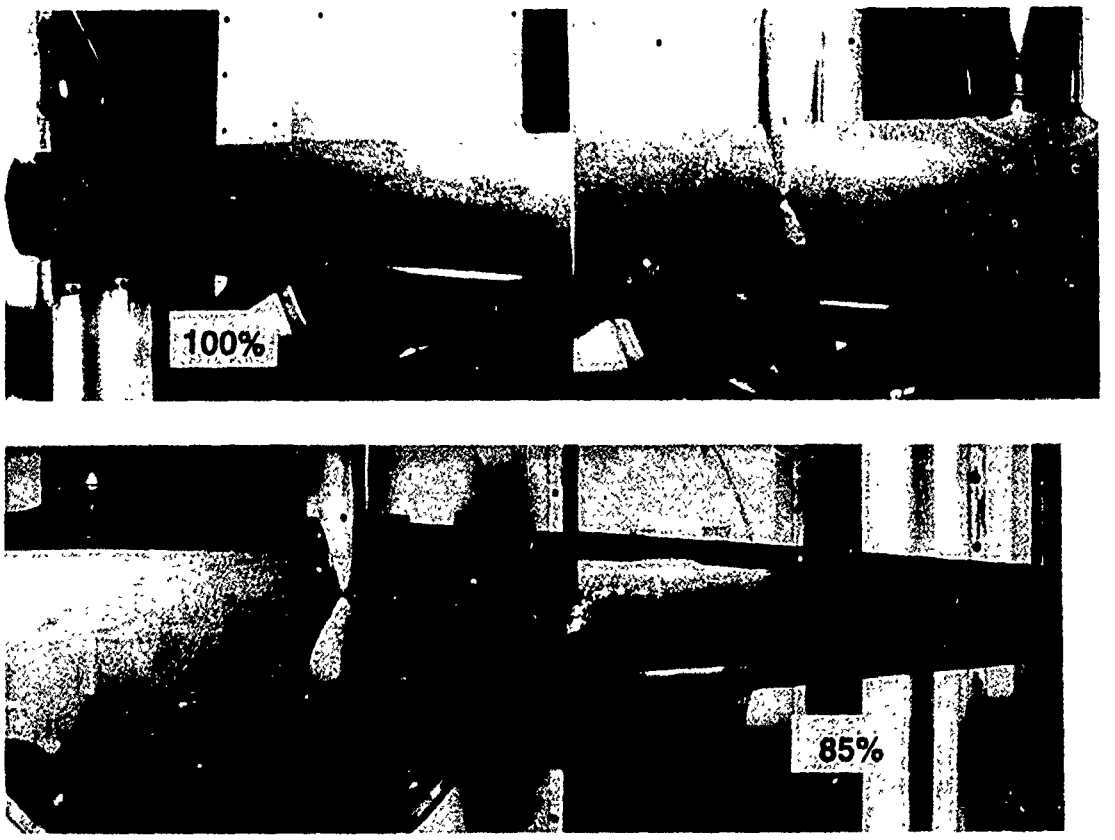

Figure 5 F27 windtunnel model with carborundum 80 on wing upper surface

Relative loss of maximum lift

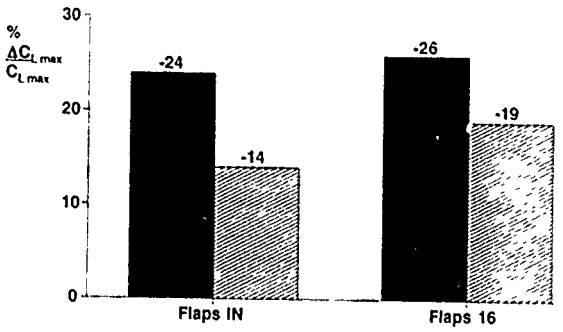

Change of α_{max}

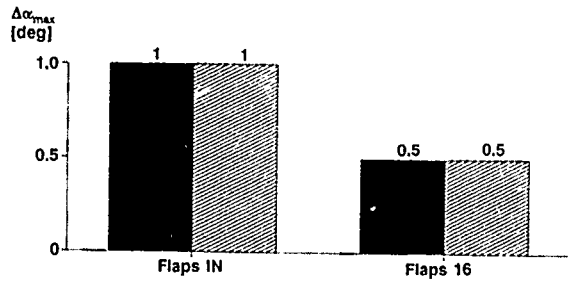

Loss of lift at $\alpha = 0°$

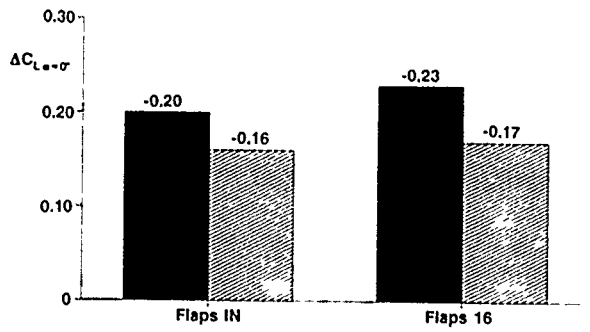

Relative increase of drag at $\alpha = 0°$

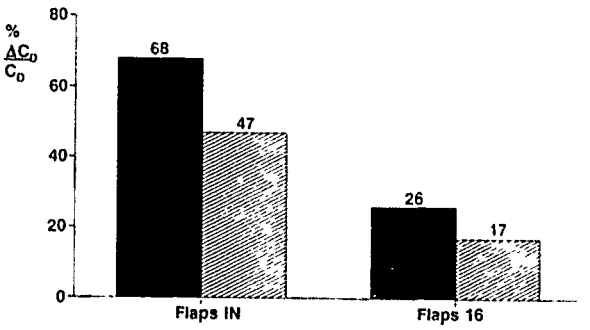

Relative loss of lift at 1.2 V_S

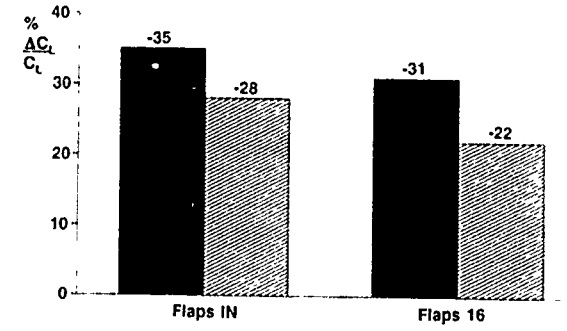

Relative increase of drag at 1.2 V_S

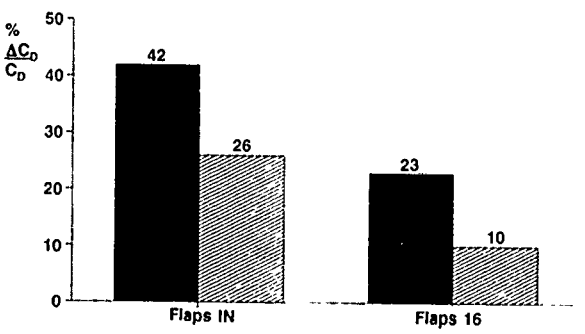

Pitch change at 1.2 V_S

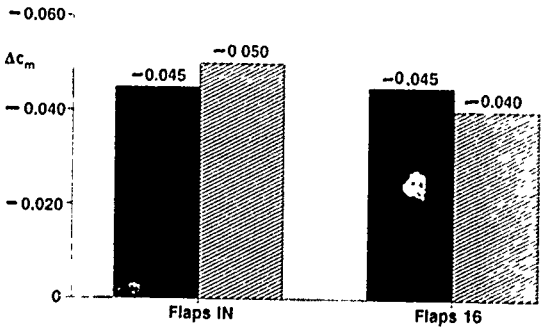

Figure 6 F27 windtunnel test results

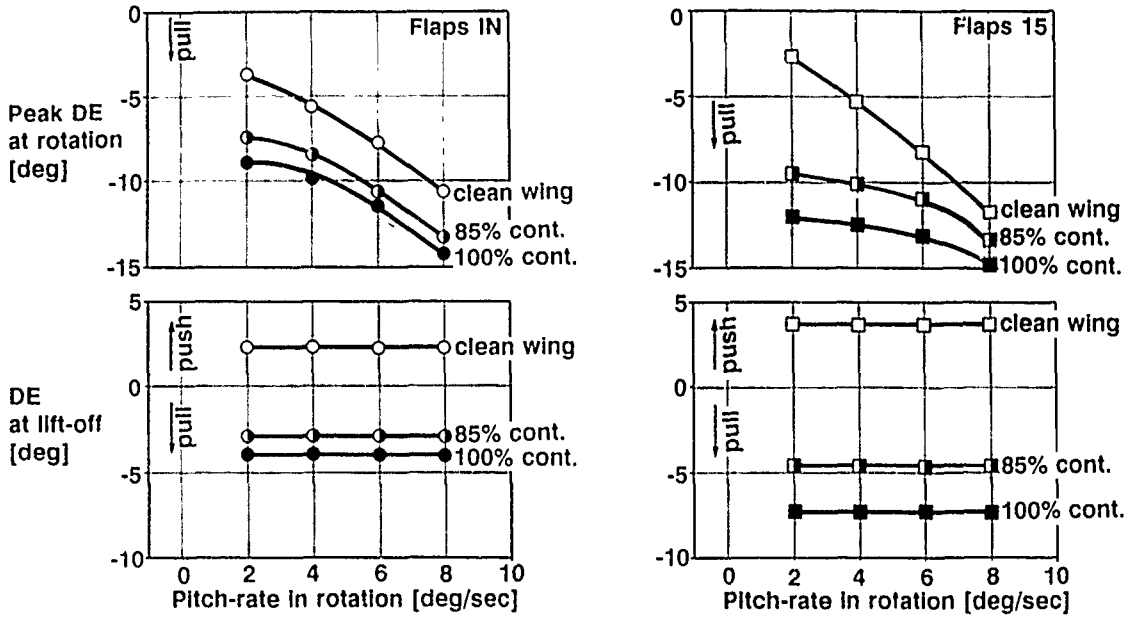

Figure 7 **Effect of frost contamination on behaviour at rotation**

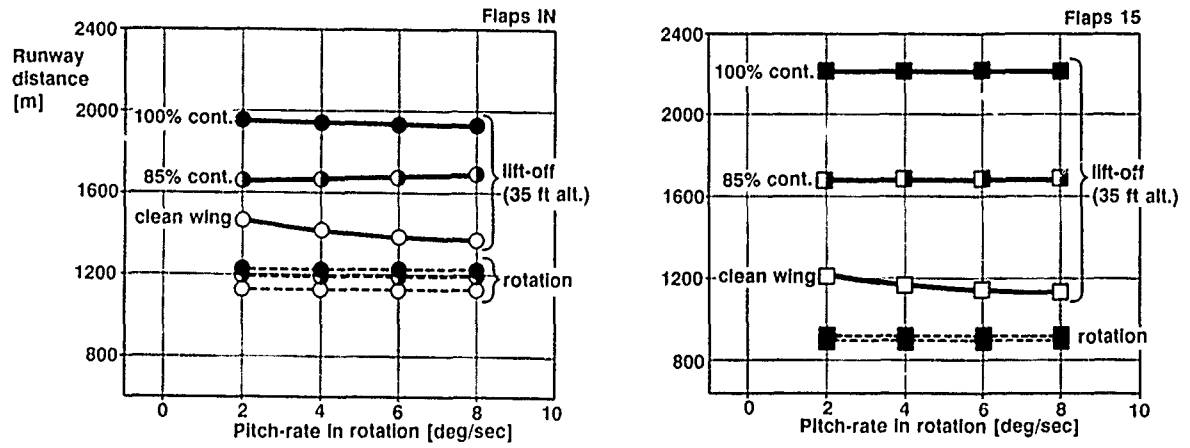

Figure 8 **Effect of frost contamination on take-off distance**

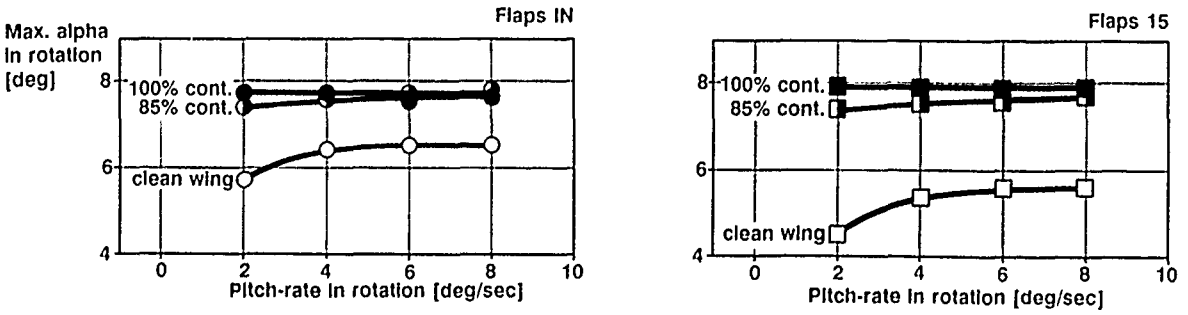

Figure 9 **Effect of frost contamination on maximum angle of attack in rotation**

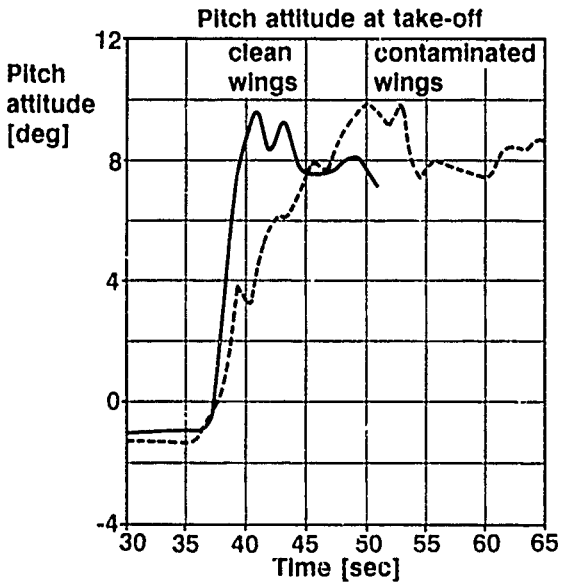

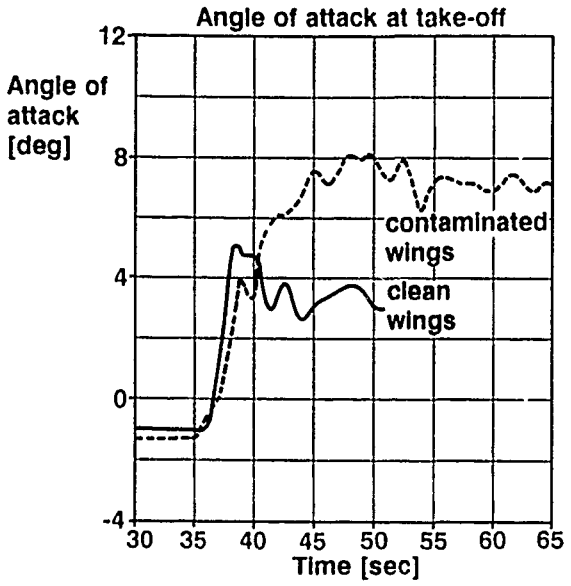

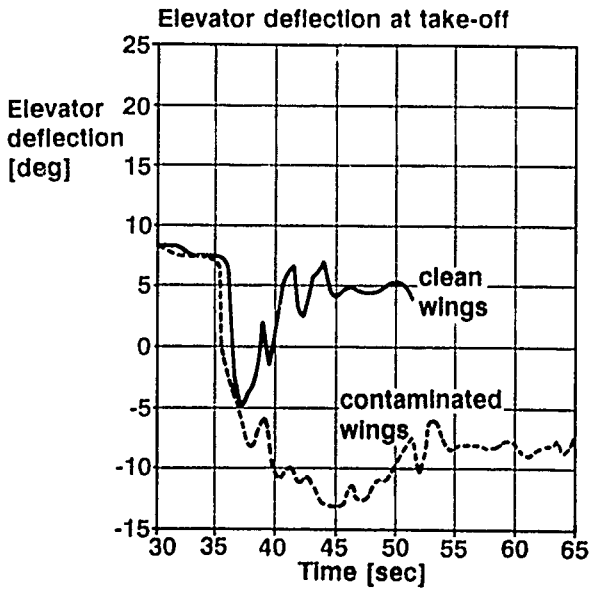

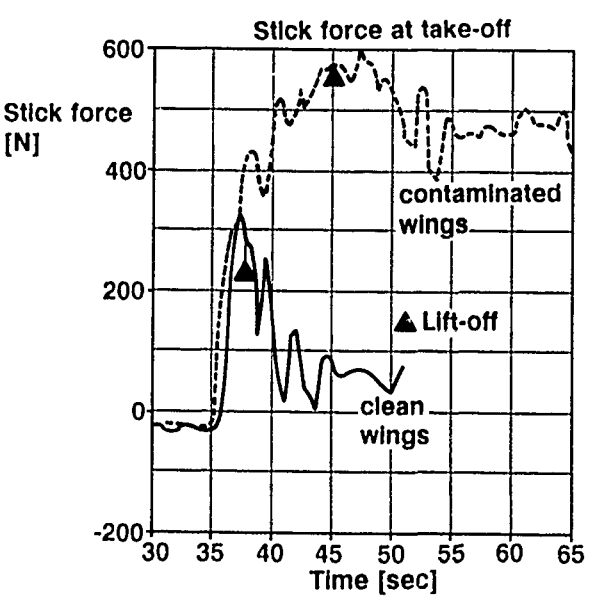

Figure 10 **Effect of 100% frost contamination on Fokker 50 take-off handling characteristics** Flaps 15

Preparation of the Ice Certification of the Dornier 328 Regional Airliner by Numerical Simulation and by Ground Test

by
D.Welte,W.Wohlrath,R.Seubert
Dornier Luftfahrt GmbH
P.O.Box 1303
W-7990 Friedrichshafen, Germany
and
W.Di Bartolomeo and R.D. Toogood
Pratt&Whitney Canada Inc.
1000 Marie Victorin
Longueuil Quebec, Canada

Abstract

The Dornier 328, a new regional airliner, is to be qualified to FAR25/JAR25 requirements for operation into known icing conditions. All lifting surfaces are pneumatically de-iced. Impingement limits have been determined using a validated CFD code. Wind tunnel tests with a model of the whole aircraft and the isolated empennage equipped with artificial ice shapes showed a degradation of handling characteristics due to ice accretion. Extensive two and three dimensional CFD calculations evaluated ice accretion at the deflected elevator horn. Icing tunnel tests have been performed with a model of the horizontal tail with icing similitude fulfilled.

The Dornier Do328 powerplant air induction system has successfully completed a program of icing tests in support of aircraft certification for operation into known icing conditions. Potential flight icing conditions were extensively analysed using a CFD potential flow code and 3D particle tracking routine to identify critical flight icing conditions. The non-altitude tunnel test configuration was similarly analysed to define the test conditions required to correctly simulate the critical flight icing conditions. The tunnel test program verified the analytically predicted critical ice accretion surfaces of the air induction system, the adequacy of the ice protection provisions and demonstrated compliance with the applicable (JAR25) regulatory material.

Notation

b	Relative Heat Factor [4]
C_i	Inlet Collection Efficiency. Quantity of water intercepted by inlet highlight area divided by quantity of water contained in an equivalent area at infinity upstream.
D_d	Volume Median Diameter (μm)
K_0	Droplet Modified Inertia Parameter
k	Model Size
LWC	Cloud Liquid Water Content (g/m^3)
L	Characteristic length (m)
n	Freezing fraction [4]
P_a	Ambient atmospheric pressure (Pa)
PP_a	Partial pressure of water vapour in the atmosphere (Pa)
t_a	Air static temperature at infinity upstream (^{0}C)
V_∞	Velocity at infinity upstream (m/s)
α	Angle of Attack (^{0})
β	Collection Efficiency
η	Flap Angle (^{0})
μ	Viscosity of air kg/m-s
ρ	Density of air kg/m^3
τ	Icing Time

Subscripts

a	Aircraft
f	Full Scale
i	Inlet
k	Ratio of the Values of a Parameter for scale k and full scale (ex.: $P_{ak} = P_{am}/P_{af}$)
m	Model
o	Flight Condition
t	Tunnel Condition

1. Introduction

The DO 328 is a new generation, high speed regional airliner with 30-33 passenger capacity in its initial configuration. It is powered by two Pratt&Whitney PW 119 turboprop engines driving six-bladed Hartzell composite propellers. The primary flight controls, comprising ailerons, elevator and rudder, are mechanically actuated with horns maintaining aerodynamic balance. The aircraft is to be qualified to FAR25/JAR25 requirements for operation into known icing conditions. Figure 1 shows the ice protection system arrangement of the Dornier 328. The leading edges of wings, vertical and horizontal stabilizers are de-iced using conventional pneumatic boots, which are totally integrated into the aerodynamic contours of the lifting surfaces. The engine inlet is also pneumatically de-iced. Elevator and rudder horns will be equipped with imbedded electrically heated mats. Windshield, pitot-static tubes and stall warning are electrically anti-iced, the propeller blades are fitted with heated mats. The last four systems will not be addressed in this paper.

2. Ice Protection of Lifting Surfaces

2.1 Extension of Protected Surfaces

As all de-icing boots have to fit into the aerodynamic contour of the surfaces there are some restrictions to their design. The spanwise extension of the boots is limited by fairings, e.g. wing-fuselage, wing-nacelle, horizontal-vertical tail or by tip sections. The chordwise extension is normally limited by front spars or nose boxes. The chordwise extension of the de-icing boots of the Do 328 was determined using a 2-D trajectory code developed by Dornier and called DROP77. The CFD-code uses the full potential equations for the flowfield of the airfoil calculated in an O-grid with normally 160 x 32 points. For the droplet the equations of motion are solved, interpolating the flow properties from the grid points. Impingement limits for upper and

lower surfaces are determined and the collection efficiency β is calculated. Figure 2 shows a typical result of the trajectory calculation code for the wing root section of the Do 328. The validation of the Dornier code has been done by comparing theoretical calculations with measurements published in NACA TM 3839 [6]. Figure 3 shows the comparison of calculated and measured impingement limits for a 15% symmetrical Joukowsky airfoil at incidences of 0^0-8^0 in dependency of the modified inertia parameter K_0. According to FAR25 requirements, for all calculations defining impingement limits a droplet diameter of 50 microns has been considered. Theoretical calculations included take-off, climb, hold, descent, approach and landing conditions using adequate center of gravity locations, flap settings, elevator and rudder deflections. For each component, such as wing, horizontal and vertical tail, an inner and an outer section was examined. In some cases, especially with flaps deflected, theoretical calculations indicated impinging droplets downstream the front spars of the wing and the horizontal stabilizer. Additional calculations determined the residual ice height at the designated end of the boots. It was shown that the residual ice height never exceeded 6mm in any case.

2.2 Wind Tunnel Tests Using Artificial Ice Shapes

2.2.1 Tests of the Whole Aircraft

To obtain information about the aerodynamic degradation due to ice accretion in the early stage of development of the Dornier 328, many different tests have been performed in the DNW windtunnel (The Netherlands) with a 1:4.2 scaled model of the whole aircraft equipped with artificial ice shapes. 12.5mm (1/2 inch, full scale) mushroom type double horns at the leading edges of the wing, horizontal and vertical stabilizer have been used to simulate a cycle between two inflations of the boots. System failures have been simulated using 75mm (3 inch, full scale) artificial ice. Different configurations have been tested to evaluate a system failure either of the inboard or the outboard wing de-icing system, also of the whole wing and of the empennage. Also a failure of the whole de-icing system has been investigated. All tests have been performed with 75mm (3 inch, full scale) artificial ice at the tips of all lifting surfaces, which are considered to be unprotected. Thus Dornier determined the influence of ice accretion on performance and handling qualities of the Do 328. It can be said that there was no indication that the airplane cannot operate safely in icing conditions. Naturally, the plane has to leave icing conditions immediately in the case of a total failure of the de-icing system. The same procedure will be recommended in case of a partial failure. In addition some restrictions on maximum flap setting may be necessary in heavy icing conditions, with a failure of the empennage de-icing system, as a result of possible limitation in pitching moment compensation.

2.2.2 Tests of the Empennage

Extensive tests with the isolated empennage have been performed in the Dornier windtunnel, especially with artificial ice. Double horns with different heights have also been tested as has hoar frost with various roughnesses and extensions of residual ice downstream of the active part of the boots. Furthermore a failure of the de-icing system at one side or one half side of the horizontal stabilizer was simulated using 75mm (3 inch, full scale) artificial ice at that part with the other areas remaining clean. Figure 4 shows the effect of ice accretion on angle of attack at maximum download for different configurations. Most important influences were seen for the 75mm (3 inch, full scale) double horns and hoar frost from the leading edge up to 35% of the chord. The tests gave significant insight into the aerodynamic qualities of the tail surfaces in icing conditions to guarantee safe operation of the Dornier 328 in heavy ice. These data form the basis for determination of the increase in landing speed and limitations in flap setting required for operation in icing conditions.

2.3 Elevator Horn Ice Accretion

Since the flight controls are mechanically actuated, both elevator and rudder need horns to maintain the aerodynamic balance. The question is now whether these horns accrete ice in any case of deflection or not? If there is ice at the leading edges of the horns the control surfaces cannot be moved. Accreted ice may also change the aerodynamic characteristics of the horn balance significantly. Ice in the chordwise gap between the fixed part of the horizontal tail and the horn may block the elevator.

2.3.1 Theoretical Investigations

Many theoretical investigations have been performed to simulate the horizontal stabilizer of the Do 328 with deflected elevator and horn in icing conditions. For 3-D calculations the AMI particle tracking code ICE [7] was used in conjunction with the VSAERO potential flow code [1]. Ice shapes at the leading edge of the horizontal tail and at the deflected horn have been calculated two-dimensionally with the ONERA Ice Accretion Code [8],[9]. For the flowfield calculations the gaps between the fixed part of the tip and the horn had to be closed. To achieve a realistic simulation of the flowfield, measurements of the pressure distribution at the tip and the horn have been performed on the model of the horizontal stabilizer in the Dornier wind tunnel for different elevator settings and angles of attack. So it was possible to estimate the quality of the theoretical methods. The calculations showed that there was ice on the deflected horn in some cases and that ice protection of the horns should be considered.

2.3.2 Icing Tunnel Tests with the Horizontal Stabilizer

Dornier used the BF Goodrich icing tunnel for some experiments, the model of the horizontal tail from the previous tests was tested in simulated icing conditions. The scale had changed to 1:4.4 according to the latest design of the Do 328 empennage. Tunnel information is as follows:

- Test Section: 0.56 m wide × 1.12 m high
- Speed: 25 - 90 m/s
- Droplet size: 14 - 40 microns
- LWC: 0.3 - 2.3 g/m³
- Temperature: -30 - 0 °C
- Altitude: Ground Level

The tests were accomplished in the BF Goodrich icing tunnel in September 1990. Figure 7 shows the installation of the model. It was fixed at one tunnel wall, such that the tip could be observed through a window of Plexiglas in the opposite wall and on top. Here the model could be investigated during the tests and final ice shapes could be documented. As the model was too large for the tunnel, only a part of it could be placed in the test section. To achieve a representative flowfield, the required distance between the tip and the tunnel wall was determined by VSAERO - calculations. The ice accretion was documented in two different spanwise sections called mid and tip section. Shapes at the leading edge were documented by photographs with a grid in the foreground. Shapes at the horn were removed by heating the surface with an imbedded hot wire and documented by a replica formed of plaster in a parafin mould. The model was protected by a metal shield in front of the leading edge until the test conditions i.e. LWC, droplet size, temperature, free stream velocity achieved nearly constant values. As time was limited, only 3 cases of the Do 328 flight envelope have been tested:

- Climb at H = 0ft with v = 150KCAS (max. negative elevator deflection)
- Approach at H = 12000ft with v = 160KCAS (max. positive elevator deflection)
- Hold at H = 12000ft with v = 200KCAS (no elevator deflection)

Atmospheric conditions are defined in FAR25/JAR25. As the horns have been considered to be unprotected, the following additional requirements have to be applied: for Intermittent Maximum Conditions a flight of 15km in clouds must be simulated, for Continuous Maximum an icing time of 30 minutes must be considered for 20 micron droplets. According to the icing similitude laws, described in AGARD 127 (Aircraft Icing) [3], droplet diameter (see equation 1), LWC (see equation 2) and icing time (see equation 3) had to be scaled from full scale to model conditions with thermodynamic similitude (see equation 5 on page 4) fulfilled.

$$k = \frac{D_{dk}^{1.61} \times V_{\infty k}^{0.61}}{P_{ak}^{0.39}} \qquad (1)$$

$$LWC_k = \frac{P_{ak}^{0.8}}{k^{0.2} \times V_{\infty k}^{0.2} \times T_{ak}^{1.6}} \qquad (2)$$

$$\tau_k = \frac{k^{1.21} \times T_{ak}^{1.6}}{V_{\infty k}^{0.8} \times P_{ak}^{0.8}} \qquad (3)$$

Only some cases have been found where thermodynamic similitude could be achieved because the tunnel can only be operated at ground level. For these cases it was impossible to scale the correct droplet diameter and/or the correct LWC because of the scaling factor of 1:4.4. In general, it was not possible to simulate droplets as small as 20 microns. Nevertheless, the mass of incoming water was calculated for 20 micron droplets with increased icing time according to conservation of mass in all cases where the required LWC could not be achieved. Thus the ice accretion results must be on the conservative side. Test cases checked with the ONERA-code showed good agreement for full scale and model conditions scaled by the similitude laws. In Figure 5 nearly the same ice shape for full scale and model can be seen, even if the conditions are absolutely different. Figure 6 shows the conditions, which could be tested with icing similitude fulfilled. Some additional testcases have been developed with similitude approximately achieved, especially for approach conditions.

2.3.3 Results

Results from 2-D and 3-D calculations are shown in comparison with measurements. Figure 8 shows the calculated pressure distributions at the tip section for the test cases Approach, Hold and Climb calculated from the 2-D ONERA code and compared to the Dornier wind tunnel tests. The leading edge is represented correctly, but the potential 2-D code overpredicts velocities at the horn in the cases of deflection. Figure 9 shows the result from the ice shape calculation with the ONERA code for Intermittent Maximum Conditions for an Approach case. Good agreement for the leading edges of the mid and the tip section can be seen. The code predicts that there is ice at the horn, but the shape shows less agreement in this case. There exists some room for improvement but the overall results look promising. Figure 10 shows the result for Hold Conditions at Intermittent Maximum. The code predicts the resulting ice shapes satisfactorily. Figure 11 shows the result for Hold Conditions at Continuous Maximum. Agreement at the tip is perfect, the shape at the mid section is correctly represented but the amount of ice is overpredicted. In Figure 12 a result for Climb Conditions at Continuous Maximum can be seen. Ice at the horn is predicted correctly by the code, only the shape is not exact. Figure 13 shows the 3-D VSAERO pressure distributions for the test cases Approach ($\alpha = -10^0, \eta = 11^0$), Hold ($\alpha = 0^0, \eta = 0^0$) and Climb ($\alpha = 2^0, \eta = -7^0$). The measured values from the Dornier wind tunnel are also shown. It can be seen that the flowfield is correctly represented in the ice accreting regions of the airfoil. Figure 14 shows droplet trajectories for the these cases, in Figure 15 the resulting collection efficiencies are shown.

3. Powerplant Air Induction System Ice Protection

3.1 Powerplant Installation

The powerplants are wing mounted and operate in the conventional tractor mode. The air induction system for each engine is of a quasi-pitot type offset below the turbomachinery centerline and incorporates a separator duct to enhance foreign object ingestion tolerance. Figure 16 shows the general configuration of the air induction system. The duct lower surface, in particular, is shaped so as to minimise significant ice accretion thus reducing the potential for ice ingestion from this location. The air induction system is designed to cater for the conflicting requirements of ice protection and good aerodynamic performance. During the initial development phase a full scale model of the air induction system was fabricated and subjected to airflow rig te-

sting at Pratt & Whitney to verify its aerodynamic characteristics. Subsequent testing with a PW119 engine has confirmed satisfactory inlet system operation.

3.2 Ice Protection Features

The Do328 powerplant air induction system incorporates ice protection features in critical areas in the form of pneumatically operated de-icing systems suplied by the B.F. Goodrich Co, Uniontown, Ohio. Figure 17 shows the protected surfaces of the air induction system. The ice protection of the Do328 air induction system is similar to that used successfully on other PW100 engine powered aircraft since 1983. (Embraer EMB120, Aerospatiale ATR42, ATR72)

3.3 Ice Protection Requirements And Qualification

The engine air induction system is to be qualified to JAR25 1093(b) requirements for operation into known icing conditions. In support of this objective it has been subjected to simulated icing conditions in the National Research Council engine laboratory facility at Ottawa, Canada. (Fig 18)

3.4 Similitude

3.4.1 Aerodynamic Similitude

In order to ensure the satisfactory simulation of the icing conditions to be encountered at altitude in the JAR25 icing environment, whilst undertaking the qualification testing in a non-altitude icing tunnel, an extensive computational analysis of potential flight icing conditions within the aircraft and JAR25 icing envelopes was undertaken. This analysis was directed at identifying critical icing conditions including the evaluation of inlet water collection efficiency in flight and in the tunnel and impingement on the inlet surfaces, both in the entry and on the critical lower inside surface.

The analysis was undertaken utilising the VSAERO [1], [2] potential flow code in conjunction with a PWC developed 3 dimensional particle tracking code. The model utilised for the altitude conditions consisted of a one half aircraft model (minus empennage) as shown in Figure 19. Typical particle trajectories in the approach flowfield in a plane approximating the nacelle vertical plane of symmetry are shown in Figures 20 - 23.

The influence of the propeller spinner profile and the approach flowfield diffusion in deflection of the droplets toward the air induction system lower lip and interior lower surfaces are clearly evident. On the basis of this phenomenon, the lower lip and interior lower surfaces were determined to be critical ice accretion surfaces, the latter especially so, as it was potentially an unprotected surface.

The non-altitude test installation incorporating the nacelle and air induction system, together with the wind tunnel configuration were also analysed using the VSAERO potential flow code and the 3D particle tracking code to provide a comparison with the flight conditions. Figure 24 show details of the analytical model of the test installation. Figures 25 - 28 inclusive show typical droplet trajectories in the tunnel approach flowfield and into the air inlet system. A reduced influence of the spinner profile, resulting from only partial immersion in the flowfield, together with the tunnel wall influences became evident during the analysis. As a result some adjustment from a true Reynolds number equivalence in the approach flowfield was made in order to obtain optimum similitude of droplet trajectories between flight and corresponding tunnel test conditions.

Droplet Modified Inertia Parameter (K_0) given by Equation 4 [5] was maintained in each test condition at the value appropriate tor the flight condition being simulated by the adjustment of the droplet median diameter.

$$K_0 = 8.192 \times 10^{-9}\left(\frac{V_\infty}{\mu}\right)^{0.6}\left(\frac{D_d^{1.6}}{L\,\rho^{0.4}}\right) \quad (4)$$

3.4.2 Thermal Similitude

Approximate thermal similitude was achieved at the critical air induction system lower surface in accordance with the approach documented in Reference [3] based on the work of Messinger [4] in defining the surface heat balance occuring in a wet icing condition. For thermal similitude of an unprotected surface Equation 5 [3] relates air temperature, velocity and pressure to the freezing fraction (n) and relative heat factor (b) [4], and should be equivalent in the flight and test conditions:

$$1.06 \times \frac{10^6}{P_s} = t_s(1+b) + 1530\frac{PP_\infty}{P_s} + 79.7nb + (3.65 + b)\frac{V_\infty{}^2}{8370} \quad (5)$$

Complete thermal similitude was not possible because of the significant effect of the pressure differences on the total heat balance. However, the residual error for the unheated critical lower surface of the air inlet system was found to be insignificant. The air stagnation temperature was slightly modified in the test condition in order to provide the optimum thermal similitude.

3.5 Qualification Test Conditions

Selection of the demonstration icing conditions for the Do328 air induction system was based on aircraft operational requirements and the guidance material of JAR25 ACJ25.1093(b) Method I as well as the results of the CFD/trajectory and thermal analyses outlined in the previous sections. The program of tunnel tests was negotiated with and approved by the JAA certification authority prior to commencement of testing. Figure 29 shows the agreed test conditions for the tunnel test program together with the simulated flight conditions. Conservation of mass of water entering the air induction system is maintained by compensation for differences in approach airspeed and inlet collection efficiency between flight and tunnel operating conditions in accordance with Equation 6.

$$LWC_t = LWC_0 \times \frac{V_0}{V_t} \times \frac{C_{t_0}}{C_{t_t}} \qquad (6)$$

3.6 Tunnel Test Program

3.6.1 Installation

In order to provide realistic air induction system operating conditions and to verify acceptability of system ice protection provisions, a PW119 engine turbomachinery module was installed together with the production configuration air induction system in a full scale nacelle lower section model.

Realistic entry flow and impingement and representative separator duct airflow were provided by operation of the tunnel in a free jet configuration. The tunnel airflow is induced primarily by a high pressure compressed air ejector located downstream of the nacelle test section and powered by a 5 MW industrial compressor. A degree of control of the tunnel air temperature is provided by a 5.5 m x 5.5 m refrigeration heat exchanger located upstream of the water spray nozzle array coupled to a refrigeration plant of nominal 130 tonnes capacity. However, prevailing atmospheric temperature conditions have a significant influence on the achievable tunnel air temperatures and testing must be scheduled accordingly.

3.6.2 Icing Simulation

The water spray nozzles are located approximately nine meters upstream of the test section and are of the air atomising type. The nozzle array consists of 48 individually selectable nozzles installed on 8 radial struts in a 2.2m diameter duct section. Droplet diameter distribution approximates the Langmuir 'D' distribution.

The spray distribution within the tunnel at the reference plane 2m upstream of the nacelle inlet plane was verified for representative test conditions with a 3 mm diameter wire mesh of 25.4 mm x 25.4 mm spacing temporarily installed for this purpose. Nozzle selection was adjusted as necessary to ensure a uniform water distribution at this location prior to commencement of the qualification test program.

The water flow rate necessary to provide the required supercooled water liquid water concentration (LWC) at the test section is calculated with an interactive routine. This routine calculates the changing psychrometric, thermodynamic and kinetic conditions within the tunnel between the spray nozzle array and the nacelle air inlet and augments the computed water flow rate as necessary to offset potential evaporation losses.

3.7 Test Conditions

Each test condition was maintained for 30 minutes (18 minutes for Climb) with alternating liquid water concentrations as appropriate for Continuous and Intermittent Maximum icing conditions in accordance with ACJ 25.1093(b) Table I. The actuation of the air induction system ice protection features was delayed 2 minutes after initiation of the icing encounter in each test to simulate a realistic delay in recognition of an icing condition. Following the icing encounter, engine acceleration from Idle to Maximum Continuous power setting was undertaken with a 1 second power lever movement to demonstrate acceptable transient operation. For test purposes the ice protecton features of the air induction system and engine were configured to be the most critical in terms of supply pressure, surface heating, surge margin etc.

3.8 Test Results

Initial testing demonstrated the need to provide additional protection to the duct lower and side surfaces to address operation in the warmer temperature icing regime. With this optimisation in place all qualification tests were conducted with satisfactory results i.e. no unacceptable power loss (including surge or flame-out), satisfactory transient operation and no engine damage. Figures 30 and 31 show the condition of the air induction system following typical qualification tests.

4. Conclusions

- Impingement limits for 50 micron droplets have been used to define the chordwise extension of the de-icing boots of the lifting surfaces of the Dornier 328.
- Wind tunnel tests with artificial ice gave information about degradation of handling characteristics due to ice accretion.
- Tests with the horizontal tail of the Dornier 328 in the BF Goodrich icing tunnel showed ice accretion at the deflected elevator horn. It could be seen that there was ice at the leading edges of the horns but no ice in the chordwise gap between the fixed part of the horizontal stabilizer and the horn.
- There still remain uncertainties caused by scaling effects and tunnel limitations. Problems with ice at the leading edges of the horns might occur if the horns were unprotected.
- To guarantee safe operation in icing conditions in compliance with the Certification Requirements, the horns of the Do 328 will therefore be anti-iced using electrical heated mats which are imbedded into the carbon structure.
- Further work remains to be done at Dornier to calculate the corresponding ice shapes at the leading edges of all lifting surfaces across the entire flight envelope according to the revised Flight Airworthiness Requirements. The most critical shapes will be determined for flight tests with artificial ice shapes before the plane will enter flight tests in natural icing conditions.
- A Do328 powerplant air induction system together with a PW119 turbomachinery module has been subjected to simulated icing conditions in support of qualification of the aircraft for operation into known icing conditions.

- A CFD analysis was undertaken to identify the required test conditions in the non-altitude test facility to correctly simulate the critical altitude flight icing conditions identified within the aircraft flight operating envelope and the icing atmospheric conditions defined in JAR25.
- The qualification test plan agreed with the certification authority was formulated on the basis of the aircraft flight envelope and the CFD analysis of the droplet trajectories and inlet enrichment for flight and tunnel regimes together with optimum thermal similitude for the unheated inlet system critical lower surface.
- The air inlet was specifically designed to minimise ice accretion whilst retaining good aerodynamic performance. Although this objective was achieved it was not possible, in the conditions tested, to achieve satisfactory operation in the critical temperature regime (TAT $\geq$ -4°C) without protection of the inlet lower surface.
- The potential flow CFD and droplet trajectory analysis was invaluable in identification of the test conditions required for similitude and in identification of critical impingement locations. However, more sophisticated analytical methods including ice accretion, ice structure and runback models, integrated with improved CFD methods capable of accomodating both separated and secondary flows would be necessary as minima for advance prediction of acceptability of potential ice accretion within the air induction system.
- The Do328 air induction system ice protection features have demonstrated satisfactory performance in a program of qualification icing tests designed to demonstrate compliance with the JAR25 1093(b) regulatory material.

References

[1]Maskew, B., *Prediction of Subsonic Aerodynamic Characteristics - A Case for Low-Order Panel Methods,* AIAA-81-0252.

[2]Clark, D.R., Maskew, B., and Dvorak, F.A. *The Application of a Second Generation Low-Order Panel Method-Program "VSAERO" - to Powerplant Installation Studies,* AIAA-84-0122.

[3]Armand, C., Charpin, F., Fasso, G., and Leclerc, G., *Techniques and Facilities Used at the Onera Modane Centre for Icing Tests,* AGARD-AR-127, Ref. 6, Appendix.

[4]Messinger, B.L., *Equilibrium Temperature of an Unheated Icing Surface as a Function of Air Speed,* Journal of Aeronautical Science, Jan. 1953

[5]Bowden, D.T., Gensemer, A.E., and Skeen, C.A., *Engineering Summory of Airframe Icing Technical Data,* FAA Technical Report ADS4, AD 608865, March 1964

[6]Gelder, T.F., Smyers, W.H., and von Glahn, U., *Experimental Droplet Impingement on Several Two-Dimensional Airfoils with Thickness Ratios Of 6 to 16 Percent,* FAA Technical NACA TN 3839, December 1956

[7]Nathman J.K., *Particle Trajectory and Ice Acretion Program, Users' Manual,* ANALYTICAL METHODS, INC., August 1990

[8]Guffond, D., Cassaing, J., Henry, R. and Bossy, M., *Overview of Icing Research at ONERA,* ONERA Note Technique 1988-123

[9]Brunet, L., *Conception et Discussion d'un Modele de Formation du Givre sur des Obstacles Varies,* ONERA Note Technique 1986-6

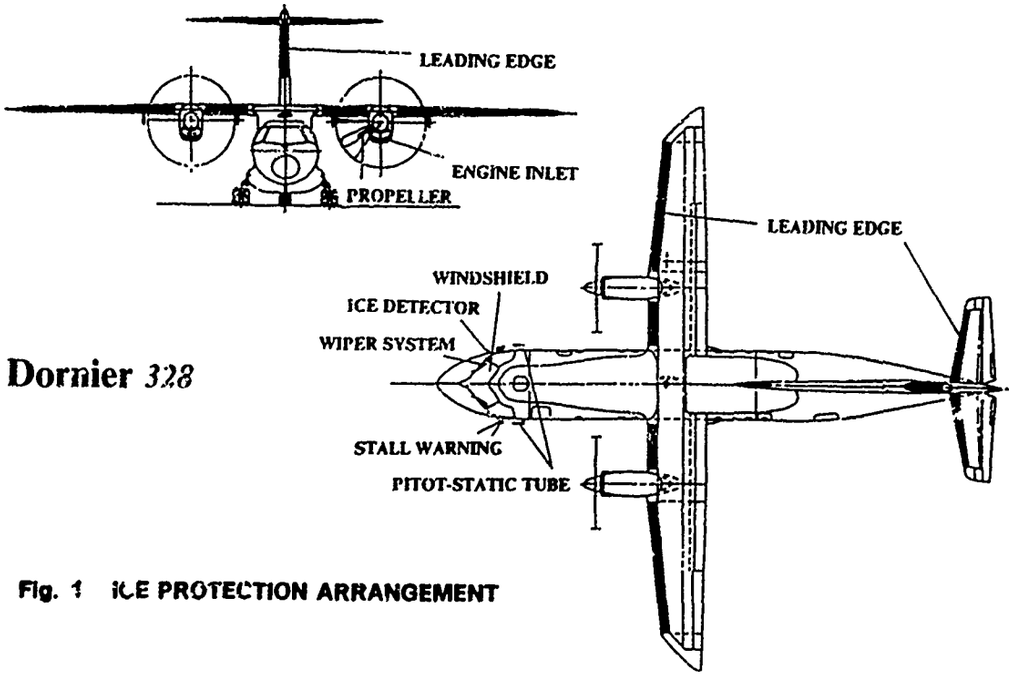

Fig. 1 ICE PROTECTION ARRANGEMENT

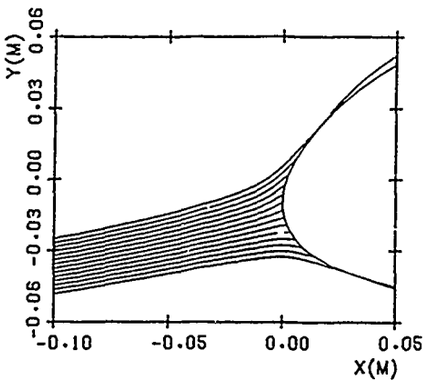

FIG. 2 : DROP77 TRAJECTORY–CALCULTION

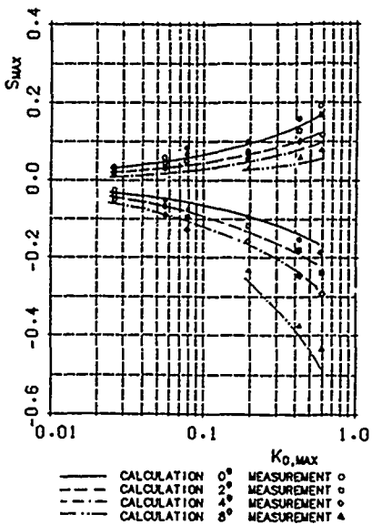

FIG. 3 : DROP77 VALIDATION
IMPINGEMENT LIMITS JOUKOWSKY (15% SYM.)
+ UPPER SIDE , – LOWER SIDE

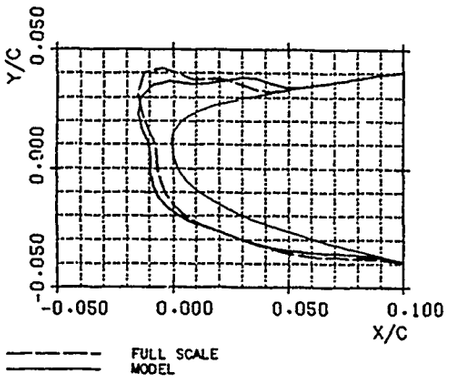

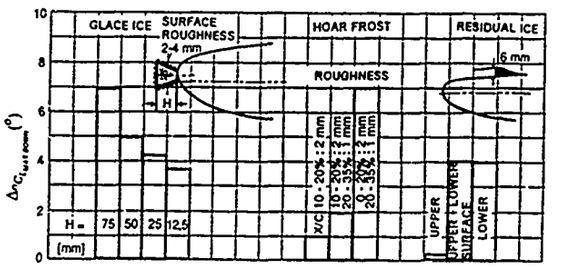

Fig 4 EFFECT OF VARIOUS ICE FORMATIONS AT THE HORZONTAL TAIL ON ANGLE OF ATTACK OF MAXIMUM DOWNLOAD (WIND TUNNEL TEST)

FIG. 5 : VALIDATION OF ICING SCALING LAWS (ONERA–CODE)
FULL SCALE: H=12400/M=0.384/P=0.634/T=–9.35/D=24.6/LWC=1.06/TAU=373
MODEL : H=0/M=0.199/P=0.9857/T=–8/D=14/LWC=2.30/TAU=75

	FULL SCALE						MODEL						
CASE (-)	H (ft)	V (KCAS)	T∞ (°C)	d (microns)	LWC (g/m³)	τ (sec)	H (ft)	V (m/sec)	T∞ (°C)	d (microns)	LWC (g/m³)	τ (sec)	COND (-)
Ho	13000	197	-4.9	27.9	1.13	365	0	90	-4	14	2.3	57	IM
Ho	12400	201	-9.4	24.6	1.06	373	0	65	-8	14	2.3	75	IM
Ho	12500	202	-13.8	20.0	0.89	465	0	30	-12	14	2.3	171	IM
Ho	13000	197	-4.9	27.9	0.7	1800	0	90	-4	14	1.42	281	CM
Ho	12400	201	-9.4	24.6	0.65	1800	0	65	-8	14	1.41	364	CM
Ho	12500	202	-13.8	20.0	0.5	1800	0	30	-12	14	1.29	662	CM
Cl	1000	148	-4	35.3	1.71	269	0	75	-4	14	2.3	46	IM
Cl	1000	149	-8	35.3	1.71	257	0	75	-8	14	2.3	43	IM
Cl	1000	150	-12	35.3	1.71	246	0	75	-12	14	2.3	41	IM
Cl	1000	152	-16	35.3	1.71	222	0	75	-16	14	2.3	37	IM
Cl	1000	153	-20	35.3	1.71	200	0	75	-20	14	2.3	34	IM
Cl	1000	148	-4	35.3	0.7	1800	0	75	-4	14	0.94	304	CM
Cl	1000	149	-8	35.3	0.65	1800	0	75	-8	14	0.87	304	CM
Cl	1000	150	-12	35.3	0.5	1800	0	75	-12	14	0.67	304	CM
App	12400	159	-4.9	24.2	1.04	398	0	50	-4	14	2.3	82	IM

Fig. 6 : TEST CONDITIONS FULL SCALE - MODEL (SCALE 4.4)

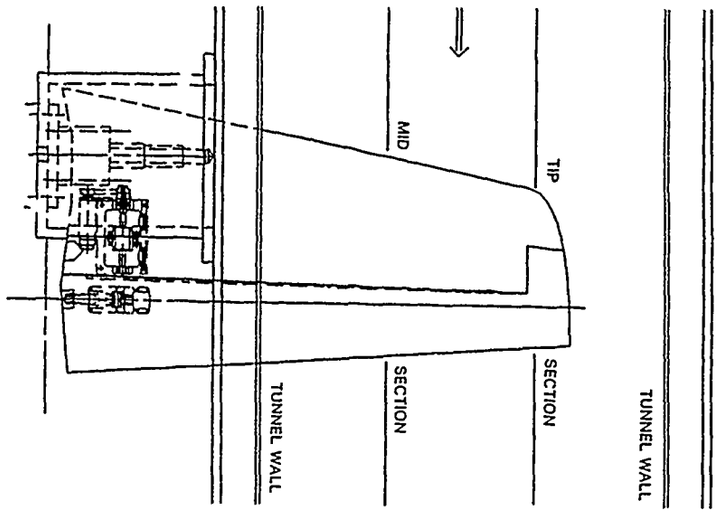

Fig. 7: MODEL INSTALLATION BF GOODRICH ICING TUNNEL

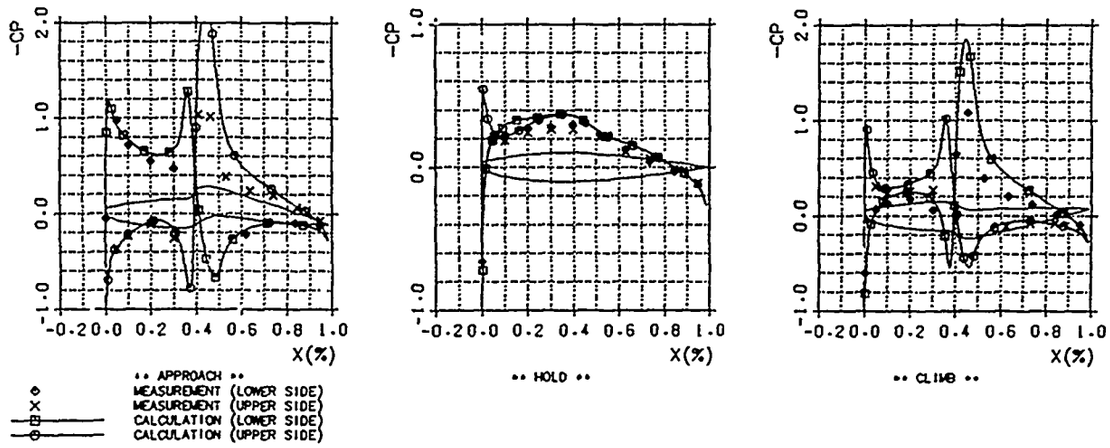

FIG. 8 : PRESSURE DISTRIBUTION (2-D ONERA-CODE)

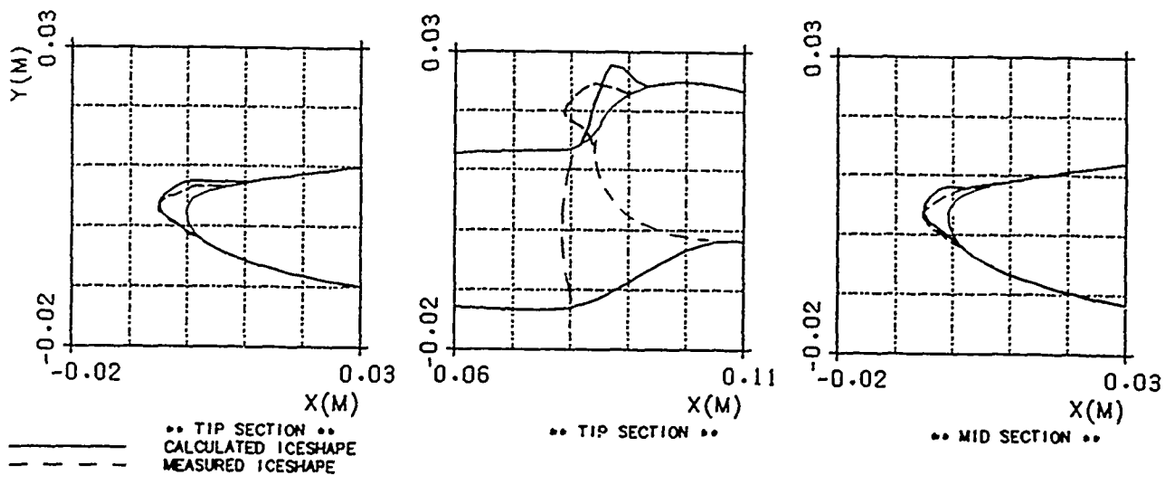

FIG. 9 : ICING TUNNEL TEST DO328 ELEVATOR (APPROACH AT INT. MAXIMUM)
••• M=0.071/D=14/T=-9.1/LWC=1.64/TAU=200 •••

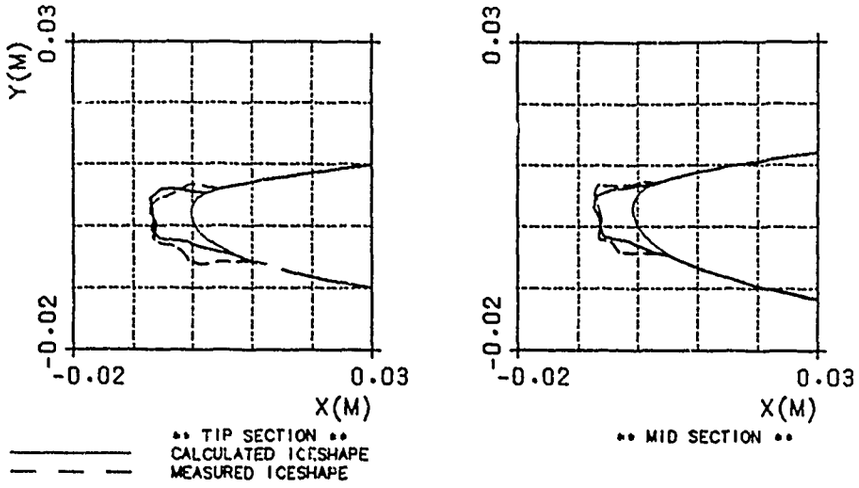

FIG.10: ICING TUNNEL TEST DO328 ELEVATOR (HOLD AT INT. MAXIMUM)
*** M=0.089/D=14/T=-11.3/LWC=[illegible]/TAU=[illegible] ***

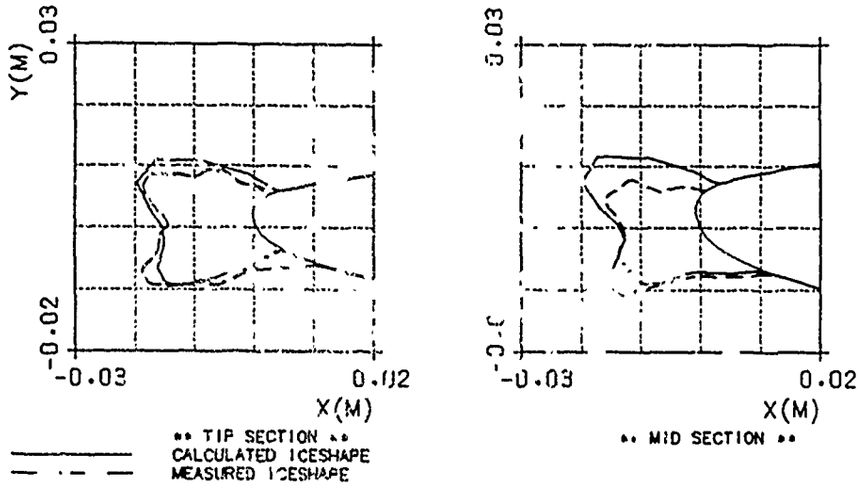

FIG.11: ICING TUNNEL TEST DO328 ELEVATOR (HOLD AT CONTINUOUS MAXIMUM)
*** M=0.196/D=14/T=-7.5/LWC=[illegible]41/TAU=364 ***

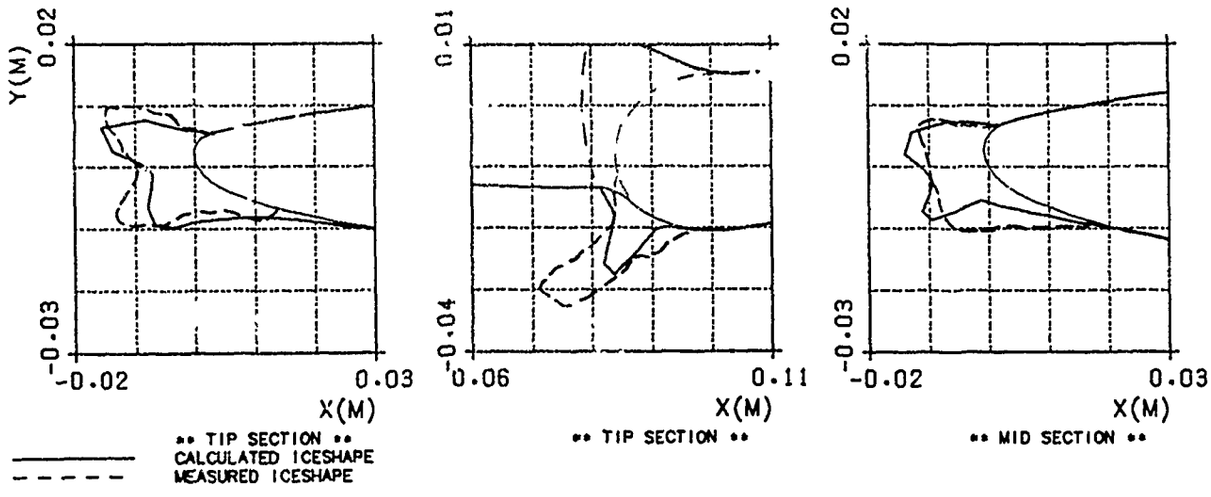

FIG.12: ICING TUNNEL TEST DO328 ELEVATOR (CLIMB AT CONTINUOUS MAXIMUM)
*** M=0.230/D=14/T=-7.7/LWC=0.84/TAU=304 ***

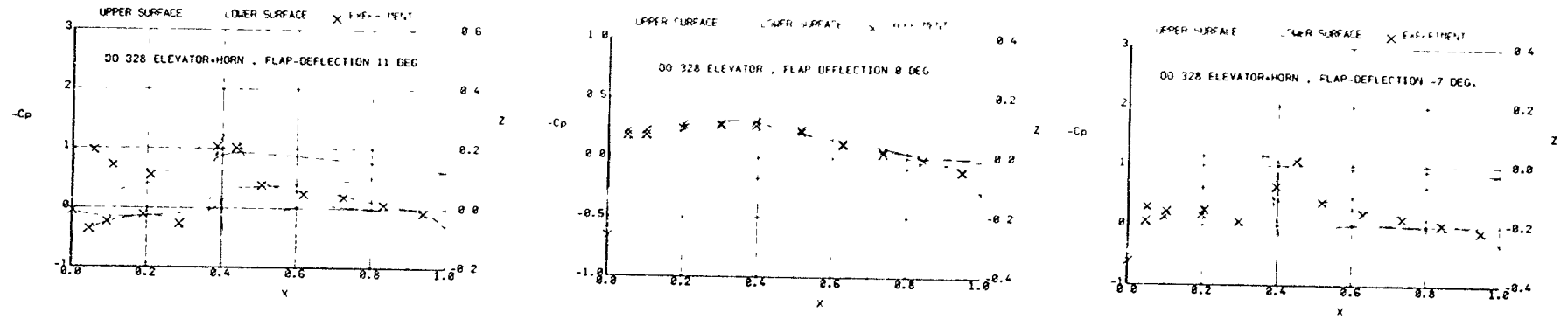

Fig. 13: PRESSURE DISTRIBUTION (3-D VSAERO)

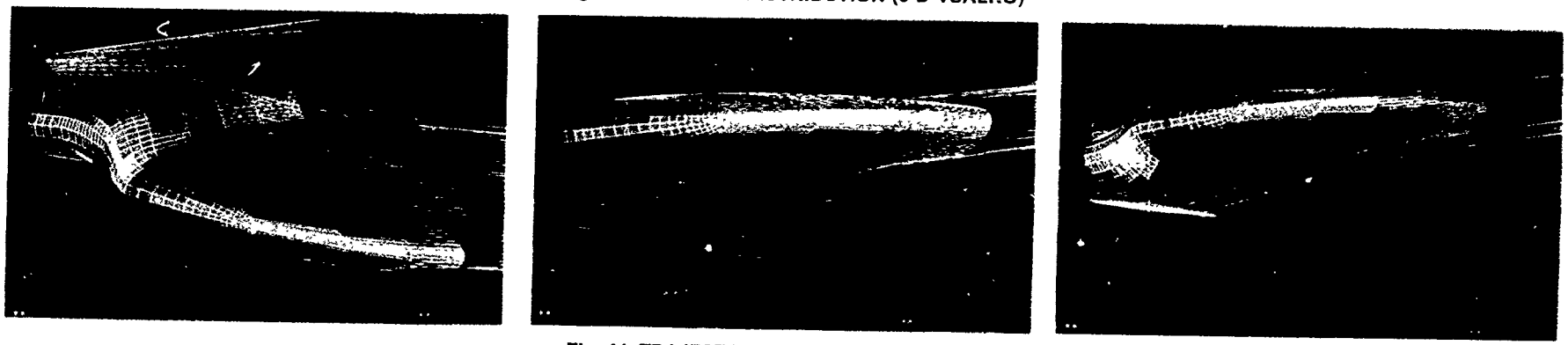

Fig. 14: TRAJECTORY CALCULATION (3-D ICE)

** DO 328 ELEVATOR+HORN , FLAP-DEFLECTION 11 DEG. (MODEL) **

** DO 328 ELEVATOR , FLAP-DEFLECTION 0 DEG. (MODEL) **

** DO 328 ELEVATOR+HORN , FLAP-DEFLECTION -7 DEG. (MODEL) **

Fig. 15: COLLECTION EFFICIENCY (3-D ICE)

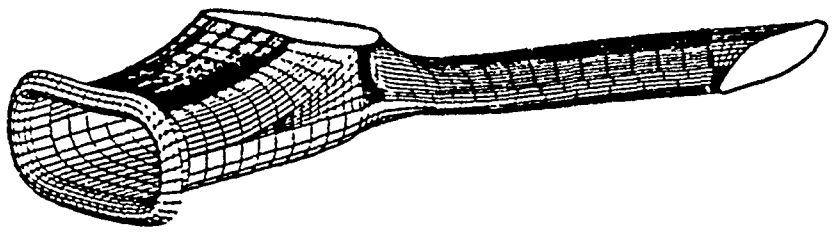

Figure 16: Dornier Do 328 Air Induction System Configuration

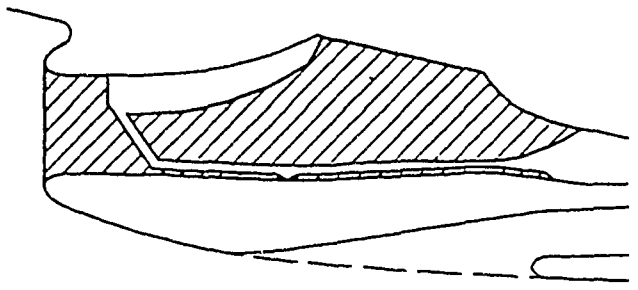

Figure 17: Dornier Do 328 Air Induction System Protected Surfaces

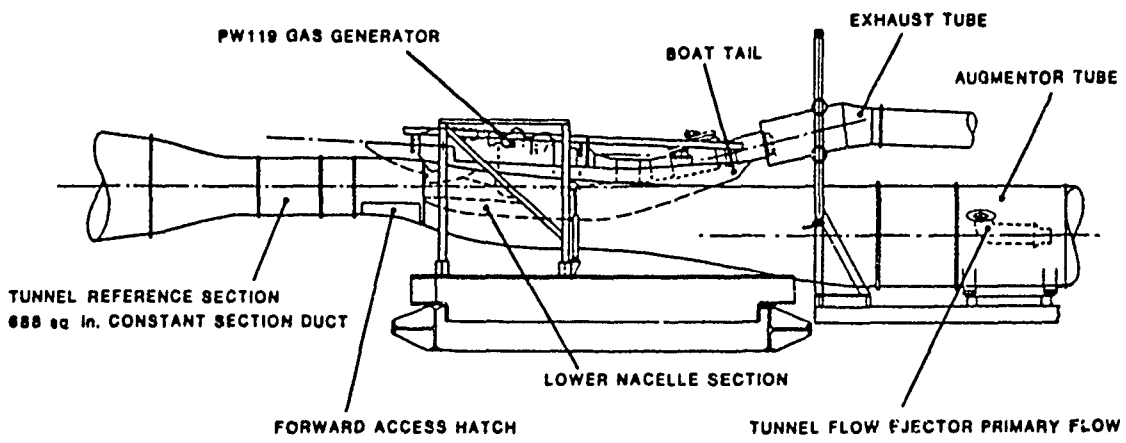

Figure 18: Dornier Do 328 Nacelle Icing Tunnel Installation

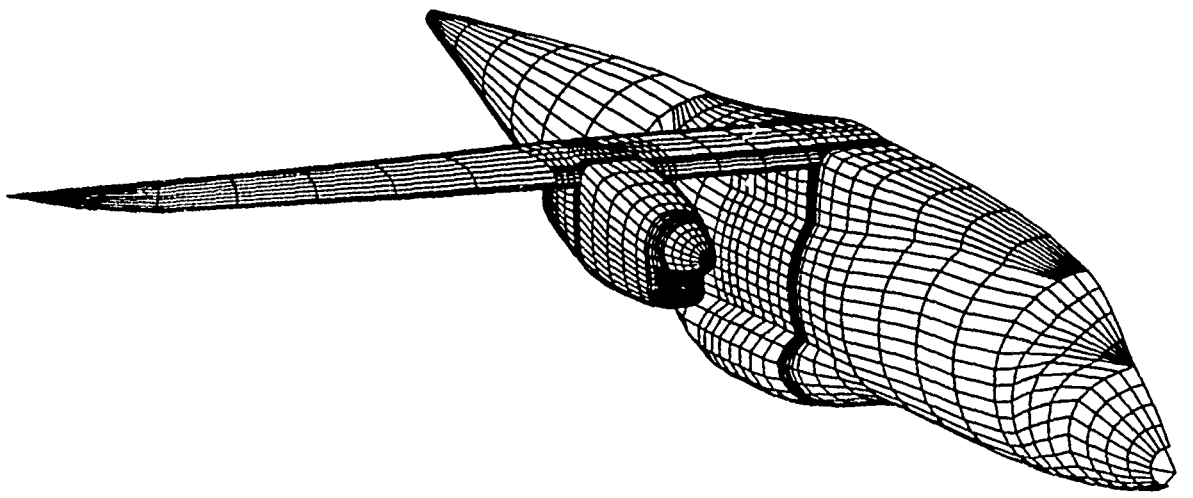

Figure 19: Dornier Do 328 Aircraft Analytical Model

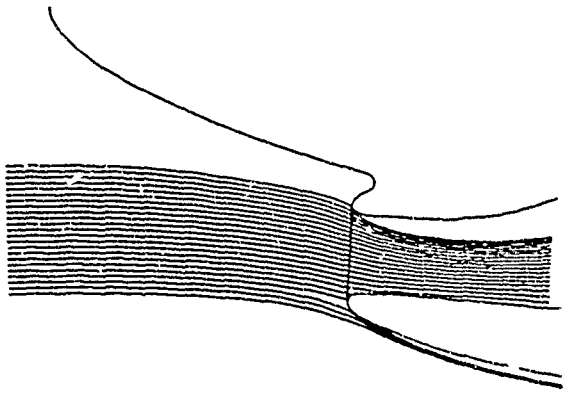

Figure 20: Flight Cond. Climb 20000 ft. $V_o = 205kts, \alpha_a = 6.2°, D_d = 20\mu m$

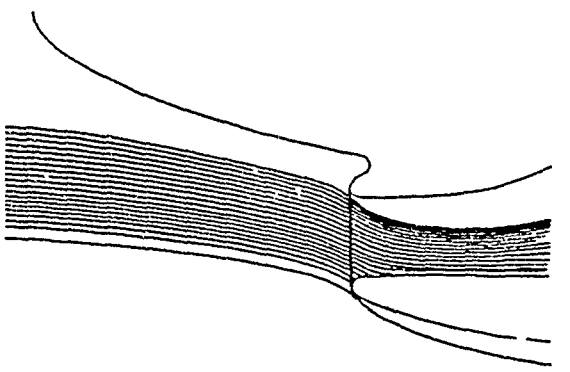

Figure 21: Flight Cond. Cruise 20000 ft. $V_o = 343kts, \alpha_a = 0°, D_d = 20\mu m$

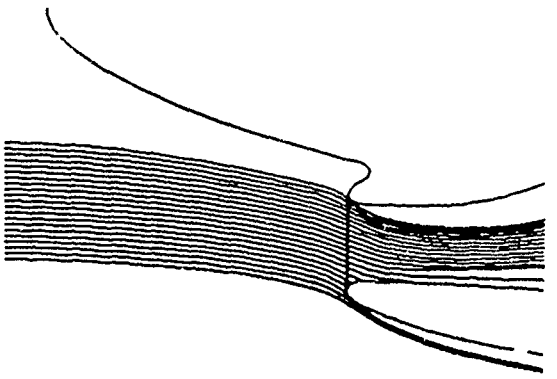

Figure 22: Flight Cond. Hold 20000 ft. $V_o = 239kts, \alpha_a = 3°, D_d = 20\mu m$

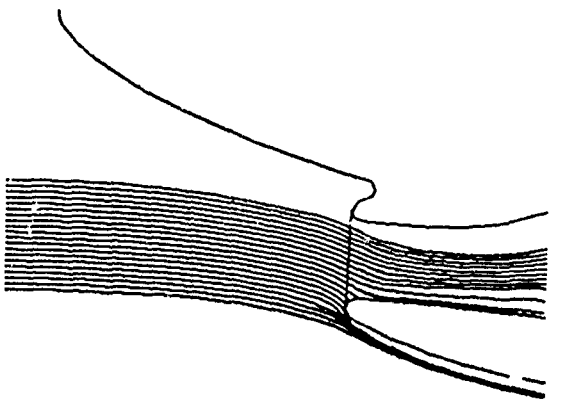

Figure 23: Flight Cond. F.I. Descent 20000 ft. $V_o = 206kts,\ \alpha_a = 5.5°,\ D_d = 20\mu m$

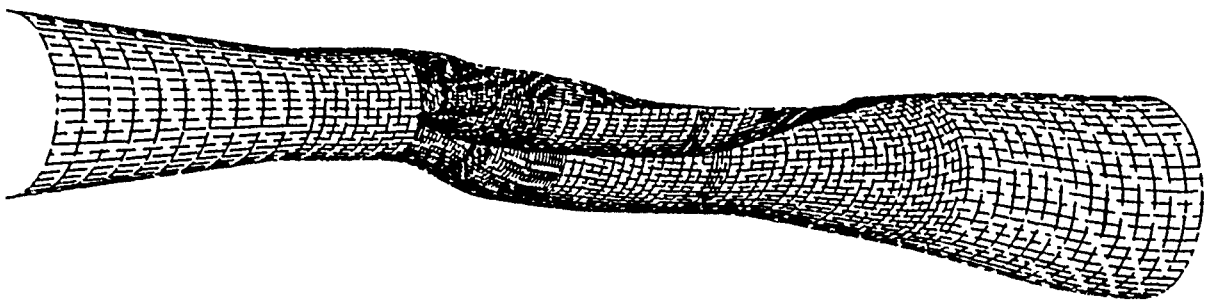

Figure 24: Dornier Do 328 Nacelle/Icing Tunnel Analytical Model

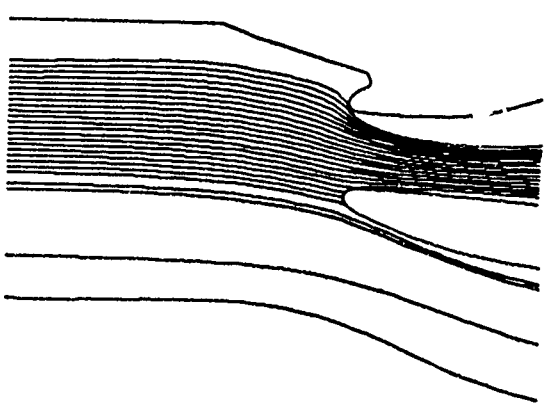

Figure 25: Tunnel Cond. Climb.
$V_o = 100kts, \alpha_i = 2.4°, D_d = 32\mu m$

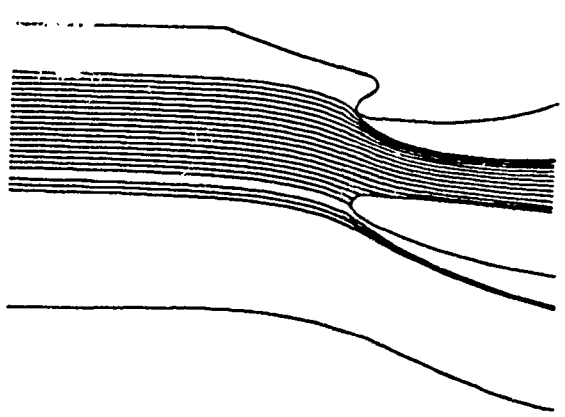

Figure 26: Tunnel Cond. Cruise.
$V_o = 210kts, \alpha_i = 2.4°, D_d = 28\mu m$

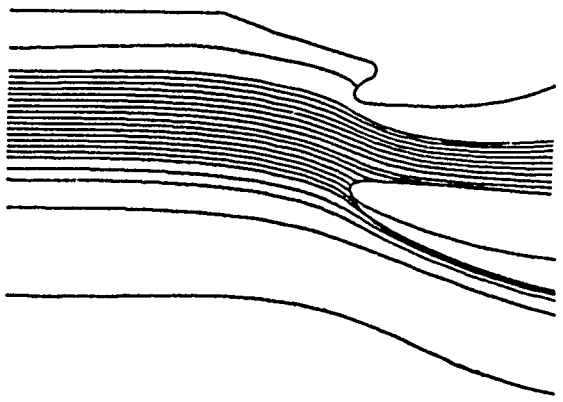

Figure 27: Tunnel Cond. Hold.
$V_o = 150kts, \alpha_i = 2.4°, D_d = 28\mu m$

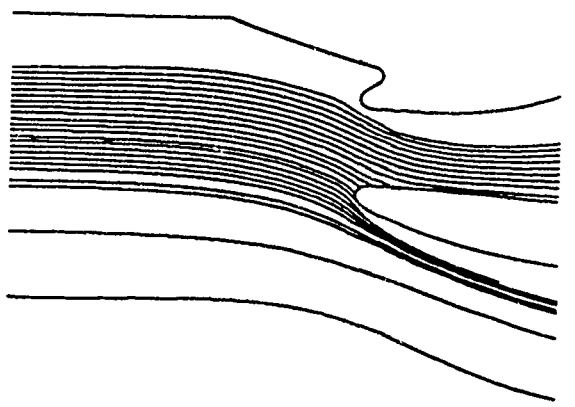

Figure 28: Tunnel Cond. F.I. Descent.
$V_o = 101kts, \alpha_i = 2.4°, D_d = 32\mu m$

SIMULATED FLIGHT CONDITION									TUNNEL CONDITION							
ALTITUDE FT.	V_∞ KTAS	α_a °	$T_{AMBIENT}$ °C	LWC GM	GM/M 3 IM	Dd µm	Ct_e	T_{TOTAL} °C	V_∞ KTAS	α_i °	Dd µm	Ct_i	$\frac{Ve}{Vi} \times \frac{Cte}{Cti}$	T_{TOTAL} °C	DURATION MINS	COMMENTS
17000	196	+6.2	-10	0.6	2.2	20	.79	-5.0	106	+2.4	30	1.01	1.42	-3.5	18	Simulated Climb Conditions.
20000	205	+6.2	-20	0.3	1.7	20	.81	-14.5	100	+2.4	32	1.11	1.50	-14.5	18	
25000	225	+6.2	-30	0.2	1.0	20	.79	-23.3	100	+2.4	32	1.05	1.69	-25.5	18	
17000	340	0	-17.5	0.35	1.86	20	.86	-2.3	207	+2.4	28	.81	1.74	-0.6	30	Simulated Cruise Conditions.
20000	343	0	-20	0.3	1.7	20	.84	-4.5	210	+2.4	28	.80	1.72	-3.2	30	
25000	345	0	-30	0.2	1.0	20	.86	-14.3	210	+2.4	30	.79	1.79	-14.8	30	
17000	225	+3.0	-10	0.6	2.2	20	.70	-3.3	157	+2.4	28	.77	1.30	-2.4	30	Simulated Hold Conditions.
20000	239	+3.0	-20	0.3	1.7	20	.71	-12.5	150	+2.4	28	.73	1.55	-12.8	30	
25000	260	+3.0	-30	0.2	1.0	20	.74	-21.1	133	+2.4	32	.83	1.74	-23.3	30	
17000	196	+5.5	-10	0.6	2.2	20	.52	-6.2	106	+2.4	30	.69	1.37	-5.2	30	Simulated Flight Idle Descent Conditions.
20000	206	+5.5	-20	0.3	1.7	20	.55	-16.2	101	+2.4	32	.73	1.54	-16.1	30	
25000	224	+5.5	-30	0.2	1.0	20	.57	-26.2	100	+2.4	32	.78	1.64	-25.7	30	
0	0	0	-2	0.3	-	20	-	-2.0	50	0	20	-	1.0	-2.0	30	Simulated Ground Idle Conditions in Freezing Fog.
0	0	0	-5	0.3	-	20	-	-5.0	50	0	20	-	1.0	-5.0	30	
0	0	0	-9	0.3	-	20	-	-9.0	50	0	20	-	1.0	-9.0	30	

Figure 29: Dornier Do 328 Air Induction System Icing Certification Test Program

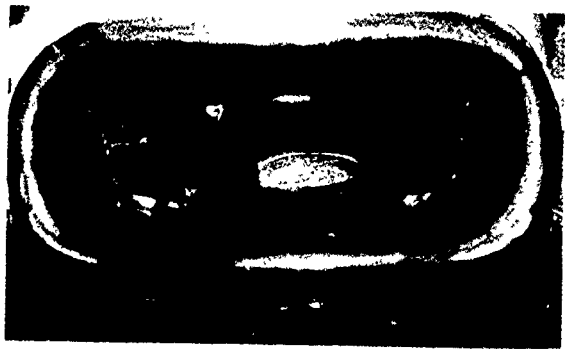

Figure 30: Air Inlet following 30 min Cruise Condition $T_o = -1.1°C$

Figure 31: Air Inlet following 18 min Climb Condition $T_o = -14.7°C$

A SUMMARY OF NASA RESEARCH ON EFFECTS OF HEAVY RAIN ON AIRFOILS

by
Dana J. Dunham, R. Earl Dunham, Jr., and Gaudy M. Bezos
NASA Langley Research Center
Mail Stop 355
Hampton, VA 23665-5225
United States

SUMMARY

This paper presents results from a broad National Aeronautics and Space Administration (NASA) research program to obtain fundamental aerodynamic information regarding the effect of heavy rain on airplane performance. The take-off and landing characteristics are of particular concern, and the aim of the program is to understand the physical phenomena associated with any aero-dynamic performance penalty that may occur during a rain encounter. This overview includes results of recent attempts to measure high-intensity, short-duration rainfall, a discussion of some of the earlier analytical investigations of rain effects on airfoils, a review of some promising experimental methods for evaluating rain effects, and some important scaling considerations for extrapolating model data.

Based on the comparisons available between the limited large-scale results and the wind-tunnel results, rain scale effects are not large and wind-tunnel results can be used to predict large-scale heavy rain effects. Although reductions in maximum lift capability and corresponding increases in drag were measured for both the cruise and high-lift configurations, the high-lift configuration was more sensitive to the rain environment than the cruise configuration. The data indicated a reduction in maximum lift capability with increasing rainfall rate and an associated decrease in the angle of attack at which maximum lift occurs. It would appear that normal transport aircraft operations would not be affected by heavy rain since most operations avoid angles of attack near stall. However, if the heavy rain encounter occurs during a severe low altitude wind shear then the piloting procedures used to counter the wind shear effects may result in operating at a higher than normal angle of attack.

NOMENCLATURE

C_d	section drag coefficient
C_D	drag coefficient
C_l	section lift coefficient
C_L	lift coefficient
LWC	liquid water content, g/m^3
R	rainfall rate in/hr or mm/hr
α	angle of attack, deg.

INTRODUCTION

Until the late seventies the recognition of weather-related safety hazards to aircraft performance and operations had included clear-air turbulence, lightning, icing, hail, low-altitude windshear, and microburst. The latter two phenomena have long been recognized as hazards to aircraft landing and take-off operations. In 1977 the United States Federal Aviation Administration (FAA) conducted a study of 25 aircraft accidents and incidents which occurred between 1964 and 1976 in which low-altitude wind shear could have been a contributing factor (ref. 1). Of the 25 cases (23 approach or landing and 2 take-off) in the study, ten cases had occurred in a rain environment, and in five cases these were classified as intense or heavy rain encounters. These results led to the reconsideration of high-intensity, short-duration rainfall as a potential weather-related aircraft safety hazard, particularly in the take-off and/or approach phases of flight.

This paper is an overview of the most recent work conducted by the NASA and others to study the potential influence of heavy rain on airfoil performance. The overview includes results of recent attempts to measure high-

intensity, short-duration rainfall, a discussion of some of the earlier analytical investigations of rain effects on airfoils, a review of some promising experimental methods for evaluating rain effects, and some important scaling considerations for extrapolating model data. The latest experimental data are also presented and discussed. A complete understanding of the influence of rain on airfoil performance will require significant additional effort both analytically and experimentally before an assessment of the degree of hazard associated with flight operations in a rain environment can be made.

THE CHARACTERISTICS OF HEAVY RAIN

In order to develop analytical models and conduct experimental studies on the effect of rain on airfoil performance, the phenomenon of naturally occuring precipitation needs to be understood. An understanding of the drop size distribution associated with heavy rain, the frequency of occurrence, and the range of rainfall rates is required in order to assess hazard potential for aircraft operation.

Two "lump parameter" quantities generally used to describe rain are rainfall rate (R) and liquid water content (LWC). Rainfall rate is the linear accumulation depth at ground level per unit time and is typically used to characterize rainfall at ground level. For airborne measurements the liquid water content, the mass of liquid water per unit volume usually expressed as g/m^3, is the meaningful parameter. The relationship between LWC and R is uniquely dependent on the type of storm and the intensity level of the storm. In the absence of a vertical wind velocity, the LWC is directly related to the rainfall rate and the drop size distribution. Figure 1 from Dunham, ref. 2, is a plot of the LWC as a function of rainfall rate for both light widespread rain and thunderstorm type rain. Rain is adequately modeled when the type of rain environment is specified (thunderstorm or continous) and either the liquid water content or rainfall rate is given.

The range of rainfall rates that an airplane could expect to encounter varies from light rain of 5-10 mm per hour up to very large rainfall rates. The ground-level world record rainfall accumulation of 1.23 inches in one minute was measured in an intense afternoon thunderstorm on July 4, 1956, (ref. 3). The volume of rain accumulated in the one minute time interval is equivalent to a rainfall rate of 1830 mm/hr (73.8 in/hr). The upper boundary for airborne measurements of liquid water content is 44 g/m^3, corresponding to approximately 2920 mm/hr (117 in/hr), measured by an instrmented F-100 airplane in 1962 by Roys and Kessler (ref. 4).

With the resurgence of interest in the characterization of high-intensity rain-fall, a review of the literature prior to 1987 pertaining to natural rainfall measurements revealed that the majority of the ground-based rainfall database was averaged over relatively long time constants using a weighing-bucket, more commonly referred to as a tipping bucket (Jones and Sims, ref. 5). According to Melson (ref. 6), this measurement technique results in lower rainfall rates being calculated and masks the short-duration, high-intensity rainfall characteristics associated with thunder-storms. The work of Jones and Sims and Melson both address the magnitude, duration and probability distribution of high-intensity rainfall.

The probability distribution data collected by Jones and Sims, measured over time constants of 1- and 4-minute accumulations at ground level, are useful for determining the potential for encountering a given rainfall rate. They analyzed data collected over a one-year period on recording weighing-bucket raingages placed throughout the world. Gages from maritime subtropical (Southeastern USA, Vietnam, Marshall Islands, Japan), continental temperate (Midwestern USA, Alaska), maritime temperate (England, France, West Germany, Northwestern USA), and midlatitude interior (Israel, Southwestern USA) regions were used. Figure 2 is a summary of the averaged zonal frequency distribution curves obtained. The probable number of minutes a given rainfall rate (or greater) can be expected in a given climatological zone can be obtained from figure 2 by converting the ordinate from percent to a fractional portion of time and multiplying by the number of minutes in a year (5.2596×10^5). The Jones and Sims data indicate that for about two minutes every year in the maritime suptropical zone,

a rainfall rate greater than 200 mm/hr (8 in/hr) could be expected at any location.

The lack of rainfall measurements over very short time constants, on the order of seconds, led to the development of a ground-based natural rainfall measurement technique by Melson. His technique acquires data over very short time constants, as short as one sample per second. Data are being acquired at 6 geographical sites: Darwin, Australia; Seattle, Washington; Denver, Colorado; Kennedy Space Center, Florida; Hampton, Virginia; and Wallops Island, Virginia. His measurement technique has verified the existence of high-intensity rainfall at ground level (ref. 7). Figure 3 is a bar chart summary of the frequency and magnitude of the events measured above 100 mm/hr (4 in/hr) and the duration times of those events. Over 7,000 events have been measured above 100 mm/hr since the test program began in 1988. The maximum rainfall rate measured of 720 mm/hr (28 in/hr) occurred for just under ten seconds at NASA Wallops Flight Facility in 1990. In figure 4 the data are presented as percentages of the total number of measurements indicating that one quarter percent of the events measured were above 20 in/hr. The rainfall rates above 20 in/hr were sustained up to 10 seconds per event. These ground-based results along with the inflight thunderstorm measurements by Roys and Kessler indicate that the probability of an airplane encountering short-duration rainfall rates greater than 200 mm/hr (8 in/hr) may be higher than the probability indicated by Jones and Sims.

ANALYTICAL WORK

The effect of rain on the aerodynamic performance of an airplane was addressed analytically as early as 1941 by Rhode (ref. 8). His analysis indicated that drag increases associated with the momentum of a DC-3 aircraft encountering a rain cloud with a water mass concentration of 50 g/m^3 (equivalent to approximately 1270 mm/hr or 50 in/hr) would cause an 18 percent reduction in airspeed. Rhode considered such an encounter to be of a short duration and of little consequence to an aircraft flying at 5000 feet.

Since low visibility take-offs and landings were not routine in 1941, the consequences of a heavy rain encounter during these phases of flight was not considered. However, for a modern day transport such an airspeed loss during take-off or landing would be significant. The influence of rain on airplane performance was addressed again in 1982 when Haines and Luers (ref. 9), under contract from NASA, evaluated the effect of rain on aircraft landing performance. In the intervening years a great deal of work had gone into calculating the motion of water drop particles in the flowfield about an airfoil (refs. 10 to 14); however these efforts were directed at calculating water drop trajectories and impingement on the airfoil for purposes of estimating ice accretion. The influence of liquid water on the airfoil performance was not calculated.

The Haines and Luers study was an attempt at refining the study of Rhode to estimate the effects of rain on a modern-day airplane. Their analysis not only included the calculation of the impact momentum of the raindrops, but also estimated the increase in skin friction drag by equating the water layer waviness and raindrop crater effects on the airfoil surface to an equivalent sand grain roughness. Using empirical data for roughness effects on airfoil lift they calculated the rain effect on the lift and drag of a 747 transport. Their analysis estimated a 2 to 5 percent increase in drag and a 7 to 29 percent reduction in maximum lift with associated reductions in stall angle from 1 to 5 degrees for rainfall rates from 100 to 1000 mm/hr (3.94 to 39.37 in/hr). These predictions, of course, constitute a substantial loss of performance.

In 1984 Calarese and Hankey (ref. 15) studied droplet drag acting as a body force in the Navier-Stokes equations. This analysis neglects the interface effects of droplet splashing, cratering, and water-layer formation. Their analysis produced a pressure distribution for an NACA 0012 airfoil for the limiting cases of a very fine rain (small drop size and a drop Reynolds number much less than 1) and for a coarse rain (large drop size and large Reynolds number). For the coarse rain little change in airfoil pressure distribution was noted. For the fine rain, significant changes in pressures were predicted which showed a small increase in lift with increasing water spray concentration.

In 1985, Kisielewski (ref 16) performed a three-dimensional Euler analysis to investigate the effects of momentum and energy exchange between the rain and the flowfield. He concluded that the rain had little effect on the calculated lift produced by a simple airfoil. Both Calarese and Hankey and Kisielewski concluded that the major influence of rain on airfoil performance was probably dominated by viscous effects of the water droplet splashing and its subsequent interaction with the air boundary layer, but these effects were not modeled in their analyses.

EXPERIMENTAL METHODS

The experimental investigation of rain effects on the aerodynamics of airfoils is a technical challenge as difficult as investigating the effects analytically. A full-scale flight test investigation would require that performance measurements be made on an airplane while in a severe rainstorm. In addition to the hazard to the test pilot, extraction of accurate performance measurements and environmental parameters would be very difficult. Because of the variability of natural rain, repeatable conditions would be difficult if not impossible to obtain.

Scale model tests of the effects of rain present a different set of challenges in that they require the simulation of properly scaled rain conditions. The three types of tests which have been used for investigating the effects of rain are (1) a rotating arm in which a model is placed at the end of a counterbalanced rotating beam, (2) conventional wind tunnels, and (3) a track in which the model is propelled down a straight track segment.

Rotating arm facilities have been quite useful for studying single-drop impact dynamics (refs. 17 and 18). Airfoil performance measurements have not been attempted with the rotating arm facility because the centrifugal effects on the water film would influence the results. Wind tunnels and track facilities are considered to be the best methods of obtaining airfoil performance data, and in both methods the technique for simulating rain and developing scaling relationships presents the areas of greatest difficulty. For the wind tunnel the difficulty lies in obtaining a uniform distribution of the water with a minimum of influence on the tunnel flow conditions. For the track the water manifolding and nozzle distribution becomes elaborate and extensive in order to cover the test area.

Wind-tunnel testing

In 1985, Bilanin (ref. 19) addressed the subject of scaling for model tests of airfoils in simulated rain. His analysis showed that the the scaling parameters which control the aerodynamic force generated by an airfoil immersed in a rain environment are the following: Reynolds number based on air; Reynolds number based on water; the Weber number; the ratio of mean droplet diameter to model chord; the ratio of the density of air to the density of water; and the angle of attack. The Weber number (We) is the ratio of inertial forces to surface tension forces and is a function of the density of water, drop velocity, volumetric mean drop diameter (the diameter at which half the volume of water is in larger or smaller drops) and the surface tension interactions between water and air. The sensitivity of the aerodynamic characteristics of an airfoil immersed in a rainstorm to each of the aforementioned parameters must be assessed to determine adequate modeling of heavy rain in the wind tunnel.

NASA has developed test techniques and procedures and conducted a series of wind-tunnel tests in the NASA Langley 14- by 22-Foot Subsonic Tunnel. The tests were conducted in the closed test section with dimensions of 14.5 feet high by 21.75 feet wide by 50 feet long. A photograph of a typical test set-up and a schematic of the test technique developed are shown in figures 5 and 6. The model hardware was located in the aft bay of the test section aligned laterally with the tunnel centerline.

The water spray distribution manifold, shown in figure 7, was located approximately 10 wing chord-lengths upstream of the model location and directed the spray horizontally at the model while aerodynamic force measurements were obtained. The shape and location of the spray manifold were selected to minimize the interference effect on tunnel freestream conditions and to allow time for the stabilization of the accelerating water

droplets. The manifold was aligned approximately 6 inches above the chord plane of the model to account for gravity effects on the water droplets. Comparisons of model aerodynamic data in and out of the simulated rain environment were made with the spray manifold in position at all times.

The wind-tunnel rainfield simulated a thunderstorm-type rain and was quantified in terms of LWC, drop size distribution and drop velocity. An extensive experimental research effort was carried out by the Jet Propulsion Laboratory (JPL), under contract to NASA, to develop a nozzle design which would simulate a range of rainfall intensity levels and a drop size distribution which would include drops 2 mm in size and larger (ref. 20). The JPL designed nozzles, shown in figure 8, consisted of a series of hypodermic tubes arranged circumferentially around a plenum which would provide control over the drop size and rainfall intensity level independently. These nozzles produced LWC values near those which occur naturally in cloudburst conditions.

Exploratory tests were conducted on a wing with a NACA 0012 airfoil section fitted with a simple, full-span trailing-edge flap at at Reynolds Number of 1.7 x 10^6. (ref. 2) The wind-tunnel rain simulation system used for the NACA 0012 tests produced LWC values ranging from 13 to 22 g/m^3. A 15 percent reduction in the maximum lift capability of both the cruise and landing configurations of the airfoil model were measured in the simulated rain environment independent of the LWC. A sample of the data is shown in figure 9. The exploratory small-scale wind-tunnel results confirmed the existence of a performance penalty in a simulated rain environment.

Following these tests, an investigation was conducted to determine the severity of the rain effect on an airfoil geometry which was representative of typical commercial transport wing sections as a function of rainfall intensity and to explore the importance of surface tension interactions of water as a scaling parameter (ref. 21). The airfoil model was an NACA 64-210 with leading-edge and trailing-edge high-lift devices tested in cruise and landing configurations. The model had a rectangular planform and was supported between two endplates in an attempt to represent a two-dimensional test set-up as shown in figure 10. The basic airfoil chord was 2.5 feet and the span between the endplates was 8 feet. Details of the cruise and landing configurations tested are shown in figure 11. The high-lift devices consisted of a leading-edge slat deflected at a fixed angle of 57° and a trailing-edge double-slotted flap deflected at a fixed angle of 35.75°.

These tests were also conducted in the Langley 14- by 22-Foot Subsonic Tunnel for Reynolds numbers of 1.8 x 10^6, 2.6 x 10^6, 3.3 x 10^6 based on airfoil chord. The rain spray system was modified to provide adequate coverage of the model at higher rainfall rates than previously tested using the JPL nozzles. The improved rain simulation system produced water mass concentrations ranging from 16 to 47 g/m^3. As shown in figure 12, a 25 percent reduction in maximum lift capability with an associated 8° decrease in the angle of attack at which maximum lift occurs was measured for the high-lift configuration at the highest water mass concentration of 46 g/m^3. For this data set the Reynolds number was 2.6 X 10^6, the Weber number 270, and the drop diameter to wing chord ratio .0018.

In general, the NACA 64-210 data indicated the same trends as the data for the NACA 0012 airfoil model. Both airfoil sections exhibited significant reductions in maximum lift and increases in drag for a given lift condition in the simulated rain environment. The most significant difference between these two airfoil sections was the sensitivity of the NACA 64-210 airfoil section to LWC. As noted previously the NACA 0012 performance losses in the rain environment were not a function of LWC. Although reductions in maximum lift capability and corresponding increases in drag were measured for both the cruise and high-lift configurations of the NACA 64-210 airfoil model, the high-lift configuration was more sensitive to the rain environment than the cruise configuration. The data indicated a reduction in maximum lift capability with increasing water mass concentration and an associated decrease in the angle of attack at which maximum lift occurs.

Campbell and Bezos (ref. 22) conducted a test using a NACA 23015 airfoil section to evaluate the time required for a wing

immersed in rain to achieve a steady state condition. They reported that the transition time for the wing to achieve a steady state condition encountering simulated heavy rain to be less than two to three seconds in most cases. These transition times are within the duration times of all the ground-based rainfall measurements reported by Melson.

The NACA 64-210 test results in terms of lift and drag characteristics in and out of the simulated rain environment represent the baseline data which was used in the evaluation of the large-scale rain effects data.

Large-scale Track Testing

In order to determine to first order if there were significant rain scaling effects, the NASA Langley Research Center and the FAA supported the development of a large-scale ground testing capability for evaluating the effect of heavy rain on airfoil lift. Figure 13 is a photograph of the facility which was developed to acquire aerodynamic data on large-scale wing sections immersed in a simulated natural rain environment. A wing section is mounted on a test vehicle and is propelled along a track through a highly-concentrated rain environment. The simulated rain is produced by a series of spray nozzles suspended above the track. This technique provides a more realistic rain simulation than can be produced in a wind tunnel. The test vehicle is propelled into an environment which exemplifies an airplane flying into a rainstorm. The generation of the rain environment in the vertical direction allows the water droplets to achieve the proper droplet size distribution and terminal velocities found in severe rainstorms. The outdoor rain simulation system developed for this investigation produced rainfall conditions from 2 to 40 in/hr.

The details of the design, development, and operation of the NASA Langley Research Center Aircraft Landing Dynamics Facility (ALDF) for large-scale heavy rain effects testing are described in references 23, 24, and 25. Although the ALDF was designed to test full-scale aircraft landing gear at operational velocities on a variety of simulated runway surfaces, its operating characteristics facilitated the conversion to a large-scale aerodynamic performance testing facility with minimal modifications to the test carriage and track test section. The ALDF is composed of three components: a test carriage, a propulsion system and an arrestment system. A high-pressure jet of water is directed into a turning bucket on the back end of the carriage to provide carriage thrust. Once the peak velocity is attained, the carriage coasts the remaining 1800 feet to the arrestment system. The large-scale wing section was mounted above the central open bay area of the carriage 22 feet above the track as shown in figure 14.

The wing section had an NACA 64-210 airfoil section with a rectangular planform and was mounted between circular endplates. The wing is equipped with leading-edge and trailing-edge high-lift devices deployed to simulate a landing configuration (fig. 15). The ALDF wing chord was chosen to be 10 feet, which corresponds to a scaling factor of 4 when compared to the wind-tunnel model chord of 2.5 feet. The wing span was constrained to a width of 13 feet by the model location chosen. The wing surfaces were painted with commercially available aircraft paint to model the wing surface/rain interaction properly. The ALDF wing structure was constructed based on a requirement to sustain high g-loads at launch. The wing angle of attack, which is set prior to launch and remains fixed during a test run, was varied from 7.5° to 19.5° in 2° increments.

The ALDF Rain Simulation System (RSS) is located approximately 800 feet downstream of the propulsion system (fig. 16) and provides uniform simulated rain over an area 30 feet wide, centered over the track, by 500 feet long. The system consists of three commercially manufactured irrigation pipes positioned length-wise along the track in 100-foot sections which are supported at both ends by a structural support frame. One leg of this frame is piping which allows the flow of water to travel from the water/air supply system up to the three irrigation pipes. Feeding off each irrigation pipe is an array of nozzles whose spacing is dependent upon the desired rainfall rate.

Dynamic pressure is measured by a standard aircraft pitot-static tube mounted on a forward extremity of the carriage. In addition to data on the wing and carriage, the measurement of wind speed and direction at the the rain simulation system location are

recorded along with temperature and barometric pressure. Because the carriage is decellerating the Reynolds number varies from 11- to 18- X 10^6. The Weber number also varies from 320-510.

The majority of the rain effects data were obtained at the maximum rain rate of 40 in/hr for an angle-of-attack range of 7.5° to 19.5°. For this rain condition the drop size to model chord ratio was .0009. This rain condition was chosen because it closely approximated a previously tested wind-tunnel condition and met one of the test objectives to investigate the significance of scale effects. A photograph of the carriage exiting the 40 in/hr rain condition is shown in figure 17. Aerodynamic data were also obtained for rainfall rates of 9 and 19 in/hr for an angle of attack range of 9.5° to 19.5°. These rain conditions have a much higher probability of occurrence than the 40 in/hr rain intensity as indicated by references 4 and 6.

The time dependent data were averaged to provide a single lift coefficient for each angle of attack. The lift coefficient versus angle of attack data exhibit the same general characteristics as the previous wind-tunnel results. The rain effect is to reduce the maximum achievable lift coefficient and to reduce the angle of attack for stall. The data shown in figure 18 for the airfoil in the rain environment reflects the fact that the wing has stalled prior to 13.5° angle of attack and attained it highest observable lift at 11.5° angle of attack. A reduction of lift capability of at least 15 to 20 percent is reflected in the data shown in figure 18 for the 40 in/hr rain condition.

SCALING CONSIDERATIONS

The large-scale data were needed to ascertain the utility of the wind-tunnel test technique for determining the effect of heavy rain at full-scale conditions. As noted in the work of Bilanin (ref. 19) difficulties arise when attempting to preserve all the scaling parameters during model testing. The functional form of the Reynolds number is linearly dependent on the test velocity; therefore, as the model size is decreased the test velocity must increase to preserve full-scale Reynolds number. Weber number, on the otherhand, varies as the square of the test velocity and, as a result, these two parameters cannot be preserved simultaneously.

Operational difficulties in achieving the desired drop size distribution and rain intensity level in the wind tunnel were also identified. The wind tunnel rain simulation technique developed during the small-scale tests identified an inherent difficulty in producing large size drops typical of natural rain while at the same time achieving the desired rainfall intensity and drop size distribution (ref. 20). When water is injected into a high velocity airstream at a velocity substantially less than the airstream velocity, the larger drops that form shatter and break up into much smaller drops. Although this difficulty can be alleviated by increasing the water injection pressure so that the initial drop velocity approaches the airstream velocity, the resulting rainfall intensity tends to be too high. The small-scale tests indicated that the drop size distribution and the rainfall intensity levels were a function of the nozzle design, the water injection pressure and the airstream velocity.

Determination of rainfall rate using the wind-tunnel test technique was subject to measurement error (ref. 22). In a wind-tunnel environment, LWC is expressed as a function of the spray area, mass flow rate, and the freestream velocity. A flowmeter measured the mass flow rate through the manifold. The spray width and height were photographically obtained at the model location using a fluorescent dye, an ultraviolet strobe light to enhance the photographic qualities of the spray and a nearfield linear length reference. Due to the dynamic nature of water drops, the boundaries of the spray region at any instant in time are not precisely straight lines, therefore an inherent inaccuracy in deriving the spray area by photographic means lies in the possible error involved in subjectively determining the usable spray region boundaries.

Despite the noted difficulties, the wind-tunnel technique appears to provide a valid estimate of the effects of heavy rain at full scale conditions (ref. 26). The lift coefficients predicted for the ALDF large-scale configuration using the wind-tunnel data are shown in figure 19 along with the ALDF large-scale data acquired at the same

test conditions. The two sets of data for the dry wing agree quite well. The ALDF lift-curve slope and maximum lift measured show excellent correlation to the wind tunnel predicted lift performance for that condition. There appears to be a reasonable degree of correlation between the two data sets for the 40 in/hr rain condition. An offset exists between the predicted lift-curve slope and the ALDF lift-curve slope in the rain. One can infer from the data shown in figure 19 that the wet wing attains its highest observable lift at approximately the same angle of attack (between 10° and 11.5°).

Comparisons of the angle of attack for maximum lift and of the percent lift loss in the various rainfall conditions in the wind tunnel and at large scale are shown in figures 20 and 21. Based on the comparisons available between the limited large-scale results and the wind-tunnel results, the difficulties in precisely simulating the rain environment in the wind tunnel do not have a first order effect on the impact of the test results. It appears that, to first order, rain scale effects are not large and that wind-tunnel results can be used to predict large-scale heavy rain effects.

CONCLUDING REMARKS

The work described herein is aimed at developing test techniques and tools for providing data which can eventually be used to assess the influence of heavy rain on airplane operations. These analysis methods and test techniques will provide valuable insight into the interpretation of heavy rain effects testing of airplane configurations. The large-scale results are not directly applicable to any airplane configuration but are applicable to understanding and interpreting future wind-tunnel tests.

The preliminary findings of the large-scale testing would seem to support earlier wind-tunnel studies of the effect of very heavy rain on airfoil performance. Extremely heavy rain of 40 in/hr produced a reduction in maximum achievable lift coefficient of at least 15 to 20 percent and an approximate reduction in the angle of attack at which the maximum observed lift occurred of 4° to 6°. Results of these small-scale studies had shown that a two-phase flow environment representing a high-intensity rainfall reduced the maximum lift by as much as 20 percent and increased the drag. Additionally, the stall angle was reduced 4 to 8 degrees in the heavy rain environment. The simulated rain seems to have little influence on the lower angle-of-attack airfoil lift performance characteristics. The severity of the effect is airfoil- and configuration-dependent and is most severe for high-lift configuration airfoils, i.e., leading-edge and trailing-edge devices deployed. Based on the wind-tunnel and large-scale results, it would appear that normal aircraft operations for transport aircraft would not be affected by heavy rain since most operations avoid high angle of attack maneuvers. However, if the heavy rain encounter occurs during a severe low altitude wind shear then the piloting procedures used to counter the wind shear effects may result in operating at a higher than normal angle of attack.

REFERENCES

1. Low-Altitude Wind Shear and Its Hazard to Aviation. National Academy Press. Library of Congress Catalog #83-63100, 1983.

2. Dunham, R. Earl, Jr.: The Potential Influence of Rain on Airfoil Performance. Lecture presented at the von Karman Institute for Fluid Dynamics, February 1987.

3. Riordan, P.: Weather Extremes Around the World. Earth Sciences Laboratory, TR-70-45-ES, January 1970.

4. Roys, G. P. and Kessler, E.: Measurements by Aircraft of Condensed Water in Great Plains Thunderstorms. National Severe Storms Laboratory Publications. TN-49-NSSP-19, 1966.

5. Jones, D. M. A. and Sims, A. L.: Climatology of Instantaneous Rainfall Rates. Journal of Applied Meteorology, Volume 17, August 1978, pg. 1135-1140.

6. Melson, W. E., Jr.: Heavy Rain Characteristics and Ground Measurement Comparisons. Presented at the WHO IAHS 8th International Workshop on Precipitation Measurement, December 1989.

7. Melson, W. Edward, Jr.: Observation and Comparison of Rainfall Measured at a High Sample Rate. Proceedings of the American Meteorological Society, 71st Annual Meeting, January 13-18, 1991, New Orleans, Lousiana.

8. Rhode, Richard V.: Some Effects of Rainfall on Flight of Airplanes and on Instrument Indications. NACA TN 803, April 1941.

9. Haines, P. A. and Luers, J. K.: Aerodynamic Penalties of Heavy Rain on Landing Aircraft. NASA CR 156885, July 1982.

10. Bergrun, Norman R.: A Method of Numerically Calculating the Area and Distribution of Water Impingement on the Leading Edge of an Airfoil. NACA TN1397, 1947.

11. Bergrun, Norman, R.: An Empirically Derived Basis for Calculating the Area, Rate, and Distribution of Water-Drop Impingement on Airfoils. NACA Report 1107, 1952.

12. Dorsch, R. G. and Brun, R. J.: A Method for Determining Cloud-Droplet Impingement on Swept Wings. NASA TN2931, 1953.

13. Morsi, S. A., and Alexander, A. J.: An Investigation of Particle Trajectories in Two-Phase Flow Systems. Journal of Fluid Mechanics, Volume 56, 1972, page 193-208.

14. Bragg, M. B.: A Similarity Analysis of the Droplet Trajectory Equation. AIAA Journal, Volume 20, December 1982, pg. 1681-1686.

15. Calarese, W. and Hankey, W. L.: "Numerical Analysis of Rain Effects on an Airfoil," AIAA-84-0539, AIAA 22nd Aerospace Sciences Meeting, Reno, NV, January 1984.

16. Kisielewski, Keith: A Numerical Investigation of Rain Effects on Lift using a Three-Dimensional Split Flux Vector Form of the Euler Equations, Master Thesis, Department of Aerospace Engineering, Mississippi State University, May 1985.

17. Feo, A.: Single Drop Impact Studies. AIAA 87-0257, AIAA 25th Aerospace Sciences Meeting, Reno, NV, January 1987.

18. Bilanin, A. J.; Quackenbush, T. R.; Feo, A.: Feasibility of Predicting Performance Degradation of Airfoils in Heavy Rain. NASA CR 181842.

19. Bilanin, A. J.: Scaling Laws for Testing of High Lift Airfoils Under Heavy Rain. AIAA-85-0259, January 1985.

20. Aaron, K. M; Hernan, M. A.; Parikh, P.; Sarohia V.: Simulation and Analysis of Natural Rain in a Wind

Tunnel via Digital Image Processing Techniques, AIAA 86-0291.

21. Bezos, G. M.; Dunham, R. E., Jr.; Gentry, G. L.; and Melson, W. E.: Wind-Tunnel Test Results of Heavy Rain Effects on Airfoil Performance. AIAA-87-0260, January 1987.

22. Campbell, B. A. and Bezos, G. M.: Steady-State and Transitional Aerodynamic Characteristics of a Wing in Simulated Heavy Rain. NASA TP 2932, August 1989.

23. Taylor, J. T.; Moore, C. T., III; Campbell, B. A.; and Melson, W. E.: The Development of a Facility for Full-Scale Testing of Airfoil Performance in Simulated Rain. AIAA-88-0055, January 1988.

24. Bezos, G. M.; Campbell, B. A. and Melson, W. E. Jr.: The Development of a Capability for Aerodynamic Testing of Large-Scale Wing Sections in a Simulated Natural Rain Environment. AIAA 89-0762.

25. Campbell, B. A.; Bezos, G. M.; Dunham, R. E., Jr.; and Melson, W. E., Jr.: Operational Considerations for Aerodynamic Testing of Large-Scale Wing Sections in a Simulated Natural Rain Environment. AIAA-89-0485, January 1990.

26. Bezos, G. M.; Dunham, R. E. Jr.; Campbell, B. A. and Melson, W. E. Jr.: Results of Aerodynamic Testing of Large-scale Wing Sections in a Natural Rain Environment. AIAA 90-0486.

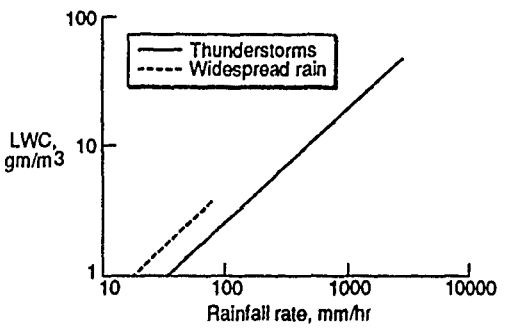

Figure 1 - Liquid water content as a function of rain rate

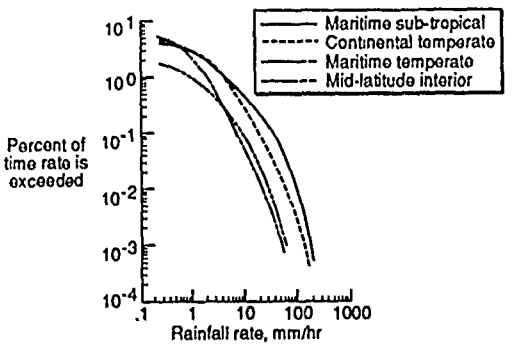

Figure 2 - Climatology of instantaneous Rainfall Rates (as defined by 1 and 4 minute accumulations)

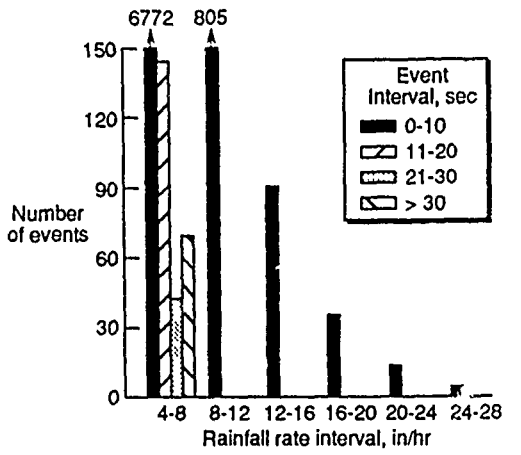

Figure 3 - Short-duration, high-intensity rain rate measurements

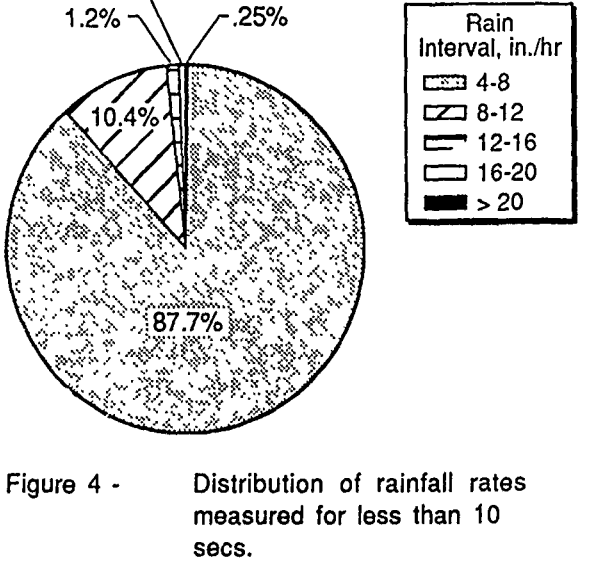

Figure 4 - Distribution of rainfall rates measured for less than 10 secs.

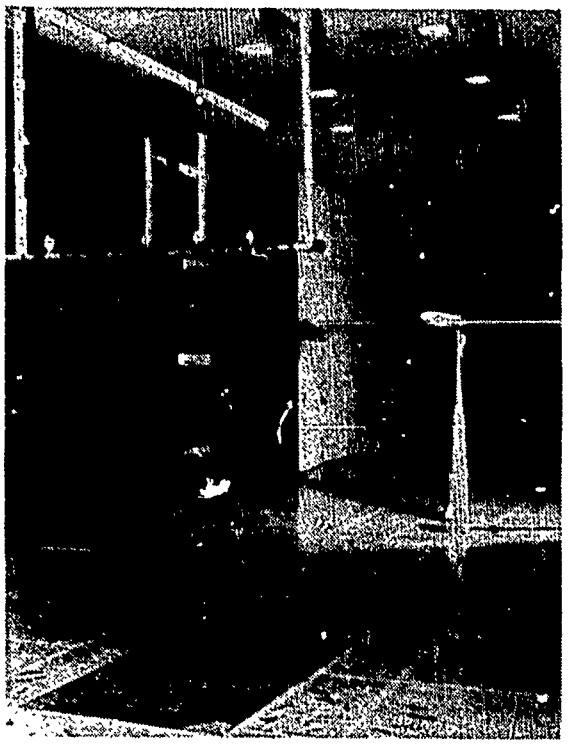

Figure 5 - Rain simulation system mounted in Langley 14- by 22-Foot Subsonic Tunnel

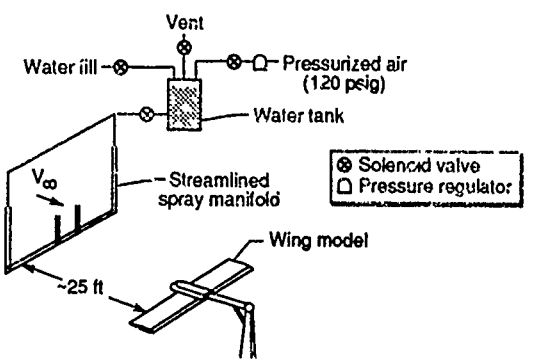

Figure 6 - Typical wind tunnel test set-up for simulated rain effects studies

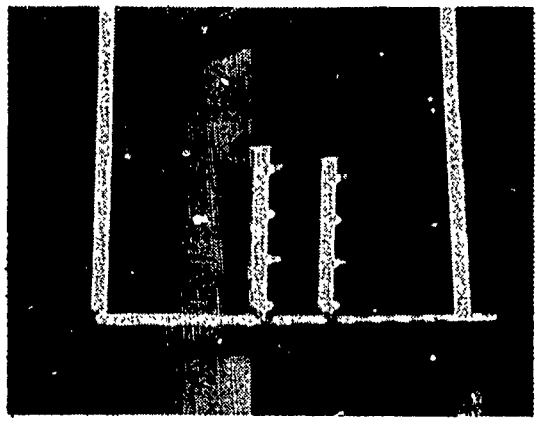

Figure 7 - Close-up detail of nozzle and solenoid arrangement on the spray manifold

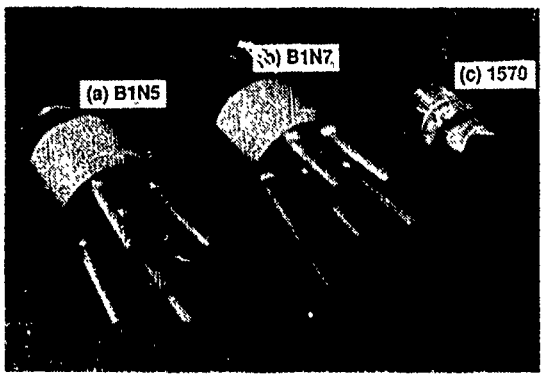

Figure 8 - Three nozzles used to vary the water spray characteristics. From left to right: 5-tube, 7-tube, and commercial nozzle

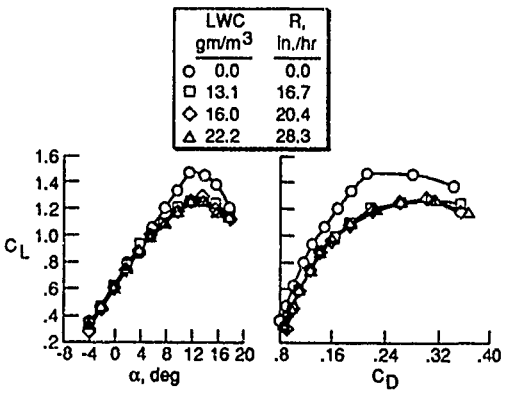

Figure 9 - Lift and drag measurements on a NACA 0012 wing model with a 30% chord flap deflected 20° while subjected to several water spray concentrations

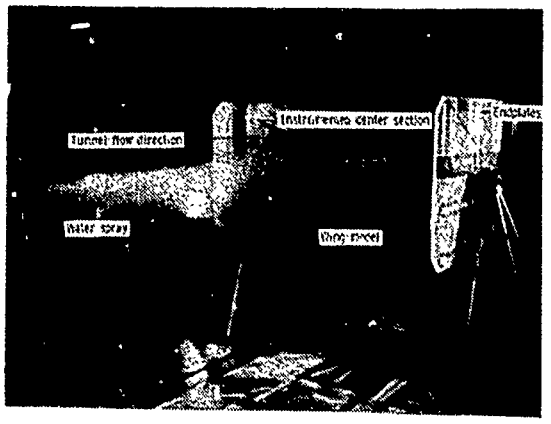

Figure 10 - Photograph of 64-210 model mounted in the wind tunnel

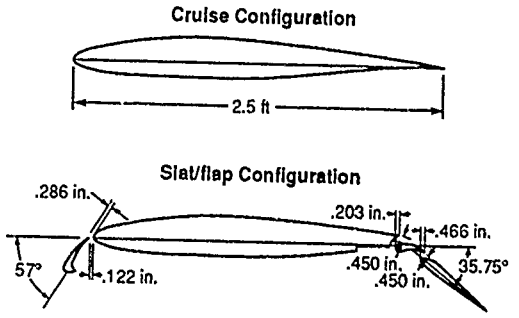

Figure 11 - A cross-section of NACA 64-210 airfoil section

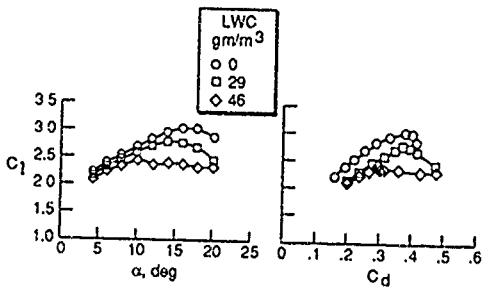

Figure 12 - Effect of rain on NACA 64-210 airfoil with flaps deflected

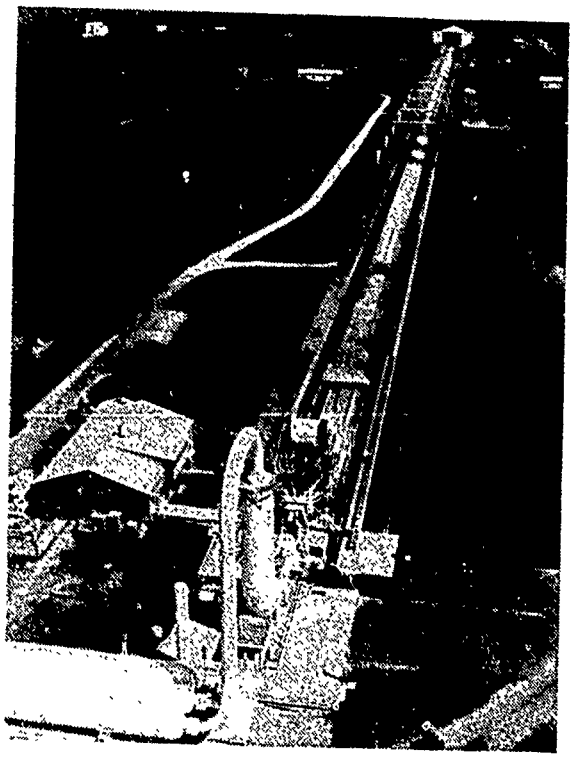

Figure 13 - Aerial photograph of modified Aircraft Landing Dynamics Facility

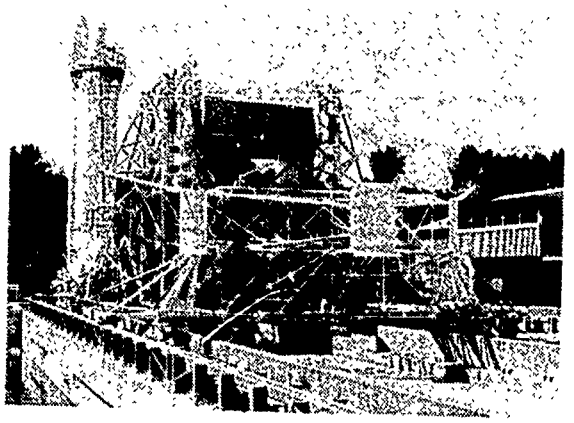

Figure 14 - Photograph of wing mounted on the ALDF carriage

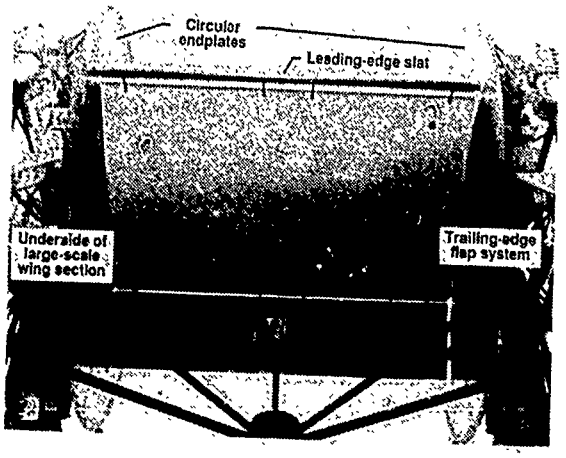

Figure 15 - An underside view of the wing hardware and endplates installed on the ALDF carriage in the high-lift configuration at an angle of attack of 18°

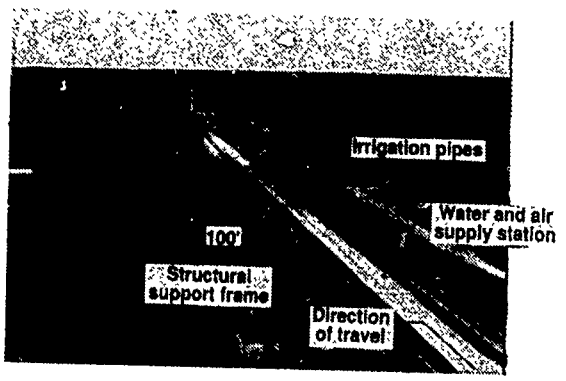

Figure 16 - An aerial view of the ALDF Rain Simulation System

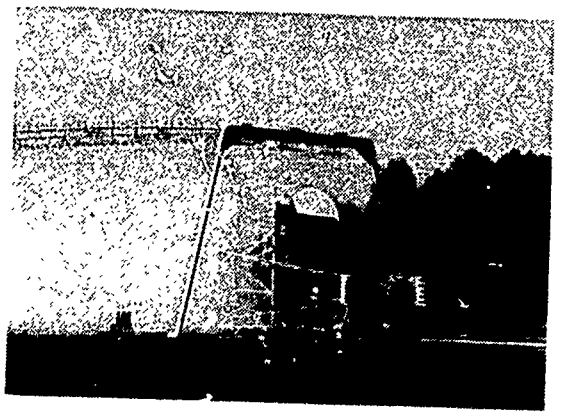

Figure 17 - Carriage exiting from RSS at 40 in/hr rain condition

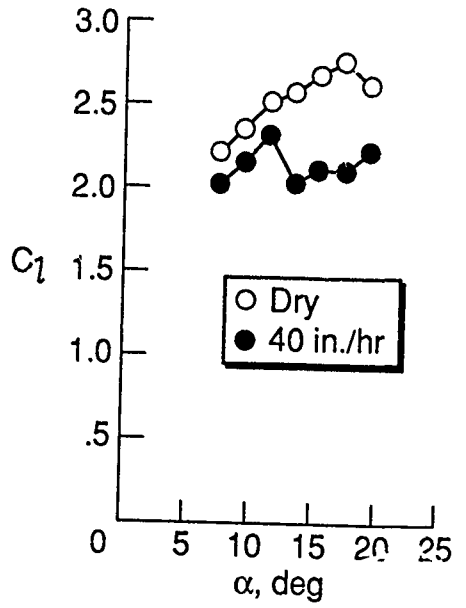

Figure 18 - Lift coefficient from ALDF high-lift data, 160 kts launch speed

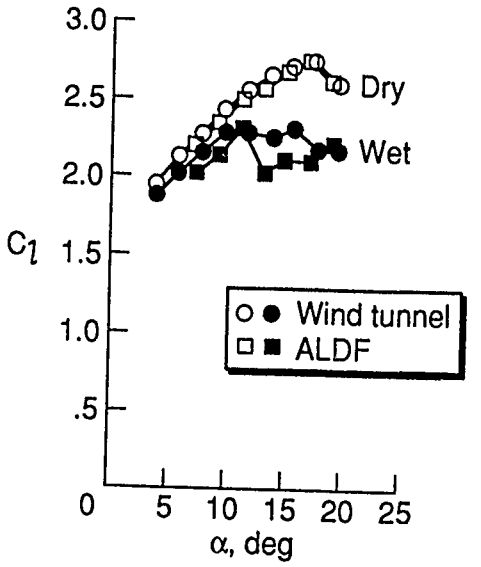

Figure 19 - A comparison between wind tunnel and ALDF data for the high-lift configuration

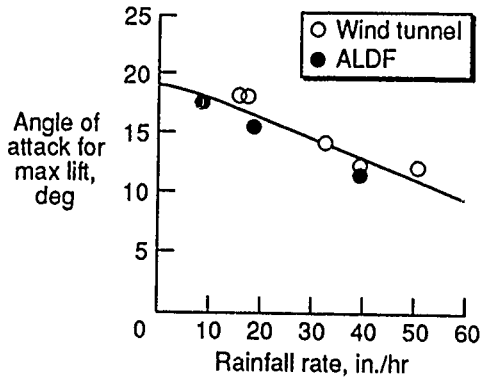

Figure 20 - Rain effect on stall angle of attack

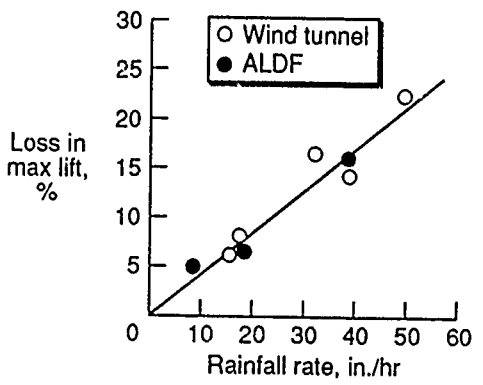

Figure 21 - Rain effect on maximum lift

THE MEASUREMENT OF WATER FILM THICKNESS ON AIRFOILS IN HEAVY RAIN CONDITIONS USING CONDUCTANCE SENSORS

A. Feo
F. Rogles
M. Urdiales

Experimental Aerodynamics Laboratory

I N T A

28850 Torrejon (Madrid) SPAIN

ABSTRACT

Calibration results of liquid film thickness using electric conductance sensors are presented. Two sensor types are analyzed. First, a double electrode sensor whose calibrations compensate liquid conductivity and secondly, a triple electrode sensor that, when properly calibrated, also compensates capacitive effects. For this second type, the electrolyitc effects can also be corrected without excessive errors. Tests conducted on a large-scale airfoil under simulated heavy rain conditions, at NASA Langley Research Center are described, and the film thickness that develop, measured.

NOMENCLATURE

d	Diameter of electrode
D	Diameter of grounded ring
ϵ_w	Liquid dielectric constant
h	Liquid film thickness
I_w	Liquid electric intensity
R, R1	Circuit resistances
V	Applied voltage
V_w	Liquid voltage drop
w	Frequency
Y_w	Liquid conductivity
Z_w	Liquid impedance
ϕ	Defined by (2)

Subscripts

0	Dry value
1	First electrode
2	Second electrode
3	Third electrode

I. INTRODUCTION

Considerable number of investigations have been conducted in recent years to determine the aerodynamic performance penalties created by heavy rain on airfoils. Haines and Luers (1) undertook an initial analytical study to estimate the performance degradation associated with heavy rain. It was followed by a report (2) in which it was suggested that the wind shear-heavy rain coupling might have been the factor on several airplane accidents. They led to the preparation of Wind Tunnel Test Programs for several airfoil sections at different Reynolds numbers (3)-(6), that indicated important reductions in maximum lift and stall angle and increase in drag coefficients. These studies document the heavy rain effects on small-scale airfoil sections. To understand its extrapolation to full scale, an study was undertaken (7), and the parameters involved in the scaling process, defined. Because of the complexity of the scaling laws, NASA decided to conduct tests on a large-scale airfoil (8), finding for the same airfoil section, lift reductions of comparable magnitude to the ones obtained in the Wind Tunnel tests. Complete overviews of heavy rain effects on airfoil aerodynamics are presented in refs. 9 and 10.

Although quantification of the performance degradation has been established for different airfoils, there is not still a comprehensive understanding of its basic causes. The most probable underlying reason is that a complete study of the wet airfoil aerodynamics requires substantial knowledge of the complex two-phase flow, dominated by the interaction between the air boundary layer and the surface water film. That process should take into account: film waviness, drop cratering, incoming and ejected droplets' interchange of momentum and energy with the airfoil air boundary layer, etc. In order to throw light on the physics of the splash-back phenomenon, some preliminary studies have been conducted (11,12). The water film thickness appears connected to all of the above mentioned physical processes, and therefore its determination is now considered necessary both by theoretical and experimental means.

A known procedure to experimentally determine a liquid film thickness is based on measuring its electrical conductance. It can be accomplished by connecting a conductance measuring circuit to a pair of electrodes, mounted flush to the surface. Determination of the water conductance value was the method initially employed in a group of heavy rain airfoil film thickness measurements (13, 14). However, the measure of the water conductance left uncompensated its conductivity and considerable errors in the film thickness measured appeared. Modification of the procedure was later proposed by the introduction of another electrode (15), and the values obtained by the indicated method, were effectively independent of water conductivity. Some measurements using the double electrode sensor concept are reported in Ref. 16.

But the double electrode method had another inherent built-in effect that was not considered. The conductance measuring circuit requires an AC signal as electrical source. The signal frequency is chosen to minimize water polarization, but it does not achieve its total elimination. This effect is responsible for the liquid's capacitive behavior that, unless properly compensated, results in errors not yet accounted. The water capacitance compensation is specially relevant for the type of heavy rain measurements that we are concerned here. The fast moving liquid film on top the sensor generates irregular patterns made of thin water rivulets, air bubbles, etc., resulting in water conductance differences when compared with the same type of water film standing still (Static). The practical consequence is that the calibration of some water in a static condition by the double electrode method, will not strictly apply to heavy rain film measurements of the same water type, unless some new sensor and calibration procedure are devised, in which the dynamic conditions are properly taken care of.

The purpose of this study is to extend the double electrode device, by the inclusion of yet another third electrode to the sensor, in a way that the compensation performed by the sensor is complete. It is also intended to establish a new film thickness calibration procedure that is finally independent of the liquid dielectric constant eliminating the instrument capacitive effects. Once this is done, the electrolytic effects, that are responsible for creating deposits at the electrode's surfaces, may be included as corrections to the clean calibration lines. Being the long-term objective in this effort, to define and fabricate an instrument with the capability of accurately measuring

water films on airfoil surfaces under heavy rain environments, some experiments have been performed and are presented in section IV. They have been obtained using a triple electrode sensor installed on a large-scale airfoil. These tests took place at NASA-Langley's acceleration track (Aircraft Landing Dynamics Facility), which was supplemented with a Rain Simulation System.

II. THEORETICAL BACKGROUND

The conductance measuring circuit employed here is sketched in Fig. 1. The measurement of V_w is directly related to the liquid impedance Z_w by:

$$V_w = \frac{V}{\frac{R+R1}{R1} + \frac{R}{Z_w}} \qquad (1)$$

$$\text{Define } \phi = \frac{1}{V_w} - \frac{1}{V_{wo}} \qquad (2)$$

being V_{wo} the voltage measured when dry. Substitution of (1) into (2) and expansion yields:

$$\phi = \frac{R}{V}\left[\frac{1}{Z_w} - \frac{1}{Z_{wo}}\right] \qquad (3)$$

which means that ϕ is proportional to the liquid conductance. Independently of the supplied frequency, the liquid equivalent impedance is represented in Fig. 2. One capacitor, C_{wp}, is dominant at low frequencies and represents the liquid polarization, while C_{ws}, that gets larger as the frequency increases, is representative of the sensor geometry and cables. Therefore:

$$V_w = f(I_w, w, Y_w, \epsilon_w, h, D, d)$$

which says that the measured voltage is an unknown function of the independent variables that result from the electric circuit, the type of liquid and the geometrical dimensions involved. They can be grouped in four non-dimensional parameters, that is:

$$\frac{V_w}{I_w} Y_w D = \bar{f}\left[\frac{Y_w}{w\epsilon_w}, \frac{d}{D}, \frac{h}{D}\right] \qquad (4)$$

Or in the terms of ϕ:

$$\frac{V\phi}{RY_wD} = F\left[\frac{Y_w}{w\epsilon_w}, \frac{d}{D}, \frac{h}{D}\right] \qquad (5)$$

If only one electrode (plus the one connected to ground) is used, the film thickness h is determined by the sensor geometrical dimensions, the known electric circuit constants, the measured ϕ, the liquid conductivity Y_w and the parameter $Y_w/w\epsilon_w$. Then, if ϕ is plotted vs h (for a given sensor), there will be as many lines as pairs of $(Y_w, Y_w/w\epsilon_w)$, as is schematically indicated in Fig. 3, and there will not be a unique h value for a ϕ measured.

Using a second electrode, very thin so is insensitive to film thickness (15), we have:

$$\phi_1 = \frac{RD_1}{V} Y_w F_1\left[\frac{Y_w}{w\epsilon_w}, \frac{d_1}{D_1}, \frac{h}{D_1}\right] \qquad (6)$$

$$\phi_2 = \frac{RD_2}{V} Y_w F_2\left[\frac{Y_w}{w\epsilon_w}, \frac{d_2}{D_2}\right] \qquad (7)$$

$$\frac{\phi_1}{\phi_2} = F_{12}\left[\frac{Y_w}{w\epsilon_w}, \frac{d_1}{D_1}, \frac{d_2}{D_2}, \frac{h}{D_1}\right] \qquad (8)$$

If ϕ_1/ϕ_2 is plotted vs h, the direct dependency with Y_w has disappeared, but the parameter $Y_w/w\epsilon_w$, indicative of the capacitive effects, still remains as shown in Fig. 4.

In order to eliminate the capacitive effects, another electrode is introduced. A new $\phi 3$ is:

$$\phi_3 = \frac{RD_3}{V} Y_w F_3 \left[\frac{Y_w}{w\epsilon_w}, \frac{d_3}{D_3}, \frac{h}{D_3} \right]$$

then:

$$\frac{\phi_3}{\phi_2} = F_{23} \left[\frac{Y_w}{w\epsilon_w}, \frac{d_2}{D_2}, \frac{d_3}{D_3}, \frac{h}{D_3} \right]$$

The parameter $Y_w/w\epsilon_w$ can now be eliminated between F_{12} and F_{23} and plotting ϕ_3/ϕ_2 vs h, and ϕ_1/ϕ_2 being included as a parameter, a unique value for the film thickness follows (Fig. 5).

III. CALIBRATIONS

III.1. Experimental apparatus

The experimental system used in the calibration of sensors consists of three elements: The calibration unit,the electrodes and the conductance measuring circuit. Brief description of each follows:

Calibration unit: The test surface is a flat stainless steel disk. It is supplemented with a bridge incorporating a needle and a micrometer (resolution 0.01 mm) (Fig. 6). Readings are made visually with backlight illumination at the touch of the needle with the liquid, and checked simultaneously with a contact electric circuit. The sensor is located beneath the needle.

Electrodes: Two types of arrangements have been used. First, a double electrode, in which the conductance ratio obtained is independent of liquid conductivity. Second, a triple electrode in which the instrument capacitive effects are also eliminated. In both cases, the configuration used were cylindrical corrosion-resistant electrodes, mounted in an insulating plastic and located flush to the surface (Fig. 7). The larger ring (ground), forms the double electrode sensor. The triple electrode sensor is formed by both rings, and the larger diameter electrode inside the smaller ring is also connected to ground. In this manner, the double electrode sensor acts as a completely independent unit.

Conductance measuring circuit: The circuit used to measure the liquid conductance on top of the electrodes is the same as was shown in Fig. 1. It is followed by the electronic conditioning elements before they are supplied to the Data Acquisition System as a DC (Fig. 8). III.2.

III.2. Calibration results

Calibrations with water in static and dynamic conditions are being considered. First, the liquid is standing still on top of the sensor (Static calibration). Second, drops being the result of a 0.8 mm broken water jet with velocity of 20 m/sec are made to impact on the sensor and its vicinity (Dynamic calibration). In this manner, it is demostrated how, different conditions are absorbed by the double and triple electrode methods.

Clean sensor calibrations: Calibrations are made with polished electrodes. The results for the double and triple electrode sensors are shown in figs. 9 and 10, respectively. They include both, static and dynamic calibrations. The static ones have been performed with three water types (tap, filtered and distilled), and the dynamic one only with tap water. For the double electrode sensor, the uncertainty is ±0.04 mm. for the lower part of the range and increasing up to ±0.10 mm. for the upper part (near 0.5 mm). The mean uncertainty for the whole range in the triple electrode case is obtained to be ±0.025 mm, which

is of the order of the inherent error in the measurement method employed.

Sensor electrolytic effects: It is known that the applied AC voltage circulates through the liquid by an electrolytic process. That is, inside the electrolite, the electric energy transfer is made by ions present in the liquid. A transformation of these ions takes place at the surface of the electrodes, by depositing of substances, effectively changing the conductance, as it is measured by the circuit defined in Fig. 1. The amount of deposits are dependent on liquid composition and temperature, geometry of the electrodes and the electrical variables in the circuit.

As an example, the sensors have been exposed to tap water with the electric current in circulation for 9 hours. Results are compared with the ones obtained when the sensors are clean. For the double electrode sensor it is shown in Fig. 11. Now, the uncertainty increases to ±0.05 mm at h≈0.05 mm and ±0.20 mm at h≈0.5 mm. The triple electrode sensor calibration is transformed into one equivalent to the clean sensor, but with the lines $R_{12}=\phi_1/\phi_2$=const, displaced (Fig. 12). The displacement, for a given sensor, is a function of liquid composition only. Tap water has been used, because among the different water types, is the one that will produce more deposits and therefore larger differences. Taking, as the correction for electroplating, lines that are displaced a fifty percent on the plots, the error obtained when these corrected lines are used is now, ±0.04 mm for the whole range.

IV. FILM THICKNESS MEASUREMENTS ON AN AIRFOIL UNDER HEAVY RAIN CONDITIONS

The double electrode sensor calibration lines (Fig. 9) have shown the differences that exist between the same water type in static and the dynamic conditions tested in the laboratory. The triple electrode calibration lines have a built-in compensation by the use of two parameters, $R_{12}=\phi_1/\phi_2$ and $K=\phi_3/\phi_1+\phi_3/\phi_2$, and any dynamic condition will be measured without nominal errors.

Then, a triple electrode sensor type was chosen for evaluation and mounted on an airfoil, that was planned to be tested under a heavy rain environment. Two main reason induced to perform those experiments:

1) To show the possibility of using this sensor type in real heavy rain conditions, and

2) To provide information of the film thickness that exists on the airfoil configuration in some specific testing conditions.

The sensor was installed on the lower surface of a large-scale airfoil mounted on a towing-type carriage. This is part of a Facility that exists at the NASA Langley Research Center, and has been modified for the Heavy Rain Effects Program (17). The sensor was located on the lower surface at 10% of the chord from the leading edge of the model, which is a 3 meters chord 64-210 airfoil section in a landing configuration, with slat and flaps extended (Fig. 13). The testing track was supplemented with an overhead rain simulation system extending for approximately 150 meters of track length.

The test conditions for which results are presented here are:

Angle of attack:	a = 7.5°
Air velocity:	V = 52 m/sec.
Rain rate:	RR = 482 mm/hour (≈15 gr water/m^3)

The same cable configuration and Data Acquisition System were used at the test and at the laboratory calibration.

The time history for the voltages (V_i) and conductances (ϕ_i) are presented in Figs. 14 and 15. It should be noticed that those jumps are much smaller than anything possible with tap water in static conditions, and the trend is consistent with dynamic laboratory calibration results. From the ϕ_i values, the time history of the parameters R_{12} and K are obtained and shown in Fig. 16. At specified time intervals, each pair of R_{12} and K defines a unique h value, that is obtained from the corresponding calibration plot. The film thickness that results, is represented in Fig. 17.

V. CONCLUDING REMARKS

Liquid film thickness electric conductance sensor calibrations and measurements, taken under a simulated heavy rain environment, at the NASA Langley Research Center, have provided the following information:

1) Single electrode sensors are only suitable to measure liquid film thickness if identical liquid sample conditions can be assumed to exist between the test and the laboratory calibration.

2) Double electrode sensors are able to compensate liquid conductivity, but do not provide a universal calibration extensive to different liquid compositions and conditions. That is, to the errors induced by the changing liquid type, there is the added uncertainty due to the unknown conditions. Therefore, they are not considered appropiate for film thickness measurements in Heavy Rain applications.

3) Triple electrode sensors compensate not only liquid conductivity, but the sensor capacitive effects. After an appropiate calibration method is established, they are valid for any liquid type and condition; therefore, these sensors are considered suitable for Heavy Rain applications. The mean error obtained in the calibration presented here is ±0.025 mm for measurements in the 0-0.5 mm range.

4) Electroplating effects can be corrected for the triple electrode calibration lines. An increase of the mean error to ±0.04 mm, after a 9 hour operation, may be considered typical.

5) Triple electrode sensor film thickness measurements conducted on a large-scale airfoil, under simulated heavy rain conditions, at the NASA Langley Research Center acceleration track (ALDF), has shown consistent trends with the values found at the laboratory dynamic calibrations. A wavy water film, with a peak of approximately 0.3 mm, has been found at the conditions indicated in Section IV.

REFERENCES

1. Haines, P. A. and Luers, J. K. **Aerodynamic Penalties of Heavy Rain on a Landing Aircraft.** NASA CR-156885, 1982.

2. National Research Council. **Low-Altitude Wind Shear and its Hazard to Aviation.** National Academy Press, 1983.

3. Dunham, R. E.; Bezos, G. M.; Gentry, G. L. and Melson, W. E. **Two-Dimensional Wind Tunnel**

Tests of a Transport-Type Airfoil in a Water Spray. AIAA-85-0258, Jan. 1985.

4. Bezos, G. M.; Dunham, R. E.; Gentry, G. L. and Melson, W. E. Wind Tunnel Tests Results of Heavy Rain Effects on Airfoil Performance. AIAA-87-0260, Jan. 1987.

5. Hansman, R. J. and Craig, A. P. Comparative Low Reynolds Number Tests of NACA 64-210, NACA 0012 and WORTMANN FX67-K170 Airfoils in Heavy Rain. AIAA 87-0259, Jan. 1987.

6. Campbell, B. A. and Bezos, G. M. Steady-State and Transitional Aerodynamic Characteristics of a Wing in Simulated Heavy Rain. NASA Technical Paper 2932, 1989.

7. Bilanin, A. J. Scaling Laws for Testing of High Lift Airfoils under Heavy Rainfall. AIAA 85-0257, Jan. 1985.

8. Bezos, G. M.; Dunham, R. E. and Campbell, B. A. Results of Aerodynamic Testing of Large-Scale Wing Sections in a Natural Rain Environment. AIAA 90-0486, Jan. 1990.

9. Dunham, R. E. Potential Influences of Heavy Rain on General Aviation Airplane Performance. AIAA 86-2606, Sept.-Oct. 1986.

10. Dunham, R. E. Potential Influences of Rain on Airfoil Performance. Influence of Environmental Factors on Aircraft Wing Performance. VKI LS-1987-03, Von Karmann Institute for Fluid Dynamics, Feb. 1987

11. Feo, A. Rotating Arms Applied to Studies of Single Angular Drop Impacts. AIAA 87-0257, Jan. 1987.

12. Bilanin, A. J.; Quackenbush, T. R. and Feo, A. Feasibility of Predicting Performance Degradation of Airfoils in Heavy Rain. NASA CR-181842, Jun. 1989.

13. Hastings, E. C. and Weinstein, L. M. Preliminary Indications of Water Film Distribution and Thickness on an Airfoil in a Water Spray. NASA TM 85796, 1984.

14. Hastings, E. C. and Manuel, G. S. Measurements of Water Film Characteristics on Airfoil Surfaces from Wind Tunnel Tests with Simulated Heavy Rain. AIAA 85-0259, Jan. 1985.

15. Weinstein, L. M. Liquid Thickness Gauge. U.S. Patent no. 4.765.187, Aug. 1987.

16. Feo, A. and Gonzalez, P. Water Film Thickness Measurements on an Airfoil Surface in a Water Spray from NASA's Langley 4x7 Meter Wind Tunnel Tests. INTA N/221/510/89004, Dec. 1988.

17. Bezos, G. M.; Campbell, B. A. and Melson, W. E. Jr. The Development of a Capability for Aerodynamic Testing of Large-Scale Wing Sections in a Simulated Natural Rain Environment. AIAA 89-0762, Jan. 1989.

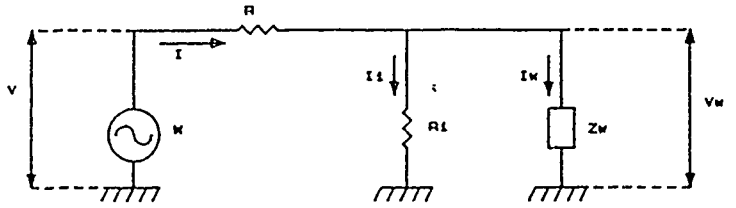

FIG.1.- CONDUCTANCE MEASURING CIRCUIT.

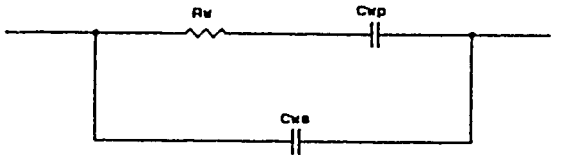

FIG.2.- LIQUID EQUIVALENT CIRCUIT.

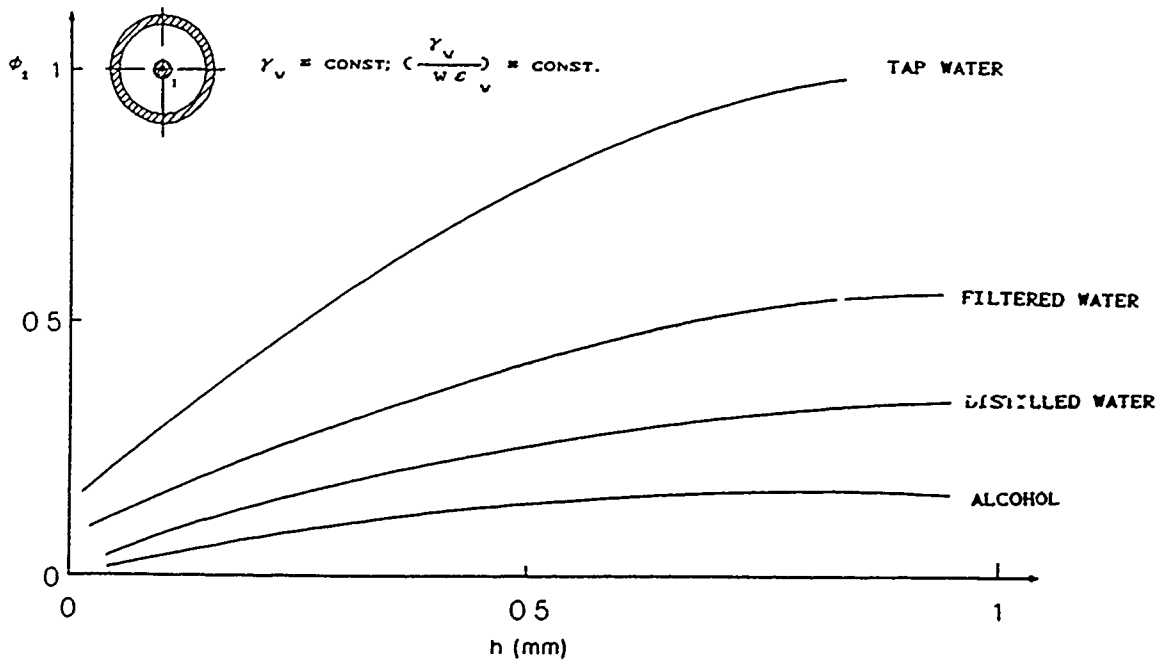

FIG.3.- SINGLE ELECTRODE REPRESENTATION. d1 ≅ 1mm;
RING ≅ 4mm (GROUND). W ≅ 1000 Hz.

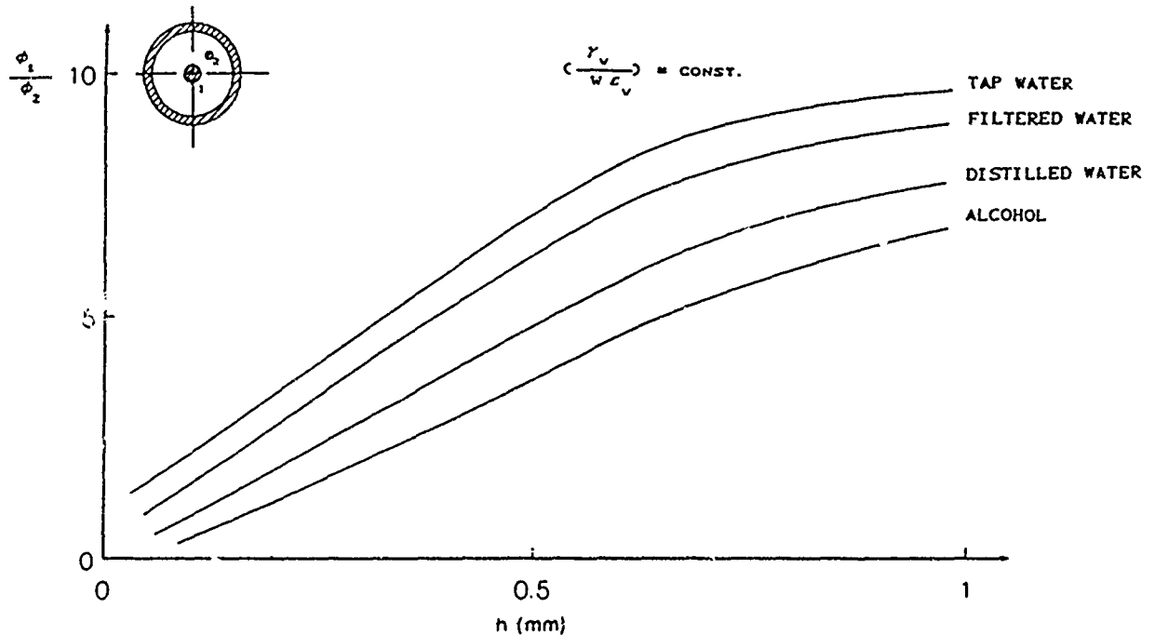

FIG.4.- DOUBLE ELECTRODE REPRESENTATION. d1 ≅ 1mm;
d2 ≅ 0.1mm; RING ≅ 4mm (GROUND). W ≅ 1000 Hz.

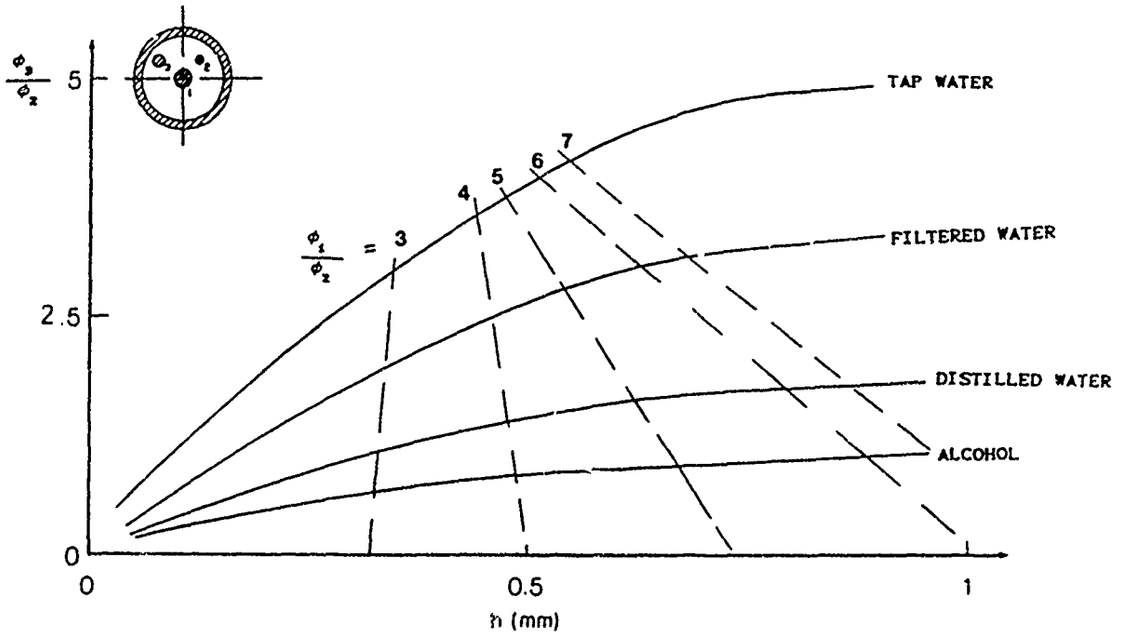

FIG.5.- TRIPLE ELECTRODE REPRESENTATION. d1≅1 mm; d2≅0.1 mm;
d3≅0.1 mm. RING≅4 mm (GROUND). W ≅ 1000 Hz.

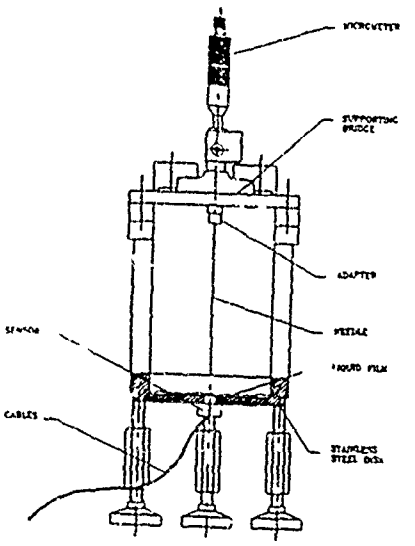

FIG.6.- CALIBRATION UNIT.

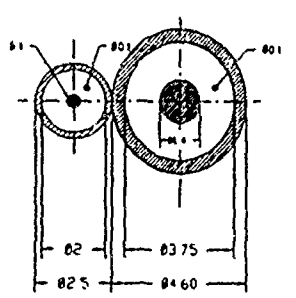

FIG.7.- TRIPLE ELECTRODE SENSOR. (DIMENSIONS IN MM)

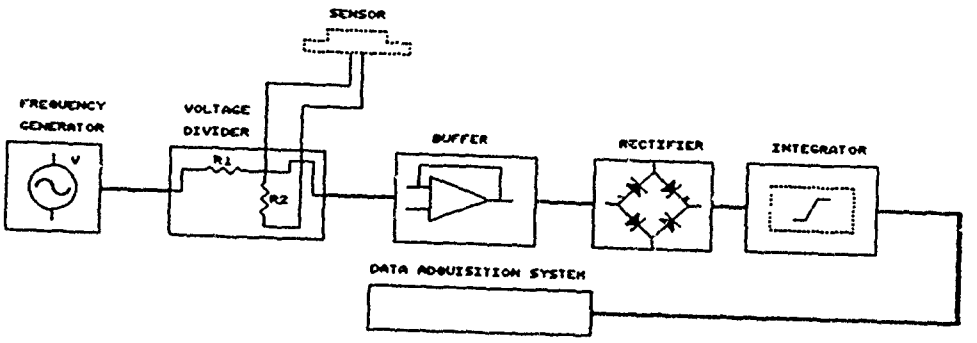

FIG.8.- CONDUCTANCE MEASURING CIRCUIT AND ELECTRONIC SIGNAL CONDITIONING.

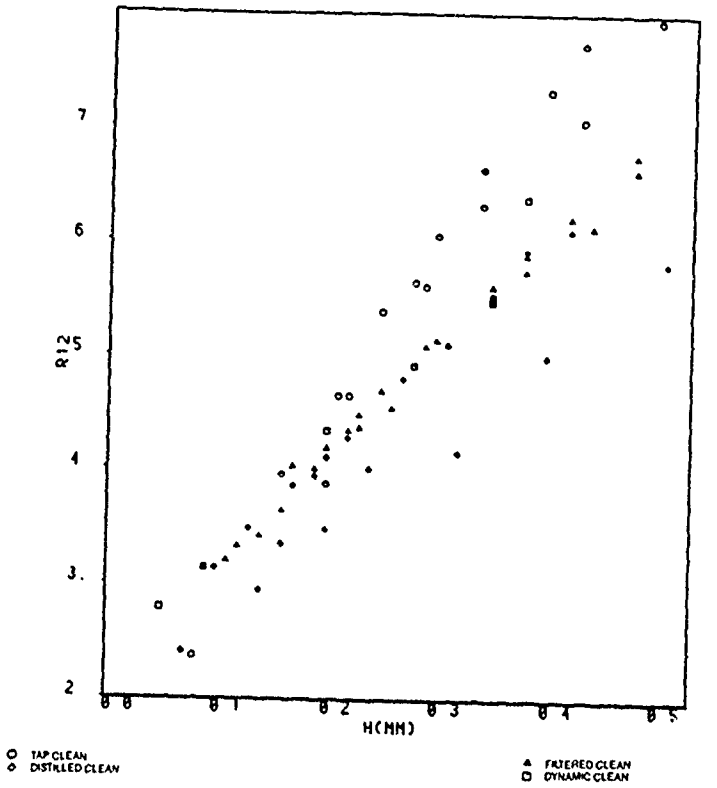

FIG.9.- CLEAN DOUBLE ELECTRODE CALIBRATION.

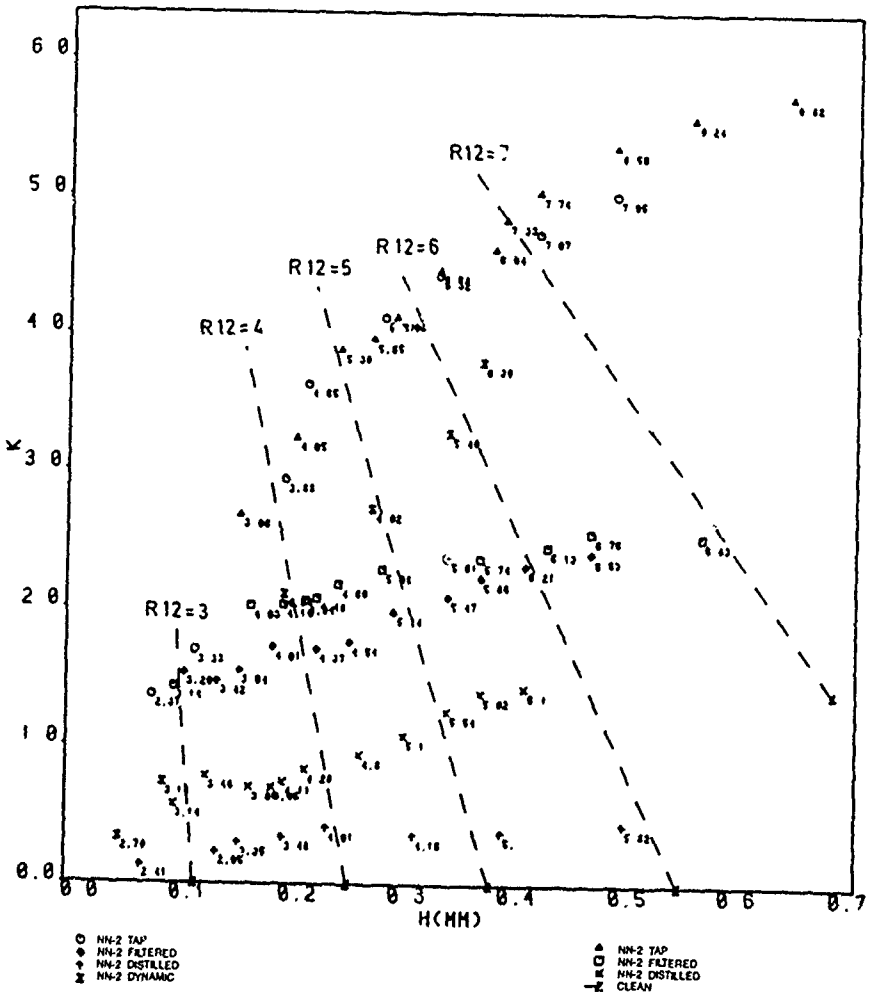

FIG.10.- CLEAN TRIPLE ELECTRODE CALIBRATION.

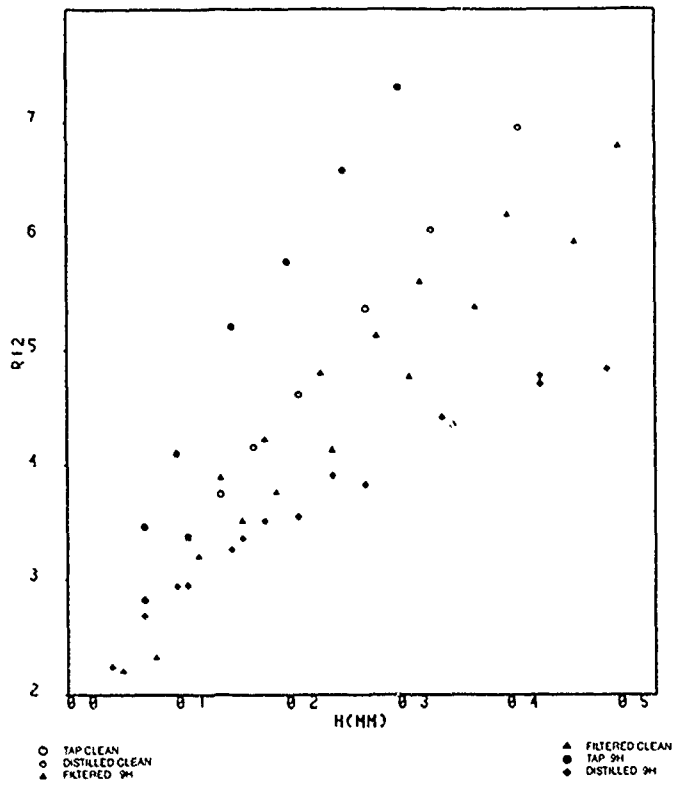

FIG.11.- DOUBLE ELECTRODE CALIBRATION RESULTS AFTER 9 HOURS OF TAP WATER CONTAMINATION.

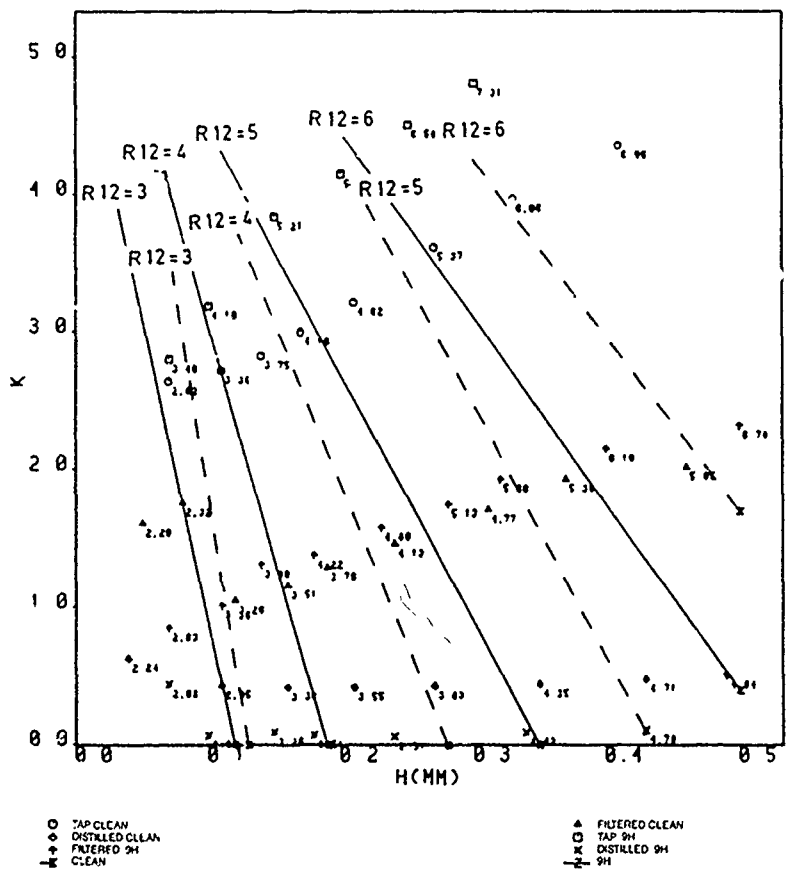

FIG.12.- TRIPLE ELECTRODE CALIBRATION RESULTS AFTER 9 HOURS OF TAP WATER CONTAMINATION.

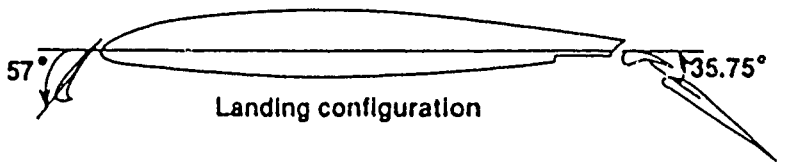

FIG.13.- AIRFOIL MODEL WITH LEADING-EDGE SLAT AND TRAILING-EDGE FLAPS EXTENDED.

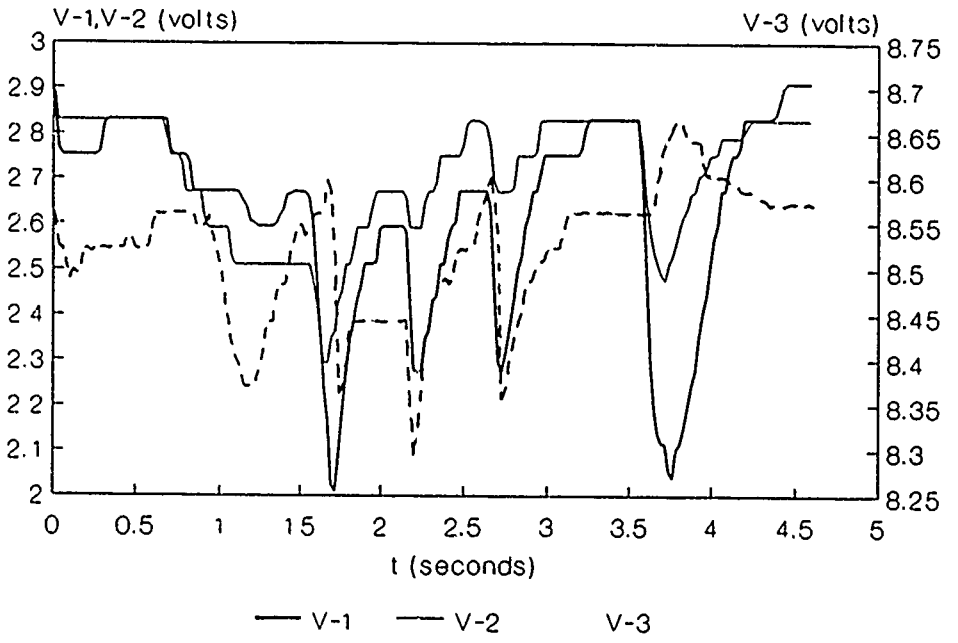

FIG.14.- TIME HISTORY OF VOLTAGES V1, V2 AND V3.
Alpha=7.5 v=53 m\s RR=482 mm\hr

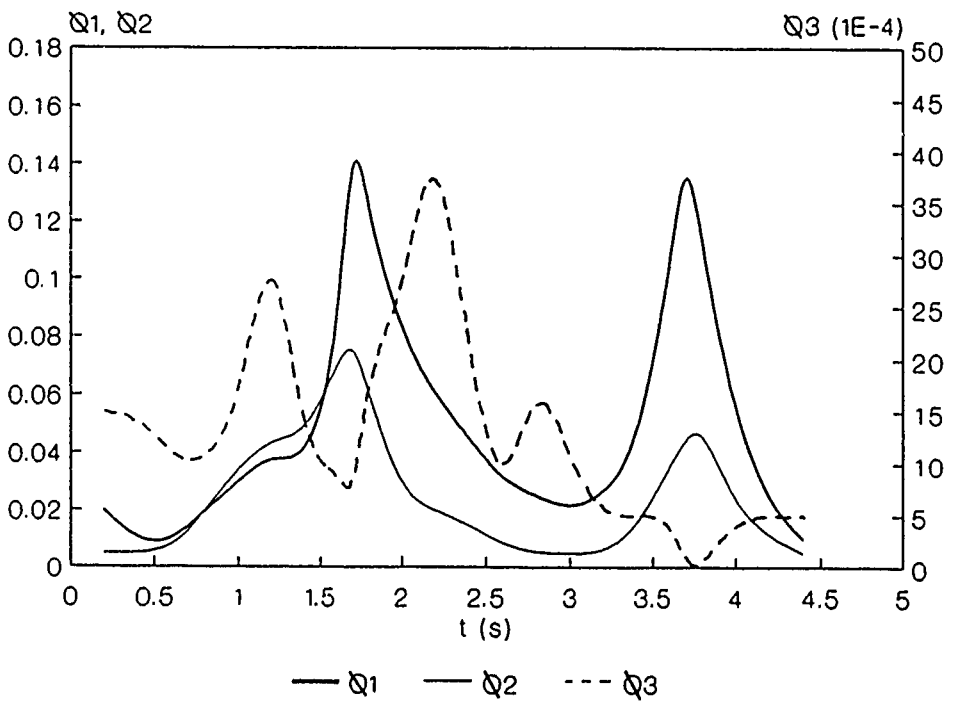

FIG.15.- TIME HISTORY OF Q1, Q2 AND Q3.

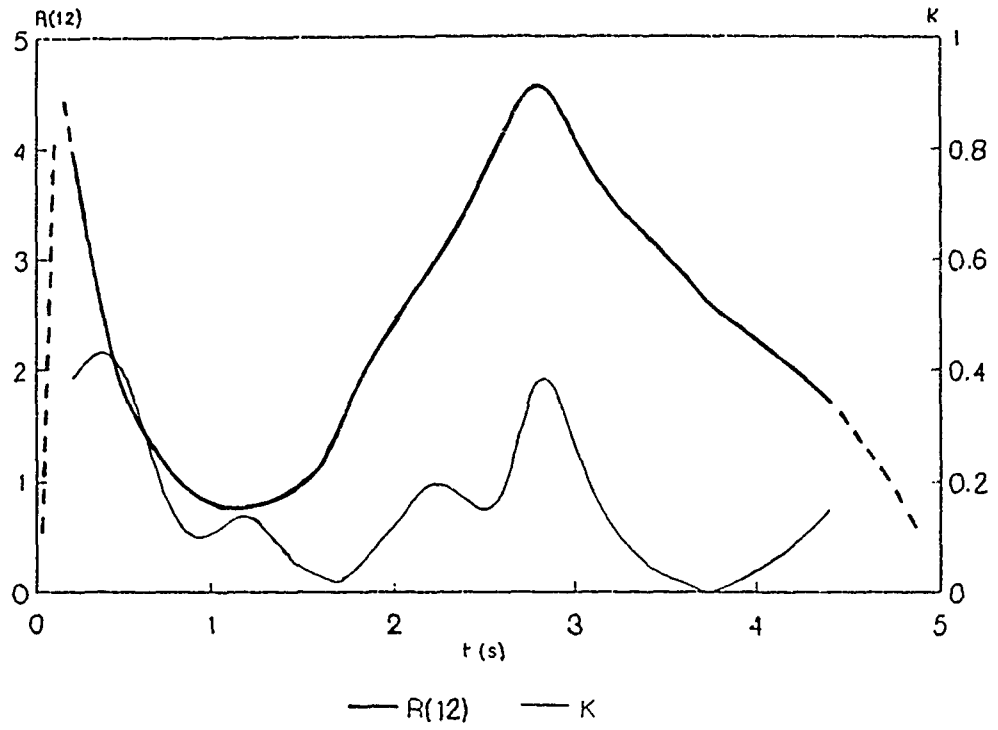

FIG.16.- TIME HISTORY OF PARAMETERS R(12) AND K.

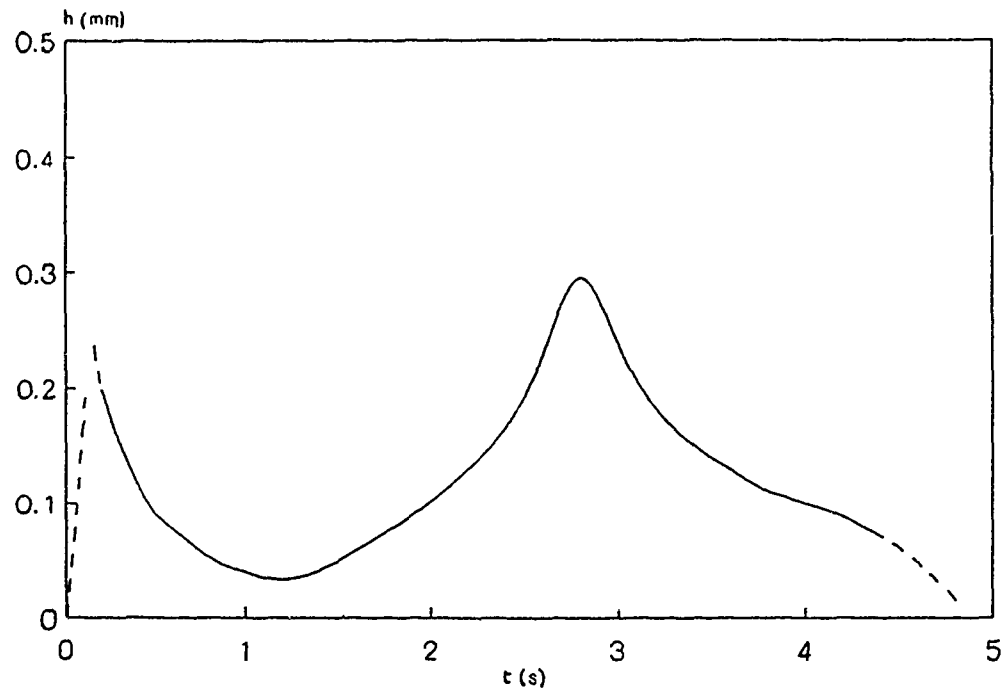

FIG.17.- TIME HISTORY OF FILM THICKNESS.

EXPERIMENTAL INVESTIGATION OF HEAVY RAINFALL EFFECT ON A 2-D HIGH LIFT AIRFOIL

by

F.C. Tang
Institute for Aerospace Research
National Research Council
Ottawa, Ontario
Canada K1A 0R6

SUMMARY

The effects of simulated heavy rainfall on a 2-D high lift airfoil have been studied in a wind tunnel experimental programme. The experiment was carried out in the 2-dimensional test section of the 1.5m X 1.5m blowdown wind tunnel of the High Speed Aerodynamics Laboratory. The model used in the investigation was a modified NACA 65_2215 multi-element airfoil with a basic chord of 254 mm. The Mach number was fixed at M=0.2, typical of the landing speed of transport type aircraft. The chord Reynolds number range was 1.7 to 8.8×10^6.

Measurements included lift, drag and pitching moment of the airfoil obtained by side wall balances and the flow rate from a water spray manifold.

The effects of the simulated rainfall to the airfoil performances are very significant. The loss in maximum lift coefficient ranged from 6% to a high of 16%. The drag levels at constant lift are up to 43% higher under wet conditions. A smaller performance degradation was noted when the model was stripped of the smooth epoxy paint with which it was originally finished.

Symbols

C_D	drag coefficient
C_L	lift coefficient
C_m	pitching moment coefficient about quarter chord
LWC	liquid water content, gm/m^3
M	freestream Mach number
RR^*	equivalent rainfall rate at R_c = 8.8×10^6, (50 mm/hr)
RR_e	equivalent rainfall rate, mm/hr
R_c	Reynolds number based on basic model chord (254 mm)
ΔC_D	drag coefficient increment between wet and dry conditions at constant lift
ΔC_L	lift coefficient increment between wet and dry conditions at constant lift
ΔC_m	pitching moment coefficient increment between wet and dry conditions at constant lift
ΔC_D^*	"normalized" drag coefficient increment between wet and dry conditions at constant lift, $\Delta C_D/RR_e \cdot RR^*$
ΔC_L^*	"normalized" lift coefficient increment between wet and dry conditions at constant lift, $\Delta C_L/RR_e \cdot RR^*$
ΔC_m^*	pitching moment coefficient increment between wet and dry conditions at constant lift, $\Delta C_m/RR_e \cdot RR^*$
α	angle of attack

INTRODUCTION

In recent years there have been a number of spectacular and often fatal weather related aircraft accidents which received a lot of attention from the news media and the concern of scientific community. The most likely cause of these weather related accidents is a meteorological phenomenon called the microburst. Severe low altitude wind shear has been noted as the major factor in a microburst, however, heavy rainfall is also observed most of the time during a microburst sighting (Reference 1). An initial study by Luers and Haines (Reference 2) on the effects of rain on aircraft aerodynamic characteristics generated substantial interest in this area. A number of experimental and theoretical studies (Reference 2-7) have since been published. Most of the experimental works were carried out in relatively low Reynolds number, around $R_c = 3\times10^5$, with the exception of Reference 5, which went up to R_c = 3.3 million. Reference 7 gives a succinct account of the results obtained in various investigations. In general, most results show a substantial reduction in maximum lift coefficient under simulated heavy rain conditions. The airfoil performance degradation has been attributed to the uneven water film distribution over the model surfaces, early flow separation due to the introduction of minute droplets as a result of rain impact on the airfoil and surface roughness effects. Water also tends to accumulate towards the airfoil trailing edge, effectively changing the camber.

This paper describes the measurements carried out in the 2-D test section of the IAR blowdown wind tunnel. Data are presented for the force and moment coefficients on the model under simulated rainfall rates of 50 mm/hr to 300 mm/hr. It should be noted that a rainfall rate of 1 mm/hr is classified as light rain; whereas heavy rain is usually referred to a rate of about 15 mm/hr. The term 'cloudburst' is reserved for the description of rainfall rates in the range of 100 mm/hr to 1000 mm/hr. Although the occurrence is very rare, rainfall rates of up to 1828 mm/hr have been recorded.

TEST FACILITY

The experiments were conducted in the Institute for Aerospace Research 1.5m blowndown wind tunnel. The 2-dimensional test section (38 cm×152 cm) of the wind tunnel as shown in Figure 1 was used. The model was located approximately 240 cm downstream of the start of the parallel section. It was mounted on two external side wall balances for measurement of axial

force, normal force and pitching moment. Solid aluminum plates were substituted for the porous Rigimesh panels normally installed on the side walls in the model area. Thus no side wall suction was applied for the removal of sidewall boundary layer, as done in more usual 2D tests.

SPRAY RIG

The spray rig (Figure 2) consists basically of an accumulator (20 l capacity), a turbine flow meter (40 l/min.), various pressure regulators and valves plus a spray manifold designed and assembled specially for these measurement. Filtered water can be pressurized up to 7 atmosphere and be delivered at a rate of up to 40 l/min. The spray manifold manufactured from streamline tubing, with up to seven commercially available spray nozzles was installed 17 chord lengths upstream of the model (Figure 3).

WATER SPRAY CHARACTERISTICS

The spray nozzles have a manufacturer quoted droplet size of 1000-2000 μm under normal, i.e. atmospheric, operating conditions. Since the water spray was to be generated in a pressurized environment, a direct measurement of the spray characteristics was required. This was done prior to mounting the airfoil model. An optical array probe was mounted inside the wind tunnel at the model location, as shown in Figure 3. In an optical array probe a linear array of photodiodes is used as a measuring grid. By means of the photodetection electronics the size of the particles passing through the probe's sample area are recorded. Illumination is provided by a He-Ne laser. When the particles pass through the optical array probe's sample area, the particle shadows are projected on the array of photodiode elements. The loss of light on an individual element results in a voltage pulse which signals the presence and size of the particle. Information about the droplets size and distribution as well as the rain rate were obtained by the optical array probe.

A few wind tunnel runs were conducted using different size nozzles and arrangements to determine the resulting particle sizes. Figure 4 shows a typical result of such a measurement, with three Spray System nozzles (1/2 G1⅝) installed on the spray manifold. The measured water droplets size ranged from under 0.1 mm to about 0.6 mm in diameter. The majority of the droplets are in the range of 0.2 mm to 0.4 mm in diameter. The rain rate was calculated to be 310 mm/hr and the liquid water content (LWC) was estimated to be 51.8 gm/m^3. The test was done at the lowest stagnation pressure (19 psia) possible to protect the probe as it is not designed to be used in a pressurized environment. The water spray was on for 5 seconds. The freestream Mach number was M=0.2. It should be stated that the droplet concentration in the wind tunnel was found to be much higher than that of the probe's design range (Reference 8). Due to the fact that water droplets that contacted the probe arms tended to stream back through the sample area, extra uncertainties and difficulties were introduced to the reduced spray data. It was estimated (Reference 8) that the deduced LWC of the water spray could in some cases be high by a factor of two.

The LWC of the water spray was also obtained from the ratio of water flow rate of the spray manifold and the wind tunnel air mass flow rate. The water flow rate was measured to be 0.448 l/sec. which corresponded to a equivalent rain rate of 290 mm/hr. This estimation of rain rate compared quite well with the optical array probe data and was adopted as a valid means of measuring the equivalent rain rate in the wind tunnel for wind tunnel runs at pressures higher than 19 psia. In general, the agreement between the two sets of measurement are within ±20% of each other.

MODEL

The airfoil model used in this investigation has a modified NACA 65_2-215 airfoil section. It has a basic chord of 254 mm and a thickness to chord ratio of 0.15. It features an 18% leading edge slat, a 13% subsidiary trailing edge flap and a 32% main trailing edge flap (Figure 5). The model was used in the landing configuration, with the leading edge slat at 48° and the main trailing edge flap at 47.5°. The main element of the airfoil was painted with aircraft grade epoxy paint that was stripped for the last phase of the test to investigate the effect of a different surface finish on the airfoil performance under wet conditions.

TEST PROCEDURE

The wind tunnel operating conditions, model orientation and spray rig operation were all pre-programmed and controlled by computer. Upon achieving the desired tunnel operating conditions, the model angle of attack would vary from nominally -10° to 20° at a rate of 1.5° per sec. to acquire the base line 'dry' data. The water spray was then turned on automatically and the model would repeat the same angle of attack range for the 'wet data'. Data were acquired (through-out the run) at 100 Hz/sec. The tunnel was kept running for another 5 seconds after the water spray had been shut off to drive water out of the test section.

RESULTS AND DISCUSSION

Case 1 (Low Reynolds number)

The variation of lift coefficient with angle of attack at a freestream Mach number of M=0.2 and chord Reynolds number of 1.7×10^6 for the dry and wet cases are shown in Figure 6. With the water spray off, a maximum C_L of 2.85 was achieved at an angle of attack of 13°. With the water spray on the maximum C_L was only 2.4, a reduction of about 16% as compared to the dry case. It is interesting to note that for the wet case the maximum C_L occurred at a higher angle of attack, about 16° versus 13° for the dry case. This increase in the maximum lift angle was also observed in Reference 7 although a single element airfoil was used in that case. Two different but quite close rain rates (280 mm/hr and 300 mm/hr) results are shown in this figure. Both lift curves for the spray on cases show considerable irregularity, especially in the 300 mm/hr rain rate case, and the stall characteristics are different. At this low

Reynolds number the water film that formed on the model was probably very uneven and is believed to be the main cause for the non-uniform lift curves. The mean lift curve slopes are significantly lower for the water spray on ($dC_L/d\alpha$ = 0.052) than for the off conditions ($dC_L/d\alpha$ = 0.064).

Figure 7 shows the drag polars obtained under the same test conditions. For a lift coefficient of 1.8, the drag coefficient was increased by 30% for the wet cases. At the higher lift coefficient of 2.3, the drag penalty was up to 43% higher under wet conditions.

Figure 8 shows the variation of pitching moment coefficient with angle of attack. The changes due to increasing angle of attack is more gradual under wet conditions. At higher angles of attack, the curves tend to converge to the same value under wet or dry conditions. Pitching moment is significantly increased by the presence of water.

Case 2 (Moderate Reynolds number)

Figure 9 shows the lift curves obtained at a chord Reynolds number of 4.6×10^6. The wet condition results were obtained at lower rain rates, 75 mm/hr and 100 mm/hr than the first case. The effect of the change in rain rate results in clearly measurable differences in C_L. It will be noted that the lift curves are now much smoother as compared with the lower Reynolds number case. A maximum lift coefficient of about 2.65 is obtained at an angle of attack of about 15° under wet conditions, while a maximum lift coefficient of 2.9 is obtained under dry condition at an angle of attack of about 16°. The increase in maximum lift under dry conditions at this higher Reynolds number is to be expected. The reduction of about 9% in maximum lift coefficient under wet condition is observed. It should be noted that the decrease in lift under wet conditions is constant over the entire angle of attack range which is not the same as in Case 1.

Figure 10 shows the drag polars obtained at $R_c = 4.6\times10^6$. The drag penalty under wet condition at low lift is relatively low, about 9% at a C_L of 1.8. This was increased to 19% at a C_L of 2.3. At their respective maximum C_L values, the drag level is almost identical under wet or dry conditions.

The variation of pitching moment coefficients with angle of attack are shown in Figure 11. The discussion for the lower Reynolds number case applies here as well.

Case 3 (High Reynolds number)

Figure 12 shows the lift curve obtained at a chord Reynolds number of 8.8×10^6, which is a more realistic value for a transport type aircraft at landing configuration, and at a rain rate of 50 mm/hr. Also shown on the same figure are lift curves from the previous two cases for comparison. Note that the rain rates are not the same for all cases. With this difference in mind, it can be seen that under wet conditions, the lift curve slopes are getting steeper as the Reynolds number increases from 1.7×10^6 to 8.8×10^6, which is the usual Reynolds number effect, while at the same time the stall angle decreases from 16° to 14°. The latter is believed to be the effect of increases in effective rain rate. In the low angle of attack range (-5° to 0°), the combined effect of Reynolds number and rain rate are very small among the wet cases. However, at -5° the lift coefficient of the wet cases is about 19% lower than that of the dry condition. The large variations in lift among the wet cases show up much more at higher angles of attack. The penalty due to wet condition to maximum C_L for the $R_c = 8.8\times10^6$ case is about 8.6%.

Figure 13 compares the drag polars of the wet and dry conditions obtained at $R_c = 8.8\times10^6$. At low lift coefficient, the differences between the dry and wet cases are small. For the $R_c = 8.8\times10^6$ case, at a lift coefficient of 1.8, the drag penalty due to the wet condition is about 6.7% and that increases to 9.5% at C_L of 2.3. The drag level at maximum lift is about the same for the wet and dry condition.

The pitching moment coefficient curves are shown in Figure 14. At 0°, there is a 17% difference in the pitching moment coefficient between 'wet' and 'dry'. The difference is reduced to a 7% difference at 19°.

The foregoing comparisons in each case have all been with respect to differing rainfall rates. In order to separate the effects of rainfall rate from Reynolds number, lift, drag and pitching moment coefficients increment from dry to wet conditions have been "normalized" by the ratio of the effective rainfall rate to the effective rainfall rate obtained at the $R_c = 8.8\times10^6$ condition (RR_e/RR^*, where RR^* = 50 mm/hr). The results are shown in Figures 15, 16 and 17 which plot ΔC_L^*, ΔC_D^* and ΔC_m^* versus C_L. They clearly show that the more serious effects occur at the higher Reynolds number cases.

Case 4 (Surface Effect)

The epoxy paint was stripped off the model to investigate the effect of different surface finish when subjected to heavy rainfall. Although the bare metal model finish is very fine, it is however not as smooth as the painted surface. Water tends to bead more readily on the painted surface than on the bare metal surface.

Figure 18 shows the C_L-α curves with the two different model surface finishes obtained under the same rain rate (50 mm/hr) and at the same Reynolds number of 8.8×10^6. When compared to the results obtained from the dry condition, the painted surface data show a larger (8.6%) degradation in lift than that from the metal surface data (5.9%). The decrease in lift is almost constant in magnitude through-out the entire angle of incidence range.

CONCLUSIONS

The following conclusions are drawn based on the limited amount of data obtained from the wind tunnel measurement:

Simulated rainfall rates of 50 mm/hr to over 300 mm/hr can be produced in a wind tunnel environment depending on the wind tunnel operating conditions. Mean droplet sizes ranging from 0.025 mm in diameter to well over 1 mm were measured using an optical array probe, although most of the droplets are in the 0.2 mm to 0.4 mm range. The estimated LWC deduced from the optical array probe data ranged from 26 gm/m^3 to 52 gm/m^3, although the values are believed to be over estimated.

Data obtained under wet conditions at low Reynolds number (1.7×10^6) shows much more irregularities than data obtained at higher Reynolds number. A drop of 16% in maximum lift coefficient was observed at the low Reynolds number case with a simulated rain rate of 300 mm/hr. The decrease in maximum lift coefficient was about 8.6% at the high Reynolds number case (8.8×10^6) with a simulated rain rate of 50 mm/hr. With the exception of the lowest Reynolds number case, the decrease in the magnitude of lift under wet conditions are almost constant with variation of angle of attack in each case.

The drag levels at constant lift are much higher under wet conditions. At a Reynolds number of 1.7×10^6 and a effective rain rate of 300 mm/hr, the drag coefficient was increased by 30% over the dry case at a constant lift coefficient of 1.8. The drag penalty increases with increasing lift. At a constant lift coefficient of 2.3, the drag penalty was up to 43% more under wet conditions. At a more realistic Reynolds number of 8.8×10^6 and an effective rain rate of 50 mm/hr, the corresponding drag penalties under wet conditions were 6.7% and 9.5% respectively. However, at the maximum lift conditions, the drag levels are almost the same for the dry and wet cases.

There is not much variation in the pitching moment coefficient with lift under wet condition at the low Reynolds number case. At higher Reynolds number cases, the increment in pitching moment due to rainfall are more pronounced at the lower lift than at the higher lift. At high angle of attack, the pitching moment curves tend to converge to the same value under wet or dry conditions. Compared to the dry case, the wet airfoil shows less change in pitching moment with incidence.

With the lift, drag and pitching moment increment "normalized" by the effective rainfall rate ratio, a more serious effects were observed with the higher Reynolds number cases.

Data obtained from a bare metal model, under identical test conditions, show a smaller performance degradation than the smoothly painted model due to simulated rainfall.

REFERENCES

1. Fujita, T.T., "Microburst-Related Aircraft Accidents". Chapter 3 in "The Downburst". The University of Chicago, 1985.

2. Luers, J.K. and Haines, P., "The Effect of Heavy Rain on Wind Shear Attributed Accidents". AIAA-81-0390, presented at the 19^{tn} Aerospace Science Meeting, St. Louis, Missouri, 1981.

3. Haines, P. and Luers, J., "Aerodynamic Penalties of Heavy Rain on Landing Airplanes". J. of Aircraft, Vol. 20, No. 2, Feb. 1983.

4. Dunham, R.E., Bezos, G.M., Gentry, G.L. and Melson, E., "Two-Dimensional Wind Tunnel Tests of A Transport-Type Airfoil in a Water Spray". AIAA-85-0258, presented at the 23rd Aerospace Science Meeting, Reno, Nevada, 1985.

5. Bezos, G.M., Dunham, R.E., Gentry, G.L. and Melson, W.E., "Wind Tunnel Test Results of Heavy Rain Effects in Airfoil Performance". AIAA-87-0260, presented at the 25th Aerospace Science Meeting, Reno, Nevada, 1987.

6. Craig, A.P. and Hansman, R.J., "An Experimental Low Reynolds Number Comparison of a Wortman FX67-K170 Airfoil, a NACA 0012 airfoil, and a NACA 64-210 Airfoil in Simulated Heavy Rain". NASA-CR-181119, June 1987.

7. Marchman, J.F. Robertson, E.A. and Emsley, H.T., "Rain Effects at Low Reynolds Number". J. of Aircraft, Vol. 24, No. 9, Sept. 1987.

8. Strapp, J.W. (Private communication), Research Meteorologist, Cloud Physics Research Division, Environment Canada.

ACKNOWLEDGEMENTS

The generosity of Cloud Physics Research Division, Environment Canada in lending the optical array probe for this wind tunnel experiment is very much appreciated. Special thanks are due to J.W. Strapp of the Cloud Physics Research Division for interpreting the spray data.

I am indebted to my colleagues in the High Speed Aerodynamics Laboratory for their efforts in setting up and carrying out this highly unusual measurements.

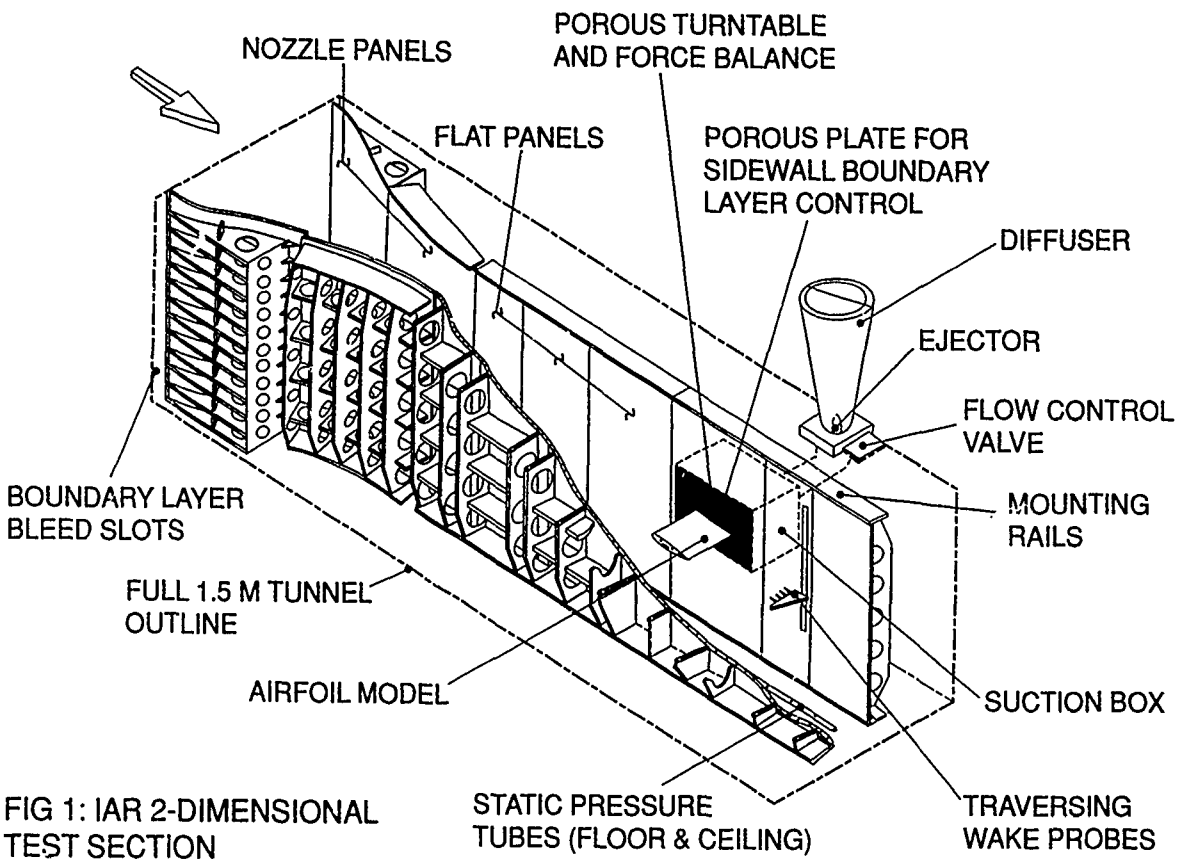

FIG 1: IAR 2-DIMENSIONAL TEST SECTION

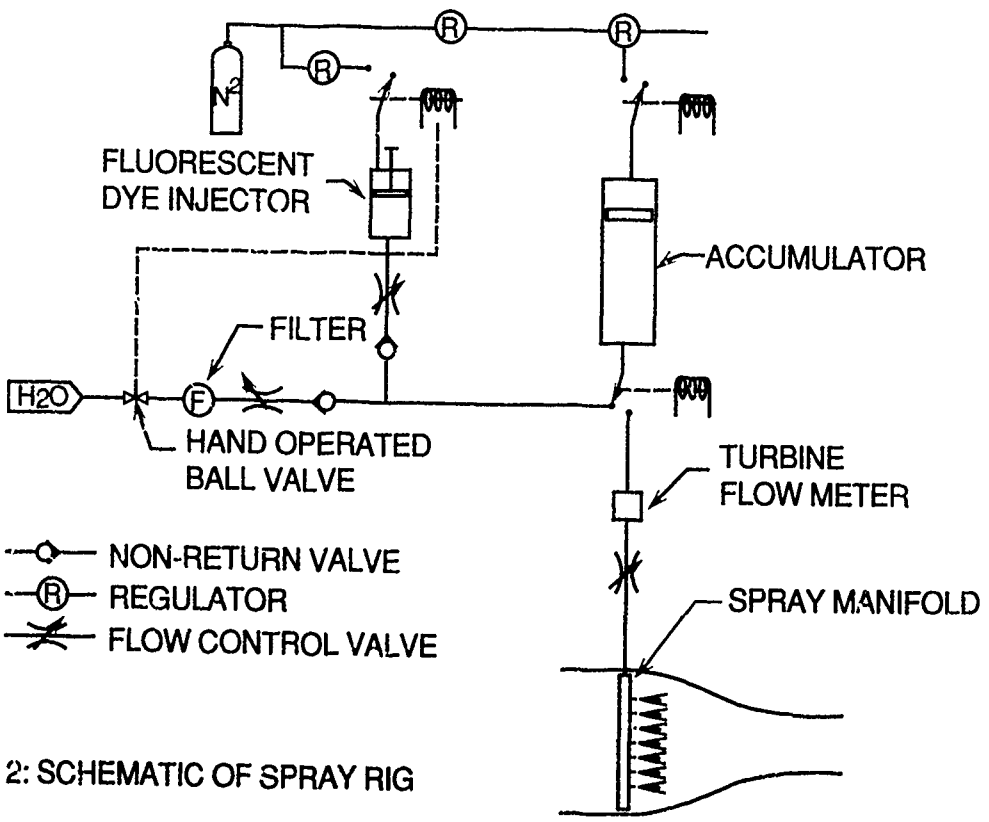

FIG. 2: SCHEMATIC OF SPRAY RIG

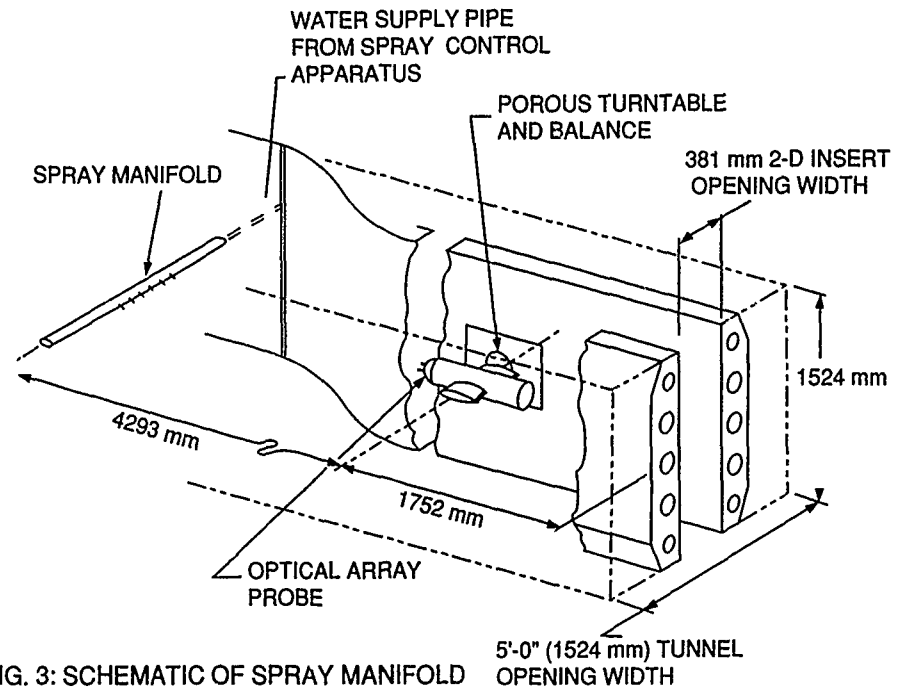

FIG. 3: SCHEMATIC OF SPRAY MANIFOLD AND OAP IN 2-D TEST SECTION

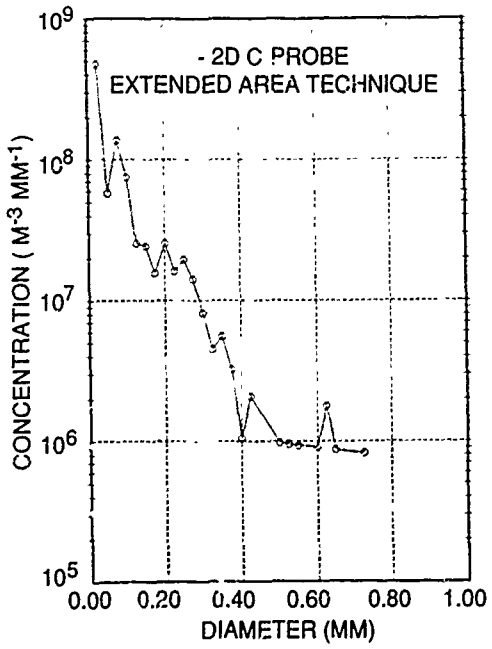

FIG. 4: SAMPLE OUTPUT OF OPTICAL ARRAY PROBE

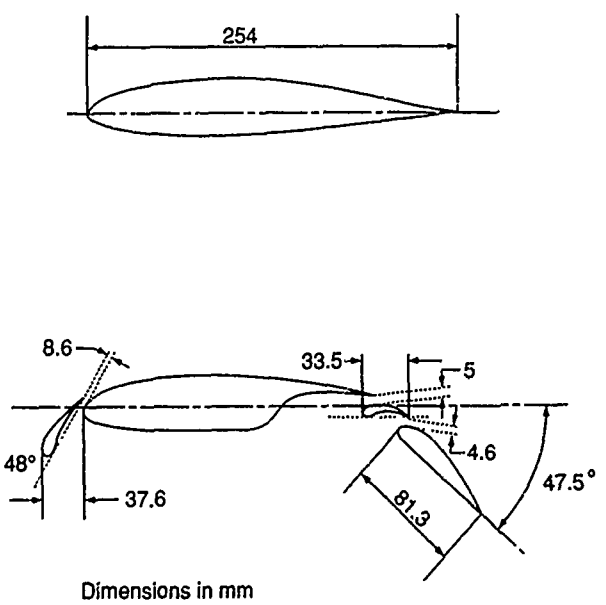

F.G. 5 BASIC AEROFOIL AND FLAP GEOMETRY

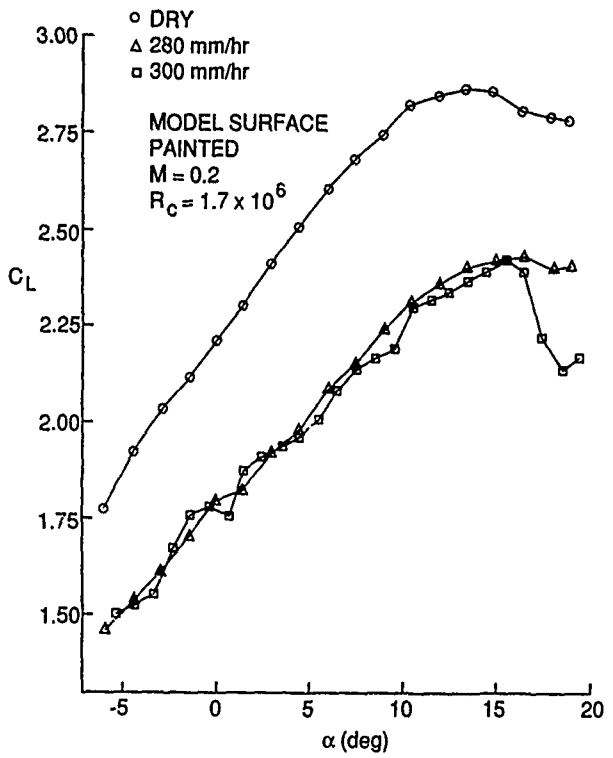

FIG. 6: LIFT COEFFICIENT VERSUS ANGLE OF ATTACK

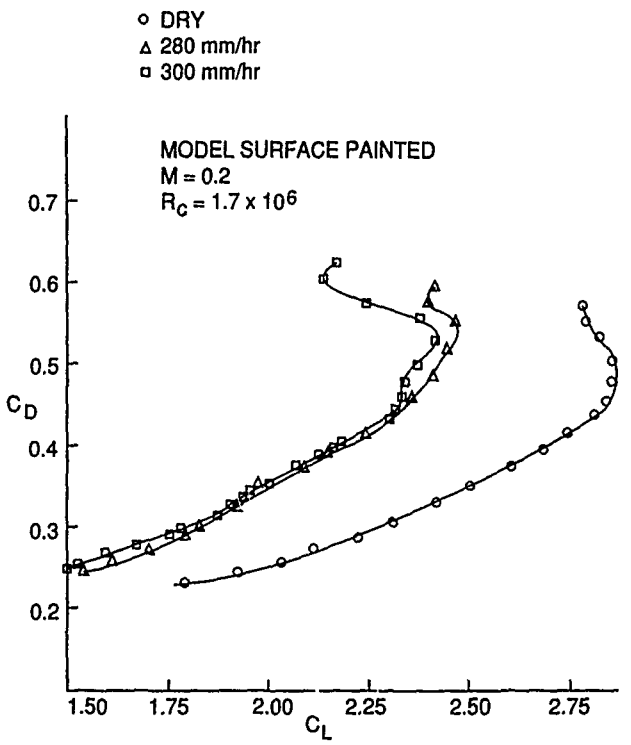

FIG 7: DRAG COEFFICIENT VERSUS LIFT COEFFICIENT

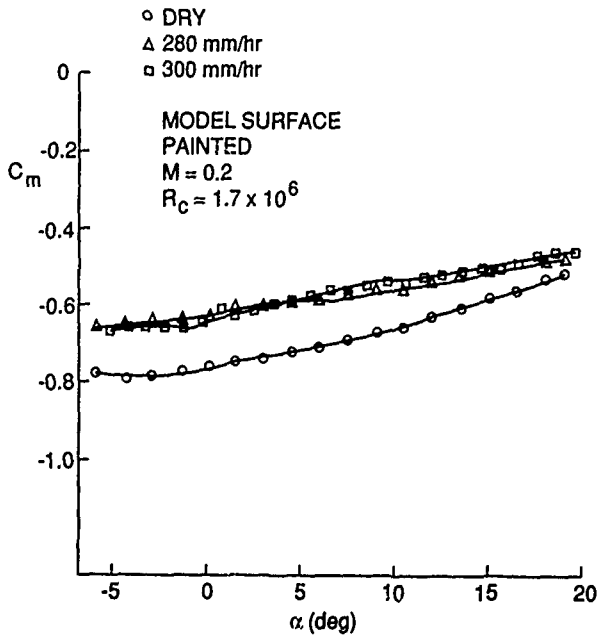

FIG. 8: PITCHING MOMENT COEFFICIENT VERSUS ANGLE OF ATTACK

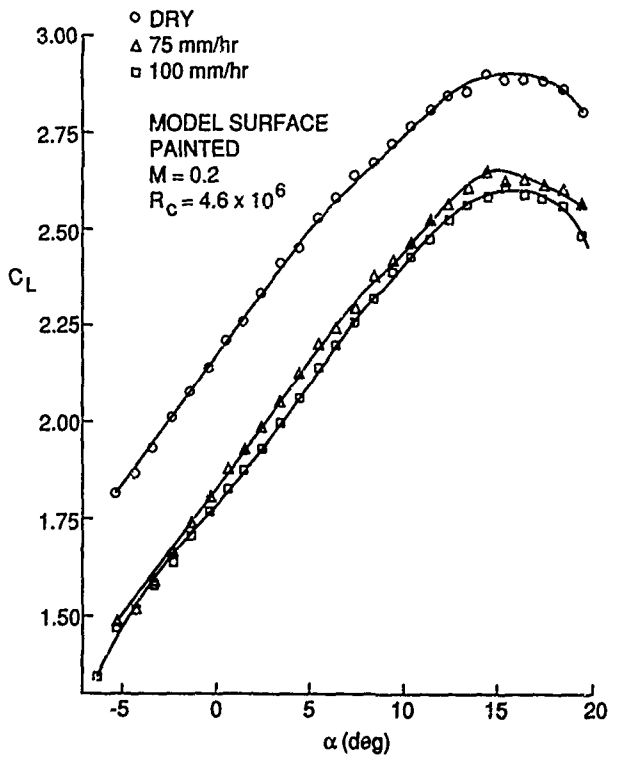

FIG. 9: LIFT COEFFICIENT VERSUS ANGLE OF ATTACK

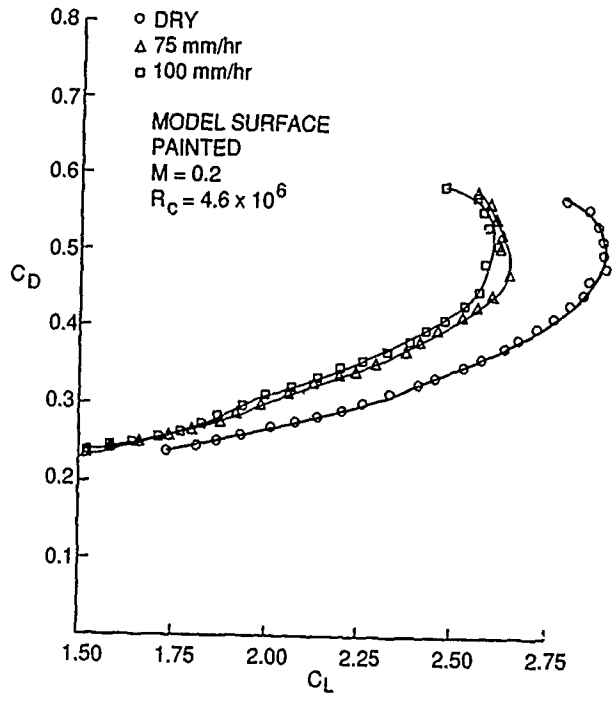

FIG. 10: DRAG COEFFICIENT VERSUS LIFT COEFFICIENT

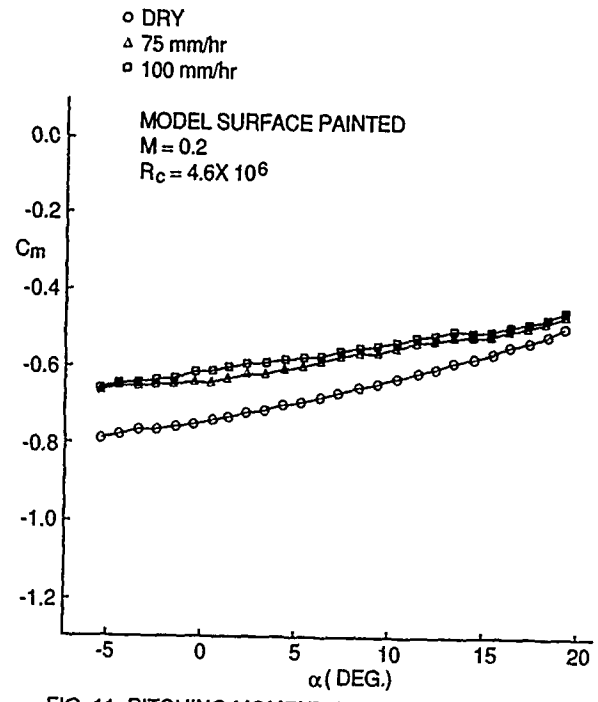

FIG. 11: PITCHING MOMENT COEFFICIENT VERSUS ANGLE OF ATTACK

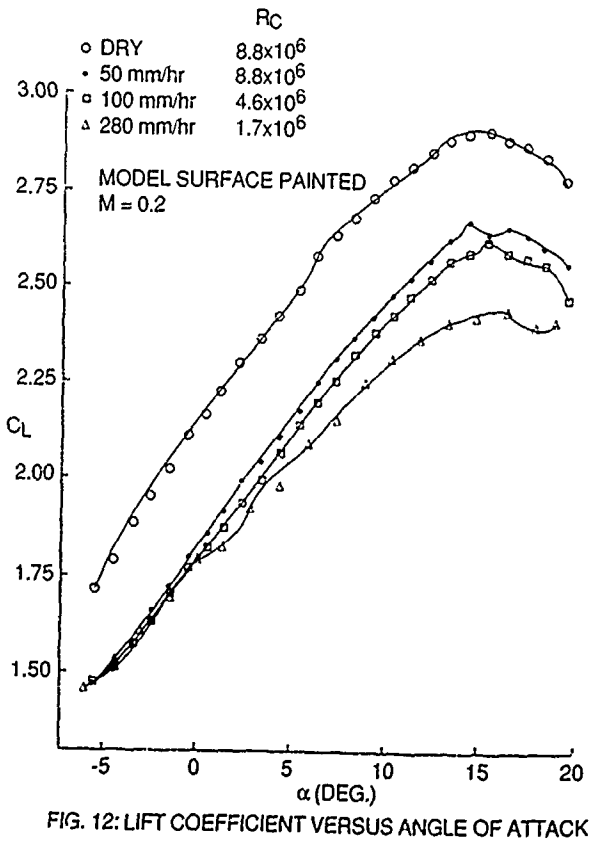

FIG. 12: LIFT COEFFICIENT VERSUS ANGLE OF ATTACK

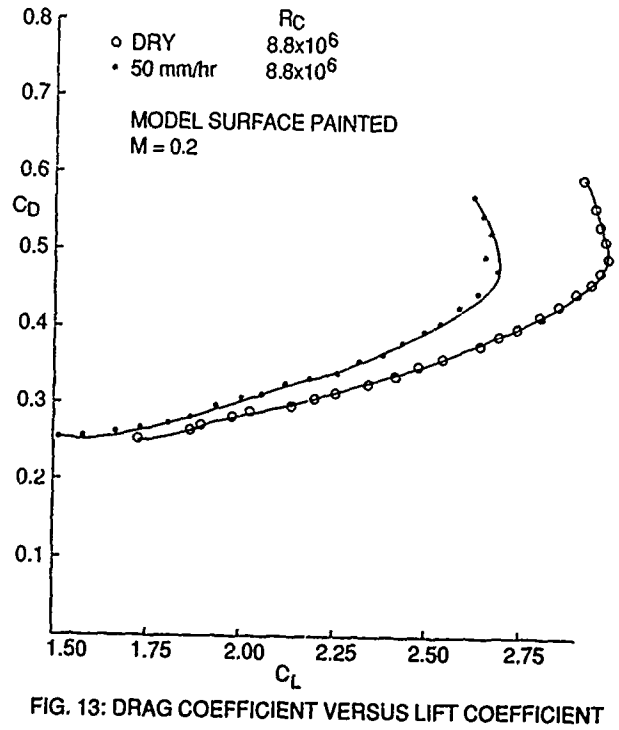

FIG. 13: DRAG COEFFICIENT VERSUS LIFT COEFFICIENT

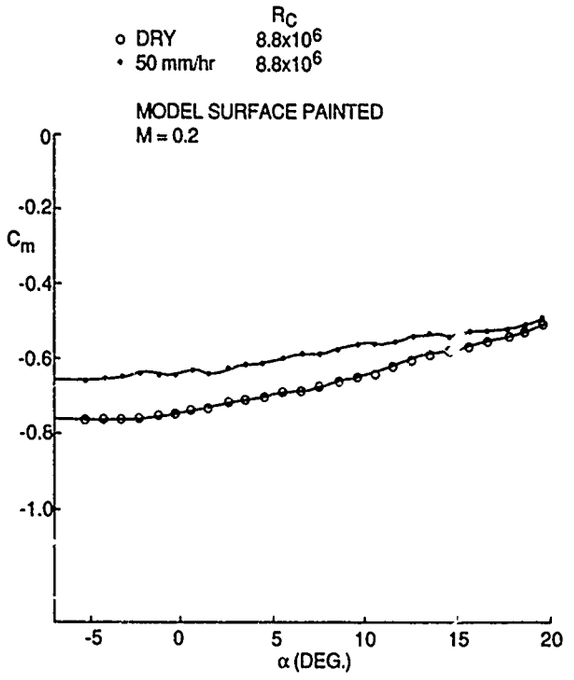

FIG. 14: PITCHING MOMENT COEFFICIENT VERSUS ANGLE OF ATTACK

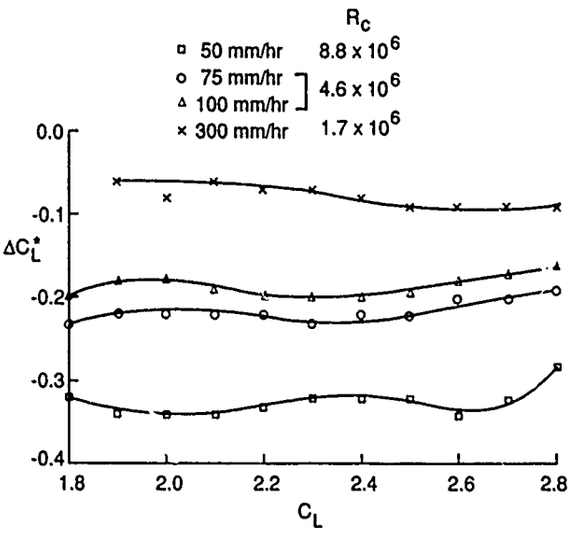

FIG. 15: VARIATIONS OF "NORMALIZED" LIFT COEFFICIENT INCREMENT VERSUS LIFT COEFFICIENT

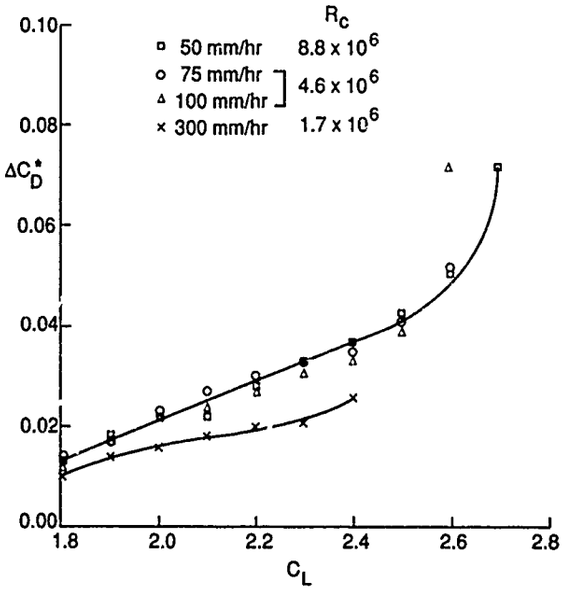

FIG. 16: VARIATIONS OF "NORMALIZED" DRAG COEFFICIENT INCREMENT VERSUS LIFT COEFFICIENT

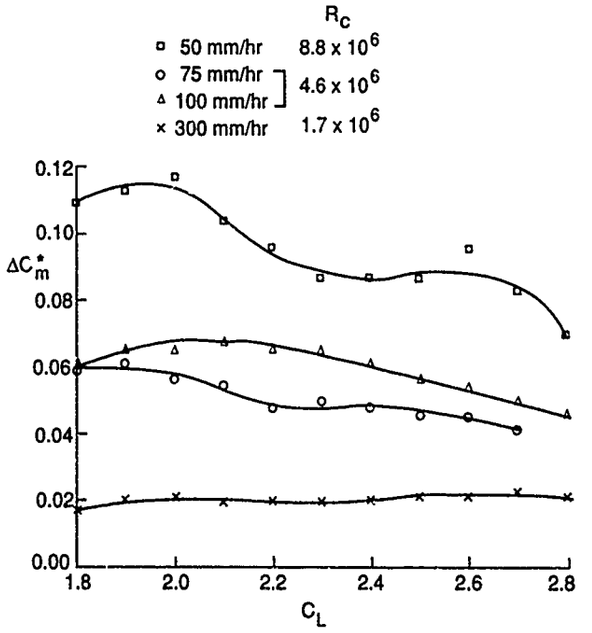

FIG. 17: VARIATIONS OF "NORMALIZED" PITCHING MOMENT COEFFICIENT INCREMENT VERSUS LIFT COEFFICIENT

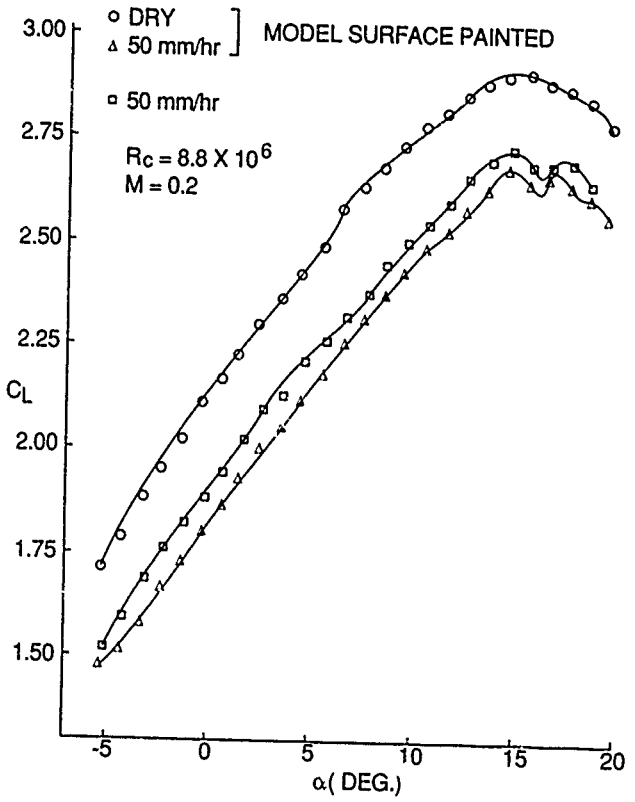

FIG 18: LIFT COEFFICIENT VERSUS ANGLE OF ATTACK (SURFACE EFFECT)

AERODYNAMIC EFFECTS OF DE/ANTI-ICING FLUIDS AND DESCRIPTION OF A FACILITY AND TEST TECHNIQUE FOR THEIR ASSESSEMENT

by
Mario CARBONARO
Professor

von Karman Institute for Fluid Dynamics
Aeronautics/Aerospace Department
72, ch. de Waterloo
1640 Rhode-Saint-Genese
Belgium

SUMMARY

Research carried out at the VKI in the period from 1984 to present on the subject of flow-off properties and aerodynamic effects at take-off of aircraft de-icing and anti-icing fluids, as well as of a test methodology for their acceptance, is described.

A small, liquid nitrogen cooled wind tunnel was developed, to study the flow of de/anti-icing fluids deposited on a flat plate and subjected to an accelerating airflow, simulating operational ground run conditions. Results indicated that substantial amounts of fluid were remaining on the plate at the time of the rotation manoeuvre, and allowed to compare the flow-off behaviour of various fluids.

Measurements of the effect of de/anti-icing fluid residuals on the aerodynamic characteristics of a two-dimensional airfoil, at conditions close to those of the full-scale take-off of a large transport aircraft were then made. This involved testing a 1.5 meter chord airfoil model, instrumented with a strain gage balance, in the VKI L1-A 3 m wind tunnel and in the BFA 2.4 m icing tunnel, the airfoil upper surface being either clean or covered by various fluids, or by solid roughness simulating frost, for comparison with Boeing flight data. Results indicated a reduction in lift coefficient and an increase in drag coefficient, due to fluid residues. Such effects were very much dependent on the specific fluid used, and could not be correlated to fluid viscosity alone.

The study was continued, to correlate the lift coefficient loss measured in large icing wind tunnels with some quantity, simply measurable in a small facility, and to define such facility, together with a methodology for determining the aerodynamic acceptability of de/anti-icing fluids for grounded aircraft.

The method proposed by the VKI involves the determination of the air and fluid boundary layer displacement thickness, for an accelerating airflow over a flat plate covered by a layer of the fluid under test. Such test is conducted in a small wind tunnel, cooled by injection of liquid nitrogen. The boundary layer displacement thickness is measured as a function of time, from the increase in test section blockage caused by its growth.

Checks of accuracy and repeatability of this procedure were conducted, by testing almost all fluids available in 1990. Results were compared with the measurements of fluid-induced degradation of the aerodynamic properties, carried out by the VKI at BFA icing tunnel, as well as by the Boeing Company at NASA Lewis Icing Research Tunnel. These comparisons indicated that good correlation was obtained, thus validating the proposed method.

1- INTRODUCTION

Research on the subject of the aerodynamic effects at take-off of deicing or anti-icing fluids was started in 1982 with a pioneering study carried out by the Boeing Company (Ref. 1). Wind tunnel measurements of lift were performed on a one-foot chord airfoil model, covered or not with a layer of anti-icing fluid. This latter was modified by addition of thickening additives, to simulate at ambient conditions the viscosity of the real fluid at low temperature. This study indicated that residuals of anti-icing fluids on aircraft wings at take-off could have very detrimental effects, as the measured loss of lift due to the presence of fluid could be as high as about 10%, for a specific anti-icing fluid.

In general anti-icing fluids are non-Newtonian, while the de-icing fluids are Newtonian. The first ones are designed to form on the surface of the wing a protective fluid layer, that should not flow off the wing under the effect of gravity when the plane is grounded, and that should prevents further re-icing of the wing for a certain "holdover" time. This fluid however, when subjected to the relative airflow of the take-off ground run, experiences a large shear stress, and because of its shear-

thinning properties, should flow-off the wing, leaving it clean at the moment of the rotation manoeuvre.

The use of non-Newtonian anti-icing fluids was widespread in Europe when Ref.1 appeared, and according to the Association of European Airlines, was offering significant operational advantages over the Newtonian products. Indeed the aircraft could be de-iced and then anti-iced well before the take-off, and so could safely wait a significant time before the actual take-off, without the danger of ice re-forming on the wings. The results of Ref.1 triggered a reaction of several European Airlines, and in early 1983 the von Karman Institute was approached by Sabena, with a request to further study the problem. The VKI was asked to verify whether or not the fluid had had the time to fully flow off the wing during the take-off ground run, before the aircraft rotation manoeuvre, and to determine what was the effect on wing lift at take-off of a possible fluid residue on the upper wing surface. This request resulted in a three-year VKI research program, carried out from 1984 to 1987, under funding of the Association of European Airlines. The main idea was to remove two scaling limitations of the earlier study, namely by using chord lenghts of the same order as the real ones, and by using the real fluids at the real subfreezing temperatures. The research program was divided in three phases. The first one was directed to the study of the flow of a fluid, deposited on a flat surface, and subjected to an accelerating airflow at operational take-off conditions, with the purpose of checking whether a fluid residue was left or not on the surface at the time corresponding to the end of the take-off ground run. The following phases were adressing the question of the effect of fluid residues on the aerodynamic performance of an airfoil.

2- FLOW OF DE/ANTI-ICING FLUID ON A FLAT PLATE

This first phase of the research (Ref. 2) required the design and construction at VKI of a special facility, the Cold Wind Tunnel CWT-1 (Fig. 1). It is a closed circuit wind tunnel, thermally insulated, and cooled by liquid nitrogen to attain temperatures as low as -30°C and below. Test section was rectangular, 0.3 m wide, 0.1 m high and 2.2 m long, and provision was made to deposit a thin layer of fluid, precooled to the test temperature, on the bottom test section wall. The tunnel could be manually accelerated from zero to maximum speed, about 65 m/s, in about 30 seconds. These values correspond to the full scale conditions of a commercial transport aircraft take-off. Soon after starting the airflow, surface waves form on the fluid surface, and fluid starts moving downstream. The instantaneous profile of thickness of the fluid layer was measured, by using an optical technique. As shown in Fig. 2, a video camera, located above the test section, was used to record pictures of the wavy and moving fluid layer, illuminated by a uniform light source, located below the test section. The fluid was dyed and therefore absorbs light, so that the picture appears darker where the layer is thicker. The instantaneous image of the fluid layer was digitized and processed on a computer. Using a suitable calibration, this allowed to obtain instantaneous profiles of fluid layer thickness. A typical example is given in Fig. 3, which shows the initial layer, with a thickness of about 3 millimiters, and 15 seconds after test start, the formation of surface waves and the overal decrease in thickness. This trend continues, at 30 seconds there is a lower thickness, and lower wave amplitude. However 30 seconds is the time at which the aircraft rotation manoeuvre should take place, and at this time there is still a significant amount of fluid left on the surface, about 1 millimiter in this specific case, which is a rather extreme one. Even after 60 seconds, there is a residual fluid layer, of about half millimiter, that according to what was observed during the tests, does not seem to evolve any more.

About 100 sets of thickness profiles like the one shown were measured, by comparing five different fluids, a Newtonian one (Kilfrost Mil-Spec fluid, mixture of ethylene and propylene glycols), and four non Newtonian anti-icing fluids, none of which is in production any more (Kilfrost ABC, SPCA AD84, Hoechst 1704/83, Union Carbide ADF 2.2), at four test temperatures (0°C, -10°C, -20°C, and ambient), for three locations on the plate, and for three initial thicknesses of the fluid layer (1, 2 and 3 mm). Fig.4 summarises the results of several tests, conducted on a specific anti-icing fluid, at various temperatures, with layers of different initial thickness. It shows that the final thickness at 30 seconds is independent of the initial layer thickness. Already at about 15 seconds the various curves merge together. This result is typical of other fluids too, and is quite important, as it demonstrates that one of the test parameters, the initial thickness, does not influence the final result.

Analysis of the results pointed out differences in flow-off of the five existing fluids: but in all cases indicated that after 30 seconds of simulated ground run fluid was still left on the surface. This led to the decision of investigating what was the effect of such residual fluid on the wing aerodynamics, and at the same time of removing the limitation of the research, namely the different pressure gradient, and shear stress distribution, as existing on a flat plate or on a real wing.

Therefore it was decided to run wind tunnel tests on a clean or contaminated, two-dimensional airfoil, and this led to the second phase of the VKI/AEA research.

3- EFFECTS OF DE/ANTI-ICING FLUIDS ON A LARGE AIRFOIL MODEL AT EXTREME CONDITIONS

Following a suggestion of Boeing, who did collaborate to the definition of this test program, the same airfoil shape as previously studied in Ref. 1 was again used for the present research (Ref. 4). It is shown in figure 5. The test airfoil had the same contour as the section (normal to leading edge) of the B737-200 wing, at 66% spanwise position, in the "flaps 5" configuration, but for simplicity, it had no slot at the flap, as also done in Ref. 1.

A goal of the research was to remove the possible limitation associated with the fact that the scaling parameters for the airflow around the model and for the

wavy fluid film are different : indeed surface roughness of an airfoil scales down with chord, while the moving surface waves on the fluid film do not depend on chord, but on fluid properties, like surface tension, viscosity or elasticity of the non-Newtonian fluid, which are temperature-dependent and do not scale down with chord.

Therefore it was decided to choose a model chord as close to full scale as reasonably possible, and this resulted (Fig. 6) in a 1.5 meter chord model, fitted with an internal strain gage balance, designed and manufactured at VKI, to measure lift, drag, and pitching moment. The model was enclosed in a wind tunnel test section insert, shown in Figure 7. The wing model, built by British Airways, was made of three parts. The central one, 0.3 meter wide, was connected to the internal balance.

Tests were conducted both in the VKI 3 meter diameter, low speed (72 m/s peak) wind tunnel L1-A, to check the setup and the instrumentation at ambient conditions, and in another wind tunnel, located in Vienna, at the Bundesversuch-und-Forschung Arsenal. This tunnel, mainly devoted to tests of railroad trains, has a test section of 2.4 X 2.2 meters, a maximum speed in excess of 150 knots, and can be cooled down to -50°C.

Tests were conducted with the airfoil either clean or covered with various fluids. Several clean airfoil tests, repeated frequently all along the test program, served the purpose of providing a reference baseline to determine fluid-induced effects, as well as of allowing a repeatability check. The same fluids as previously tested for flow-off in the VKI CWT-1 during the previous research phase were again used.

Test procedure was as follows: at temperatures of -20°C, -10°C, and 0°C, a sufficient amount of unsheared, dyed fluid was poured on the airfoil model to completetely cover its centre portion, and the excess fluid was left drip off. Then the tunnel was started and accelerated up to about 107 knots, with an almost linear velocity-time variation, as encountered during a take-off ground run. After about 30 seconds the airfoil was pitched up, to simulate a rotation manoeuvre. Recording of the balance measurements was made at a 5 Hertz sampling frequency, fluid motion was continously recorded on videotape, and photographs of the upper surface were taken every 3 seconds. .

A sample sequence of such photographs is reproduced as Fig. 8, showing the formation of surface waves soon after the starting of the flow (a). A typical triangular shape is apparent, as the initial surface perturbation widens laterally as it is convected downstream. Some time after, the various perturbations have merged together (b), and form a wave front propagating downstream, almost reaching the trailing edge (c), when the rotation of the airfoil starts. At the end of the rotation fluid was observed to be still present in the trailing edge region. The forward part of the airfoil seemed to be clean, but indeed it was not, as a thin layer of fluid was still present, as revealed by close visual inspection and by quantitative measurements with a mechanical depth gage after the test.

Figure 9 shows how different the formation of the surface waves can be for a Newtonian and a non-Newtonian fluid. In the first case small surface riddles, due to capillarity forces, are formed, while in the second case much larger waves appear.

Figure 10 shows another unexpected phenomenon, of a second wave front, appearing after the rotation manoeuvre. Its existence has been for a time controversial : in these tests, conducted in May 1986, it appeared when the airfoil pitch-up was important, and not for a moderate pitch-up. Its formation was thought to be due to the increase of shear stress over the forward part of the airfoil upper surface, which is associated with the change of incidence, and which sweeps downstream some of the fluid remaining on the forward part of the airfoil.

As a result of this second phase of the VKI/AEA research, the aerodynamic characteristics of the fluid-contaminated airfoil were measured at extreme conditions, ie at relatively low velocity (about 107 knots) and at high incidences (from 10 to 14 degrees), close to stall. Indeed this was the most unfavourable case, to be investigated first, and it indicated the existence of a lift loss, that could be quite high : a maximum value of 17% for the lift loss coefficient was reached, and intermittent stall observed, when testing a specific anti-icing fluid, not in production any more.

Amongst the non-Newtonian fluids tested, those with lower viscosity seemed to yield lower lift losses, and a tentative correlation showing this dependence was established. However, also the Newtonian Mil Spec fluid yielded non negligible lift losses at the lowest test temperature of -20°C. These results triggered the third phase of the research, directed to repeat the experiments at lower incidences and higher velocities, as encountered during a real take-off manoeuvre.

These results also encouraged fluid manufacturers, at the request of the Association of European Airlines, to stop production of the existing fluids and to develop new products with reduced viscosity, to improve their flow-off behaviour and thence their aerodynamic characteristics, and to make them available during the next coming winter 1986/87.

4- EFFECTS OF FLUIDS ON A LARGE AIRFOIL MODEL AT CONDITIONS CLOSE TO OPERATIONAL

The same airfoil model, with some improvements of the set-up to allow higher test velocities and a variable pitch-up angle, was again used for this third phase of the VKI/AEA research. Tests were again conducted at BFA, in May 1987, following the same procedure as in previous year, but with test conditions simulating those of a normal B737-200 take-off, as well as those of a one-engine-only take-off. Thus a wind tunnel speed of 145

knots and a pitch-up angle of 4 degrees were used for the first case, and of 130 knots and 7 degrees for the second.

Amongst the fluids tested, there were the three new products designed following the results of the second VKI/AEA research phase, i.e. Kilfrost ABC-2, Hoechst 1704 LTV-87, and SPCA AD-99/6, as well as one of the fluids tested the previous year, and four experimental products made available by Union Carbide Canada, amongst which there was the UC 250/3 fluid.

During this third phase of the research, also the effect of solid roughness on the wing upper surface was examined. According to procedures defined by Boeing (Ref. 6) this roughness, which simulates the presence of frost, was obtained by glueing on the wing surface an adhesive anti-slip safety walk sheet, commercially available from 3M. Two different roughnesses were tested: 3M stock No.61-2091-5102-8, and No.61-2080-3073-6, respectively denominated Frost 1 and 2, with a roughness of approximately 0.36 mm and 0.48 mm. A more rough coverage (Frost 3) was obtained, as done in Ref. 6, by applying an epoxy putty material to the Frost 1 safety walk, and then roughening it with a paint roller.

Results of tests on solid roughness contamination are shown in Figure 11, where the lift coefficient versus alpha curve shows a progressive decrease with increasing roughness, as could be expected. A decrease in stalling angle and in maximum lift coefficient is also present. This test demonstrated the validity of the measurements, because the measured decreases of lift agreed with results of flight tests carried out by Boeing on a B737 (Ref. 7) using artificially roughened wings to simulate two frost cases, denominated Frost A (similar to Frost 1 and 2) and Frost B (similar to Frost 3).

Tests were then run with and without fluid, and similar results were obtained (Fig 12). Using the "dry" tests as a reference baseline, losses of lift coefficient were again found to be present, for the various fluids, at three temperatures (Fig. 13). However these lift coefficient losses are lower than those found during the previous research phase. This is due to the improvements in fluids achieved by their manufacturers, and to the less critical test conditions (lower wing incidence, and higher test speed), closer to those of a real take-off.

However, these wind tunnel tests indicated that the reduction of lift loss was not as important as could be expected by the reduction of viscosity of the new fluids tested, on the basis of the tentative correlation previously established (Ref 3). Indeed it was noticed that lift loss was not correlated with viscosity alone, as a fluid of high viscosity could yield lower losses than another fluid with lower viscosity. This is important, because it means that a quality control of the de/anti-icing fluid cannot be made by a viscosity check, but that an aerodynamic test is required, at least untill the mechanism of fluid flow-off and lift loss is fully understood and modelled. It is also important to stress that this aerodynamic test, if it is to be made on a routine basis for quality control or for the development of new fluids, cannot consist in force measurements on airfoils in large wind tunnels as used, because of the associated high costs and delays, and an alternative test methodology was needed.

At this stage the research on airfoils was taken over by Boeing, who conducted wind tunnel tests in NASA Lewis Icing Research Tunnel, and flight tests on a B737 in Kuopio (Finland) to extend these results to the real 3D case and to validate wind tunnel studies (Ref.8). A comparison of the wind tunnel results on the 2D airfoil, as obtained by VKI/AEA and by Boeing/NASA-IRT, is shown in Fig. 14. Considering that these tests were conducted in different tunnels, on models of different scale, with different instrumentation and experimenters, the agreement is very reasonable. A further study was also conducted by Boeing in the NASA Lewis icing tunnel in February 1990 (Ref. 9) to investigate most of the presently existing fluids.

5- ANALYSIS OF THE LIFT LOSS MECHANISM

After the conclusion of the three phases of the VKI/AEA research just described, another problem was adressed by VKI in 1987/88, i.e. the definition of a simplified test for aerodynamic acceptance of de/anti-icing fluids. This independent, self-supported VKI work resulted towards the end of 1988 in the proposal of an original test methodology (Ref. 10), that was presented to AIA and AECMA member companies, and further investigated in 1989 by VKI under the sponsorship of Airbus, British Aerospace and Fokker.

The fundamental question refers to the nature of the mechanism of lift loss of a fluid-contaminated airfoil. It can be recognised that the wavy fluid layer produces an increase of the aerodynamic roughness of the wing surface, thus thickening the airflow boundary layer. This in turn modifies the effective shape of the airfoil, as felt by the external inviscid flow, by an amount which is the boundary layer displacement thickness. Therefore this last quantity must be related to the variation of the aerodynamic characteristics of the airfoil.

To investigate this concept, a numerical model was developed (Ref. 11), using an inviscid panel method for the external airflow, based on Hess and Smith approach, coupled with a simple integral boundary layer calculation based on Head's entrainment approach, proposed long ago by Dvorak (Ref. 12) for turbulent flow over a rough surface. In this approach the usual Ludwig-Tillmann formula for skin friction, valid for smooth walls, was replaced with another one, proposed by Betterman (Ref. 13) for walls with a periodic roughness, characterised by two parameters, a roughness height and wave lenght. This model was selected because of its analogy with the periodic waves on the fluid surface. Its applicability was verified by Pitot boundary layer surveys over a periodically rough flat plate (Ref. 14). Calculations were run for the test airfoil, and indicated, as was expected, that the lift coefficient loss was an increasing function of the displacement thickness over the rough airfoil surface, irrespective of the roughness wave lenght.

6- DEFINITION OF AN AERODYNAMIC ACCEPTANCE TEST

As explained, one could characterize the aerodynamic effects of a fluid layer deposited on an airfoil, by the displacement thickness of the airflow boundary layer above it. Furthermore, a basic simplifying assumption was made, i.e. to refer such aerodynamic effects to a measurement of boundary layer thickness over a flat plate, not over an airfoil. The two situations are of course different, but might be related one to another, and a study, supported by Airbus, British Aerospace and Fokker was carried out at VKI to investigate the correlation between the boundary layer thickness over a flat plate covered with fluid and the lift loss experienced by a contaminated airtoil, as determined by the wind tunnel tests of References 4 and 8.

For this study the VKI cold wind tunnel CWT-1 was again used. It was however modified (Ref. 11) to improve flow quality and test procedures, by adding a computer-controlled drive to ensure a repeatable velocity-time sequence, and by performing the injection of liquid nitrogen in a similar way as done in cryogenic tunnels. Figure 1 illustrates the present, modified state of the CWT-1.

Figure 15 shows the boundary layer profile measured in the CWT-1 test section, at ambient conditions, on the bottom and top walls, when the bottom wall is smooth or covered with two different roughnesses. The effect of roughness in increasing the bottom wall boundary layer is evident, as could be expected.

However, it would have been quite difficult to measure the time-dependent airflow boundary layer with a Pitot survey during an actual test with moving fluid, so an alternative method was devised, based on a wind tunnel blockage concept: the increase in boundary layer displacement thickness causes an acceleration of the inviscid flow outside of the boundary layer, and this in turn causes a variation of the static pressure difference along the test section.

The test setup is illustrated in Fig. 16. Wall pressures are measured in the settling chamber, at inlet and outlet of test section. From Bernoulli theorem the velocities at inlet and outlet are obtained, and their ratio gives the ratio of effective cross sectional areas, which equals the geometrical area minus the area blocked by the boundary layer, which is in turn the test section perimeter multiplied by the boundary layer displacement thickness. In the case when a fluid is deposited on the bottom wall, and no fluid is present on the side and top walls, an average of the displacement thickness over the perimeter is obtained. The net displacement thickness over the wet bottom wall is then obtained from the expression of its perimeter-averaged value, by subtraction of the value for a dry wall.

This allows the determination of the displacement thickness over a fluid covered flat plate, as function of two measurements of pressure difference. These measurements are carried out continously during all the test run, and result in a graph like shown on Fig. 17, which gives the tunnel velocity variation with time, first increasing steadily then flattening to a constant level, and the instantaneous value of the measured displacement thickness. This latter is first increasing and then decreasing, as at the beginning of the test, big surface waves form, and then fluid is entrained downstream by the airflow. Over a dry plate, as shown for comparison on the same figure, a much lower displacement thickness, independent of time, is measured. Figure 19 refers to another fluid, and demonstrates that, as already found during the VKI/AEA first research phase, the effect of different initial fluid thicknesses tends to disappear very quickly, before reaching the time of 30 seconds after test start, which corresponds to thebeginning of the take-off rotation manoeuvre. These graphs are then used to extract the value of displacement thickness at 30 seconds after test start, and this value is plotted versus the test temperature in Fig. 19, that fully characterises the flow off behaviour of a given fluid. Curves for two fluids are shown in Fig. 19: an early fluid, not in production any more, with poor flow-off and yielding rather large lift losses; and another non-Newtonian fluid, with quite good flow-off and low lift loss, despite of its non-small viscosity.

The effect of dilution of an anti-icing fluid with water, was also studied, by testing two fluids at full strength, as well as diluted with 25% and 50% of demineralized water. Results, given in Fig. 20, indicate that depending on the specific fluid nature, dilution can lead either to a better or a worse flow-off.

Finally, what remained to be done was to correlate these measured boundary layer displacement thicknesses over a flat plate to the lift loss of an airfoil. Such a correlation for the fluids tested by VKI at BFA in 1886, at the three temperatures of 0°C, -10°C and -20°C, is shown in Fig. 21. Fluid 1A is an ethylene/propylene glycol Newtonian fluid as described by Military Specification 8243-D. Fluid 2A and fluid 4, both non-Newtonian, are respectively the early anti-icing fluid with poor flow-off, and the high-viscosity product with good flow-off, already referred to in Fig. 19. Correlation looks reasonable, and was also made for the other improved products, tested by Boeing in the NASA Lewis icing tunnel. Such results are here shown in Fig. 22, and correlation is again evident, despite some scatter for a few products, which were not in industrial production and therefore were prepared in different batches, at different times for the Boeing/NASA and the VKI CWT-1 tests.

On the basis of these results, and as a result of extended discussions with US and European aircraft manufacturers, carried out in the context of the Aerospace Industries of America (AIA) Transport Committe (TC) Project 218-4, a procedure was agreed (Ref. 14), of comparing the displacement thickness versus temperature curve of a candidate fluid with that of a smooth wall and that of a reference de-icing Newtonian fluid, having a well defined composition, as for instance prescribed by Military Specication 8243-D . Appropriate factoring of the curve for the Mil Spec fluid allows to

define a limit curve, below which the curve of a candidate fluid should fall, in order for it to pass the aerodynamic acceptance test.

7- CONCLUSIONS

The research carried out at the VKI in the period 1984 to present was summarized. A facility, cooled by liquid nitrogen was developed, to study the flow of de/anti-icing fluids on a flat plate, at conditions close to those of take-off of a transport aircraft. Measurements of aerodynamic degradation of a 2D wing profile were also carried out, in presence of solid and fluid surface contamination. A correlation was established relating such degradation to the boundary layer displacement thickness over a fluid contaminated flat plate, and a simple wind tunnel blockage method was devised to measure such displacement thickness. This resulted in a procedure allowing the asessment of the aerodynamic quality of a de-icing or anti-icing fluid.

REFERENCES

1-NARK T.: Wind tunnel investigation of the aerodynamic effects of type II anti-icing fluids when applied to airfoils. Boeing Commercial Aircraft Co.,Document D6-37730, December 1983.

2-CARBONARO M.,LOCATELLI C.,MANTEGAZZA C.,MCSPADDEN C.,MOLLER I.: Experimental study of the flow of a film of aircraft de-icing fluid during a simulated take-off at subfreezing temperature. VKI Contract Report 1985-02, May 1985.

3-CARBONARO M.: Experimental study of the aerodynamic characteristics of a two-dimensional wing model covered with de/anti-icing fluid during a simulated take-off at subfreezing temperature. VKI Contract Report 1986-22, August 1986.

4-CARBONARO M.: Further study of the aerodynamic performance of a two-dimensional wing model covered with simulated frost or with de/anti-icing fluid during a wind tunnel-simulated take-off at subfreezing temperature. VKI Contract Report 1987-29, July 1987.

5-HENDRICKSON G.S., HILL E.G.: Effects of aircraft de/anti-icing fluids on airfoil characteristics. Paper presented at the VKI Lecture Series on "Influence of environmental factors on aircraft wing performance", VKI LS 1987-03, February 1987

6-ZIERTEN T.A., HILL E.G.: Effects of wing simulated frost on airplane performance. Paper presented at the VKI Lecture Series on "Influence of environmental factors on aircraft wing performance", VKI LS 1987-03, February 1987

7-MULALLY A.R., SHIRKEY M.D., HIGGINS C.R.: Winter operations: keep it clean. Boeing Airliner, October-December 1983.

8-RUNYAN L.J., ZIERTEN T.A., HILL E.G.: Flight and wind tunnel invetsigation of aerodynamic effects of aircraft ground deicing/anti-icing fluids. AGARD Conference proceedings 470, Flight in adverse environmental conditions, Gol, Norway, May 1989.

9-ZIERTEN T.A., HILL E.G.: Wind tunnel investigation of the aerodynamic effects of aircraft ground deicing/anti-icing fluids and criteria for aerodynamic acceptance. AGARD FDP Specialist Meeting "Effects of adverse weather on aerodynamics", Toulouse, France, April 1991.

10-MACRI L., CARBONARO M.: Tentative correlation between lift loss on a fluid-contaminated wing and boundary layer modification. VKI Stagiaire Report 1988-33, September 1988.

11-MOYAUX B., CARBONARO M.: Aerodynamic effects of aircraft anti-icing fluids. VKI Project Report 1989-15, June 1989.

12-DVORAK F.A.: Calculation of turbulent boundary layers on rough surfaces in pressure gradient. AIAA Journal, Vol.7 No.9, September 1969.

13-BETTERMANN D.: Contribution a l'etude de la couche limite turbulente le long de plaques rugueuses. Laboratoire d'Aerothermique du C.N.R.S., Rapport No. 65-6, 1965.

14-SPAZZINI P.G., CARBONARO M.: Boundary layer measurements over a 2D discrete roughness wall. VKI Stagiaire Report 1991-05, November 1990.

15-CARBONARO M.: Proposed specification for aerodynamic acceptance tests of aircraft de/anti-icing fluids. VKI Preprint 1990-20, presented at AIA TC Project 218-4 / AECMA Meeting, Amsterdam, April 1990.

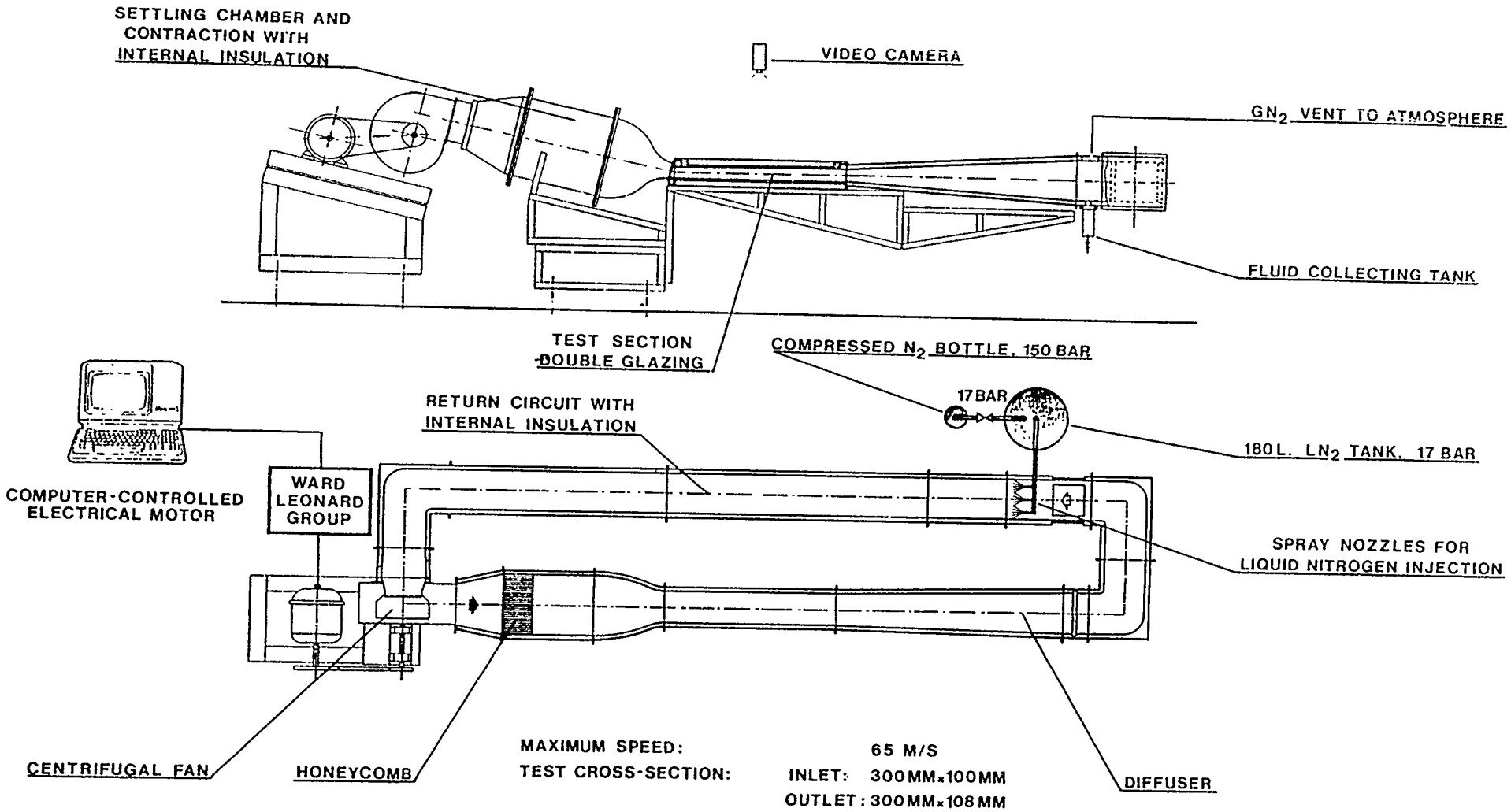

MAXIMUM SPEED:		65 M/S
TEST CROSS-SECTION:	INLET:	300MM×100MM
	OUTLET:	300MM×108MM
TEST SECTION LENGTH:		1.60M
DRIVE POWER:		6.7 KW
MINIMUM TEMPERATURE:		-50°C
LIQUID N_2 CONSUMPTION:		~3L/MIN
TIME TO GET -20°C:		~15 MIN

Fig. 1 THE VKI COLD WIND TUNNEL CWT-1

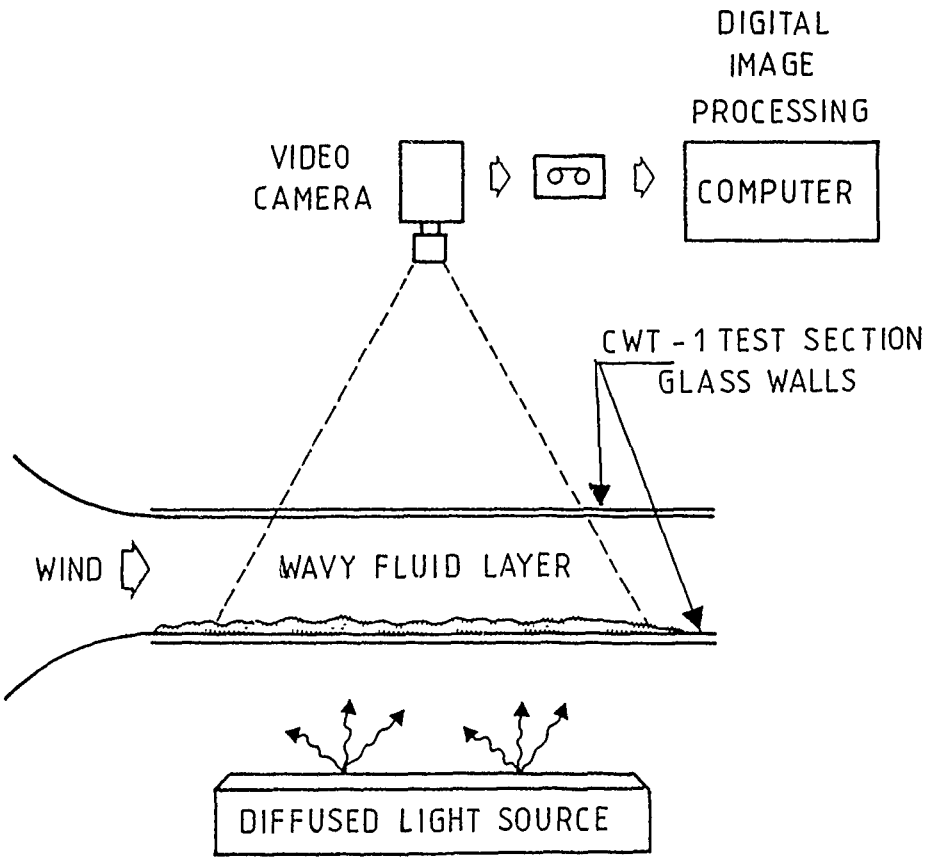

Fig. 2 SET-UP FOR MEASUREMENT OF LOCAL THICKNESS OF A DYED FLUID LAYER BY A LIGHT ABSORPTION TECHNIQUE

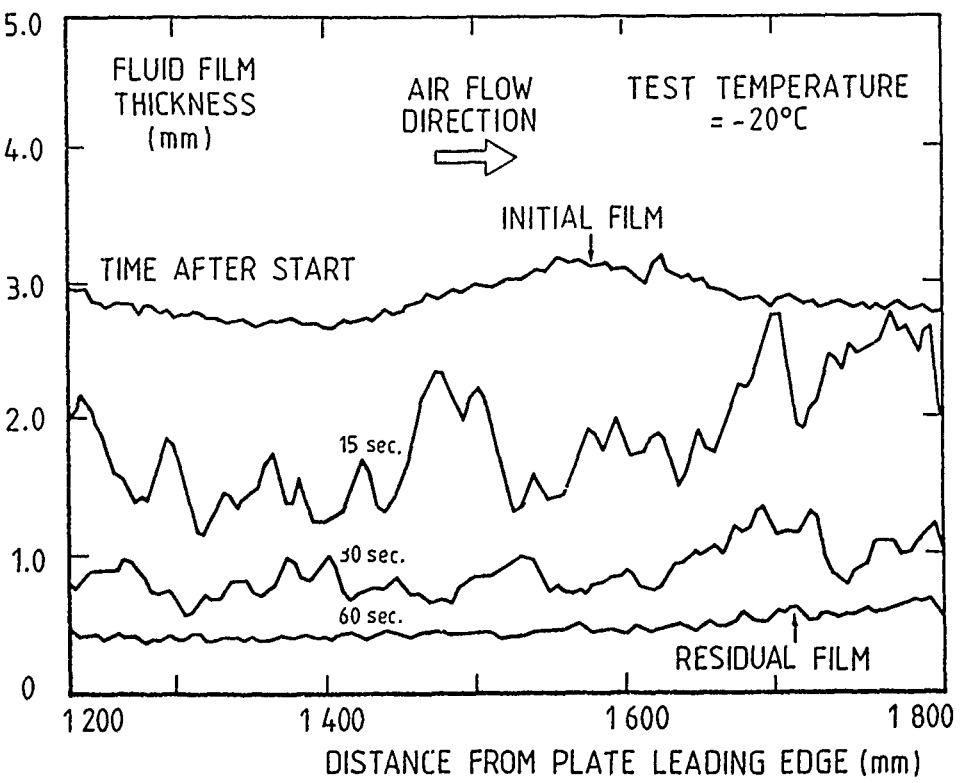

Fig. 3 TIME-DEPENDENT THICKNESS PROFILE OF A LAYER OF A SPECIFIC ANTI-ICING FLUID ON A FLAT PLATE UNDER EFFECT OF AN ACCELERATING AIRFLOW

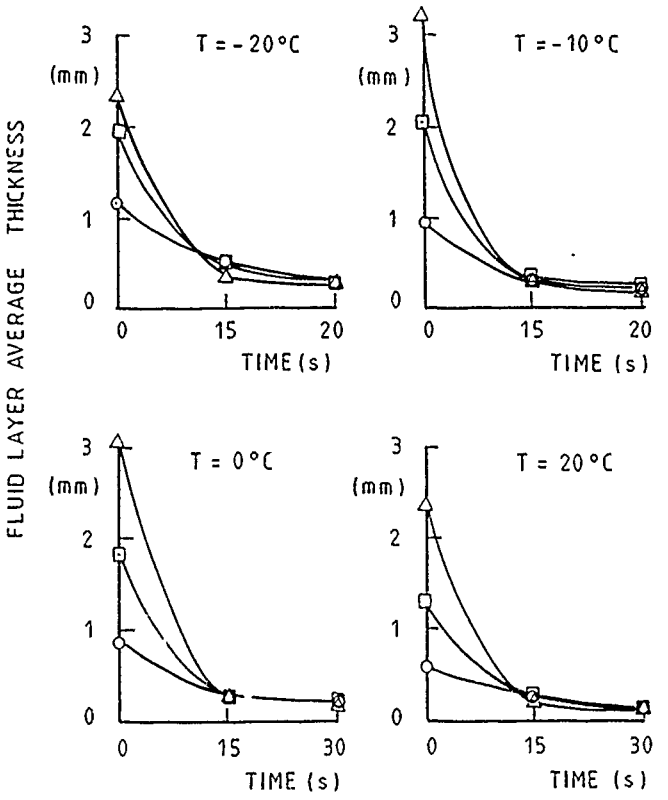

Fig. 4 VARIATION WITH TIME OF SPACE-AVERAGED THICKNESS OF AN ANTI-ICING FLUID LAYER FOR VARIOUS INITIAL THICKNESSES AND TEST TEMPERATURES

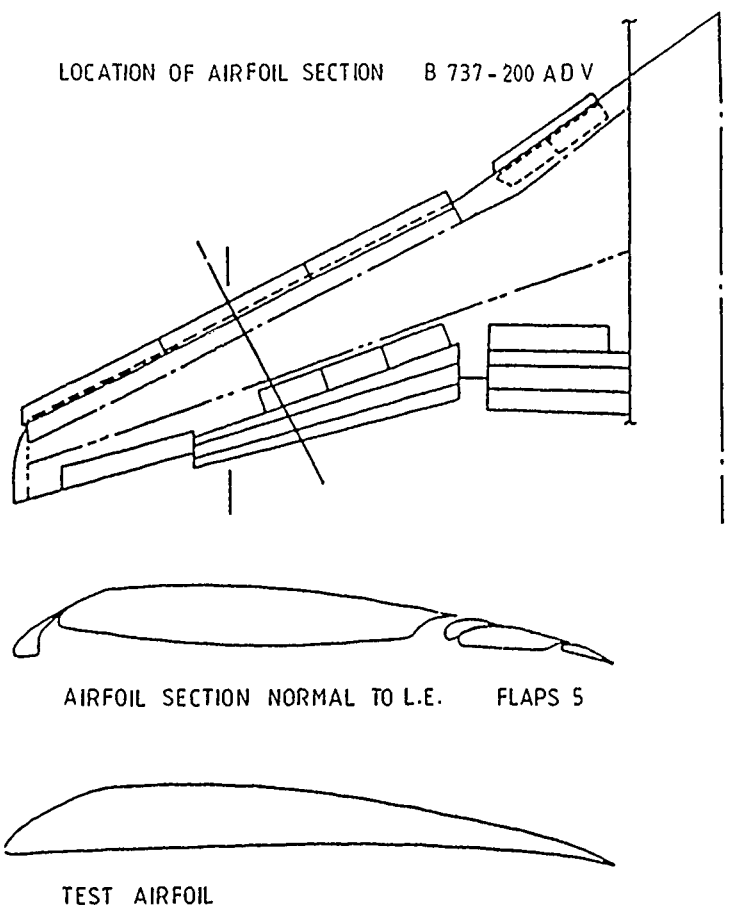

Fig. 5 SECTION OF THE B737 WING SELECTED AS TEST AIRFOIL

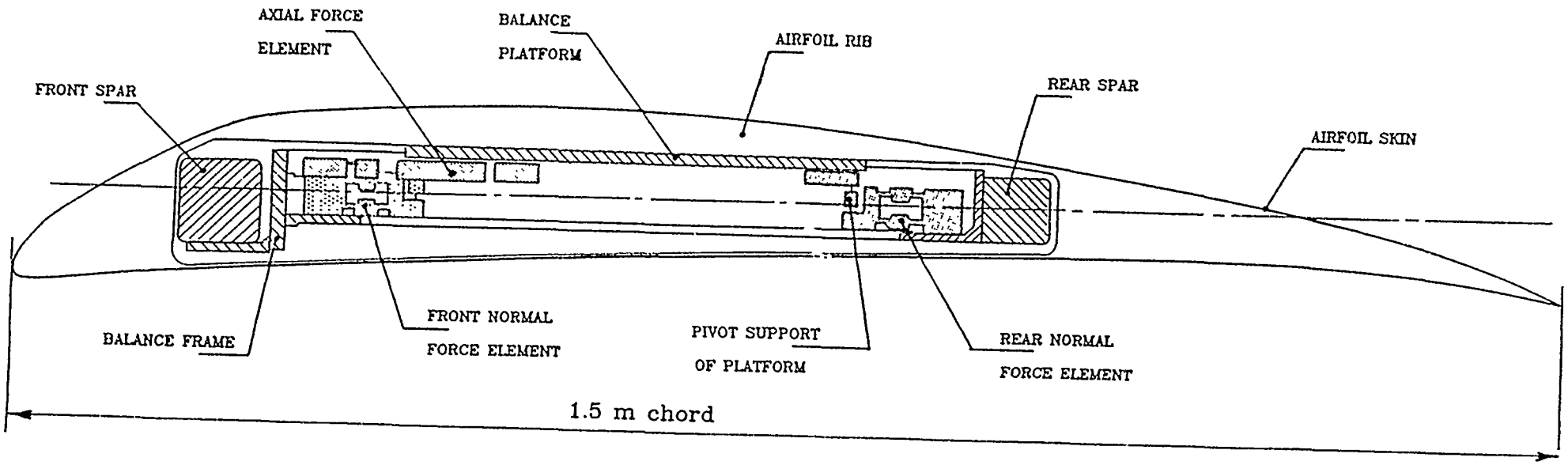

Fig. 6 TEST AIRFOIL MODEL AND INTERNAL BALANCE ARRANGEMENT

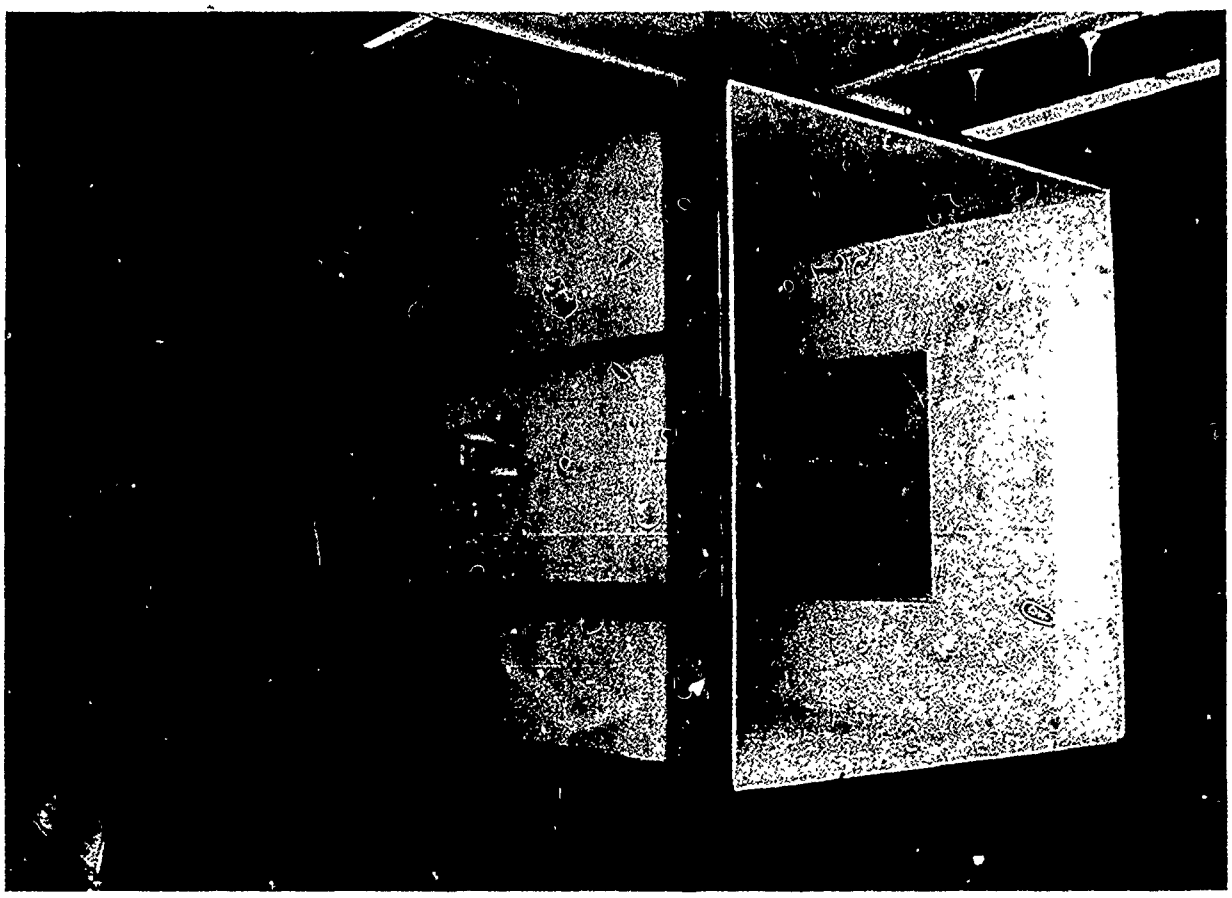

Fig. 7 AIRFOIL MODEL IN TEST SECTION INSERT FOR VKI L1-A AND BFA WIND TUNNELS

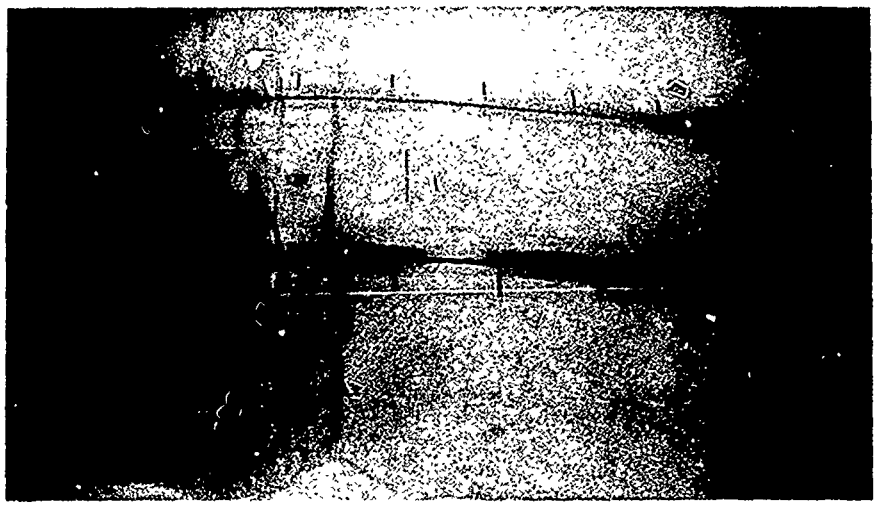

a) Initial wave formation

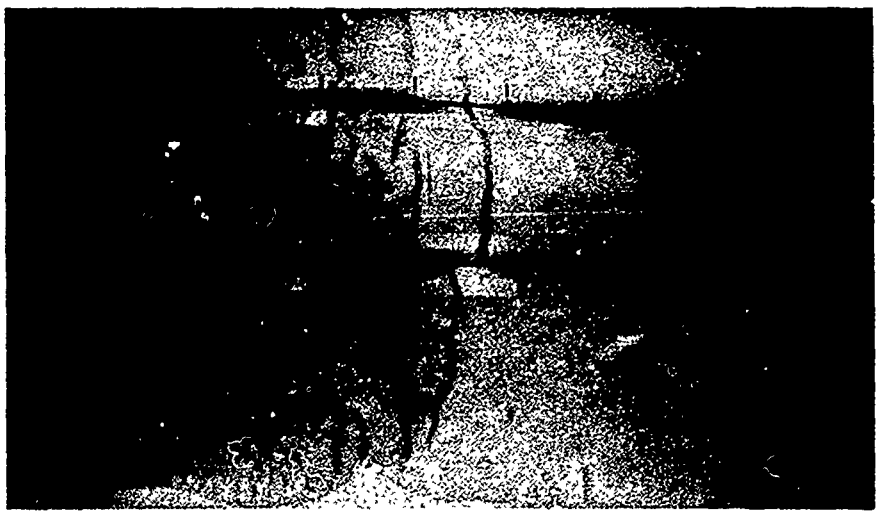

b) Merging of waves to form a single front

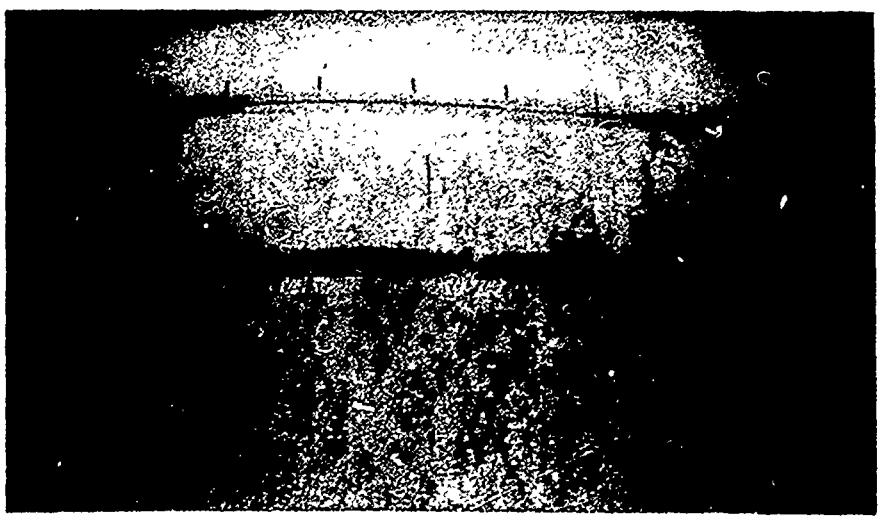

c) Wave front approaching trailing edge

Fig. 8 WIND-INDUCED SURFACE WAVES ON AN ANTI-ICING FLUID LAYER DEPOSITED ON UPPER WING SURFACE

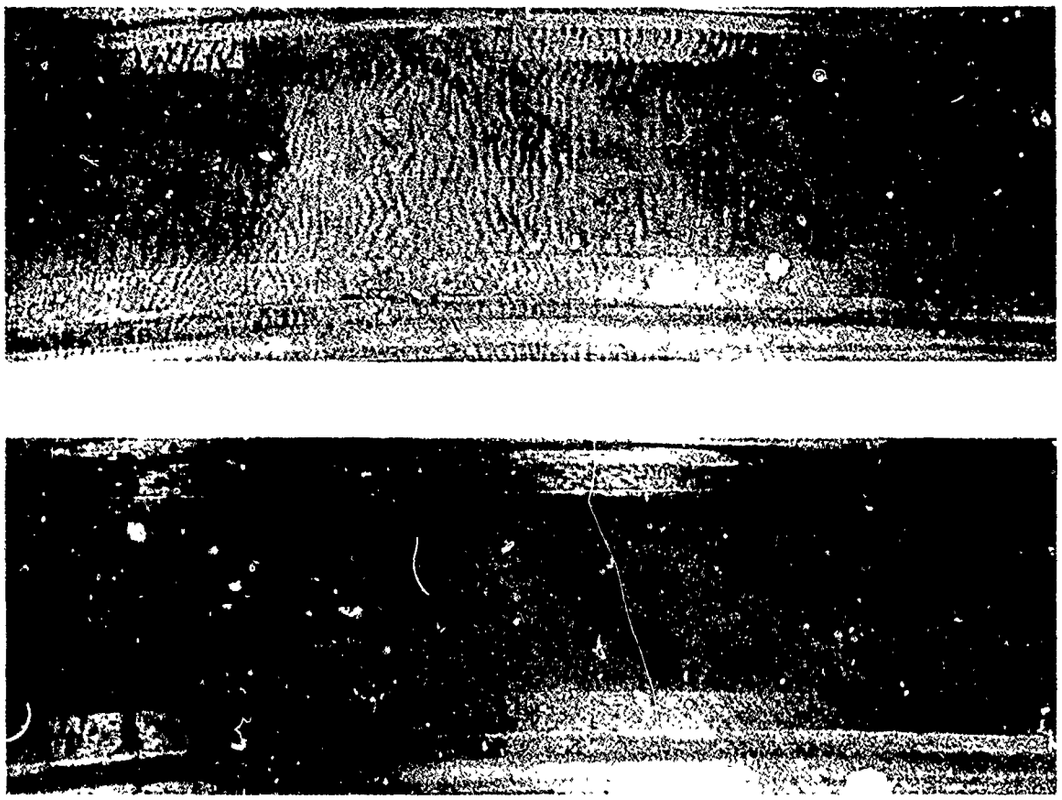

Fig. 9 DIFFERENCE IN WIND-INDUCED SURFACE WAVES FOR A NEWTONIAN DE-ICING FLUID (a) AND A NON-NEWTONIAN ANTI-ICING FLUID (b)

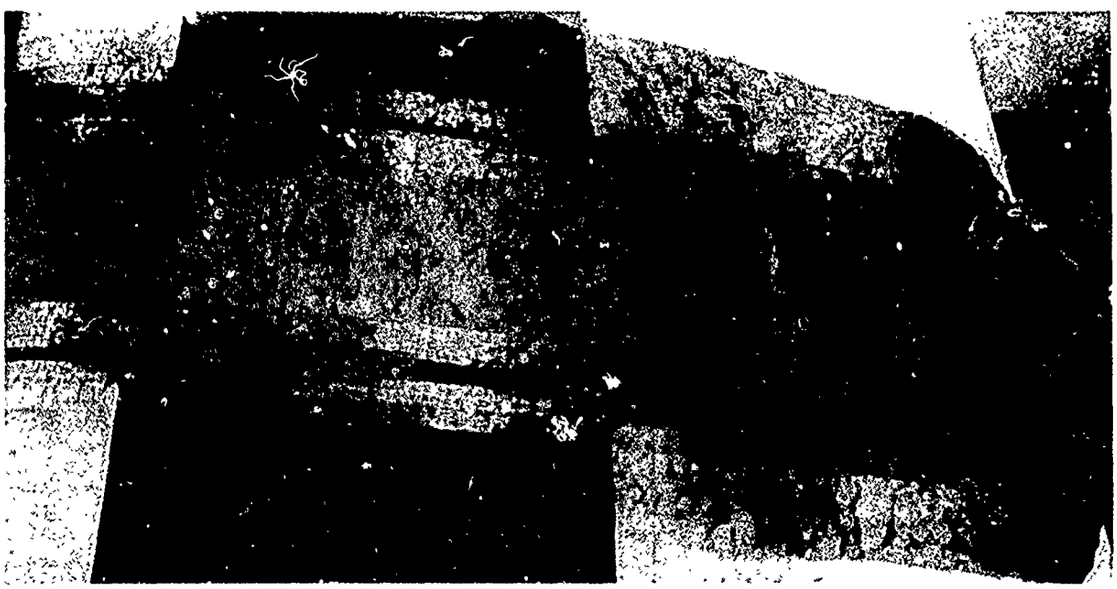

Fig. 10 SECOND WAVE FRONT APPEARING AFTER THE WING ROTATION MANOEUVRE

d. Adequate takeoff acceleration and climb capabilities

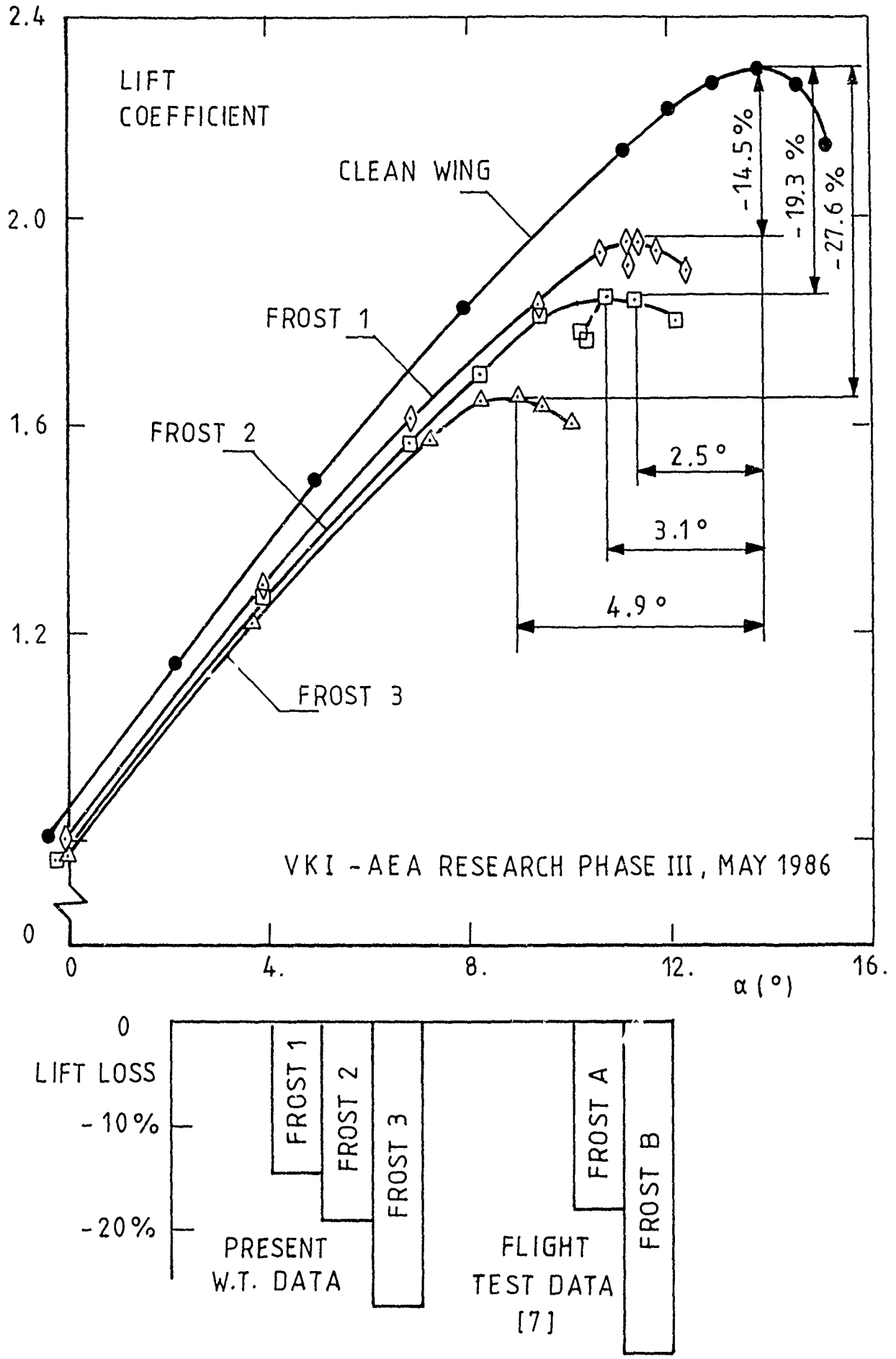

Fig. 11 LIFT VS INCIDENCE CURVE OF WING, CLEAN OR WITH ROUGHNESS-SIMULATED FROST ON UPPER SURFACE

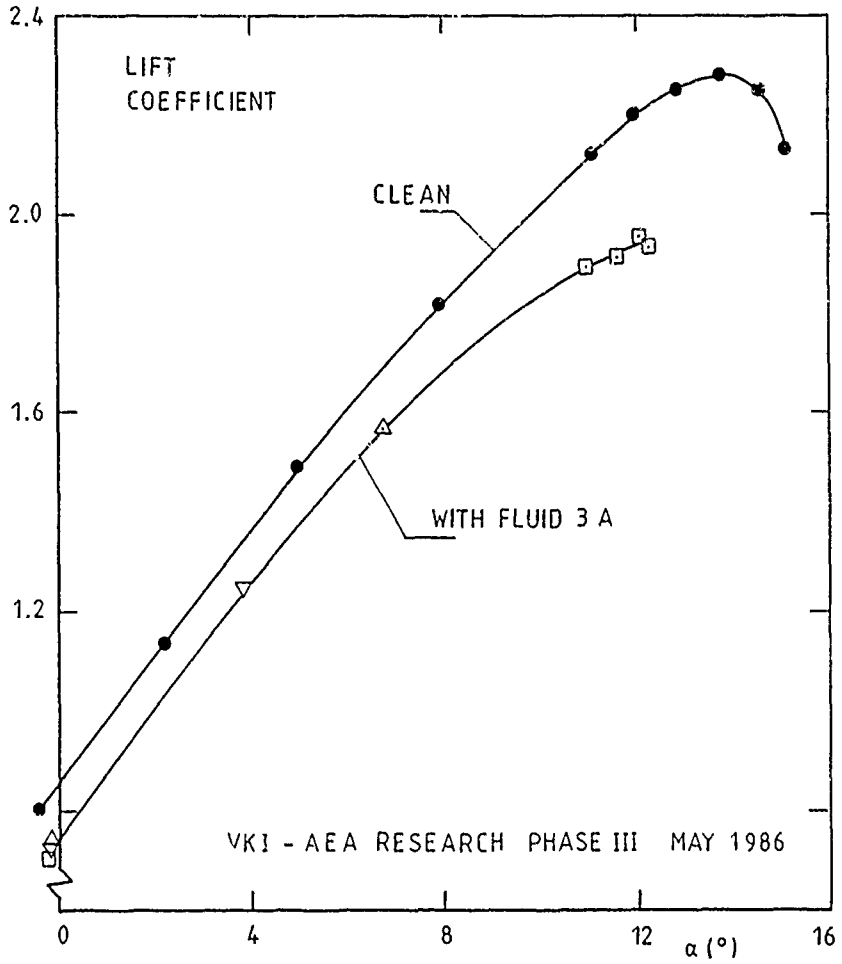

Fig. 12 LIFT VS INCIDENCE CURVE OF WING, CLEAN OR WITH AN ANTI-ICING FLUID DEPOSITED ON UPPER SURFACE

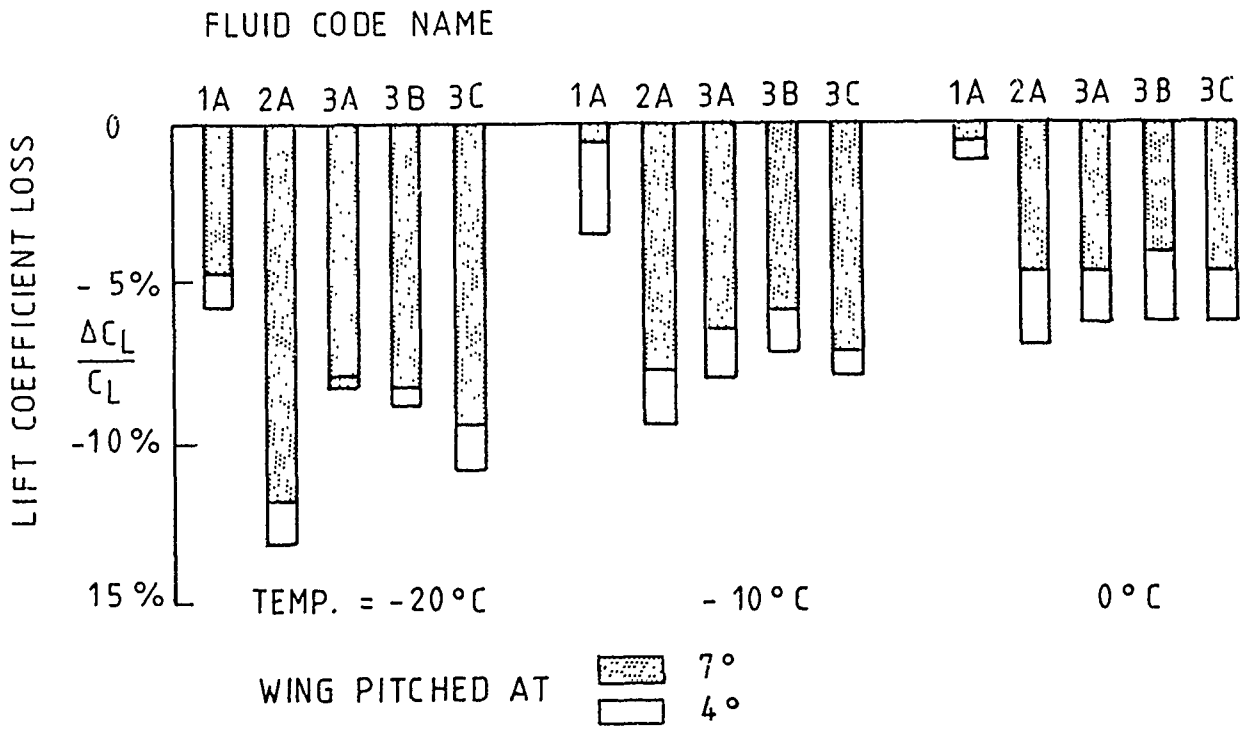

Fig. 13 LOSS IN WING LIFT COEFFICIENT AT TWO POST-ROTATION INCIDENCES, FOR VARIOUS FLUIDS AND TEMPERATURES

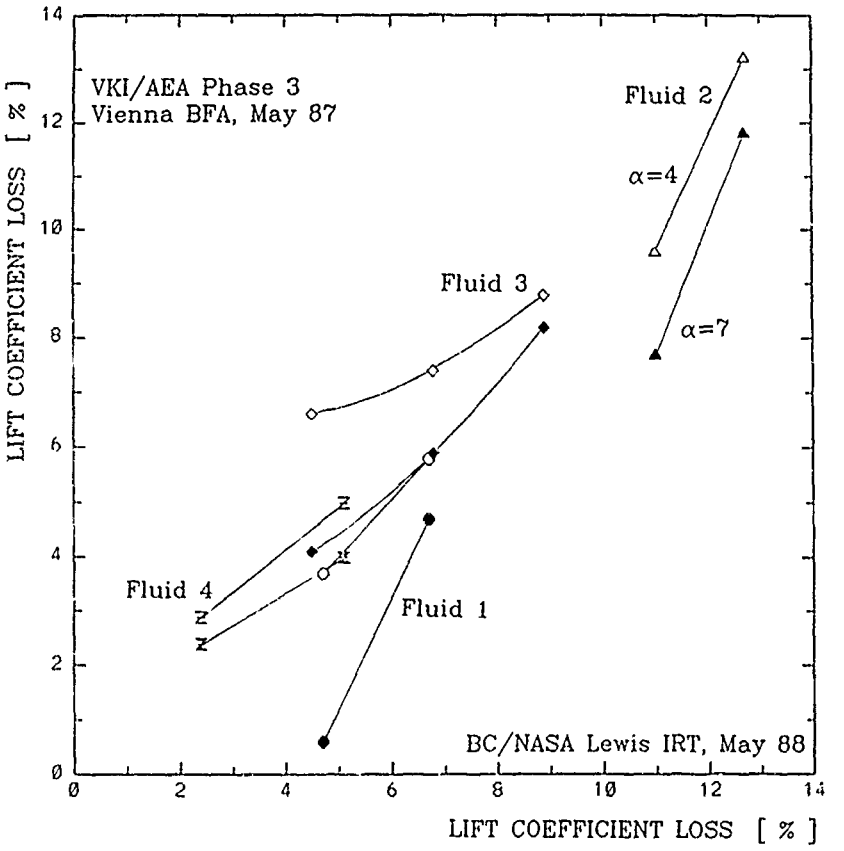

Fig. 14 COMPARISON OF LIFT COEFFICIENT LOSSES MEASURED IN BFA AND NASA-LEWIS ICING TUNNELS

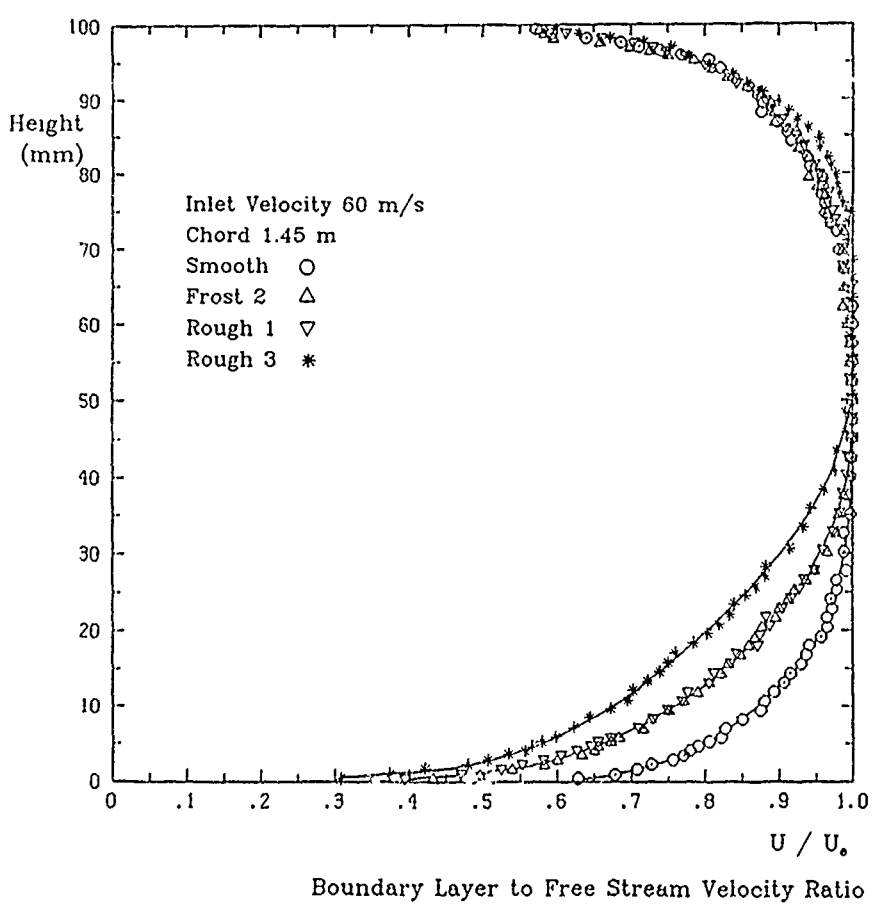

Fig. 15 VERTICAL PROFILE OF VELOCITY AT THE EXIT OF THE TEST SECTION OF THE VKI CWT-1 FACILITY

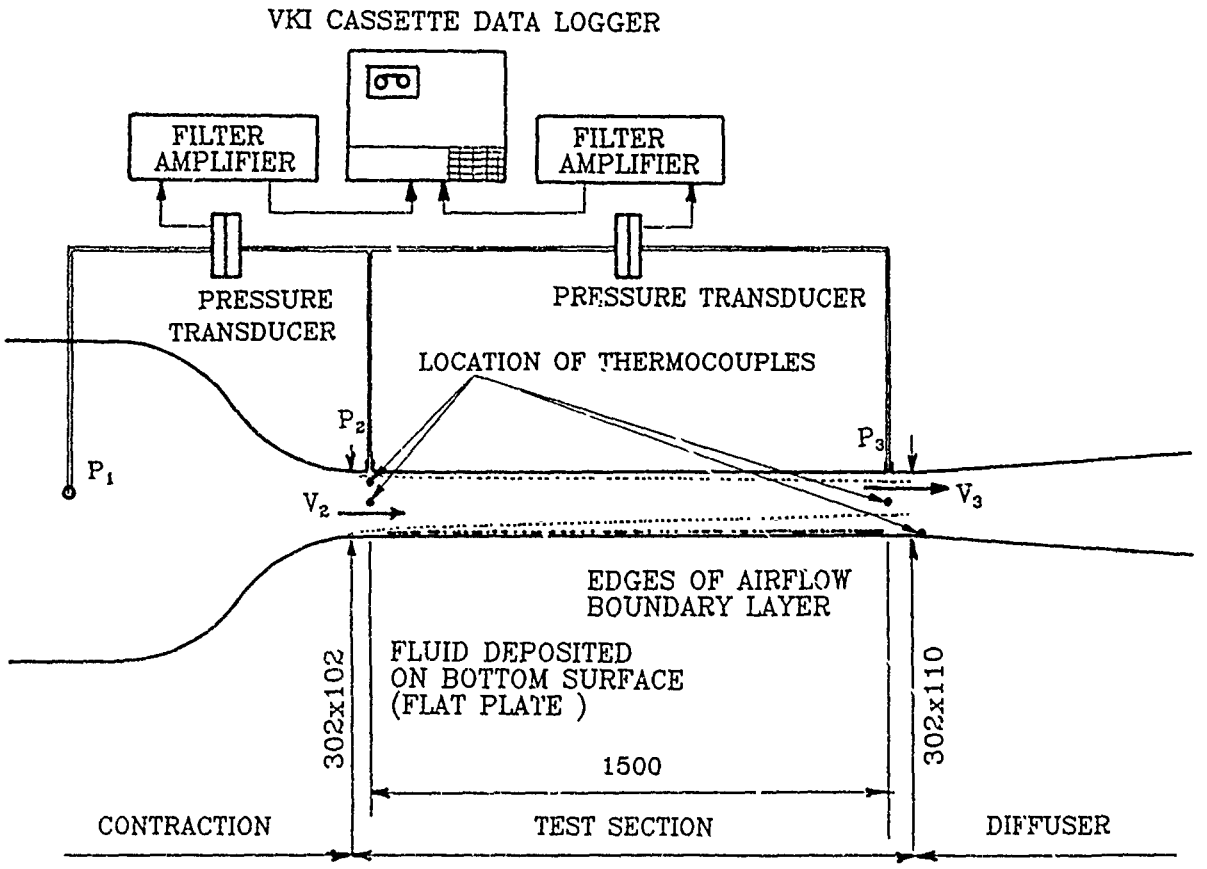

Fig. 16 CWT-1 TEST SECTION AND INSTRUMENTATION SET-UP

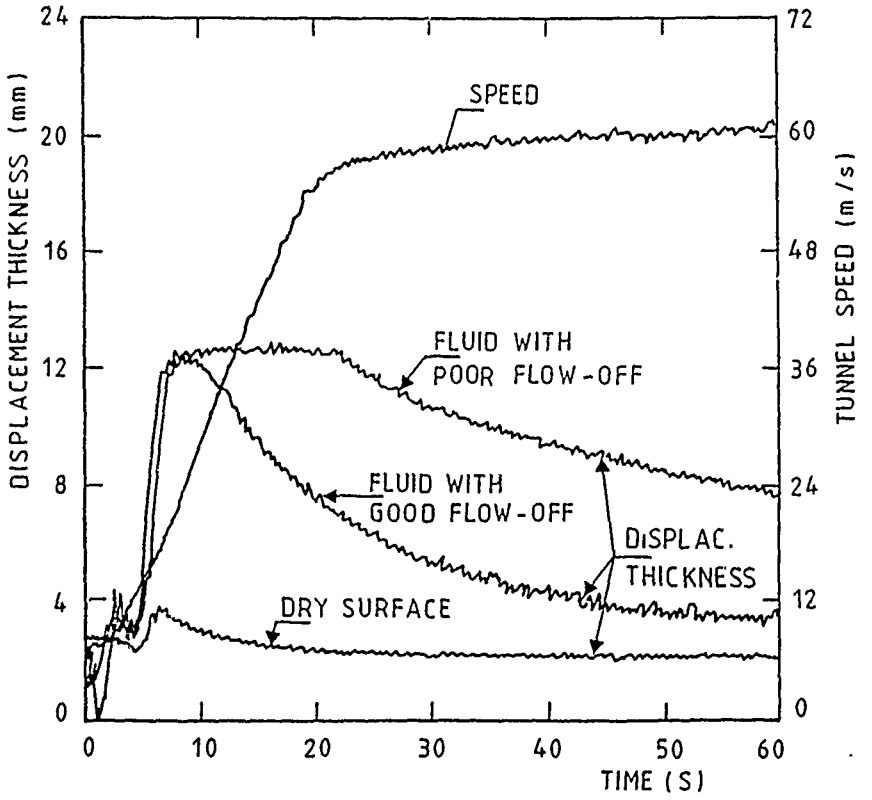

Fig. 17 TYPICAL RESULTS OF CWT-1 FLOW-OFF TESTS, WITH BOTTOM FLAT WALL OF TEST SECTION CLEAN OR COVERED WITH FLUID

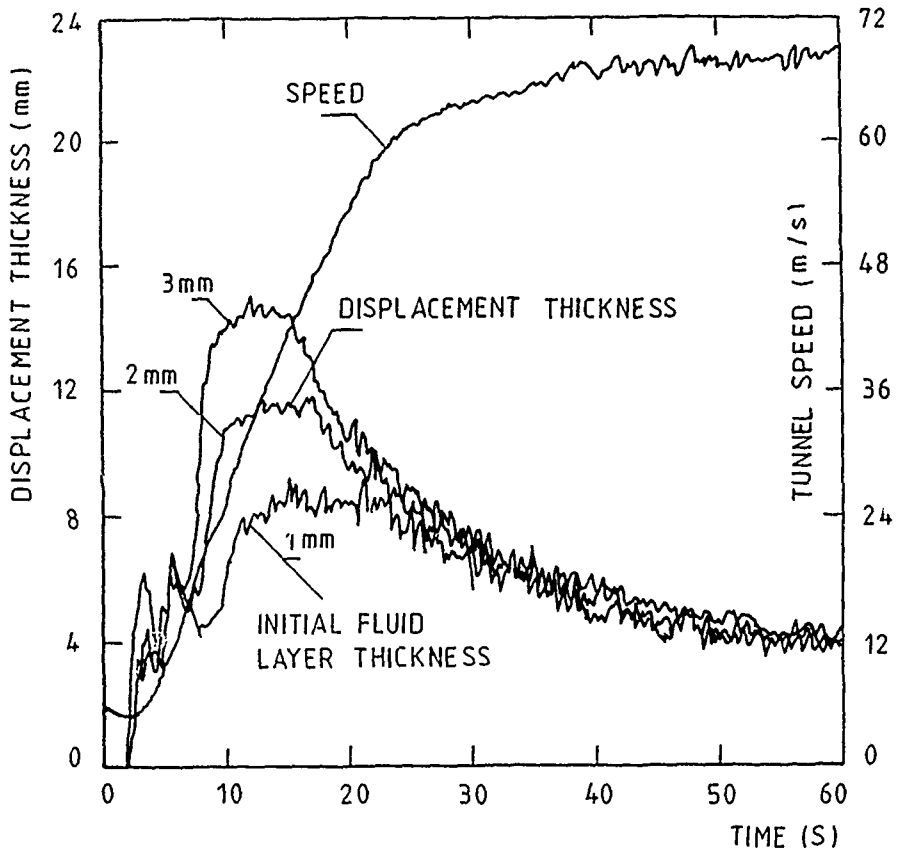

Fig. 18 EFFECT OF INITIAL THICKNESS OF FLUID LAYER ON THE MEASURED BOUNDARY LAYER DISPLACEMENT THICKNESS

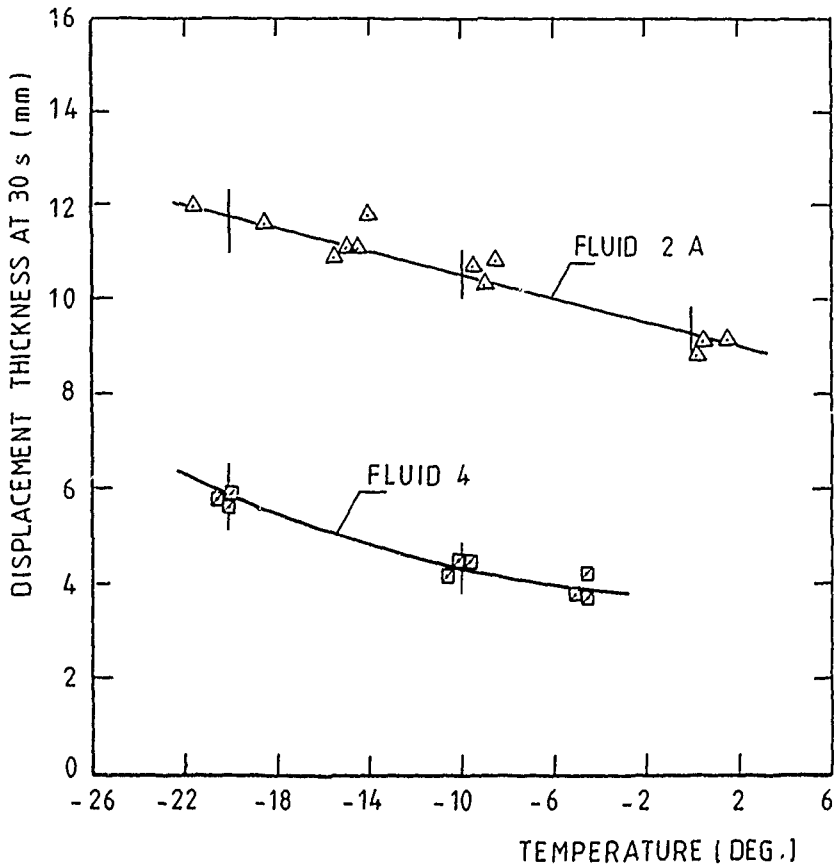

Fig. 19 CHARACTERIZATION OF THE TEMPERATURE-DEPENDENT FLOW-OFF BEHAVIOUR OF A FLUID

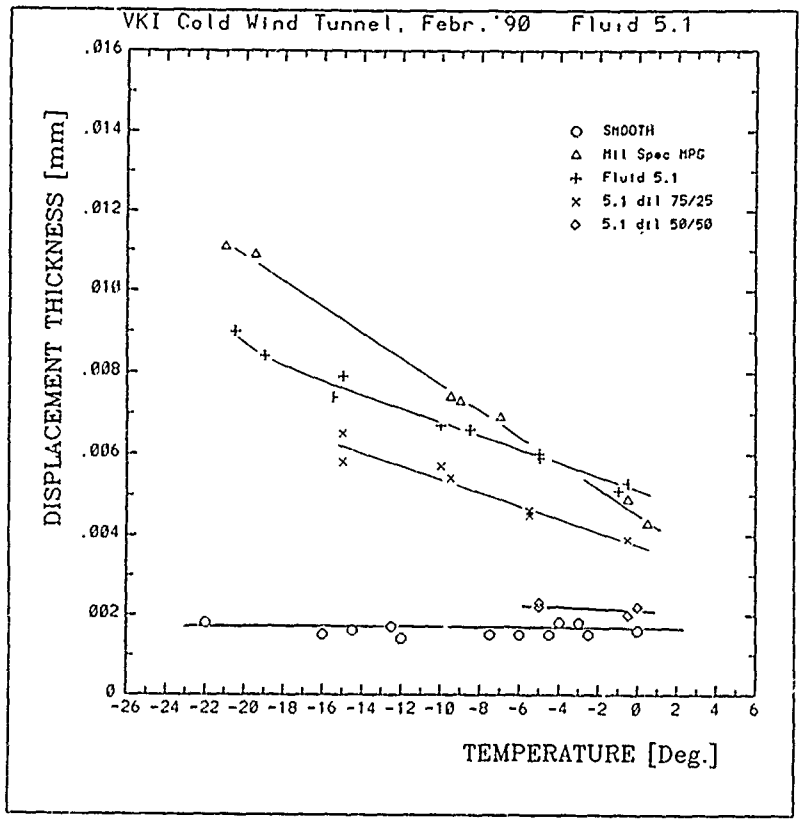

(a)

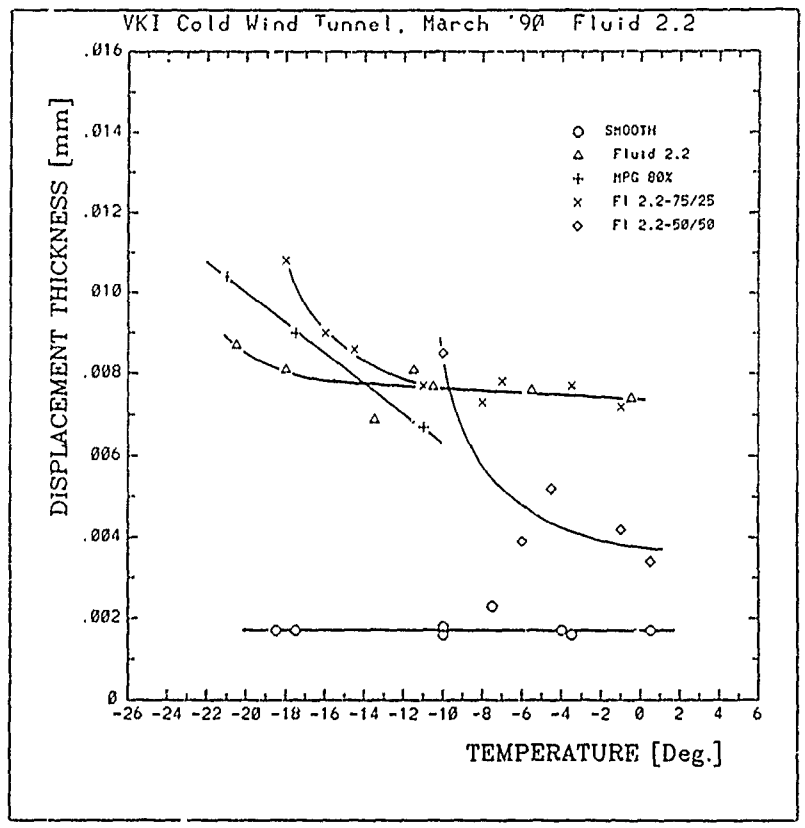

(b)

Fig. 20 EFFECT OF WATER DILUTION ON THE FLOW-OFF BEHAVIOUR OF TWO DIFFERENT ANTI-ICING FLUIDS

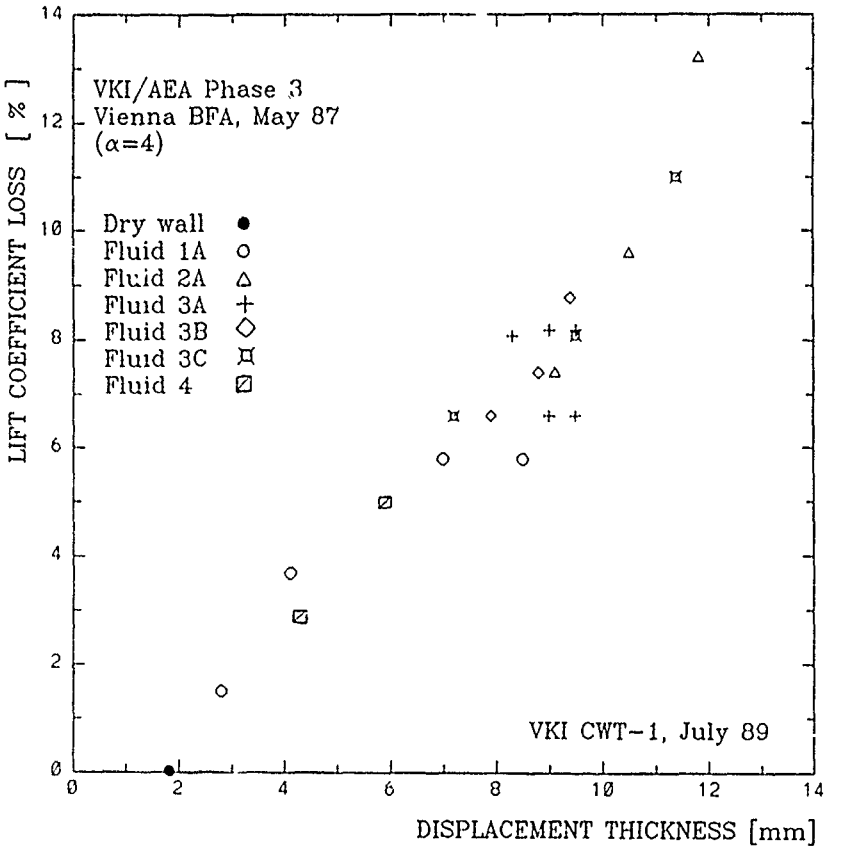

DISPLACEMENT THICKNESS [mm]

Fig. 21 CORRELATION BETWEEN BOUNDARY LAYER DISPLACEMENT THICKNESS IN CWT-1 AND AIRFOIL LIFT COEFFICIENT LOSS MEASURED IN BFA ICING TUNNEL

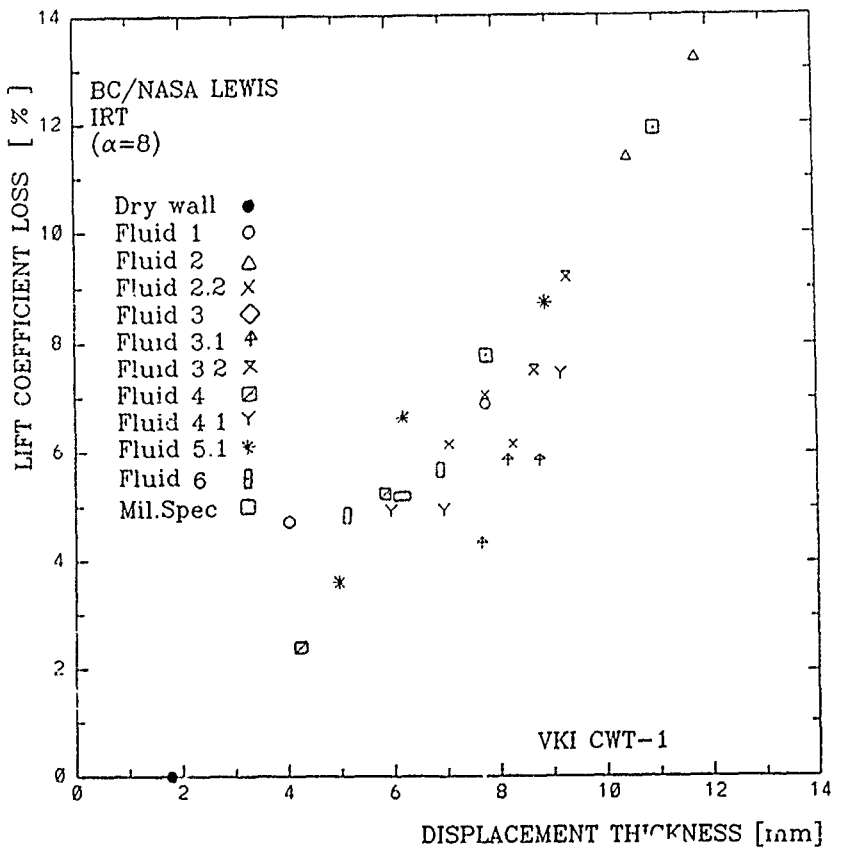

Fig. 22 CORRELATION BETWEEN BOUNDARY LAYER DISPLACEMENT THICKNESS IN CWT-1 AND AIRFOIL LIFT COEFFICIENT LOSS MEASURED IN NASA LEWIS ICING TUNNEL

WIND TUNNEL INVESTIGATION OF THE AERODYNAMIC EFFECTS OF AIRCRAFT GROUND DEICING/ANTI-ICING FLUIDS AND CRITERIA FOR AERODYNAMIC ACCEPTANCE

Thomas A. Zierten* and Eugene G. Hill**
***Principal Engineer**
****Manager**
Boeing Commercial Airplane Group
Configurations and Basic Certification
Renton Division Aerodynamics
P.O. Box 3707
Seattle, Washington 98124-2207
U.S.A.

SUMMARY

A follow-on wind tunnel investigation of the aerodynamic effects of aircraft ground deicing/anti-icing fluids was performed to supplement earlier reported flight and wind tunnel tests and support the development of aerodynamic acceptance criteria for aircraft ground deicing/anti-icing fluids. The test was conducted at the NASA Lewis Research Center Icing Research Tunnel using both a two-dimensional model and a three-dimensional half model of the 737-200ADV airplane. The fluids that were tested included three Type I Newtonian fluids, which use ethylene, diethylene, and propylene glycol as the freezing point depressant; four Type II non-Newtonian fluids, which are currently in production; eight developmental fluids; and a Mil Spec fluid to be used as a reference fluid in the aerodynamic acceptance test. The Type I and current Type II fluids were tested neat and diluted to determine basic aerodynamic effects. Dilution of the Type II fluids did not significantly alter the aerodynamic effects of the fluids. Diluting the Type I fluids did result in a significant reduction in the adverse aerodynamic effects of these fluids, especially at temperatures of -10°C and colder. Boundary layer displacement thickness, δ*, measurements made with the fluids on the two-dimensional model show excellent correlation with lift loss due to the fluids at maximum lift and at operating angles of attack and with the boundary layer displacement thickness measured on a flat plate in the small von Karman Institute wind tunnel. This correlation validated the future use of flat plate boundary layer displacement thickness measurement as the criterion for the aerodynamic acceptability of a fluid. The limiting boundary layer displacement thickness, which identifies a fluid as being aerodynamically acceptable, is correlated with a loss in maximum lift that results in an allowed specific reduction in aerodynamic performance margins.

LIST OF SYMBOLS AND ABBREVIATIONS

C	Celsius
c	Mean aerodynamic chord
C_D	Coefficient of drag, three-dimensional
CDSA	Stability axis coefficient of drag, three-dimensional
C_l	Coefficient of lift, two-dimensional
C_L	Coefficient of lift, three-dimensional
CLSA	Stability axis coefficient of lift, three-dimensional
cm	Centimeters
C_M	Coefficient of pitching moments, three-dimensional
EG	Ethylene glycol
ETHY	Ethylene
ft	Feet
Fwd	Forward
GLY	Glycol
hp	Horsepower
in	Inches
kW	Kilowatts
m	Meters
mi/h	Miles per hour
mm	Millimeters
Mil Spec	Military specification
mPas	Millipascal seconds
Pa	Pascals
PG	Propylene glycol
PROPY	Propylene
s, sec	Seconds
t	Time, seconds
T, TEMP	Temperature
u	Local velocity
U_∞	Freestream velocity
V	Velocity
X_{NF}	Center of normal force in fraction of chord length
α	Angle of attack, deg
δ*	Boundary layer displacement thickness
μ	Absolute viscosity

Subscripts

B	Body
DRY	Dry surface
FLUID	Surface wetted with fluid
keas	Knots equivalent airspeed
MAX	Maximum
R	Takeoff rotation speed
S_{1g}	1g stall speed
W	Wing
0	Time zero
2	Takeoff safety speed
$\alpha_w 8$	At 8-deg wing angle of attack

1.0 INTRODUCTION

Investigation of the aerodynamic effects of aircraft ground deicing/anti-icing fluids has been carried out extensively in both wind tunnel tests and flight tests (Refs. 1, 2, 3, 4, and 5). For the most part these investigations have concentrated on development of test techniques for obtaining basic aerodynamic data on a single Newtonian deicing fluid and several non-Newtonian deicing/anti-icing fluids. From this primary database, development of the non-Newtonian fluids with less severe aerodynamic effects has progressed to the point where these fluids can be used on most large transport aircraft without requiring performance penalties. However, some questions remain that were not addressed in the previous investigation. In particular, does the behavior of the Type I Newtonian fluids differ depending the glycol used as the freezing point depressant in the formulation of the fluid? Previously only Association of European Airlines (AEA) Type I fluid was tested, whereas the aerodynamic effects of Type I fluids using ethylene or propylene glycol were as yet undetermined. Also, the effects of dilution and/or precipitation contamination of either Type I or Type II fluids were not addressed previously.

Further, to continue development of fluids that could provide improved deicing/anti-icing capability without degrading aerodynamic performance, criteria for aerodynamic acceptance needed to be established. Economy and timing of the development cycle demanded the capability to determine compliance with these criteria using some method other than a wind tunnel test program requiring a facility such as the NASA Lewis Research Center Icing Research Tunnel (IRT).

2.0 AIRCRAFT GROUND DEICING/ANTI-ICING FLUIDS

The Type I fluids, characterized by Newtonian viscosity behavior (i.e., viscosity is principally a function of temperature only), have a relatively low viscosity except at very cold temperatures. At colder temperatures, the viscosity of Type I fluids can vary significantly, depending on the glycol used as the freezing point depressant in the formulation of the fluid. Monoethylene glycol has been widely used in the United States and has a relatively

low viscosity throughout the normal temperature range of use. Diethylene and propylene glycol-based Type I fluid formulations are used in Europe and are becoming more common in North America. At colder temperatures these latter glycols exhibit viscosities much higher than that of (mono) ethylene glycol The specific Type I fluids evaluated are listed in Table I.

Table I. Fluids Evaluated.

Current Type I Fluids

Hoechst VP 1732 (AEA Type I)
Octagon ADF 1427 (propylene glycol-based)
UCAR ADF IID (ethylene glycol-based)
MIL-A-8243D Type I

Current Type II Fluids

Dow Flightgard® 2000 (Hoechst 1704 LTV/88)
Kilfrost ABC-3
SPCA AD 104
UCAR AAF 250-3

Developmental Fluids by

BASF AG	Kilfrost Ltd.	Octagon Processes
Technoshield	Texaco (2)	Union Carbide (Canada) (2)

The other deicing/anti-icing fluids, Type II, are characterized by non-Newtonian viscosity behavior (i.e., viscosity is a function of temperature and shear stress). These non-Newtonian fluids are characterized by extremely high viscosity that dramatically decreases with increasing shear stress, approaching viscosity levels of Type I fluids at shear stress levels associated with typical takeoff and climb speeds of large commercial air transports. Fluid designers are able to control other characteristics of Type II fluids, such as the variation of viscosity with temperature, flow-off behavior, and the affinity of the fluid to absorb melted precipitants into solution Type II fluid products tend to have unique characteristics as compared to "generic" Type I fluid products. Figure 1 illustrates typical viscosity characteristics of Type I and II fluids. The specific Type II fluids evaluated are also listed in Table I.

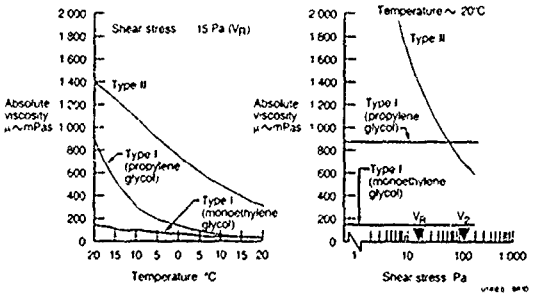

Figure 1. Undiluted Aircraft Ground Deicing/Anti-Icing Fluids Characteristics.

3.0 WIND TUNNEL TEST

The wind tunnel evaluation of the fluids was performed at the NASA Lewis Research Center IRT during February 1990. The testing was a joint effort of Boeing, NASA, and various fluid manufacturers. Boeing provided the wind tunnel models and conducted the tests in cooperation with NASA. The NASA Lewis Research Center provided and operated the IRT. Final documentation of the test results will be performed by NASA. Fluids were provided by a variety of fluid manufacturers, as noted in Table I. This test was a follow-on of the test reported earlier in Reference 5.

3.1 Test Facility, Models, and Technique

The NASA Lewis IRT layout is shown in Figure 2. Tunnel temperature can be varied from 27°C to -29°C (81°F to -20°F) in the 6.1m (20-ft) long test section. Boeing provided force balances, a data acquisition system, and photographic and video equipment to supplement the NASA Lewis IRT data system and instrumentation. The data acquisition system consisted of 28 channels of analog-to-digital converters and signal conditions that were sampled at 4 Hz by an HP9845 computer. Data were then

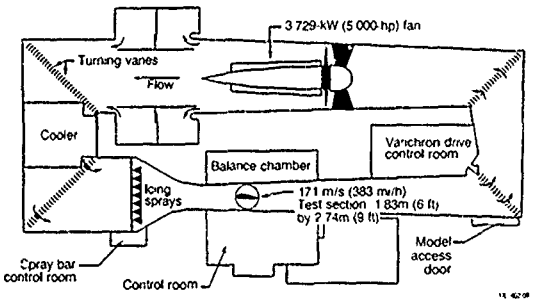

Figure 2. NASA Lewis Icing Research Tunnel.

transferred from the HP9845 memory to a DEC MicroVAX minicomputer for processing, analysis, and plotting.

Figures 3 and 4 show details of the models tested The 0.46m (1.5-ft) chord two-dimensional model was a 0.18-scale model of the 737-200ADV airfoil at approximately 65% semispan. The size of the two-dimensional model was limited to 25% of the wind tunnel height to avoid excessive wall effects. The model was mounted to turntables and balances located within a pair of splitter walls The three-dimensional model was a 0.091-scale half model of the 737-200ADV that was mounted to one of the splitter walls by a turntable and balance. Most of the three-dimensional model testing was performed with a ground plane in place. The models provided the capability of testing the configurations shown in Figure 5; however, testing was only performed at Flaps 5 with sealed slats configuration.

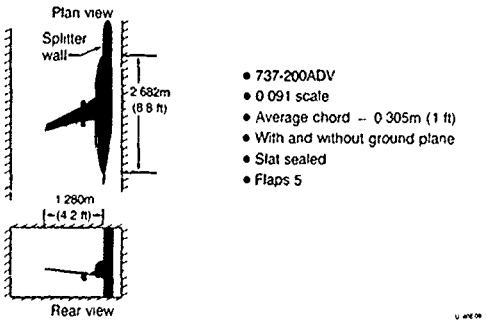

Figure 3. Three-Dimensional Half Model.

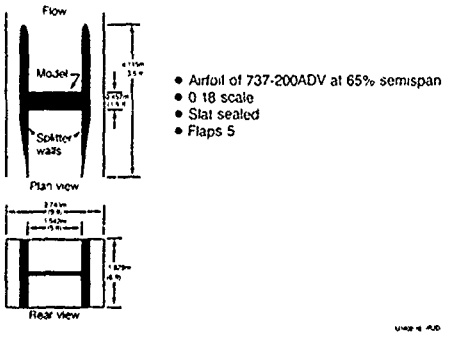

Figure 4. Two-Dimensional Model.

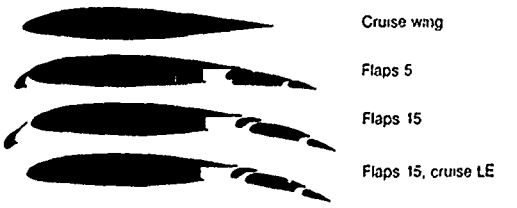

Figure 5. Two-Dimensional Model Configurations.

After the model was cleaned, wiped with a cloth dampened with a 50:50 water/Type I fluid mixture, and the fluid specimen poured from a 2L container and leveled to the desired film depth, the model and fluid were exposed to the cooled wind tunnel

environment for 5 min under essentially static conditions. The 5-min exposure time allowed the temperature of the precooled fluid specimen to come into equilibrium with the temperature of the model and wind tunnel. Also, the exposure time was representative of time required for an aircraft to taxi to a runway for takeoff after deicing/anti-icing had been completed. The wind tunnel flow velocity was linearly increased to 69 m/s (135 keas) in approximately 30 sec, and the model was rotated from the taxi attitude (0 deg) to the desired attitude at a rotation rate of 3 deg/s at 25 sec after the start of the tunnel acceleration. The tunnel flow velocity increase and model rotation simulated the shear stress history that would occur during a typical all-engines-operating takeoff for a large commercial jet transport. Data were continuously acquired from the start of the tunnel flow to 30 sec after the model was rotated through the stall angle of attack. Data acquired in the previous test using a pitch-and-pause technique verified that accurate data could be obtained using the more efficient continuous pitch data acquisition technique. The typical online data plot shown in Figure 6 illustrates the testing technique used and the force data acquired.

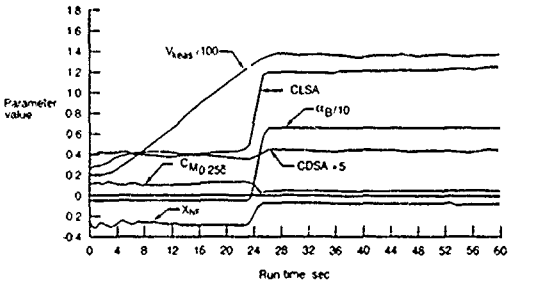

Figure 6. Typical Online Data Plot

3.2 Results

The following is a detailed description of results from the Phase II (1990) wind tunnel test that are of general interest. Additional testing was performed during Phase II to evaluate new and experimental deicing/anti-icing fluids. All the data from Phase II will be provided in a forthcoming NASA report on the test.

The opportunity to collaborate with NASA and the fluid manufacturers in a second entry into the NASA Lewis IRT 2 years after Phase I allowed the earlier limited database to be expanded to include:

a. Aerodynamic evaluations of currently available undiluted and diluted Type II fluids on both the three-dimensional half model and the two-dimensional model.

b. Examination of the difference in effects between the various glycol temperature depressants used in Type I fluids.

c. Acquisition of data to support development of an aerodynamic acceptance test for deicing/anti-icing fluids.

d. Further aerodynamic experimentation for fluid manufacturers to develop technology for improved fluids.

e. A cursory look at the effect of precipitation on the flow-off characteristics of a Type II fluid.

Figure 7 is a synopsis of the 737-200ADV half model data obtained with currently available deicing/anti-icing fluids. Maximum lift loss and the lift loss measured at 8-deg angle of attack, extracted from Figures 7a and 7b, respectively, for neat deicing/anti-icing fluids, are shown at specific temperatures in Figure 8. The 8-deg angle of attack attitude is representative of an engine-inoperative takeoff climb attitude at model Reynolds number. For the fluids shown, the ethylene glycol-based Type I and Union Carbide AAF 250-3 Type II fluids are the least intrusive. At a representative cold day temperature of -20°C (-4°F), the aerodynamic effects of Kilfrost ABC-3 and SPCA AD 104 Type II fluids are similar to the European AEA Type I fluid; however, the effects of the AEA Type I diminish rapidly with increasingly warmer temperatures. The comparatively high sensitivity of the proplyene glycol Type I fluid lift loss with temperature is also evident. The comparative results of the ethylene and propylene glycol Type I fluids reflect the viscosity differences between the fluids, as shown in Figure 1.

The effects of dilution on maximum lift loss and lift loss measured at 8-deg angle of attack, with data again extracted from Figures 7a and 7b, respectively, for the neat and diluted Type I and Type II fluids, are shown at specific temperatures in Figure 9. Because of economics and the eutectic nature of glycol mixtures, Type I fluids are diluted before they are applied to aircraft. For this reason the diluted Type I fluid lift losses, which are significantly less than those of neat AEA and propylene glycol-based Type I fluids, are most representative of what would be encountered in operational use. Conversely, Type II fluids are used operationally either neat or diluted. The temperatures selected for display are representative of the approximate lower limit temperatures for operational use of the particular dilutions of the Type II fluids. Figure 9 shows that a 25% dilution of the Type II fluids did not result in significant maximum lift loss differences when compared to undiluted fluid results. The dilution investigation was conducted to address concerns with the characteristic of some Type II fluids to have higher viscosity when diluted approximately 25% with water. Results of the investigation suggested that the aerodynamic effects of the increased viscosity were compensated by the change in elasticity of the diluted fluid.

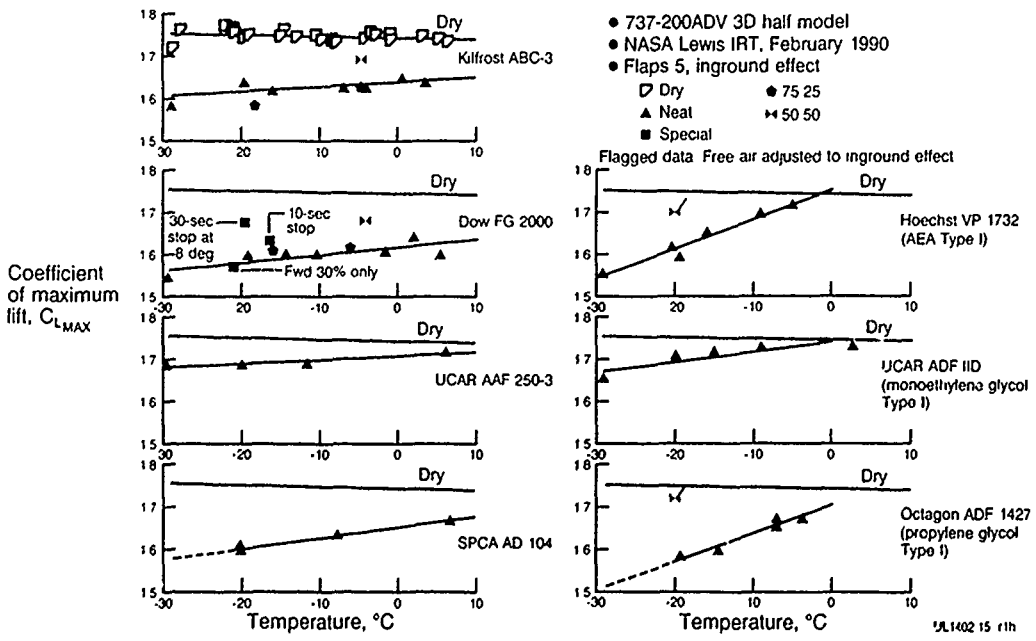

Figure 7a. Fluid Effect on Maximum Lift.

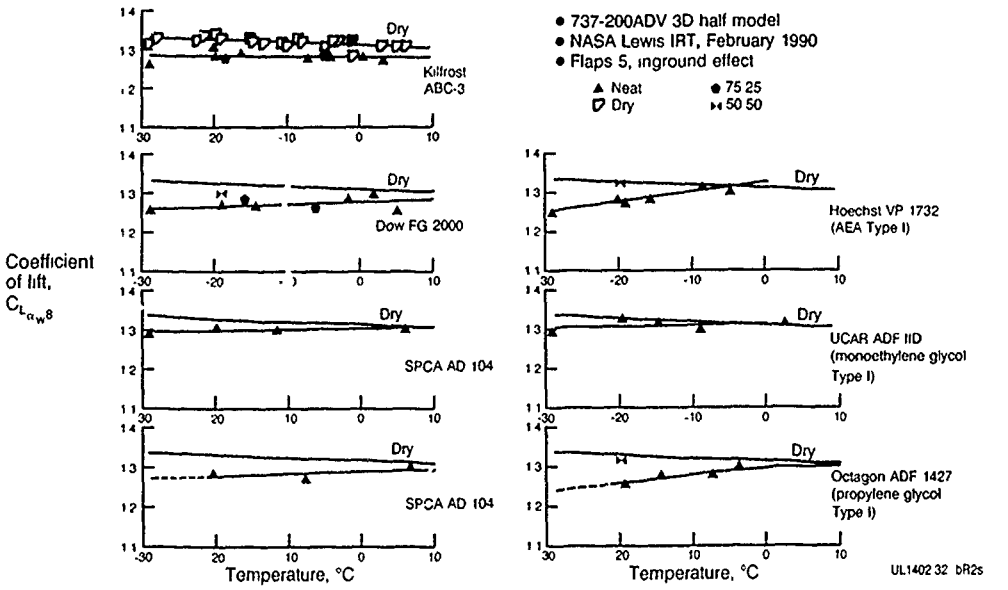

Figure 7b. Fluid Effect on Lift at Wing 8-deg Angle of Attack.

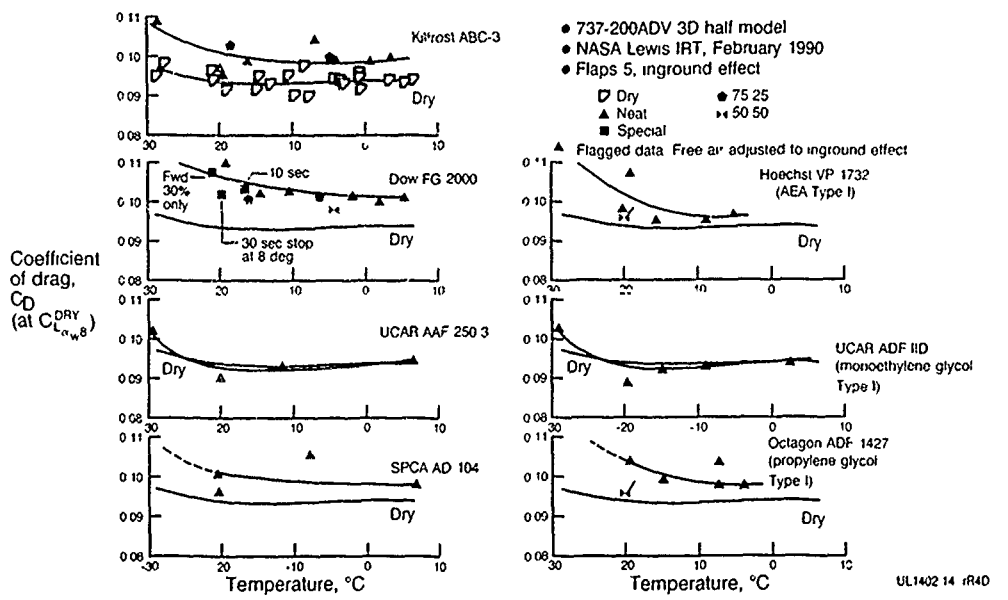

Figure 7c. Fluid Effect on Drag at Dry Wing 8-deg Angle of Attack Lift.

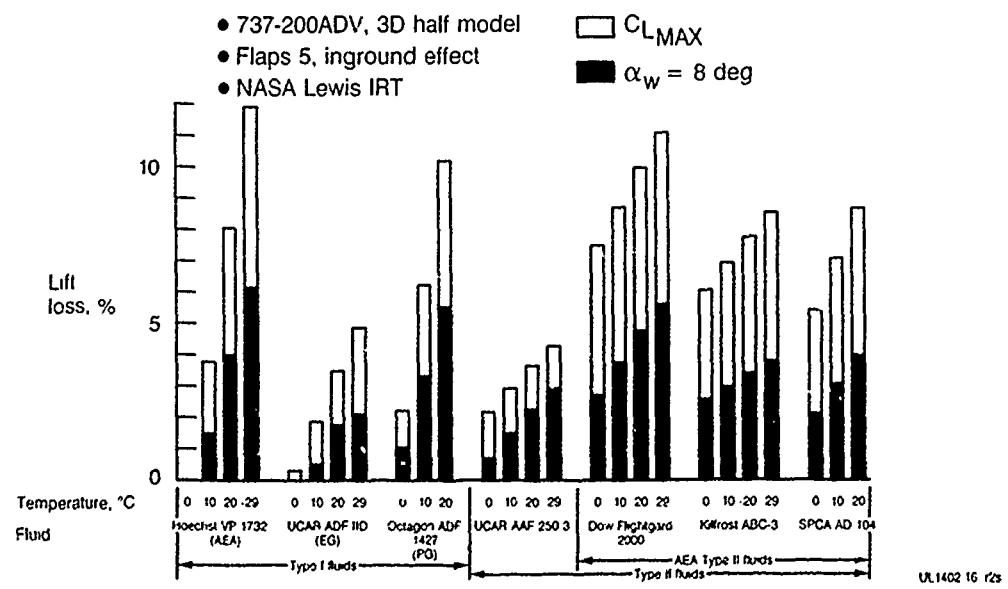

Figure 8. Lift Loss Due to Undiluted Deicing/Anti-Icing Fluids at Liftoff.

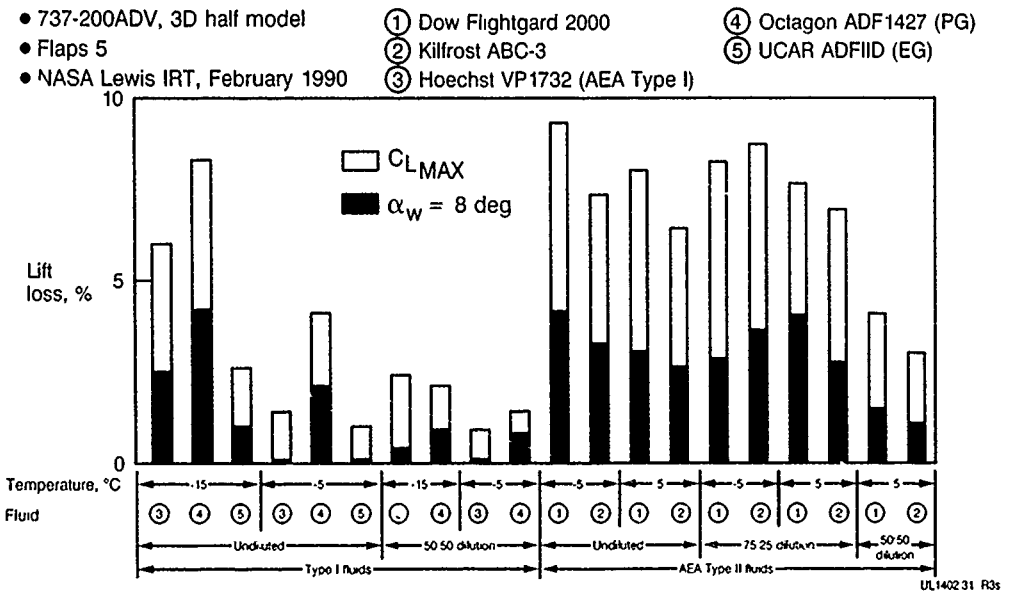

Figure 9. Aerodynamic Effects of Deicing/Anti-Icing Fluids at Operational Concentrations.

The transitory nature of deicing/anti-icing fluids is shown in Figure 10. These data were obtained by pausing for approximately 10 and 30 sec at the 8-deg angle of attack attitude and then resuming the pitch sweep to the test limit pitch attitude. These data proved useful when evaluating the additional time-dependent effects of the fluid on airplane takeoff and climb performance.

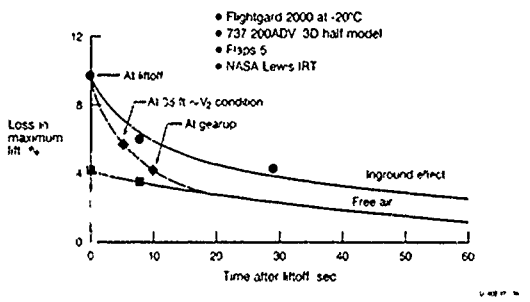

Figure 10a. Maximum Lift Loss Variation With Time.

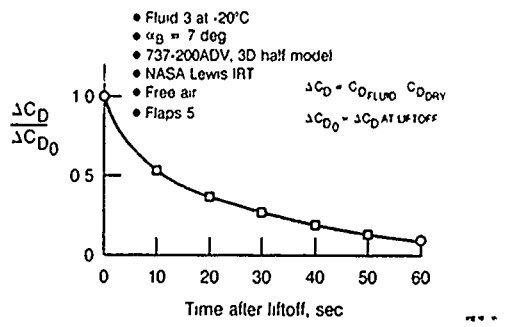

Figure 10b. Drag Increase Variation With Time.

The effects of precipitation contamination on the flow-off behavior of Type II fluids were evaluated on the two-dimensional model by spraying an amount of water over the model that was equivalent to 10% and 20% of the undiluted fluid that had been applied to the model. Results of this evaluation are shown in Figure 11. At the colder temperatures the lift losses either are higher with the sprayed water than with equivalent water mixed into solution with the Type II fluid, or the lift loss did not diminish with the simulated precipitation. Video recordings revealed that at the colder temperatures the simulated precipitation formed a sheet of ice on top of the deicing/anti-icing fluid layer rather than being melted, if frozen before reaching the deicing/anti-icing fluid, and absorbed into solution. This evaluation is not considered conclusive, but does suggest that further study is needed.

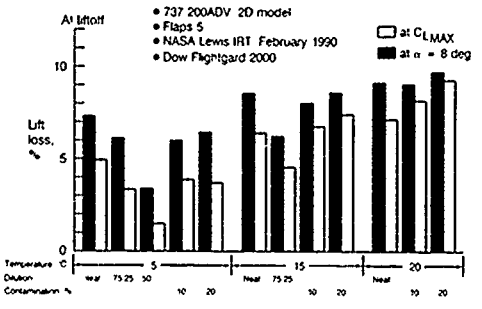

Figure 11. Lift Loss Due to Fluids With Simulated Precipitation.

Results shown in Figure 11 for the two-dimensional model indicate percentage lift losses at 8-deg angle of attack that are larger than those at maximum lift. This trend is different from that observed on the three-dimensional model and indicates the importance of three-dimensional and configuration-specific testing

Boundary layer data were obtained on the two-dimensional model using a rake of 10 total pressure probes and one static pressure probe located at the trailing edge of the airfoil's fixed trailing edge. The effect of the fluid as well as of solid roughness on the boundary layer profile is clearly evident in Figures 12a and 12b. The time-dependent nature of the fluid effect on the boundary layer and its relation to lift loss is also shown in Figure 12b. Data below 5.08 mm (0.2 in) were not obtained with fluid on the model because the lower total pressure probes were plugged to prevent fluid contamination. From these data, the boundary layer displacement thicknesses, δ*, were computed for several currently used deicing/anti-icing fluids.

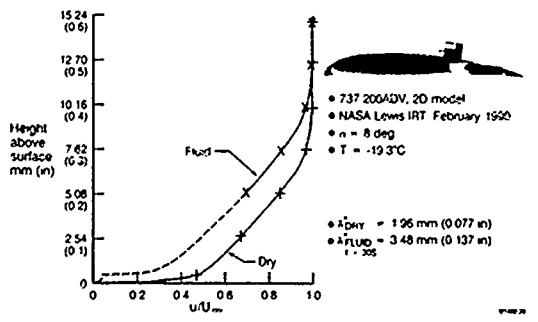

Figure 12a. Two-Dimensional Model Boundary Layer Velocity Profile.

Fig. 8 WIND-INDUCED SURFACE WAVES ON AN ANTI-ICING FLUID LAYER DEPOSITED ON UPPER WING SURFACE

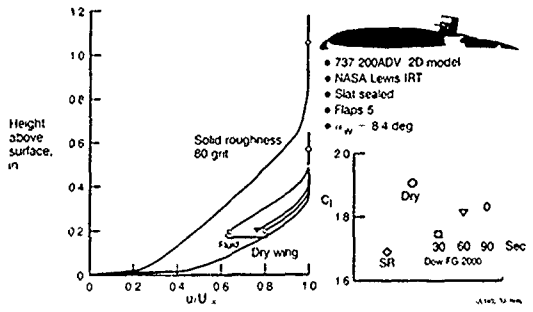

Figure 12b. Boundary Layer Velocity Profiles and Lift Level With Solid Roughness and Fluid.

If the hypothesis is valid that the mechanism of the fluid effect on the aerodynamics of the wing is premature growth of the boundary layer, then a correlation between the prematurely thickened boundary layer and the aerodynamic effects can be anticipated. Figure 13 illustrates the excellent correlation obtained with the two-dimensional model between the boundary layer displacement thickness with fluids and the resultant lift loss at 8-deg angle of attack. Because the two-dimensional model airfoil was extracted from the critical (relative to stall progression) 737-200ADV wing section, and assuming that the thickened boundary layer measured at 8-deg angle of attack was an indicator of the effect of the fluid at maximum lift, an acceptable correlation between the two-dimensional model boundary layer thickness and the three-dimensional model maximum lift loss can also be anticipated. This correlation is shown in Figure 14. These results indicate that the fluid effects on the boundary layer thickness are an indicator of the fluid effects on airplane performance. The extrapolation of lift loss measured in the wind tunnel to full scale on a 1:1 basis have been discussed in Reference 6. Similar correlations were found for simulated frost (i.e., solid roughness) lift and drag increments during earlier Boeing flight and wind tunnel tests (Ref. 7).

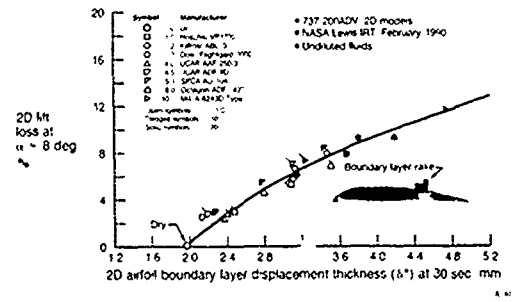

Figure 13. 737-200ADV Two-Dimensional Lift Loss/ Boundary Layer Displacement Thickness Correlation.

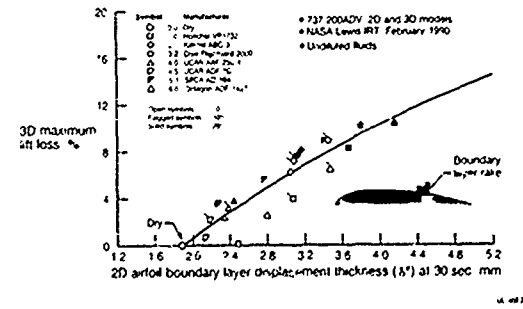

Figure 14. Lift Loss/Boundary Layer Displacement Thickness Correlation.

3.3 Conclusions

Conclusions drawn from the wind tunnel test include the following:

a. Depending on temperature, Newtonian Type I and non-Newtonian Type II fluids produce measurable adverse aerodynamic effects.

b. For the full three-dimensional model, lift loss at maximum lift is greater than that at lower angles of attack.

c. Fluid aerodynamic effects are transitory.

d. The fluid effects vary with airplane configuration.

e. Aerodynamic effects of the fluids correlate well with boundary layer thickening caused by the fluids.

f. Aerodynamic effects of the fluid vary with specific fluids, and viscosity is not the only governing rheological parameter.

4.0 AERODYNAMIC ACCEPTANCE CRITERIA

Traditionally, aircraft have been deiced and anti-iced and dispatched without concern for airplane performance effects. Whatever effects the fluids had on airplane performance were considered within the safety margins provided by airworthiness and operational regulations. Results of flight and wind tunnel tests, discussed previously and in References 5 and 6, clearly show that the transitory aerodynamic effects of the fluids are not negligible.

Therefore, an international group was formed during 1988 under the auspices of the Aerospace Industries of America Transport Committee (AIA TC) to consider the aerodynamic effects of the fluids. The AIA TC 218-4 group consisted of active representatives from Airbus Industrie, Boeing, British Aerospace, Fokker, and McDonnell Douglas, with assistance from the AEA and the von Karman Institute for Fluid Dynamics. The result of the group's efforts was definition of an aerodynamics acceptance test that establishes minimum standards for deicing/anti-icing flow-off characteristics.

4.1 Airplane Performance Considerations

With all engines operating, the effects of deicing/anti-icing fluids on airplane performance are considered negligible. However, with an engine failure at the critical engine failure speed, V_1, and when the aircraft is operating at minimum allowable performance levels, adverse aerodynamic effects of the fluids can become more evident and significantly affect takeoff and climb performance. Because of the low probability of a performance-limited airplane having an engine failure at V_1 with the fluid present, previous unrestricted use of deicing/anti-icing fluids has had an excellent operational record. However, airworthiness regulations do require consideration of an engine failure at V_1 when scheduling airplane performance. Prudence dictates that criteria be defined to ensure adequate airplane performance when operating near minimum performance levels with a failed engine and the fluids present.

The criteria that have been established encourage proper aircraft ground deicing/anti-icing procedures, so that the intent of regulations requiring that aircraft be free of ice, snow, and frost are met without undue takeoff performance adjustments. Underlying considerations of the takeoff performance criteria include the following:

a. Aircraft safety is paramount.

b. The fluid effects are transitory.

c. Newtonian fluids have been safely used without operational performance adjustments.

d. Non-Newtonian fluids' aerodynamic characteristics are similar to some Newtonian fluids at colder temperatures.

e. Non-Newtonian fluids have been successfully used by European, Asian, and North American airlines.

f. Both Newtonian and non-Newtonian fluids will be used, depending on anti-ice protection requirements.

g. Caution is required when considering use of fluids on a contaminated runway.

Specific aspects of the takeoff maneuver addressed by the criteria include:

a. Adequate margin between the takeoff safety speed, V_2, and the 1g stall speed.

b. Adequate margins between liftoff and minimum unstick speeds.

c. Adequate aftbody runway clearance during takeoff.

d. Adequate takeoff acceleration and climb capabilities.

e. Adequate maneuver capability to stall warning.

Of these five criteria, the first is most critical. A minimum V_2 speed of 1.1 $V_{S_{1g}}$ was selected. The 10% V_2 speed margin to the 1g stall speed compares with a 13% margin airworthiness requirement currently used for the nominal dry, clean wing. For aircraft whose normal V_2 speeds are at the minimum margin, 1.13 $V_{S_{1g}}$, the acceptable maximum lift loss resulting from reducing the minimum margin V_2 speed to 1.10 $V_{S_{1g}}$ for the fluids is 5.24%. Note that for aircraft whose V_2 speed margin to the 1g stall speed is larger, the concern for adverse effects of the fluids on stall speed is diminished. The acceptable 5.24% maximum lift loss defines a criterion for acceptable fluid flow-off behavior. The above discussion can be expressed by the following relations.

Criteria:

Dry $\qquad V_2 = 1.13\ V_{S_{1G}}^{Fluid}$

With fluid $\qquad V_2 \geq 1.10\ V_{S_{1G}}^{Fluid}$

Equations:

$$V_{S_{1G}} = \frac{K}{\sqrt{C_{L_{MAX}}}}$$

$$C_{L_{MAX}}^{Fluid} = C_{L_{MAX}}^{Dry} - \Delta C_{L_{MAX}}^{Fluid}$$

To meet minimum 10% speed margin:

$$\frac{\Delta C_{L_{MAX}}^{Fluid}}{C_{L_{MAX}}^{Dry}} \leq 5.24\%$$

4.2 Fluids Aerodynamic Acceptance Test

In light of the results of the flight and wind tunnel evaluations of the deicing/anti-icing fluids and the influence of the fluids on airplane performance, the AIA TC 218-4 group established an aerodynamic acceptance test for the fluids.

Research performed at the von Karman Institute indicated that fluid flow-off behavior could be observed on a flat surface in a small cooled wind tunnel that was capable of operational takeoff speeds and temperatures. Also, correlation was shown between lift losses measured on two-dimensional wind tunnel models and the flat plate fluid boundary layer displacement thickness (Ref 8). These results suggested that a relatively simple cost-effective aerodynamic acceptance test for ground deicing fluids could be established by measuring the fluid's boundary layer displacement thickness on a flat plate in a small, cooled wind tunnel.

Further validation of the aerodynamic acceptance test was provided by the force and boundary layer data obtained during this 1990 reentry into the NASA Lewis IRT. Figures 13 and 14 illustrate correlations between lift losses measured on the two-dimensional and three-dimensional 737-200ADV wind tunnel models and the boundary layer displacement thickness measured on the two-dimensional model at 8-deg angle of attack. Figure 15 illustrates the correlation between the two-dimensional model fluid boundary layer thickness measurements and the flat plate fluid boundary layer thickness measurements made at the von Karman Institute. The correlations shown in Figures 13 through 15 suggest that 737-200ADV lift losses resulting from a fluid can be directly correlated with the fluid's boundary layer displacement thickness measured on a flat surface. This correlation is shown in Figure 16.

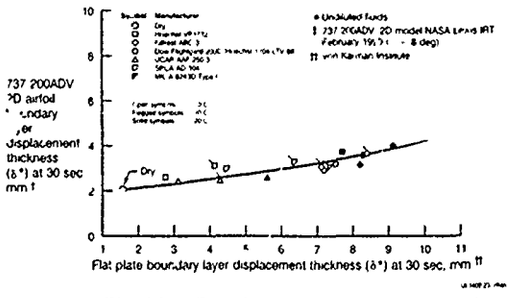

Figure 15. Flat Plate/Two-Dimensional Airfoil Correlation of Boundary Layer Displacement Thickness.

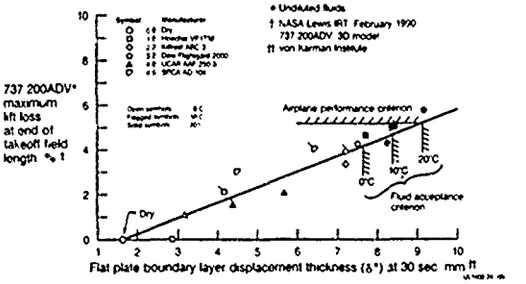

Figure 16. Airplane Performance/Fluid Acceptance Correlation.

Based on the allowable maximum lift loss of 5.24%, the 737-200ADV correlation shown in Figure 16 indicates that a maximum fluid boundary layer displacement thickness of 9.15 mm would be acceptable. Specific values of maximum acceptable fluid boundary layer displacement thickness, δ*, will depend on the values obtained for the dry flat δ* and reference fluid δ* obtained in the particular acceptance test facility. Boundary layer thickness measurements, made at the von Karman Institute, of several currently used deicing/anti-icing fluids, shown in Figure 17, indicate that the fluid boundary layer thickness tends to become thinner at warmer temperatures. This trend suggests that requiring a thinner boundary layer displacement thickness at the warmer temperature would be prudent because lower lift losses would be required at temperatures where contaminated runways might be encountered. The resulting fluid boundary layer displacement thickness acceptance criterion is shown in Figure 17. Details of the acceptance test are provided in Reference 9.

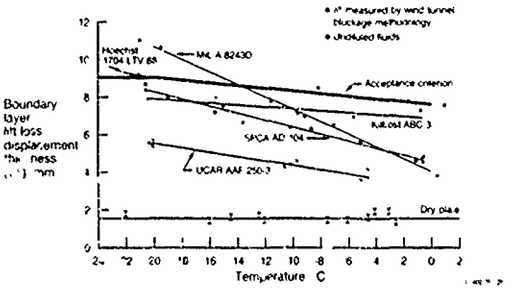

Figure 17. Aircraft Ground Deicing/Anti-Icing Fluids Acceptance Criterion.

Compliance with the acceptance test is considered a minimum requirement for acceptable aircraft ground deicing/anti-icing fluids. An airframe manufacturer may impose additional requirements that reflect considerations for airplane designs that are different from the 737-200ADV and for performance criteria not addressed by the acceptance test. The acceptance test is being incorporated as a requirement by fluid specifications promulgated by the AEA, the Society of Automotive Engineers, and the International Standardization Organization. In addition to the von Karman Institute, the University of Quebec at Chicoutimi has recently provided facilities and services to perform the test.

5.0 CONCLUSIONS

The latest wind tunnel tests have shown that, depending on temperature and specific fluid characteristics, Type I and Type II ground deicing/anti-icing fluids measurably affect airplane lift and drag. Limiting the adverse aerodynamic effects of the fluids is considered prudent, especially for one-engine-inoperative, performance-limited takeoffs. An aerodynamic acceptance test standard has been established and is being incorporated into recognized fluid specifications to ensure that fluids used by airlines to deice/anti-ice large commercial air transports have acceptable flow off and aerodynamic characteristics.

REFERENCES

1. G. S. Hendrickson and E. G. Hill, "Effects of Aircraft De-/Anti-Icing Fluids on Airfoil Characteristics," paper presented at the von Karman Institute for Fluid Dynamics Lecture Series entitled "Influence of Environmental Factors on Aircraft Performance," Brussels, Belgium, February 16–19, 1987.

2. M. Carbonaro, *Experimental Study of the Flow of a Film of Aircraft Deicing Fluid During a Simulated Take Off at Subfreezing Temperature*, von Karman Institute for Fluid Dynamics report CR 1985-02, May 1985.

3. M. Carbonaro, *Experimental Study of the Aerodynamic Characteristics of a Two Dimensional Wing Model Covered With De/Anti-Icing Fluid During a Simulated Take Off at Subfreezing Temperature*, von Karman Institute for Fluid Dynamics report CR 1986-22, August 1986

4. M. Carbonaro, *Further Study of the Aerodynamic Performance of a 2-D Wing Model Covered With Simulated Frost or With De/Anti-Icing Fluid During a Simulated Take Off at Subfreezing Temperature*, von Karman Institute for Fluid Dynamics report CR 1987.

5. L. J. Runyan, T. A. Zierten, and E. G. Hill, "Flight and Wind Tunnel Investigation of Aerodynamic Effects of Aircraft Ground Deicing/Anti-Icing Fluids," AGARD Conference Proceedings No. 470 (Flight in Adverse Environmental Conditions), Göl, Norway, May 8–11, 1989, pp. 24-1 to 24-11.

6. E. G. Hill and T. A. Zierten, "Flight and Wind Tunnel Tes of the Aerodynamic Effects of Aircraft Ground Deicing/Anti-Icing Fluids," AIAA paper 91-0762, presented at the 29th Aerospace Sciences Meeting, Reno, Nevada, January 7–10, 1991.

7. T. A. Zierten and E. G. Hill, "Effects of Wing Simulated Ground Frost on Airplane Performance," paper presented at the von Karman Institute for Fluid Dynamics Lecture Series "Influence of Environmental Factors on Aircraft Performance," Brussels, Belgium, February 16–19, 1987.

8. M. Carbonaro, "Aerodynamic Aspects of De/Anti-Icing Fluids, and Description of a Facility and Test Technique for Their Assessment," paper No. 18, AGARD Fluid Dynamics Panel Specialists Meeting on Effects of Adverse Weather on Aerodynamics, Toulouse, France, April 29–May 1, 1991.

9. E. G. Hill, *Aerodynamic Acceptance Test for Aircraft Ground Deicing/Anti-IcingFluids*, Boeing document number D6-55573, October 11, 1990

ROUND TABLE DISCUSSION

EFFECTS OF ADVERSE WEATHER ON AERODYNAMICS

Prof. Ir. J.W. Sloof, National Aerospace Laboraory NLR, Netherlands
Good morning. This brings us to the final part of this Specialists' meeting which consists of two parts; the first part is the Technical Evaluator's remarks and after that we will hopefully have an interesting and aggressive discussion of issues that came up during the past three days. As I said on Monday, the Program Committee was very happy that we found Mr. Reinmann ready to take up the job as the Technical Evaluator. For those of you who are not familiar with AGARD procedures, I should perhaps mention that the technical evaluator has two tasks; one is to give an on-the-spot verbal evaluation of the meeting which is going to be held in a minute or so, and secondly he has to provide a written report afterwards that I am sure you will all be interested in reading.

Mr. Jack Reinmann got his Bachelor's and Master's in Mechanical Engineering from Case Institute of Technology in Ohio and also a Master's in Physics from John Carroll University. After that he spent six years with TRW Inc. working on zero gravity heat transfer and fluid mechanics problems of liquid metals for space power applications. He spent fifteen years at NASA Lewis Research Center in Cleveland, Ohio working in advanced space propulsion concepts conducting design studies for thermonuclear propulsion systems and conducted experimental high temperature plasma physics research. It is since 1978 that he has been active in the adverse weather business, if I may say so. He started up, in that year, a program on aircraft icing and has continued to work in that area since then. As you will all have experienced these last few days, he is an internationally recognized expert in that field and I am very happy that we have him to do the technical evaluation job. So, Jack, if I may ask you to take the microphone.

Mr. J. Reinmann, NASAS Lewis Research Center, USA
I thank the committee for inviting me to be the technical evaluator and I want to start off by reviewing the purpose of this meeting as stated in some literature that I received. It is to review the state of the art with respect to (1) prediction (which would be code work), (2) simulation (which is the experimental), and (3) measurements of the effects of icing, anti-icing fluids and precipitation (which in our case was frost and heavy rain) on the aerodynamic characteristics of flight vehicles. I think that this committee has done an excellent job of getting representative papers in every one of those areas. I just want to congratulate the committee for that good selection of papers.

There were several review papers at the beginning of this meeting. They reviewed previous meetings that were relevant to this meeting. The first was "Flight and Adverse Environmental Conditions", held in Gol, Norway in May 1989. There is a conference publication available on that, AGARD CP-470. Mr. Ranaudie presented the results relevant to this meeting. One important point was on wind shear and crew procedure during a downburst. You should avoid it if you can, but if you get caught in a downburst, pull up to an attitude of 15 degrees, full throttle, and forget all previous experience. He made the strong point by his illustrations that pilots need simulator training in downbursts. I thought that another interesting point that came out of that meeting was on the flight control laws for the A320, which has stall protection. It is the only airplane that can fly near CL max. The A320 has auto triggering at full thrust at high alpha when the pilot pulls pitch control. In the future, they will have built into those control laws a wind shear warning and automatic reaction system.

Prof. Jacques presented a review of another related meeting. It was on "Low Temperature Environmental Operations of Turboengines (Design and Users Problems)", held in Brussels, Belgium in October 1990. There is an AGARD Conference Pre-Publication Report 480, and I believe that there is also going to be a Conference Publication Report on that. Prof. Jacques reviewed operational concerns for engines; one is ice build-up in the inlet, which can cause flow distortion that in turn leads to compressor surge and stalls. Ice ingestion can damage fan blades. He showed several solutions to inlet screen icing and ice build-up problems in the inlet ducts; most solutions involved some kind of a by-pass system. He discussed icing test facilities available worldwide and some of the calibration concerns. He also indicated that extensive use is now being made of water droplet trajectory codes and ice accretion prediction codes, which is one of the major topics of this meeting.

The invited presentation by Mr. Cattaneo was "The Evolution of Regulation Addressed to Certification of Airplanes in Icing Conditions". I will do my best here to summarize what I think was said in that paper. The FAR/JAR 25 regulations are clear on what must be demonstrated for icing certification, but they are fuzzy on how to demonstrate compliance regarding the flight safety for performance and handling qualities in icing. Mr. Cattaneo suggested more standarized methodologies for demonstrating flight safety compliance. He recommended extensive flight testing with artificial ice shapes as predicted by computer codes on the leading edges of the airfoils. For takeoff, he pointed out that some aircraft cannot turn on their ice protection system until airborne. For some small transport aircraft, the ice protection system can't be turned on until at about 400 feet, and it can take about 4 minutes to reach that altitude. Extensive ice could build up during climbout. It is his suggestion that if that is the case then the forward leading edge of the wings and tail should be modelled with an artificial ice shape. Under cruise, the ice shapes needed are only on the unprotected surfaces. For ice protection failure in flight he recommends what size ice to use. He stresses heavily that performance and handling qualities must be validated in natural icing. But as I recall, his artificial ice shape test results were always more conservative than the natural icing test results, so he felt that he could rely on the artificial testing. When the pilot turns the ice protection system on, stall warning should occur at the angle of attack appropriate to lower stall angle found with ice contamination. That is an important point.

Next we shall discuss paper number 2 in the program by Mr. Ralph Brumby. He was unable to attend the meeting and present the paper, but I think it is an important paper. It sets the stage for much of what is going to follow. I thought I would spend some time on it. This figure is a plot of percent increase in stall speed (on the left hand ordinate)and percent decrease in CL max (on the right hand ordinate) against roughness height ratio, the height ratio divided by the wing chord, K/C. The left most curve is for roughness over the entire upper surface with the slats retracted. The dotted line is for slats fully

extended. The point that he made here is that if you have the slats fully extended, you can recover some of the lift loss caused by upper surface roughness. That is the point that Tom Zierten was making earlier in the meeting. If you have roughness on the leading edge only, you get these right hand curves. And with the slats extended you again get considerable recovery. Unfortunately, he didn't do the case for roughness over only a portion of the upper surface. It would have been interesting to see what he got for roughness over say the first 30% or so, or for roughness removed over the first 30%. Let's put some other numbers on here. Three tenths of a millimeter roughness height for a ten foot chord airplane wing gives a K/C of 0.0001 and .5 millimeters, about 0.00016. We heard from Professor Kind that it is difficult to find frost greater than about .5 millimeter. We are looking at a K/C of 0.00016, and if you have roughness over the entire surface, you see that when you extend the flaps you do get a little performance back. At .3 mm or a K/C of 0.0001 you get more, but not that much as I expected. Now if you go to 2 millimeters, which was the full-scale thickness used in a couple of papers, you get a K/C of about 0.0007. I think the Fokker 50 study came out to be somewhere between 2 and 3 millimeters of roughness full-scale. Mr. Boer indicated that the slats and flaps did not help recover lift, and that clearly agrees with what is shown here. If you have very heavy surface roughness, slats do not help you. These much thicker roughnesses are probably more representative of freezing rain, slush, and snow.

There are some scaling problems and so forth, however, the main point is that you better keep the roughness and contamination off the wing. This quote is from Brumby's concluding remarks: "From an aerodynamic viewpoint there is no such thing as a little ice. Strict attention should be focussed on ensuring that critical aircraft surfaces are free of ice contamination at the initiation of takeoff". This goes along with the FAA policy of 'clean wing concept'. They continually emphasize to 'keep it clean'. I can say that we continually see cases where they are taking off and not following that policy. I mention that in Cleveland, Ohio, in February of this year a jet airplane crashed on takeoff in moderate snow conditions. It was a mail plane, the pilot and co-pilot were killed. There is speculation that wing ice or snow contamination was a contributing factor.

I want to try to group some of the papers. I think that we covered the invited papers, except for one of the invited papers that was given by Mark Potapczuk and myself in the second session. That had to do with a survey of icing simulation, which included first, computer modelling, second, experimental facilities, such as the use of either icing wind tunnels or inflight spray tankers, and third, leading edge artificial ice shapes. Our survey paper basically set the stage for the beginning of that second session which dealt with the prediction or simulation of ice contamination and its effects on aerodynamics. Paper number 6, by Mr. Prel, presented methods of calculating the droplet collection efficiency on three-dimensional bodies.

I think that the important point that was made in the paper by Mr. Prel was that if you are going to put instruments on board an aircraft to record the cloud conditions you are flying through, you should do a three-dimensional water droplet trajectory analysis around the airplane. Many parts of the airplane are shadowed from the clouds, and the effect of the airplane flow field is to concentrate or disperse the water droplets, and different size droplets will concentrate differently. Unless you know what those concentrations are you could measure a water droplet size spectrum that is different from the free-stream cloud. In some cases you may miss the cloud totally. So I think that droplet trajectory calculations should be done, and they are being done.

Drs. Potapczuk and Bragg gave a paper on analyses and measurements of airfoil performance of finite-length swept and straight wings with leading edge ice shape.

Papers 9 and 10 of that session were on helicopter icing and again we see that we are beginning to develop rotor performance codes that include the effects of icing on the rotors. The paper by Mr. Fleming also indicated that there appears to be promise in using sub-scale model rotor testing in an icing wind tunnel. The results were reproducible, they made sense, the trends were all correct. He used a rotor performance code, he incorporated into that rotor performance code an empirical icing aero-performance effect on rotor blades and was able to match the performance measured in the tunnel very accurately under certain conditions. Under other conditions, he overpredicted penalties and in some conditions he underpredicted penalties. It appeared to be a very promising technique.

Mr. Roger Gent wrote his rotor performance code and he also made predictions against the same wind tunnel data. I thought he showed good agreement in some cases, and the trends were always right. Mr. Gent also compared his rotor performance prediction with inflight full-scale helicopter icing data. He showed a fair amount of scatter, but the trends again were in the right direction. I think that this is encouraging. One point that Mr. Gent made was that he would like to see the empirical aero-performance icing correlation in his code replaced by an analytical code that could predict both ice shape and the resulting aero-penalties caused by the ice. That is now beginning to be done. We are doing that at NASA, and I think others are also looking at developing analytical models - boundary layer models or Navier-Stokes models to predict aero-performance penalties on iced rotor blades.

Papers 8, 11 and 12 dealt with the effects of roughness on airplane aero-performance. One very interesting paper, number 8, by Prof. Kind, talked about the effects of frost on wing aerodynamics and airplane takeoff performance. He obtained samples of hoar frost and replicated the frost with a dissolved liquid plastic technique that I don't quite understand, but I would like to know more about that. He indicated that he found it difficult to realize frost any thicker than about 0.5 mm. He was able to put the replicated frost in a wind tunnel on a flat plate and obtain air boundary layer velocity profiles over the frosted surface. He got a delta u/u* shift by plotting the velocity profiles on a log-log plot and using the law of the wall. He incorporated these results into a boundary layer development for rough surfaces coupled with a non-viscous panel method and computed the effects of hoar frost on airfoil performance. I was impressed that he could predict up to and beyond CL max. He showed the effect of frost to be very significant on CL max loss and the loss of stall angle. He also indicated that if the roughness starts where the boundary layer is thin, such as at the pressure suction peak, the impact on lift is very strong. If it starts further downstream, it is not a problem. He did point out that .4 millimeter can produce dramatic effects. His suggestion was to clean off the first 20% of the airfoil and it might be alright.

Paper 11 was a wind tunnel investigation of powered propellar model effects on airfoil performance degradation due to distributed upper surface roughness and leading edge ice shapes. This was a very interesting paper, it considered not only the upper surface roughness but also the propeller effects. He also investigated the effect of the propellar slip stream on scrubbing the roughness off of that region. He described a wind tunnel test of an airfoil on which a propeller was mounted. I was impressed with the effort there. The roughness height of the model scaled to about 1 to 3 millimeters on a 10 foot chord, and according to Ralph Brumby's plot, that thick roughness is going to give you very serious effects. I guess that there are going to be some questions about the interpretation if you are using that large a frost. But it would be a very heavy contamination if you are going to interpret it. He found that the forward 25 to 30 % of the chord was sensitive to roughness, but again, at one point he said that if you just removed 5 to 10% of the wing leading edge ice you got back to clean wing performance. But the important finding was that the roughened powered wing CL max dropped significantly below the clean unpowered wing. The conclusions were that reduced lift slope and maximum lift were 30% due to roughness and could be very significant in the case of engine failure during take-off.

Paper number 13, by Mr. Boer presented a study on the effects of surface contamination on takeoff aerodynamics of the Fokker 50. They conducted scale-model tests of a Fokker 27 in a wind tunnel. The wind tunnel test results were used in a fixed base engineering simulator to investigate degradation in performance of handling qualities. The roughness in their model corresponded to a very heavy roughness, 2 millimeter frost at full scale. With a clean wing, the airplane is designed to stall first at the nacelle and work its way out. This gives the pilot some time to respond. But with roughness, the complete leading edge of the wing stalled out simultaneously. He also mentioned that the pilot will not notice the effect of contamination until rotation and then he will need extreme stick force to recover and probably try to abort the take-off and he will be in big trouble. In this case, Mr. Boer pointed out that the use of slats and flaps did not affect the CL vs alpha curves, and I think that with the large 2 millimeter frost thickness that would agree with the first paper by Brumby. Again, his message was to clearly indicate the need for clean wing at takeoff, and he believes it applies to all airplanes.

There was another paper on the full airplane, number 14. It described the initial analysis and wind tunnel testing in preparation for the icing certification of the Dornier 328 regional airliner. Again, I think that the significant point was that there was a great deal of computer code work used in that certification process. A computer code was used to predict ice shapes on the leading edges; one was also used to predict limits of impingement for the water droplets. The water trajectories inside the engine ducts were also computed with the computer code, and for this particular aircraft, they had a by-pass duct to separate out particles that shed during de-icer activation. They used a non-viscous panel flow code coupled with a 3D droplet trajectory code to calculate water droplet trajectories on the wings. Pratt & Whitney used the VSAERO code with their own 3D trajectory code for the inlet duct work.

Also used was ONERA's two-dimensional ice accretion code to calculate ice growth on the balance horns. These two-dimensional ice growth calculations agreed qualitatively with the experimental data that was obtained in the BF Goodrich icing tunnel on the balance horns. There was no ice in the gap of the balance horns, but they determined that they would have to electro-thermally heat the gap to make sure the horn would not lock up with ice. A most important conclusion for the air intake, Mr. Toogood pointed out, was that the FAR/JAR 25 requires a test demonstration at -5°C and below. P&W has found a worst case to be somewhere between -5°C and 0°C. Under these conditions he had to use a higher liquid water content (LWC) that goes with the warmer temperatures, and this higher LWC leads to water runback beyond the protected areas. The water can run back into the duct, build up ice, and that ice can be dislodged and can fod the engine. His recommendation would be that the FAA considers a test at a temperature above -5°C.

That summarizes through Session 2, and I am going into Session 3, now, on the effects of heavy rain and de-icing/anti-icing fluids.

The first paper that was presented was on NASA Langley Research on Heavy Rain Effects, and Dr. Ed Waggoner presented that paper. Results were given for both scale-model testing conducted in the 14 x 22 foot Langley tunnel and full-scale testing conducted in their long track. They had a very impressive heavy rain spray system involved there. They were also able to record rain rates in several locations around the world, and as Dr. Waggoner pointed out, these intensities can be extremely high. They recorded rain rates greater than 28 inches per hour, but they only lasted for short times; they can last for as long as 20 seconds, and in 20 seconds an airplane can get into a lot of trouble. They also found that there definitely is a serious aero-performance loss, CL loss, CL max loss, and alpha stall loss. It is interesting that there is a difference between the frost effects and the heavy rain. In the cruise configuration heavy rain does not cause a serious degradation on aero-performance. But with the slats deployed they do have an aero-degradation problem. Waggoner suspects that it might be caused by blockage of the slat gap due to water. He is just not sure what it is. He feels that analytical techniques to model the rain cannot be done until they get a good understanding of the physics. He also did not find a strong scaling effect. The results of the wind tunnel agreed with the results of the full-scale testing. He said that the wind tunnel test is valid for first order effects on rain. I would mention here that Tom Zierten, from Boeing, in the discussion cautioned that this research should be done very carefully before they try to get it into pilot procedures for wind shear. The effects would definitely be serious because pilot wind shear procedures require high angles of attack, and there will be a tremendous lift loss if heavy rain is present during the wind shear.

The second paper on heavy rain was by Mr. Tang from Canada. He also found for his system, which again was a multi-element configuration with slats and flaps, losses in CL max between 6 and 16%, and drag increases by as much as 43%. But in contrast to the Langley research, which said that scale size did not seem to have a strong effect on the results, Tang found that the higher the Reynolds number the more serious the aero-degradation. The interesting thing to observe was that lift loss increments (normalized to a common rain rate) increased with increasing Reynolds number. In the discussion period this raised a real dilema. One study was insensitive to Reynolds number effects; the other appeared to be very sensitive. The conclusion seems to be that a lot more work has to be done on the exact type of wing geometry that you are dealing with. One wing geometry may be very sensitive and another not so sensitive.

Another paper in that group was presented by Dr. Feo from Spain. He presented a development of a three element conductance sensor for liquid film thickness. Presently at Langley they are using a two element sensor. Dr. Feo showed that the three element sensor would give a more accurate reading of the depth. The two element apparently gave about 60% of the real depth whereas the three element gave the correct measurement. He also pointed out with the three element system the practical effect of electrolytic corrosion on these triple element sensors is not as pronounced as with a two element system. It looks to be a good system to use in the future. They also had good dynamic response, something like a tenth of a millisecond.

I don't know whether I can summarize the last two ground de-icing papers. The main point is that in combination with Dr. Carbonaro's work at VKI, the work done by Boeing at the Lewis Icing Research Tunnel, and the flight test work, they (VKI and Boeing) were able to develop a relatively simple aerodynamic acceptance criteria for any future ground de-icing, anti-icing fluids that are submitted for this purpose. It amounts to putting a fluid on a flat plate on the floor of the wind tunnel and measuring the air boundary layer displacement thickness at the trailing edge of the plate. They actually measure the boundary layer displacement thickness by measuring the pressure drop across the tunnel. A plot of boundary layer displacement thickness versus temperature will tell them whether they are above or below the acceptance criteria limit. One of the points that Dr. Carbonaro made in private was that one must be extremely careful in measuring the dimensions of the tunnel because if you don't you can get big errors in your results.

That summarizes my work. Put up the last slide. This is just an introduction to some conclusions and recommendations which I hope can be extended by discussion. Someone pointed out after seeing a lot of slightly different results with the surface roughness, that they felt that, as had been done for wind tunnels some time ago, we may need a systematic experimental study of the effects of Reynolds numbers on surface roughness effects. That sounds like a good idea. Again, we need a very careful study of heavy rain effects. Don't change pilot procedures in wind shear until research has been done. From what I have seen and what I know about code development I think that we must continue the development of ice accretion modelling codes for three dimension and for predicting aero-performance penalties caused by ice. It is a very active area which will be going on for several years.

Prof. Slooff
Thank you, Jack, for sharing your expert's view on the contents of this meeting and for your comments and recommendations. We are all looking forward to the written version of your report.

This should be the beginning of the Round Table Discussion. As you may have noticed we are running a little late and our manoeuvering friends are breathing down our necks, I am afraid. Nevertheless, I would like to suggest that we spend a few minutes on two important questions. One is perhaps to get some comments on the recommendations by Jack Reinmann on where research in this area should be directed. The second question, perhaps, should be that if we look at our current facilities and tools, both experimental and computational, what is lacking there and what is needed. What sort of new facilities or upgraded facilities are needed. If anyone has comments or suggestions related to such questions, I think it would be a good idea to communicate them. One thing that I should mention perhaps is that this discussion is being recorded on tape. You shouldn't worry about that, nothing you will say will be held against you, but it is useful to clearly state your name and affiliation because the transcript of the discussion will be sent to you for corrections and editing. So make sure if you say something that you state your name and affiliation clearly.

Could we put up Mr. Reinmann's last viewgraph again so that we have a look at his recommendations and see if anyone else would like to add something to that or comment on it.

Mr. R. J. Flemming, Sikorsky Aircraft, USA
One thing that seems to be apparent from a lot of the discussions is a need for a theoretical method that would delve into the boundary layer effect of water or ice or frost on the airfoil in a very micro nature. One of the problems that we may be experiencing with our helicopter correlation is the effect, not of heavy rain on the airfoil, but of something that is more closely associated with flying through a wet cloud. The same problem right now is trying to use the heavy rain analysis for something else, but we need to have a handle on the physics. We don't know the physics right now, so that some research and possibly the use of programs requiring super computers for analysis may start to answer a number of the questions that we have, in terms of frost, heavy rain and flight through non-supercooled and supercooled clouds.

Prof. Slooff
Thank you for that remark. Is there a boundary layer specialist here that would like to comment on that?

Prof. R. J. Kind, Carleton University, USA
I don't claim to be a boundary layer specialist, but it certainly is a tall order, in the case of frost maybe not as tall, because at least the frost is there, it is rigid, whereas in the case of liquids there could very well be some sort of coupling. In fact we saw those ripples and so on in the film from Fokker and that was maybe where the supercomputers come in. Having done calculation methods maybe I could feel safe in saying this too, that they are very interesting, they enable you to see a lot of detail that is very difficult to see experimentally, but one must always recognize that they are calculation methods and I don't know to what degree one can trust them without validation. Validation is really quite difficult because you get into these Reynolds number effects and so on. So it is a difficult order, but it would be well worth working towards.

Prof. Slooff
Is there anybody else that would like to comment on one of these three recommendations here? One remark comes to my mind at this point in time with respect to the effect of surface roughness on boundary layer development. There should be quite a volume of data from the naval hydrodynamicist. They have a problem with all kinds of little creatures growing on their boats. That is roughness and I think that they have quite a volume of experimental towing tank material there probably. That, perhaps, could be of some help to us also.

Professor Dr. C. Ciray, Middle East Technical University, Turkey
With respect to the first recommendation, i.e., the need for research for Reynolds number effects on surface roughness, I think civil engineers have been working on these kinds of problems for years. The irrigation people or the highway engineers have similar types of problems with rain dropping on a thin sheet layer of water flowing on the surface of the pavement. I think, if aerodynamic engineers are interested in these kind of problems, there might be a lot of information existing somewhere but they may need to be adapted to our own conditions.

Prof. Slooff
Anybody else that would like to say something on recommendations for future research? If not, I would like to address the second question, that is, looking at the tools that are available when trying to solve our problems in this area, experimental as well as computational tools, what is missing? Would anybody like to comment on what is lacking here and what we should do to try to improve the situation; also perhaps in terms of experimental techniques.

Apparently we all feel very happy with what we have. Jack, do you have a comment on that.

Mr. Reinmann
I think the important point that we see is that we don't know very much about how to model roughness effects on ice, and how to get good aero-performance penalty calculations. If you go to Navier-Stokes approaches you probably have to modify your turbulence models, for example. To start doing that, you get into a lot of work. There are other approaches. We think we could do a lot more in understanding the boundary layer approach to surface roughness. Right now ice presents a very grotesque ice shape. There are feathers behind the large piece of ice that may act like turbulence generators. It is just very complicated and we think that it is going to take a lot of work to sort it out. I think these things will occupy fluid dynamicists for a number of years yet.

Mr. E. Waggoner, NASA Langley Research Center, USA
I will comment on the computational aspects associated with the heavy rain. We too have found it difficult to get CFD personnel really interested in this problem. It is a very, very difficult problem. We have been successful in initiating a grant with Professor Rand Decker at the University of Utah and he will be staying with us three months this summer to get the work started and he will be looking at very detailed calculations of raindrop trajectories and their interactions with an airfoil and then the subsequent computations with a Navier-Stokes code. Perhaps in a year we will have a better feel for the success of this program.

Prof. Slooff
Thank you for that information. I am sure people will be looking forward to the results of that. Anybody else at this point in time that would like to make a comment or suggestion or perhaps ask a question to one of the authors if he didn't have a chance in the discussion period for a particular paper. If not, then in view of the time, I think this is the end of this meeting. It has been a pleasure working with you these past three days. I thank all the authors for their efforts and their presentations, particularly the Technical Evaluator, Mr. Reinmann, for his close listening and scrutinization of the material, and finally of course, the audience for their interest and participation in the discussions. I now have a hunch that AGARD's Fluid Dynamics Panel Chairman wants to say something.

Dr. W. J. McCroskey, US Army Aeroflightdynamics Directorate, USA
You are very good at picking up the hint. Thanks to you, Professor Slooff and your Program Committee for putting together this specialist meeting. Thanks to the authors of course. I would like to acknowledge the contributions here of the representative of the Flight Mechanics Panel, Monsieur Renaudie and the representative of the Propulsion and Energetics Panel, Professor Jacques. Also thanks very much to Mr. Reinmann for your part and to all of you for your parts contributing to the success of this meeting. I hope you found it profitable and stimulating. Thanks also to our translators, our host Sup'Aero and our local coordinators, Monsieur and Madame Dujarric. Thanks to Aerospatiale, to Airbus Industrie, to ONERA and specifically to Monsieur Bosquet for the tours and dinners that were arranged yesterday.

Just quickly I would like to say that AGARD is unique. Nevertheless, like many institutions it is now under pressure to justify its existence. Therefore, I would like to say that if you found this meeting useful, we would request that you please acknowledge this to your management. If you have suggestions for improvement, we would like you to address them to the Panel Members, and we would really like to hear from you. Now just a few quick administrative announcements. We will take a short coffee break in the registration area. During this time you are asked to manoeuver rapidly and to buy tickets for lunch if you have not already done so. If you have a companion who would like to make the walking tour, or those of you finishing this conference who want to join the walking tour of Toulouse this afternoon, also please buy the tickets at the coffee break.

Panel members are asked to start lining up to buy dinner tickets for tomorrow night and to look into the arrangement for transportation that is being provided after the business meeting. Finally, there will be a bus leaving at 11:15 going back to Place Wilson, to the train station and to the airport.

This is not the end. FDP will be continuing and I would like to just mention very briefly our future programs. In addition to the Manoeuvering Aerodynamics Specialists Meeting that will start in another 20 minutes or so, we have a fall symposium on Aerodynamic Engine Airframe Integration that will occur in Texas in early October. Symposia next year include one on Hypersonics in Torino in May, one on Highlift Aerodynamics in Canada in the fall and two special courses that are put on in conjunction with the von Karman Institute. Now in conclusion thanks again to all of you for your participation. We hope to see you at these future AGARD meetings, including the Specialists Meeting. As I say, please now manoeuver rapidly and let's come back from the coffee promptly at 11:05.

REPORT DOCUMENTATION PAGE

1. Recipient's Reference	2. Originator's Reference	3. Further Reference	4. Security Classification of Document
	AGARD-CP-496	ISBN 92-835-0644-8	UNCLASSIFIED

5. Originator: Advisory Group for Aerospace Research and Development
North Atlantic Treaty Organization
7 rue Ancelle, 92200 Neuilly sur Seine, France

6. Title EFFECTS OF ADVERSE WEATHER ON AERODYNAMICS

7. Presented at the Fluid Dynamics Panel Specialists' Meeting
held in Toulouse, France, 29th April—1 May 1991.

8. Author(s)/Editor(s)	9. Date
Various	December 1991
10. Author's/Editor's Address	**11. Pages**
Various	292

12. Distribution Statement This document is distributed in accordance with AGARD policies and regulations, which are outlined on the back covers of all AGARD publications.

13. Keywords/Descriptors

Aerodynamic characteristics	Ice formation
Aerodynamics	Deicing
Aircraft	Deicers
Weather	Precipitation / meteorology
NATO, NATO Flight	France

14. Abstract

The 19 technical papers developed for the AGARD Fluid Dynamics Panel (FDP) Specialists' Meeting on "Effects of Adverse Weather on Aerodynamics" held from 28th April—1 May 1991 in Toulouse, France are documented in this Conference Proceedings. In addition, introductory material from the Program Chairman and the results of the Round Table Discussion held after the meeting are also included.

The FDP organized this meeting to provide a timely review of the progress being made in advancing the state-of-the-art of predicting, simulating, and measuring the effects of icing, anti-icing fluids, and various forms of precipitation on the aerodynamic characteristics of flight vehicles. Topics included results from both theoretical and experimental programs and material related to procedures and regulations for certification and operation. International participation for the meeting included authors from eight nations and representatives from most of the 16 NATO nations. (25)

\GARD Conference Proceedings 496 .'.dvisory Group for aerospace Research and Development, NATO EFFECTS OF ADVERSE WEATHER ON AERODYNAMICS Published December 1991 292 pages The 19 technical papers developed for the AGARD Fluid Dynamics Panel (FDP) Specialists' Meeting on "Effects of Adverse Weather on Aerodynamics" held from 28th April—1 May 1991 in Toulouse, France are documented in this Conference Proceedings. In addition, introductory material from the Program Chairman and the results of the Round Table Discussion held after the meeting are also included. P.T.O.	AGARD-CP-496 Aerodynamic characteristics Aerodynamics Aircraft Weather Ice formation Deicing Deicers Precipitation — meteorology	AGARD Conference Proceedings 496 Advisory Group for aerospace Research and Development, NATO EFFECTS OF ADVERSE WEATHER ON AERODYNAMICS Published December 1991 292 pages The 19 technical papers developed for the AGARD Fluid Dynamics Panel (FDP) Specialists' Meeting on "Effects of Adverse Weather on Aerodynamics" held from 28th April—1 May 1991 in Toulouse, France are documented in this Conference Proceedings. In addition, introductory material from the Program Chairman and the results of the Round Table Discussion held after the meeting are also included. P.T.O.	AGARD-CP-496 Aerodynamic characteristics Aerodynamics Aircraft Weather Ice formation Deicing Deicers Precipitation — meteorology
AGARD Conference Proceedings 496 Advisory Group for aerospace Research and Development, NATO EFFECTS OF ADVERSE WEATHER ON AERODYNAMICS Published December 1991 292 pages The 19 technical papers developed for the AGARD Fluid Dynamics Panel (FDP) Specialists' Meeting on "Effects of Adverse Weather on Aerodynamics" held from 28th April—1 May 1991 in Toulouse, France are documented in this Conference Proceedings. In addition, introductory material from the Program Chairman and the results of the Round Table Discussion held after the meeting are also included. P.T.O.	AGARD-CP-496 Aerodynamic characteristics Aerodynamics Aircraft Weather Ice formation Deicing Deicers Precipitation — meteorology	AGARD Conference Proceedings 496 Advisory Group for aerospace Research and Development, NATO EFFECTS OF ADVERSE WEATHER ON AERODYNAMICS Published December 1991 292 pages The 19 technical papers developed for the AGARD Fluid Dynamics Panel (FDP) Specialists' Meeting on "Effects of Adverse Weather on Aerodynamics" held fr 28th April—1 May 1991 in Toulouse, France are documented in this Conference Proceedings. In addition, introductory material from the Program Chairman and the results of the Round Table Discussion held after the meeting are also included. P.T.O.	AGARD-CP-496 Aerodynamic characteristics Aerodynamics Aircraft Weather Ice formation Deicing Deicers Precipitation — meteorology

The FDP organized this meeting to provide a timely review of the progress being made in advancing the state-of-the-art of predicting, simulating, and measuring the effects of icing, anti-icing fluids, and various forms of precipitation on the aerodynamic characteristics of flight vehicles. Topics included results from both theoretical and experimental programs and material related to procedures and regulations for certification and operation. International participation for the meeting included authors from eight nations and representatives from most of the 16 NATO nations.

ISBN 92-835-0644-8

The FDP organized this meeting to provide a timely review of the progress being made in advancing the state-of-the-art of predicting, simulating, and measuring the effects of icing, anti-icing fluids, and various forms of precipitation on the aerodynamic characteristics of flight vehicles. Topics included results from both theoretical and experimental programs and material related to procedures and regulations for certification and operation. International participation for the meeting included authors from eight nations and representatives from most of the 16 NATO nations.

ISBN 92-835-0644-8

The FDP organized this meeting to provide a timely review of the progress being made in advancing the state-of-the-art of predicting, simulating, and measuring the effects of icing, anti-icing fluids, and various forms of precipitation on the aerodynamic characteristics of flight vehicles. Topics included results from both theoretical and experimental programs and material related to procedures and regulations for certification and operation. International participation for the meeting included authors from eight nations and representatives from most of the 16 NATO nations.

ISBN 92-835-0644-8

The FDP organized this meeting to provide a timely review of the progress being made in advancing the state-of-the-art of predicting, simulating, and measuring the effects of icing, anti-icing fluids, and various forms of precipitation on the aerodynamic characteristics of flight vehicles. Topics included results from both theoretical and experimental programs and material related to procedures and regulations for certification and operation. International participation for the meeting included authors from eight nations and representatives from most of the 16 NATO nations.

ISBN 92-835-0644-8

AGARD

NATO OTAN

7 RUE ANCELLE · 92200 NEUILLY-SUR-SEINE

FRANCE

Téléphone (1)47.38.57.00 · Télex 610 176
Télécopie (1)47.38.57.99

DIFFUSION DES PUBLICATIONS AGARD NON CLASSIFIEES

L'AGARD ne détient pas de stocks de ses publications, dans un but de distribution générale à l'adresse ci-dessus. La diffusion initiale des publications de l'AGARD est effectuée auprès des pays membres de cette organisation par l'intermediaire des Centres Nationaux de Distribution suivants. A l'exception des Etats-Unis, ces centres disposent parfois d'exemplaires additionnels, dans les cas contraire, on peut se procurer ces exemplaires sous forme de microfiches ou de microcopies auprès des Agences de Vente dont la liste suite.

CENTRES DE DIFFUSION NATIONAUX

ALLEMAGNE
Fachinformationszentrum,
Karlsruhe
D-7514 Eggenstein-Leopoldshafen 2

BELGIQUE
Coordonnateur AGARD-VSL
Etat-Major de la Force Aérienne
Quartier Reine Elisabeth
Rue d'Evere, 1140 Bruxelles

CANADA
Directeur du Service des Renseignements Scientifiques
Ministère de la Défense Nationale
Ottawa, Ontario K1A 0K2

DANEMARK
Danish Defence Research Board
Ved Idraetsparken 4
2100 Copenhagen Ø

ESPAGNE
INTA (AGARD Publications)
Pintor Rosales 34
28008 Madrid

ETATS-UNIS
National Aeronautics and Space Administration
Langley Research Center
M/S 180
Hampton, Virginia 23665

FRANCE
O.N.E.R.A. (Direction)
29, Avenue de la Division Leclerc
92320, Châtillon sous Bagneux

GRECE
Hellenic Air Force
Air War College
Scientific and Technical Library
Dekelia Air Force Base
Dekelia, Athens TGA 1010

ISLANDE
Director of Aviation
c/o Flugrad
Reykjavik

ITALIE
Aeronautica Militare
Ufficio del Delegato Nazionale all'AGARD
Aeroporto Pratica di Mare
00040 Pomezia (Roma)

LUXEMBOURG
Voir Belgique

NORVEGE
Norwegian Defence Research Establishment
Attn: Biblioteket
P.O. Box 25
N-2007 Kjeller

PAYS-BAS
Netherlands Delegation to AGARD
National Aerospace Laboratory NLR
Kluyverweg 1
2629 HS Delft

PORTUGAL
Portuguese National Coordinator to AGARD
Gabinete de Estudos e Programas
CLAFA
Base de Alfragide
Alfragide
2700 Amadora

ROYAUME UNI
Defence Research Information Centre
Kentigern House
65 Brown Street
Glasgow G2 8EX

TURQUIE
Milli Savunma Başkanlığı (MSB)
ARGE Daire Başkanlığı (ARGE)
Ankara

LE CENTRE NATIONAL DE DISTRIBUTION DES ETATS-UNIS (NASA) NE DETIENT PAS DE STOCKS DES PUBLICATIONS AGARD ET LES DEMANDES D'EXEMPLAIRES DOIVENT ETRE ADRESSEES DIRECTEMENT AU SERVICE NATIONAL TECHNIQUE DE L'INFORMATION (NTIS) DONT L'ADRESSE SUIT.

AGENCES DE VENTE

National Technical Information Service
(NTIS)
5285 Port Royal Road
Springfield, Virginia 22161
Etats-Unis

ESA/Information Retrieval Service
European Space Agency
10, rue Mario Nikis
75015 Paris
France

The British Library
Document Supply Division
Boston Spa, Wetherby
West Yorkshire LS23 7BQ
Royaume Uni

Les demandes de microfiches ou de photocopies de documents AGARD (y compris les demandes faites auprès du NTIS) doivent comporter la dénomination AGARD, ainsi que le numéro de série de l'AGARD (par exemple AGARD-AG-315). Des informations analogues, telles que le titre et la date de publication sont souhaitables. Veuiller noter qu'il y a lieu de spécifier AGARD-R-nnn et AGARD-AR-nnn lors de la commande de rapports AGARD et des rapports consultatifs AGARD respectivement. Des références bibliographiques complètes ainsi que des résumés des publications AGARD figurent dans les journaux suivants:

Scientifique and Technical Aerospace Reports (STAR)
publié par la NASA Scientific and Technical
Information Division
NASA Headquarters (NTT)
Washington D.C. 20546
Etats-Unis

Government Reports Announcements and Index (GRA&I)
publié par le National Technical Information Service
Springfield
Virginia 22161
Etats-Unis

(accessible également en mode interactif dans la base de données bibliographiques en ligne du NTIS, et sur CD-ROM)

Imprimé par Specialised Printing Services Limited
40 Chigwell Lane, Loughton, Essex IG10 3TZ